Tools for the Design and Characterization of Covalent Cysteine Protease Inhibitors

Dissertation

zur Erlangung des Grades

"Doktor der Naturwissenschaften"

im Promotionsfach Medizinische Chemie

am Fachbereich Chemie, Pharmazie und Geowissenschaften

der Johannes Gutenberg-Universität

in Mainz

Fabian Barthels

geb. in Velbert

Mainz, 2022

Submitted at the Faculty of Chemistry, Pharmacy, Geography, and Geoscience.

Dean: [redacted]

Name of the 1st reviewer: [redacted]

Name of the 2nd reviewer: [redacted]

Date of the doctoral examination: 23.03.2022.

Declaration of Authorship

I, Fabian Barthels, declare that this thesis titled, “Tools for the Design and Characterization of Covalent Cysteine Protease Inhibitors” and the work presented in it are my own. I confirm that:

• This work was done wholly or mainly while in candidature for a research degree at this university.

• Where any part of this thesis has previously been submitted for a degree or any other qualification at this University or any other institution, this has been clearly stated.

• Where I have consulted the published work of others, this is always clearly attributed.

• Where I have quoted from the work of others, the source is always given. Except for such quotations, this thesis is entirely my own work.

• I have acknowledged all main sources of help.

• Where the thesis is based on work done by myself jointly with others, I have made clear exactly what was done by others and what I have contributed myself.

_____

Abstract

The research of covalent cysteine protease inhibitors is on the cutting edge of drug discovery, as the recent U.S. Food and Drug Administration's approval of the very first registered inhibitor nirmatrelvir demonstrated that covalent inhibitors of this target class have finally arrived in reality. The repertoire of potential cysteine-reactive inhibitors was yet found to be tremendous and new chemotypes are constantly being discovered and characterized. In this regard, tuning the reactivity of the electrophilic warhead is essential for the successful development of cysteine protease inhibitors, and hence, the search for those is often synonymous with the quest for new covalent warheads.

In this dissertation, novel warheads for addressing the catalytic cysteine residues of *S. aureus* sortase A and *T. brucei rhodesiense* cathepsin L (rhodesain) were developed and characterized. Rhodesain and sortase A each represent a drug target with disease relevance; rhodesain for the neglected parasite-borne African sleeping sickness and sortase A for antibiotic-resistant pathogenic Gram-positive bacteria such as *S. aureus*. However, rhodesain and sortase A are unrelated cysteine proteases that prefer different warhead chemotypes highlighted by their very distinctive catalytic mechanisms.

In the course of this work, mechanistic investigations and optimizations of six warhead chemotypes were performed. Enzyme kinetic, biophysical, and quantum chemical methods were used to elucidate the underlying reaction mechanisms and to find rational approaches to increase biological effectiveness and selectivity. Disulfanylbenzamides and sulfonylpyrimidines were shown to be potent and selective irreversible inhibitors of the *S. aureus* sortase A, and these were investigated as novel resistance-preventing anti-virulence agents during cell-based biofilm inhibition experiments. Four additional rhodesain-targeting warheads were investigated, namely substituted naphthoquinones, fluorodinitroarenes, fluorovinyl sulfones, and vinylogous arginine Michael acceptors. The first three of which featured a covalent-reversible course of inhibition which proved to be an advantageous property across all chemotypes for avoiding off-target reactivity and cellular toxicity.

Instrumental hurdles arose recurrently during the investigation of the new warhead entities which were addressed by the development of open-source hardware and software that contributed to the solution of synthetic and biochemical questions. The development of a liquid-handling and peptide synthesis robot (FINDUS), a differential scanning fluorometer (openDSF), and a web toolkit for crystallographic analysis of normalized B-factors (BANΔIT) highlight the focus of this work to invent chemical, technical, and conceptual tools for drug discovery.

Zusammenfassung

Die Erforschung kovalenter Cysteinprotease-Inhibitoren ist ein wichtiger Bestandteil der gegenwärtigen Wirkstoffforschung, denn die jüngste Zulassung des ersten registrierten Inhibitors Nirmatrelvir durch die US-amerikanische Food and Drug Administration hat gezeigt, dass kovalente Inhibitoren dieser Enzymklasse endlich in der Realität angekommen sind. Das Repertoire potenzieller Cystein-reaktiver Inhibitoren ist unerschöpflich und es werden ständig neue Chemotypen entdeckt und charakterisiert. In dieser Hinsicht ist die Modulation der Reaktivität des elektrophilen *Warheads* von entscheidender Bedeutung für die Entwicklung von klinisch-erfolgreichen Cysteinprotease-Inhibitoren.

In dieser Dissertation wurden neuartige *Warheads* für die katalytischen Cysteinreste von *S. aureus* Sortase A und *T. brucei rhodesiense* Cathepsin L (Rhodesain) entwickelt und mechanistisch charakterisiert. Rhodesain und Sortase A stellen jeweils ein pharmakologisch-relevantes Zielenzym für eine humanpathogene Erkrankung dar. Rhodesain für die vernachlässigte, durch Parasiten übertragene Afrikanische Schlafkrankheit und Sortase A für antibiotikaresistente pathogene Gram-positive Bakterien. Rhodesain und Sortase A sind nicht miteinander verwandte Cysteinproteasen, die aufgrund ihres unterschiedlichen Katalysemechanismus recht unterschiedliche *Warhead*-Chemotypen bevorzugen.

Im Rahmen dieser Arbeit wurden mechanistische Untersuchungen und Optimierungen von sechs verschiedenen *Warhead*-Chemotypen durchgeführt. Enzymkinetische, biophysikalische und quantenchemische Methoden wurden eingesetzt, um die zugrundeliegenden Reaktionsmechanismen aufzuklären und rationale Ansätze zur Verbesserung der biologischen Wirksamkeit und Selektivität zu finden. Disulfanylbenzamide und Sulfonylpyrimidine erwiesen sich als potente und selektive Inhibitoren der *S. aureus* Sortase A und wurden in zellbasierten Biofilm-Experimenten als neuartige resistenzarme Antivirulenz-Wirkstoffe untersucht. Vier weitere für Rhodesain entwickelte *Warheads* (substituierte Naphthochinone, Fluordinitroarene, Fluorvinylsulfone und vinyloge Arginin-Michael-Akzeptoren) wurden zudem mechanistisch untersucht. Dabei wiesen die drei erstgenannten einen kovalent-reversiblen Hemmmechanismus auf, was sich bei allen Chemotypen als vorteilhaftes Attribut zur Vermeidung von Off-Target-Reaktivität und zellulärer Toxizität erwies.

Bei der Untersuchung der neuartigen *Warheads* traten immer wieder instrumentelle Hürden auf, die durch die Entwicklung von Open-Source-Hardware und -Software überwunden werden konnten, welche zur Lösung synthetischer und biochemischer Fragen beitrugen. Die Entwicklung eines Roboters zur Assayvorbereitung und Peptidsynthese (FINDUS), eines *Differential-Scanning*-Fluorometers (openDSF) und eines Web-Toolkits für die kristallografische Analyse normalisierter B-Faktoren (BANΔIT) verdeutlichen den Schwerpunkt dieser Arbeit auf der Entwicklung chemischer, technischer und konzeptioneller Werkzeuge für die grundlegende Wirkstofferforschung.

Acknowledgment

Table of Contents

List of Abbreviations

ACE	Angiotensin-converting enzyme
Ala	Alanine
Arg	Arginine
Asn	Asparagine
Asp	Aspartic acid
CAD	Computer-aided design
ClfA/B	Clumping factors A/B
CnA	Collagen-binding protein
CNS	Central nervous system
Cys	Cysteine
DPP IV	Dipeptidyl peptidase-4
DSF	Differential scanning fluorimetry
EbpS	Elastin-binding protein
EPS	Extracellular polymeric substance
ESI-MS	Electrospray ionization mass spectrometry
FDA	U.S. Food and Drug Administration
FDM	Fused deposition modeling
FnbpA/B	Fibronectin-binding protein
Gln	Glutamine
Glu	Glutamic acid
Gly	Glycine
HAV-2	Human adenovirus-2
HCV	Hepatitis C virus
His	Histidine
HIV	Human immunodeficiency virus
IgG	Immunoglobulin G
IsdA–H	Iron-regulated surface determinant A–H
LC/MS	Liquid chromatography/mass spectrometry
Leu	Leucine
MALDI-TOF	Matrix-assisted laser desorption/ionization time-of-flight
PAINS	Pan-assay interference compounds
MD	Molecular dynamics
MIC	Minimum inhibitory concentration
MSCRAMM	Microbial surface components recognizing adhesive matrix molecules
NAG	*N*-acetylglucosamin
NAM	*N*-acetylmuramic acid
NC-IUBMB	Nomenclature Committee of the International Union of Biochemistry and Molecular Biology
NMR	Nuclear magnetic resonance
PAR2	Protease-activated receptor-2

PCR	Polymerase chain reaction
PETG	Polyethylene terephthalate glycol-modified
PGP1	Pyroglutamyl peptidase I
Phe	Phenylalanine
PKC	Proteinkinase C
PLC	Phospholipase C
POM	Polyoxymethylene
QM/MM	Quantum mechanics/molecular mechanics
qPCR	Real-time polymerase chain reaction
SaeRS	*S. aureus* two-component system
SAR	Structure-activity relationship
SARS-CoV	Severe acute respiratory syndrome coronavirus
SasA–K	*Staphylococcus aureus* surface protein A–K
SdrC/D/E	Serine-aspartic acid repeat proteins C/D/E
Sec pathway	Secretory pathway
Ser	Serine
SINV	Sindbis virus
siRNA	Small interfering ribonucleic acid
SpA	*S. aureus* protein A
SrtA	Sortase A
SUMO	Small ubiquitin-like modifier
TCI	Targeted covalent inhibition
Thr	Threonine
TLF	Trypanosome lytic factors
Tyr	Tyrosine
Val	Valine
VSG	Variant surface glycoproteins

1 Introduction

1.1 Cysteine Proteases and Their Inhibitors

1.1.1 Function and Classification of Proteases

In 1905, P.A. LEVENE published his research article titled “The Cleavage Products of Proteoses” which is widely recognized as the first study of functional protease research.[1] More than 100 years and 500,000 scientific publications later, the understanding of protease function has fundamentally changed, yet their study remains at the forefront of fundamental and applied research. By historic definition, proteases are the protein executors of a ubiquitous (bio)chemical reaction: the hydrolysis of an amide bond in a proteinogenic macromolecule.[2] In recent years, however, the perspective has broadened, so that under certain circumstances the catalysis of other reactions might also be inherent for the characteristic function of a protease. Under appropriate conditions, proteases are able to synthesize peptide bonds (reverse proteolysis), accept non-peptidic substrates (general hydrolysis), or combine these two capabilities in immediate sequence (transpeptidation).[3,4] These are by no means marginal phenomena which becomes clear, as each of these aspects will play its role in the drug discovery research during this doctoral work.[5–7]

In evolutionary terms, the catalysis of the amide bond hydrolysis is probably one of the oldest achievements of protein evolution which enabled the simplest organisms to obtain amino acid nutrients through the catabolism of proteins.[8] In close succession to the works of LEVENE, scientific studies on proteases during the first half of the 20th-century focused likewise on the predominantly non-specific, degradative functions of proteases during nutritional metabolism. However, the realization that a predominant number of proteases catalyze highly specific reactions dawned a new research era in which proteases were rather regarded as the “Swiss Army knife” of enzymes.[9,10] On a cellular level, proteases regulate the localization, activity, and fate of almost all human proteins, as these form new post-translational modifications, modulate the interactions within protein complexes, and play an important role during signal transduction.[11–17] Unlike other mechanisms of post-translational modification, proteolytic processing is mostly an irreversible process which is why the functionality of proteases is rigorously controlled at the cellular level. Using bioinformatic analysis of eukaryotic genomes, at least 500 proteases (2% of all protein genes) have been identified per organism,[18] many of which are regulated by gene expression, zymogen inactivation, endogenous inhibitors, or compartmentation to organelles such as lysosomes or mitochondria.[19–21]

The unmatched diversity of protease functions is a direct result of the evolutionary process which has produced a variety of different forms and functions of proteolytic enzymes. The "form follows function" paradigm can also be applied when describing the architecture of proteases which range from small single-fold proteins (papain, 23 kDa)[22] to highly sophisticated molecular types of machinery (proteasomes, 2.5 MDa).[23] Proteases are distinguished in terms of their function mainly by their specificity of the cleaved substrates. To structure this diverse mosaic of proteolytic enzymes, the classification of proteases is a task by itself which is primarily guided by the classification of the EC system by the NC-IUBMB (Nomenclature Committee of the International Union of Biochemistry and Molecular Biology).[24]

According to the EC system, enzymes can be classified based on their catalyzed reaction types, and thus, proteases belong to the group of hydrolases (EC 3.4). Proteases are further divided into exo- (EC 3.4.11–19) and endopeptidase (EC 3.4.21–99) depending on the cleavage site of the polypeptide chain. Exopeptidases are divided into amino- and carboxypeptidase, according to the cleavage at the outermost N- or the C-terminus, whereas endopeptidases cleave at specific sites within the polypeptide sequence. Additional classification by the MEROPS system categorizes subsets of proteases with respect to the composition of their active-site and the associated catalytic mechanism.[25,26] Hence, proteases can be classified into aspartate (EC 3.4.23), cysteine (EC 3.4.22), glutamate (also EC 3.4.23), metallo (EC 3.4.24), serine (EC 3.4.21), threonine (EC 3.4.25), and unknown-type (EC 3.4.99) proteases. Recently, a seventh group (asparagine lyases) has been discovered which, since the reaction does not involve the consumption of water, is counted among the lyases (EC 4.3.2).[27] An overview of the functional relationship of proteases in the context of the enzymatically competent proteome is shown in Figure 1.

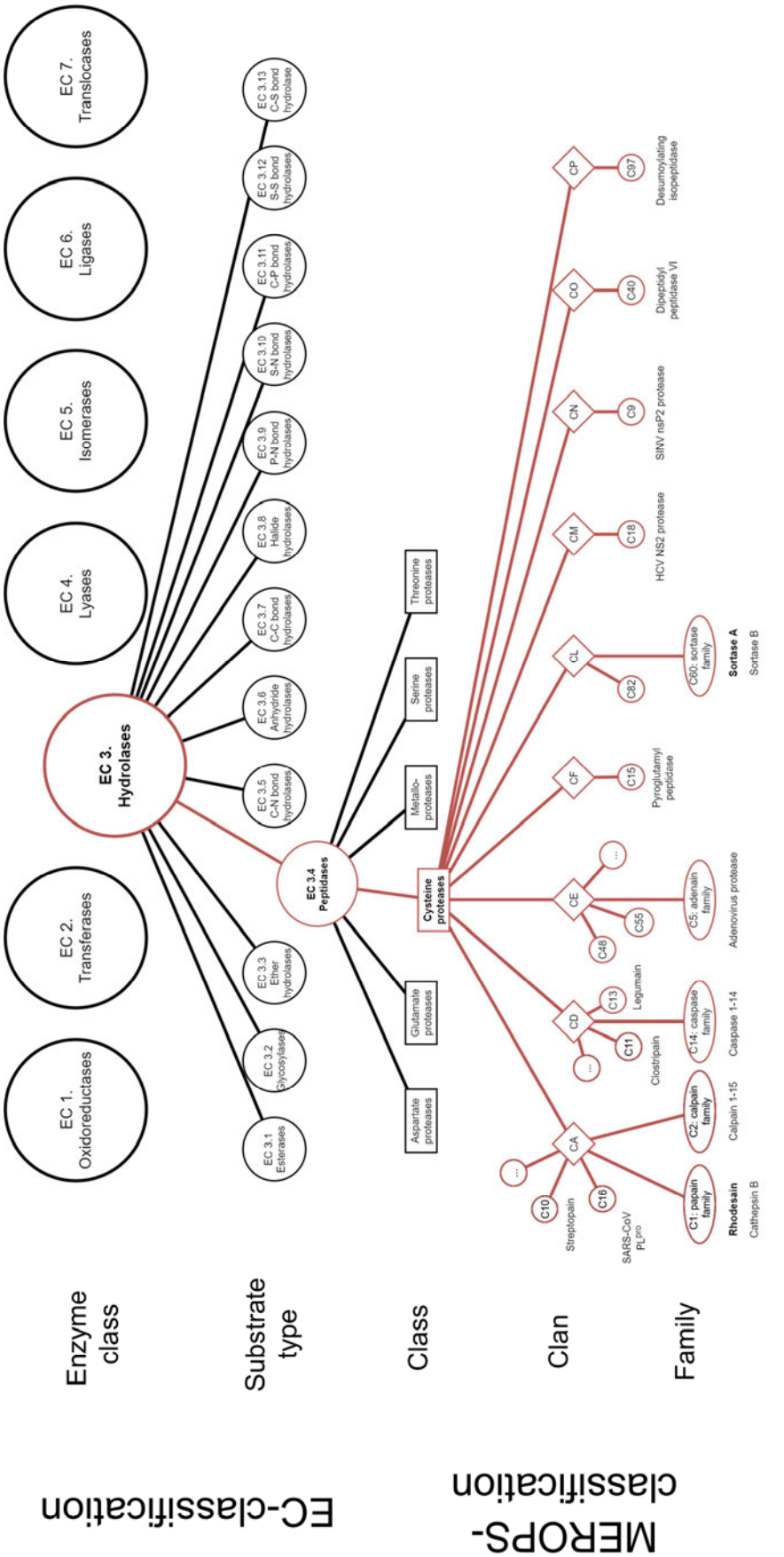

Figure 1: **Assignment of proteases in the genealogical tree of the enzymes. (top)** Classification of proteolytic enzymes according to the EC system. **(bottom)** More detailed classification of cysteine proteases into clans, families, and species according to the MEROPS system, in which the proteases can be grouped on the basis of evolutionary and structural relationships. The two enzymes *T. brucei rhodesiense* rhodesain and *S. aureus* sortase A focused on in this work are highlighted with bold font.

Proteases bind their substrates via hydrogen bonds, hydrophobic, and electrostatic interactions which ultimately determine the substrate specificity to the proteolytically processed substrates. These substrates share a general conformational requirement for host-guest recognition across almost all protease classes; they typically bind in an extended β-sheet fold to the active-site cleft. This conformational selection accounts for the resistance of folded or diversely structured regions of proteins to proteolytic cleavage, and on the other hand, facilitates efficient degradation of mis- and unfolded proteins by the presentation of proteolytically labile sequences.[28,29] According to the standard nomenclature for proteases by BERGER and SCHECHTER, substrate residues are designated P1 to P_n (non-primed site) starting from the cleavage site in the direction of the N-terminus and P1' to P_n' (primed site) in the direction of the C-terminus. Similarly, the binding pockets in the enzyme are given the corresponding designations S1 to S_n and S1' to S_n' (Figure 2A).[30]

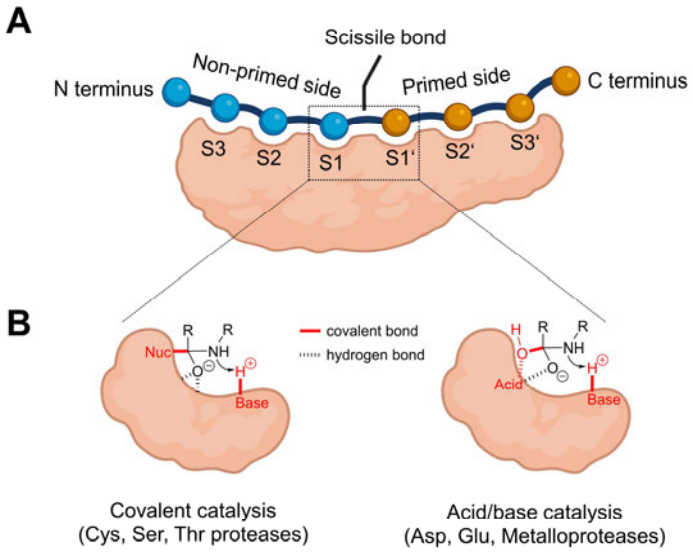

Figure 2: **General principles at the protease-substrate interface.** (**A**) Schematic representation of substrate binding according to the nomenclature proposed by SCHECHTER and BERGER.[30] (**B**) There are two proposed tetrahedral transition states for the six common types of proteases. Serine, cysteine, and threonine proteases involve the nucleophilic residue of the eponymous amino acid side chain for a covalent catalysis mechanism. In the case of aspartate, glutamate, and metalloproteases, the nucleophile is an activated non-covalently bound water molecule resulting in so-called general acid/base catalysis. The figure was created inspired by an illustration published by TURK.[31]

Once a substrate is bound to its protease, the cleavage of the C-N bond occurs by a nucleophilic attack on the sp^2-hybridized carbonyl atom mostly with an intermediary tetrahedral transition state.[32] The five classes of proteases found in mammals (glutamate proteases have so far been identified only in fungi, bacteria, and viruses) make use of two fundamentally different catalytic mechanisms to stabilize the tetrahedral intermediate during hydrolysis (Figure 2B). Serine, cysteine, and threonine proteases use covalent catalysis by their active-site residues acting as nucleophiles, whereas in aspartate, glutamate, and metalloproteases hydrolysis proceeds without covalent involvement but by the generation of a highly reactive water molecule (non-covalent catalysis).[31,33]

1.1.2 Structural and Mechanistic Phylogeny of Cysteine Proteases

A closer look at the subgroup of cysteine proteases shows that this is neither a structurally nor a functionally homogeneous class of enzymes. Cysteine proteases can be further classified into clans and families according to the MEROPS system (Figure 1, bottom).[25] Decisive factors for this classification are the similarity of the amino acid sequence, the occurrence of similar secondary structural elements, and the cleavage specificity for natural substrates. Proteases that are similar in terms of their amino acid sequence, and thus in tertiary or quaternary structure, were grouped into families. And on a level above, if diverse proteases are found to be evolutionarily descended from a common "primordial protein", these families were additionally grouped into clans which are often named after the prototypical protease.[34] However, despite the structural commonalities, diverse cysteine proteases within the same clan can differ significantly by their substrate specificity.[35]

Until today, cysteine proteases were divided into nine different clans: the papain clan (CA), the caspase clan (CD), the adenain clan (CE), the pyroglutamyl peptidase clan (CF), the sortase clan (CL), and the unnamed clans CM, CN, CO, and CP.[24,25,34] In addition, there is a number of cysteine proteases that cannot be assigned to any of the above clans,[36–38] and proteases that are part of the mixed chymotrypsin-like clan (PA) in which some proteases use serine as the nucleophile, whereas others use cysteine.[39] The origin of this clan is therefore an example of divergent evolution, wherein the only known cysteine-catalyzed PA proteases are of viral origin.[40] An overview of the tertiary structures for a characteristic protease of all known cysteine protease clans can be seen in Figure 3.

Although the protein topology differs significantly across the nine resp. ten different cysteine protease clans, there is one border-crossing characteristic of all cysteine proteases: in addition to the name-giving catalytic cysteine residue, the active-site always contains a catalytically involved histidine residue which performs multifunctional tasks during the catalytic mechanism.[41] In this regard, different protease clans can also be distinguished by their protonation state of the catalytically active cysteine residue, while the neighboring histidine residue is the decisive factor in determining the two possible thiol protonation forms (Cys-SH or Cys-S^-). If the catalytic cysteine and histidine residues of a protease are both in sufficient proximity and suitable orientation, an intramolecular proton transfer might occur, leading to permanent stabilization of a zwitterionic inner salt consisting of an imidazolium cation and a thiolate anion (Cys^-/His^+). In this regard, the polarization and deprotonation of a proteinogenic thiol to the thiolate leads to a significant increase in the nucleophilicity of the corresponding cysteine residue, and thus, this is a key factor for the discrimination of catalysis mechanisms between differently protonated enzymes (see mechanisms below).

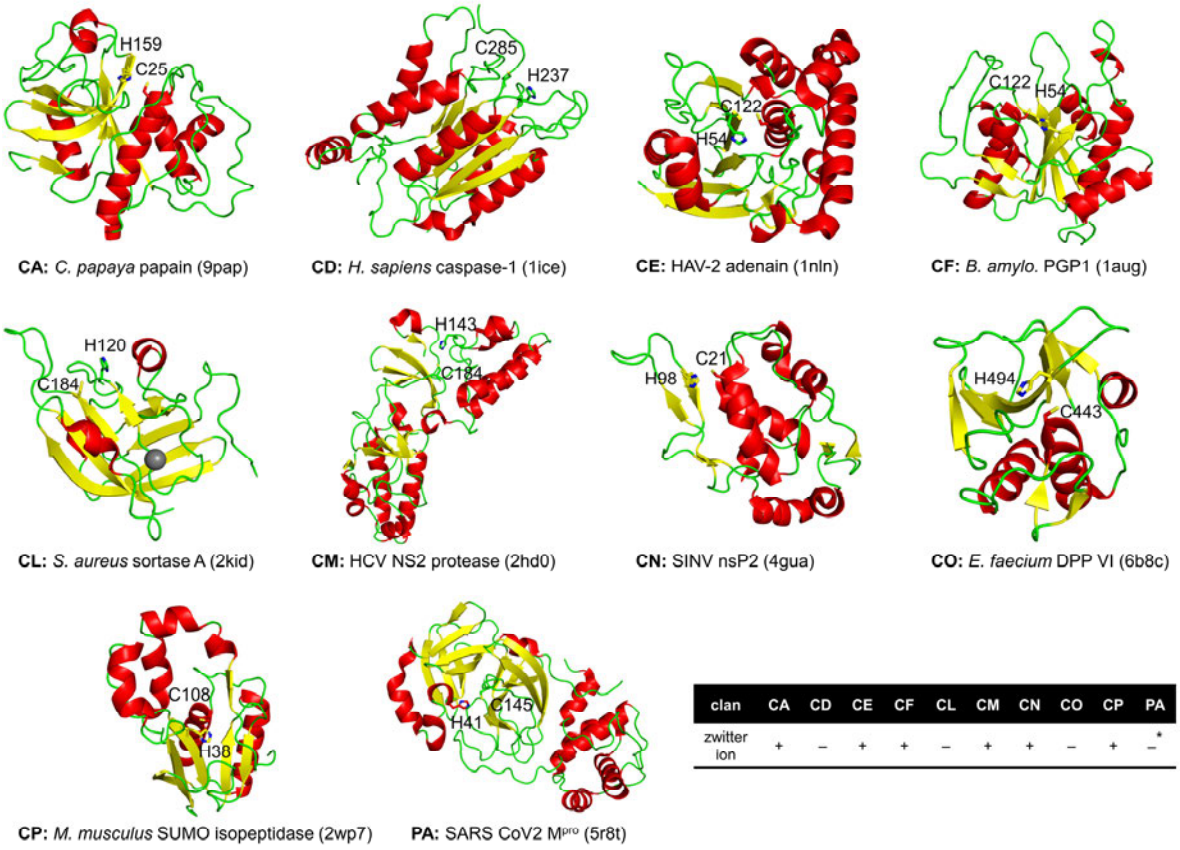

Figure 3: **Overview of the ten different cysteine protease clans based on the tertiary structure of a clan-characteristic protease.** Shown is the topology of the respective cysteine protease from the organism first published as a crystal structure with the pdb accession ID in parentheses.[22,42–50] The catalytically involved cysteine and histidine residues are highlighted in the stick representation and labeled according to the crystallographic residue numbering. The table on the bottom lists the generally accepted protonation state of the respective cysteine/histidine dyad within a clan: "+" corresponds to a zwitterionic dyad with the charge distribution of Cys^{-}/His^{+} and "–" corresponds to an uncharged dyad (Cys^{o}/His^{o}).[34] *For the PA clan cysteine proteases, there are sporadic reports of a zwitterionic dyad with the vast majority of studies assuming an uncharged dyad.[51]

For the best-studied cysteine proteases, such as papain (clan CA), caspase 1 (clan CD), or *S. aureus* sortase A (clan CL), the characterization of the cysteine protonation state is largely undisputed today, but this has not always been the case and even presently there are cases of surprising revision,[52,53] so that cysteine protonation often resembles rather a wavering hologram than an unshakable dogma. A recent example discusses the protonation of the SARS-CoV main protease (M^{pro}) from the PA clan which has long been cited as a prime example of an uncharged cysteine-histidine dyad consistent with the reports of homologous 3C-like proteases from diverse viral origin.[54,55] Theoretical and biochemical studies subsequently appeared to have shown that an imidazolium-thiolate zwitterion forms in situ upon substrate binding to the active-site pocket.[56] Only recently, several thousand crystal structures were recorded for the SARS-CoV2 M^{pro} which consistently seemed to confirm the uncharged dyad configuration of the resting-state by a large number of datasets recorded,[50] until a high-resolution

neutron diffraction study of analogous M^{pro} crystals clearly showed the formation of an imidazolium-thiolate dyad in its apo resting-state configuration.[51]

To simplify this complexity, two archetypal mechanisms of cysteine protease catalysis based on the well-characterized protonation status of clans CA (papain) and CD (legumain) are presented in the following. Mechanistic studies on proteases from other clans, such as *S. aureus* sortase (CL) or SARS-CoV M^{pro} (PA), have also been performed at the atomistic (QM/MM) level.[56–60] However, the results of different publications are too contradictory to give a hint on an undisputed catalysis mechanism in this chapter.

Clan CA-type papain-like catalysis mechanism:

The largest proportion of the cysteine proteases discovered to date belongs to the papain (CA) clan.[61] Papain was the first cysteine protease to be isolated from the juice of the papaya fruit in 1879,[62] and nearly one century later, papain was also the first cysteine protease whose crystal structure was solved in 1968.[63] It is therefore not surprising that papain has been extensively characterized mechanistically and is used as a model system to describe the catalytic mechanism of cysteine proteases with a zwitterionic imidazolium-thiolate dyad. Most proteases from the CA, CE, EF, CM, CN, and CP clans are thought to follow the catalysis mechanism of the primordial papain protease.[34] The active-site residues Cys25 and His159 form the catalytic dyad of papain, while two other functionally important residues are conserved in papain and its homologs: Gln19 which might assist the formation of the tetrahedral transition state (termed as “oxyanion hole”), and Asn175 which is thought to pre-orientate the imidazolium ring of His159.[64]

For clan CA cysteine proteases, the ion pair mechanism is commonly accepted and supported by potentiometric resp. NMR titrations of the active-site residues.[65–67] In the native resting-state of the papain protease, the catalytic dyad is present as an imidazolium-thiolate pair which increases the nucleophilicity of Cys25, while the basic His159 serves as a proton acceptor. The involvement of a rigid water network to stabilize this zwitterionic state has also been assumed.[68] Mechanistically, the catalytic cycle of the papain-mediated peptide hydrolysis can be divided into two phases: 1.) acylation and 2.) deacylation. The individual steps of possible proton movements during both steps were extensively examined by computations and kinetic studies for papain.[69–77] Since these studies draw slightly different mechanistic conclusions from their results, it is likely that not a single trajectory along the reaction hypersurface determines the reaction coordinate, but, depending on the actual enzymatic conditions, different parallel pathways might characterize the catalysis mechanism of papain proteolysis. The proposed mechanism pathway with stabilized intermediates is shown in Figure 4A–C.

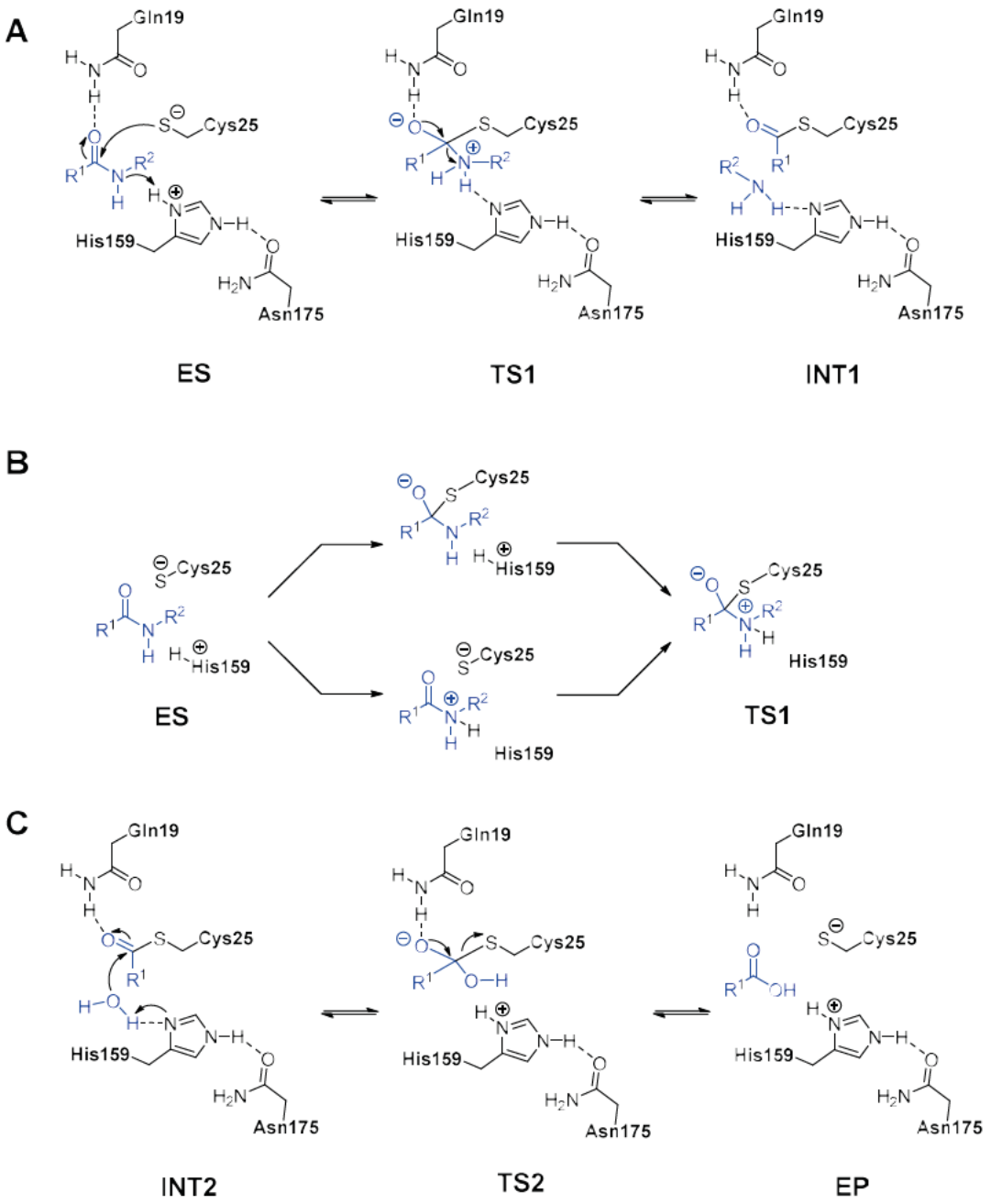

Figure 4: **Proposed reaction mechanism for the catalysis cycle of papain-like proteases.** (**A**) Two-step mechanism of the acylation reaction: nucleophilic attack by the negatively charged thiolate on the carbonyl atom of the P1 residue yields the tetrahedral intermediate (INT1). Upon protonation of the amide nitrogen, the scissile bond breaks yielding the covalent acyl-enzyme adduct. (**B**) Different hypotheses for the temporal sequence of protonation transfer states during the acylation step. (**C**) Mechanism of deacylation: the acyl-enzyme intermediate (INT2) is attacked by the nucleophilic water and yields a second tetrahedral transition state (TS2). Subsequent release of the cleaved carboxylic acid regenerated the enzyme's resting-state (EP).

A two-step mechanism was proposed for the formation of the acyl-enzyme intermediate (INT1) involving a thiohemiketal transition state (TS1). The first step is the nucleophilic attack on the carbonyl carbon of the substrate by the Cys25 thiolate accompanied with the proton transfer from the N^{δ} atom of His159 to the amide nitrogen and subsequently breaking the amide bond of the substrate. The thiohemiketal transition state (TS1) is believed to be stabilized by the Gln19 side chain via hydrogen bonding similar to the mechanism known from serine proteases' "oxyanion holes".[78] A controversy between different studies in the acylation step is the question of the temporal sequence for the generation of the acyl-enzyme intermediate. While the most recent studies assume an initial nucleophilic attack,[74,77] earlier studies conclude from their calculations either the protonation of the amide prior to the nucleophilic attack or a concerted reaction course without the intervention of the tetrahedral thiohemiketal transition state (Figure 4B).[70,71,75,76]

Regarding deacylation (Figure 4C), there is a consensus in the literature that this mechanism proceeds under general base catalysis mediated by His25 which is uncharged during this stage. The nucleophile is a single water molecule that is coordinated in the binding pocket and polarized at the His159 imidazole ring for the nucleophilic attack (TS2). Computations revealed that the deacylation consists of two distinct reaction steps involving a tetrahedral intermediate (INT2): first, the nucleophilic attack on the thioacyl carbon atom by the water molecule with the simultaneous transfers of a proton to the N^{δ} atom of His159. Subsequently, the S-C bond is broken to generate the final product with a new carboxy terminus (EP).

Clan CD-type legumain-like catalysis mechanism:

The clan CD contains cysteine proteases with a protein fold similar to those found in the caspase family (C14), all of which contain a Cys/His catalytic dyad that is thought to act with a mechanism distinct from papain-like proteases.[34] Experimental and computational results indicate that the catalytic Cys189 must be present in the protonated thiol form (Cys-SH) for a productive nucleophilic attack and cleavage of the scissile peptide bond.[52,79] A QM/MM study investigating the human protease legumain showed that this caspase-like protease requires a protonated catalytic Cys189 (ES) for the nucleophilic attack and the concerted formation of an acyl-enzyme intermediate (INT1) without the intervention of a tetrahedral transition state.[80] The presumed legumain catalysis mechanism as an example of cysteine proteases with an uncharged dyad (Cys^{o}/His^{o}) is shown in Figure 5.

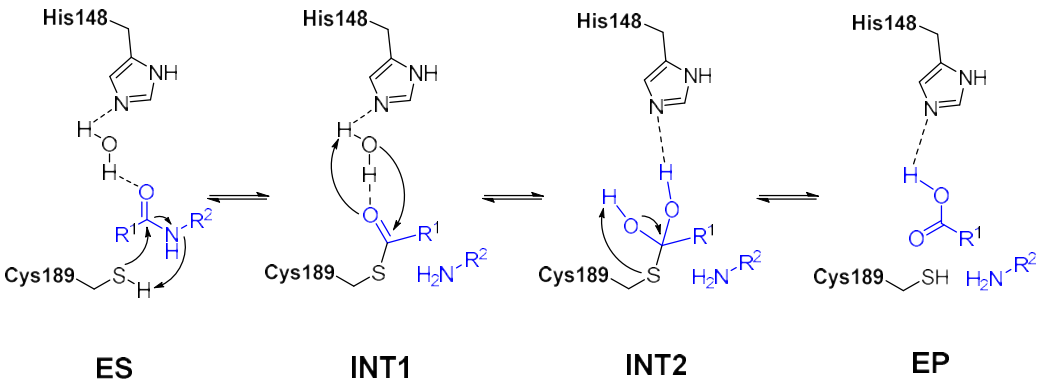

Figure 5: **Proposed reaction mechanism for the catalysis cycle of legumain-like proteases.** The three-step reaction mechanism of legumain-like proteases involves the concerted attack of the protonated Cys189 on the P1 carbonyl atom resulting in a covalent acyl-enzyme intermediate without the stabilization of a transient tetrahedral transition state (INT1). Deacylation is triggered by a nucleophilic attack of a hydrolytic water molecule and stabilizes a tetrahedral diol intermediate (INT2) which subsequently releases the product by an intramolecular proton transfer and regenerates the catalytically competent protease (EP).

The role of the oxyanion hole, formed by the nucleophilic water molecule and the backbone NH atoms of Gly149, Ala189 was found to be of greater importance for the acylation step compared to the papain-like protease mechanism discussed above. On the one hand, the oxyanion hole polarizes the C=O bond and weakens the scissile C−N bond, and on the other hand, it stabilizes the acyl-enzyme intermediate (INT1) which is generated during the concerted-type of acylation reaction. During deacylation, the catalytic His148 does not serve as a general base moiety but rather stabilizes the orientation of the nucleophilic water molecule. Subsequently, the water proton is abstracted by the substrate's P1 carbonyl atom and the remaining hydroxyl anion attacks the same carbonyl atom to produce a tetrahedral geminal diol intermediate (INT2). To dissociate the covalent bond to the protease, this tetrahedral intermediate is resolved by a proton transfer to the catalytic Cys189. The cleaved carboxylic acid product can now leave the enzyme pocket, restoring the initial state of the protease (EP).

1.1.3 Protease Inhibitors for Drug Discovery

It is estimated that 5–10% of all pharmaceutical drug targets are proteases.[33] Impaired regulation of proteases can lead to inappropriate proteolysis which in turn plays an important role in cancer, cardiovascular, inflammatory, neurodegenerative, and infectious diseases. Excessive proteolysis can be prevented pharmacologically by blocking the proteases involved, and hence, many proteases have become the focus of the pharmaceutical industry as potential drug targets or biomarkers.[81] To date, 64 small-molecule drugs have been approved by the U.S. Food and Drug Administration (FDA) between 1964–2022 with a primary indication for a protease target, highlighting four characteristic eras in the regulatory history (Figure 6).

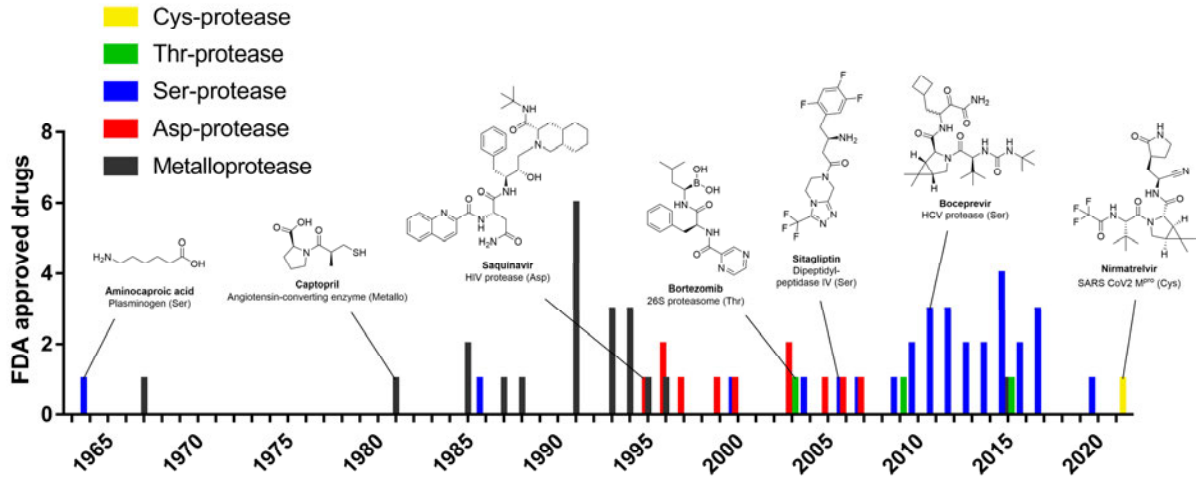

Figure 6: **Timeline for the annual FDA approval of new protease inhibitors.** The coloring of the bar diagram indicates the protease class of the approved drugs. Milestones of some first-in-class approved protease inhibitors are highlighted with their respective structures and target description. Regulatory data were retrieved from the ChEMBL28 database and curated according to the annotation of LEESON et al.[82]

The very first FDA-approved protease inhibitor, aminocaproic acid (1964), is atypical in many respects, but in this chapter, these attributes can be used to describe what has characterized the development of clinical protease inhibitors over the past six decades. During the 1950s, phenotypic efficacy trials demonstrated a beneficial effect of aminocaproic acid in the treatment of acute bleeding due to elevated fibrinolytic activity.[83] Thus, the proteolytic enzymes of the coagulation cascade around human plasmin were quickly identified as the site of action, although the molecular target was rather vague than concretely thought to be one of the plasminogen-activating proteases.[84] It was not until 1971 – seven years after the initial approval – that the target was identified beyond doubt: aminocaproic acid binds the catalytic inactive proenzyme plasminogen and prevents its cleavage and subsequent activation.[85] Yet, it took another 20 years to elucidate the binding mode from a ligand-bound plasminogen crystal structure.[86]

In contrast to this early example, the general development of protease inhibitors is considered synonymous with the structure-based drug design of known enzyme structures and defined binding mechanisms.[87] It is not surprising that the approval of protease inhibitors did not significantly pick up until the 1980s. Primarily through the Nobel Prize-winning innovation of the PCR method, the recombinant protein expression of numerous proteases, and thus, the functional characterization of their inhibitors was accomplished.[82] In contrast to the aminocaproic acid example, more than 95% of the approved inhibitors bind to the active form of the addressed protease and compete with their endogenous substrates for active-site occupation.[31,33] Inhibitors during early development, just like the approved protease targeting drugs, are mostly peptidomimetic in nature which makes pharmacokinetic optimization a central dogma of the development.[88,89]

The 64 protease inhibitors approved to date can be classified into 4 eras of regulatory history, with each first-in-class inhibitor having itself a story of success. The first story tells of the angiotensin-covering enzyme (ACE) inhibitors for the treatment of hypertension and heart failure with annual sales of around $6 billion during the 1980s/90s.[90] Started by the approval of the ACE inhibitor captopril in 1981, the period from 1980 to 1995 can therefore be described as the era of metalloprotease inhibitors. The second era of protease inhibitors began in the 1990s primarily due to the significant increase of computer performance in the search for HIV protease inhibitors as antiviral agents. Once the crystal structure of the viral aspartate protease was elucidated,[91] it took only six years for the first inhibitor, saquinavir, to be approved in 1995 followed by nine more approvals until 2006 primarily to help contain the HIV pandemic.[92] The third era of protease inhibitors began in two ways with the approval of the first proteasome inhibitor bortezomib (2003) for the treatment of multiple myeloma. This boronic acid-containing inhibitor was the first to target a threonine protease, and secondly, bortezomib was the first approved protease inhibitor with a covalent mechanism of action, as it forms a chemical bond with the catalytic threonine residue.[93]

Covalent ligands have a prolonged residence time at their protein receptor compared to non-covalent inhibitors which leads to improved pharmacokinetic properties and enhanced inhibition potency.[94] Out of the 64 protease inhibitors approved to date, only 10 show a covalent mechanism, however, this is a contemporary trend, as all of these have been approved in the last 20 years.[95] Over the last 10 years, serine protease inhibitors have dominated approvals (19/22 drugs), with all 19 inhibitors targeting only three protease targets: HCV NS3 protease,[96] dipeptidyl peptidase IV (DPP IV),[97] and coagulation factor X.[98] The approvals of the first DPP IV inhibitor sitagliptin (2007) and the HCV protease inhibitor boceprevir (2011) represent the status quo in the current development: a peptidomimetic serine protease inhibitor with either a non-covalent or a covalent-reversible mode of action.[99,100]

It is noteworthy that until 2021 no cysteine protease inhibitor has received FDA approval, although fundamental research on this class of inhibitors is been ongoing since the 1990s.[101] Many potential inhibitors failed in clinical development, with the main problems being lack of inhibitor selectivity and limited understanding of the complex regulatory mechanisms.[102,103] However, recently, some cysteine protease inhibitors have shown remarkable progress in clinical trials (Table 1), with cathepsin K inhibitor odanacatib showing promising prospects for approval by reaching phase 3 in clinical trials.[104] The SARS-CoV2 M^{pro} inhibitor nirmatrelvir (PF-07321332) has recently received emergency approval from the FDA, making it the very first cysteine protease inhibitor to be approved in 2021.[105,106] Six additional cysteine protease inhibitors have also reached or completed phase 2 clinical trials – all of which have achieved this goal in the last seven years, making it likely that additional approvals will occur in the next few years. Given that all clinically studied cysteine protease inhibitors target their enzyme with a covalent mechanism, it is likely that this type of mechanism is privileged for cysteine protease targeting drugs (Table 1).

Table 1: **Listing of all cysteine protease inhibitors that have reached or completed FDA clinical phases 2 and 3 to date.** Indicated are the generic drug name, the primary target determined at study enrolment, and the date when phase 2 or 3 was entered. For covalent inhibitors, a red arrow indicates the electrophilic center for the bond formation with the catalytic cysteine residue. Regulatory data were retrieved from the ChEMBL28 database.

Name	Structure	Target	Phase (year)	Literature
Nirmatrelvir	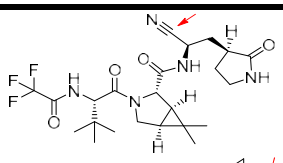	SARS-CoV2 M^{pro}	*approval* (2021)	[105]
Odanacatib	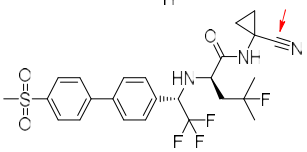	Cathepsin K	3 (2019)	[107]
AZD-7986	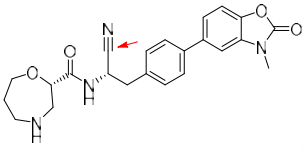	Cathepsin C	2 (2020)	[108]
Belnacasan	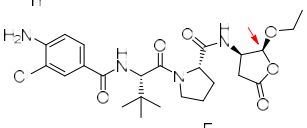	Caspase 1	2 (2020)	[109]
Petesicatib	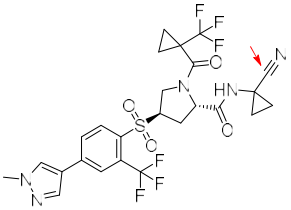	Cathepsin S	2 (2018)	[110]
Emricasan	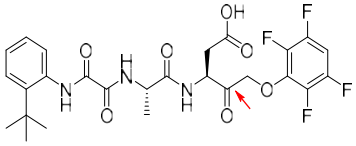	Pan-Caspase	2 (2017)	[111]
Balicatib	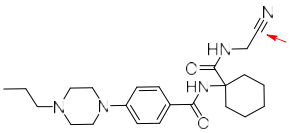	Cathepsin K	2 (2017)	[112]
Nivocasan	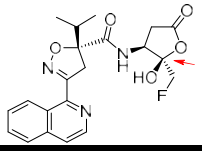	Pan-Caspase	2 (2014)	[113]

1.1.4 Covalent Inhibition of Cysteine Proteases

As can be seen from the clinically studied cysteine protease inhibitors (Table 1), the most promising drug candidates consist of a peptidomimetic recognition unit with an electrophilic warhead that can form a covalent bond with the active-site cysteine residue. Therefore, the search for new cysteine protease inhibitors is often synonymous with the quest for new covalent inhibitors.[101–103] In this regard, tuning the reactivity of the electrophilic warhead is essential for the successful development of cysteine protease inhibitors, and hence, targeted covalent inhibition (TCI) was titled a recent concept to optimize the covalent inhibition properties of a ligand by rational design.[114,115] In addition to the established medicinal chemistry toolbox of structure-based drug discovery, TCI tries to capture the thermodynamics and kinetics of the reaction between the active-site cysteine and the electrophilic warhead by empirical or calculated parameters. From a thermodynamic point of view, the binding of a covalent ligand to a protein can be described by a model that can be divided into at least two separate mechanistic steps (Figure 7A).[116,117]

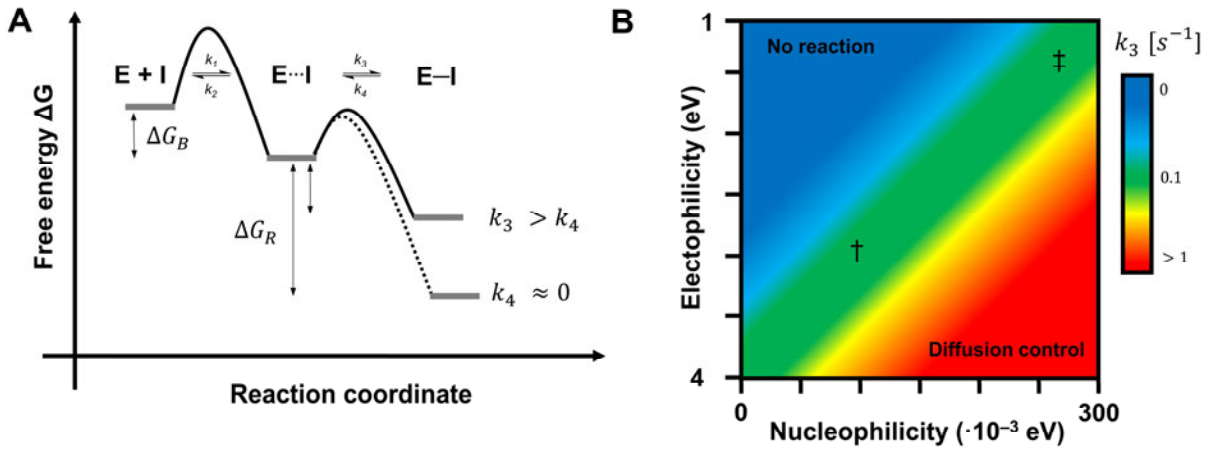

Figure 7: **Thermodynamic and kinetic description of covalent cysteine protease inhibition.** (**A**) Free energy diagram for the inhibition mechanism of a covalent inhibitor. Created in the style of SCHIRMEISTER et al.[116] (**B**) Semiquantitative 2D model of organic reactivity according to MAYR et al.[118] To achieve a targeted covalent reaction, nucleophilicity and electrophilicity have to be adjusted so that the reaction rates of the warhead reaction (k_3) are in the range of 10^{-4}–10^{0} s^{-1} (green area). The nucleophilicity of a cysteine residue with a protonated thiol (†, Cys-SH) and a deprotonated thiolate (‡, Cys-S^-) is labeled in the diagram.

During the first, non-covalent binding event, the ligand associates to the active-site pocket of the protein. The stability of this non-covalent complex (E···I) depends on the energy barrier required to dissociate the enzyme-inhibitor interactions and is the sum of the free binding enthalpy of the complex formation (ΔG_B) and its activation energy. The geometrical arrangement of this complex is mainly influenced by the interactions between the recognition unit of the inhibitor and the proteinogenic environment of the binding pocket. In the second step, if the warhead is positioned appropriately to the cysteine residue, a bond formation can occur, resulting in a covalent protein-inhibitor complex (E—I). The free reaction energy ΔG_R of this subsequent chemical reaction depends mainly on the chemical properties of the

warhead chemotype. Thus, the reaction barrier for the reverse reaction (k_4) is often the decisive factor for the reversibility of covalent bond formation: highly exothermic reactions (< –25 kcal/mol) mostly lead to an irreversible bond formation, while covalent-reversible inhibition is observed if the reversed reaction barrier is smaller or in the range of 20 kcal/mol.[116]

From a kinetic perspective, the two microscopic rate constants k_1 and k_2 determine the formation and stability of the non-covalent protein-inhibitor complex.[116,117] In a two-step model, the kinetics of covalent bond formation is described mainly by k_3 which depends on the electrophilicity of the warhead and the nucleophilicity of the addressed cysteine residue (Figure 7B). Kinetic constant k_4 determines whether the inhibition is reversible ($k_4 > 0$) or irreversible ($k_4 \approx 0$). The reversibility of the covalent reaction step may be a desirable property for the pharmacodynamic profile of the inhibitor because covalent-reversible binding retains the benefits of covalent binding such as increased inhibition potency but reduces patient risks like off-target modification, idiosyncratic toxicity, and auto-immune reactions (haptenization).[119,120]

The reactivity of a covalent inhibitor (characterized by k_3) can be described by a function of the Patz-Mayr relationship between the electrophilicity of the warhead (E) and the nucleophilicity of the cysteine residue (N): $\log(k_3)=S_N(N+E)$.[118] To avoid hyperreactivity (e.g., diffusion-controlled reaction velocity) and prevent toxicity risks, it is important to fine-tune the reactivity of the warhead reaction to maintain the reaction rates in a reasonable range ($k_3=10^{-4}$–10^{-0} s^{-1}).[116,121] The nucleophilicity of the cysteine's thiol moiety is primarily determined by the proteinogenic environment of the enzyme binding pocket and can rarely be modulated pharmacologically (e.g., by basic groups of an inhibitor).[122,123] In contrast, the electrophilicity of the warhead is freely modulable and can be quantified experimentally and computationally.[124,125]

LOPACHIN et al. and MAYER et al. have studied the nucleophilicity of bioorganic thiols and found that proteinogenic cysteine residues differ significantly in their nucleophilicity (ω^- [eV]) depending on their protonation state.[126,127] Thiols (†, R-SH, ω^-=0.098 eV) require comparatively stronger electrophiles than thiolates (‡, R-S^-, ω^-=0.261 eV) to react with covalent inhibitors (Figure 7B). In this context, for the rational design of specific covalent inhibitors of cysteine protease, it is important to be aware of their different protonation and enzymatic mechanisms (see chapter 1.1.2). The repertoire of potential cysteine-reactive warheads is almost unlimited and new chemotypes are constantly being discovered and characterized.[121] Trends in drug development showed that some warheads are more suitable than others for the inhibition of cysteine proteases.[101] A look at the cysteine protease inhibitors currently in clinical trials reveals that five of eight covalent drugs contain a nitrile warhead, while the other three have ketone/aldehyde-based warheads (Table 1). The nitrile warhead is the most frequently used chemotype for the development of cysteine protease inhibitors because of its mild electrophilicity and covalent reversible mode of action.[128]

Among the clinical targets of nitrile-containing drugs are the papain-like cathepsins C, S, K, and the SARS-CoV2 M^{pro}. All of these have in common that they possess a zwitterionic catalytic dyad (Cys^{-}/His^{+}) which undergoes a quantitative reaction with the relatively unreactive nitrile warhead. Quantum chemical calculations between nitrile warheads and biogenic thiols have shown that the reaction with negatively charged thiolate cysteine residues is privileged which could be substantiated by QM/MM studies for the clinical targets cathepsin K and SARS-CoV2 M^{pro}.[129–131] Here, it was shown that the zwitterionic dyad in both proteases mediates a two-step covalent mechanism with the formation of a thioimidate (Figure 8A): first, the thiolate anion of Cys25 attacks the electrophilic carbon atom of the nitrile warhead to form a covalent bond, and subsequently, the negatively charged thioylidene amide abstracts a proton from the imidazolium cation of His159 forming a stable thioimidate.

Ketones and aldehydes are more electrophilic than nitriles, and thus, they are the more reactive warheads.[132,133] Therefore, it is not surprising this warhead chemotype has been developed for targets with a less nucleophilic cysteine residue. The caspase 3 inhibitor emricasan has a substrate-mimetic ketone warhead in the position of the P1 carbonyl atoms which reacts in a covalent-reversible reaction with the catalytic cysteine residue (Figure 8B).[111] Nivocasan contains a fluoromethyl ketone warhead (masked as a ketale ester prodrug) which in contrast to the free ketone warhead modifies the active-site cysteine of caspase 3 with an irreversible covalent reaction. The reaction proceeds with a three-step mechanism involving the thiol addition to form the thiohemiketal, subsequent rearrangement to the three-membered sulfonium intermediate, and finally the elimination of the fluoride anion to form the covalent β-thioether (Figure 8C).[134] In analogy to the catalytic mechanism of legumain, the unique nature of the oxyanion hole plays a major role in the covalent inhibition mechanism for clan CD proteases (see chapter 1.1.2). Here, the crystal structure of a caspase 3 fluoromethyl ketone complex was used to show that the oxyanion hole favors the attack of the protonated thiol on the ketone warhead by charge stabilization.[135]

In addition to the mechanisms described in Figure 8, nitrile, ketone, and aldehyde warheads also exhibit inherent reactivity to serine proteases, which complicates the development of class-selective inhibitors.[136] The use of other family-specific warheads for cysteine proteases is known from preclinical research, but these have not yet been able to progress to the clinical stages.[101–103] In this regard, an overview of diverse SrtA and rhodesain warheads is presented in chapters 1.2.4 and 1.3.3. During the course of this work, new warheads for addressing the catalytic cysteine residues of *S. aureus* Sortase A and *T. brucei rhodesiense* cathepsin L (rhodesain) were developed and characterized. The elaborated mechanisms of the covalent reactions are presented during the respective result sections.

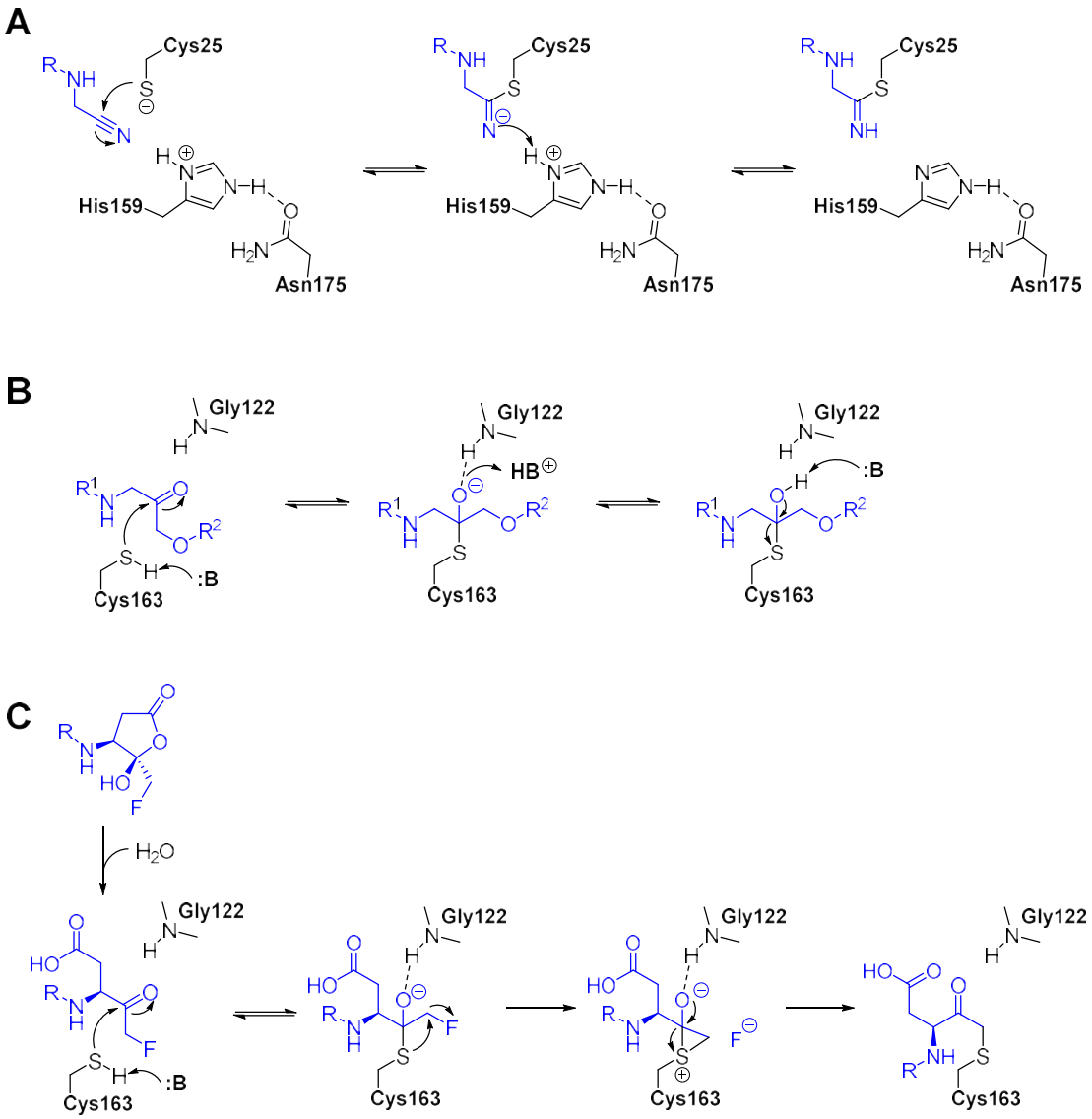

Figure 8: **Warhead mechanisms of clinically relevant cysteine protease inhibitors.** (**A**) Reversible mechanism of nitrile-based warheads. In the first step, a thioylidene amide is formed upon attack of the nucleophilic thiolate which is converted to a stable thioimidate by His159-mediated reprotonation. (**B**) Mechanism of covalent-reversible inhibition of caspase 3 by ketones/aldehydes. Formation of a tetrahedral thiohemiketal occurs which is stabilized by either an oxyanion hole or reprotonation. (**C**) 5-Fluoromethyldihydrofuran-2-ones are prodrugs and form the irreversible fluoromethyl ketone warhead upon hydrolysis with water. This chemotype reacts with caspase 3 in a three-step mechanism to form the respective β-thioether.

1.2 *Staphylococcus aureus* Sortase A

1.2.1 Physiological Role and Catalytic Mechanism

To date, about 3000 sortase-encoding genes have been identified across nearly one thousand Gram-positive bacterial species.[137] Based on their sequence identity, these sortase homologs can be classified into six differentiable subfamilies (class A–F).[138] For the past 20 years, the *Staphylococcus aureus* sortase A (SrtA) has been the longest studied sortase enzyme and is often considered archetypal for the entire class A subfamily.[139,140] *S. aureus* SrtA is a type II membrane transpeptidase that performs cellular housekeeping roles by anchoring numerous microbial surface components recognizing adhesive matrix molecules (MSCRAMMs) to the staphylococcal cell wall which are utilized for adherence to endothelial host cells and immune evasion.[141,142] All sortases characterized until now recognize surface protein precursors by their cell wall sorting signal and attach these to the peptidoglycan layer through a multistep transpeptidation process (Figure 9).

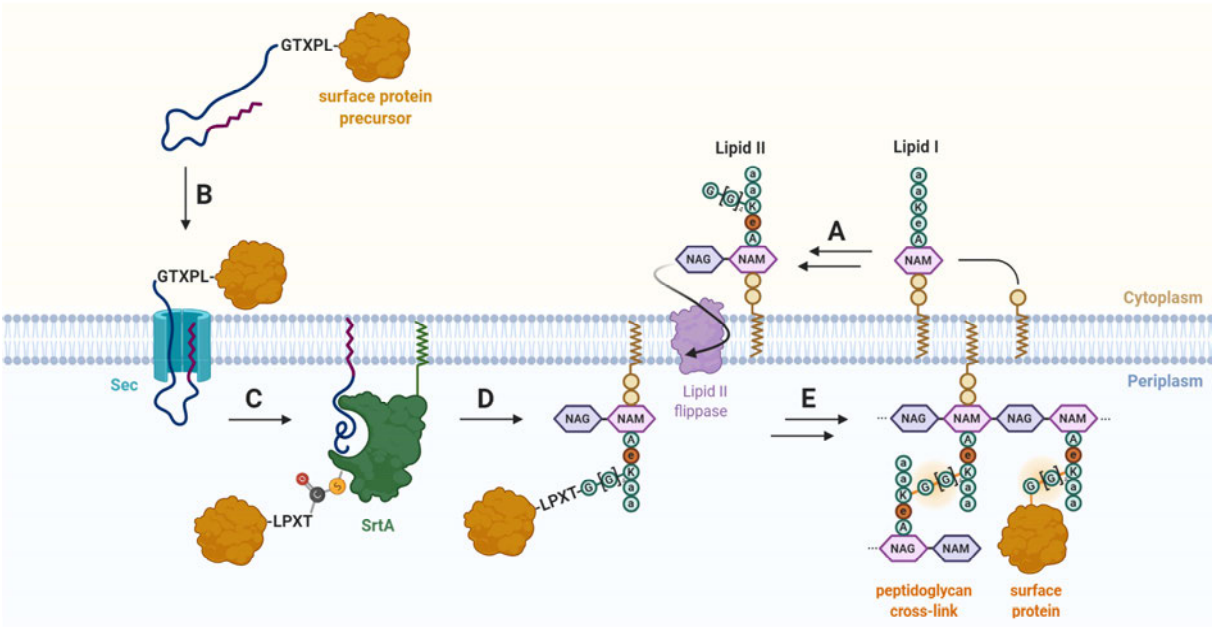

Figure 9: **Cell wall sorting reaction catalyzed by *S. aureus* SrtA.** (**A**) Lipid II, a ubiquitous building block for peptidoglycan biosynthesis, is synthesized from the bactoprenol-conjugate lipid I via a multistep process and transported into the periplasm by a membrane flippase. (**B**) Surface proteins (orange) that are to be anchored to the staphylococcal cell wall are synthesized in the cytosol containing a Sec pathway signal peptide (purple) and a cell wall sorting signal (LPXTG). (**C**) After the passage of the Sec translocon, the MSCRAMM precursor protein is retained in the periplasm with a membrane anchor, until it is recognized as an LPXTG-substrate by SrtA (green) to yield the covalent MSCRAMM-SrtA thioester. (**D**) The pentaglycine moiety from lipid II nucleophilically attacks the thioester intermediate to form a membrane-anchored lipid II-MSCRAMM conjugate. (**E**) Surface protein-tagged lipid II molecules are incorporated into the cell wall by transglycosylation and transpeptidation reactions to yield the staphylococcal peptidoglycan network.

The canonical cell wall sorting signal consists of a five-amino acid SrtA substrate sequence (mostly LPXTG) followed by a hydrophobic membrane anchor domain.[143] MSCRAMMs are mainly synthesized as cytoplasmic precursor proteins with N-terminal signal peptides for Sec-mediated secretion and export to the periplasm (Figure 9B). Here, the LPXTG-motif of the sorting signal is cleaved between threonine and glycine by the proteolytic functionality of SrtA, resulting in a thioacyl-enzyme intermediate attached to the SrtA active-site Cys184 (Figure 9C).[139,140] Subsequently, the reactive MSCRAMM-SrtA thioester is relieved by a nucleophilic attack of the pentaglycine moiety in lipid II (Figure 9D), and hence, MSCRAMMs, covalently linked to lipid II, are incorporated into the peptidoglycan network via consecutive transglycosylation and transpeptidation reactions during bacterial cell wall biosynthesis (Figure 9E).[53,144]

All sortases belong to the clan CL cysteine proteases and use a Cys-His-Arg catalytic triad in their active sites for catalysis.[145–147] The reaction mechanism of the sortase-catalyzed reaction was controversially debated during the early 2000s but is now considered to be mostly elucidated to proceed through a ping-pong catalysis mechanism.[148,149] The structural elucidation of the LPXTG-substrate complex has made its contribution to the understanding of the catalytic mechanism, however, since the atomistic binding mode of lipid II remains elusive to date, parts of the catalytic mechanism persist in controversy.[150] The reaction mechanism currently accepted is shown in Figure 10.

A central question in elucidating the SrtA reaction mechanism is the protonation state of the catalytic Cys184.[53,151] Based on pK_a measurements of the catalytic residues Cys184 and His120, less than 0.1% are in the zwitterionic form.[148,151,152] In contrast to legumain-like proteases (see chapter 1.1.2), which have an active uncharged catalytic dyad due to their prominent oxyanion hole, the SrtA enzyme must contain the catalytic residues in their thiolate and imidazolium forms, respectively. An enzyme system in which the majority of the population adopts an inactive protonation form is called “reversely protonated”.[153] Such reverse protonation of the catalytic dyad results in relatively low catalysis rates and is therefore rarely observed in nature while being also poorly understood.[154,155] This catalytic dormancy could be substantiated by the NMR and crystal structures of *S. aureus* SrtA, where Cys184 and His120 are too far apart (>7Å) for an ionic interaction.[146,156]

In the statistically unlikely condition that Cys184 and His120 are appropriately protonated, catalysis begins by a nucleophilic attack of the active-site thiolate on the P1 carbonyl carbon between threonine and glycine in the sorting signal (Figure 10).[150] This leads to the formation of a tetrahedral thiohemiketal transition state stabilized by an oxyanion hole mediated by Arg197 and the side chain of the P1 threonine residue.[58,157] This unstable thiohemiketal was found to collapse rapidly, breaking the bond to the primed side glycine residue to form a more stable acyl thioester.[158] During this step, His120 presumably serves the role of a catalytic acid assisting in the protonation of the leaving glycine amine.

SrtA recognizes lipid II as a secondary natural substrate and mediates the nucleophilic attack of the terminal pentaglycine amine on the enzyme-linked thioester, while His120 is believed to increase the nucleophilicity by the concerted deprotonation of the primary amine (Figure 10).[144,159] This results in the formation of a second tetrahedral thiohemiketal which is stabilized by an oxyanion hole, and subsequently, it resolves to yield a covalent amide-linked lipid II-MSCRAMM conjugate.[57,150] The symmetry of the reaction sequence leads to the reversibility of all reaction steps and an equilibrium yield of the transpeptidation products.[160]

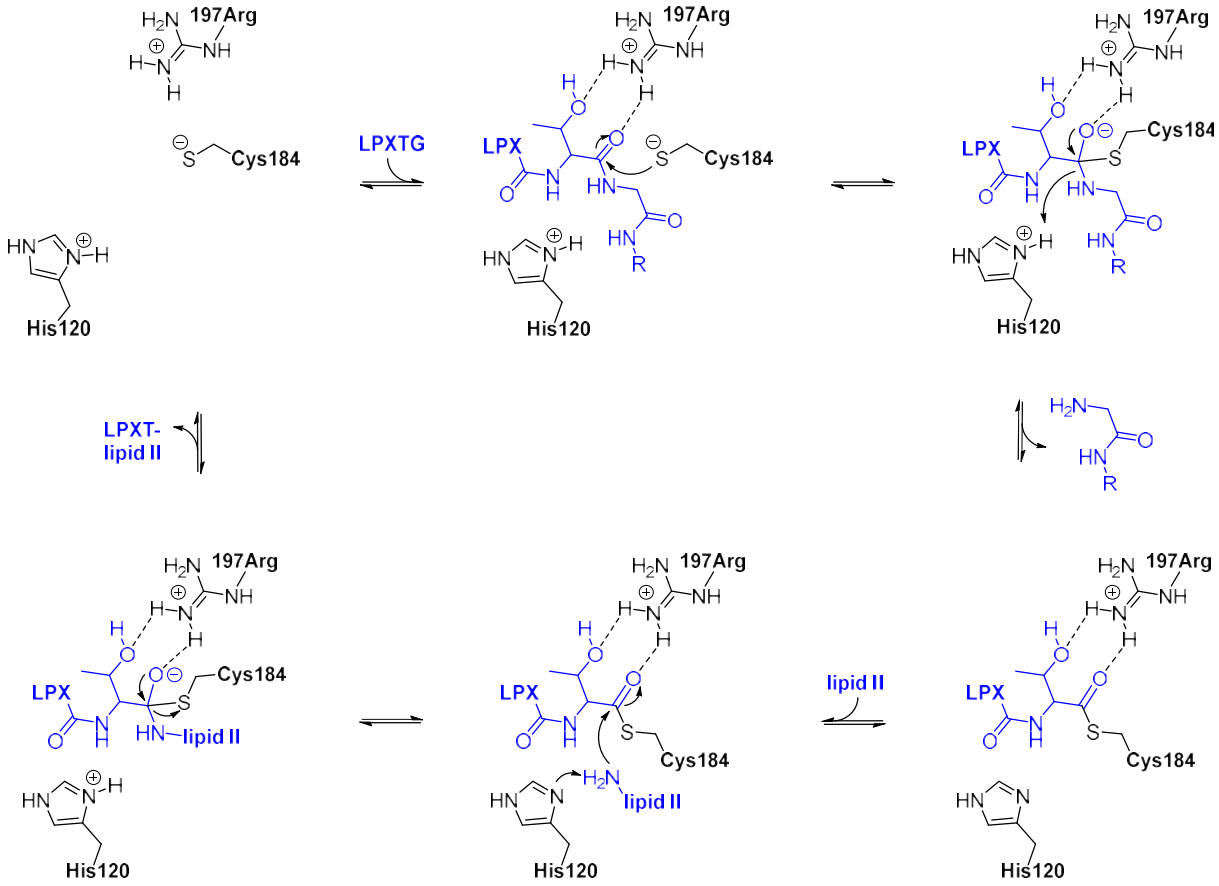

Figure 10: **Transpeptidation catalysis mechanism of *S. aureus* SrtA.** The active-site of *S. aureus* SrtA contains three catalytically active residues Cys184, His120, and Arg197, with the catalytically active form characterized by an imidazolium-thiolate dyad. In the first step, the canonical sorting signal substrate (LPXTG) binds into the active-site and a nucleophilic attack of the Cys183 thiolate on the P1 carbonyl carbon induces ionization to a transient thiohemiketal. Breaking the amide bond to the primed site glycine residue is facilitated by a proton transfer from His120 resulting in an uncharged thioacyl intermediate. Subsequent deacylation is triggered by a nucleophilic attack of a glycine nucleophile (lipid II) and stabilizes a second tetrahedral thiohemiketal which subsequently releases the product and regenerates the catalytically competent protease.

1.2.2 Structural Biology of Sortase A

The primary sequence of *S. aureus* SrtA consists of three structural elements that are mostly conserved in other sortase homologs: an N-terminal signal peptide that determines export via the Sec pathway translocon, a hydrophobic membrane anchor that keeps SrtA in the periplasm, and an 18 kDa catalytic domain containing the Cys-His-Arg triad.[140,147] Early in the study of sortases, the structure of the catalytic domain (residue 60–206) was elucidated, with the NMR and crystal structures postulating a nearly identical topology (RMSD: 1.97 Å).[146,156] The characteristic fold of SrtA is defined by a closed eight-stranded β-barrel, with the three catalytic residues (Cys184, His120, Arg184) located in a shallow groove at the bottom of this barrel (strands β4 and β7), while the walls of the barrel are formed by the flexible loops that connect the rigid β-sheets (β3/β4 loop, β6/β7 loop, β7/β8 loop). As a result, the binding pocket is dominated by disordered loop elements which lead to high intrinsic flexibility of the enzyme structure (Figure 11A). Interestingly, the *S. aureus* SrtA requires a calcium ion for its catalytic activity, while the binding site of the calcium ion is determined by acidic side chain residues of the β3/β4 and β6/β7 loops (Figure 11B).[146,161]

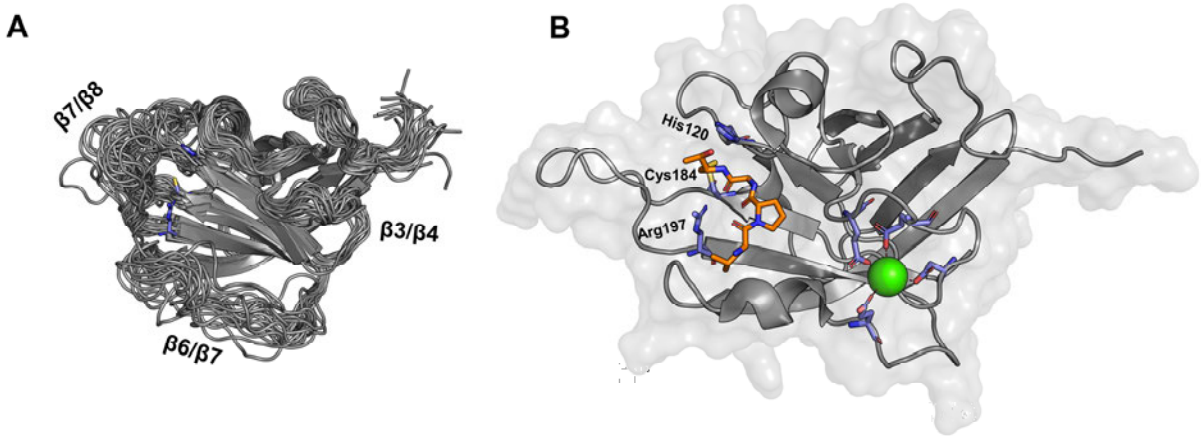

Figure 11: **NMR structures of *S. aureus* SrtA.** (**A**) NMR ensemble of the *S. aureus* SrtA apo structure (pdb: 1ija) highlighting the high intrinsic flexibility of the binding pocket-determining loops β3/β4, β6/β7, and β7/β8. (**B**) NMR structure of the SrtA-LPAT complex (pdb: 2kid) with the labeling of the catalytic triad (Cys184, His 120, Arg197) and highlighting the calcium-binding residues.

Nearly 10 years after the first publication of the apo sortase structure, a SrtA-LPAT substrate complex was elucidated by NMR spectroscopy, thus providing the molecular basis for sorting signal recognition.[45] The structure of the complex showed that the substrate-binding pocket is in close proximity to the catalytic Cys184 and is defined by the strands of β4 resp. β7, the β6/β7 loop, and the β3/β4 loop (Figure 11B). In this process, binding of the LPXTG-substrate leads to a fundamental reorganization of the binding pocket with a disordered-to-order transformation of the β6/β7 loop and an opening of the β-barrel's lateral wall by displacement of the β7/β8 loop.[162] The β6/β7 and β7/β8 loops, which showed high intrinsic flexibility in the apo structure (Figure 11A), are tightly rigidized in complex with the LPAT substrate and a single calcium ion (Figure 11B).[45,161] In this structure, the interaction of

the LPAT substrate with the β6/β7 loop explains how SrtA recognizes the P3 (proline) and P4 (leucine) amino acids of the sorting signal. The side chain of the P4 leucine residue interacts with a sub-pocket formed by the hydrophobic residues of the newly formed 3^{10}-helix (Val161–Leu169). In a crystal structure of the LPAT-SrtA substrate complex without a calcium ion, this P4 interaction was not observed which led to the hypothesis that the binding of the calcium ion is required for the preorganization of the β6/β7 loop.[156] Additional NMR titrations revealed that calcium-binding alters the mobility of the β6/β7 loop, thereby allosterically regulating the affinity for the sorting signal.[163,164] The P3 position in sorting signals is conserved across all sortase classes with a strong preference for a proline residue. This can be explained by the L-shaped topology of the SrtA binding pocket because only with a *cis*-peptide configuration the catalytically attacked threonine residue reaches Cys184.

In addition to the structural biology discoveries, molecular dynamics calculations have led to further insights into molecular substrate recognition by SrtA. A multistep model, based on conformational selection and induced-fit mechanisms, seems to be the most plausible (Figure 12A).[157,165] In the apo state of SrtA, the binding pocket is characterized by the intrinsic flexibility of the β6/β7 and β7/β8 loops, while the β6/β7 loop adopts a predominantly open conformation and the β7/β8 loop exhibits a closed conformation. After titration with calcium ions, the β6/β7 loop seems to follow a mechanism of conformational selection, as the interaction of the cation leads to rigidization and partial closure of the loop.[163] Subsequent binding of an LPXTG-substrate leads to complete closure of the β6/β7 loop and simultaneous opening of the β7/β8 loop, suggesting an induced-fit mechanism.[45] In this regard, the rigidization of the β6/β7 loop seems to be mainly responsible for the specificity of substrate recognition, whereas the displacement of the β7/β8 loop allows the opening of the binding pocket for lipid II as a second substrate (Figure 12A).[165]

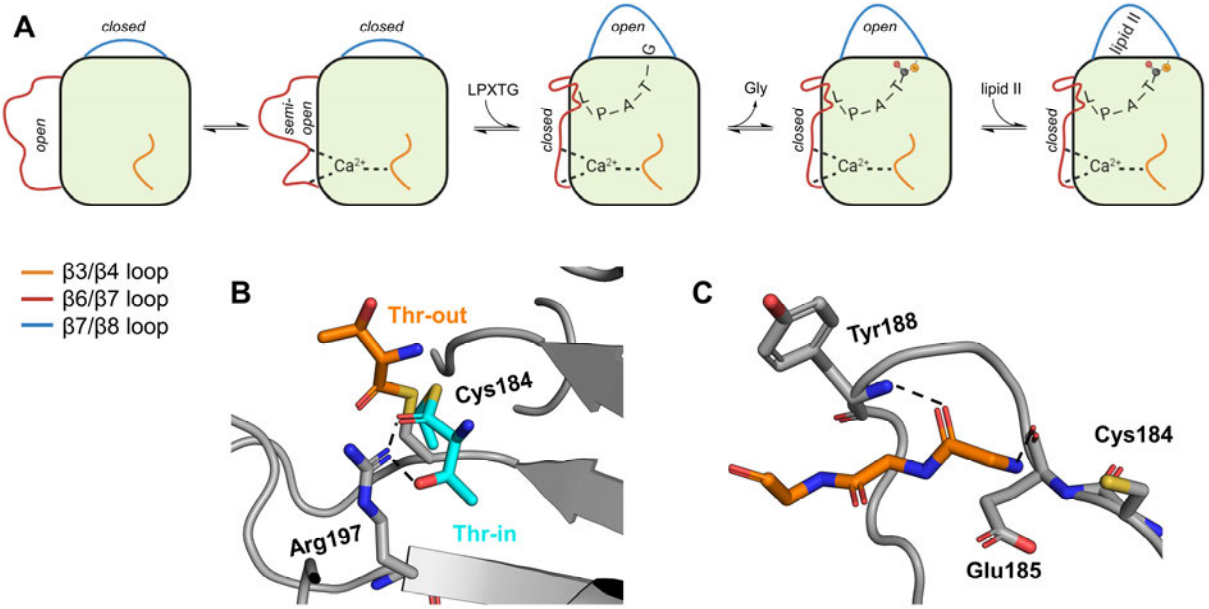

Figure 12: **Model of the substrate recognition by *S. aureus* SrtA.** (**A**) Mechanistic model of LPXTG-substrate binding. The mobility changes in the β6/β7 and β7/β8 loops characterize the induced-fit mechanism and mediate the allosteric cooperativity between the three ligands: LPXTG, lipid II, and the calcium ion. (**B**) Energy-minimized model of the P1 residue binding modes Thr-out and Thr-in, with only the latter interacting productively with Arg197 and representing the catalytically competent configuration.[157] The model was built based on a template (pdb: 2kid) and with an OPLS3 minimization using Schrödinger Maestro. (**C**) Binding mode of a triglycine ligand in the *S. aureus* srtB crystal structure (pdb: 1qxa) with interactions in the β7/β8 loop and close proximity of the glycine nucleophile to Cys184. The residue numbering was adapted to the *S. aureus* SrtA nomenclature.

In contrast to the agreement between P3/P4 coordinates in NMR structures and molecular dynamic calculations, the NMR and crystal coordinates for the P1 (threonine) and P2 (variable position) do not match the biochemical and bioinformatics research data.[142,166] In the NMR structure of the SrtA-LPAT complex, the side chain of the threonine P1 residue points to the solvent and is consequently not recognized by the enzyme (Figure 11B). On the other hand, the variable P2 position (here: alanine) points deep into the binding pocket, so that larger amino acids, which are accepted in vitro and in vivo experiments, could not bind with this conformation.[166]

This so-called “Thr-out” conformation appears to be artificially caused by the covalent linkage of the LPXTG-substrate to the Cys184.[157] By using a larger amino acid residue (glutamine) in the variable P2 position, a “Thr-in” binding mode could be achieved for *S. aureus* srtB, where the P1 threonine is buried in the active-site and involves interactions with Arg197 as predicted by QM calculations.[167] For a recently resolved *B. anthracis* SrtA-LPAT complex, this Thr-in conformation could be confirmed too, so that this “Thr-in” conformation is substantiated for both sortase classes A and B.[168] As described in chapter 1.2.1, the *S. aureus* srtB and *B. anthracis* SrtA substrate complexes support the mechanistic idea that the P1 threonine side chain interacts with the Arg197 catalytic residue to stabilize an oxyanion hole.[57,58] An energy-minimized model of the thioacyl intermediate with “Thr-in” and “Thr-out” conformations for the *S. aureus* SrtA binding pocket is shown in Figure 12B.

In contrast to the molecular recognition of the LPXTG-sorting signal, the binding of the secondary substrate lipid II remains poorly understood for the lack of a SrtA crystal structure. However, for the homologous *S. aureus* srtB, a crystal structure with a triglycine ligand was elucidated, but the elaborated binding mode at the β7/β8 loop is not transferable to SrtA because the β7/β8 loops between the two sortase homologs are fundamentally different (Figure 12C).[169] NMR shift mapping data from titration of the *S. aureus* SrtA-LPAT complex with triglycine confirmed an interaction surface at the SrtA β7/β8 loop, but no conclusions can be drawn about the exact binding mode.[45] Furthermore, only the SrtA-LPAT complex but not the SrtA apo form showed an affinity for triglycine which is compatible with the proposed ping-pong bi-bi mechanism and can be used to explain the induced-fit model with opening of the β7/β8 loop only after sorting signal binding (Figure 12A).[148,149]

1.2.3 The Role of SrtA for the *S. aureus* Virulence

S. aureus possesses an extensive arsenal of virulence factors to establish infectious diseases. In this context, the term virulence describes the non-metrified degree of disease-related properties of a pathogen.[170] Staphylococcal infections are initiated by a breach of the skin or mucosal barrier, allowing the bacteria to gain access to vulnerable tissues or the bloodstream.[171] The complexity of virulence in *S. aureus* infections is remarkable, as these bacteria colonize a wide variety of tissues as commensal such as nares, skin, or pharynx.[172,173] The tissue tropism of different staphylococcal strains cannot be attributed solely to passive spreading by the bloodstream, but it is the result of complex host-virulence factor interactions in the establishment of which SrtA plays a central role.[174,175] Virulence factors of *S. aureus* are mostly proteinogenic in nature and generally fulfill one of the four competencies: 1.) support of colonization (adhesins), 2.) evasion of the host immune system (etablins), 3.) damage to host tissues (toxins), or 4.) recruitment of nutrients (hemophores).[175–177]

S. aureus pathogenesis can be described by a biofilm life cycle in which virulence factors are crucially involved in the host-pathogen interactions at each stage (Figure 13).[171] Biofilms are sessile microbial communities, as they are formed by the adhesion of cells to the surface of animate tissues or inanimate surfaces.[178] The formation of a biofilm was attributed to reduce the susceptibility of pathogens to antimicrobial therapy and the development of resistance.[179] Initial attachment during biofilm formation involves the reversible binding of bacterial cells to proteins located on the surface of host cells (fibronectin, fibrinogen, collagen, etc.). This binding occurs by means of intercellular adhesion mechanisms through surface-associated virulence factors on the bacterial cell membrane.[178] Subsequent cell division and secretion of a surrounding extracellular polymeric substance (EPS) lead to the formation of the biofilm.[178]

Within the biofilm, other bacterial species or mammalian cells (e.g., platelets) might be incorporated. Dispersion of individual cells leads to reactivation of the planktonic state and can initiate the formation of new biofilms after metastasis.[171,179] In the last step of the biofilm life cycle, the biofilm undergoes maturation by diversification of the metabolic profile of the bacterial cells. The formation of cells with stationary phase-like dormancy is closely associated with tolerance to antibiotic chemotherapy.[179]

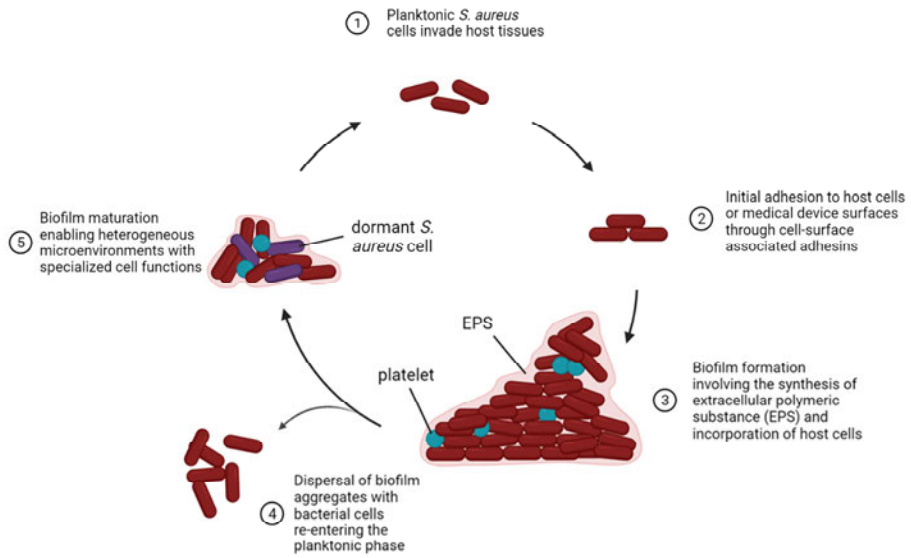

Figure 13: **The *S. aureus* biofilm life cycle.** Biofilm formation in *S. aureus* proceeds through five characteristic stages that are closely related to SrtA-mediated virulence mechanisms: 1.) the planktonic stage, 2.) initial adhesion, 3.) biofilm mass accumulation, 4.) dispersal of excess cells, and 5.) biofilm maturation and cell differentiation.

Several *S. aureus* virulence factors have been described as SrtA substrates (MSCRAMMs) such as protein A (SpA), α-hemolysine (α-toxin), collagen/fibronectin/elastin-binding proteins (Cna, FnbpA/B, EbpS), clumping factors (ClfA/B), serine-aspartic acid repeat proteins (SdrC/D/E), iron-regulated surface determinant (IsdA–H), and staphylococcal surface proteins (SasA–K).[175,180] An overview of *S. aureus* virulence factors is shown in Figure 14. During the first phase of the biofilm life cycle, adhesins attach the bacterial cell to the host matrix.[174,181] These surface proteins for adhesion share common structural features: a C-terminal cell-anchoring region and the N-terminal ligand-binding domain required to function as adhesins.[175] Adhesins include collagen-, fibronectin-, and elastin-binding proteins (Cna, FnbpA/B, EbpS). These proteins enable adhesion to the extracellular matrix of the host tissue.[175] The surface of the bacterium also contains virulence factors against the host's immune defense. Among these etablins, that consolidate the infection of the host, is protein A (SpA). This protein binds to IgG antibodies, and as a result, the bacterial cell might be able to escape phagocytosis.[182] In addition, *S. aureus* secretes proteins (exotoxins) which lead to damage or destruction of host cells or matrix. The most studied α-toxin (α-hemolysin) causes pore formation by binding to the host cell membrane and leading to apoptosis through cell wall rupture.[183] In addition, *S. aureus* harbors clumping factors (ClfA/B) for tissue damage which activates host blood clotting through the formation of fibrin.[184] The virulence factors of the Isd gene locus (iron-regulated surface determinant) function as hemophores and

recruit heme from porated and lysed host cells, contributing to the nutritional requirements of the bacterial cell.[185]

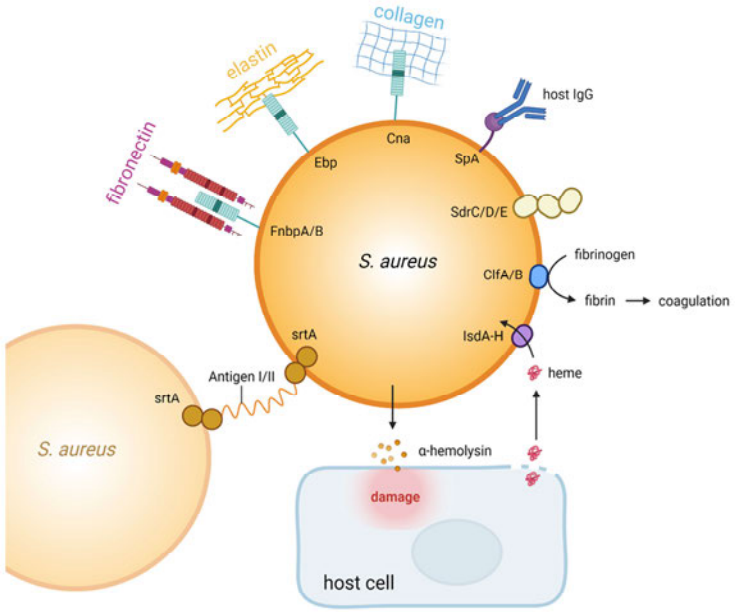

Figure 14: **Intercellular network of *S. aureus* virulence factors.** Several *S. aureus* virulence factors have been described as SrtA substrates, such as protein A (SpA), α-hemolysine, collagen/fibronectin/elastin-binding proteins (Cna, FnbpA/B, EbpS), clumping factors (ClfA/B), serine-aspartic acid repeat proteins (SdrC/D/E), and iron-regulated surface determinant (IsdA–H).

In infection model systems, the SrtA substrates clumping factor B (ClfB) and iron-regulated surface determinant A (IsdA) have been identified as major drivers of human *S. aureus* pathogenesis, making SrtA favorable as a drug target to reduce the virulence in *S. aureus* infections.[186,187] Mutation or deletion of SrtA in *S. aureus* has been shown to be one of the most effective ways to prevent pathogenicity and lethal disease progression in mouse models.[139,188,189] However, inhibition of SrtA as an anti-virulence drug target differs from the paradigm of 20th-century antibiotics, as anti-virulence drugs disarm rather than kill pathogenic bacteria.[190] SrtA inhibitors are likely to interfere with host-pathogen adherence but not with bacterial growth, thus imposing a lower selective pressure to avoid resistance development.[191,192] Since neither genetic deletion nor selective chemical inhibition of *S. aureus* SrtA was found to cause cytotoxic or growth inhibitory effects on *S. aureus* cells, the SrtA enzyme meets the requirements of an anti-virulence target.[192–194]

The concept of anti-virulence inhibitors has recently been demonstrated for SaeRS (*S. aureus* two-component system) inhibitors leading to FDA approval of streptozotocin and floxuridine.[195] However, the development of SrtA inhibitors as anti-virulence drugs has not yet progressed beyond preclinical studies of potential inhibitors, as the privileged position of SrtA is protected against pharmacological manipulation by three structural features of the enzyme: (i) The reverse protonation of Cys184 makes it a weaker nucleophile than the catalytic cysteine residues of most papain-like proteases,[146,148] and hence, mild protease-specific warheads such as nitriles or Michael acceptors are largely unsuitable for covalent inhibition of *S. aureus* SrtA.[53,151,166,196,197] (ii) The substrate-binding pocket of the enzyme is determined

by the intrinsic flexibility of the β6/7- and β7/8-loops.[165] Binding of the LPXTG-substrate or small-molecule inhibitors usually leads to strong protein rigidization and is therefore entropically penalized, as reflected by the high K_M value of 5.5 mM and only a few inhibitors with a potency of <10 µM.[45,166,192] (iii) Co-localization of SrtA with the LPXTG- and pentaglycine substrate leads to high local concentrations and efficient complex formation *in cellulo* which is difficult to disrupt with reversible-competitive inhibitors. Therefore, most of the SrtA inhibitors identified to date are covalent-irreversible in nature and react with the active-site Cys184.[192]

1.2.4 Covalent Inhibitors of *S. aureus* SrtA

After the identification of *S. aureus* SrtA as a drug target for the development of anti-bacterial agents, the search for suitable inhibitors began which has yielded mainly covalent-irreversible inhibitors in the past 20 years.[192,198] Besides this trend, our validations of published non-covalent inhibitors have shown that these substances often interfere with the assays system and do not possess significant SrtA inhibition.[193,199–201] The electrophilic warheads of the identified covalent inhibitors, however, differ widely from the typical warheads to address cysteine proteases such as carbonyl compounds or nitriles (see chapter 1.1.4), as these chemotypes showed only weak reactivity to the catalytic Cys184.[196,197] Instead, the most potent inhibitors identified included predominantly electrophilic sulfur-containing warheads that form a disulfide bond with Cys184. These warheads include chemotypes such as thioamides, benzisothiazolinones, thiopyridazinones, thiadiazoles, and thiadiazolidinones (Table 2).[202–206] Despite the long development history for SrtA inhibitors, the K_I-values of the most potent inhibitors are still in the low micromolar range, which explains why no inhibitor has yet advanced to clinical trials.[207]

Table 2: **Selected covalent *S. aureus* srtA inhibitors.** For covalent inhibitors, a red arrow indicates the electrophilic center for the disulfide bond formation with the catalytic cysteine residue. *The thiadiazolidinone inhibitor tideglusib shows a covalent-reversible course of inhibition.

Chemotype	Structure	K_I	Literature
Thioamide	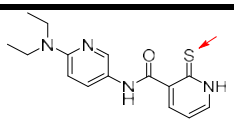	n.d.	202
Benzisothiazolinone	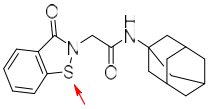	6.11 µM	203
Thiopyridazinone	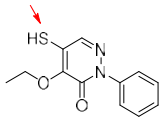	13.0 µM	204
Thiadiazole	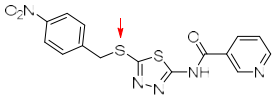	3.8 µM	205
Thiadiazolidinone	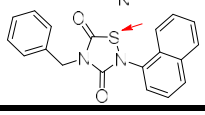	0.6 µM*	206

In this regard, the aim of this dissertation is the development and optimization of potent covalent SrtA inhibitors and their further mechanistic and cellular investigation as *S. aureus* anti-virulence drugs. The following two publications are part of the results obtained in this sortase project:

(1) **Barthels, F.**; Meyr, J.; Hammerschmidt, SJ.; Marciniak, T.; Räder, HJ.; Ziebuhr, W.; Engels, B.; Schirmeister, T. 2-Sulfonylpyrimidines as Privileged Warheads for the Development of S. Aureus Sortase A Inhibitors *Front. Mol. Biosci.* **2022**, *8*, 1284.

(2) **Barthels, F.**; Marincola, G.; Marciniak, T.; Konhäuser, M.; Hammerschmidt, S.; Bierlmeier, J.; Distler, U.; Wich, P. R.; Tenzer, S.; Schwarzer, D.; Ziebuhr, W.; Schirmeister, T. Asymmetric Disulfanylbenzamides as Irreversible and Selective Inhibitors of Staphylococcus Aureus Sortase A. *ChemMedChem* **2020**, *15* (10), 839–850.

1.3 *Trypanosoma brucei rhodesiense* Cathepsin L (Rhodesain)

1.3.1 Physiological Role of Rhodesain

Trypanosoma brucei rhodesiense cathepsin L, also called rhodesain, is the major lysosomal protease of the harboring parasite.[208–210] Rhodesain, is a member of the papain family, making it a part of the CA clan (see chapter 1.1.2). Trypanosomes are a family of unicellular, flagellate-bearing parasites which are classified as kinetoplastids.[211] Within *T. brucei*, there are two human pathogenic subspecies: *T. b. gambiense* (the causative agent of West African sleeping sickness) and *T. b. rhodesiense* (East African sleeping sickness).[212] African sleeping sickness or Human African Trypanosomiasis is caused by the infection with trypanosomes which are transmitted by the bite of the tsetse fly.[213] Although several 10,000 new cases were reported each year, sleeping sickness is considered a neglected tropical disease.[214] The diverse physiological roles of rhodesain include evading the human immune system, overcoming the blood-brain barrier, and promoting parasitic iron homeostasis (Figure 15).[215,216]

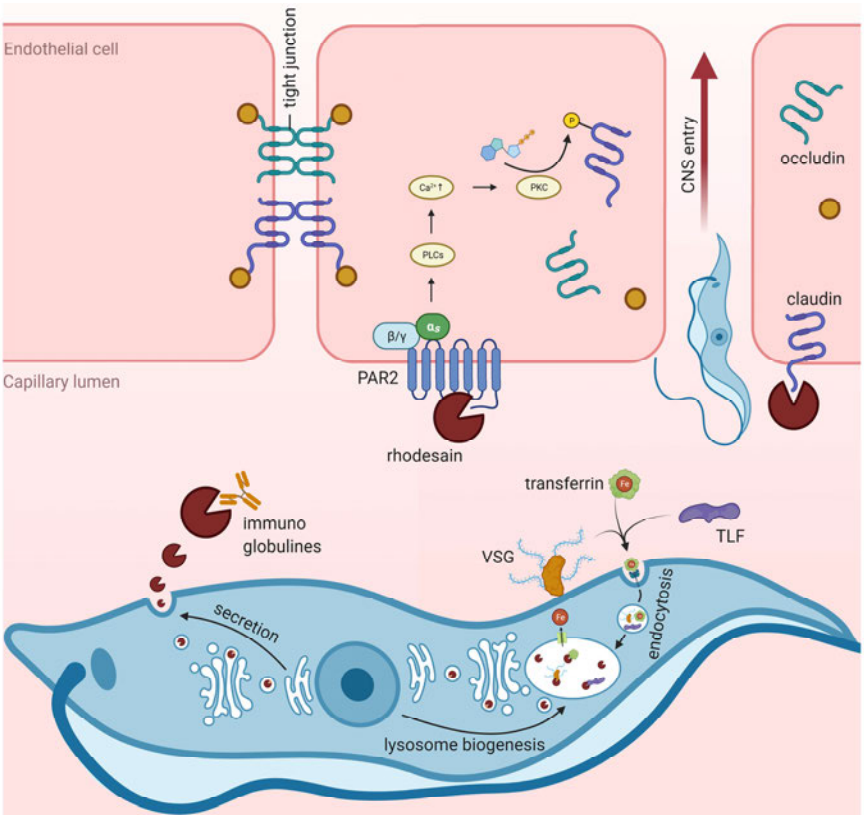

Figure 15: **Physiological roles of *Trypanosoma brucei rhodesiense* cathepsin L (rhodesain).** Rhodesain acts in the parasitic lysosome, where it digests internalized host proteins (VSG, transferrin, and TLF), or it is secreted from the parasite and exerts its effect in human blood plasma, where it cleaves host proteins (PAR2, immunoglobulines, claudin, and occludin) to help cross the blood-brain barrier and to evade the immune system.

Once the parasite enters the host's bloodstream, the disease progresses in two stages.[212] During the first, hemolymphatic stage, the parasites spread in the blood and the lymphatic system of the host. During this stage, malaria-like symptoms appear such as headache, pain in the limbs, fever, and weakness. If the infection remains untreated, the second stage trypanosomes cross the blood-brain barrier, resulting in characteristic symptoms such as neurological disorders, seizures, and coma.[217]

In the event of a trypanosomal infection, the human innate immune system responds by releasing trypanosome lytic factors (TLF) which are forced to endocytosis into the parasite after binding to a trypanosomal receptor. After transport into the lysosome, the pore-forming subunits of TLF lead to organelle permeation and parasite apoptosis.[218] However, in *T. b. rhodesiense*, two resistance mechanisms to TLF intervention have evolved, allowing the parasite to survive in human blood: the parasite serum resistance-associated protein can bind and neutralize human TLF.[219] Furthermore, lysosomal cathepsins, among which rhodesain belongs, cleave TLF at their site of action, thus weakening the effect of the immune response.[220] In addition, the parasites have developed mechanisms to evade the adaptive immune system. In this way, they present a layer of *N*-glycosylated variant surface glycoproteins (VSG) on their cell surface.[221] This impenetrable layer prevents host immune proteins from reaching the cell surface of the parasite. The VSG coat is continuously internalized by endocytosis, glycolytically resp. proteolytically modified, and renewed on the cell surface, so that it cannot be recognized by adaptive immunoglobulines.[222] Internalized VSG are transported to the lysosome, where they are trimmed or degraded by rhodesain and other proteases.[223]

For iron uptake, trypanosomes exploit the iron-containing host protein transferrin.[224] After binding of transferrin to a parasitic receptor and subsequent endocytosis, the receptors are transported into endosomes. Here, acidic pH leads to the release of bound iron, while the transferrin receptors are transported back to the cell surface and the transferrin protein is degraded by lysosomal cathepsins (*T. b.* cathepsin B and rhodesain).[208,215] In addition, *T. b. rhodesiense* uses secreted rhodesain to cross the host blood-brain barrier.[216] In this process, rhodesain induces Ca^{2+} release in host endothelial cells by hydrolysis of the protease-activated receptor-2 (PAR2) which after activation of protein kinase C (PKC), subsequent phosphorylation of claudin, and loss of the tight junctions allow trypanosomes to enter the central nervous system (CNS). Direct proteolysis of tight junction proteins between endothelial cells by secreted rhodesain and the degradation of soluble immunoglobulines is also hypothesized.[225]

1.3.2 Structural Biology and Catalytic Mechanism

Rhodesain is a papain-like protease with 60% sequence similarity to human cathepsin L, and thus, it is structurally very similar to the CA clan proteases.[209] During lysosome biogenesis, rhodesain is originally expressed as an inactive precursor protein (zymogen).[226,227] Among the 450 residues of pro-rhodesain, the first N-terminal amino acids form a signal peptide, followed by a 105 residue pro-peptide and a catalytic domain (214 amino acids) which is concluded by a trypanosome-specific C-terminal domain

(Figure 16A).[210,227] The rhodesain pro-domain acts as an intramolecular inhibitor of the protease, preventing nonspecific proteolysis until the protease reaches its subcellular destination: the lysosome.[228,229] During the secretory transport pathway from the endoplasmic reticulum (pH 7.2) to the lysosome (pH 5.5), rhodesain is exposed to an increasingly acidic pH.[227] When the zymogen reaches the lysosome, pH-dependent activation occurs by cleavage of the pro-domain; a process known as maturation.[229]

In all known structures of cathepsin L zymogens, the pro-domain consists of three α-helices and a short β-strand.[226,229] Helix 1 and 2 are connected by a flexible loop region and oriented orthogonally to each other. Helix 3 transitions to a disordered region resting over the active-site cleft of the protease, thereby blocking access to the catalytic center of the enzyme. The trypanosomal pro-domain differs from those of non-parasitic cathepsins in having an additional α-helical region (helix 4) that blocks the S2 and S3 substrate-binding pockets of the protease with aromatic residues (Tyr107, Phe108) similar to the binding mode of the anti-protozoal inhibitor K11777 (Figure 16C).[229] The acidic pH value found in lysosomes results in a loss of affinity between the catalytic domain and pro-domain in cathepsin L-like proteases by disrupting conserved salt bridges of this interaction interface.[230] MD simulations and mutagenesis studies demonstrated that for rhodesain, the protonatable groups Asp194 and Asp242 in the protease domain form a pH-switchable interdomain lock with the basic residues Arg114 and Arg116 of the pro-domain and lead to activation of rhodesain at pH values <5.5 (Figure 16C).[229]

After autoactivation by proteolysis of the pro-domain, deblocking of the catalytic center occurs which is located between an α-helical-dominated L- and a β-sheet-dominated R-domain of the papain-like fold (Figure 16B).[209] Along the active-site cleft, shallow substrate-binding pockets are formed, with the S2 binding pocket being primarily responsible for substrate recognition and having a preference for large hydrophobic side chains such as the phenylalanine residue of the covalent inhibitor K11777.[231] The S1 pocket, on the other hand, prefers basic amino acids such as arginine but also tolerates non-polar residues such as the homophenylalanine moiety of K11777. No preferences were found for the S3 and primed side binding pockets which can be explained by their open and flat topology.[232]

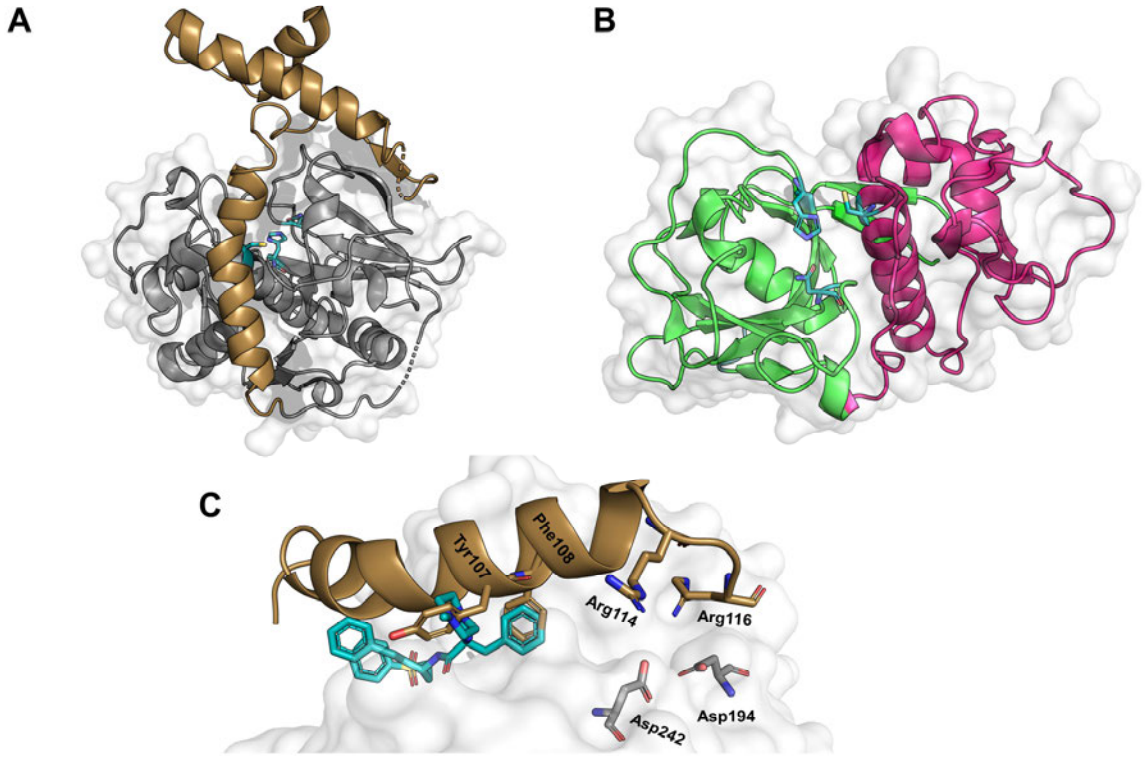

Figure 16: **Structural biology of *T. brucei* rhodesain.** (**A**) The structure of pro-rhodesain Cys25Ala mutant (pdb: 7avm) is shown with the protease domain in grey, the pro-domain in gold, and the catalytic residues (Cys25*, His162, Asn182) highlighted in cyan. *The Cys25 residue was generated by in silico mutagenesis with Schrödinger PyMol. (**B**) Crystal structure of catalytically active rhodesain (pdb: 2p7u). The protease fold can be separated into an α-helical dominated L-domain (magenta) and a β-sheet dominated R-domain (green). The active-site, with the catalytic residues Cys25, His162, Asn182 (cyan), is located in the cleft between the two domains. (**C**) Selected interactions between the protease domain and pro-domain residues. The superposition of the pro-peptide (gold, pdb: 7avm) and the crystallographic binding mode of K11777 (cyan, pdb: 2p7u) reveals overlaps between the S2 and S3 residues with Tyr107 and Phe108. Salt bridges between the pro-domain (Arg114, Arg116) and the catalytic domain (Asp194, Asp242) presumably act as a pH-switchable interdomain lock to prevent premature activation.

The proteolysis mechanism of rhodesain is similar to most CA clan papain-like proteases (see chapter 1.1.2).[233] Within the active-site, there is a catalytic triad consisting of Cys25, His162, and Asn182 which forms a strongly nucleophilic imidazolium-thiolate dyad.[66,209] Asn182 thereby stabilizes the correct orientation and tautomeric form of the His162 imidazole ring and polarizes the catalytic Cys25 to the thiolate form.[64] For rhodesain, there are no quantum chemical studies of the catalytic mechanism available to date, however, QM/MM simulations of the proteolysis have been investigated for *T. cruzi* cruzain and these can be considered as a surrogate due to the high similarity (identity: 70%, similarity: 81%) between the two proteases (Figure 17).[234,235] The postulated mechanism follows a stepwise acylation-deacylation scheme, where in the case of cruzain, protonation of the S1-amide nitrogen appeared to occur prior to nucleophilic attack by Cys25. In turn, bond breakage was postulated to occur with a concerted mechanism without the formation of a tetrahedral transition state. For deacylation, the thioacyl intermediate was hydrolyzed by a general base-catalyzed mechanism which also appeared to occur in a concerted manner due to high energy barriers.

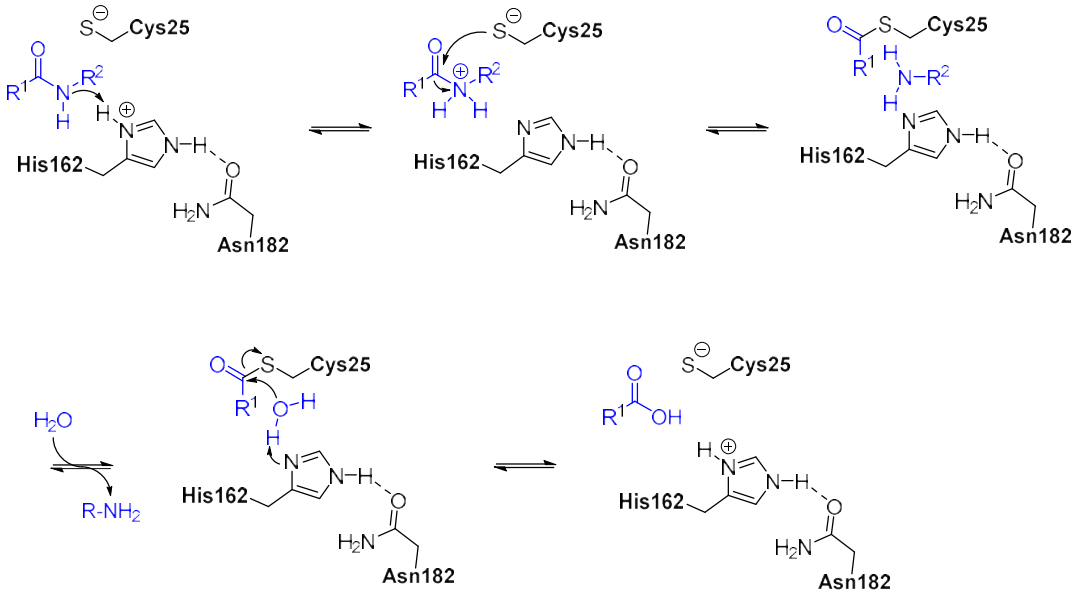

Figure 17: **Proteolysis mechanism of *T. brucei* rhodesain.** The active-site of rhodesain contains three catalytically active residues Cys25, His162, and Asn182, with the catalytically competent form characterized by an imidazolium-thiolate dyad. In the first step, the rhodesain substrate binds to the active-site and protonation of the S1-amide bond occurs. Breaking the amide bond is facilitated by a nucleophilic attack of the Cys25 thiolate on the P1 carbonyl carbon resulting in an uncharged thioacyl intermediate. Subsequent deacylation is triggered by a nucleophilic attack of a polarized water molecule which subsequently releases the product and regenerates the catalytically competent protease.

Rhodesain has come in the focus as an anti-trypanosomal drug target because silencing of rhodesain using siRNA resulted in a decreased growth rate of trypanosomes.[236] In addition, studies on *T. brucei* cultures showed that inhibition of rhodesain by selective inhibitors resulted in a marked effect on trypanosomal survival.[237–239] However, in the case of rhodesain, selective inhibition is complicated by the high similarity of the catalytic domain to other members of the cathepsin L family.[233] This similarity may lead to simultaneous inhibition of human cathepsin L and off-target-related toxicity. Recently solved crystal structures of rhodesain in complex with specific inhibitors can be exploited to rationally design selective covalent inhibitors.[116,231,240,241]

1.3.3 Covalent inhibitors of *T. brucei* rhodesain

Most rhodesain inhibitors are typically for their target class peptidomimetic in nature and possess a covalent inhibition mechanism with potency in the low nanomolar range or even below.[242] Some inhibitors with the clinically investigated carbonyl and nitrile warheads have already been developed (see chapter 1.1.4).[237,243–247] In addition, derived aryl nitriles have also been investigated as covalent-reversible inhibitors of rhodesain.[241,248] However, the majority of rhodesain inhibitors follow a different leitmotif: the long history of Michael acceptor inhibitors suggests that vinylogous C-electrophiles are privileged for addressing the catalytic Cys25 of rhodesain (Table 3).[233] Here, an electron-withdrawing group (EWG=SO_2Ph, $COCH_3$, $COOCH_3$, CN, NO_2) polarizes the sp^2-hybridized system and makes the β-position of the olefin a suitable soft electrophile for reaction with the Cys25 thiolate.[249]

Based on the initial work by CAFFREY et al. who identified a dipeptidic vinyl sulfone (Cbz-Phe-hPhe-VS) as the first irreversible inhibitor of rhodesain, various derived vinyl sulfones have been developed over the last 20 years.[227,231,250–254] Related Michael acceptors such as vinyl ketones, crotonates, cyanoalkenes, and oxoenoates were subsequently involved to modulate the electrophilicity, among which the covalent-reversible inhibition mechanism of nitroalkenes and fluorovinyl sulfones mitigates the toxicity risks of covalent inhibition (see chapter 1.1.3).[116,255–257] In addition to the Michael acceptor-based chemotypes, other alkylating inhibitors such as epoxy esters, bromoisoxazolines, and aziridines have also been investigated, but widely have lower potencies in the triple-digit nanomolar range.[258–262]

Table 3: **Selected covalent *T. brucei* rhodesain inhibitors.** For covalent inhibitors, a red arrow indicates the electrophilic center for the bond formation with the catalytic cysteine residue. For some warhead chemotypes, more than one possible site of bond formation is labeled. *Flurovinyl sulfones and nitroalkene show a unique type of covalent-reversible inhibition.

Chemotype	Structure	K_I	Literature
	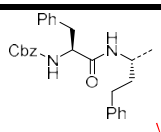		
Vinyl sulfone		5.0 nM	227
Fluorovinyl sulfone		128 nM*	116
Vinyl ketone		0.038 nM	255
Crotonate	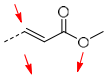	2.0 nM	255
Cyanoalkene		46 nM	255
Nitroalkene		4.2 nM*	257
Oxoenoate	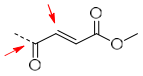	30 nM	256
Epoxy ester	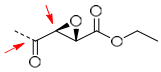	30 nM	258
Aziridine	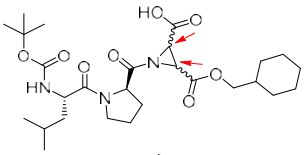	120 nM	262
Bromoisoxazoline	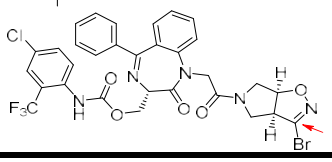	960 nM	259

The aim of this dissertation is the mechanistic investigation of new *T. brucei* rhodesain-targeting warheads with a special focus on covalent-reversible chemotypes. The following four publications are part of the results obtained in this rhodesain project:

(3) Jung, S.[†]; Fuchs, N.[†]; Johe, P.; Wagner, W.; Diehl, E.; Yuliani, T.; Zimmer, C.; **Barthels, F.**; Zimmermann, RA.; Klein, P.; Waigel, W.; Meyr, J.; Opatz, T.; Tenzer, S.; Distler, U.; Räder, HJ.; Kersten, C.; Engels, B.; Klein, J.; Schirmeister, T. Fluorovinyl sulfones and -Sulfonates as Potent Covalent Reversible Inhibitors of the Trypanosomal Cysteine Protease Rhodesain: Structure–Activity Relationship, Inhibition Mechanism, Metabolism, and In Vivo Studies. *J. Med. Chem.* **2021**, *64* (16), 12322–12358.

(4) Klein, P.; **Barthels, F.**; Johe, P.; Wagner, A.; Tenzer, S.; Distler, U.; Le, T. A.; Schmid, P.; Engel, V.; Engels, B.; Hellmich, U. A.; Opatz, T.; Schirmeister, T. Naphthoquinones as Covalent Reversible Inhibitors of Cysteine Proteases—Studies on Inhibition Mechanism and Kinetics. *Molecules* **2020**, *25* (9), 2064.

(5) Klein, P.; Johe, P.; Wagner, A.; Jung, S.; Kühlborn, J.; **Barthels, F.**; Tenzer, S.; Distler, U.; Waigel, W.; Engels, B.; Hellmich, U. A.; Opatz, T.; Schirmeister, T. New Cysteine Protease Inhibitors: Electrophilic (Het)Arenes and Unexpected Prodrug Identification for the Trypanosoma Protease Rhodesain. *Molecules* **2020**, *25* (6), 1451.

(6) Roman, D.; Raguž, L.; Keiff, F.; Meyer, F.; **Barthels, F.**; Schirmeister, T.; Kloss, F.; Beemelmanns, C. Modular Solid-Phase Synthesis of Antiprotozoal Barnesin Derivatives. *Org. Lett.* **2020**, *22* (10), 3744–3748.

1.4 Open-Source Tools for Life Sciences

The open-source movement, which originated with do-it-yourself software developers during the 1960s, has endured the previous decades of life sciences research and has gained significant momentum only in the last 5 years as the paradigm of source code accessibility has shifted towards the public domain for hardware and instrumentation.[263,264] Most developers of scientific instrumentation share their results under an open-source license along with detailed engineering instructions in online repositories or peer-reviewed journals so that a reader can reverse engineer, modify, and further improve this hardware.[265–267]

During this doctoral work, several instrumental challenges have been encountered in the study of covalent *S. aureus* SrtA and *T. brucei* rhodesain inhibitors which could not be solved with the available hardware. To address these synthetic and molecular biology requirements, a combination of computer-aided design (CAD), 3D printing, and microcontrollers have proven successful to expand the functionality of existing hardware or to build new instruments. The combination of these three concepts has become popular only in the last 5 years, due to advances in accessibility, especially in 3D printing and microcontrollers.[268] This can be seen in the publication history of articles containing the keywords "3D-print" and "microcontroller". PubMed shows that articles containing "3D-print" have been increasing exponentially since 2010, while "microcontroller" has been used more and more frequently in the life sciences since 2000 (Figure 18A).[269] The combination of microcontrollers and 3D printing is an even younger trend with just 86 studies indexed by PubMed, the oldest of which is dated 2017 (Figure 18B).[269] This trend was fueled by the foundation of the HardwareX journal in 2016 which exclusively publishes open-source instrumentation.[270]

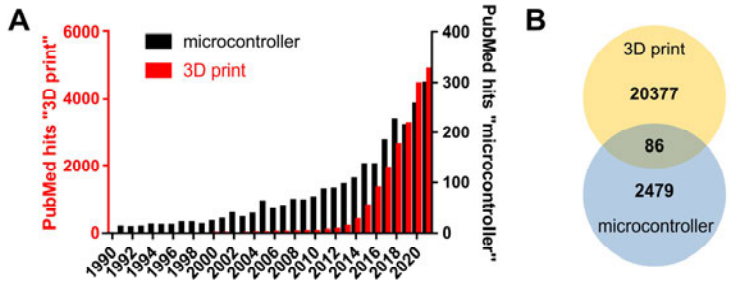

Figure 18: **Publication history of open-source hardware instrumentations for life sciences.** (**A**) Annual publications indexed in the PubMed database for the search terms "3D-print" and "microcontroller" between 1990 and 2021. (**B**) Between 1990 and 2021, 20,377 articles were published with the keyword "3D-print" and 2,479 contained the keyword "microcontroller". Only 86 articles contained the combination of both keywords, with the oldest article dated 2017.

Microcontrollers are at the heart of an open-source instrument because these enable to build low-cost machines that receive input from sensors or generate electrical output to control motors, lights, etc. In principle, microcontrollers are full-fledged board-sized computers that consist of a processor, memory, and inputs resp. outputs for signal transmission. Among the most popular microcontrollers are the Raspberry Pi and the Arduino microcontrollers ESP8266 and ESP32.[271–273] Current microcontrollers are inexpensive (10–20 €) and these can be used both stand-alone and in combination with desktop computers or smartphones. Recently, scientists developed several open-source devices with low-budget microcontrollers yielding highly specialized life science instruments that have already been summarized in reviews.[274–277]

3D printing is a transformative technology that enables the rapid fabrication of structural elements, housings, and chemical or biological labware.[263,278,279] The most commonly used technology, stereolithography, was invented and first patented by CHARLES W. HULL in 1986, with additional patents on adjacent technologies following in the next years.[280–283] 3D printing is an even more recent trend for life sciences, as 3D printers were prohibitively expensive for academic research 10 years ago, but the costs have dramatically decreased since 2013 after the expiration of the original fused deposition modeling (FDM) patents.[264,284] 3D printers based on the FDM principle operate by melting a plastic filament (e.g. PETG) at a heated nozzle and extruding the rapidly solidifying plastic on a printing table so that the 3D object is built layer by layer from the bottom up.[285] A variety of 3D-printed scientific objects have already been developed, published, and summarized in reviews.[278,284–286] In the fields of life sciences, most notable is the extensive pioneering work of JOSHUA M. PEARCE to develop instrumentation for biochemical applications.[287,288] In addition to designing instrumentation to accomplish a functional task in the process of research, 3D-printed models have also proven useful in structure-based research for illustrative purposes.[289] Historically, the physical construction of 3D models of biological structures has played an essential role in elucidating Watson-Crick's DNA double helix and Pauling's α-helix.[290,291]

Due to the emerging synthetic and biological questions during this work, several functional 3D models were designed, printed, and transformed into open-source instrumentations with ESP32 microcontrollers, LED lamps, and stepper motors. An overview of the partially published open-source devices is shown in Figure 19. The following three publications are part of the results obtained in the open-source tools project:

(7) **Barthels, F.**; Hammerschmidt, SJ.; Fischer, TR.; Zimmer, C.; Kallert, K.; Helm, M.; Kersten, C.; Schirmeister, T. A Low-cost 3D-printable Differential Scanning Fluorometer for Protein and RNA Melting Experiments. *HardwareX*, **2022**, *11* (2022), e00256.

(8) **Barthels, F.**; Schirmeister, T.; Kersten, C. BANΔIT: B'-factor Analysis for Drug Design and Structural Biology. *Mol. Inf.* **2020**, *40* (1), 202000144.

(9) **Barthels, F.**; Barthels, U.; Schwickert, M.; Schirmeister, T. FINDUS: An Open-Source 3D Printable Liquid-Handling Workstation for Laboratory Automation in Life Sciences. *SLAS Technol.* **2020**, *25* (2), 190–199.

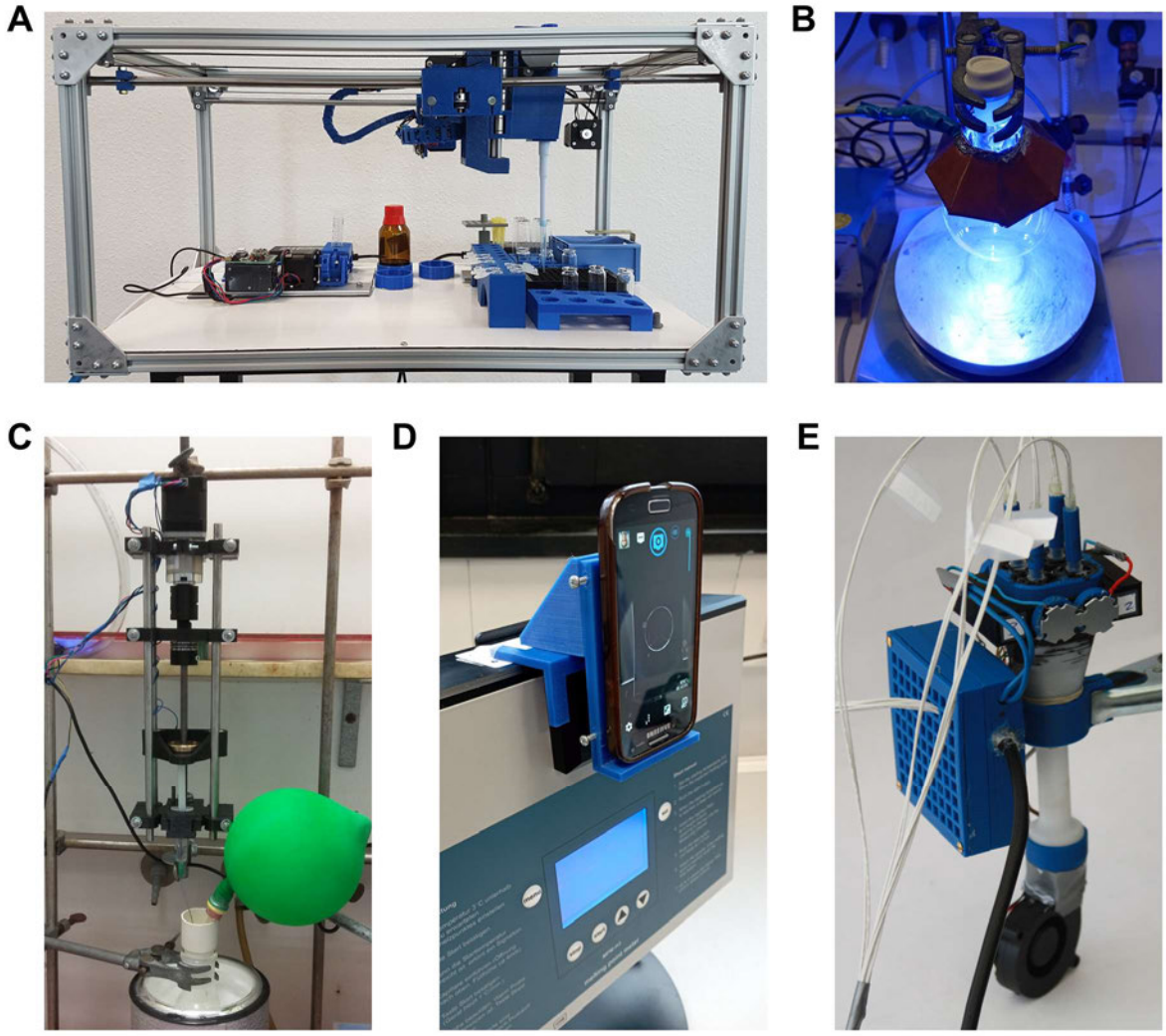

Figure 19: **Open-source instruments designed and constructed during this work.** (**A**) FINDUS liquid-handling system for high-throughput screenings and automated solid-phase peptide synthesis, material costs: 400 €; (**B**) High-power blue light LED reflector umbrella (λ_{em}=430 nm, W_{max}=25 W, ϕ_E=5000 mW) for mounting on round bottom flasks, material costs: 40 €; (**C**) Spindle-driven syringe pump for slow addition of reagents (e.g., 1 µL/min), material costs: 120 €; (**D**) Smartphone adapter for automated melting point meter usage, material costs: 3 € (**E**) openDSF instrument for protein and RNA differential scanning fluorimetry, material costs: 180 €.

2 List of Publications

2.1 Publications as Part of this Doctoral Thesis

2.1.1 Project 1: Design, synthesis, and characterization of covalent *S. aureus* SrtA inhibitors

(1) **Barthels, F.**; Meyr, J.; Hammerschmidt, SJ.; Marciniak, T.; Räder, HJ.; Ziebuhr, W.; Engels, B.; Schirmeister, T. 2-Sulfonylpyrimidines as Privileged Warheads for the Development of S. Aureus Sortase A Inhibitors *Front. Mol. Biosci.* **2022**, *8*, 1284.

(2) **Barthels, F.**; Marincola, G.; Marciniak, T.; Konhäuser, M.; Hammerschmidt, S.; Bierlmeier, J.; Distler, U.; Wich, P. R.; Tenzer, S.; Schwarzer, D.; Ziebuhr, W.; Schirmeister, T. Asymmetric Disulfanylbenzamides as Irreversible and Selective Inhibitors of Staphylococcus Aureus Sortase A. *ChemMedChem* **2020**, *15* (10), 839–850.

Contributions as part of this doctoral thesis: Within the two publications of this project, 68 final compounds were synthesized as potential sortase inhibitors which were evaluated for their inhibition of *S. aureus* SrtA and selectivity to other cysteine proteases. Furthermore, enzymatic, mass spectrometric, and biophysical techniques were employed to investigate the covalent mechanism of these novel inhibitors.

2.1.2 Project 2: Mechanistic investigations of covalent-reversible *T. brucei* rhodesain inhibitors

(3) Jung, S.[†]; Fuchs, N.[†]; Johe, P.; Wagner, W.; Diehl, E.; Yuliani, T.; Zimmer, C.; **Barthels, F.**; Zimmermann, RA.; Klein, P.; Waigel, W.; Meyr, J.; Opatz, T.; Tenzer, S.; Distler, U.; Räder, HJ.; Kersten, C.; Engels, B.; Klein, J.; Schirmeister, T. Fluorovinyl sulfones and -Sulfonates as Potent Covalent Reversible Inhibitors of the Trypanosomal Cysteine Protease Rhodesain: Structure–Activity Relationship, Inhibition Mechanism, Metabolism, and In Vivo Studies. *J. Med. Chem.* **2021**, *64* (16), 12322–12358.

(4) Klein, P.; **Barthels, F.**; Johe, P.; Wagner, A.; Tenzer, S.; Distler, U.; Le, T. A.; Schmid, P.; Engel, V.; Engels, B.; Hellmich, U. A.; Opatz, T.; Schirmeister, T. Naphthoquinones as Covalent Reversible Inhibitors of Cysteine Proteases—Studies on Inhibition Mechanism and Kinetics. *Molecules* **2020**, *25* (9), 2064.

(5) Klein, P.; Johe, P.; Wagner, A.; Jung, S.; Kühlborn, J.; **Barthels, F.**; Tenzer, S.; Distler, U.; Waigel, W.; Engels, B.; Hellmich, U. A.; Opatz, T.; Schirmeister, T. New Cysteine Protease Inhibitors: Electrophilic (Het)Arenes and Unexpected Prodrug Identification for the Trypanosoma Protease Rhodesain. *Molecules* **2020**, *25* (6), 1451.

(6) Roman, D.; Raguž, L.; Keiff, F.; Meyer, F.; **Barthels, F.**; Schirmeister, T.; Kloss, F.; Beemelmanns, C. Modular Solid-Phase Synthesis of Antiprotozoal Barnesin Derivatives. *Org. Lett.* **2020**, *22* (10), 3744–3748.

Contributions as part of this doctoral thesis: Within the four publications of this project, enzymatic and mass spectrometric methodologies were used to investigate the covalent-reversible mechanism of novel *T. brucei* rhodesain inhibitors.

2.1.3 Project 3: Development of open-source tools for medicinal chemistry applications

(7) **Barthels, F.**; Hammerschmidt, SJ.; Fischer, TR.; Zimmer, C.; Kallert, K.; Helm, M.; Kersten, C.; Schirmeister, T. A Low-cost 3D-printable Differential Scanning Fluorometer for Protein and RNA Melting Experiments. *HardwareX*, **2022**, *11* (2022), e00256.

(8) **Barthels, F.**; Schirmeister, T.; Kersten, C. BANΔIT: B'-factor Analysis for Drug Design and Structural Biology. *Mol. Inf.* **2020**, *40* (1), 202000144.

(9) **Barthels, F.**; Barthels, U.; Schwickert, M.; Schirmeister, T. FINDUS: An Open-Source 3D Printable Liquid-Handling Workstation for Laboratory Automation in Life Sciences. *SLAS Technol.* **2020**, *25* (2), 190–199.

Contributions as part of this doctoral thesis: Within the three publications of this project, selected hard- and software tools to assist medicinal chemistry research were conceptualized, built, and validated with exemplary applications.

2.2 Publications beyond this Doctoral Thesis

(10) Amiri Rudbari, H.; Kordestani, N.; Cuevas-Vicario, J.; Zhou, M.; Efferth, T.; Correia, I.; Schirmeister, T.; **Barthels, F.**; Enamullah, M.; Fernandes, A.; Micale, N. Investigation of the Influence of Chirality and Halogen Atoms on the Anticancer Activity of Enantiopure Palladium(II) Complexes Derived from Chiral Amino-alcohol Schiff Bases and 2-Picolylamine. *New. J. Chem.* **2022**, *accepted.*

(11) Volynets, GP; **Barthels, F**; Hammerschmidt, SJ; Moshynets, OV; Lukashov, SS; Starosyla, SA; Vyshniakova, HV; Iungin, OS; Bdzhola, VG; Prykhod'ko, AO; Syniugin, AR; Sapelkin, VM; Yarmoluk, SM; Schirmeister, T. Identification of Novel Small-molecular Inhibitors of Staphylococcus Aureus Sortase A Using Hybrid Virtual Screening. *J. Med. Chem.* **2022**, *submitted*.

(12) Maus, H.[†]; **Barthels, F.**[†]; Hammerschmidt, SJ.; Kopp, K.; Millies, B.; Gellert, A.; Ruggieri, A.; Schirmeister, T. SAR of Novel Benzothiazoles Targeting an Allosteric Pocket of DENV and ZIKV NS2B/NS3 Proteases. *Bioorg. Med. Chem.* **2021**, *47* (2021), 116392.

(13) Millies, B.; von Hammerstein, F.; Gellert, A.; Hammerschmidt, S.; **Barthels, F.**; Göppel, U.; Immerheiser, M.; Elgner, F.; Jung, N.; Basic, M.; Kersten, C.; Kiefer, W.; Bodem, J.; Hildt, E.; Windbergs, M.; Hellmich, U. A.; Schirmeister, T. Proline-Based Allosteric Inhibitors of Zika and Dengue Virus NS2B/NS3 Proteases. *J. Med. Chem.* **2019**, *62* (24), 11359–11382.

(14) Schmohl, L.; Bierlmeier, J.; von Kügelgen, N.; Kurz, L.; Reis, P.; **Barthels, F.**; Mach, P.; Schutkowski, M.; Freund, C.; Schwarzer, D. Identification of Sortase Substrates by Specificity Profiling. *Bioorg. Med. Chem.* **2017**, *25* (18), 5002–5007.

3 Covalent Inhibitors of *Staphylococcus aureus* Sortase A

3.1 2-Sulfonylpyrimidines as Privileged Warheads for the Development of *S. aureus* Sortase A Inhibitors

3.1.1 Context, Project Summary, and own Contribution

Recently, JAUDZEMS et al. performed a high-throughput screening identifying 28 irreversible inhibitors of SrtA.[202] One of these compounds *N*-(2-benzylphenyl)-5-chloro-2-(methylsulfonyl)pyrimidine-4-carboxamide attracted our interest because 2-sulfonylpyrimidines were previously found to be mild and selective warheads for the reaction with non-catalytic and protonated cysteine residues.[292–295] However, the molecular background of this behavior was not investigated until now. The unique structural properties of *S. aureus* SrtA (see chapter 1.2.3) appear to favor such covalent-irreversible chemotypes, however, rational design of covalent SrtA warheads using quantum chemical methods has not yet been attempted because the flexibility of the enzyme makes it difficult to predict the inhibitor-binding enzyme conformation.[296] In this study, by using methods from molecular biology and quantum chemical calculations, we aimed to elucidate the underlying reaction mechanism which might help to explain the mild yet efficient reactivity towards protonated thiols, and beyond SrtA, 2-sulfonylpyrimidines might be applied to target other low-nucleophilic and non-catalytic cysteines in future drug design campaigns.

By the synthesis of 28 diverse 2-sulfonylpyrimidines and structure-activity relationships, we were able to increase the potency of JAUDZEMS' parent compound by a factor of 32 (k_{2nd}=870 to 28,185 $M^{-1}min^{-1}$) which subsequently was confirmed using ESI-MS and MALDI-TOF MS as a covalent modifier of the catalytic Cys184. Comprehensive enzymatic, chemical kinetics, and computational studies indicated that the isoform of the enzyme addressed by this warhead must be different from the catalytically active imidazolium-thiolate species. This fits well with our results of protease selectivity assay which showed that 2-sulfonylpyrimidines do not inhibit cathepsin-like proteases with an inherent thiolate nucleophile. In solution QM calculations revealed that the warhead reaction involves a ternary transition state consisting of a 2-sulfonylpyrimidine, a protonated thiol, and a conjugated base moiety. Using molecular docking and pH-dependent inhibition assays, we showed that this base moiety is likely represented by the catalytic His120 residue in the SrtA context. In summary, we demonstrated that the 2-sulfonylpyrimidine warhead is suitable for the selective inhibition of *S. aureus* SrtA, and after adjustment of the inhibitor recognition sequence, it might be potentially useful for inhibition of other disease-related proteins with conserved protonated cysteine residues.

Own contributions: Synthesis of all inhibitors, Sortase A inhibition assays, Protease selectivity assays, ESI mass spectrometry, MALDI-TOF mass spectrometry, Cysteine reactivity assays, Molecular modeling & Writing of the manuscript.

Contributions from other authors: Protein expression and purification, Quantum chemical investigations & Writing of the chapter "Theoretical Investigations".

This work has been published in: Frontiers in Molecular Biosciences (impact factor: 5.24).

The appended 'Supporting Information' represents an abridged version. The full version can be accessed online at doi: 10.3389/fmolb.2021.804970.

3.1.2 Publication

The following publication quoted (within “”) from page 44 to page 98 is exactly the same as the manuscript cited on page 43:”

frontiers in Molecular Biosciences

ORIGINAL RESEARCH
published: 03 January 2022
doi: 10.3389/fmolb.2021.804970

2-Sulfonylpyrimidines as Privileged Warheads for the Development of *S. aureus* Sortase A Inhibitors

Fabian Barthels[1], *Jessica Meyr*[2], *Stefan J. Hammerschmidt*[1], *Tessa Marciniak*[3], *Hans Joachim Räder*[4], *Wilma Ziebuhr*[3], *Bernd Engels*[2] *and Tanja Schirmeister*[1]*

[1]*Institute for Pharmaceutical and Biomedical Sciences, Johannes Gutenberg-University, Mainz, Germany,* [2]*Institute of Physical and Theoretical Chemistry, Julius-Maximilians-University of Würzburg, Würzburg, Germany,* [3]*Institute for Molecular Infection Biology, Julius-Maximilians-University of Würzburg, Würzburg, Germany,* [4]*Max Planck Institute for Polymer Research, Mainz, Germany*

Staphylococcus aureus is one of the most frequent causes of nosocomial and community-acquired infections, with emerging multiresistant isolates causing a significant burden to public health systems. We identified 2-sulfonylpyrimidines as a new class of potent inhibitors against *S. aureus* sortase A acting by covalent modification of the active site cysteine 184. Series of derivatives were synthesized to derive structure-activity relationship (SAR) with the most potent compounds displaying low micromolar K_I values. Studies on the inhibition selectivity of homologous cysteine proteases showed that 2-sulfonylpyrimidines reacted efficiently with protonated cysteine residues as found in sortase A, though surprisingly, no reaction occurred with the more nucleophilic cysteine residue from imidazolinium-thiolate dyads of cathepsin-like proteases. By means of enzymatic and chemical kinetics as well as quantum chemical calculations, it could be rationalized that the S_NAr reaction between protonated cysteine residues and 2-sulfonylpyrimidines proceeds in a concerted fashion, and the mechanism involves a ternary transition state with a conjugated base. Molecular docking and enzyme inhibition at variable pH values allowed us to hypothesize that in sortase A this base is represented by the catalytic histidine 120, which could be substantiated by QM model calculation with 4-methylimidazole as histidine analog.

Keywords: covalent inhibition, sortase, quantum mechanics, anti-virulence, drug discovery

OPEN ACCESS

Edited by:
Jerônimo Lameira,
Federal University of Pará, Brazil

Reviewed by:
Martin D. Witte,
University of Groningen, Netherlands
Steven Verhelst,
KU Leuven, Belgium

***Correspondence:**
Tanja Schirmeister
schirmei@uni-mainz.de

Specialty section:
This article was submitted to Biological Modeling and Simulation, a section of the journal Frontiers in Molecular Biosciences

Received: *29 October 2021*
Accepted: *03 December 2021*
Published: *03 January 2022*

Citation:
Barthels F, Meyr J, Hammerschmidt SJ, Marciniak T, Räder H-J, Ziebuhr W, Engels B and Schirmeister T (2022) 2-Sulfonylpyrimidines as Privileged Warheads for the Development of S. aureus Sortase A Inhibitors. Front. Mol. Biosci. 8:804970. doi: 10.3389/fmolb.2021.804970

1 INTRODUCTION

The emergence of bacterial strains resistant to antibiotic therapy is one of the greatest medical challenges of our time. In addition to conventional antibiotics, there are efforts to develop drugs that can interfere with the virulence mechanisms of bacteria to reduce their pathogenicity (Allen et al., 2014; Dickey et al., 2017). The cysteine transpeptidase sortase A (SrtA) has been discussed as an anti virulence drug target for nearly 20 years since SrtA mediates the attachment of virulence associated surface proteins to the bacterial cell wall (Perry et al., 2002). It was shown that the *S. aureus* ΔSrtA knock out mutant is attenuated in mouse infection models compared to the wild type (Mazmanian et al., 2000; Weiss et al., 2004). Neither genetic deletion (Mazmanian et al., 1999) nor selective chemical inhibition (Cascioferro et al., 2014; Zhang et al., 2014; Mu et al., 2018) of *S. aureus* SrtA was found to affect the growth properties of bacterial cells, thus deducing a lower selective pressure for resistance development compared to bactericidal antibiotics.

At the bacterial cell wall, virulence associated surface proteins with C terminal LPXTG tagged sorting signals (e.g., protein A, fibronectin binding proteins, clumping factors) are cleaved between threonine and glycine by the membrane anchored SrtA and subsequently ligated to the pentaglycine tail of the peptidoglycan layer to yield covalent attachment of these surface proteins (Tsompanidou et al., 2012; Schneewind and Missiakas, 2019). The fact that SrtA plays a key role in the pathogenesis of *S. aureus* and the enzyme is drug accessible on the outside of the bacterial cell membrane makes SrtA seemingly a well druggable target for the development of anti virulence agents (Cascioferro et al., 2015).

However, the privileged position of SrtA is protected from pharmacological manipulation by several structural and biochemical properties of this enzyme. *S. aureus* SrtA is an eight stranded β barrel protein with three conserved catalytic residues: His^{120}, Cys^{184}, and Arg^{197}, each of which cannot be mutated without disrupting enzymatic functionality (Ton That et al., 2002; Bentley et al., 2008; Clancy et al., 2010). Three SrtA characteristics were identified that complicate the development of small molecule SrtA inhibitors:

1) The catalytic Cys^{184} is "reversely protonated," which means it does not form a thiolate imidazolium pair under physiological conditions (<0.1%) and is therefore significantly less nucleophilic than structurally related cysteine proteases such as enzymes of the papain family (Ilangovan et al., 2001; Frankel et al., 2005). Hence, covalent modification of the catalytic Cys^{184} is inefficient with cysteine protease specific warheads such as Michael acceptors and similar electrophiles (Ton That and Schneewind, 1999; Scott et al., 2002; Connolly et al., 2003; Kruger et al., 2004a; Liew et al., 2004).
2) The active site is predominantly defined by the intrinsic flexibility of the β6/7 and β7/8 loops (Kappel et al., 2012). Binding of the LPXTG substrate leads to strong protein rigidization, observable from the NMR structure, and is therefore entropically penalized, which is expressed in the substrates' high K_M value of 5.5 mM (Kruger et al., 2004b; Suree et al., 2009a).
3) To compensate for the low activity and the high KM value, both the LPXTG and the pentaglycine substrate are co localized with the SrtA enzyme at the bacterial outer membrane (Ton That et al., 1999). Spatial co localization yields high local concentrations, which cannot easily be competed with reversible competitive inhibitors *in cellulo*. Hence, most active compounds were found to be irreversible covalent inhibitors containing an electrophilic warhead that reacts with the active site Cys^{184} of SrtA, such as disulfides, benzisothiazolinones, thiadiazolidine 3,5 diones, and 1,3,4 thiadiazoles (Maresso et al., 2007; Suree et al., 2009b; Zhulenkovs et al., 2014; Chan et al., 2017; Wehrli et al., 2019; Barthels et al., 2020; Yang et al., 2020).

Previously, Jaudzems et al. have performed a high throughput screening with a library of 50,000 compounds and identified 27 novel covalent modifiers of SrtA (Jaudzems et al., 2020). One of these inhibitors, parent compound sulfonylpyrimidine **4** (**Table 1**), showed 97% inhibition after 16 h of incubation with 100 μM inhibitor. The irreversibility of the reaction was confirmed by 2D ^{15}N ^{1}H HSQC NMR, however, characterization of the inhibition kinetics and detection of the covalent adduct were still to be determined.

TABLE 1 | Inhibition constants (K_I, k_{inact}, k_{2nd}) of the compounds **4** and **5a–k** for *S. aureus* SrtA; n. i. <20% inhibition at 100 μM.

Cpd.	Structure	K_I [μM]	k_{inact} [s^{-1}]	k_{2nd} [$M^{-1}min^{-1}$]
4	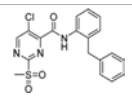	47.1 ± 15.7	0.00065 ± 0.00007	870 ± 170
5a	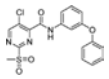	57.6 ± 3.55	0.00774 ± 0.00007	8,088 ± 464
5b	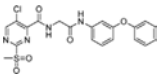	42.37 ± 4.62	0.00082 ± 0.00004	1,175 ± 67
5c			n. i.	
5d	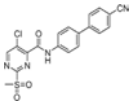		n. i.	
5f			n. i.	
5g	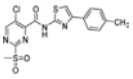		n. i.	
5h			n. i.	
5i			n. i.	
5k			n. i.	

The use of 2 sulfonylpyrimidines as electrophilic building blocks has been documented in the synthesis of heterocyclic compounds for nearly 100 years (Sprague and Johnson, 1936). In a more biological context, heteroaromatic methyl sulfones, such as 2 methylsulfonyl benzothiazole, are well established as bioorthogonal reagents for the selective modification of non catalytic cysteine residues (Zhang et al., 2012). Regardless of the knowledge of this potential cysteine

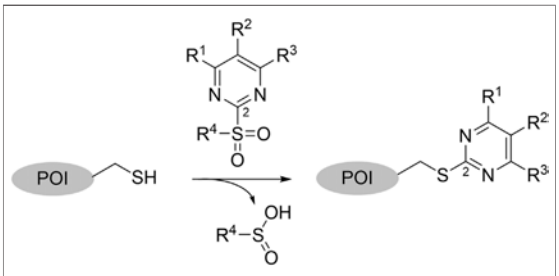

FIGURE 1 | Covalent Reaction of 2-sulfonylpyrimidines. Reaction mechanism of 2-sulfonylpyrimidines with cysteine residues of a respective protein of interest (POI) yielding a covalent 2-pyrimidyl cysteine adduct. The electrophilic C-2 atom was highlighted with a small numeral "2."

reactivity, 2 sulfonylpyrimidines have been previously considered almost exclusively as reversible modulators of pharmacological targets during drug design campaigns. Besides the studies by Jaudzems et al., 2 sulfonylpyrimidines have just recently come into the spotlight for mechanistic studies of irreversible inhibition. In the last few years, four independent studies identified 2 sulfonylpyrimidines as covalent and pharmacologically active modifiers of the following disease associated protein targets: p53 (Bauer et al., 2016), kinesin HSET (Förster et al., 2019), succinate dehydrogenase subunit B (Li L. et al., 2017), and *S. mansoni* thioredoxin glutathione reductase (Lyu et al., 2020). All these targets share a covalently addressed cysteine residue, that is not catalytically activated and thus predominantly protonated under physiological conditions (Hallenbeck et al., 2017).

A preference for the reactivity with protonated thiols is also reflected in the ability of sulfonylpyrimidine mediated glutathione depletion in a cellular context (Bauer et al., 2016; Wilke et al., 2018). However, compared to other electrophilic warheads, which react quantitatively with protonated cysteine residues under physiological conditions, the second order rate constant (60 200 M ^{1}min ^{1}) is lower by a factor of 10 1,000 and thus 2 sulfonylpyrimidines may have the potential to be mild enough to achieve favorable target *vs.* off target selectivity (Schoonen et al., 2005; Böhme et al., 2009; Chipinda et al., 2010; Wilke et al., 2018).

2 Sulfonylpyrimidines react with thiols under nucleophilic aromatic substitution (S_NAr) to form the respective pyrimidyl thioether and release the corresponding sulfinic acid (Bauer et al., 2016). Electron withdrawing substituents on the aromatic ring (R^1 R^3) increase the polarization of the electrophilic C 2 atom and generally lead to higher reaction rates (Buděšínský and Vavřina, 1972). A schematic representation of the reaction mechanism between 2 sulfonylpyrimidines and proteinogenic cysteine residues is shown in **Figure 1**.

In this work, evidence of the covalent modification by 2 sulfonylpyrimidines, as well as the characterization of the SrtA inhibition kinetics were conducted in following up on the previously reported parent compound **4** (Jaudzems et al., 2020). Further, by using methods from molecular biology, enzyme kinetics, and quantum chemical calculations, we

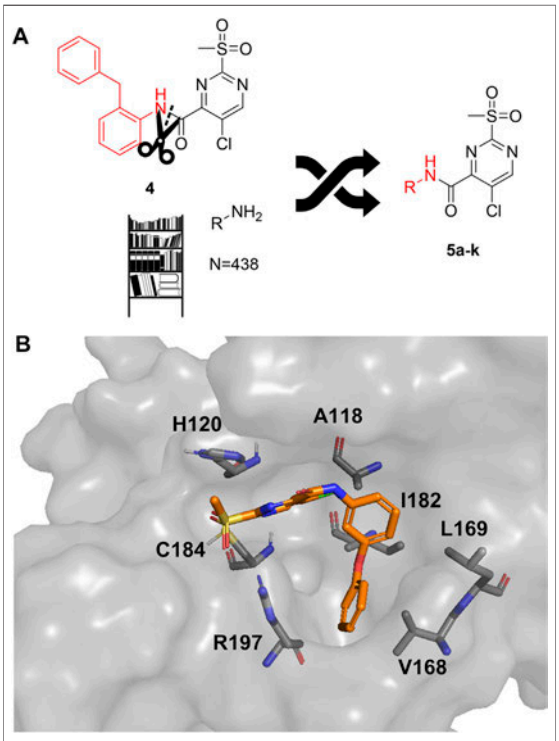

FIGURE 2 | Optimization strategy overview. **(A)** Virtual synthesis strategy to optimize the inhibition properties of parent compound **4** by synthesis of the sulfonylpyrimidines **5a–k**. Carboxylic acid **5c** was coupled *in silico* with 438 amines and the resulting amides were docked into a receptor of the SrtA active site. Subsequently, virtual screening hits **5a–k** were synthesized. **(B)** Docking pose of virtual screening hit **5a** with the labeling of interacting residues in the SrtA binding pocket (pdb: 2kid).

aimed to elucidate the underlying reaction mechanism of the 2 sulfonylpyrimidine warhead with cysteine residues, which might help to explain the mild yet efficient reactivity towards protonated thiols.

2 RESULTS AND DISCUSSION

2.1 Kinetic Characterization and Inhibitor Optimization Strategy

To evaluate the inhibition potency of the parent sulfonylpyrimidine **4**, this compound was tested by means of a fluorometric enzyme assay with recombinantly expressed *S. aureus* SrtA (Schmohl et al., 2017b) and Abz LPETG Dap (Dnp) OH as substrate. Parent compound **4** was found to act as a time dependent and irreversible inhibitor, which is in agreement with the literature data (Lit.: 97% inhibition after 16 h of incubation with 100 µM inhibitor; Jaudzems et al., 2020). To verify the irreversible mode of inhibition, we determined the maximum inactivation rate k_{inact}, the

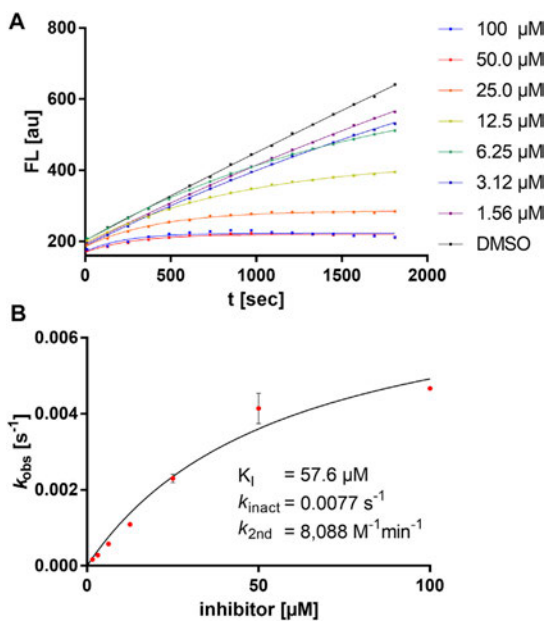

FIGURE 3 | Kinetic characterization of compound **5a**. **(A)** Fluorometric assay with compound **5a** showing time-dependent enzyme inhibition with hyperbolic substrate conversion plots. The fluorescence was recorded for 30 min every 30 s. For clarity, only every fourth data point is shown. **(B)** k_{obs} vs. (I) for the determination of inhibition constants (K_I, k_{inact}).

dissociation constant of the reversible enzyme inhibitor complex K_I, and the second order rate of inhibition k_{2nd}. For compound **4**, a k_{inact} = 0.00065 s^{-1} was found, which is very low compared to other covalent SrtA inhibitors (Chan et al., 2017; Barthels et al., 2020; Jaudzems et al., 2020). The K_I value was as high as 47.1 µM, thus, we decided to increase the potency of the sulfonylpyrimidine inhibitors by rational optimization before conducting mechanistic studies of this new inhibitor class.

In order to increase the affinity of the sulfonylpyrimidine inhibitors, a first strategy was applied to optimize the recognition sequence while maintaining the warhead functionality. Previously, we have performed a recognition sequence optimization study on disulfanylbenzamide SrtA inhibitors (Barthels et al., 2020). Therefore, we designed and tested two chimeric inhibitors (**5b,c Supplementary Figure S1**). In general, sulfonylpyrimidines were synthesized based on multi step procedures according to literature protocols. Detailed synthesis instructions can be found in the supporting information. Briefly, 2 (methanesulfanyl)pyrimidinecarboxylic acids (**2a d**) were coupled to various commercially available or synthesized amines (**1a o**) in the presence of 2 (1*H* benzotriazole 1 yl) 1,1,3,3 tetramethylaminium tetrafluoroborate (TBTU) to provide the inhibitor scaffold precursors (**3a z**). The potential sulfonylpyrimidine inhibitors (**4, 5a k, 6a n, 7a e**) were subsequently synthesized by oxidation with potassium peroxymonosulfate (Webb, 1994).

TABLE 2 | Inhibition constants (K_I, k_{inact}, k_{2nd}) of the compounds **6a–n** for *S. aureus* SrtA; n. i. <20% inhibition at 100 µM.

Cpd.	Structure	K_I [µM]	k_{inact} [s^{-1}]	k_{2nd} [$M^{-1}min^{-1}$]
6a	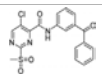	29.6 ± 9.39	0.00986 ± 0.00128	20,785 ± 4,074
6b		47.5 ± 4.62	0.00578 ± 0.00033	7,305 ± 294
6c		78.8 ± 9.92	0.00864 ± 0.00092	6,593 ± 243
6d		60.3 ± 6.40	0.00618 ± 0.00025	6,181 ± 489
6e		—	—	882 ± 43
6f		—	—	588 ± 48
6g		n. i.		
6h		n. i.		
6i		n. i.		
6k		n. i.		
6l		n. i.		
6m	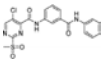	n. i.		
6n		n. i.		

The chimeric 3 phenoxyphenyl glycine derivative (**5b**) showed slightly higher overall inhibition potency (k_{2nd} = 1,175 $M^{-1}min^{-1}$) than parent compound **4** (**Table 1**). In contrast, the adapted fragment inhibitor (**5c**) showed no SrtA inhibition even at a final inhibitor concentration of 300 µM. From the inhibition results, we concluded that the binding geometry of the previously optimized disulfanylbenzamide recognition sequence (**5b**, **Supplementary Figure S1**) is probably not optimally transferable to the novel sulfonylpyrimidine derivates because of the different aromatic substitution pattern of the warheads' electrophilic center (ortho vs. meta).

TABLE 3 | Inhibition constants (K_I, k_{inact}, k_{2nd}) of the compounds **7a–e** for *S. aureus* SrtA; n. i. <20% inhibition at 100 μM.

Cpd.	Structure	K_I (μM)	k_{inact} (s^{-1})	k_{2nd} ($M^{-1}min^{-1}$)
7a	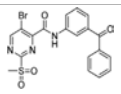	32.0 ± 5.07	0.01493 ± 0.00132	28,185 ± 2,117
7b	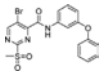	55.9 ± 11.6	0.01285 ± 0.00147	13,998 ± 1,462
7c	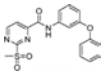	33.8 ± 11.2	0.00239 ± 0.00047	4,364 ± 596
7d	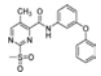	—	—	1,204 ± 139
7e	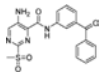		n. i.	

As a second attempt, we tried an *in silico* supported optimization approach (**Figure 2A**): Using virtual synthesis, we combined the warhead function of parent compound **4** with our in house inventory of aliphatic and aromatic amines (N = 438). Subsequently, molecular docking to the binding pocket of SrtA was carried out using the Glide docking algorithm (Friesner et al., 2004). Potential binders were discriminated in this virtual screening approach by a distance scan of the electrophilic C 2 atom in the pyrimidine ring from the catalytic Cys^{184} in the binding pocket. Structures that showed a distance of less than 5 Å were sorted according to their docking score and manual inspection of the binding pose. The seven best sulfonylpyrimidines were synthesized for *in vitro* evaluation (**5a,d k**).

The exchange of the 2 benzylaniline fragment (**4**) for the 3 phenoxyaniline fragment (**5a**) led to a significant improvement of the overall inhibition potency by a factor of 10 (**Table 1**, k_{2nd} = 8,088 $M^{-1}min^{-1}$). The docking pose of **5a** with putative interactions in the SrtA binding pocket can be seen in **Figure 2B**. Here, the sulfonylpyrimidine warhead is positioned orthogonally to the axis of the three catalytic residues (His^{120}, Cys^{184}, Arg^{197}) and is thus reasonably positioned for a nucleophilic attack of the Cys^{184} thiol to the pyrimidine ring. The 3 phenoxyaniline moiety fits well to the L shaped binding pocket of SrtA and shows interactions with the hydrophobic residues (Ala^{118}, Val^{168}, Leu^{169}, Ile^{182}) in the S3/S4 substrate binding pockets.

Exemplarily, the substrate conversion plot with time dependent inhibition is shown in **Figure 3**. The apparent first order rate constant (k_{obs}) in the presence of inhibitor **5a** varied hyperbolically with the concentration of the inhibitor. A limiting value was approached asymptotically at higher inhibitor concentrations indicating two step mechanism inactivation kinetics.

The other virtual screening hits (**5d k**) were also assayed using the fluorometric enzyme assay at an inhibitor concentration of 100 μM but showed no measurable inhibition of SrtA (**Table 1**). For achieving warhead selectivity towards off targets, such a strong dependence on a recognition sequence for a covalent inhibitor might be desirable (Copeland, 2005; Awoonor Williams and Rowley, 2018). The inhibition data and structures of the sulfonylpyrimidines **4** and **5a k** are summarized in **Table 1**.

2.2 SAR Study Around Hit Compound 5a

The subtle structural transformation from 2 benzylaniline derivate (**4**) to 3 phenoxyaniline derivate (**5a**) resulted in a tenfold increase of the inhibitory potency (k_{2nd} = 870 vs. 8,088 $M^{-1}min^{-1}$), hence, we hypothesized that the inhibitor's recognition sequence can be further systematically optimized. Therefore, we conducted a SAR study around virtual screening hit **5a**. The inhibition results of the synthesized compounds **6a n** are shown in **Table 2**.

Six out of 13 sulfonylpyrimidines (**6a f**) did inhibit SrtA in the fluorometric enzyme assay, but with varying potency. Strikingly, we observed a drop in SrtA inhibition for most modifications on the 3 phenoxyaniline motif. These structural "activity cliffs" highlight the importance of the accurate positioning of the warhead towards the catalytic Cys^{184} for a successful covalent reaction (Bajorath, 2019).

Only small changes in inhibition potency were observed upon changes of the aryl ether connecting group of compound **5a** to the analogous aryl thioether (**6b**) or the methylene derivate (**6d**). However, the exchange to a ketone connecting unit (**6a**) resulted in a significant increase of inhibition potency which might be due to beneficial interactions with Arg^{197}. Based on the k_{2nd} value, compound **6a** (k_{2nd} = 20,785 $M^{-1}min^{-1}$) appeared to be 2.5 fold more potent than virtual screening hit **5a**. Alteration of the *meta* substitution pattern resulted in the complete abolition of inhibition for the *ortho* (**6g**) and *para* (**6h**) derivatives. After truncation of the connecting group to the biphenyl derivative (**6f**), only minor inhibition potency remained (k_{2nd} = 588 $M^{-1}min^{-1}$). On the other hand, with connector elongation to the benzyl ether (**6k**) or an amide derivate (**6m**), the inhibition was completely abolished.

Modifications of the terminal phenyl ring were well tolerated in the case of an exchange to an aliphatic cyclohexyl ring (**6c**, k_{2nd} = 6,593 $M^{-1}min^{-1}$) but resulted in a severe loss of inhibition when downsized to a methoxy group (**6e**, k_{2nd} = 882 $M^{-1}min^{-1}$). Other transformations such as amide inversion at the sulfonylpyrimidine ring (**6i**), rigidization to a benzofuran derivative (**6l**), or decyclization of the central phenyl ring (**6n**) resulted in complete loss of inhibition. For derivatives **6e,f**, two step kinetics could not be confirmed because of a lacking k_{obs} saturation at higher inhibitor concentrations. The K_I values of these compounds were estimated to be significantly higher than 100 μM. In these cases, the inhibition potency (k_{2nd} value) was determined by Lineweaver Burk linearization.

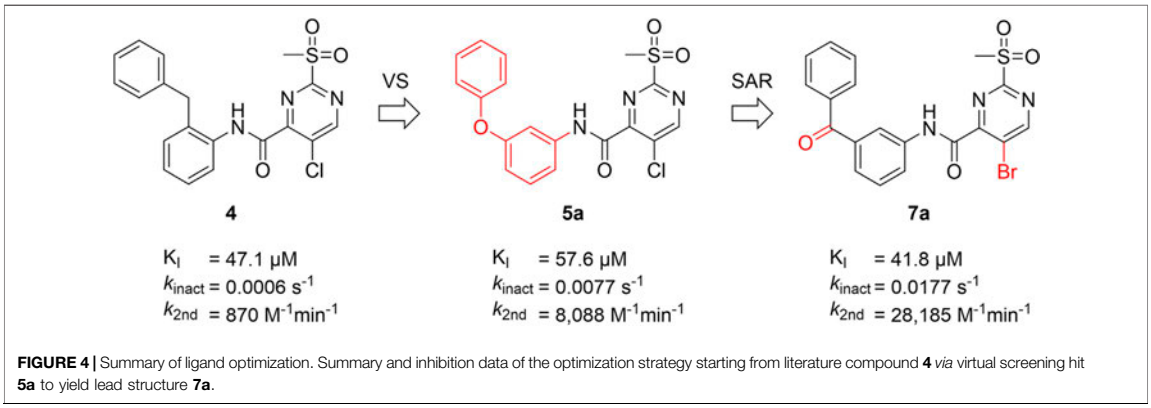

FIGURE 4 | Summary of ligand optimization. Summary and inhibition data of the optimization strategy starting from literature compound **4** *via* virtual screening hit **5a** to yield lead structure **7a**.

In addition to the modification of the recognition sequence, the chlorine substituent on the sulfonylpyrimidine ring was also varied and derivatives **7a e** were synthesized (**Table 3**).

A positive correlation was found between the intensity of the electron withdrawing properties of the substituents and the inhibition potency: Br (**7b**) > Cl (**5a**) > H (**7c**) > CH_3 (**7d**) >> NH_2 (**7e**). The increase in inhibition was mainly caused by an increase in the k_{inact} value and was not due to affinity changes for the target (K_I value). The electronic effects of the substituents on the pyrimidine ring predominantly influenced the warhead reactivity, which can be quantified and is discussed by the analysis of the Hammett constants (**Section 2.7**). In summary, starting from virtual screening hit **5a**, two SAR transformations proved to be beneficial: Conversion of the aryl ether connecting group to the ketone derivative **6a** and the halogen exchange at the pyrimidine ring from chlorine to bromine derivative **7b**. Subsequently, the two modifications were combined and inhibitor **7a** was synthesized. Considering the k_{2nd} value, **7a** was the most potent irreversible inhibitor of this study (k_{2nd} = 28,185 M ^{1}min ^{1}). The optimization strategy is summarized in **Figure 4**.

2.3 Identification of Covalent Adducts by Mass Spectrometry

For electron deficient heteroaromatic compounds, S_NAr reactions often occur at the aromatic carbon atom with the substituent representing the best leaving group (Rohrbach et al., 2019). For 2 sulfonylpyrimidines, this is generally the sulfonyl group (Buděšínský and Vavřina, 1972; Bauer et al., 2016; Förster et al., 2019). However, the scaffold used here also carried a halogen substituent which, depending on the reaction conditions, might represent the actual leaving group during organic synthesis (Buděšínský and Vavřina, 1972). Thus, we determined the point of nucleophilic thiol attack by means of ESI mass spectrometry between the reaction of compound **7a** and cysteine in phosphate buffered solution at pH 7.5. The reaction between compound **7a** (100 µM) and cysteine (100 µM) occurred quantitatively in less than 10 min to form the 2 pyrimidyl cysteine adduct (m/z = 501.03) as described by the mechanism in **Figure 1**. As expected, the isotope pattern specific for bromine (m/z = 502.97) was preserved for the adduct mass (**Figure 5A**). Similarly, for the chlorine substituted compound **5c**, the analogous reaction adduct could be detected by LC/MS (**Supplementary Figure S2**). Accordingly, it was confirmed that under physiological conditions, the sulfonyl group was the leaving group and stable 2 pyrimidyl adducts were formed.

By using MALDI TOF mass spectrometry, we aimed to determine the mode of inhibitory action in an enzymatic context. For the native SrtA, we found a protein mass at m/z = 17,806. Treatment with inhibitor **7a** resulted in quantitative conversion and showed a single mass peak at m/z = 18,185 (**Figure 5B**), which matches the corresponding 2 pyrimidyl adduct and proves the covalent inhibition mechanism (**Figure 5C**).

2.4 Protease Inhibition Selectivity

The sulfonylpyrimidines studied in this work were characterized as mild covalent inactivators of the SrtA enzyme (**Table 3** and **Figure 5**) and exhibited a strong scaffold dependence for their inhibitory potency (**Table 2**). To investigate how these sulfonylpyrimidines affect the activity of other cysteine and serine proteases, a selectivity panel was constructed from a matrix of 6 diverse sulfonylpyrimidines and 6 different proteases. The compounds were assayed at a final compound concentration of 100 µM for the cysteine proteases human cathepsin B (hCatB), cathepsin L (hCatL), and *T. brucei* rhodesain (Rd). Furthermore, the serine proteases NS2B NS3 from Zika virus (ZIKV), the homologous protease from Dengue virus (DENV), and the human protease urokinase plasminogen activator (uPA) were tested for their susceptibility. The results of the inhibition data are summarized in **Table 4**.

Cathepsin B/L, rhodesain, and SrtA are all structurally related to papain like proteases, thus, we used their relatedness to study the selectivity of our inhibitors (Bradshaw et al., 2015). The selected sulfonylpyrimidines appear to have good selectivity for SrtA, as the other three proteases were inhibited at most 29.4% by compound **6g**. A time dependent inhibition, as with SrtA, could not be observed over the measurement duration of 30 min, which leads to the

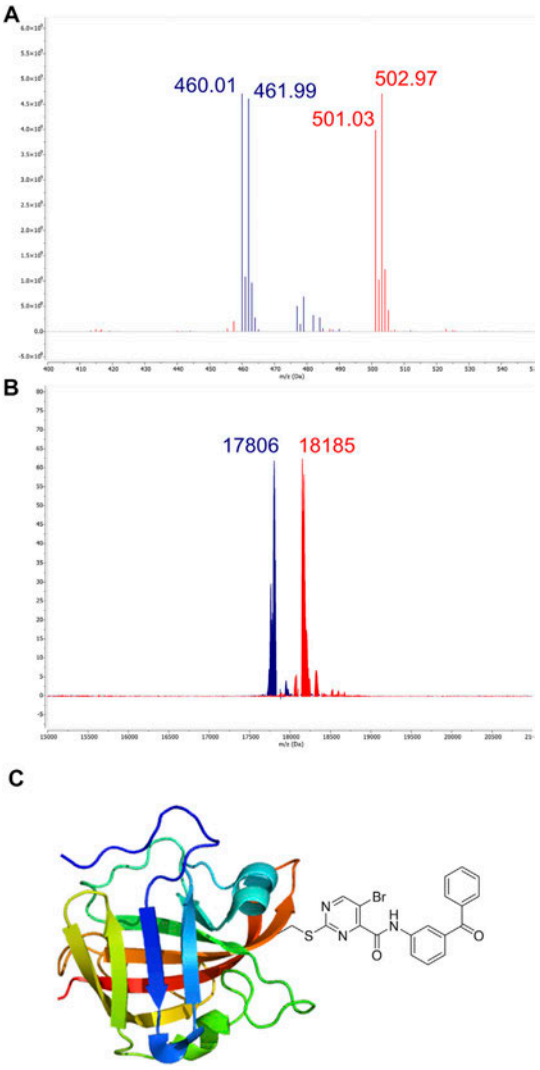

FIGURE 5 | Identification of covalent adducts by mass spectrometry. **(A)** ESI-MS of compound **7a** (blue, m/z 460.01) treated with free cysteine revealed the formation of a distinct adduct (red, m/z 501.03) corresponding to the respective 2-pyrimidyl cysteine (see the mechanism in **Panel 1**). **(B)** MALDI-TOF-MS of SrtA (blue, m/z 17,806) treated with compound **7a**. The peak at m/z 18,185 (red) corresponds to the modification of the active site Cys^{184} by compound **7a**. **(C)** The predominant mode of SrtA inhibition is the transfer of the pyrimidyl-fragment to Cys^{184}.

conclusion that sulfonylpyrimidines probably do not react covalently with cathepsin related proteases.

A significant difference between cathepsin B/L, rhodesain, and SrtA is that in contrast to SrtA, the catalytically active cysteine is present in thiolate form in the first three proteases (Otto and Schirmeister, 1997; Ehmke et al., 2013; Klein et al., 2020b). This observation seems counterintuitive at first since the reversely protonated thiol of SrtA has a lower nucleophilicity than the thiolate in cathepsin related proteases. The reaction of electrophiles such as sulfonylpyrimidines should react favorably with the thiolate as a stronger nucleophile (Zhang et al., 2012). A theoretical examination of these observations is provided later in this study through docking and quantum chemical calculations (**Section 2.8**).

The ZIKV NS2B/NS3 protease is a serine protease and contains two non catalytic cysteine residues, thus as expected, only <30% inhibition at 100 μM inhibitor concentration was found. The related DENV NS2B/NS3 protease has no cysteine residues in its protein sequence and was inhibited by a maximum of only 15% (Li Y. et al., 2017). The urokinase plasminogen activator, which is also a serine protease, was inhibited by less than 25% by most compounds. Compound **6g**, however, showed 67% inhibition, but this inhibition was observed to be not time dependent and thus presumably due to reversible binding.

2.5 Solvent Effects on SrtA Inhibition

To investigate which thiol protomer (Cys SH or Cys S) of SrtA Cys^{184} is responsible for the reaction with sulfonylpyrimidines, enzyme assays were performed at different pH values and in different enzyme buffers. It is known that the catalytical Cys^{184} of SrtA is predominantly (99.94%) in the protonated thiol form under physiological conditions at pH 7.5 (van't Hof et al., 2015). The pK_a value was previously determined to be 9.4 by NMR titration (Connolly et al., 2003). Thus, increasing the pH value of the enzyme solution above pH 7.5 resulted in a significant increase in the thiolate species content. This on one hand led to increased enzyme activity, on the other hand, made SrtA also more vulnerable for covalent modification by electrophiles such as Michael acceptors leading to an increase in the observed rate of irreversible enzyme inactivation (Connolly et al., 2003; Frankel et al., 2005; Schmohl et al., 2015; Barthels et al., 2020). Enzyme assays were performed at five pH values between 6.5 and 8.5 in Tris or Bis Tris buffers within the possible buffer capacities. Both the relative enzyme activity k_{cat} (RFU·s ^{1}) of the DMSO control and the inhibition potency k_{2nd} (M ^{1}min ^{1}) of compound **5a** were determined at each pH value (**Figure 6A**).

The observed activity increase of SrtA (k_{cat}) at pH values above pH 7.5 is in agreement with the literature (Frankel et al., 2005; Barthels et al., 2020). However, the inhibitory potency of compound **5a** showed no significant differences at varying pH values between 7.0 and 8.5. This is contrary to the inactivation kinetics of known SrtA targeting warheads, which have been shown to react preferentially with the thiolate species (Connolly et al., 2003; Frankel et al., 2005; Schmohl et al., 2015; Barthels et al., 2020). We take this, in addition to the protease selectivity results (**Table 4**), as further evidence that sulfonylpyrimidines might react preferentially with protonated thiols in this proteinogenic context (**Figure 6B**). Albeit yet unclear, we aimed to elucidate the molecular background by *in vitro* and *in silico* methods. In addition to the cationic Tris and Bis Tris buffers, inhibition experiments of SrtA by compound **5a** were also performed in the zwitterionic HEPES buffer at pH 7.5 (k_{2nd} = 7,956 M ^{1}min ^{1}). Hence, the inhibitory potency at pH 7.5 did not

TABLE 4 | Protease inhibition selectivity of a representative compound set. Compounds were tested at a final concentration of 100 μM inhibitor. The inhibition is expressed relative to the DMSO control in (%); n. i. no inhibition at 100 μM.

Cpd	Structure	SrtA (%)	CatB (%)	CatL (%)	Rd	ZIKV (%)	DENV	uPA
5a	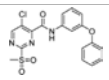	99.0	6.6	8.8	24.6%	6.4	n. i.	23.0%
5c		19.6	5.8	6.6	20.0%	7.7	n. i.	n. i.
6a	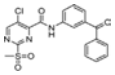	98.4	5.6	18.0	n. i.	18.6	5.1%	2.2%
6g	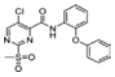	21.8	11.8	29.4	15.0%	18.3	2.6%	67.0%
6i	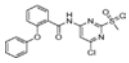	36.0	9.5	21.3	9.2%	29.3	15.0%	59.4%
7b	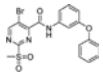	99.2	12.5	28.5	4.7%	18.3	5.2%	11.2%

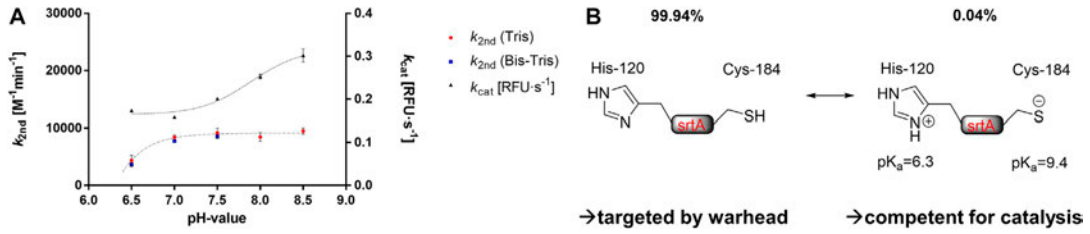

FIGURE 6 | Buffer effects on SrtA inhibition. **(A)** pH- and buffer dependence of the enzymatic activity [k_{cat} (RFU·s ^{1})] and the inhibitory potency of compound **5a** [k_{2nd} (M ^{1}min ^{1})]. **(B)** Hypothesis for the covalent inhibition mechanism by sulfonylpyrimidines. The catalytically competent form presumably differs from the warhead-targeted form in terms of the protonation of the catalytic dyad.

differ significantly between all three investigated buffers indicating no involvement of a buffer molecule for the reaction in an enzymatic context.

In contrast, when the pH value was lowered to 6.5, a substantial decrease in SrtA inhibitory potency was observed (pH 7.0: k_{2nd} = 8,436 M ^{1}min ^{1}; pH 6.5: k_{2nd} = 4,384 M ^{1}min ^{1}). However, the enzymatic activity (k_{cat}) did not decrease as much with this pH change, which is in agreement with the literature reports (Zong et al., 2004). The reduction in inhibitory potency at pH < 7.0 must be due to other SrtA residues than Cys^{184} since the proportions of the thiol/thiolate ratio do not change significantly at pH 6.5 7.0. However, the pK$_a$ value of the neighboring His^{120} is 6.3 leading to a significant protonation change when the pH is lowered from pH 7.0 to pH 6.5 (Connolly et al., 2003).

It is conceivable that the protonated imidazolinium form prevents the reaction of Cys^{184} with the sulfonylpyrimidine warhead. This would also hint at an explanation for the selectivity over the cysteine proteases with zwitterionic dyad (**Table 4**) since these have such an imidazolinium ion adjacent to their catalytic cysteine residue which might prevent reversible binding to the cathepsin B/L or rhodesain binding pockets (Mladenovic et al., 2007; Ehmke et al., 2013; Paasche et al., 2014).

2.6 In-Solution Cysteine Reactivity

Next, the reaction of sulfonylpyrimidines was studied kinetically in a non proteinogenic context with the free amino acid cysteine as a nucleophile to gather additional evidence for the reaction mechanism of sulfonylpyrimidines with thiols.

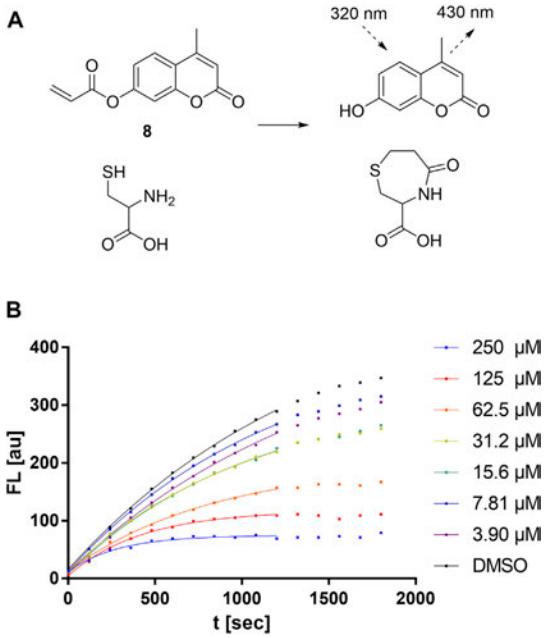

FIGURE 7 | Cysteine reactivity assay. **(A)** Mechanism of the fluorescent probe **8** reacting with cysteine. **(B)** Cysteine reactivity assay with variable concentrations of compound **5a** showing hyperbolic substrate conversion plots. The fluorescence was recorded for 30 min every 30 s. For clarity, only every fourth data point is shown.

In order to study the kinetics of sulfonylpyrimidines reacting with free cysteine in solution, a strategy for a competitive fluorescence based assay was adapted from previous works (Epps and Taylor, 2001; Sameshima et al., 2017). For this purpose, a novel cysteine reactive probe **8** was synthesized, which, in terms of signal to noise ratio, was superior to the probes used in the previous cysteine assays (Zeng et al., 2017). The reaction of probe **8** with cysteine liberates 4 methylumbelliferone as a fluorometrically detectable product (**Figure 7A**), and thus, the fluorescence increase can be described by the second order rate constant k_{probe} (**Equation 1**).

Upon the addition of competitive and irreversible cysteine modifiers such as sulfonylpyrimidines, the fluorescence increase of the probe reaction was hyperbolically attenuated (**Figure 7B**). According to the conceptual deduction described previously (Epps and Taylor, 2001; Sameshima et al., 2017), the experimental fluorescence curves can be analyzed by nonlinear regression as first order reaction progress curves (**Equation 2**). The parameter k_{obs} describes the curvature corresponding to the sum of the competing kinetics (**Equation 3**). Under the assumptions that 1) the competitive reaction between sulfonylpyrimidines *vs.* probe with cysteine is started by simultaneous addition, and 2) sulfonylpyrimidines are added at a much higher concentration than cysteine (5 µM) and the probe (5 µM), the k_{obs} values depend substantially on the k_{chem} value. The compound specific second order inactivation parameter k_{chem} can be determined by linear regression from the k_{obs} values of the dilution series (**Equation 4**).

$$\frac{d[FL]}{dt} = k_{probe}[Cys][probe] \quad (1)$$

$$FL = \frac{[Cys]_{total} \cdot k_{probe}[probe]}{k_{probe}[probe] + k_{chem}[sulfonylpyrimidine]}\left(1 - e^{-k_{obs} \cdot t}\right) \quad (2)$$

$$k_{obs} = k_{chem}[sulfonylpyrimidine] + k_{probe}[probe] \quad (3)$$

$$k_{chem} = \frac{k_{obs}}{[sulfonylpyrimidine]} \quad (4)$$

The observed k_{chem} values of a comprehensive set of sulfonylpyrimidines are shown in **Table 5**. Bauer et al. have already determined a k_{chem} value of compound **5c** vs. glutathione (k_{chem} = 82 $M^{-1}min^{-1}$). Our determined k_{chem} for the reaction of the identical compound with cysteine is 63 $M^{-1}min^{-1}$ and thus, as expected, in the same order of magnitude. The determined k_{chem} values ranged from 6 to 104 $M^{-1}min^{-1}$, i e., they are 10 10,000 times lower than for the reactions of the reported Michael acceptors 1 penten 3 one, methyl propiolate, and methyl acrylate with GSH (Böhme et al., 2009). This confirms the previous reports that sulfonylpyrimidines are mild cysteine modifiers with potential application in a cellular context (Bauer et al., 2016; Li L. et al., 2017; Förster et al., 2019; Jaudzems et al., 2020).

From the kinetic constants k_{chem} (cysteine assay) and k_{2nd} (SrtA inhibition), selectivity indices (S.I.) were calculated that compare how efficient the inactivation of SrtA was in comparison with the in solution reactivity towards free cysteine (**Table 5**). It was found that the S.I. values do not depend on the halogen substituent, but rather on the recognition sequence: 3 benzoylaniline derivatives **6a** and **7a** were superior to 3 phenoxyaniline derivatives **5a** and **7b** in terms of the S.I. by about a factor of two. This is in agreement with findings from the enzymatic context that the recognition sequence mainly influences the affinity of binding (K_I), with the halogen substituent influencing the reaction rate (k_{inact}, k_{chem}).

Furthermore, the influence of different solvents on the reaction of sulfonylpyrimidines with thiols in solution was investigated. No reactivity was observed between cysteine and **5a** or **5c** in water/DMSO mixtures. Likewise, no reactivity was detected between **5c** and 2 phenylethanethiol in chloroform. These observations are in agreement with the literature. In organic synthesis, such reactions required a base and elevated temperature (Sprague and Johnson, 1936; Buděšínský and Vavřina, 1972). However, between **5a** and cysteine, quantitative turnover (<10 min) was observed in phosphate buffered solution during the preparation of ESI MS experiments (**Figure 5A**) and cysteine reactivity assays (**Figure 7**). The buffer component appeared to be essential for the reaction in an aqueous solution.

In support of this qualitative statement, a quantitative estimation of the buffer dependent reaction between sulfonylpyrimidines and cysteine was also performed: The

TABLE 5 | Kinetic constants (k_{chem} and k_{2nd}) of the selected compound set investigated by the cysteine reactivity assay. Selectivity indices were calculated from k_{2nd}/k_{chem}.

Cpd.	Structure	Cysteine k_{chem} (M ^{1}min ^{1})	SrtA k_{2nd} (M ^{1}min ^{1})	S. I.
5a	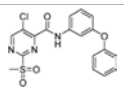	50.8 ± 16.6	8,088 ± 464	159
5c		63.0 ± 2.01	0	—
6a	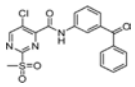	63.3 ± 8.37	20,785 ± 4,074	327
6i	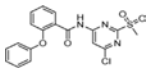	0	0	—
7a	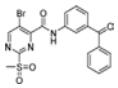	104.9 ± 22.5	28,185 ± 2,117	268
7b	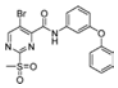	104.1 ± 19.4	13,998 ± 1,462	134
7c	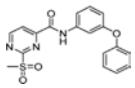	33.58 ± 2.93	4,364 ± 596	129
7d	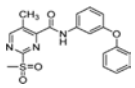	6.14 ± 1.71	1,204 ± 139	196
7e	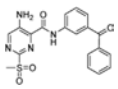	0	0	—

cysteine reactivity assay of compound **5c** was performed in addition to the usage of phosphate buffer (k_{chem} = 63.0 ± 2.01 M ^{1}min ^{1}) also in bicarbonate buffered solution at an identical pH 7.5. The reaction rate in bicarbonate buffer appeared to be significantly reduced (k_{chem} = 21.9 ± 1.27 M ^{1}min ^{1}). Mechanistic participation of the buffer molecule is discussed during the quantum chemical investigations (**Section 2.8**).

2.7 Mechanistic Evaluation by Hammett Plot Analysis

Table 3 shows that sulfonylpyrimidine derivatives, whose halogen substituent was varied, exhibited significantly different reaction rates in the inactivation of SrtA. The same was found for the cysteine reactivity assays (**Table 5**). If the pyrimidine ring is regarded as a pseudo atom, according to Hammett's theory, linear logarithmic relationships can be established between rate constants (M ^{1}min ^{1}) and Hammett's substituent constants (σ), which allow qualitative mechanistic conclusions to be drawn (Hammett, 1937; Flynn, 1980). For this purpose, a substituent series based on compound **5a** (R = Cl, Br, H, CH_3) was investigated (**Figure 8A**). Plotting the logarithmic normalized second order rate constants (k_{2nd}, k_{chem}) allowed us to generate Hammett plots for the reaction of sulfonylpyrimidines with SrtA (**Figure 8B**) and for the in solution reaction with free cysteine (phosphate buffer pH 7.5, **Figure 8C**). From these, we found positive ρ values (slope) of 2.64 resp. 2.51σ, which are consistent with the rate limiting nucleophilic attack (Kiemele et al., 2016), and strongly suggest a concerted S_NAr mechanism without stabilization of a Meisenheimer intermediate (Choi et al., 2009). The ρ values obtained from enzymatic reactions and reactions with free cysteine are almost identical suggesting an analogous reaction mechanism for covalent modification of SrtA and free cysteine.

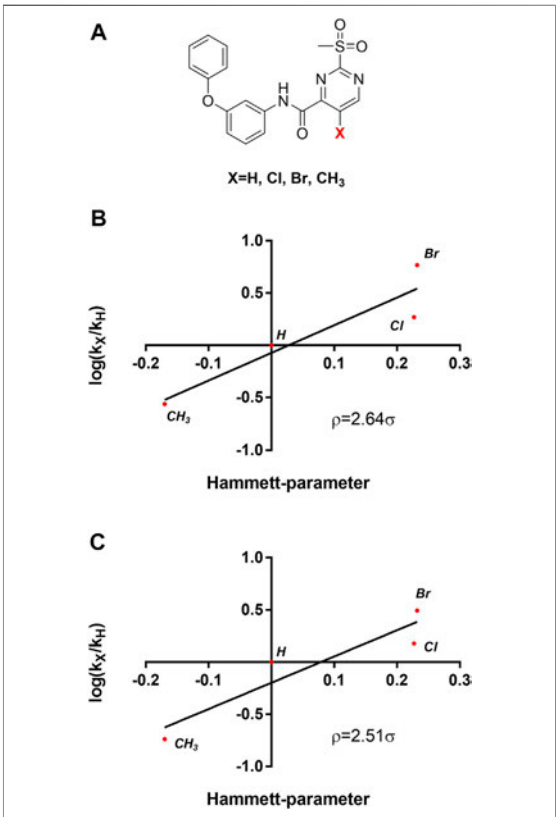

FIGURE 8 | Mechanistic analysis by Hammett plots. **(A)** Substituent series based on compound **5a** used for kinetic characterization. **(B)** Hammett plot for the inactivation of SrtA by sulfonylpyrimidines. **(C)** Hammett plot for the reaction of sulfonylpyrimidines with cysteine in solution (phosphate buffer pH 7.5).

2.8 Theoretical Investigations

To gain insights into the mechanism of 2 sulfonylpyrimidine inhibitors in an enzymatic environment, QM/MM calculations would be desirable. However, the available X ray structures of *S. aureus* SrtA differ strongly in the geometrical structure of their active site, and it is yet unclear which one represents the reactive conformation. Additionally, the enzyme is very flexible which makes it difficult to select appropriate conformations for the computation. Thus, unambiguous QM/MM computations were thought to be not available. Hence, we focused on the comparison of the warhead reaction in solution with the available experimental data. These findings were then applied to shed some light on the reaction of 2 sulfonylpyrimidines with SrtA. The reaction of inhibitor **5c** with methanethiol in (implicit) aqueous solution was selected as a model system. The relative orientation of the reactants together with the main reaction coordinate is depicted in **Supplementary Figure S3**. As the main reaction coordinate of the nucleophilic substitution of the sulfonyl group by the thiol (ate) we selected the distance between the sulfur center of thiol and the C 2 atom of the inhibitor (R (S_{thiol} C $2_{inhibitor}$)). To obtain single points of the corresponding reaction paths this distance was frozen while all other degrees of freedom were optimized. In the course of the calculations, only the R (S_{thiol} C $2_{inhibitor}$) distance was frozen but not the relative orientation of the two fragments to each other. Hence, the corresponding reaction path represents the minimum energy path (MEP) of the reaction. More details about the calculations are described in the experimental section.

First, the reactions of **5c** with methanethiol as well as methanethiolate were investigated. As shown in **Supplementary Figure S4**, the reaction with negatively charged methanethiolate occurs without any barrier, while the reaction with neutral methanethiol shows a barrier of 142 kJ/mol. Due to the high reaction barrier, a reaction of **5c** with a neutral thiol is not expected to take place. This is in line with the experimental findings that a reaction is not observed in organic solvents or neutral water/DMSO mixtures (**Section 2.6**) but only in a buffered medium. We also investigated if structures, which resemble the Meisenheimer complex, represent local minima on the potential surface. This is not the case as corresponding structures for the reaction with the thiol were found to be about 150 kJ/mol above the separated fragments. For the reaction with the thiolate, these were calculated to be more stable than the fragments but also do not represent local minima.

To elucidate possible mechanisms of buffer mediated reactions, we modeled reactions in which possible buffer molecules act as intermediate storage for the thiol proton before transferring it to the sulfonyl leaving group. At the investigated pH of 7.5, the majority of the bicarbonate buffer is composed of HCO_3, but small fractions of CO_3^2 and H_2CO_3 are found as well. To include all these possibilities, we computed reaction paths for all protonation states of H_2CO_3. The results are depicted in **Figure 9**. Besides the reaction paths, **Figure 9** depicts the variations in the geometrical arrangements for selected points along the reaction coordinate. Additional structures for the other paths can be found in **Supplementary Table S1**.

The reaction of methanethiol with HCO_3 as buffer molecule shows an activation barrier of 56 kJ/mol which is significantly lower than the reaction barrier of the thiol without any buffer molecule (142 kJ/mol). The proton transfer to the buffer occurs at R (S_{thiol} C $2_{inhibitor}$) = 2.3 Å. This point represents the top of the barrier. For the thiol, the top of the barrier is at about R (S_{thiol} C $2_{inhibitor}$) = 2.0 Å. Neutral buffer molecules of H_2CO_3 are not able to bind the additional proton, hence no catalysis would be expected. Indeed, our computation predicted a reaction barrier of 124 kJ/mol, which lies only 20 kJ/mol below the barrier computed for unbuffered thiol (142 kJ/mol). CO_3^2 as buffer molecule facilitates a fast reaction with a barrier height of merely 24 kJ/mol. For this species, the proton transfer occurs earlier in the reaction at R (S_{thiol} C $2_{inhibitor}$) = 2.5 Å. For the reaction catalyzed by HCO_3 structures resembling the Meisenheimer complex are found to be about 50 kJ/mol higher in energy than the fragments, showing that no Meisenheimer complex is formed. These predictions that Meisenheimer complexes are energetically unfavorable supports the conclusion drawn by Hammett's analysis (**Section 2.7**).

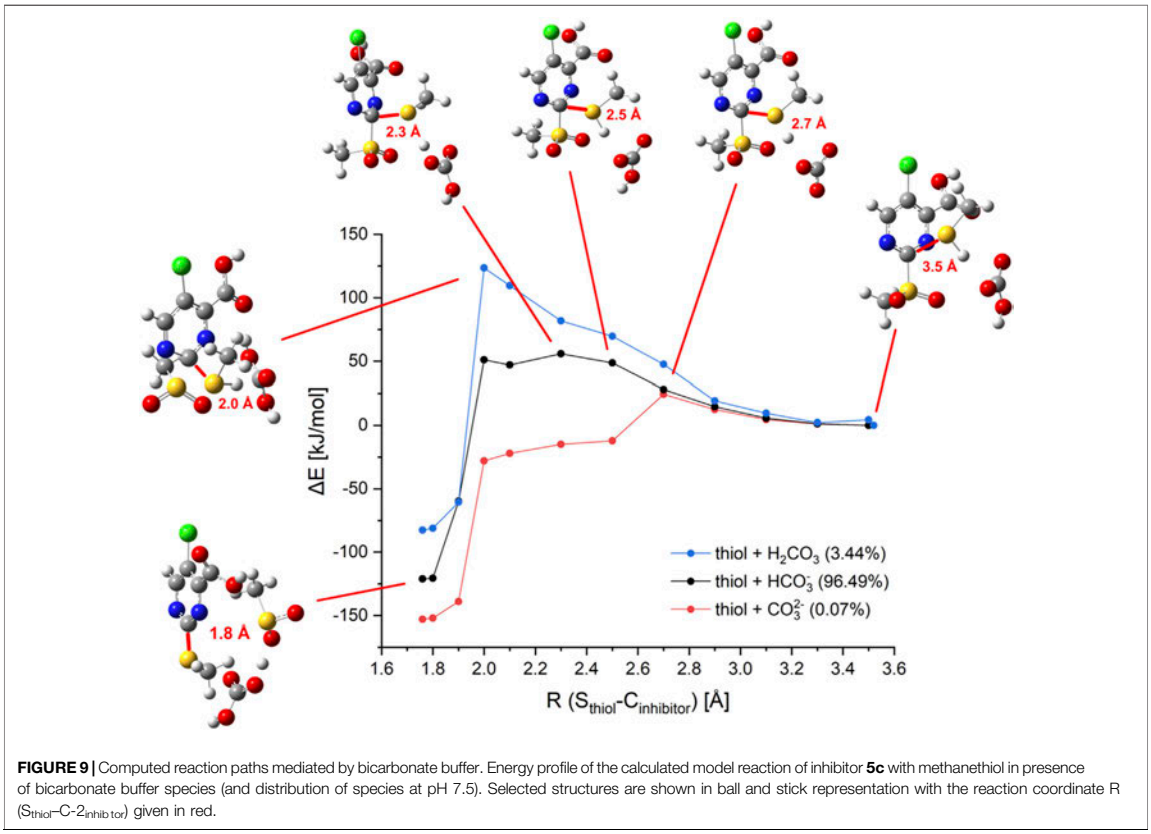

FIGURE 9 | Computed reaction paths mediated by bicarbonate buffer. Energy profile of the calculated model reaction of inhibitor **5c** with methanethiol in presence of bicarbonate buffer species (and distribution of species at pH 7.5). Selected structures are shown in ball and stick representation with the reaction coordinate R (S_{thiol}–C-$2_{inhibitor}$) given in red.

For further examination, the reaction paths for all phosphate buffer species were computed as well. The major component at pH 7.5 is HPO_4^{2} , the computation yields an activation barrier of 31 kJ/mol, which is lower than that for HCO_3 and comparable to the one found for CO_3^{2} (**Supplementary Figure S6**). This could be confirmed experimentally since a faster reaction was observed by using a phosphate buffer instead of a bicarbonate buffer (**Section 2.6**). The H_2PO_4 fraction of the phosphate buffer system shows a reaction barrier of 64 kJ/mol similar to the HCO_3 mediated reaction.

To determine whether the reaction can occur *via* the His^{120} residue in SrtA, the model reaction path was calculated with 4 methylimidazole as a conjugated base, yielding a barrier height of 64 kJ/mol. Consequently, the inhibition reaction in presence of histidine could lead to a reaction path analogous to the reaction mediated by bicarbonate or phosphate buffers. Our computations indicate that thiolates would react with 2 sulfonylpyrimidines without any barrier while the reaction with thiol requires a base as a catalyst. This stands in contrast to the experimental finding that 2 sulfonylpyrimidines inhibit a reversely protonated Cys/His dyad in enzymes like SrtA (as shown in **Table 4**), but not enzymes with zwitterionic Cys/His^{+} dyad as cathepsin like proteases (**Section 2.4**). According to Zhang et al. and our model calculations, the nucleophilic reaction with a deprotonated cysteine residue should be preferred over the reaction with a neutral cysteine (Zhang et al., 2012). To address this question, we docked inhibitor **5a** to the SrtA receptors mimicking the zwitterionic and the neutral Cys/His dyads. The most advantageous docking poses are depicted in **Figures 10A,B**. For the neutral dyad, **5a** forms a quite stable complex blocking the active site. For the zwitterionic receptor, the inhibitor stays outside of the binding pocket with a distance (Cys^{184} SH/C 2) = 7.8 Å. A similar result is found for the docking pose of inhibitor **5a** in the zwitterionic cathepsin like protease rhodesain (**Figure 10C**) which also shows an enlarged Cys^{25} S/C 2 distance of 7.8 Å.

Thus, the docking indicates that the possibility of a reaction does not result from the reactivity of the thiol or thiolate group but rather from the possibility to form an enzyme inhibitor complex which can result in a covalent reaction. According to our findings for a zwitterionic dyad, the reaction would be very fast. However, it does not take place because the 2 sulfonylpyrimidine warhead does not fit into the active site due to unfavorable intermolecular interactions. For a neutral Cys/His dyad, the 2 sulfonylpyrimidine fits into the pocket, however, according to the experimental and theoretical

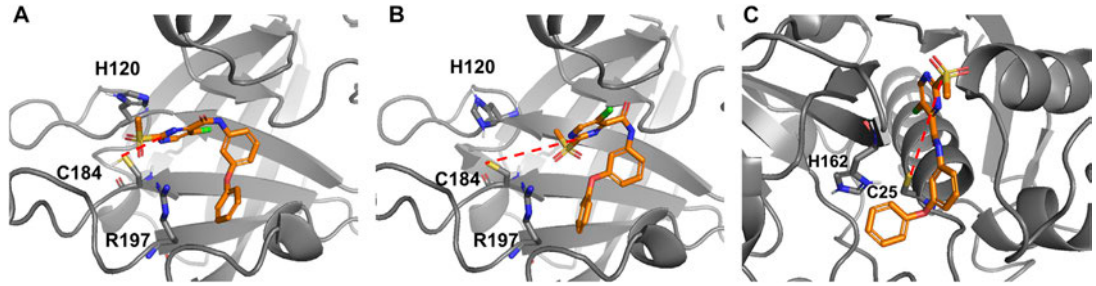

FIGURE 10 | Docking poses of compound **5a** reversibly bound to SrtA and rhodesain. **(A)** Docking to a SrtA receptor with reversely protonated Cys/His dyad (pdb: 2kid). Distance (Cys^{184}-SH/C-2) 4.6 Å. **(B)** Docking to a SrtA receptor with an artificial zwitterionic Cys/His^+ dyad (pdb: 2kid). Distance (Cys^{184}-S /C-2) 7.8 Å. **(C)** Docking to a rhodesain receptor (pdb: 2p7u). Distance (Cys^{25}-S /C-2) 7.8 Å.

findings, a base catalyst is needed that acts as a proton buffer. Our computations show that the histidine could be this catalyst if it is sufficiently close. This role of His^{120} as a proton buffer is supported by the fact that the inhibition potency decreases between pH 7.0 and 6.5 for which His^{120} undergoes a significant protonation change (Connolly et al., 2003).

3 CONCLUSION

In summary, our investigations show that 2 sulfonylpyrimidines act as irreversible inhibitors for *S. aureus* SrtA possessing a neutral Cys/His dyad. Considerably weaker inhibition is found for enzymes with zwitterionic Cys^-/His^+ dyads as found in cathepsin like proteases. Inactivation measurements at higher pH values show no increase in the inhibitory potency of 2 sulfonylpyrimidines which, in this regard, stands in contrast to other known SrtA inhibitors. Measurements in solution show that no reaction takes place in a DMSO/water mixture. Only in presence of a buffer like bicarbonate or phosphate buffered solution (pH ~7.5), a reaction was observed.

While the enzyme inactivation measurements indicate that 2 sulfonylpyrimidines react preferentially with protonated thiols, the investigations of in solution cysteine reactivity indicate that this reaction is hampered. To get a better understanding of these conflicting data, we performed quantum chemical model calculations in water/DMSO, bicarbonate, and phosphate buffers. Our computations predict that thiolates react with 2 sulfonylpyrimidines without any barrier. This is not the case for a protonated thiol for which a very high barrier of 142 kJ/mol is computed. The barrier is considerably lowered for bicarbonate or phosphate buffer solutions because the conjugated bases, e.g., HCO_3^-, CO_3^{2-}, act as base catalysts. The barriers drop because these bases induce a proton transfer from the thiol, thus increasing the nucleophilicity of the attacking agent. As expected, the decrease of the barrier heights correlates with the basicity of the catalyst. Additional computations show that imidazole can also act as a catalyst. It reduces the reaction barrier from 142 kJ/mol to about 64 kJ/mol.

The computations predict that a deprotonated cysteine should react considerably more efficiently with 2 sulfonylpyrimidines than protonated cysteine moieties. In contrast, our enzyme inhibition measurements only show an efficient inhibition of SrtA with neutral Cys/His dyads while enzymes possessing a zwitterionic Cys^-/His^+ dyad in their reactive center are less affected. This contradiction is resolved by docking studies, which predict that 2 sulfonylpyrimidines only enter the active sites of enzymes with neutral Cys/His dyads. If the dyad of SrtA is artificially switched to a Cys^-/His^+ dyad, the 2 sulfonylpyrimidine does not fit the active site. For rhodesain, which possesses a zwitterionic Cys^-/His^+ dyad, the same results are found. Intermolecular interactions prevent the formation of an enzyme inhibitor complex whose geometrical arrangements allow the reaction. As a catalyst for the reaction of 2 sulfonylpyrimidines with SrtA, the His^{120} moiety can act as a base catalyst. In line with the Hammett plots, our computations indicate that Meisenheimer complexes are energetically unfavorable for the energy surface of the S_NAr substitution reaction.

4 MATERIALS AND METHODS

4.1 Synthesis

Synthesis protocols of all compounds with their analytical data and the spectral appendix are provided in the supporting information.

4.2 Protein Expression and Purification

Expression of the *S. aureus* SrtA was performed as described previously (Schmohl et al., 2017a). The pET23b expression construct was transformed into *E. coli* strain BL21 Gold (DE3) cells (Agilent Technologies, Santa Clara, California) and grown in LB medium with 100 µM ampicillin at 37 °C to an OD_{600} of ~0.7. Expression was then induced with 1 mM isopropyl D thiogalactoside (IPTG) for 16 h at 20 °C. Harvested cells were resuspended in lysis buffer (20 mM Tris HCl, pH 6.9, 300 mM NaCl, 0.1% Triton X 100, RNase, DNase, lysozyme) and lysed by multiple cycles of sonication (Sonoplus, Bandelin,

Berlin, Germany). After centrifugation (45 min at 15 krpm), the cleared lysate was subjected to IMAC (HisTrap HP 5 ml column, GE Healthcare, Chicago, Illinois) to isolate crude SrtA. For further purification, SrtA containing fractions were subsequently subjected to a gel filtration step (HiLoad 16/60 Superdex 200 column, GE Healthcare) and eluted in the storage buffer (20 mM Tris HCl, pH 7.50, 150 mM NaCl, 5 mM $CaCl_2$). For storage at −80°C, the pure SrtA was concentrated, aliquoted and shock frozen in liquid nitrogen. Throughout all steps, protein concentrations were determined *via* absorbance at 280 nm and sample purity was assessed *via* sodium dodecyl sulfate polyacrylamide gel electrophoresis (SDS PAGE).

4.3 Inhibition of Sortase A

Inhibition assays of *S. aureus* SrtA transpeptidation reactions were performed as described previously (Barthels et al., 2020). Briefly, the recombinantly expressed SrtA (final concentration: 1 μM) was incubated in assay buffer (50 mM Tris, 150 mM NaCl, 5 mM $CaCl_2$, pH 7.50) with 25 μM of the FRET pair substrate Abz LPETG Dap (Dnp) OH (Genscript, Piscataway, New Jersey) and 0.5 mM tetraglycine (Sigma Aldrich, St. Louis, Missouri). Inhibitors were added from DMSO stocks. Reactions were initiated by addition of SrtA and monitored for 30 min at 30°C in an Infinite M200 Pro plate reader with λ_{ex} 320 nm/λ_{em} 430 nm (Tecan, Männedorf, Switzerland). Three technical replicates were carried out for each inhibitor in black flat bottom 96 well plates (Greiner bio one, Kremsmünster, Austria). The enzyme kinetics of irreversible SrtA inactivation were analyzed as described previously (Barthels et al., 2020).

4.4 Protease Inhibition Selectivity

Fluorometric assays of the ZIKV/DENV NS2B/NS3 protease were performed as described previously (Maus et al., 2021). The assay was carried out in triplicates at 25°C in assay buffer (50 mM Tris, pH 9.0, 20% glycerol (v/v), and 1 mM CHAPS). 100 μM Boc Gly Arg Arg AMC (Bachem, Bubendorf, Switzerland) was used as a substrate. Fluorometric assays for cathepsin B, cathepsin L, and rhodesain (Calbiochem, Merck Millipore, Burlington, Massachusetts) were performed as described previously (Klein et al., 2020a). Cbz Phe Arg AMC (Bachem, Bubendorf, Switzerland) was used as substrate (100 μM for cathepsin B, 6.5 μM for cathepsin L, and 10 μM for rhodesain). Fluorometric assays for urokinase plasminogen activator were performed as described previously (Angelini et al., 2012). 240 μM Cbz Gly Arg Arg AMC (Bachem, Bubendorf, Switzerland) was used as a substrate.

4.5 Mass Spectrometry

4.5.1 ESI-MS

To a solution of 100 μM cysteine in phosphate buffered saline (1×, pH 7.5), compound **5a** or **7a** (100 μM, 5% DMSO) was added and incubated for 10 min at room temperature. The negative labeling control was performed by mock treatment with DMSO. Samples were analyzed by LC/MS using an Agilent 1100 series HPLC system with an Agilent Poroshell 120 EC C18 column (150 × 2.10 mm 4 μm; mobile phase: ACN/H2O 45:55 + 0.1% formic acid; flow rate: 0.4 ml/min) and electron spray ionization with the Agilent 1100 series LC/MSD Trap in positive ionization mode.

4.5.2 MALDI-MS

An *S. aureus* SrtA stock solution was diluted in 100 μL assay buffer (50 mM Tris, 150 mM NaCl, 5 mM CaCl2, pH 7.50) to a final concentration of 10 μM. Compound **7a** was dissolved in DMSO and added to SrtA at a final concentration of 100 μM. The protein samples were allowed to react for 1 h at room temperature and subsequently, these were desalted using Zeba™ Spin desalting columns (7 kDa MWCO, 0.5 ml; Thermo Scientific) according to the manufacturer's instructions. For MALDI sample preparation, the desalted solution was mixed 1:1 with a matrix combination of equal amounts α cyano 4 hydroxycinnamic acid (20 mg/ml dissolved in 70% acetonitrile and 30% of formic acid in water at a concentration of 5%) and 2,5 dihydroxybenzoic acid (20 mg/ml dissolved in 70% acetonitrile and 30% of trifluoroacetic acid in water at a concentration of 0.1%). The resulting mixture was allowed to dry slowly on the MALDI target prior to introduction into the mass spectrometer. The measurements were carried out on a rapiflex™ MALDI TOF/TOF mass spectrometer (Bruker Daltonik GmbH, Bremen, Germany). The instrument is equipped with a scanning smartbeam 10 kHz Nd:YAG laser at a wavelength of 355 nm and a 10 bit 5 GHz digitizer. The acceleration voltage was set to 20 kV and the mass spectra were recorded in positive ion linear mode. Calibration was done with the Bruker protein calibration standard II in a mass range from 10 to 70 kDa. Samples were measured at a laser power of 60% with random walk ionization across the sample spot.

4.6 Cysteine Reactivity Assay

Kinetic characterization of the reaction between sulfonylpyrimidines and cysteine was performed in degassed phosphate buffer (1×PBS, pH 7.5) or individual cases in bicarbonate buffer (20 mM $NaHCO_3$, 100 mM NaCl, pH 7.5). Three technical replicates were carried out for each sulfonylpyrimidine in black flat bottom 96 well plates. For this purpose, 50 μL buffered solution (including 5% (v/v) DMSO) of the respective sulfonylpyrimidine derivative (final: 250 3 μM) and the cysteine reactive probe **8** (final: 5 μM) were premixed. Reactions were initiated by the addition of 50 μL cysteine (final: 5 μM), dissolved in the respective buffer, and monitored for 30 min at 30°C in an Infinite M200 Pro plate reader with λ_{ex} 380 nm/λ_{em} 460 nm. To calculate k_{obs} and k_{chem} values, fluorescence curves were fitted using the same non linear regression as for *in vitro* inhibition of SrtA (Barthels et al., 2020).

4.7 Molecular Modeling

JChem for Office (Excel) was used for the virtual synthesis of an in house docking library. JChem for Office 20.18.0, 2020, ChemAxon (http://www.chemaxon.com) (Bode, 2004). For this purpose, a database of 438 in house available amine building blocks was amide coupled *in silico* with the sulfonylpyrimidine carboxylic acid **5c**. The resulting product structures were exported in the SDF file format. For virtual screening of this compound library, a Glide docking protocol was conducted

within the Schrödinger Maestro 2020.04 worksuite (Friesner et al., 2004). The protein structures pdb: 2kid (frame 1, SrtA) and 2p7u (rhodesain) were downloaded from the Protein Databank (PDB). Before docking, the alkylated active site Cys^{184} (SrtA) or Cys^{25} (rhodesain) were untethered and reprotonated. Receptor preparation was performed using the automated binding site, protonation, and energy minimization routine within Maestro "Protein preparation" and "Receptor grid generation." Ligands were energy minimized using the "LigPrep" routine. The docking protocol was performed under default parameters with extra precision (XP) settings. Subsequently, predicted binding modes were analyzed to select the most promising candidate compounds for wet lab synthesis. Ranking of the virtual screening output was performed according to the total docking score and in a second step according to the predicted binding mode (i.e., positioning and distance of the warhead relative to the Cys^{184}).

4.8 Quantum Chemical Methods

All calculations were carried out with the Gaussian16 program (Frisch et al., 2020). The DFT functional B3LYP (Vosko et al., 1980; Lee et al., 1988; Becke, 1993) with Grimme's D3 correction (Grimme et al., 2010) and the Pople basis set 6 31+G (d,p) were employed. Implicit solvation in water was included with the SMD solvation method (Marenich et al., 2009). The geometry of the reactants was optimized to obtain the starting structures. Subsequently, a scan was performed in which the distance of the methanethiol (ate) to the attacking carbon atom of the inhibitor (C 2) was gradually shortened. Reaction profiles were calculated for the reaction of the inhibitor with methanethiolate, methanethiol, and with methanethiol in presence of a buffer molecule. As buffer molecules, all species of the bicarbonate buffer and phosphate buffer species, respectively, were considered. For the reaction of the thiolate anion with the inhibitor, the dihedral angle between the thiolate carbon, thiolate sulfur, C 2 and C 5 of the inhibitor was frozen, because otherwise the thiolate was not oriented towards the attacking carbon. However, for the distances R ($S_{thiolate}$ C $2_{inhibitor}$) = 1.8/1.9 Å the restraint was removed to ensure the correct product geometry. Reactants and products were confirmed by calculations without restraints and frequency calculations.

DATA AVAILABILITY STATEMENT

The original contributions presented in the study are included in the article/**Supplementary Material**, further inquiries can be directed to the corresponding author.

AUTHOR CONTRIBUTIONS

TS, BE, WZ, and FB conceived and designed the research; FB, JM, SH, and H JR performed the research; FB, JM, TM, and BE analyzed the data; FB, BE, JM, TS, and SH wrote the manuscript. The final manuscript has been seen and approved by all authors, and we have taken due care to ensure the integrity of the work.

FUNDING

The work of WZ is funded by the German Research Council (DFG) ShARE (ZI665/3 1) and the German Federal Ministry of Education and Research (BMBF) (16GW0297).

ACKNOWLEDGMENTS

We thank Prof. Dirk Schwarzer (University of Tuebingen) for providing the expression plasmid of *S. aureus* SrtA. The authors gratefully acknowledge ChemAxon Ltd. for the donation of the academic license to the JChem package.

SUPPLEMENTARY MATERIAL

The Supplementary Material for this article can be found online at: https://www.frontiersin.org/articles/10.3389/fmolb.2021.804970/full#supplementary material

REFERENCES

Allen, R. C., Popat, R., Diggle, S. P., and Brown, S. P. (2014). Targeting Virulence: Can We Make Evolution-Proof Drugs? *Nat. Rev. Microbiol.* 12, 300–308. doi:10.1038/nrmicro3232

Angelini, A., Cendron, L., Chen, S., Touati, J., Winter, G., Zanotti, G., et al. (2012). Bicyclic Peptide Inhibitor Reveals Large Contact Interface with a Protease Target. *ACS Chem. Biol.* 7, 817–821. doi:10.1021/cb200478t

Awoonor-Williams, E., and Rowley, C. N. (2018). How Reactive Are Druggable Cysteines in Protein Kinases? *J. Chem. Inf. Model.* 58, 1935–1946. doi:10.1021/acs.jcim.8b00454

Bajorath, J. (2019). Duality of Activity Cliffs in Drug Discovery. *Expert Opin. Drug Discov.* 14, 517–520. doi:10.1080/17460441.2019.1593371

Barthels, F., Marincola, G., Marciniak, T., Konhäuser, M., Hammerschmidt, S., Bierlmeier, J., et al. (2020). Asymmetric Disulfanylbenzamides as Irreversible and Selective Inhibitors ofStaphylococcus aureusSortase A. *ChemMedChem* 15, 839–850. doi:10.1002/cmdc.201900687

Bauer, M. R., Joerger, A. C., and Fersht, A. R. (2016). 2-Sulfonylpyrimidines: Mild Alkylating Agents with Anticancer Activity toward P53-Compromised Cells. *Proc. Natl. Acad. Sci. USA* 113, E5271–E5280. doi:10.1073/pnas.1610421113

Becke, A. D. (1993). Density-functional Thermochemistry. III. The Role of Exact Exchange. *J. Chem. Phys.* 98, 5648–5652. doi:10.1063/1.464913

Bentley, M. L., Lamb, E. C., and McCafferty, D. G. (2008). Mutagenesis Studies of Substrate Recognition and Catalysis in the Sortase A Transpeptidase from *Staphylococcus aureus*. *J. Biol. Chem.* 283, 14762–14771. doi:10.1074/jbc.M800974200

Bode, J. W. (2004). *Reactor ChemAxon Ltd*. Maramaros koz 2/a. Budapest, 1037 Hungary: ChemAxon. Available at: www.chemaxon.com.

Böhme, A., Thaens, D., Paschke, A., and Schüürmann, G. (2009). Kinetic Glutathione Chemoassay to Quantify Thiol Reactivity of Organic Electrophiles-Application to α,β-Unsaturated Ketones, Acrylates, and Propiolates. *Chem. Res. Toxicol.* 22, 742–750. doi:10.1021/tx800492x

Bradshaw, W. J., Davies, A. H., Chambers, C. J., Roberts, A. K., Shone, C. C., and Acharya, K. R. (2015). Molecular Features of the Sortase Enzyme Family. *FEBS J.* 282, 2097–2114. doi:10.1111/febs.13288

Buděšínský, Z., and Vavřina, J. (1972). Nucleophilic Substitutions in the 2-methanesulfonylpyrimidine Series. *Collect. Czech. Chem. Commun.* 37, 1721–1733. doi:10.1135/cccc19721721

Cascioferro, S., Raffa, D., Maggio, B., Raimondi, M. V., Schillaci, D., and Daidone, G. (2015). Sortase A Inhibitors: Recent Advances and Future Perspectives. *J. Med. Chem.* 58, 9108–9123. doi:10.1021/acs.jmedchem.5b00779

Cascioferro, S., Totsika, M., and Schillaci, D. (2014). Sortase A: An Ideal Target for Anti-virulence Drug Development. *Microb. Pathogenesis* 77, 105–112. doi:10.1016/j.micpath.2014.10.007

Chan, A. H., Yi, S. W., Weiner, E. M., Amer, B. R., Sue, C. K., Wereszczynski, J., et al. (2017). NMR Structure-Based Optimization ofStaphylococcus Aureussortase A Pyridazinone Inhibitors. *Chem. Biol. Drug Des.* 90, 327–344. doi:10.1111/cbdd.12962

Chipinda, I., Ajibola, R. O., Morakinyo, M. K., Ruwona, T. B., Simoyi, R. H., and Siegel, P. D. (2010). Rapid and Simple Kinetics Screening Assay for Electrophilic Dermal Sensitizers Using Nitrobenzenethiol. *Chem. Res. Toxicol.* 23, 918–925. doi:10.1021/tx100003w

Choi, Hojune., Lee, Jong-Pal., Park, Jong. Keun., Yang, Kiyull., and Koo, In. Sun. (2009). Kinetic Studies on the Nucleophilic Substitution Reaction of 4-X-Substituted-2,6-Dinitrochlorobenzene with Pyridines in MeOH-MeCN Mixtures. *Bull. Korean Chem. Soc.* 30, 1579–1582. doi:10.5012/BKCS.2009.30.7.1579

Clancy, K. W., Melvin, J. A., and McCafferty, D. G. (2010). Sortase Transpeptidases: Insights into Mechanism, Substrate Specificity, and Inhibition. *Biopolymers* 94, 385–396. doi:10.1002/bip.21472

Connolly, K. M., Smith, B. T., Pilpa, R., Ilangovan, U., Jung, M. E., and Clubb, R. T. (2003). Sortase from *Staphylococcus aureus* Does Not Contain a Thiolate-Imidazolium Ion Pair in its Active Site. *J. Biol. Chem.* 278, 34061–34065. doi:10.1074/jbc.M305245200

Copeland, R. A. (2005). *Evaluation of Enzyme Inhibitors in Drug Discovery: A Guide for Medicinal Chemists and Pharmacologists*. Second Edition. Hoboken, NJ.: John Wiley & Sons, 572. doi:10.1002/9781118540398

Dickey, S. W., Cheung, G. Y. C., and Otto, M. (2017). Different Drugs for Bad Bugs: Antivirulence Strategies in the Age of Antibiotic Resistance. *Nat. Rev. Drug Discov.* 16, 457–471. doi:10.1038/nrd.2017.23

Ehmke, V., Winkler, E., Banner, D. W., Haap, W., Schweizer, W. B., Rottmann, M., et al. (2013). Optimization of Triazine Nitriles as Rhodesain Inhibitors: Structure-Activity Relationships, Bioisosteric Imidazopyridine Nitriles, and X-ray Crystal Structure Analysis with Human Cathepsin L. *ChemMedChem* 8, 967–975. doi:10.1002/cmdc.201300112

Epps, D. E., and Taylor, B. M. (2001). A Competitive Fluorescence Assay to Measure the Reactivity of Compounds. *Anal. Biochem.* 295, 101–106. doi:10.1006/abio.2001.5173

Flynn, G. L. (1980). Substituent Constants for Correlation Analysis in Chemistry and Biology. *J. Pharm. Sci.* 69, 1109. doi:10.1002/jps.2600690938

Förster, T., Shang, E., Shimizu, K., Sanada, E., Schölermann, B., Huebecker, M., et al. (2019). 2-Sulfonylpyrimidines Target the Kinesin HSET via Cysteine Alkylation. *Eur. J. Org. Chem.* 2019, 5486–5496. doi:10.1002/ejoc.201900586

Frankel, B. A., Kruger, R. G., Robinson, D. E., Kelleher, N. L., and McCafferty, D. G. (2005). *Staphylococcus aureus* Sortase Transpeptidase SrtA: Insight into the Kinetic Mechanism and Evidence for a Reverse Protonation Catalytic Mechanism. *Biochemistry* 44, 11188–11200. doi:10.1021/bi050141j

Friesner, R. A., Banks, J. L., Murphy, R. B., Halgren, T. A., Klicic, J. J., Mainz, D. T., et al. (2004). Glide: A New Approach for Rapid, Accurate Docking and Scoring. 1. Method and Assessment of Docking Accuracy. *J. Med. Chem.* 47, 1739–1749. doi:10.1021/jm0306430

Frisch, M. J., Trucks, G. W., Schlegel, H. B., Scuseria, G. E., Robb, M. A., Cheeseman, J. R., et al. (2020). *Gaussian 16, Revision C. 01*. Wallingford CT: Gaussian, Inc.

Grimme, S., Antony, J., Ehrlich, S., and Krieg, H. (2010). A Consistent and Accurate Ab Initio Parametrization of Density Functional Dispersion Correction (DFT-D) for the 94 Elements H-Pu. *J. Chem. Phys.* 132, 154104. doi:10.1063/1.3382344

Hallenbeck, K., Turner, D., Renslo, A., and Arkin, M. (2016). Targeting Non-catalytic Cysteine Residues through Structure-Guided Drug Discovery. *Ctmc* 17, 4–15. doi:10.2174/1568026616666160719163839

Hammett, L. P. (1937). The Effect of Structure upon the Reactions of Organic Compounds. Benzene Derivatives. *J. Am. Chem. Soc.* 59, 96–103. doi:10.1021/ja01280a022

Ilangovan, U., Ton-That, H., Iwahara, J., Schneewind, O., and Clubb, R. T. (2001). Structure of Sortase, the Transpeptidase that Anchors Proteins to the Cell wall of *Staphylococcus aureus*. *Proc. Natl. Acad. Sci.* 98, 6056–6061. doi:10.1073/pnas.101064198

Jaudzems, K., Kurbatska, V., Jekabsons, A., Bobrovs, R., Rudevica, Z., and Leonchiks, A. (2020). Targeting Bacterial Sortase A with Covalent Inhibitors: 27 New Starting Points for Structure-Based Hit-To-Lead Optimization. *ACS Infect. Dis.* 6, 186–194. doi:10.1021/acsinfecdis.9b00265

Kappel, K., Wereszczynski, J., Clubb, R. T., and McCammon, J. A. (2012). The Binding Mechanism, Multiple Binding Modes, and Allosteric Regulation ofStaphylococcus aureusSortase A Probed by Molecular Dynamics Simulations. *Protein Sci.* 21, 1858–1871. doi:10.1002/pro.2168

Kiemele, E. R., Wathier, M., Bichler, P., and Love, J. A. (2016). Total Synthesis of K777: Successful Application of Transition-Metal-Catalyzed Alkyne Hydrothiolation toward the Modular Synthesis of a Potent Cysteine Protease Inhibitor. *Org. Lett.* 18, 492–495. doi:10.1021/acs.orglett.5b03535

Klein, P., Barthels, F., Johe, P., Wagner, A., Tenzer, S., Distler, U., et al. (2020a). Naphthoquinones as Covalent Reversible Inhibitors of Cysteine Proteases-Studies on Inhibition Mechanism and Kinetics. *Molecules* 25, 2064. doi:10.3390/molecules25092064

Klein, P., Johe, P., Wagner, A., Jung, S., Kühlborn, J., Barthels, F., et al. (2020b). New Cysteine Protease Inhibitors: Electrophilic (Het)arenes and Unexpected Prodrug Identification for the Trypanosoma Protease Rhodesain. *Molecules* 25, 1451. doi:10.3390/molecules25061451

Kruger, R. G., Barkallah, S., Frankel, B. A., and McCafferty, D. G. (2004a). Inhibition of the *Staphylococcus aureus* Sortase Transpeptidase SrtA by Phosphinic Peptidomimetics. *Bioorg. Med. Chem.* 12, 3723–3729. doi:10.1016/j.bmc.2004.03.066

Kruger, R. G., Dostal, P., and McCafferty, D. G. (2004b). Development of a High-Performance Liquid Chromatography Assay and Revision of Kinetic Parameters for the *Staphylococcus aureus* Sortase Transpeptidase SrtA. *Anal. Biochem.* 326, 42–48. doi:10.1016/j.ab.2003.10.023

Lee, C., Yang, W., and Parr, R. G. (1988). Development of the Colle-Salvetti Correlation-Energy Formula into a Functional of the Electron Density. *Phys. Rev. B* 37, 785–789. doi:10.1103/PhysRevB.37.785

Li, L., Jiang, X., Huang, S., Ying, Z., Zhang, Z., Pan, C., et al. (2017a). Discovery of Highly Potent 2-Sulfonyl-Pyrimidinyl Derivatives for Apoptosis Inhibition and Ischemia Treatment. *ACS Med. Chem. Lett.* 8, 407–412. doi:10.1021/acsmedchemlett.6b00489

Li, Y., Phoo, W. W., Loh, Y. R., Zhang, Z., Ng, E. Y., Wang, W., et al. (2017b). Structural Characterization of the Linked NS2B-NS3 Protease of Zika Virus. *FEBS Lett.* 591, 2338–2347. doi:10.1002/1873-3468.12741

Liew, C. K., Smith, B. T., Pilpa, R., Suree, N., Ilangovan, U., Connolly, K. M., et al. (2004). Localization and Mutagenesis of the Sorting Signal Binding Site on Sortase A fromStaphylococcus Aureus. *FEBS Lett.* 571, 221–226. doi:10.1016/j.febslet.2004.06.070

Lyu, H., Petukhov, P. A., Banta, P. R., Jadhav, A., Lea, W. A., Cheng, Q., et al. (2020). Characterization of Lead Compounds Targeting the Selenoprotein Thioredoxin Glutathione Reductase for Treatment of Schistosomiasis. *ACS Infect. Dis.* 6, 393–405. doi:10.1021/acsinfecdis.9b00354

Marenich, A. V., Cramer, C. J., and Truhlar, D. G. (2009). Universal Solvation Model Based on Solute Electron Density and on a Continuum Model of the Solvent Defined by the Bulk Dielectric Constant and Atomic Surface Tensions. *J. Phys. Chem. B* 113, 6378–6396. doi:10.1021/jp810292n

Maresso, A. W., Wu, R., Kern, J. W., Zhang, R., Janik, D., Missiakas, D. M., et al. (2007). Activation of Inhibitors by Sortase Triggers Irreversible Modification of the Active Site. *J. Biol. Chem.* 282, 23129–23139. doi:10.1074/jbc.M701857200

Maus, H., Barthels, F., Hammerschmidt, S. J., Kopp, K., Millies, B., Gellert, A., et al. (2021). SAR of Novel Benzothiazoles Targeting an Allosteric Pocket of DENV and ZIKV NS2B/NS3 Proteases. *Bioorg. Med. Chem.* 47, 116392. doi:10.1016/j.bmc.2021.116392

Mazmanian, S. K., Liu, G., Jensen, E. R., Lenoy, E., and Schneewind, O. (2000). *Staphylococcus aureus* Sortase Mutants Defective in the Display of Surface Proteins and in the Pathogenesis of Animal Infections. *Proc. Natl. Acad. Sci.* 97, 5510–5515. doi:10.1073/pnas.080520697

Mazmanian, S. K., Liu, G., Ton-That, H., and Schneewind, O. (1999). *Staphylococcus aureus* Sortase, an Enzyme that Anchors Surface Proteins to the Cell Wall. *Science* 285, 760–763. doi:10.1126/science.285.5428.760

Mladenovic, M., Schirmeister, T., Thiel, S., Thiel, W., and Engels, B. (2007). The Importance of the Active Site Histidine for the Activity of Epoxide- or Aziridine-Based Inhibitors of Cysteine Proteases. *ChemMedChem* 2, 120–128. doi:10.1002/cmdc.200600159

Mu, D., Xiang, H., Dong, H., Wang, D., and Wang, T. (2018). Isovitexin, a Potential Candidate Inhibitor of Sortase A of *Staphylococcus aureus* USA300. *J. Microbiol. Biotechnol.* 28, 1426–1432. doi:10.4014/jmb.1802.02014

Otto, H.-H., and Schirmeister, T. (1997). Cysteine Proteases and Their Inhibitors. *Chem. Rev.* 97, 133–172. doi:10.1021/cr950025u

Paasche, A., Zipper, A., Schäfer, S., Ziebuhr, J., Schirmeister, T., and Engels, B. (2014). Evidence for Substrate Binding-Induced Zwitterion Formation in the Catalytic Cys-His Dyad of the SARS-CoV Main Protease. *Biochemistry* 53, 5930–5946. doi:10.1021/bi400604t

Perry, A. M., Ton-That, H., Mazmanian, S. K., and Schneewind, O. (2002). Anchoring of Surface Proteins to the Cell Wall of *Staphylococcus aureus*. *J. Biol. Chem.* 277, 16241–16248. doi:10.1074/jbc.M109194200

Rohrbach, S., Smith, A. J., Pang, J. H., Poole, D. L., Tuttle, T., Chiba, S., et al. (2019). Concerted Nucleophilic Aromatic Substitution Reactions. *Angew. Chem. Int. Ed.* 58, 16368–16388. doi:10.1002/anie.201902216

Sameshima, T., Miyahisa, I., Yamasaki, S., Gotou, M., Kobayashi, T., and Sakamoto, J. (2017). High-Throughput Quantitative Intrinsic Thiol Reactivity Evaluation Using a Fluorescence-Based Competitive Endpoint Assay. *SLAS DISCOVERY: Advancing Sci. Drug Discov.* 22, 1168–1174. doi:10.1177/2472555217704654

Schmohl, L., Bierlmeier, J., Gerth, F., Freund, C., and Schwarzer, D. (2017a). Engineering Sortase A by Screening a Second-Generation Library Using Phage Display. *J. Pept. Sci.* 23, 631–635. doi:10.1002/psc.2980

Schmohl, L., Bierlmeier, J., von Kügelgen, N., Kurz, L., Reis, P., Barthels, F., et al. (2017b). Identification of Sortase Substrates by Specificity Profiling. *Bioorg. Med. Chem.* 25, 5002–5007. doi:10.1016/j.bmc.2017.06.033

Schmohl, L., Wagner, F. R., Schümann, M., Krause, E., and Schwarzer, D. (2015). Semisynthesis and Initial Characterization of Sortase A Mutants Containing Selenocysteine and Homocysteine. *Bioorg. Med. Chem.* 23, 2883–2889. doi:10.1016/j.bmc.2015.03.057

Schneewind, O., and Missiakas, D. (2019). Sortases, Surface Proteins, and Their Roles inStaphylococcus aureusDisease and Vaccine Development. *Protein Secret. Bact.* 7, 173–188. doi:10.1128/microbiolspec.PSIB-0004-201810.1128/9781683670285.ch15

Schoonen, W. G. E. J., Westerink, W. M. A., de Roos, J. A. D. M., and Débiton, E. (2005). Cytotoxic Effects of 100 Reference Compounds on Hep G2 and HeLa Cells and of 60 Compounds on ECC-1 and CHO Cells. I Mechanistic Assays on ROS, Glutathione Depletion and Calcein Uptake. *Toxicol. Vitro* 19, 505–516. doi:10.1016/j.tiv.2005.01.003

Scott, C. J., McDowell, A., Martin, S. L., Lynas, J. F., Vandenbroeck, K., and Walker, B. (2002). Irreversible Inhibition of the Bacterial Cysteine Protease-Transpeptidase Sortase (SrtA) by Substrate-Derived Affinity Labels. *Biochem. J.* 366, 953–958. doi:10.1042/bj20020602

Sprague, J. M., and Johnson, T. B. (1936). Researches on Pyrimidines. CXLIX. Reactions of Some 2-Ethylsulfonylpyrimidines. *J. Am. Chem. Soc.* 58, 423–426. doi:10.1021/ja01294a010

Suree, N., Liew, C. K., Villareal, V. A., Thieu, W., Fadeev, E. A., Clemens, J. J., et al. (2009a). The Structure of the *Staphylococcus aureus* Sortase-Substrate Complex Reveals How the Universally Conserved LPXTG Sorting Signal Is Recognized. *J. Biol. Chem.* 284, 24465–24477. doi:10.1074/jbc.M109.022624

Suree, N., Yi, S. W., Thieu, W., Marohn, M., Damoiseaux, R., Chan, A., et al. (2009b). Discovery and Structure-Activity Relationship Analysis of *Staphylococcus aureus* Sortase A Inhibitors. *Bioorg. Med. Chem.* 17, 7174–7185. doi:10.1016/j.bmc.2009.08.067

Ton-That, H., Liu, G., Mazmanian, S. K., Faull, K. F., and Schneewind, O. (1999). Purification and Characterization of Sortase, the Transpeptidase that Cleaves Surface Proteins of *Staphylococcus aureus* at the LPXTG Motif. *Proc. Natl. Acad. Sci.* 96, 12424–12429. doi:10.1073/pnas.96.22.12424

Ton-That, H., Mazmanian, S. K., Alksne, L., and Schneewind, O. (2002). Anchoring of Surface Proteins to the Cell Wall of *Staphylococcus aureus*. *J. Biol. Chem.* 277, 7447–7452. doi:10.1074/jbc.M109945200

Ton-That, H., and Schneewind, O. (1999). Anchor Structure of Staphylococcal Surface Proteins. *J. Biol. Chem.* 274, 24316–24320. doi:10.1074/jbc.274.34.24316

Tsompanidou, E., Denham, E. L., Sibbald, M. J. J. B., Yang, X.-m., Seinen, J., Friedrich, A. W., et al. (2012). The Sortase A Substrates FnbpA, FnbpB, ClfA and ClfB Antagonize Colony Spreading of *Staphylococcus aureus*. *PLoS One* 7, e44646. doi:10.1371/journal.pone.0044646

van't Hof, W., Mañásková, S. H., Veerman, E. C. I., and Bolscher, J. G. M. (2015). Sortase-mediated Backbone Cyclization of Proteins and Peptides. *Biol. Chem.* 396, 283–293. doi:10.1515/hsz-2014-0260

Vosko, S. H., Wilk, L., and Nusair, M. (1980). Accurate Spin-dependent Electron Liquid Correlation Energies for Local Spin Density Calculations: a Critical Analysis. *Can. J. Phys.* 58, 1200–1211. doi:10.1139/p80-159

Webb, K. S. (1994). A Mild, Inexpensive and Practical Oxidation of Sulfides. *Tetrahedron Lett.* 35, 3457–3460. doi:10.1016/S0040-4039(00)73209-6

Wehrli, P. M., Uzelac, I., Olsson, T., Jacso, T., Tietze, D., and Gottfries, J. (2019). Discovery and Development of Substituted Thiadiazoles as Inhibitors of *Staphylococcus aureus* Sortase A. *Bioorg. Med. Chem.* 27, 115043. doi:10.1016/j.bmc.2019.115043

Weiss, W. J., Lenoy, E., Murphy, T., Tardio, L., Burgio, P., Projan, S. J., et al. (2004). Effect of srtA and srtB Gene Expression on the Virulence of *Staphylococcus aureus* in Animal Models of Infection. *J. Antimicrob. Chemother.* 53, 480–486. doi:10.1093/jac/dkh078

Wilke, J., Kawamura, T., Watanabe, N., Osada, H., Ziegler, S., and Waldmann, H. (2018). Identification of Cytotoxic, Glutathione-Reactive Moieties Inducing Accumulation of Reactive Oxygen Species via Glutathione Depletion. *Bioorg. Med. Chem.* 26, 1453–1461. doi:10.1016/j.bmc.2017.11.009

Yang, T., Zhang, T., Guan, X.-N., Dong, Z., Lan, L., Yang, S., et al. (2020). Tideglusib and its Analogues as Inhibitors of *Staphylococcus aureus* SrtA. *J. Med. Chem.* 63, 8442–8457. doi:10.1021/acs.jmedchem.0c00803

Zeng, R.-F., Lan, J.-S., Li, X.-D., Liang, H.-F., Liao, Y., Lu, Y.-J., et al. (2017). A Fluorescent Coumarin-Based Probe for the Fast Detection of Cysteine with Live Cell Application. *Molecules* 22, 1618. doi:10.3390/molecules22101618

Zhang, D., Devarie-Baez, N. O., Li, Q., Lancaster, J. R., and Xian, M. (2012). Methylsulfonyl Benzothiazole (MSBT): A Selective Protein Thiol Blocking Reagent. *Org. Lett.* 14, 3396–3399. doi:10.1021/ol301370s

Zhang, J., Liu, H., Zhu, K., Gong, S., Dramsi, S., Wang, Y.-T., et al. (2014). Antiinfective Therapy with a Small Molecule Inhibitor ofStaphylococcus Aureussortase. *Proc. Natl. Acad. Sci. USA* 111, 13517–13522. doi:10.1073/pnas.1408601111

Zhulenkovs, D., Rudevica, Z., Jaudzems, K., Turks, M., and Leonchiks, A. (2014). Discovery and Structure-Activity Relationship Studies of Irreversible Benzisothiazolinone-Based Inhibitors against *Staphylococcus aureus* Sortase A Transpeptidase. *Bioorg. Med. Chem.* 22, 5988–6003. doi:10.1016/j.bmc.2014.09.011

Zong, Y., Bice, T. W., Ton-That, H., Schneewind, O., and Narayana, S. V. L. (2004). Crystal Structures of *Staphylococcus aureus* Sortase A and its Substrate Complex. *J. Biol. Chem.* 279, 31383–31389. doi:10.1074/jbc.M401374200

Conflict of Interest: The authors declare that the research was conducted in the absence of any commercial or financial relationships that could be construed as a potential conflict of interest.

Publisher's Note: All claims expressed in this article are solely those of the authors and do not necessarily represent those of their affiliated organizations, or those of the publisher, the editors, and the reviewers. Any product that may be evaluated in this article, or claim that may be made by its manufacturer, is not guaranteed or endorsed by the publisher.

frontiers

Supplementary Material

1 General synthetic procedures

All reagents and solvents were of reagent/analytical grade quality and purchased from *Sigma-Aldrich*, *BLDpharmatech*, or *FisherScientific*. Chemicals were used without further purification. Solvents were purified by distillation and desiccated by standard methods if necessary. ^{1}H and ^{13}C spectra were recorded on a *Bruker* Fourier 300 using DMSO-d_6 or $CDCl_3$ as solvent. Chemical shifts δ are given in parts per million (ppm) using residual proton peaks of the solvent as internal standard (^{1}H / ^{13}C: DMSO: 2.50 / 39.52 ppm, $CHCl_3$: 7.26 / 77.16 ppm). Mass spectra were obtained by LC-MS consisting of an 1100 series HPLC system from *Agilent* with an *Agilent* Poroshell 120 EC-C_{18} 150 x 2.10 mm, 4 μm column. The detection wavelength was 254 nm. The molecular mass was detected by an *Agilent* 1100 series LC/MSD Trap with electron spray ionization (ESI) in positive mode. Column chromatography was performed with silica gel (0.06–0.02 mm) obtained from *Carl Roth*. All reactions were monitored by thin-layer chromatography using *Macherey-Nagel* ALUGRAM Xtra SIL G/UV254 silica gel 60 plates for detection at 254 nm. Melting points (uncorrected) were determined in open capillaries using a Schorpp MPM-H3 melting point device.

2 Synthesis of precursor compounds (1a–o, 2c–d)

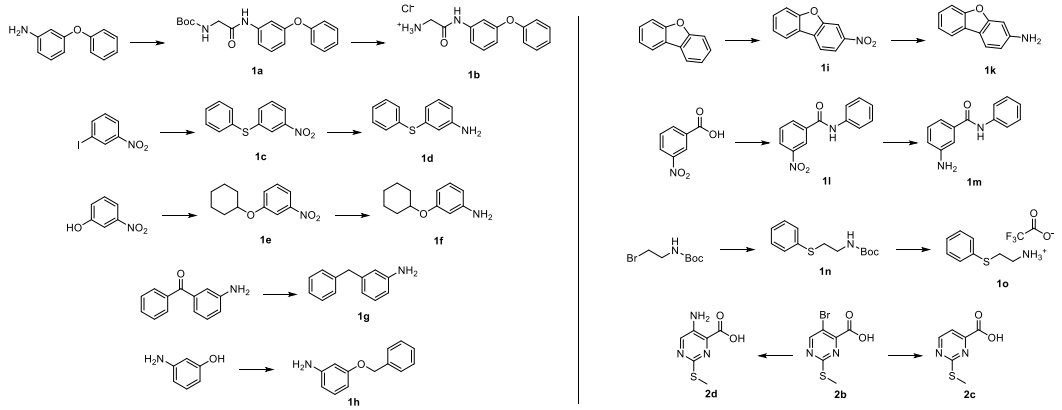

2-Sulfonylpyrimidines as Sortase A Inhibitors

***Tert*-butyl *N*-{[(3-phenoxyphenyl)carbamoyl]methyl}carbamate (1a)**

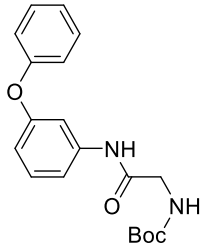

A solution of 3-phenoxyaniline (370 mg, 2.00 mmol), Boc-glycine (350 mg, 2.00 mmol), TBTU (642 mg, 2.00 mmol), and DIPEA (1047 µL, 6.00 mmol) in ethyl acetate (20 mL) was stirred for 16 h at room temperature. The organic phase was extract with $NaHCO_3$ sat., HCl (1 M) and filtered through a pad of silica. Evaporation of the solvent yielded the title compound **1a** as an orange solid (509 mg, 74%); mp: 122 °C; ^{1}H NMR (300 MHz, DMSO-d_6) δ= 9.99 (s, 1H), 7.46 – 7.35 (m, 2H), 7.35 – 7.24 (m, 3H), 7.20 – 7.10 (m, 1H), 7.07 – 6.95 (m, 3H), 6.75 – 6.64 (m, 1H), 3.68 (d, *J* = 6.1 Hz, 2H), 1.37 (s, 9H); ^{13}C NMR (75 MHz, DMSO-d_6) δ= 168.8, 157.5, 156.8, 156.3, 140.9, 130.5, 130.5 (2C), 124.0, 119.3 (2C), 114.2, 113.6, 109.3, 78.5, 44.2, 28.6 (3C); FT-IR (neat): ṽ [cm^{-1}]= 1671, 1589, 1533, 1485, 1440, 1366, 1285, 1220, 1159, 1057, 954, 896, 861, 757, 687.

[(3-Phenoxyphenyl)carbamoyl]methanamine hydrochloride (1b)

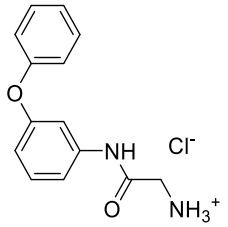

Boc-protected amide **1a** (171 mg, 0.50 mmol) was dissolved in tetrahydrofuran (5 mL). Concentrated hydrochloric acid (5 mL) was added dropwise and the mixture was stirred for 1 h at room temperature. The solvent was evaporated, and the residual was lyophilized from ACN/H_2O (1:1, 5 mL) to give the title compound **1b** as a colourless solid (112 mg, 80%). mp: 235 °C; ^{1}H NMR (300 MHz, DMSO-d_6) δ= 10.83 (s, 1H), 8.55 – 8.01 (m, 3H), 7.47 – 7.27 (m, 5H), 7.16 (t, *J* = 7.4 Hz, 1H), 7.03 (d, *J* = 8.0 Hz, 2H), 6.79 – 6.70 (m, 1H), 3.75 (q, *J* = 5.5 Hz, 2H); ^{13}C NMR (75 MHz, DMSO-d_6) δ= 165.3, 157.7, 156.6, 140.2, 130.7, 130.5 (2C), 124.2, 119.5 (2C), 114.2, 114.0, 109.2, 41.4; FT-IR (neat): ṽ [cm^{-1}]= 3040, 2832, 1679, 1594, 1557, 1478, 1445, 1286, 1246, 1211, 1165, 1130, 967, 938, 895, 882, 818, 790, 768, 743, 688,.

(3-Nitrophenyl)(phenyl)sulfane (1c)

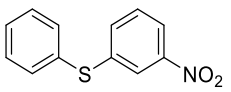

A suspension of 1-iodo-3-nitrobenzene (461 mg, 1.85 mmol), K_2CO_3 (415 mg, 3.00 mmol), thiophenol (234 µL, 2.30 mmol) and copper(I)iodide (145 mg, 0.76 mmol) in dimethylsulfoxide (5 mL) was thoroughly degassed with argon and transferred to an oxygen-free reflux apparatus. Under argon atmosphere, the reaction mixture was heated for 16 h to 140 °C. Subsequently, the solvent was distilled off and the residual was resolved in ethyl acetate. The organic phase was extract with $NaHCO_3$ sat. and HCl (1 M). Purification by column chromatography (CH/EA 20:1) afforded the title compound **1c** as an orange oil (178 mg, 41%); ^{1}H NMR (300 MHz, $CDCl_3$) δ= 8.06 – 7.95 (m, 2H), 7.54 – 7.36 (m, 7H); ^{13}C NMR (75 MHz, $CDCl_3$) δ= 148.8, 140.7, 134.3, 133.5 (2C), 132.2, 130.0 (2C), 129.8, 129.0, 123.2, 121.0; FT-IR (neat): ṽ [cm^{-1}]= 1522, 1475, 1463, 1439, 1344, 1125, 1066, 875, 799, 749, 728, 689, 667.

3-(Phenylthio)aniline (1d)

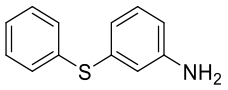

To a solution of nitroarene **1c** (173 mg, 0.75 mmol) in ethyl acetate/methanol (10+1 mL), tin(II)chloride (903 mg, 4.00 mmol) and HCl (1 mL, 1 M) were added. The reaction mixture was stirred for 2 h at 60 °C and subsequently quenched by the addition of $NaHCO_3$ sat. (5 mL). Extraction with ethyl acetate and filtration through a pad of silica afforded the title compound **1d** as a yellowish oil (108 mg, 71%); ^{1}H NMR (300 MHz, $CDCl_3$) δ= 7.28 – 7.19 (m, 2H), 7.18 – 7.07 (m, 3H), 6.93 (t, *J* = 7.9 Hz, 1H), 6.65 – 6.56 (m, 1H), 6.50 (t, *J* = 2.0 Hz, 1H), 6.38 (dd, *J* = 7.9, 2.3 Hz, 1H), 3.44 (s, 2H); ^{13}C NMR (75 MHz, $CDCl_3$) δ= 147.2, 136.3, 135.7, 131.0 (2C), 129.9, 129.1 (2C), 126.9, 120.9, 117.1, 113.9; FT-IR (neat): ṽ [cm^{-1}]= 3365, 1616, 1589, 1525, 1476, 1437, 1299, 1264, 1164, 1075, 1023, 991, 887, 857, 773, 739, 685.

1-(Cyclohexyloxy)-3-nitrobenzene (1e)

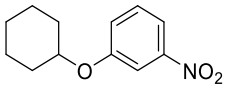

To an ice-cooled solution of 3-nitrophenol (278 mg, 2.00 mmol), cyclohexanol (832 µL, 8.00 mmol) and triphenylphosphine (1049 mg, 4.00 mmol) in tetrahydrofuran (10 mL) diisopropyl azodicarboxylate (785 µL, 4.00 mmol) was added. The reaction mixture was stirred under argon atmosphere for 168 h at room temperature. Purification by column chromatography (CH/EA 10:1) afforded the title compound **1e** as a yellowish oil (224 mg, 50%); ^{1}H NMR (300 MHz, $CDCl_3$) δ= 7.82 – 7.73 (m, 1H), 7.71 (t, *J* = 2.3 Hz, 1H), 7.39 (t, *J* = 8.2 Hz, 1H), 7.23 – 7.14 (m, 1H), 4.47 – 4.21 (m, 1H), 2.06 – 1.92 (m, 2H), 1.87 – 1.73 (m, 2H), 1.67 – 1.49 (m, 3H), 1.46 – 1.32 (m, 3H); ^{13}C NMR (75 MHz, $CDCl_3$) δ= 158.5, 149.3, 130.0, 122.9, 115.5, 110.2, 76.2, 74.4, 31.5, 25.5, 23.6, 21.7; FT-IR (neat): ṽ [cm^{-1}]= 2935, 2859, 1773, 1616, 1578, 1525, 1478, 1449, 1346, 1284, 1237, 1094, 1043, 1021, 999, 975, 892, 845, 811, 794, 736, 673.

3-(Cyclohexyloxy)aniline (1f)

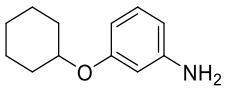

To a solution of nitroarene **1e** (177 mg, 0.80 mmol) in tetrahydrofuran (10 mL), Pd/C (20 mg) was added. The reaction mixture was stirred for 16 h under H_2-atmosphere (15 psi) at room temperature. Subsequently, the catalyst was filtered off and the solvent was removed *in vacuo* to afford the title compound **1f** as an orange oil (150 mg, 98%); ^{1}H NMR (300 MHz, $CDCl_3$) δ= 6.97 – 6.85 (m, 1H), 6.26 – 6.19 (m, 1H), 6.18 – 6.09 (m, 2H), 4.14 – 4.01 (m, 1H), 3.59 (s, 2H), 1.95 – 1.81 (m, 2H), 1.76 – 1.60 (m, 2H), 1.52 – 1.11 (m, 6H); ^{13}C NMR (75 MHz, $CDCl_3$) δ= 158.4, 147.3, 129.5, 107.3, 105.6, 102.8, 74.7, 31.4, 29.8, 25.1, 23.3, 21.4; FT-IR (neat): ṽ [cm^{-1}]= 2932, 2855, 1721, 1596, 1492, 1448, 1372, 1288, 1231, 1181, 1148, 1107, 1046, 1021, 984, 928, 888, 843, 762, 687.

3-Benzylaniline (1g)

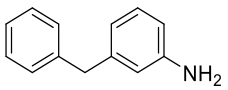

To a solution of 3-benzoylaniline (296 mg, 1.50 mmol) in tetrahydrofuran (10 mL), trifluoroacetic acid (1 mL) and Pd/C (30 mg) were added. The reaction mixture was stirred for 5 h under H_2-atmosphere (80 psi) at room temperature.

Subsequently, the catalyst was filtered off and the solvent was removed *in vacuo*. The residual was suspended in $NaHCO_3$ sat. and extracted twice with ethyl acetate. The organic phase was filtered through a pad of silica and evaporated to afford the title compound **1g** as a brownish oil (270 mg, 98%); ^{1}H NMR (300 MHz, $CDCl_3$) δ= 7.44 – 7.17 (m, 7H), 6.64 (d, *J* = 7.6 Hz, 1H), 6.59 – 6.51 (m, 1H), 3.92 (s, 2H), 3.47 (s, 2H); ^{13}C NMR (75 MHz, $CDCl_3$) δ= 146.4, 142.4, 141.2, 129.4, 129.0 (2C), 128.5 (2C), 126.1, 119.5, 115.9, 113.1, 42.0; FT-IR (neat): ṽ [cm^{-1}]= 3025, 2916, 1673, 1599, 1492, 1451, 1288, 1200, 1135, 1073, 1029, 995, 764, 724, 694.

3-(Benzyloxy)aniline (1h)

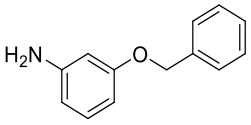

The title compound **1h** was synthesized by a procedure according to Tröster et al. 3-aminophenol (546 mg, 5.00 mmol) and KO*t*Bu (673 mg, 6.00 mmol) were solved in dimethylformamide (5 mL). Benzyl bromide (593 µL, 5.00 mmol) was added dropwise and the reaction mixture was stirred for 16 h at room temperature. Subsequently, the mixture was diluted with water (50 mL) and extracted thrice with ethyl acetate. The combined organic phases were washed with $NaHCO_3$ sat. and brine. Filtration through a pad of silica and evaporation of the solvent yielded the title compound **1h** as a beige solid (713 mg, 71%); mp: 62 °C; ^{1}H NMR (300 MHz, DMSO-*d*$_6$) δ= 7.55 – 7.28 (m, 5H), 7.13 – 6.97 (m, 1H), 6.46 – 6.37 (m, 1H), 6.36 – 6.27 (m, 2H), 5.03 (s, 2H), 3.65 (s, 2H); ^{13}C NMR (75 MHz, DMSO-*d*$_6$) δ= 160.1, 147.9, 137.3, 130.2, 128.6, 127.9, 127.5, 108.3, 105.0, 102.1, 69.9; FT-IR (neat): ṽ [cm^{-1}]= 1492, 1453, 1371, 1336, 1294, 1218, 1186, 1176, 1162, 1012, 989, 937, 911, 842, 758, 739, 689.

3-Nitrodibenzo[*b,d*]furan (1i)

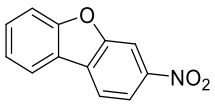

The title compound **1i** was synthesized by a procedure according to Li et al. Dibenzo[*b,d*]furan (505 mg, 3.00 mmol) was suspended in trifluoroacetic acid (1.2 mL) and cooled to –20 °C. Red fuming nitric acid (145 µL, 1.17 mmol) was carefully mixed with trifluoroacetic acid (1.0 mL) and the nitrating agent was added dropwise to the reaction. Subsequently, the reaction mixture was warmed to room temperature and stirred for 3 h until completion of the conversion. The precipitated product was isolated by filtration, washed with water and dried by lyophilization. The title compound **1i** was yielded as a beige solid (588 mg, 91%); mp: 179 °C; ^{1}H NMR (300 MHz, $CDCl_3$) δ= 8.44 (d, *J* = 2.0 Hz, 1H), 8.28 (dd, *J* = 8.5, 2.0 Hz, 1H), 8.09 – 7.99 (m, 2H), 7.70 – 7.53 (m, 2H), 7.50 – 7.39 (m, 1H); ^{13}C NMR (75 MHz, $CDCl_3$) δ= 158.4, 155.1, 130.3, 129.7, 126.6, 123.9, 121.9, 120.6, 118.6, 112.4, 111.7, 108.1; FT-IR (neat): ṽ [cm^{-1}]= 3102, 1629, 1522, 1457, 1421, 1359, 1340, 1263, 1231, 1197, 1107, 1061, 1018, 929, 871, 846, 820, 758, 733, 719, 688.

Dibenzo[*b,d*]furan-3-amine (1k)

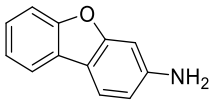

To a solution of nitroarene **1i** (320 mg, 1.50 mmol) in ethyl acetate/dichloromethane (10+10 mL), Pd/C (30 mg) was added. The reaction mixture was stirred for 6 h under H_2-atmosphere (60 psi) at room temperature. Subsequently, the catalyst was filtered off and the solvent was removed *in vacuo*

to afford the title compound **1k** as a yellowish solid (259 mg, 94%); mp: 89 °C; ^{1}H NMR (300 MHz, $CDCl_3$) δ= 7.85 – 7.77 (m, 1H), 7.71 (d, *J* = 8.2 Hz, 1H), 7.54 – 7.43 (m, 1H), 7.41 – 7.23 (m, 2H), 6.87 (d, *J* = 2.0 Hz, 1H), 6.71 (dd, *J* = 8.2, 2.0 Hz, 1H), 3.83 (s, 2H); ^{13}C NMR (75 MHz, $CDCl_3$) δ= 158.0, 156.0, 146.8, 125.2, 124.9, 122.6, 121.3, 119.4, 115.7, 111.3, 111.2, 97.6; FT-IR (neat): ṽ [cm^{-1}]= 3364, 1635, 1602, 1507, 1456, 1354, 1303, 1273, 1186, 1149, 1127, 1014, 940, 844, 810, 777, 747, 720.

3-Nitro-*N*-phenylbenzamide (1l)

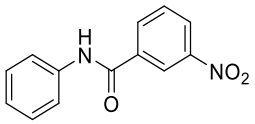

A solution of aniline (159 µL, 1.75 mmol), 3-nitrobenzoic acid (292 mg, 1.75 mmol), TBTU (562 mg, 1.75 mmol) and DIPEA (916 µL, 5.25 mmol) in ethyl acetate (20 mL) was stirred for 16 h at room temperature. The organic phase was extract with $NaHCO_3$ sat., HCl (1 M), and filtered through a pad of silica. Evaporation of the solvent yielded the title compound **1l** as an orange solid (344 mg, 81%); mp: 149 °C; ^{1}H NMR (300 MHz, $CDCl_3$) δ= 8.69 (t, *J* = 2.0 Hz, 1H), 8.43 – 8.32 (m, 1H), 8.31 – 8.20 (m, 1H), 8.19 – 8.08 (m, 1H), 7.73 – 7.58 (m, 3H), 7.44 – 7.30 (m, 2H), 7.23 – 7.11 (m, 1H); ^{13}C NMR (75 MHz, $CDCl_3$) δ= 163.5, 148.3, 137.4, 136.7, 133.5, 130.2, 129.3 (2C), 126.4, 125.4, 122.0, 120.7 (2C); FT-IR (neat): ṽ [cm^{-1}]= 3322, 1648, 1597, 1525, 1495, 1444, 1345, 1326, 1258, 1135, 1073, 1002, 914, 813, 752, 715, 689, 667.

3-Amino-*N*-phenylbenzamide (1m)

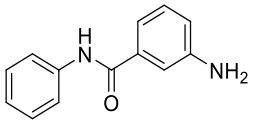

To a solution of nitroarene **1l** (291 mg, 1.20 mmol) in ethyl acetate (10 mL), Pd/C (30 mg) was added. The reaction mixture was stirred for 16 h under H_2-atmosphere (60 psi) at room temperature. Subsequently, the catalyst was filtered off and the solvent was removed *in vacuo* to afford the title compound **1m** as a beige solid (230 mg, 90%); mp: 124 °C; ^{1}H NMR (300 MHz, $CDCl_3$) δ= 7.95 (s, 1H), 7.68 – 7.57 (m, 2H), 7.39 – 7.30 (m, 2H), 7.23 – 7.08 (m, 4H), 6.84 – 6.75 (m, 1H), 3.82 (s, 2H); ^{13}C NMR (75 MHz, $CDCl_3$) δ= 166.2, 147.1, 138.1, 136.2, 129.7, 129.1 (2C), 124.5, 120.3 (2C), 118.3, 116.4, 113.9; FT-IR (neat): ṽ [cm^{-1}]= 3363, 1638, 1619, 1592, 1517, 1489, 1456, 1435, 1321, 1241, 1175, 1077, 994, 905, 880, 792, 750, 688.

***Tert*-butyl (2-(phenylthio)ethyl)carbamate (1n)**

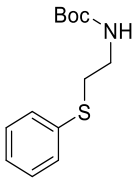

tert-butyl *N*-(2-bromoethyl)carbamate (448 mg, 2.00 mmol), thiophenol (204 µL, 2.00 mmol), DIPEA (1.0 mL, 6.00 mmol) and potassium iodide (332 mg, 2.00 mmol) were suspended in acetonitrile (5 mL) and stirred for 16 h at room temperature under argon atmosphere. Subsequently, the solvent was evaporated and the residual was resolved in ethyl acetate (10 mL). The organic phase was extract with $NaHCO_3$ sat., HCl (1 M), and filtered through a pad of silica. Evaporation of the solvent yielded the title compound **1n** as a colourless oil (414 mg, 81%); ^{1}H NMR (300 MHz, $CDCl_3$) δ= 7.40 – 7.32 (m, 2H), 7.31 – 7.23 (m, 2H), 7.21 – 7.11 (m, 1H), 3.31 (q, *J* = 6.5 Hz, 2H), 3.02 (t, *J* = 6.5 Hz, 2H), 1.43 (s, 9H); ^{13}C NMR (75 MHz, $CDCl_3$) δ= 155.3, 134.8, 129.2 (2C), 128.5 (2C), 125.9, 78.9,

39.2, 33.5, 27.9 (3C); FT-IR (neat): $\tilde{\nu}$ [cm^{-1}]= 3315, 2915, 1687, 1639, 1506, 1478, 1364, 1334, 1249, 1160, 1088, 1025, 947, 889, 736, 690.

2-(Phenylthio)ethan-1-amine trifluoroacetate (1o)

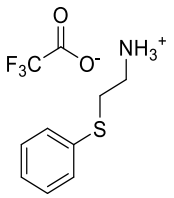

The Boc-protected amine **1n** (304 mg, 1.20 mmol) was suspended in dichloromethane (1.0 mL). Subsequently, trifluoroacetic acid (1.0 mL) was added and the reaction was stirred for 4 h at room temperature. Evaporation of the solvent and lyophilization from acetonitrile/water (1:1) yielded the title compound **1o** as a colourless oil (320 mg, 99%); ^{1}H NMR (300 MHz, DMSO-d_6) δ= 8.02 (s, 3H), 7.46 – 7.30 (m, 4H), 7.29 – 7.18 (m, 1H), 3.25 – 3.12 (m, 2H), 3.03 – 2.90 (m, 2H); ^{13}C NMR (75 MHz, DMSO-d_6) δ= 158.5 (d, J = 34.1 Hz), 134.2, 129.4 (2C), 128.8 (2C), 126.5, 38.2, 29.5; FT-IR (neat): $\tilde{\nu}$ [cm^{-1}]= 2903, 1669, 1475, 1439, 1328, 1134, 1024, 889, 840, 797, 740, 723, 690.

2-(Methylthio)pyrimidine-4-carboxylic acid (2c)

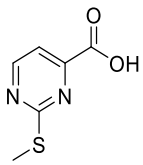

The title compound **2c** was synthesized by a procedure according to Arukwe et al. 5-bromo-2-(methylsulfanyl)pyrimidine-4-carboxylic acid **2a** (400 mg, 1.60 mmol) was solved in anhydrous tetrahydrofuran (15 mL) and cooled to –78 °C. A solution of *n*-butyllithium (1.3 mL, 2.5 M in hexanes) was added dropwise under argon atmosphere. The reaction mixture was stirred for 2 h at –78 °C and subsequently quenched by the addition of HCl (2 mL, 1 M). The mixture was warmed to room temperature and stirred for additional 30 min. The solvent was evaporated and the residual was extracted twice from dichloromethane/water. The combined organic layers were filtered through a pad of silica. Evaporation of the solvent yielded the title compound **2c** as a yellowish solid (57 mg, 20%); mp: 198 °C; ^{1}H NMR (300 MHz, DMSO-d_6) δ= 8.86 (d, J = 4.9 Hz, 1H), 7.64 (d, J = 4.9 Hz, 1H), 2.55 (s, 3H); ^{13}C NMR (75 MHz, DMSO-d_6) δ= 172.2, 164.9, 159.9, 156.1, 115.9, 13.6; FT-IR (neat): $\tilde{\nu}$ [cm^{-1}]= 1670, 1588, 1512, 1484, 1404, 1355, 1321, 1225, 1160, 1125, 1058, 966, 855, 766, 737, 693, 668.

5-Amino-2-(methylthio)pyrimidine-4-carboxylic acid (2d)

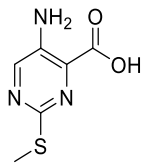

The title compound **2d** was synthesized by a procedure according to Grant et al. 5-bromo-2-(methylsulfanyl)pyrimidine-4-carboxylic acid **2a** (623 mg, 2.50 mmol) and copper(II)sulfate (24 mg, 0.15 mmol) were solved in NH_3 aq. (5 mL, 25%). The reaction mixture was heated in a sealed tube for 4 h to 100 °C. The cooled reaction mixture was adjusted to pH=1 with conc. HCl and the precipitate was isolated by filtration. The solid residual was washed with water and dichloromethane. After drying, the title compound **2d** was obtained as a yellow solid (195 mg, 42%); mp: 190 °C; ^{1}H NMR (300 MHz, DMSO-d_6) δ= 8.44 (s, 1H), 2.47 (s, 3H); ^{13}C NMR (75 MHz, DMSO-d_6) δ= 167.7, 154.8, 150.2, 140.6, 131.5, 13.6; FT-IR (neat): $\tilde{\nu}$ [cm^{-1}]= 3439, 3327, 2436, 1865, 1656, 1603, 1566, 1463, 1408, 1320, 1290, 1211, 1136, 985, 947, 905, 787, 736, 696, 663.

3 Synthesis of 2-(methylthio)pyrimidine-4-carboxamides (3a–z)

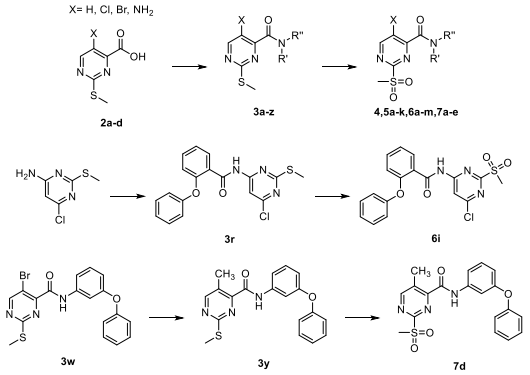

General procedure (I) for the synthesis of 2-(methylthio)pyrimidine-4-carboxamides

The respective pyrimidinecarboxylic acid (1.0 eq.), the corresponding amine component (1.0 eq.), TBTU (1.0 eq.) and DIPEA (3.0 eq.) were suspended in ethyl acetate and stirred for 24 h at room temperature. The organic phase was extracted with $NaHCO_3$ sat., HCl (1 M), and filtered through a pad of silica. Evaporation of the solvent yielded the corresponding 2-(methylthio)pyrimidine-4-carboxamides (**3a–z**), which were used without further purification.

N-(2-benzylphenyl)-5-chloro-2-(methylthio)pyrimidine-4-carboxamide (3a)

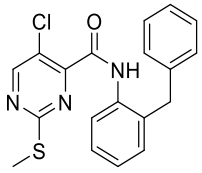

According to the general procedure (I), the title compound **3a** was obtained from **2a** and 2-benzylaniline as a yellowish solid (80 mg, 30%); mp: 150 °C; ^{1}H NMR (300 MHz, $CDCl_3$) δ= 9.45 (s, 1H), 8.67 (s, 1H), 8.20 (d, *J* = 7.7 Hz, 1H), 7.43 – 7.16 (m, 8H), 4.10 (s, 2H), 2.47 (s, 3H); ^{13}C NMR (75 MHz, $CDCl_3$) δ= 170.0, 160.8, 159.3, 151.5, 138.7, 135.1, 131.3, 131.0, 129.0 (2C), 128.6 (2C), 127.8, 126.8, 125.8, 125.3, 123.1, 38.2, 14.6; FT-IR (neat): ṽ [cm^{-1}]= 3345, 1702, 1585, 1547, 1529, 1511, 1473, 1453, 1434, 1397, 1315, 1299, 1214, 1154, 1072, 1046, 962, 754, 726, 694, 672, 655.

5-Chloro-2-(methylthio)-*N*-(3-phenoxyphenyl)pyrimidine-4-carboxamide (3b)

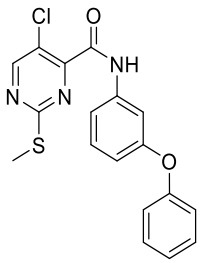

According to the general procedure (I), the title compound **3b** was obtained from **2a** and 3-phenoxyaniline as a yellow solid (170 mg, 91%); mp: 148 °C; ^{1}H NMR (300 MHz, DMSO-d_6) δ= 10.89 (s, 1H), 8.94 (s, 1H), 7.51 – 7.33 (m, 6H), 7.17 (t, *J* = 7.4 Hz, 1H), 7.07 (d, *J* = 8.0 Hz, 2H), 6.82 (dd, *J* = 8.0, 2.3 Hz, 1H), 2.57 (s, 3H); ^{13}C NMR (75 MHz, DMSO-d_6) δ= 169.9, 161.2, 158.5, 157.4, 157.2, 156.1, 139.4, 130.4, 130.1 (2C), 123.8, 122.1, 119.0 (2C), 114.4, 109.4, 14.0; FT-IR (neat): ṽ [cm^{-1}]= 3367, 1693, 1589, 1534, 1509, 1485, 1418, 1394, 1312, 1270, 1213, 1175, 1157, 1050, 964, 865, 809, 787, 773, 734, 687, 675.

2-Sulfonylpyrimidines as Sortase A Inhibitors

5-Chloro-2-(methylthio)-*N*-(2-oxo-2-((3-phenoxyphenyl)amino)ethyl)pyrimidine-4-carboxamide (3c)

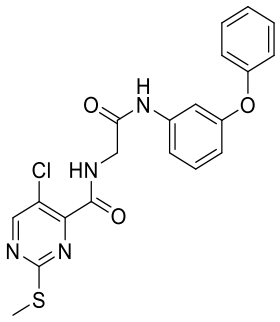

According to the general procedure (I), the title compound **3c** was obtained from **2a** and **1b** as a colourless solid (112 mg, 52%); mp: 193 °C; ^{1}H NMR (300 MHz, DMSO-d_6) δ= 10.19 (s, 1H), 9.08 (t, J = 5.8 Hz, 1H), 8.88 (s, 1H), 7.47 – 7.35 (m, 2H), 7.35 – 7.26 (m, 3H), 7.21 – 7.09 (m, 1H), 7.08 – 6.98 (m, 2H), 6.79 – 6.66 (m, 1H), 4.08 (d, J = 5.8 Hz, 2H), 2.57 (s, 3H); ^{13}C NMR (75 MHz, DMSO-d_6) δ= 169.4, 166.8, 162.6, 158.9, 157.1, 156.3, 156.0, 140.2, 130.2, 130.0 (2C), 123.6, 122.9, 118.9 (2C), 113.8, 113.3, 108.8, 42.7, 14.0; FT-IR (neat): ṽ [cm^{-1}]= 3321, 1700, 1668, 1609, 1594, 1536, 1506, 1480, 1419, 1388, 1312, 1257, 1216, 1171, 1149, 947, 886, 795, 756, 693, 663.

5-Chloro-*N*-(4'-cyano-[1,1'-biphenyl]-4-yl)-2-(methylthio)pyrimidine-4-carboxamide (3d)

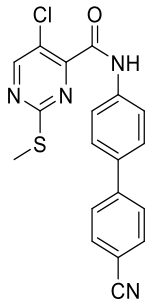

According to the general procedure (I), the title compound **3d** was obtained from **2a** and 4'-amino-[1,1'-biphenyl]-4-carbonitrile as a yellowish solid (115 mg, 60%); mp: 225 °C; ^{1}H NMR (300 MHz, DMSO-d_6) δ= 11.01 (s, 1H), 8.97 (s, 1H), 7.97 – 7.77 (m, 8H), 2.59 (s, 3H); ^{13}C NMR (75 MHz, DMSO-d_6) δ= 169.9, 161.2, 158.5, 157.4, 143.8, 138.5, 134.1, 132.8 (2C), 127.7 (2C), 127.1 (2C), 122.2, 120.2 (2C), 118.9, 109.7, 14.1; FT-IR (neat): ṽ [cm^{-1}]= 3339, 2222, 1678, 1603, 1590, 1550, 1532, 1501, 1419, 1399, 1311, 1217, 1183, 1154, 1050, 962, 809, 741, 719, 707, 679, 656.

***Tert*-butyl 5-(5-chloro-2-(methylthio)pyrimidine-4-carboxamido)-1*H*-indazole-1-carboxylate (3e)**

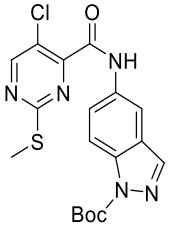

According to the general procedure (I), the title compound **3e** was obtained from **2a** and *tert*-butyl 5-amino-1*H*-indazole-1-carboxylate as an orange solid (200 mg, 95%); mp: 187 °C; ^{1}H NMR (300 MHz, $CDCl_3$) δ= 9.76 (s, 1H), 8.70 (s, 1H), 8.48 – 8.37 (m, 1H), 8.24 – 8.10 (m, 2H), 7.61 (dd, J = 9.0, 2.1 Hz, 1H), 2.65 (s, 3H), 1.73 (s, 9H); ^{13}C NMR (75 MHz, $CDCl_3$) δ= 169.6, 160.6, 158.9, 150.7, 148.7, 139.2, 136.8, 132.6, 126.0, 125.0, 121.8, 114.8, 111.3, 84.8, 27.8 (3C), 14.4; FT-IR (neat): ṽ [cm^{-1}]= 1734, 1686, 1602, 1546, 1517, 1431, 1385, 1349, 1305, 1289, 1245, 1214, 1159, 1146, 1030, 896, 873, 844, 829, 792, 764, 669.

2-Sulfonylpyrimidines as Sortase A Inhibitors

5-Chloro-2-(methylthio)-*N*-(4-(*p*-tolyl)thiazol-2-yl)pyrimidine-4-carboxamide (3f)

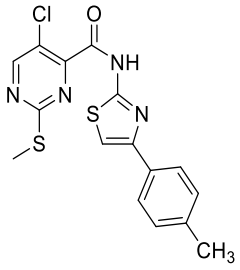

According to the general procedure (I), the title compound **3f** was obtained from **2a** and 4-(*p*-tolyl)thiazol-2-amine as a yellowish solid (80 mg, 42%); mp: 162 °C; ^{1}H NMR (300 MHz, DMSO-d_6) δ= 13.12 (s, 1H), 8.98 (s, 1H), 7.82 (d, J = 8.1 Hz, 2H), 7.71 – 7.61 (m, 2H), 7.00 (s, 1H), 2.60 (s, 3H), 2.33 (s, 3H); ^{13}C NMR (75 MHz, DMSO-d_6) δ= 168.8, 158.6, 155.8, 137.5, 131.2, 129.3, 129.2 (2C), 125.7, 125.5 (2C), 122.6, 108.5, 100.9, 20.8, 14.0; FT-IR (neat): ṽ [cm^{-1}]= 1688, 1627, 1537, 1518, 1434, 1380, 1334, 1321, 1306, 1268, 1206, 1182, 1150, 1131, 1063, 1040, 820, 794, 753, 730, 708, 676.

(5-Chloro-2-(methylthio)pyrimidin-4-yl)(3,4-dihydroisoquinolin-2(1*H*)-yl)methanone (3g)

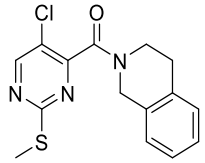

According to the general procedure (I), the title compound **3g** was obtained from **2a** and 1,2,3,4-tetrahydroisoquinoline as a beige solid (151 mg, 94%); mp: 141 °C; ^{1}H NMR (300 MHz, $CDCl_3$) δ= 8.58 (d, J = 3.7 Hz, 1H), 7.32 – 6.90 (m, 4H), 5.03 – 4.35 (m, 2H), 4.08 – 3.45 (m, 2H), 2.97 (dt, J = 26.9, 6.0 Hz, 2H), 2.56 (d, J = 7.0 Hz, 3H); ^{13}C NMR (75 MHz, $CDCl_3$) δ= 171.5, 163.4, 163.2, 159.4, 157.3, 134.4, 133.6, 132.0, 131.7, 129.1, 128.8, 127.3, 126.9, 126.8, 126.7, 126.0, 122.6, 47.9, 44.2, 44.0, 39.9, 30.0, 29.5, 28.3, 14.7; FT-IR (neat): ṽ [cm^{-1}]= 3342, 1696, 1593, 1569, 1522, 1474, 1434, 1386, 1333, 1306, 1261, 1247, 1207, 1148, 1117, 1043, 986, 943, 885, 862, 770, 737, 686, 665.

5-Chloro-2-(methylthio)-*N*-(pentan-3-yl)pyrimidine-4-carboxamide (3h)

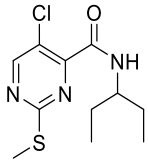

According to the general procedure (I), the title compound **3h** was obtained from **2a** and pentan-3-amine as a colourless solid (123 mg, 89%); mp: 125 °C; ^{1}H NMR (300 MHz, $CDCl_3$) δ= 8.62 (s, 1H), 7.30 (d, J = 9.2 Hz, 1H), 4.04 – 3.77 (m, 1H), 2.57 (s, 3H), 1.76 – 1.39 (m, 4H), 0.95 (t, J = 7.4 Hz, 6H); ^{13}C NMR (75 MHz, $CDCl_3$) δ= 169.8, 161.5, 160.4, 152.5, 125.0, 52.6, 27.4 (2C), 14.7, 10.4 (2C); FT-IR (neat): ṽ [cm^{-1}]= 2922, 1647, 1546, 1526, 1464, 1445, 1386, 1361, 1332, 1308, 1284, 1250, 1197, 1105, 1039, 929, 841, 814, 780, 753, 731, 657.

***N,N*-dibenzyl-5-chloro-2-(methylthio)pyrimidine-4-carboxamide (3i)**

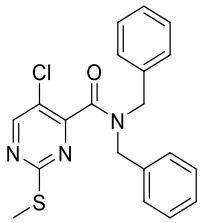

According to the general procedure (I), the title compound **3i** was obtained from **2a** and *N,N*-dibenzylamine as a beige solid (190 mg, 99%); mp: 120 °C; ^{1}H NMR (300 MHz, $CDCl_3$) δ= 8.98 (s, 1H), 7.91 – 7.58 (m, 10H), 5.14 (s, 2H), 4.67 (s, 2H), 2.97 (s, 3H); ^{13}C NMR (75 MHz, $CDCl_3$) δ= 171.4, 164.9, 159.4, 157.3, 135.8, 135.0, 129.1, 128.9 (2C), 128.6 (2C), 128.3 (2C), 127.9 (2C), 126.5, 122.6, 50.6, 46.6, 14.6; FT-IR (neat): ṽ [cm^{-1}]= 1645, 1529, 1494, 1473, 1452, 1439, 1417, 1386, 1366, 1355, 1334, 1304, 1263, 1201, 1166, 1025, 1009, 959, 784, 743, 729, 699, 665.

***N*-(3-benzoylphenyl)-5-chloro-2-(methylthio)pyrimidine-4-carboxamide (3k)**

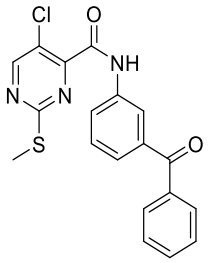

According to the general procedure (I), the title compound **3k** was obtained from **2a** and 3-benzoylaniline as a beige solid (237 mg, 88%); mp: 158 °C; ^{1}H NMR (300 MHz, $CDCl_3$) δ= 9.72 (s, 1H), 8.70 (s, 1H), 8.23 – 8.10 (m, 1H), 7.98 (t, *J* = 1.9 Hz, 1H), 7.89 – 7.76 (m, 2H), 7.67 – 7.42 (m, 5H), 2.64 (s, 3H); ^{13}C NMR (75 MHz, $CDCl_3$) δ= 196.1, 170.2, 161.1, 159.4, 151.0, 138.7, 137.3, 137.2, 132.8, 130.2 (2C), 129.3, 128.5 (2C), 126.8, 125.4, 123.9, 121.1, 14.8; FT-IR (neat): ṽ [cm^{-1}]= 3323, 1687, 1648, 1593, 1532, 1509, 1483, 1415, 1395, 1317, 1215, 1157, 1125, 1055, 968, 893, 856, 814, 787, 719, 707, 693, 669.

5-Chloro-*N*-(3-(cyclohexyloxy)phenyl)-2-(methylthio)pyrimidine-4-carboxamide (3l)

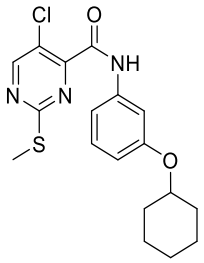

According to the general procedure (I), the title compound **3l** was obtained from **2a** and **1f** as a reddish oil (220 mg, 97%); ^{1}H NMR (300 MHz, $CDCl_3$) δ= 9.55 (s, 1H), 8.61 (s, 1H), 7.40 (t, *J* = 2.2 Hz, 1H), 7.24 – 7.08 (m, 2H), 6.78 – 6.62 (m, 1H), 4.34 – 4.19 (m, 1H), 2.57 (s, 3H), 2.04 – 1.85 (m, 2H), 1.84 – 1.67 (m, 2H), 1.57 – 1.14 (m, 6H); ^{13}C NMR (75 MHz, $CDCl_3$) δ= 169.8, 160.5, 159.1, 158.4, 151.6, 138.0, 129.7, 125.0, 112.8, 112.0, 107.9, 75.3, 38.5, 31.7, 25.6, 23.5, 21.9, 14.6; FT-IR (neat): ṽ [cm^{-1}]= 3338, 2937, 1691, 1593, 1536, 1513, 1442, 1393, 1310, 1273, 1213, 1153, 1046, 1000, 985, 941, 867, 767, 736, 684, 670.

***N*-(3-benzylphenyl)-5-chloro-2-(methylthio)pyrimidine-4-carboxamide (3m)**

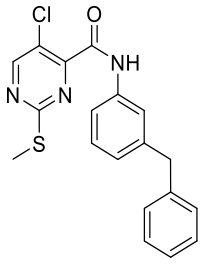

According to the general procedure (I), the title compound **3m** was obtained from **2a** and **1g** as a beige solid (138 mg, 53%); mp: 153 °C; ^{1}H NMR (300 MHz, $CDCl_3$) δ= 9.97 (s, 1H), 9.13 (s, 1H), 8.01 (d, *J* = 8.3 Hz, 2H), 7.77 – 7.58 (m, 7H), 7.46 (d, *J* = 7.3 Hz, 1H), 4.45 (s, 2H), 3.07 (s, 3H); ^{13}C NMR (75 MHz, $CDCl_3$) δ= 169.9, 161.0, 159.1, 151.4, 142.5, 140.8, 137.1, 129.3, 129.0 (2C), 128.6 (2C), 126.3, 125.9, 125.4, 120.5, 117.9, 42.0, 14.8; FT-IR (neat): ṽ [cm^{-1}]= 3350, 1688, 1609, 1535, 1514, 1489, 1452, 1420, 1393, 1307, 1214, 1153, 1050, 883, 810, 784, 759, 734, 699, 661.

5-Chloro-*N*-(3-methoxyphenyl)-2-(methylthio)pyrimidine-4-carboxamide (3n)

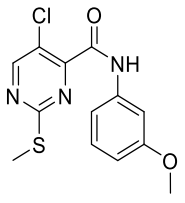

According to the general procedure (I), the title compound **3n** was obtained from **2a** and 3-methoxyaniline as a beige solid (185 mg, 85%); mp: 151 °C; ^{1}H NMR (300 MHz, $CDCl_3$) δ= 9.98 (s, 1H), 9.08 (s, 1H), 7.90 (t, *J* = 2.3 Hz, 1H), 7.71 – 7.61 (m, 1H), 7.57 – 7.50 (m, 1H), 7.13 (dd, *J* = 8.2, 2.5 Hz, 1H), 4.24 (s, 3H), 3.03 (s, 3H); ^{13}C NMR (75 MHz, $CDCl_3$) δ= 170.0, 161.0, 160.4, 159.1, 151.3, 138.2, 129.9, 125.3, 112.2, 111.3, 105.5, 55.5, 14.7; FT-IR (neat): ṽ [cm^{-1}]= 3318, 1691, 1595, 1540, 1515, 1469, 1454, 1430, 1385, 1336, 1287, 1206, 1180, 1158, 1084, 1036, 958, 855, 798, 770, 737, 688, 675.

_N_-([1,1'-biphenyl]-3-yl)-5-chloro-2-(methylthio)pyrimidine-4-carboxamide (3o)

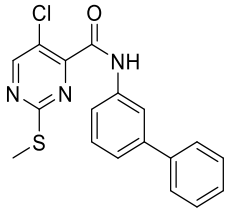

According to the general procedure (I), the title compound **3o** was obtained from **2a** and [1,1'-biphenyl]-3-amine as a beige solid (225 mg, 90%); mp: 189 °C; ^{1}H NMR (300 MHz, $CDCl_3$) δ= 9.67 (s, 1H), 8.70 (s, 1H), 8.00 (t, *J* = 1.9 Hz, 1H), 7.76 – 7.57 (m, 3H), 7.50 – 7.32 (m, 5H), 2.65 (s, 3H); ^{13}C NMR (75 MHz, $CDCl_3$) δ= 170.0, 161.0, 159.2, 151.3, 142.5, 140.6, 137.4, 129.6, 128.9 (2C), 127.7, 127.4 (2C), 125.4, 124.0, 118.8, 14.8; FT-IR (neat): ṽ [cm^{-1}]= 3367, 1691, 1601, 1537, 1504, 1449, 1406, 1392, 1315, 1214, 1153, 963, 868, 820, 802, 757, 738, 697, 673.

5-Chloro-2-(methylthio)-_N_-(2-phenoxyphenyl)pyrimidine-4-carboxamide (3p)

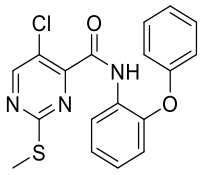

According to the general procedure (I), the title compound **3p** was obtained from **2a** and 2-phenoxyaniline as a yellowish solid (191 mg, 73%); mp: 126 °C; ^{1}H NMR (300 MHz, $CDCl_3$) δ= 10.50 (s, 1H), 8.70 – 8.61 (m, 2H), 7.44 – 7.30 (m, 2H), 7.23 – 7.01 (m, 5H), 6.93 (dd, *J* = 8.1, 1.5 Hz, 1H), 2.39 (s, 3H); ^{13}C NMR (75 MHz, $CDCl_3$) δ= 170.1, 161.1, 159.1, 156.6, 151.1, 146.1, 130.1 (2C), 129.3, 125.4, 125.0, 124.5, 124.1, 120.5, 118.4 (2C), 118.2, 14.6; FT-IR (neat): ṽ [cm^{-1}]= 3313, 1697, 1588, 1541, 1516, 1491, 1449, 1383, 1333, 1302, 1248, 1205, 1100, 1046, 876, 787, 745, 693, 675.

5-Chloro-2-(methylthio)-_N_-(4-phenoxyphenyl)pyrimidine-4-carboxamide (3q)

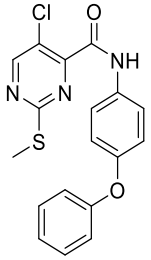

According to the general procedure (I), the title compound **3q** was obtained from **2a** and 4-phenoxyaniline as a yellowish solid (221 mg, 84%); mp: 181 °C; ^{1}H NMR (300 MHz, $CDCl_3$) δ= 9.56 (s, 1H), 8.69 (s, 1H), 7.75 – 7.62 (m, 2H), 7.40 – 7.29 (m, 2H), 7.17 – 6.96 (m, 5H), 2.64 (s, 3H); ^{13}C NMR (75 MHz, $CDCl_3$) δ= 170.0, 161.0, 159.0, 157.4, 154.3, 151.4, 132.4 (2C), 129.9, 125.4, 123.4, 121.7 (2C), 119.7 (2C), 118.7 (2C), 14.7; FT-IR (neat): ṽ [cm^{-1}]= 3352, 1684, 1595, 1508, 1488, 1394, 1316, 1249, 1212, 1155, 1105, 1047, 959, 849, 813, 798, 738, 687.

_N_-(6-chloro-2-(methylthio)pyrimidin-4-yl)-2-phenoxybenzamide (3r)

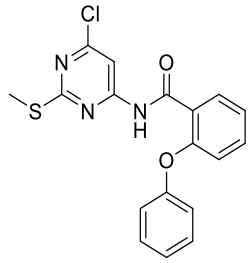

To a solution of 2-phenoxybenzoic acid (214 mg, 1.00 mmol) in toluene (1 mL), thionyl chloride (725 µL, 10.0 mmol) was added. The mixture was refluxed for 1 h and evaporated *in vacuo.* Subsequently, the isolated acyl chloride was added dropwise to a solution of 4-amino-6-chloro-2-(methylthio)pyrimidine (176 mg, 1.00 mmol) and DIPEA (524 µL, 3.00 mmol) in dichloromethane (5 mL). The reaction mixture was stirred for 168 h at room temperature, evaporated, and resolved in ethyl acetate. Extraction with $NaHCO_3$ sat. and purification by silica column

chromatography (CH/EA 10:1 + 1% TFA) afforded the title compound **3r** as a yellowish solid (22 mg, 5.9%); mp: 148 °C; ^{1}H NMR (300 MHz, DMSO-*d*$_6$) δ= 10.24 (s, 1H), 8.25 (dd, *J* = 7.9, 1.8 Hz, 1H), 8.07 (s, 1H), 7.52 – 7.37 (m, 3H), 7.31 – 7.20 (m, 2H), 7.16 – 7.08 (m, 2H), 6.95 – 6.88 (m, 1H), 2.46 (s, 3H); ^{13}C NMR (75 MHz, DMSO-*d*$_6$) δ= 172.8, 164.3, 162.5, 158.6, 156.2, 155.3, 134.9, 133.1, 130.9, 125.8, 124.5, 120.1, 118.9, 118.4, 105.8, 28.5; FT-IR (neat): ṽ [cm^{-1}]= 3252, 2903, 1657, 1544, 1500, 1458, 1415, 1359, 1307, 1207, 1167, 1112, 1020, 778, 755, 710, 665.

_N_-(3-(benzyloxy)phenyl)-5-chloro-2-(methylthio)pyrimidine-4-carboxamide (3s)

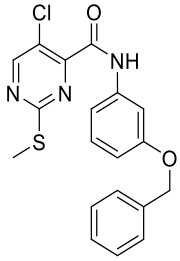

According to the general procedure (I), the title compound **3s** was obtained from **2a** and **1h** as a beige solid (188 mg, 97%); mp: 62 °C; ^{1}H NMR (300 MHz, $CDCl_3$) δ= 9.51 (s, 1H), 8.62 – 8.56 (m, 1H), 7.52 (t, *J* = 2.2 Hz, 1H), 7.40 – 7.04 (m, 7H), 6.72 (dd, *J* = 8.2, 2.5, Hz, 1H), 5.01 (s, 2H), 2.54 (s, 3H); ^{13}C NMR (75 MHz, $CDCl_3$) δ= 170.0, 161.0, 159.5, 159.1, 151.3, 138.2, 136.8, 129.9, 128.6 (2C), 128.1, 127.6 (2C), 125.3, 112.4, 112.0, 106.5, 70.2, 14.7; FT-IR (neat): ṽ [cm^{-1}]= 3367, 1692, 1599, 1536, 1511, 1493, 1454, 1418, 1393, 1314, 1247, 1213, 1193, 1156, 1083, 1050, 1009, 992, 922, 835, 786, 736, 700, 684, 673.

5-Chloro-_N_-(dibenzo[*b,d*]furan-1-yl)-2-(methylthio)pyrimidine-4-carboxamide (3t)

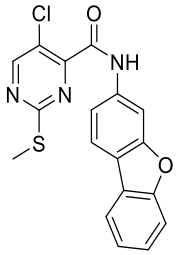

According to the general procedure (I), the title compound **3t** was obtained from **2a** and **1k** as a beige solid (214 mg, 82%); mp: 195 °C; ^{1}H NMR (300 MHz, DMSO-*d*$_6$) δ= 10.37 – 10.16 (m, 1H), 8.73 – 8.57 (m, 1H), 8.32 – 8.16 (m, 1H), 7.99 – 7.76 (m, 2H), 7.61 – 7.19 (m, 4H), 2.59 (s, 3H); ^{13}C NMR (75 MHz, DMSO-*d*$_6$) δ= 170.0, 156.1, 155.5, 126.2, 123.4, 123.3, 122.3, 122.1, 120.2, 120.1, 119.7, 114.9, 114.9, 111.1, 110.9, 103.1, 14.0; FT-IR (neat): ṽ [cm^{-1}]= 3333, 1687, 1597, 1513, 1453, 1419, 1391, 1310, 1212, 1047, 960, 854, 824, 771, 751, 737, 722, 673.

5-Chloro-2-(methylthio)-_N_-(3-(phenylcarbamoyl)phenyl)pyrimidine-4-carboxamide (3u)

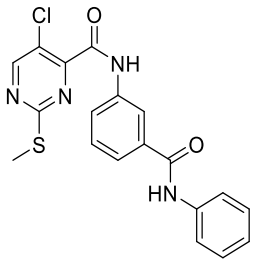

According to the general procedure (I), the title compound **3u** was obtained from **2a** and **1m** as a colourless solid (162 mg, 58%); mp: 168 °C; ^{1}H NMR (300 MHz, $CDCl_3$) δ= 11.04 (s, 1H), 10.33 (s, 1H), 8.97 (s, 1H), 8.30 – 8.12 (m, 1H), 7.97 – 7.86 (m, 1H), 7.84 – 7.70 (m, 3H), 7.56 (t, *J* = 7.9 Hz, 1H), 7.36 (t, *J* = 7.9 Hz, 2H), 7.21 – 6.98 (m, 1H), 2.60 (s, 3H); ^{13}C NMR (75 MHz, $CDCl_3$) δ= 169.9, 165.3, 161.3, 158.6, 157.4, 139.0, 138.0, 136.0, 129.1, 128.6 (2C), 123.7, 123.5, 122.7, 122.2, 120.3 (2C), 119.3, 14.1; FT-IR (neat): ṽ [cm^{-1}]= 3356, 1690, 1651, 1597, 1531, 1510, 1483, 1442, 1416, 1394, 1314, 1218, 1177, 1153, 1049, 963, 895, 810, 789, 751, 688, 667.

2-Sulfonylpyrimidines as Sortase A Inhibitors

***N*-(3-benzoylphenyl)-5-bromo-2-(methylthio)pyrimidine-4-carboxamide (3v)**

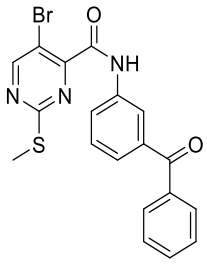

According to the general procedure (I), the title compound **3v** was obtained from **2b** and 3-benzoylaniline as a yellowish solid (276 mg, 92%); mp: 165 °C; ^{1}H NMR (300 MHz, $CDCl_3$) δ= 11.06 (s, 1H), 9.02 (s, 1H), 8.12 (t, *J* = 1.8 Hz, 1H), 8.03 – 7.95 (m, 1H), 7.80 – 7.74 (m, 2H), 7.73 – 7.66 (m, 1H), 7.64 – 7.49 (m, 4H), 2.57 (s, 3H); ^{13}C NMR (75 MHz, $CDCl_3$) δ= 195.4, 170.4, 162.1, 160.7, 159.1, 138.1, 137.7, 136.8, 132.8, 129.6 (2C), 129.4, 128.6 (2C), 125.7, 123.6, 120.6, 110.9, 14.0; FT-IR (neat): ṽ [cm^{-1}]= 3324, 1691, 1646, 1594, 1528, 1505, 1484, 1447, 1414, 1393, 1313, 1295, 1259, 1212, 1177, 1155, 1026, 999, 968, 893, 863, 810, 787, 719, 706, 693, 671.

5-Bromo-2-(methylthio)-*N*-(3-phenoxyphenyl)pyrimidine-4-carboxamide (3w)

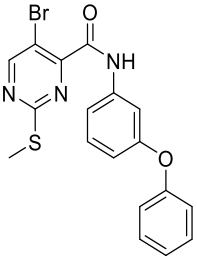

According to the general procedure (I), the title compound **3w** was obtained from **2b** and 3-phenoxyaniline as a yellowish solid (250 mg, 85%); mp: 136 °C; ^{1}H NMR (300 MHz, $CDCl_3$) δ= 9.61 (s, 1H), 8.81 (s, 1H), 7.54 – 7.41 (m, 2H), 7.39 – 7.29 (m, 3H), 7.16 – 7.08 (m, 1H), 7.06 – 6.99 (m, 2H), 6.90 – 6.75 (m, 1H), 2.61 (s, 3H); ^{13}C NMR (75 MHz, $CDCl_3$) δ= 170.7, 163.4, 159.4, 157.9, 157.0, 153.0, 138.3, 130.2, 129.8 (2C), 123.5, 119.0 (2C), 115.5, 114.9, 112.5, 110.9, 14.6; FT-IR (neat): ṽ [cm^{-1}]= 3365, 1693, 1589, 1530, 1509, 1484, 1418, 1393, 1308, 1250, 1212, 1174, 1157, 1027, 964, 915, 865, 806, 786, 772, 734, 687, 674.

2-(Methylthio)-*N*-(3-phenoxyphenyl)pyrimidine-4-carboxamide (3x)

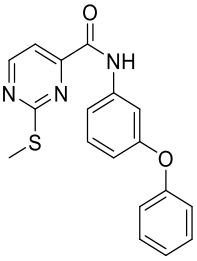

According to the general procedure (I), the title compound **3x** was obtained from **2c** and 3-phenoxyaniline as a beige solid (89 mg, 87%); mp: 117 °C; ^{1}H NMR (300 MHz, $CDCl_3$) δ= 10.19 – 10.02 (m, 1H), 9.20 (d, *J* = 5.0 Hz, 1H), 8.23 (d, *J* = 5.0 Hz, 1H), 7.92 – 7.84 (m, 2H), 7.82 – 7.71 (m, 3H), 7.59 – 7.51 (m, 1H), 7.50 – 7.43 (m, 2H), 7.30 – 7.16 (m, 1H), 3.05 (s, 3H); ^{13}C NMR (75 MHz, $CDCl_3$) δ= 172.4, 160.1, 159.8, 158.1, 156.9, 156.5, 138.3, 130.3, 129.9 (2C), 123.6, 119.2 (2C), 115.3, 114.8, 113.5, 110.6, 14.4; FT-IR (neat): ṽ [cm^{-1}]= 3328, 1691, 1669, 1587, 1513, 1486, 1445, 1415, 1320, 1218, 1155, 1124, 1056, 1022, 968, 859, 762, 738, 692.

5-Methyl-2-(methylthio)-*N*-(3-phenoxyphenyl)pyrimidine-4-carboxamide (3y)

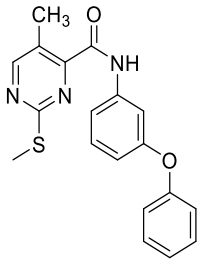

A solution of 2-(methylthio)pyrimidine **3w** (125 mg, 0.30 mmol) and $Pd(PPh)_3$ (35 mg, 0.03 mmol) in anhydrous tetrahydrofuran (5 mL) was thoroughly degassed with argon and transferred to an argon-flushed sealed tube. Trimethylaluminium (1.2 mL, 2 M in toluene) was added via septum and the reaction mixture was heated for 2 h to 70 °C. The reaction was quenched by the addition of water (1 mL) and evaporation of the volatiles. Purification by silica column chromatography (CH/EA 5:1) afforded the title compound **3y** as a colourless solid (35 mg, 33%); mp: 112 °C; ^{1}H NMR (300 MHz, $CDCl_3$) δ= 9.88 (s, 1H), 8.54 (s, 1H), 7.51 – 7.41 (m, 2H), 7.40 – 7.28 (m, 3H), 7.16 – 7.07 (m, 1H), 7.07 – 7.00 (m, 2H), 6.85 – 6.73 (m, 1H), 2.66 (s, 3H), 2.61 (s, 3H); ^{13}C NMR (75 MHz, $CDCl_3$) δ= 169.1, 162.6, 161.8, 157.9, 157.1, 152.8, 138.7, 130.2, 129.9 (2C), 126.6, 123.5, 119.0 (2C), 115.2, 114.8, 110.8, 16.8, 14.3; FT-IR (neat): ṽ [cm^{-1}]= 3314, 2970, 1697, 1640, 1588, 1525, 1448, 1387, 1361, 1278, 1250, 1170, 1149, 1065, 1041, 968, 918, 897, 873, 762, 720, 688.

5-Amino-*N*-(3-benzoylphenyl)-2-(methylthio)pyrimidine-4-carboxamide (3z)

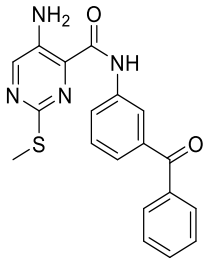

According to the general procedure (I), the title compound **3z** was obtained from **2d** and 3-benzoylaniline as a yellow solid (73 mg, 50%); mp: 178 °C; ^{1}H NMR (300 MHz, DMSO-d_6) δ= 10.43 (s, 1H), 8.28 (t, J = 1.9 Hz, 2H), 8.09 – 7.97 (m, 1H), 7.85 – 7.46 (m, 7H), 6.74 – 6.58 (m, 2H), 2.57 (s, 3H); ^{13}C NMR (75 MHz, DMSO-d_6) δ= 195.6, 164.8, 154.7, 150.4, 139.8, 138.0, 137.5, 137.0, 132.8, 132.8, 129.7 (2C), 129.0, 128.6 (2C), 125.4, 124.8, 121.4, 13.8; FT-IR (neat): ṽ [cm^{-1}]= 3443, 3324, 1678, 1644, 1585, 1527, 1436, 1410, 1317, 1273, 1237, 1206, 1141, 1107, 985, 921, 806, 783, 710, 683, 664.

4 Synthesis of 2-(methylsulfonyl)pyrimidines (4, 5a–k, 6a–n, 7a–e)

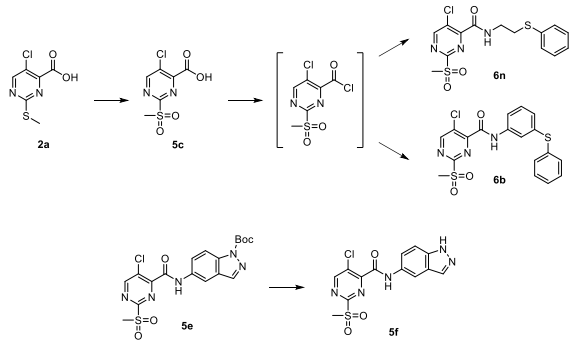

2-Sulfonylpyrimidines as Sortase A Inhibitors

General procedure (II) for the synthesis of 2-(methylsulfonyl)pyrimidines

2-(methylsulfonyl)pyrimidines were synthesized according to a procedure by Webb. To a solution of the respective 2-(methylthio)pyrimidine **3a–z** (1.0 eq.) in tetrahydrofuran/water (1:1) potassium peroxymonosulfate (3.0 eq., OXONE®) was added and the mixture was stirred for 16 h at room temperature. The solvent was evaporated and the residual was extracted from dichloromethane/water. Purification by silica column chromatography (isocratic, CH/EA 5:1–2:1) yielded the corresponding 2-(methylsulfonyl)pyrimidines (**4, 5a–k, 6a–m, 7a–e**)

***N*-(2-benzylphenyl)-5-chloro-2-(methylsulfonyl)pyrimidine-4-carboxamide (4)**

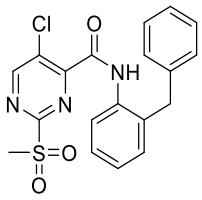

According to the general procedure (II), the title compound **4** was obtained from **3a** as a yellowish solid (52 mg, 86%); mp: 250 °C; ^{1}H NMR (300 MHz, $CDCl_3$) δ= 9.26 (s, 1H), 8.94 (s, 1H), 8.03 (d, *J* = 8.0 Hz, 1H), 7.39 – 7.00 (m, 8H), 4.03 (s, 2H), 3.19 (s, 3H); ^{13}C NMR (75 MHz, $CDCl_3$) δ= 162.0, 160.1, 158.0, 153.7, 138.6, 134.5, 133.6, 132.1, 131.2, 129.0 (2C), 128.6 (2C), 127.8, 126.8, 126.4, 123.4, 39.7, 38.2; FT-IR (neat): ṽ [cm^{-1}]= 3380, 1737, 1692, 1584, 1522, 1465, 1451, 1396, 1308, 1178, 1145, 1131, 1091, 1057, 963, 917, 787, 761, 731, 712, 696, 670; ESI-MS *m/z*: $[M+H]^+$ 402.15 (100%), 403.37 (4.82%), 404.12 (33.88%); purity (HPLC)= 95.6%.

5-Chloro-2-(methylsulfonyl)-*N*-(3-phenoxyphenyl)pyrimidine-4-carboxamide (5a)

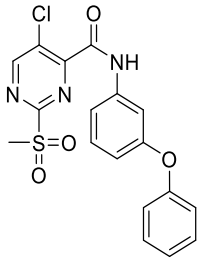

According to the general procedure (II), the title compound **5a** was obtained from **3b** as a yellowish solid (34 mg, 49%); mp: 156 °C; ^{1}H NMR (300 MHz, DMSO-d_6) δ= 11.05 (s, 1H), 9.44 (s, 1H), 7.51 – 7.35 (m, 5H), 7.18 (t, *J* = 7.6 Hz, 1H), 7.08 (d, *J* = 7.6 Hz, 2H), 6.85 (dt, *J* = 7.6, 2.0 Hz, 1H), 3.49 (s, 3H); ^{13}C NMR (75 MHz, DMSO-d_6) δ= 162.8, 160.3, 158.3, 157.3, 156.1, 139.1, 130.6, 130.1 (2C), 129.9, 123.9, 119.1 (2C), 114.7, 114.6, 109.5, 39.4; FT-IR (neat): ṽ [cm^{-1}]= 3332, 1692, 1610, 1588, 1529, 1484, 1429, 1392, 1319, 1302, 1261, 1208, 1183, 1157, 1136, 1059, 1023, 973, 912, 870, 809, 787, 777, 733, 690, 671; ESI-MS *m/z*: $[M+H]^+$ 404.08 (100%), 405.28 (6.56%), 406.09 (33.7%); purity (HPLC)= 95.4%.

5-Chloro-2-(methylsulfonyl)-*N*-(2-oxo-2-((3-phenoxyphenyl)amino)ethyl)pyrimidine-4-carboxamide (5b)

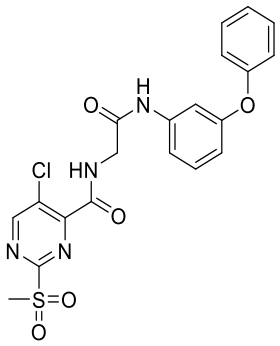

According to the general procedure (II), the title compound **5b** was obtained from **3c** as a colourless solid (50 mg, 60%); mp: 91 °C; ^{1}H NMR (300 MHz, DMSO-d_6) δ= 10.24 (s, 1H), 9.36 (s, 1H), 9.28 (t, J = 5.8 Hz, 1H), 7.45 – 7.36 (m, 2H), 7.35 – 7.29 (m, 3H), 7.21 – 7.11 (m, 1H), 7.07 – 6.99 (m, 2H), 6.77 – 6.68 (m, 1H), 4.14 (d, J = 5.8 Hz, 2H), 3.48 (s, 3H); ^{13}C NMR (75 MHz, DMSO-d_6) δ= 166.6, 162.5, 161.9, 160.5, 157.2, 156.3, 140.2, 130.5, 130.2, 130.0 (2C), 123.6, 118.9 (2C), 113.8, 113.3, 108.8, 42.8, 39.4; FT-IR (neat): ṽ [cm^{-1}]= 3340, 2361, 1674, 1589, 1508, 1486, 1440, 1315, 1216, 1163, 1133, 1006, 961, 874, 767, 689, 664; ESI-MS *m/z*: [M+H]$^{+}$ 461.28 (100%), 463.19 (62.9%), 464.22 (3.48%); purity (HPLC)= 95.3%.

5-Chloro-2-(methylsulfonyl)pyrimidine-4-carboxylic acid (5c)

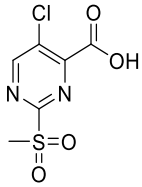

According to the general procedure (II), the title compound **5c** was obtained from **2a** as a beige solid (70 mg, 98%); mp: 180 °C; ^{1}H NMR (300 MHz, DMSO-d_6) δ= 9.38 (s, 1H), 3.44 (s, 3H); ^{13}C NMR (75 MHz, DMSO-d_6) δ= 163.5, 162.8, 160.4, 156.8, 129.6, 39.4; FT-IR (neat): ṽ [cm^{-1}]= 2930, 1728, 1568, 1433, 1395, 1306, 1277, 1231, 1193, 1158, 1141, 1065, 1036, 973, 937, 896, 811, 774, 749, 732, 657; ESI-MS *m/z*: [M+H]$^{+}$ 236.92 (100%), 237.91 (10.7%), 238.92 (38.09%); purity (HPLC)= 95.7%.

5-Chloro-*N*-(4'-cyano-[1,1'-biphenyl]-4-yl)-2-(methylsulfonyl)pyrimidine-4-carboxamide (5d)

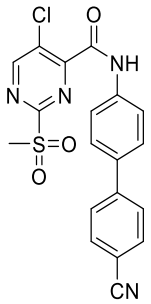

According to the general procedure (II), the title compound **5d** was obtained from **3d** as a yellow solid (38 mg, 54%); mp: 267 °C; ^{1}H NMR (300 MHz, DMSO-d_6) δ= 11.17 (s, 1H), 9.47 (s, 1H), 7.96 – 7.87 (m, 4H), 7.85 (s, 4H), 3.52 (s, 3H); ^{13}C NMR (75 MHz, DMSO-d_6) δ= 162.8, 160.4, 158.3, 143.8, 138.2, 134.4, 132.9 (2C), 130.0, 127.8 (2C), 127.2 (2C), 120.4 (2C), 118.9, 109.8, 39.4; FT-IR (neat): ṽ [cm^{-1}]= 2227, 1688, 1605, 1590, 1525, 1509, 1420, 1398, 1315, 1229, 1187, 1146, 1128, 1058, 974, 949, 819, 800, 780, 764, 741, 676; ESI-MS *m/z*: [M+H]$^{+}$ 413.07 (100%), 414.14 (15.8%), 415.06 (60.82%); purity (HPLC)= 95.3%.

2-Sulfonylpyrimidines as Sortase A Inhibitors

***Tert*-butyl 5-(5-chloro-2-(methylsulfonyl)pyrimidine-4-carboxamido)-1*H*-indazole-1-carboxylate (5e)**

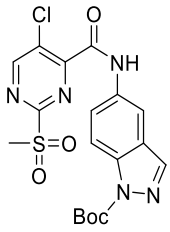

According to the general procedure (II), the title compound **5e** was obtained from **3e** as a yellow solid (83 mg, 76%); mp: 180 °C; ^{1}H NMR (300 MHz, $CDCl_3$) δ= 9.82 (s, 1H), 9.04 (s, 1H), 8.35 (d, *J* = 2.1 Hz, 1H), 8.21 – 8.11 (m, 2H), 7.64 (dd, *J* = 8.9, 2.1 Hz, 1H), 3.41 (s, 3H), 1.72 (s, 9H); ^{13}C NMR (75 MHz, $CDCl_3$) δ= 162.3, 161.9, 158.2, 154.0, 149.1, 139.6, 137.4, 133.6, 132.6, 126.2, 122.6, 115.3, 112.4, 85.3, 39.7, 28.2 (3C); FT-IR (neat): ṽ [cm^{-1}]= 1737, 1693, 1508, 1393, 1354, 1318, 1289, 1243, 1152, 1131, 1029, 980, 902, 848, 819, 758, 686.

5-Chloro-*N*-(1*H*-indazol-5-yl)-2-(methylsulfonyl)pyrimidine-4-carboxamide (5f)

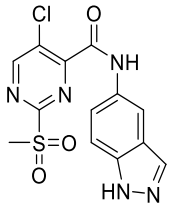

The Boc-protected 2-(methylsulfonyl)pyrimidine **5e** (42 mg, 0.10 mmol) was suspended in dichloromethane (3.0 mL). Subsequently, trifluoroacetic acid (1.5 mL) was added and the reaction mixture was stirred for 16 h at room temperature. Evaporation of the solvent and lyophilization from acetonitrile/water (1:1) yielded the title compound **5f** as a yellow solid (35 mg, 99%); mp: 231 °C; ^{1}H NMR (300 MHz, DMSO-d_6) δ= 13.12 (s, 1H), 10.99 (s, 1H), 9.45 (s, 1H), 8.28 – 8.22 (m, 1H), 8.11 (s, 1H), 7.63 – 7.47 (m, 2H), 3.51 (s, 3H); ^{13}C NMR (75 MHz, DMSO-d_6) δ= 162.8, 160.2, 160.1, 158.8, 130.6, 130.0, 129.8, 122.6, 120.3, 111.0, 106.3, 99.9, 39.3; FT-IR (neat): ṽ [cm^{-1}]= 3307, 3012, 2929, 1687, 1587, 1536, 1501, 1455, 1404, 1312, 1292, 1257, 1218, 1187, 1132, 1067, 1052, 965, 940, 894, 855, 798, 753, 730, 665; ESI-MS *m/z*: $[M+H]^+$ 352.06 (100%), 353.05 (15.16%), 354.04 (34.78%); purity (HPLC)= 99.5%.

5-Chloro-2-(methylsulfonyl)-*N*-(4-(*p*-tolyl)thiazol-2-yl)pyrimidine-4-carboxamide (5g)

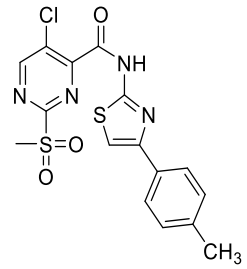

According to the general procedure (II), the title compound **5g** was obtained from **3f** as a yellow solid (18 mg, 33%); mp: 280 °C; ^{1}H NMR (300 MHz, DMSO-d_6) δ= 13.22 (s, 1H), 9.43 (d, *J* = 29.4 Hz, 1H), 7.82 (d, *J* = 7.9 Hz, 2H), 7.76 (d, *J* = 3.2 Hz, 1H), 7.26 (d, *J* = 7.9 Hz, 2H), 3.53 (s, 3H), 2.33 (s, 3H); ^{13}C NMR (75 MHz, DMSO-d_6) δ= 171.4, 162.7, 160.7, 156.3, 137.4, 131.2, 131.1, 130.6, 129.3 (2C), 128.5, 125.7 (2C), 108.8, 39.8, 20.8; FT-IR (neat): ṽ [cm^{-1}]= 3384, 1701, 1534, 1445, 1391, 1323, 1303, 1184, 1143, 1067, 1054, 962, 932, 824, 750, 737, 710, 674; ESI-MS *m/z*: $[M+H]^+$ 409.14 (100%), 410.13 (20.03%), 411.12 (42.91%); purity (HPLC)= 97.7%.

2-Sulfonylpyrimidines as Sortase A Inhibitors

(5-Chloro-2-(methylsulfonyl)pyrimidin-4-yl)(3,4-dihydroisoquinolin-2(1*H*)-yl)methanone (5h)

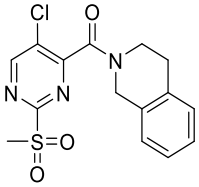

According to the general procedure (II), the title compound **5h** was obtained from **3g** as a yellowish solid (20 mg, 28%); mp: 218 °C; ^{1}H NMR (300 MHz, DMSO-*d*$_6$) δ= 9.50 – 9.25 (m, 1H), 7.39 – 7.09 (m, 4H), 4.95 – 4.40 (m, 2H), 3.97 – 3.49 (m, 2H), 3.42 (d, *J* = 8.5 Hz, 3H), 3.01 – 2.74 (m, 2H); ^{13}C NMR (75 MHz, DMSO-*d*$_6$) δ= 163.2, 161.5, 161.3, 159.8, 159.8, 159.7, 134.0, 133.7, 132.5, 131.9, 129.6, 128.7, 128.6, 126.8, 126.6, 126.5, 126.4, 126.2, 126.0, 46.8, 43.3, 39.9, 28.6, 27.4; FT-IR (neat): ṽ [cm^{-1}]= 2925, 1644, 1483, 1459, 1402, 1372, 1311, 1255, 1188, 1134, 1066, 1044, 964, 927, 814, 794, 770, 757, 714; ESI-MS *m/z*: [M+H]$^{+}$ 352.10 (100%), 353.08 (13.95%), 354.07 (31.77%); purity (HPLC)= 96.5%.

5-Chloro-2-(methylsulfonyl)-*N*-(pentan-3-yl)pyrimidine-4-carboxamide (5i)

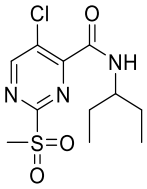

According to the general procedure (II), the title compound **5i** was obtained from **3h** as a yellowish solid (55 mg, 71%); mp: 146 °C; ^{1}H NMR (300 MHz, $CDCl_3$) δ= 8.99 (s, 1H), 7.32 (d, *J* = 9.2 Hz, 1H), 4.08 – 3.86 (m, 1H), 3.38 (s, 3H), 1.82 – 1.46 (m, 4H), 0.96 (t, *J* = 7.4 Hz, 6H); ^{13}C NMR (75 MHz, $CDCl_3$) δ= 162.4, 161.5, 160.2, 154.7, 133.2, 53.3, 39.7, 27.4 (2C), 10.5 (2C); FT-IR (neat): ṽ [cm^{-1}]= 3268, 2966, 1650, 1533, 1459, 1413, 1318, 1197, 1125, 1060, 969, 954, 926, 782, 715, 676; ESI-MS *m/z*: [M+H]$^{+}$ 306.07 (100%), 307.07 (9.57%), 308.07 (40.32%); purity (HPLC)= 99.3%.

***N*,*N*-dibenzyl-5-chloro-2-(methylsulfonyl)pyrimidine-4-carboxamide (5k)**

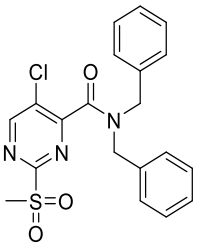

According to the general procedure (II), the title compound **5k** was obtained from **3i** as a yellowish solid (74 mg, 89%); mp: 68 °C; ^{1}H NMR (300 MHz, $CDCl_3$) δ= 8.87 (s, 1H), 7.45 – 7.24 (m, 8H), 7.18 – 7.10 (m, 2H), 4.74 (s, 2H), 4.24 (s, 2H), 3.23 (s, 3H); ^{13}C NMR (75 MHz, $CDCl_3$) δ= 163.4, 160.8, 158.9, 135.4, 134.5, 131.0, 129.0 (2C), 129.0 (2C), 128.7 (2C), 128.4, 128.2, 127.7 (2C), 50.9, 47.7, 39.4; FT-IR (neat): ṽ [cm^{-1}]= 2926, 1769, 1646, 1553, 1495, 1473, 1452, 1394, 1317, 1184, 1132, 1080, 1061, 1029, 1001, 958, 796, 747, 715, 697; ESI-MS *m/z*: [M+H]$^{+}$ 438.04 (100%), 439.03 (19.28%), 440.02 (32.13%); purity (HPLC)= 96.9%.

2-Sulfonylpyrimidines as Sortase A Inhibitors

***N*-(4-benzoylphenyl)-5-chloro-2-(methylsulfonyl)pyrimidine-4-carboxamide (6a)**

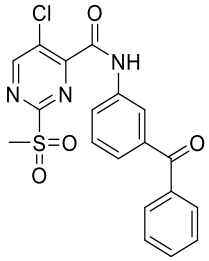

According to the general procedure (II), the title compound **6a** was obtained from **3k** as a yellowish solid (80 mg, 64%); mp: 175 °C; ^{1}H NMR (300 MHz, DMSO-d_6) δ= 11.24 (s, 1H), 9.46 (s, 1H), 8.19 – 8.07 (m, 1H), 8.02 (d, J = 8.0 Hz, 1H), 7.81 – 7.74 (m, 2H), 7.73 – 7.53 (m, 5H), 3.51 (s, 3H); ^{13}C NMR (75 MHz, DMSO-d_6) δ= 194.3, 162.8, 160.5, 160.4, 158.0, 137.8, 137.7, 136.8, 132.8, 130.0, 129.6 (2C), 129.5, 128.6 (2C), 126.0, 123.8, 121.4, 39.4; FT-IR (neat): ṽ [cm^{-1}]= 3303, 1677, 1650, 1588, 1533, 1513, 1482, 1401, 1323, 1292, 1225, 1135, 1058, 962, 904, 854, 758, 721, 707, 694, 669; ESI-MS *m/z*: [M+H]$^{+}$ 416.04 (100%), 417.05 (22.14%), 418.03 (36.43%); purity (HPLC)= 99.2%.

5-Chloro-2-(methylsulfonyl)-*N*-(3-(phenylthio)phenyl)pyrimidine-4-carboxamide (6b)

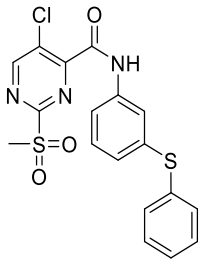

At 0 °C, 5-chloro-2-(methylsulfonyl)pyrimidine-4-carboxylic acid **5c** (106 mg, 0.45 mmol) and single drop of dimethylformamide were added stepwise to thionyl chloride (580 µL, 8.00 mmol). The mixture was refluxed for 1 h and evaporated *in vacuo.* Subsequently, the isolated acyl chloride was added dropwise to a solution of the arylamine **1d** (81 mg, 0.40 mmol) and triethylamine (168 µL, 1.20 mmol) in dichloromethane (10 mL). The reaction mixture was stirred for 16 h at room temperature, evaporated and resolved in ethyl acetate. The organic phase was extracted with $NaHCO_3$ sat. and HCl (1 M). Purification by silica column chromatography (CH/EA 2:1) afforded the title compound **6b** as a yellow solid (66 mg, 39%); mp: 135 °C; ^{1}H NMR (300 MHz, $CDCl_3$) δ= 9.51 (s, 1H), 8.94 (s, 1H), 7.61 – 7.49 (m, 2H), 7.38 – 7.12 (m, 6H), 7.08 – 6.94 (m, 1H), 3.29 (s, 3H); ^{13}C NMR (75 MHz, $CDCl_3$) δ= 162.2, 161.8, 158.1, 154.2, 137.7, 137.3, 134.8, 133.5, 131.9 (2C), 129.9, 129.4 (2C), 127.6, 127.5, 122.1, 119.0, 39.7; FT-IR (neat): ṽ [cm^{-1}]= 3329, 1689, 1592, 1523, 1513, 1478, 1438, 1407, 1386, 1319, 1301, 1226, 1181, 1151, 1135, 1081, 1059, 1025, 972, 881, 858, 821, 780, 769, 745, 684, 665; ESI-MS *m/z*: [M+H]$^{+}$ 420.14 (100%), 421.08 (11.65%), 422.12 (34.38%); purity (HPLC)= 95.4%.

5-Chloro-*N*-(3-(cyclohexyloxy)phenyl)-2-(methylsulfonyl)pyrimidine-4-carboxamide (6c)

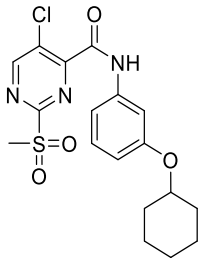

According to the general procedure (II), the title compound **6c** was obtained from **3l** as a yellowish solid (46 mg, 37%); mp: 144 °C; ^{1}H NMR (300 MHz, $CDCl_3$) δ= 9.40 (s, 1H), 8.97 (s, 1H), 7.33 (t, J = 2.2 Hz, 1H), 7.25 – 7.08 (m, 2H), 6.74 – 6.64 (m, 1H), 4.30 – 4.16 (m, 1H), 3.34 (s, 3H), 2.01 – 1.81 (m, 2H), 1.81 – 1.62 (m, 2H), 1.57 – 1.14 (m, 6H); ^{13}C NMR (75 MHz, $CDCl_3$) δ= 162.3, 162.0, 158.6, 157.8, 154.2, 137.6, 133.6, 130.0, 113.7, 112.6, 108.4, 75.6, 39.8, 31.8 (2C), 25.7, 23.7 (2C); FT-IR (neat): ṽ [cm^{-1}]= 3344, 2935, 1702, 1604, 1540, 1495, 1422, 1389, 1325, 1274, 1205, 1146, 1130, 1049, 1020, 979, 850, 785, 765, 730, 690, 669; ESI-MS *m/z*: [M+Na]$^{+}$ 432.15 (100%), 433.12 (15.81%), 434.14 (44.39%); purity (HPLC)= 95.6%.

2-Sulfonylpyrimidines as Sortase A Inhibitors

***N*-(3-benzylphenyl)-5-chloro-2-(methylsulfonyl)pyrimidine-4-carboxamide (6d)**

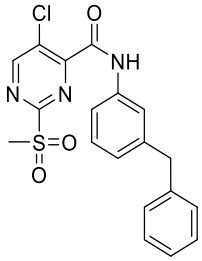

According to the general procedure (II), the title compound **6d** was obtained from **3m** as a yellow solid (88 mg, 87%); mp: 148 °C; ^{1}H NMR (300 MHz, $CDCl_3$) δ= 9.53 (s, 1H), 9.01 (s, 1H), 7.65 – 7.49 (m, 2H), 7.36 – 7.24 (m, 3H), 7.24 – 7.14 (m, 3H), 7.09 – 6.99 (m, 1H), 4.00 (s, 2H), 3.38 (s, 3H); ^{13}C NMR (75 MHz, $CDCl_3$) δ= 162.2, 161.8, 160.0, 158.0, 154.3, 142.5, 140.7, 136.7, 133.4, 129.3, 129.0 (2C), 128.6 (2C), 126.4, 126.3, 120.9, 118.3, 41.9, 39.7; FT-IR (neat): ṽ [cm^{-1}]= 3336, 1686, 1593, 1534, 1494, 1443, 1393, 1305, 1189, 1145, 1058, 972, 898, 820, 785, 761, 732, 695, 669; ESI-MS *m/z*: $[M+H]^+$ 402.13 (100%), 403.18 (17.85%), 404.17 (32.18%); purity (HPLC)= 98.4%.

5-Chloro-*N*-(3-methoxyphenyl)-2-(methylsulfonyl)pyrimidine-4-carboxamide (6e)

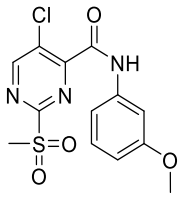

According to the general procedure (II), the title compound **6e** was obtained from **3n** as a yellow solid (113 mg, 86%); mp: 185 °C; ^{1}H NMR (300 MHz, DMSO-d_6) δ= 10.97 (s, 1H), 9.44 (s, 1H), 7.37 – 7.21 (m, 3H), 6.84 – 6.74 (m, 1H), 3.77 (s, 3H), 3.50 (s, 3H); ^{13}C NMR (75 MHz, DMSO-d_6) δ= 172.0, 162.8, 160.3, 159.7, 158.6, 138.8, 130.0, 129.9, 112.1, 110.4, 105.7, 55.1, 39.5; FT-IR (neat): ṽ [cm^{-1}]= 3339, 1687, 1596, 1531, 1454, 1432, 1392, 1307, 1292, 1268, 1212, 1178, 1161, 1147, 1058, 1044, 971, 865, 818, 766, 738, 690, 668; ESI-MS *m/z*: $[M+H]^+$ 342.08 (100%), 343.10 (22.39%), 344.09 (29.87%); purity (HPLC)= 98.1%.

***N*-([1,1'-biphenyl]-3-yl)-5-chloro-2-(methylsulfonyl)pyrimidine-4-carboxamide (6f)**

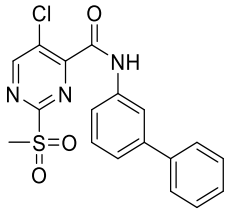

According to the general procedure (II), the title compound **6f** was obtained from **3o** as a yellowish solid (122 mg, 78%); mp: 164 °C; ^{1}H NMR (300 MHz, DMSO-d_6) δ= 11.10 (s, 1H), 9.46 (s, 1H), 8.04 – 7.97 (m, 1H), 7.77 – 7.61 (m, 3H), 7.57 – 7.46 (m, 4H), 7.45 – 7.27 (m, 1H), 3.52 (s, 3H); ^{13}C NMR (75 MHz, DMSO-d_6) δ= 162.8, 160.3 (2C), 158.4, 141.2, 139.7, 138.2, 130.0, 129.8, 129.0 (2C), 127.8, 126.7 (2C), 123.3, 119.0, 118.2, 39.4; FT-IR (neat): ṽ [cm^{-1}]= 3289, 1675, 1593, 1576, 1539, 1500, 1453, 1422, 1400, 1350, 1310, 1219, 1153, 1136, 1121, 1055, 967, 948, 881, 793, 751, 691, 668; ESI-MS *m/z*: $[M+H]^+$ 388.12 (100%), 389.18 (27.86%), 390.15 (24.35%); purity (HPLC)= 97.6%.

5-Chloro-2-(methylsulfonyl)-*N*-(2-phenoxyphenyl)pyrimidine-4-carboxamide (6g)

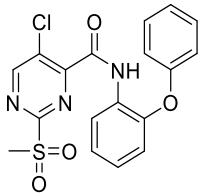

According to the general procedure (II), the title compound **6g** was obtained from **3p** as a yellowish solid (57 mg, 47%); mp: 177 °C; ^{1}H NMR (300 MHz, $CDCl_3$) δ= 10.17 (s, 1H), 9.06 (s, 1H), 8.59 (dd, *J* = 8.0, 1.7 Hz, 1H), 7.40 – 7.31 (m, 2H), 7.25 – 7.09 (m, 3H), 7.09 – 7.03 (m, 2H), 6.99 (dd, *J* = 8.0, 1.7 Hz, 1H), 3.21 (s, 3H); ^{13}C NMR (75 MHz, $CDCl_3$) δ= 162.6, 162.4, 157.6, 156.4, 153.0, 146.1, 133.4, 130.2 (2C), 128.8, 125.7, 124.6, 124.1, 120.8, 118.7 (2C), 118.2, 39.3; FT-IR (neat): ṽ [cm^{-1}]= 3360, 1705, 1602, 1588, 1517, 1447, 1414, 1389, 1311, 1249,

1210, 1174, 1142, 1102, 1054, 1029, 967, 873, 849, 802, 784, 767, 748, 694, 669; ESI-MS *m/z*: $[M+H]^+$ 404.14 (100%), 405.13 (19.81%), 406.13 (40.53%); purity (HPLC)= 97.5%.

5-Chloro-2-(methylsulfonyl)-*N*-(4-phenoxyphenyl)pyrimidine-4-carboxamide (6h)

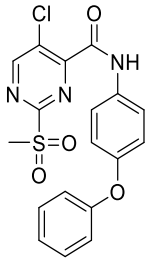

According to the general procedure (II), the title compound **6h** was obtained from **3q** as a yellowish solid (75 mg, 61%); mp: 195 °C; ^{1}H NMR (300 MHz, $CDCl_3$) δ= 9.61 (s, 1H), 9.03 (s, 1H), 7.78 – 7.61 (m, 2H), 7.34 (t, *J* = 7.7 Hz, 2H), 7.11 (t, *J* = 7.4 Hz, 1H), 7.06 – 6.96 (m, 4H), 3.40 (s, 3H); ^{13}C NMR (75 MHz, $CDCl_3$) δ= 162.3, 161.9, 157.9, 157.2, 154.8, 154.2, 133.6, 131.9, 129.9 (2C), 123.5, 122.2 (2C), 119.5 (2C), 118.9 (2C), 39.8; FT-IR (neat): ṽ [cm^{-1}]= 3297, 1669, 1587, 1513, 1483, 1403, 1323, 1254, 1227, 1160, 1125, 1058, 1023, 967, 927, 876, 855, 840, 766, 734, 693, 669; ESI-MS *m/z*: $[M+H]^+$ 404.14 (100%), 405.17 (21.05%), 406.16 (36.77%); purity (HPLC)= 96.6%.

***N*-(6-chloro-2-(methylsulfonyl)pyrimidin-4-yl)-2-phenoxybenzamide (6i)**

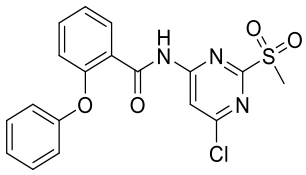

According to the general procedure (II), the title compound **6i** was obtained from **3r** as a colourless solid (14 mg, 57%); mp: 184 °C; ^{1}H NMR (300 MHz, $CDCl_3$) δ= 10.48 (s, 1H), 8.54 (s, 1H), 8.17 (dd, *J* = 7.9, 1.8 Hz, 1H), 7.46 – 7.30 (m, 3H), 7.23 – 7.13 (m, 2H), 7.10 – 7.01 (m, 2H), 6.82 (dd, *J* = 8.4, 1.1 Hz, 1H), 3.21 (s, 3H); ^{13}C NMR (75 MHz, $CDCl_3$) δ= 165.2, 164.2, 163.8, 159.7, 156.3, 154.5, 135.1, 132.8, 130.6 (2C), 125.7, 124.0, 121.5, 120.1 (2C), 118.2, 112.7, 39.0; FT-IR (neat): ṽ [cm^{-1}]= 3310, 1686, 1600, 1537, 1479, 1450, 1342, 1320, 1289, 1243, 1207, 1140, 1111, 1093, 975, 906, 863, 785, 770, 748, 708, 687; ESI-MS *m/z*: $[M+H]^+$ 404.12 (100%), 405.12 (23.57%), 406.13 (33.48%); purity (HPLC)= 99.0%.

***N*-(3-(benzyloxy)phenyl)-5-chloro-2-(methylsulfonyl)pyrimidine-4-carboxamide (6k)**

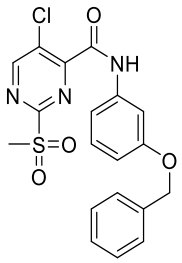

According to the general procedure (II), the title compound **6k** was obtained from **3s** as a yellowish solid (66 mg, 68%); mp: 154 °C; ^{1}H NMR (300 MHz, $CDCl_3$) δ= 9.52 (s, 1H), 8.94 (s, 1H), 7.45 (t, *J* = 2.2 Hz, 1H), 7.39 – 7.08 (m, 7H), 6.80 – 6.70 (m, 1H), 5.00 (s, 2H), 3.31 (s, 3H); ^{13}C NMR (75 MHz, $CDCl_3$) δ= 162.2, 161.9, 159.5, 158.0, 154.1, 137.7, 136.8, 133.5, 130.0, 128.7 (2C), 128.1, 127.6 (2C), 112.9, 112.6, 106.9, 70.2, 39.7; FT-IR (neat): ṽ [cm^{-1}]= 3282, 1675, 1596, 1536, 1441, 1402, 1382, 1351, 1310, 1277, 1202, 1121, 1053, 1027, 954, 871, 850, 767, 728, 690, 668; ESI-MS *m/z*: $[M+H]^+$ 418.15 (100%), 419.17 (30.79%), 421.16 (13.05%); purity (HPLC)= 98.7%.

2-Sulfonylpyrimidines as Sortase A Inhibitors

5-Chloro-*N*-(dibenzo[*b*,*d*]furan-3-yl)-2-(methylsulfonyl)pyrimidine-4-carboxamide (6l)

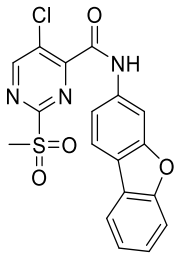

According to the general procedure (II), the title compound **6l** was obtained from **3t** as a yellow solid (68 mg, 42%); mp: 250 °C; ^{1}H NMR (300 MHz, DMSO-d_6) δ= 11.31 (s, 1H), 9.48 (s, 1H), 8.24 – 8.08 (m, 3H), 7.81 – 7.33 (m, 4H), 3.53 (s, 3H); ^{13}C NMR (75 MHz, DMSO-d_6) δ= 162.8, 160.3, 158.3, 155.9, 155.6, 137.2, 133.3, 130.0, 127.2, 123.3, 123.3, 121.5, 120.8, 120.3, 115.5, 111.6, 103.0, 39.5; FT-IR (neat): ṽ [cm^{-1}]= 1692, 1600, 1530, 1455, 1423, 1397, 1306, 1181, 1141, 1116, 1054, 962, 846, 831, 776, 752, 739, 719, 677, 654; ESI-MS *m/z*: [M+H]$^+$ 402.09 (100%), 403.07 (19.92%), 404.09 (44.97%); purity (HPLC)= 95.0%.

5-Chloro-2-(methylsulfonyl)-*N*-(3-(phenylcarbamoyl)phenyl)pyrimidine-4-carboxamide (6m)

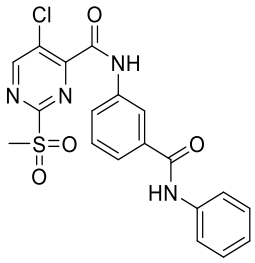

According to the general procedure (II), the title compound **6m** was obtained from **3u** as a yellowish solid (120 mg, 92%); mp: 237 °C; ^{1}H NMR (300 MHz, DMSO-d_6) δ= 11.20 (s, 1H), 10.35 (s, 1H), 9.47 (s, 1H), 8.21 (d, J = 2.0 Hz, 1H), 7.93 (d, J = 8.2 Hz, 1H), 7.83 – 7.73 (m, 3H), 7.59 (t, J = 7.9 Hz, 1H), 7.36 (t, J = 7.9 Hz, 2H), 7.11 (t, J = 7.4 Hz, 1H), 3.52 (s, 3H); ^{13}C NMR (75 MHz, DMSO-d_6) δ= 165.2, 162.8, 160.4, 160.4, 158.2, 139.0, 137.7, 136.0, 130.0, 129.2, 128.6 (2C), 123.8, 123.7, 122.9, 120.3 (2C), 119.5, 40.0; FT-IR (neat): ṽ [cm^{-1}]= 3370, 1683, 1655, 1598, 1531, 1484, 1442, 1420, 1394, 1324, 1257, 1212, 1177, 1148, 1128, 1054, 972, 896, 867, 833, 809, 770, 750, 728, 666; ESI-MS *m/z*: [M+H]$^+$ 431.15 (100%), 432.16 (24.92%), 433.15 (37.69%); purity (HPLC)= 95.0%.

5-Chloro-2-(methylsulfonyl)-*N*-(2-(phenylthio)ethyl)pyrimidine-4-carboxamide (6n)

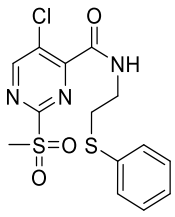

At 0 °C, 5-chloro-2-(methylsulfonyl)pyrimidine-4-carboxylic acid **5c** (130 mg, 0.55 mmol) and single drop of dimethylformamide were added stepwise to oxalyl chloride (428 µL, 5.00 mmol). The mixture was refluxed for 1 h and evaporated *in vacuo*. Subsequently, the isolated acyl chloride was added dropwise to a solution of the amine **1o** (134 mg, 0.50 mmol) and triethylamine (168 µL, 1.20 mmol) in dichloromethane (5 mL). The reaction mixture was stirred for 16 h at room temperature, evaporated and resolved in ethyl acetate. The organic phase was extracted with $NaHCO_3$ sat. and HCl (1 M). Purification by silica column chromatography (CH/EA 2:1) afforded the title compound **6n** as an orange oil (50 mg, 26%);^{1}H NMR (300 MHz, $CDCl_3$) δ= 8.90 (s, 1H), 8.07 – 7.99 (m, 1H), 7.37 – 7.25 (m, 2H), 7.25 – 7.14 (m, 2H), 7.14 – 7.02 (m, 1H), 3.59 (q, J = 6.6 Hz, 2H), 3.29 (s, 3H), 3.10 (t, J = 6.6 Hz, 2H); ^{13}C NMR (75 MHz, $CDCl_3$) δ= 162.2, 161.5, 160.4, 153.9, 134.7, 133.0, 130.0 (2C), 129.2 (2C), 126.7, 39.6, 39.2, 32.9; FT-IR (neat): ṽ [cm^{-1}]= 3299, 1667, 1531, 1515, 1477, 1439, 1404, 1317, 1284, 1209, 1177, 1131, 1073, 1033, 955, 831, 791, 764, 739, 687, 667; ESI-MS *m/z*: [M+H]$^+$ 372.02 (100%), 373.08 (18.01%), 374.01 (50.99%); purity (HPLC)= 96.0%.

2-Sulfonylpyrimidines as Sortase A Inhibitors

***N*-(4-benzoylphenyl)-5-bromo-2-(methylsulfonyl)pyrimidine-4-carboxamide (7a)**

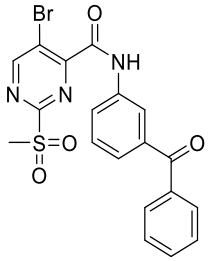

According to the general procedure (II), the title compound **7a** was obtained from **3v** as a yellowish solid (91 mg, 65%); mp: 174 °C; ^{1}H NMR (300 MHz, DMSO-d_6) δ= 11.23 (s, 1H), 9.53 (s, 1H), 8.11 (s, 1H), 8.00 (d, J = 7.9 Hz, 1H), 7.86 – 7.45 (m, 7H), 3.49 (s, 3H); ^{13}C NMR (75 MHz, DMSO-d_6) δ= 195.3, 163.4, 162.6, 161.3, 160.1, 137.9, 137.8, 136.8, 132.8, 129.6 (2C), 129.5, 128.6 (2C), 126.0, 123.7, 120.7, 119.5, 39.4; FT-IR (neat): ṽ [cm^{-1}]= 1691, 1652, 1589, 1530, 1483, 1434, 1396, 1311, 1177, 1133, 1035, 961, 860, 785, 762, 723, 709, 683, 668; ESI-MS *m/z*: [M+H]$^{+}$ 460.01 (100%), 461.01 (23.12%), 461.99 (97.81%); purity (HPLC)= 99.7%.

5-Bromo-2-(methylsulfonyl)-*N*-(3-phenoxyphenyl)pyrimidine-4-carboxamide (7b)

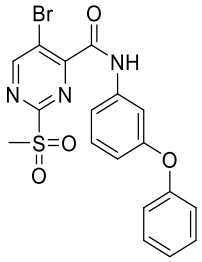

According to the general procedure (II), the title compound **7b** was obtained from **3w** as a yellowish solid (90 mg, 66%); mp: 153 °C; ^{1}H NMR (300 MHz, $CDCl_3$) δ= 9.56 (s, 1H), 9.27 – 9.13 (m, 1H), 7.49 – 7.40 (m, 2H), 7.39 – 7.29 (m, 3H), 7.16 – 7.07 (m, 1H), 7.07 – 6.97 (m, 2H), 6.91 – 6.78 (m, 1H), 3.39 (s, 3H); ^{13}C NMR (75 MHz, $CDCl_3$) δ= 164.7, 163.1, 158.3, 158.1, 156.9, 155.1, 137.9, 130.3, 129.9 (2C), 123.7, 121.8, 119.2 (2C), 116.0, 115.3, 111.3, 39.7; FT-IR (neat): ṽ [cm^{-1}]= 3330, 1691, 1669, 1611, 1587, 1507, 1483, 1420, 1319, 1302, 1256, 1210, 1182, 1156, 1126, 1057, 1036, 970, 912, 856, 839, 802, 767, 733, 691, 669; ESI-MS *m/z*: [M+H]$^{+}$ 448.12 (100%), 449.09 (22.43%), 450.37 (21.65%); purity (HPLC)= 97.2%.

2-(Methylsulfonyl)-*N*-(4-phenoxyphenyl)pyrimidine-4-carboxamide (7c)

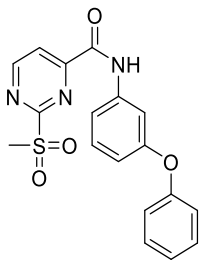

According to the general procedure (II), the title compound **7c** was obtained from **3x** as a yellowish solid (38 mg, 51%); mp: 149 °C; ^{1}H NMR (300 MHz, $CDCl_3$) δ= 9.76 (s, 1H), 9.13 (d, J = 5.0 Hz, 1H), 8.39 (d, J = 5.0 Hz, 1H), 7.51 (t, J = 2.2 Hz, 1H), 7.48 – 7.42 (m, 1H), 7.40 – 7.28 (m, 3H), 7.15 – 7.08 (m, 1H), 7.06 – 6.98 (m, 2H), 6.87 – 6.76 (m, 1H), 3.41 (s, 3H); ^{13}C NMR (75 MHz, $CDCl_3$) δ= 165.2, 160.8, 158.7, 158.7, 158.1, 156.7, 137.8, 130.3, 129.9 (2C), 123.8, 121.4, 119.2 (2C), 115.8, 115.2, 111.0, 39.5; FT-IR (neat): ṽ [cm^{-1}]= 3373, 1701, 1597, 1529, 1492, 1445, 1353, 1310, 1278, 1226, 1186, 1154, 1131, 975, 880, 797, 755, 697, 686, 672; ESI-MS *m/z*: [M+H]$^{+}$ 370.09 (100%), 371.10 (23.95%), 372.08 (4.81%); purity (HPLC)= 97.8%.

5-Methyl-2-(methylsulfonyl)-*N*-(4-phenoxyphenyl)pyrimidine-4-carboxamide (7d)

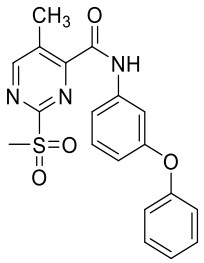

According to the general procedure (II), the title compound **7d** was obtained from **3y** as a yellow solid (54 mg, 70%); mp: 164 °C; ^{1}H NMR (300 MHz, DMSO-d_6) δ= 10.79 (d, J = 18.0 Hz, 1H), 9.21 – 9.07 (m, 1H), 7.68 – 7.47 (m, 3H), 7.46 – 7.36 (m, 2H), 7.22 – 7.12 (m, 1H), 7.06 (d, J = 7.7 Hz, 2H), 6.90 – 6.80 (m, 1H), 3.56 (d, J = 38.9 Hz, 3H), 2.53 (s, 3H); ^{13}C NMR (75 MHz, DMSO-d_6) δ= 162.8, 162.4, 162.2, 157.1, 156.3, 139.4, 132.7, 131.5, 131.4, 130.1 (2C), 128.8, 128.7, 123.7, 118.9 (2C), 115.0, 114.6, 110.1, 39.5, 15.5; FT-IR (neat): ṽ [cm^{-1}]= 3376, 2931, 1687, 1612, 1593, 1532, 1486, 1458, 1423, 1304, 1259, 1213, 1189, 1150, 1121, 970, 909, 873, 774, 742, 722, 688, 673, 657; ESI-MS *m/z*: [M+Na]$^{+}$ 406.08 (100%), 407.04 (23.79%), 408.04 (6.54%); purity (HPLC)= 99.1%.

5-Amino-*N*-(4-benzoylphenyl)-2-(methylsulfonyl)pyrimidine-4-carboxamide (7e)

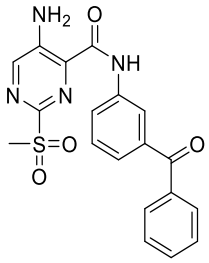

According to the general procedure (II), the title compound **7e** was obtained from **3z** as a beige solid (12 mg, 23%); mp: 280 °C; ^{1}H NMR (300 MHz, DMSO-d_6) δ= 9.73 (s, 1H), 7.78 (s, 1H), 7.47 – 7.36 (m, 1H), 7.29 – 7.16 (m, 1H), 6.97 – 6.90 (m, 2H), 6.89 – 6.82 (m, 1H), 6.80 – 6.63 (m, 6H), 2.64 (s, 3H); ^{13}C NMR (75 MHz, DMSO-d_6) δ= 195.5, 164.1, 150.7, 149.0, 144.4, 137.7, 137.5, 136.9, 132.8, 130.8, 129.6 (2C), 128.9, 128.6 (2C), 125.7, 125.2, 121.9, 39.6; FT-IR (neat): ṽ [cm^{-1}]= 3414, 3307, 1678, 1650, 1605, 1528, 1481, 1427, 1318, 1294, 1213, 1122, 982, 972, 890, 833, 807, 789, 775, 717, 687, 674, 660; ESI-MS *m/z*: [M+Na]$^{+}$ 419.08 (100%), 420.08 (23.26%), 421.11 (6.31%); purity (HPLC)= 99.5%.

5 Cysteine-reactive probe

4-Methyl-2-oxo-2*H*-chromen-7-yl acrylate (8)

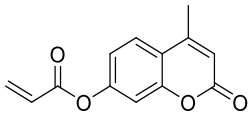

The title compound **8** was synthesized by a procedure according to Zeng et al. To a solution of 4-methylumbelliferone (88 mg, 0.50 mmol) in dichloromethane (10 mL), acryloyl chloride (72 µL, 0.90 mmol) and DIPEA (87 µL, 0.50 mmol) were added dropwise. The reaction mixture was stirred for 16 h at room temperature and extracted with $NaHCO_3$ sat. and HCl (1 M). Purification by silica column chromatography (CH/EA 5:1) afforded the title compound **8** as a colourless solid (20 mg, 17%); mp: 159 °C; ^{1}H NMR (300 MHz, DMSO-d_6) δ= 7.83 (d, J = 8.6 Hz, 1H), 7.35 (d, J = 2.2 Hz, 1H), 7.24 (dt, J = 8.6, 2.2 Hz, 1H), 6.59 (dd, J = 17.2, 1.6 Hz, 1H), 6.51 – 6.35 (m, 2H), 6.20 (dd, J = 10.1, 1.6 Hz, 1H), 2.45 (s, 3H); ^{13}C NMR (75 MHz, DMSO-d_6) δ= 163.6, 159.6, 153.5, 152.9, 152.6, 134.3, 127.3, 126.4, 118.3, 117.6, 113.8, 110.1, 18.1; FT-IR (neat): ṽ [cm^{-1}]= 1730, 1614, 1386, 1371, 1292, 1263, 1159, 1074, 1066, 1019, 985, 970, 903, 875, 845, 824, 803, 794, 750, 706, 671; ESI-MS *m/z*: [M+H]$^{+}$ 230.81 (100%), 231.35 (10.35%), 232.26 (3.31%); purity (HPLC)= 99.9%.

6 Strategy to design the chimeric sulfonylpyrimidine inhibitors 5b,c

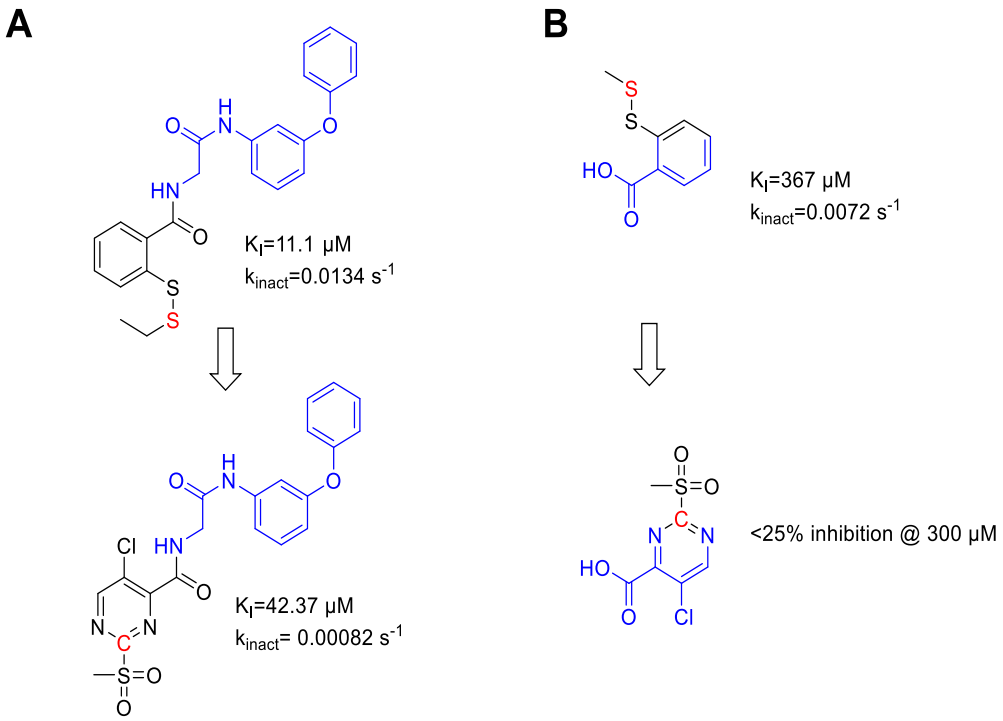

Figure 1: Scheme of the design strategy to derive the chimeric sulfonylpyrimidines 5b,c from previously published SrtA inhibitors (Barthels et al., 2020; doi: 10.1002/cmdc.201900687). (**A**) The previously published disulfanylbenzamide (original manuscript compound numbering: **7a**) was used to design the chimeric inhibitor **5b**. The electrophilic center of the warhead chemotype is highlighted in red. The preserved sequence of the recognition motif (3-PhOPh-NH-Glycine) is marked in blue. (**B**) The previously published disulfide-substituted benzoic acid (original manuscript compound numbering: **3a**) was used to design the chimeric fragment inhibitor **5c**. The electrophilic center of the warhead chemotype is highlighted in red. The preserved sequence of the recognition motif (aromatic carboxylic acid) is marked in blue.

7 Mass spectrometry data supporting the cysteine reactivity experiments

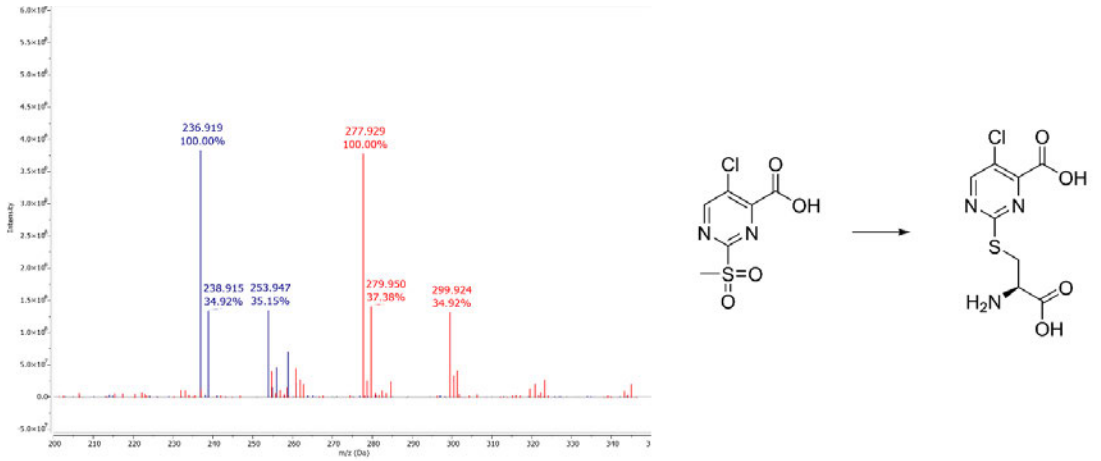

Figure 2: ESI-MS of compound 5c (blue, m/z=236.91) treated with free cysteine revealed the formation of a distinct adduct (red, m/z=277.92) corresponding to the respective 2-pyrimidyl cysteine.

8 Quantum mechanical calculations

To investigate the reaction in solution, the model reaction of inhibitor **5c** with methanethiol was chosen. The reaction coordinate is labeled with R(S_{thiol}-$C_{inhibitor}$) and describes the distance between the thiol(ate) sulfur atom and the C-2 atom of the inhibitor (Figure 3).

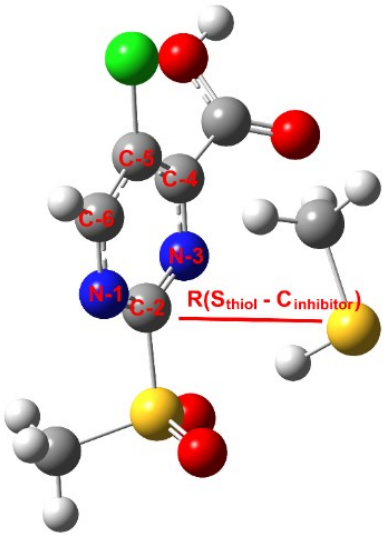

Figure 3: Selected model for QM calculations between inhibitor 5c and methanethiol.

2-Sulfonylpyrimidines as Sortase A Inhibitors

Computed reaction paths of inhibitor **5c** with methanethiol or methanethiolate are shown in Figure 4.

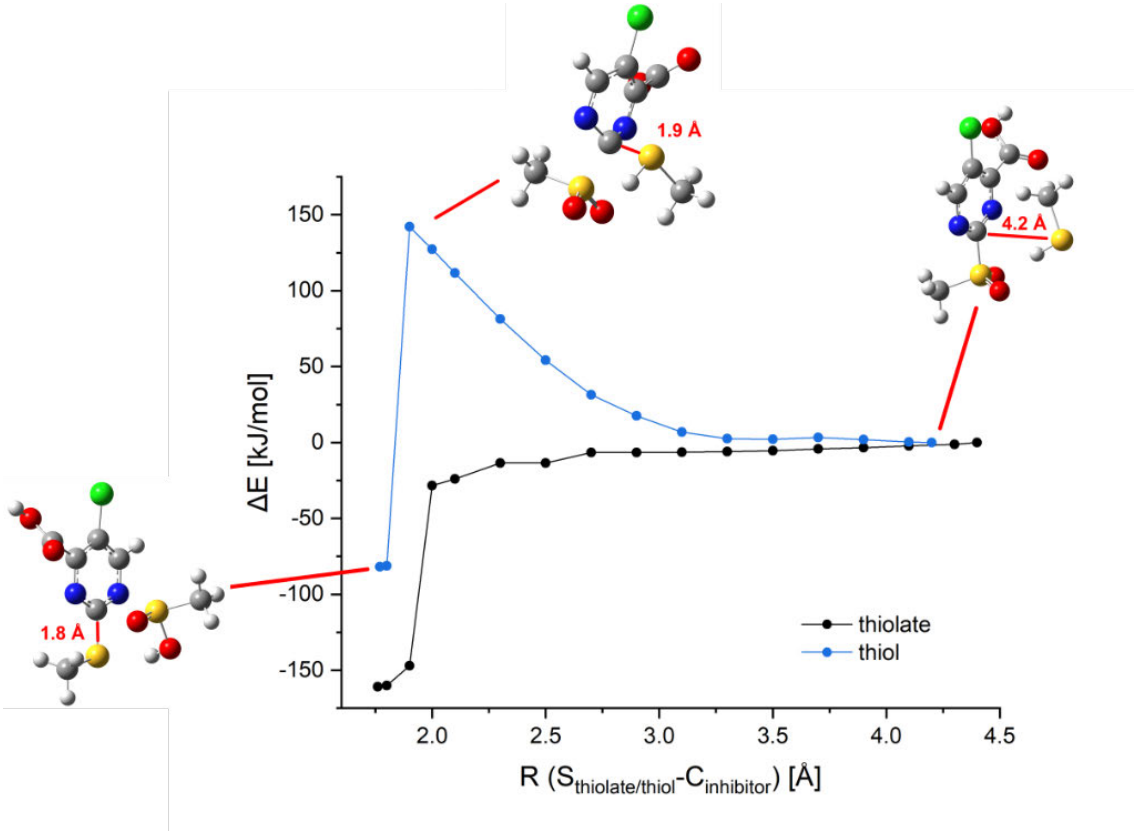

Figure 4: Computed reaction paths with thiolate and thiol: Energy profile of the calculated model reaction of inhibitor **5c** with methanethiolate or methanethiol.

Calculated reaction paths of inhibitor **5c** with methanethiol in the presence of all possible bicarbonate and phosphate species are shown in Figure 5 and Figure 6.

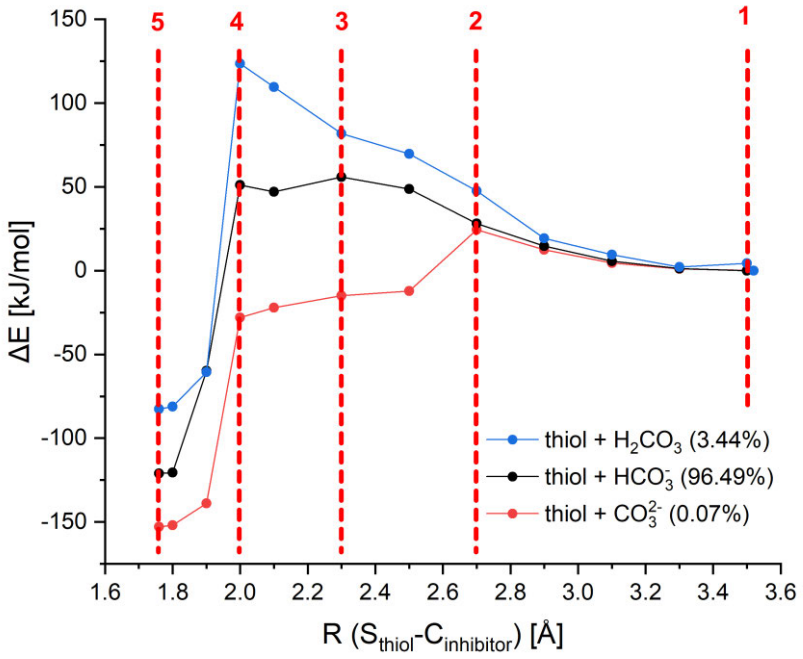

Figure 5: Computed reaction paths mediated by bicarbonate buffer: Energy profile of the calculated model reaction between inhibitor **5c** and methanethiol in the presence of bicarbonate buffer species, the dashed red lines indicated the structures depicted in the following Table 1.

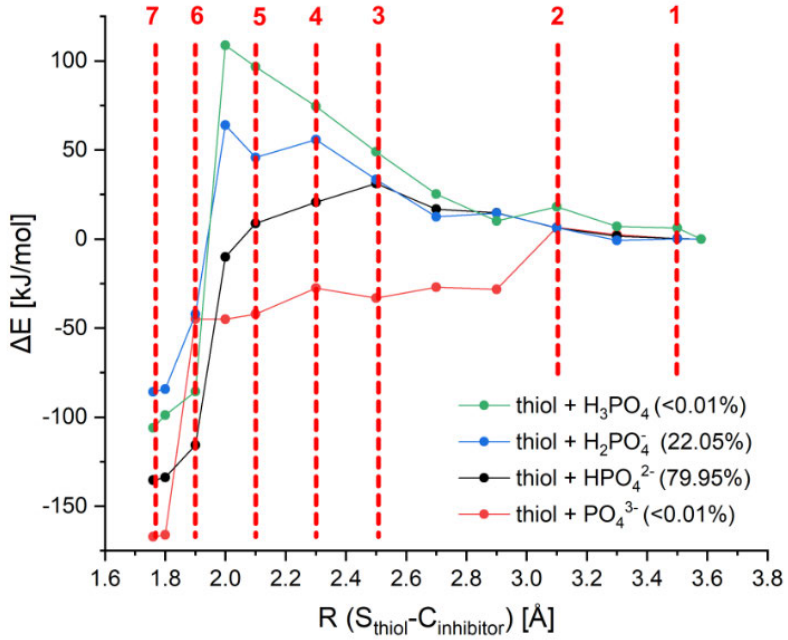

Figure 6: Computed reaction paths mediated by phosphate buffer: Energy profile of the calculated model reaction between inhibitor **5c** and methanethiol in the presence of phosphate buffer species, the dashed red lines indicated the structures depicted in the following Table 2.

Table 1: Selected structures from the calculated reaction paths of inhibitor **5c** and all bicarbonate buffer species.

	R (S_{thiol}-C_{inh}) [Å]	thiol + H_2CO_3	thiol + HCO_3^-	thiol + CO_3^{2-}
1	3.5	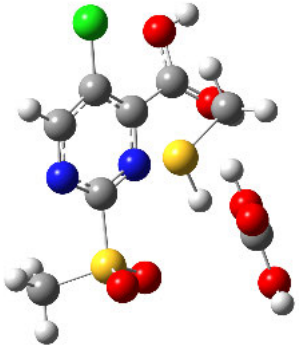	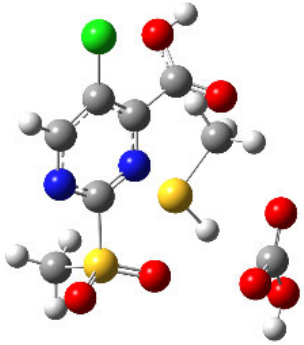	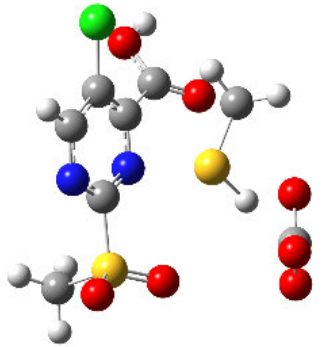
2	2.7	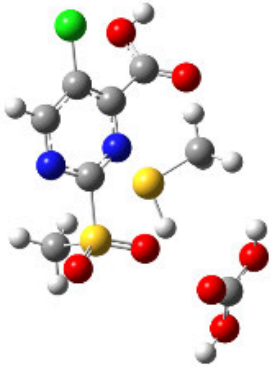	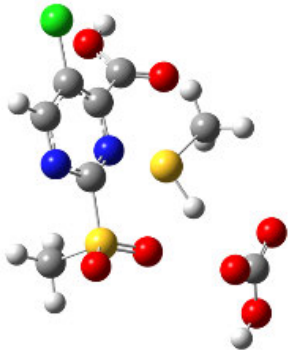	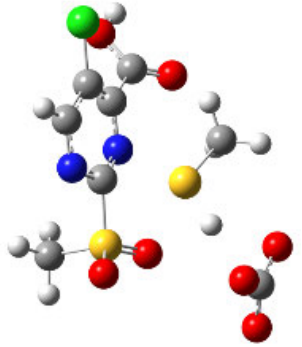

3	**2.3**	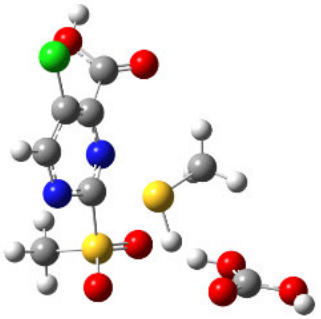	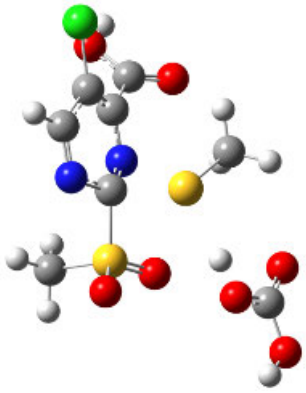	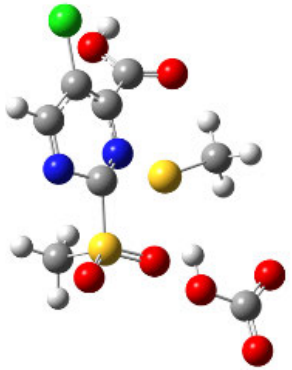
4	**2.0**	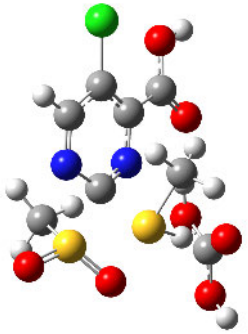	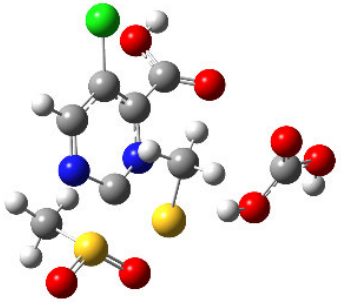	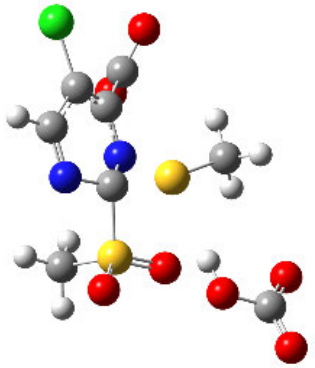

5	**1.76**	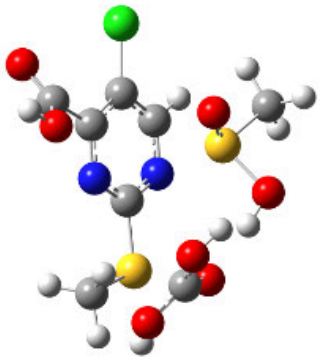	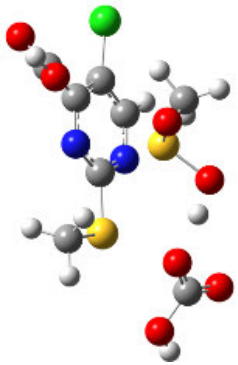	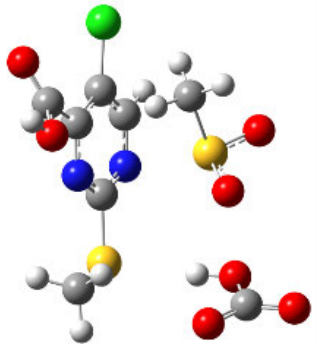

Table 2: Selected structures from the calculated reaction paths of inhibitor **5c** and all phosphate buffer species.

	R (S_{thiol}-C_{inh}) [Å]	**thiol + H_3PO_4**	**thiol + $H_2PO_4^-$**	**thiol + HPO_4^{2-}**	**thiol + PO_4^{3-}**
1	**3.5**		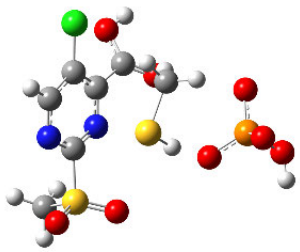	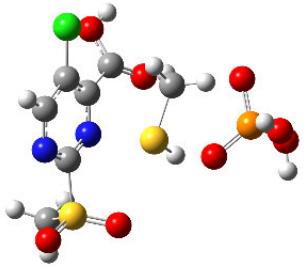	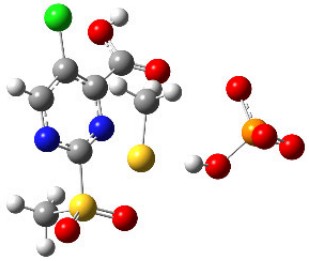

2	2.9	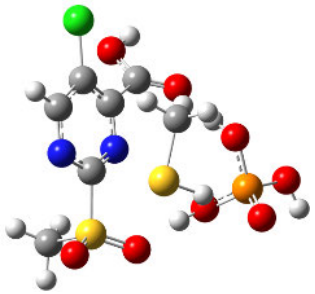	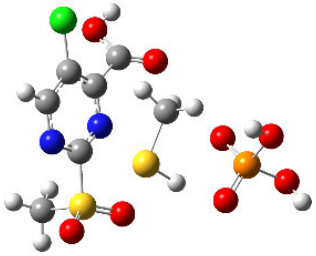	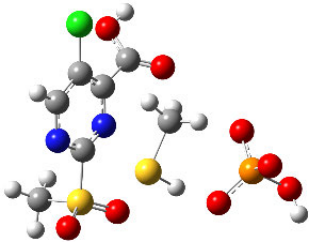	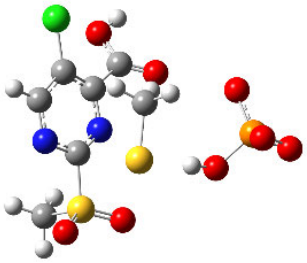
3	2.5	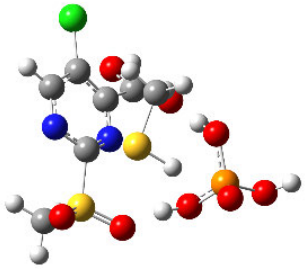	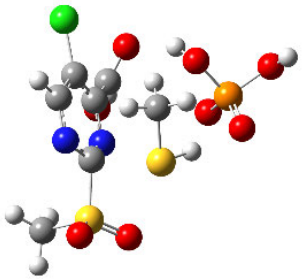	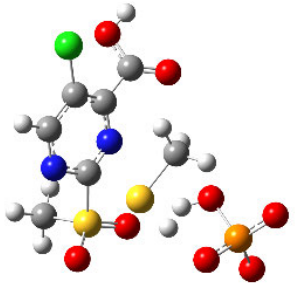	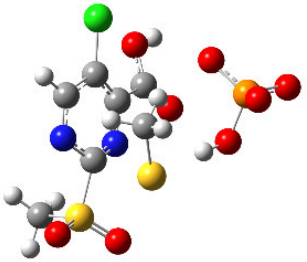
4	2.3	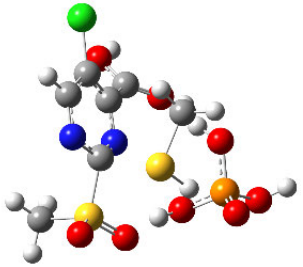	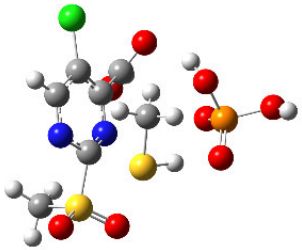	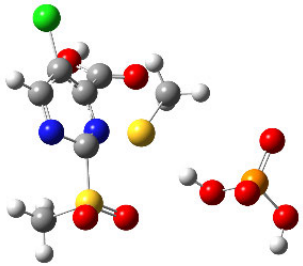	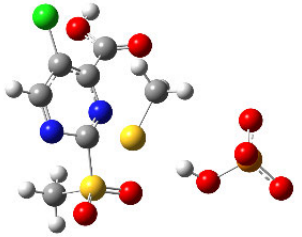

5	**2.1**		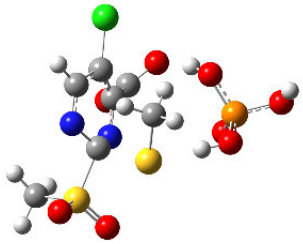	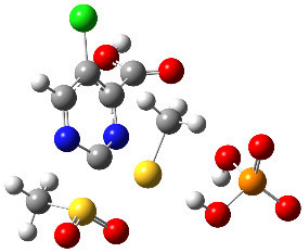	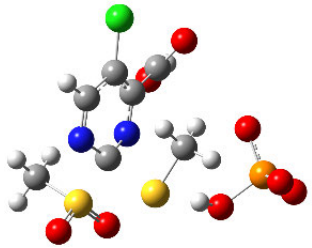
6	**1.9**	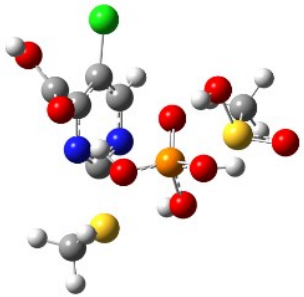	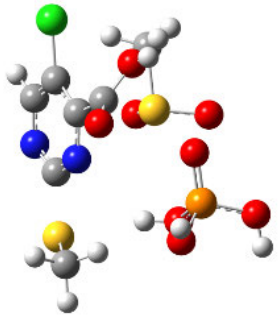	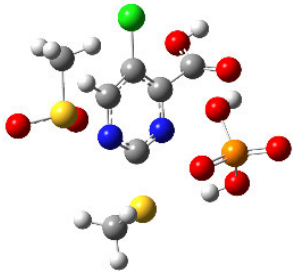	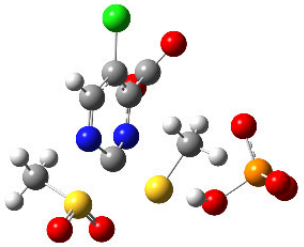
7	**1.76**	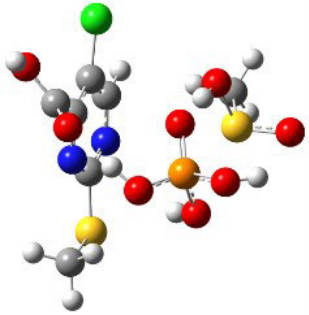	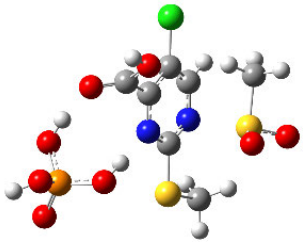	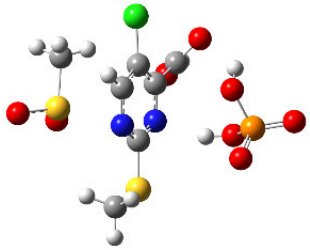	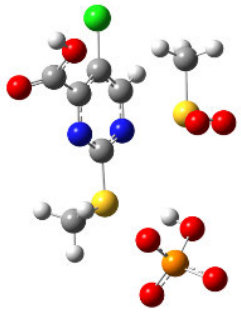

The reaction path of inhibitor **5c** with methanethiol in the presence of 4-methylimidazole is shown in Figure 7.

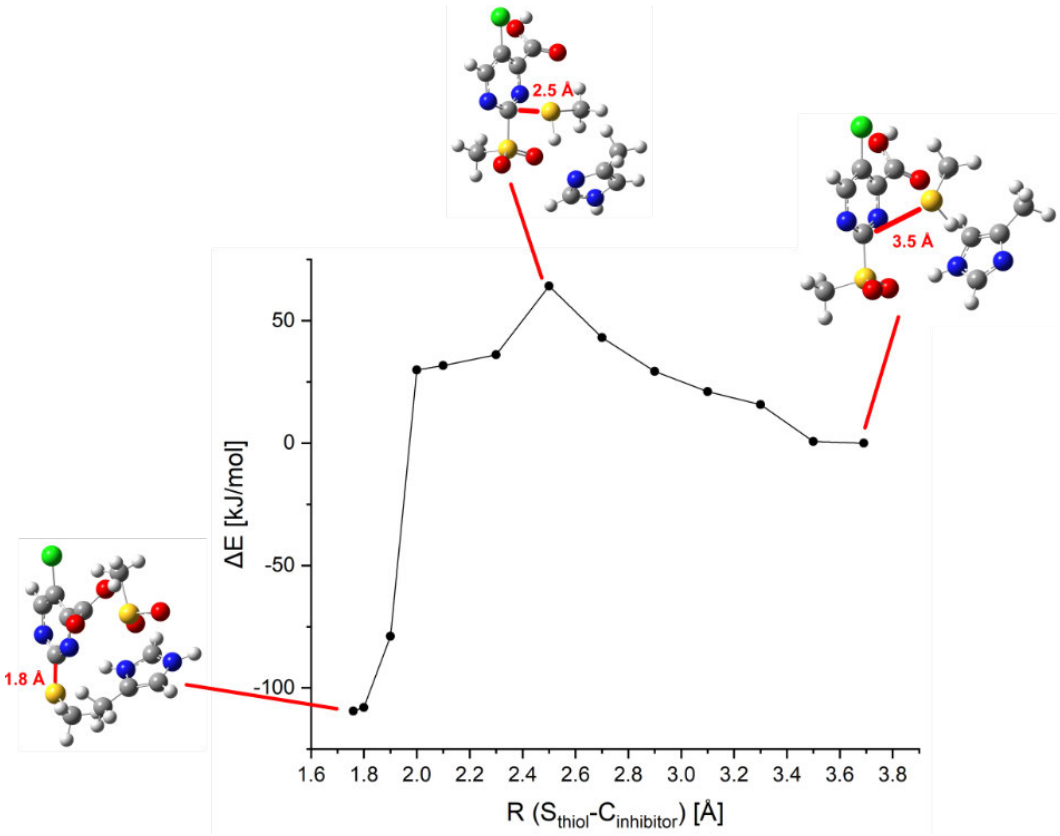

Figure 7: Computed reaction paths mediated by 4-methylimidazole: Energy profile of the calculated model reaction between inhibitor **5c** and methanethiol in the presence of 4-methylimidazole.

2-Sulfonylpyrimidines as Sortase A Inhibitors

In the following Table 3 an overview of all computed barrier heights, product energies, and distances R(S_{thiol}-C-$2_{inhibitor}$), at which the proton is transferred, is shown.

Table 3: Computed model reactions of inhibitor 5c: Reaction barrier, product energy, and distances R(S_{thiol}-C-$2_{inhibitor}$), at which the proton is transferred, of the calculated model reaction between inhibitor **5c** and methanethiol(ate).

	thiolate	**thiol**	**thiol + HCO_3^-**	**thiol + H_2CO_3**	**thiol + CO_3^{2-}**	**thiol + HPO_4^{2-}**	**thiol + $H_2PO_4^-$**	**thiol + H_3PO_4**	**thiol + PO_4^{3-}**	**thiol + 4-Me-imidazol**
barrier [kJ/mol]	–	142	56	123	24	31	64	109	7	64
product [kJ/mol]	–161	–82	–121	–82	–153	–135	–86	–106	–167	–110
proton transfer (R_{S-C-2}) [Å]	–	1.8	2.3	1.9	2.5	2.3	2.1	1.9	2.9	2.3

9 References

Arukwe, J., Undheim, K., Skjetne, T., and Darzynkiewicz, E. (1986). Lithiation in the Synthesis of 5-Pyrimidinyl Ketones. *Acta Chem. Scand.* 40b, 588–592. doi:10.3891/acta.chem.scand.40b-0588.

Barthels, F., Marincola, G., Marciniak, T., Konhäuser, M., Hammerschmidt, S., Bierlmeier, J., et al. (2020). Asymmetric Disulfanylbenzamides as Irreversible and Selective Inhibitors of Staphylococcus aureus Sortase A. *ChemMedChem* 15, 839–850. doi:10.1002/cmdc.201900687.

Grant, G. A., Seemann, C. V., and Winthrop, S. O. (1956). Basic Esters Of Substituted Pyrimidine-4-Carboxylic Acids. *Can. J. Chem.* 34, 1444–1446. doi:10.1139/v56-185.

Li, W., Li, J., Wu, Y., Wu, J., Hotchandani, R., Cunningham, K., et al. (2009). A Selective Matrix Metalloprotease 12 Inhibitor for Potential Treatment of Chronic Obstructive Pulmonary Disease (COPD): Discovery of (*S*)-2-(8-(Methoxycarbonylamino)dibenzo[*b* , *d*]furan-3-sulfonamido)-3-methylbutanoic acid (MMP408). *J. Med. Chem.* 52, 1799–1802. doi:10.1021/jm900093d.

Tröster, A., Bauer, A., Jandl, C., and Bach, T. (2019). Enantioselective Visible-Light-Mediated Formation of 3-Cyclopropylquinolones by Triplet-Sensitized Deracemization. *Angew. Chem. Int. Ed.* 58, 3538–3541. doi:10.1002/anie.201814193.

Webb, K. S. (1994). A mild, inexpensive and practical oxidation of sulfides. *Tetrahedron Lett.* 35, 3457–3460. doi:10.1016/S0040-4039(00)73209-6.

Zeng, R.-F., Lan, J.-S., Li, X.-D., Liang, H.-F., Liao, Y., Lu, Y.-J., et al. (2017). A Fluorescent Coumarin-Based Probe for the Fast Detection of Cysteine with Live Cell Application. *Molecules* 22, 1618. doi:10.3390/molecules22101618.

3.2 Asymmetric Disulfanylbenzamides as Irreversible and Selective Inhibitors of *Staphylococcus aureus* Sortase A

3.2.1 Context, Project Summary, and own Contribution

Chemotype analysis of *S. aureus* SrtA targeting warheads revealed many of those contain electrophiles that form disulfide bonds with the active-site Cys184 such as benzisothiazolinones, thiadiazolidine-3,5-diones, disulfides, thioamides, and 1,3,4-thiadiazoles.[202,203,205,206,297,298] ZHULENKOV et al. identified benzisothiazolinones as a potent class of *S. aureus* SrtA inhibitors. However, in addition to strong inhibition in vitro, these compounds showed no effect of biofilm inhibition in cellulo, as they were found to be hyperreactive causing toxicity and bactericidal effect even at low doses.[203] In this context, benzothiazolinones were frequently classified as pan-assay interference compounds (PAINS) which should be avoided during hit optimization and inhibitor design.[299,300] However, if there is structural evidence for enzyme binding, a more recent view of PAINS pursues the strategy to tame these chemical entities, meaning to modulate the hyperreactive groups and to conserve the productive interactions of the inhibitor with the binding pocket.[301]

In this project, we analyzed the NMR structure of the SrtA-benzisothiazolinone complex (pdb: 2mlm) which allowed the rational design of selective SrtA inhibitors by using asymmetric alkyl-aryl disulfides as warhead chemotypes. In an inhibitor SAR study, we identified a proline-based inhibitor with a k_{2nd}=57,529 $M^{-1}min^{-1}$ that furthermore exhibited low bactericidal activity (MIC=116 µM) and no toxicity to human cells (CC_{50}=253 µM). Protease selectivity assays showed favorable selectivity towards SrtA which could be substantiated by cellular *S. aureus* SrtA reporter inhibition assays and potent biofilm inhibition in the single-digit micromolar range. Tryptic digestion of the covalently modified enzyme coupled with ESI-MS and differential scanning fluorimetry experiments allowed us to conclude mechanistic insights of the warhead reaction: The reaction between the catalytic Cys184 and the disulfide warheads proceeds via a bi-molecular disulfide metathesis reaction. In principle, for asymmetric alkyl-aryl disulfides, two covalent adducts to Cys184 are possible. Here, however, we could show that only the alkyl group of the inhibitor is transferred to the catalytic Cys184, yielding an irreversible disulfide SrtA conjugate.

Unfortunately, the additionally investigated multidrug-resistant *S. aureus* strain USA300 showed very little biofilm reduction upon treatment with the inhibitors which could mean that strain-specific resistances to SrtA inhibitors are already inherent, as known from conventional antibiotics. In summary, we demonstrated that the asymmetric disulfide warhead is suitable for the selective inhibition of *S. aureus* SrtA and might be useful for anti-virulence studies in diseases-related animal studies.

Own contributions: Synthesis of all inhibitors, Sortase A inhibition assays, Protease selectivity assays, Differential scanning fluorimetry, Molecular modeling & Writing of the manuscript.

Contributions from other authors: Protein expression and purification, Cell viability assays, Bacterial growth inhibition assays, Biofilm inhibition assays & Protein mass spectrometry.

This work has been published in: ChemMedChem (impact factor: 3.46).

The appended 'Supporting Information' represents an abridged version. The full version can be accessed online at doi: 10.1002/cmdc.201900687.

3.2.2 Publication

The following publication quoted (within "") from page 101 to page 146 is exactly the same as the manuscript cited on page 100:"

ChemMedChem | Full Papers
doi.org/10.1002/cmdc.201900687

Asymmetric Disulfanylbenzamides as Irreversible and Selective Inhibitors of *Staphylococcus aureus* Sortase A

Fabian Barthels,[a] Gabriella Marincola,[b] Tessa Marciniak,[b] Matthias Konhäuser,[a] Stefan Hammerschmidt,[a] Jan Bierlmeier,[c] Ute Distler,[d, e] Peter R. Wich,[a, f] Stefan Tenzer,[d] Dirk Schwarzer,[c] Wilma Ziebuhr,[b] and Tanja Schirmeister*[a]

Staphylococcus aureus is one of the most frequent causes of nosocomial and community-acquired infections, with drug-resistant strains being responsible for tens of thousands of deaths per year. *S. aureus* sortase A inhibitors are designed to interfere with virulence determinants. We have identified disulfanylbenzamides as a new class of potent inhibitors against sortase A that act by covalent modification of the active-site cysteine. A broad series of derivatives were synthesized to derive structure-activity relationships (SAR). *In vitro* and *in silico* methods allowed the experimentally observed binding affinities and selectivities to be rationalized. The most active compounds were found to have single-digit micromolar K_i values and caused up to a 66% reduction of *S. aureus* fibrinogen attachment at an effective inhibitor concentration of 10 μM. This new molecule class exhibited minimal cytotoxicity, low bacterial growth inhibition and impaired sortase-mediated adherence of *S. aureus* cells.

Introduction

The ongoing spread of antibiotic resistance among Gram-positive bacteria such as *Staphylococcus aureus* highlights the need for new treatment options beyond traditional antibiotics. In this respect, exploring virulence mechanisms as drug targets might provide novel opportunities to interfere with bacterial pathogenicity.[1] The cysteine transpeptidase sortase A (SrtA) was considered as a putative anti-virulence drug target, which may be addressed also in combination with classical antibiotics' target structures.[2] SrtA mediates the attachment of surface proteins to the bacterial cell wall and it was shown that an *S. aureus* Δ*SrtA* mutant is clearly attenuated in mouse infection models compared to the wild type.[3,4] SrtA inhibitors are likely to interfere with adherence and intercellular communication rather than with bacterial growth, thus imposing a lower selective pressure to promote resistance development.[5] Since neither genetic deletion[6] nor selective chemical inhibition[7–9] of *S. aureus* SrtA was found to cause cytotoxic or growth inhibitory effects on bacterial cells, the enzyme meets the requirements of an anti-virulence target. Microbial surface components recognizing adhesive matrix molecules (MSCRAMMs) are bacterial surface proteins utilized during pathogenesis for adherence to endothelial host cells and playing a role in immune evasion.[10] Many of these virulence-associated proteins are secreted as precursors with C-terminal LPXTG-tagged sorting-signals. At the bacterial cell wall, they are recognized and cleaved between threonine and glycine by the membrane-anchored transpeptidase SrtA.[11] Subsequent ligation to the pentaglycine tail of the peptidoglycan layer yields the covalent attachment to the bacterial outer surface.[12] In *S. aureus*, approximately 20 surface proteins have been identified as naturally occurring SrtA substrates, including several factors that are involved in pathogenicity, such as protein A (SpA), fibronectin-binding proteins (FnbpA/B), clumping factors (ClfA/B), serine-aspartic acid repeat proteins (SdrC/D/E) and staphylococcal surface proteins (Sas).[13,14]

The eight-stranded β-barrel protein SrtA possesses three conserved residues within the sortase family: His62, Cys126, and Arg139, each of which cannot be mutated without disrupting enzymatic functionality.[15] Structural similarities between the transpeptidase SrtA and the papain protease were noticed,[16] however, enzymatic characteristics of the *S. aureus* SrtA differ significantly from most proteases: (i) The catalytic Cys126 is "reversely protonated", which means it does not form a

[a] *F. Barthels, M. Konhäuser, S. Hammerschmidt, Jun.-Prof. Dr. P. R. Wich, Prof. Dr. T. Schirmeister*
Institute for Pharmacy and Biochemistry
Johannes-Gutenberg-University of Mainz
Staudinger Weg 5, 55128 Mainz, Germany
E-mail: schirmei@uni-mainz.de
[b] *Dr. G. Marincola, T. Marciniak, Dr. W. Ziebuhr*
Institute for Molecular Infection Biology
Julius-Maximilians-University of Würzburg
Josef-Schneider-Strasse 2, 97080 Würzburg, Germany
[c] *J. Bierlmeier, Prof. Dr. D. Schwarzer*
Interfaculty Institute of Biochemistry
Eberhard-Karls-University of Tübingen
Hoppe-Seyler-Strasse 4, 72076 Tübingen, Germany
[d] *Dr. U. Distler, Prof. Dr. S. Tenzer*
Institute for Immunology, University Medical Center
Johannes-Gutenberg-University of Mainz
Langenbeckstr. 1, 55131 Mainz, Germany
[e] *Dr. U. Distler*
Focus Program Translational Neuroscience (FTN), University Medical Center
Langenbeckstr. 1, 55131 Mainz, Germany
[f] *Jun.-Prof. Dr. P. R. Wich*
School of Chemical Engineering, University of New South Wales
Science and Engineering Building, Sydney, NSW 2052, Australia

Supporting information for this article is available on the WWW under https://doi.org/10.1002/cmdc.201900687

ChemMedChem
Full Papers
doi.org/10.1002/cmdc.201900687
Chemistry Europe
European Chemical Societies Publishing

thiolate-imidazolium pair, and thus, only a small fraction (< 0.1%) of SrtA is competent for catalysis at physiological pH 7.4.[17] (ii) The active site is predominantly defined by the intrinsic flexibility of the β6/7- and β7/8-loops.[18] (iii) The most active form of SrtA is constituted as a homo-dimer with a K_D= 55 μM.[19] (iv) The K_M values for both, the LPXTG- and Gly_n-substrates are exceptionally high (K_M= 5.5 mM and 0.14 mM), probably due to the fact that the enzyme and both substrates are spatially co-localized at the outer membrane yielding high local concentrations.[20] (v) The high redox potential of the catalytic Cys126 (1.27 V) makes SrtA insensitive towards oxidation stress contributing to *S. aureus* phagocytotic survival.[21]

Previous research campaigns investigated competitive-reversible *S. aureus* SrtA inhibitors including promising scaffolds such as 2-morpholinobenzoates,[22] thiadiazoles,[7,23] 2-phenylthiazoles,[24] macrocyclic peptides,[25] 2-phenylbenzoxazoles,[26] and various other inhibitors.[8,27,28] However, the most active compounds were found to be irreversible covalent inhibitors containing an electrophilic warhead that reacts with the active-site Cys126 of SrtA.[29–33] While having significant inhibition in the low micromolar range, they typically exhibit poor target selectivity or are cytotoxic such as quinones,[34] rhodanines,[30] or benzisothiazolinones.[32] Zhulenkovs *et al.* solved the NMR structure of SrtA in complex with a covalent benzisothiazolinone adduct. Reaction with the active-site Cys126 occurred via ring-opening of the isothiazolinone moiety yielding a covalent disulfide bond (Figure 1A).

In the corresponding NMR structure (PDB: 2MLM), the ligand displayed a reasonable fit, mimicking substrate binding in the active-site pocket (Figure 1B). Asymmetric disulfides are known inhibitors of cysteine proteases,[35–37] thus, we decided to investigate a disulfide warhead chemotype exchange and systematic scaffold optimization to generate more selective and less cytotoxic disulfide-based SrtA inhibitors (Figure 1C).

Results and Discussion

Synthesis of the inhibitors

Disulfanylbenzamides were synthesized based on a known procedure for asymmetric disulfides (Scheme 1).[38] Commercially available sulfanylbenzoic acids **2a–c** were activated at 50 °C with trichloroisocyanuric acid (TCCA) to form electrophilic sulfenyl chlorides *in situ*. The subsequent conversion with nucleophilic alkyl thiols provided the disulfanylbenzoic acids **3b–g**. Since methyl mercaptan is gaseous at room temperature, for 2-(methyldisulfanyl)benzoic acid **3a** a different strategy was employed. *S*-methyl methanethiosulfonate as thiomethyl-transferring reagent was utilized to convert thiosalicylic acid **2a** to 2-(methyldisulfanyl)benzoic acid **3a**.[39] Boc-protected amino acids **4a–l** were coupled to various aromatic and aliphatic amines (R^1) in the presence of 2-(1*H*-benzotriazole-1-yl)-1,1,3,3-tetramethylaminium tetrafluoroborate (TBTU) to provide the inhibitor scaffold precursors **5a–v**. The deprotection of the Boc group was achieved by treatment with hydrochloric acid. Finally, the disulfanylbenzoic acids **3a–g** were coupled in the presence of TBTU with the appropriate amine hydrochlorides **6a–v** to provide the desired test compounds **7a–w** and **7α–ζ** (Scheme 1). Parent compound **1** was prepared in a one-pot procedure from **3a** and **6a**. Both reactants were coupled by means of TBTU. The subsequent treatment with lithium

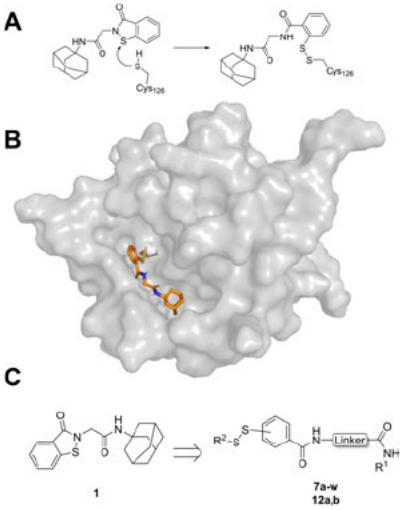

Figure 1. A) The reaction of benzisothiazolinones with the active-site Cys126 in *S. aureus* SrtA. B) NMR structure of the benzisothiazolinone inhibitor (**1**) covalently bound to *S. aureus* SrtA (PDB: 2MLM). C) Warhead chemotype exchange and scaffold-hopping strategy to transform the known inhibitor **1** to disulfanylbenzamides (**7a–w** and **12a,b**).[32]

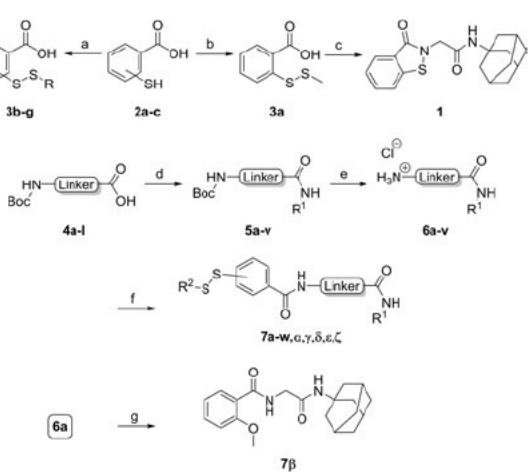

Scheme 1. a) Trichloroisocyanuric acid, R-SH, ACN, −50 °C to RT, 15 min; 56–69%; b) *S*-methyl methanethiosulfonate, MeOH, RT, 16 h, 86%; c) (i) **6a**, TBTU, DIPEA, DMF, RT, 16 h (ii) 4 M $LiOH_{aq}$, 60 °C, 4 h, 75%; d) R^1–NH_2, TBTU, DIPEA, EtOAc, RT, 72 h, 24–96%; e) 12 M HCl_{aq}/THF (1:1), RT, 1 h, 74–99%; f) R^2–SS–PhCOOH, TBTU, DIPEA, EtOAc, RT, 16 h, 23–89%; g) *o*-anisic acid, TBTU, DIPEA, EtOAc, RT, 72 h, 82%.

ChemMedChem
Full Papers
doi.org/10.1002/cmdc.201900687
Chemistry Europe
European Chemical Societies Publishing

hydroxide at 60 °C yielded the elimination of methyl mercaptan and provided the benzisothiazolinone inhibitor **1**.[40]

For the synthesis of the aspartic acid-based inhibitors **12a,b** a different protection group strategy was used (Scheme 2). Briefly, the Cbz/*t*Bu-protected aspartic acid derivates **8a,b** were coupled by means of TBTU to yield the amides **9a,b**. The deprotection of the N-terminal Cbz group was achieved by Pd-catalyzed hydrogenolysis to yield the amines **10a,b**. The disulfanylbenzoic acids **3a** or **3d** were coupled to the appropriate amines in the presence of TBTU yielding the inhibitor scaffold precursors **11a,b**. Finally, the deprotection of the *tert*-butyl ester with trifluoroacetic acid yielded the compounds **12a,b**.

Substrate-based diacyl hydrazide inhibitors (**16a,b**) were synthesized starting from proline benzyl ester **13** and Boc-leucine to yield the dipeptide ester **14**. Hydrazinolysis of the benzyl ester gave the hydrazide **15**, which was either TBTU-coupled with **3a** to yield the disulfanylbenzamide **16a** or converted with maleic anhydride to the monomaleamide **16b** (Scheme 3).

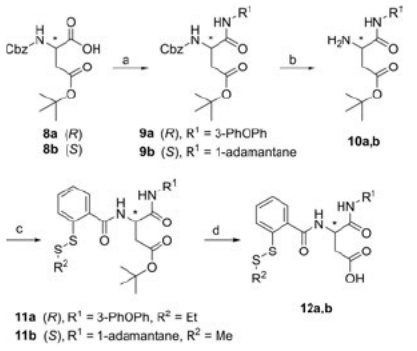

Scheme 2. a) R^1–NH_2, TBTU, DIPEA, EtOAc, RT, 72 h, 68–96%; b) H_2 (60 psi), Pd/C, MeOH, RT, 16 h, 92–99%; c) R^2–SS–PhCOOH, TBTU, DIPEA, EtOAc, RT, 16 h, 79–83%; d) TFA/DCM, RT, 2 h, 91–99%.

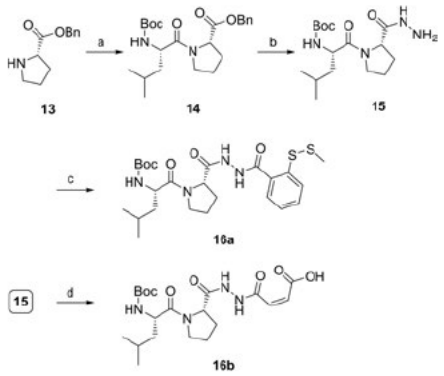

Scheme 3. a) Boc–Leu–OH, TBTU, DIPEA, EtOAc, RT, 72 h, 56%; b) hydrazine hydrate, MeOH, RT, 16 h, 74%; c) **3a**, TBTU, DIPEA, EtOAc, RT, 16 h, 16%; d) maleic anhydride, AcOH, RT, 16 h, 79%.

Irreversible inhibition of *S. aureus* sortase A

To evaluate the inhibition potency of the compounds, these were tested by means of a fluorometric enzyme assay with recombinantly expressed *S. aureus* SrtA[41] and Abz-LPETG-Dap (Dnp)-OH as substrate. The inhibitors **7a–w** and **12a,b** were found to act as time-dependent and irreversible inhibitors. Exemplarily, the substrate conversion plot in the presence of inhibitor **12a** is showing the time-dependency of inhibition (Figure 2). The apparent first-order rate constant (k_{obs}) varied hyperbolically with the concentration of the inhibitor. A limiting value was approached asymptotically at higher inhibitor concentrations indicating two-step mechanism kinetics for all inhibitors except for the fragment-like inhibitor **3a** (K_i = 367 μM). Benzisothiazolinone **1** was used as a reference inhibitor with a literature reported IC_{50} = 6.11 μM.[32] For time-dependent inhibitors, reporting IC_{50} values is less suitable since the IC_{50} is strongly depending on the incubation time of enzyme and inhibitor. Moreover, the IC_{50} is depending on the substrate used for the enzyme assays, its K_M value and its concentration.[42] Therefore, we determined the maximum inactivation rate k_{inact}, the dissociation constant of the reversible enzyme-inhibitor complex K_i, and the second-order rate of inhibition k_{2nd}. For compound **1** a k_{inact} = 0.0307 s^{-1} was found, which is quite high compared to other targeted covalent

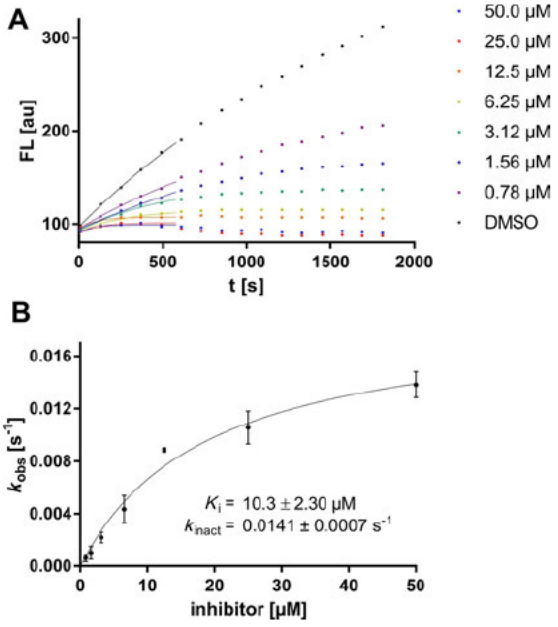

Figure 2. A) Fluorometric assay with compound **12a** showing time-dependent enzyme inhibition with hyperbolic substrate conversion plots. The fluorescence was recorded for 30 min every 30 s. For clarity, only every fourth data point is shown. Lines represent nonlinear fits for $t < 10$ min. A magnification plot of the crucial initial phase can be found in Figure S8 in the Supporting Information. B) k_{obs} vs. [I] for the determination of inhibition constants (K_i, k_{inact}).

ChemMedChem
Full Papers
doi.org/10.1002/cmdc.201900687
Chemistry Europe
European Chemical Societies Publishing

Table 1. Inhibition constants (K_i, k_{inact}, k_{2nd}) of the compounds **1**, **3a** and **16a,b** for *S. aureus* SrtA.

Cpd.	structure	K_i [μM]	k_{inact} [s^{-1}]	k_{2nd} [$M^{-1} min^{-1}$]
1	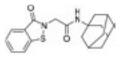	34.2 ± 5.87	0.0307 ± 0.0016	53860 ± 6665
3a		367 ± 24.4	0.0072 ± 0.0012	1177 ± 119
16a	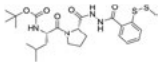	16.6 ± 2.88	0.0044 ± 0.0003	15904 ± 1735
16b	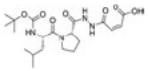	IC_{50} 20.4 ± 1.30 μM[a]		

[a] Two-hour preincubation of the enzyme with inhibitor at pH 7.50. All results include the mean value and standard deviations from triplicate measurements.

inhibitors,[43,44] but gives reason to its bactericidal effects[32] and the unspecific cysteine labeling by benzisothiazolinones.[45]

To date, only a few studies characterized irreversible SrtA inhibitors by their inactivation kinetics.[31,46,47] Most of these inhibitors contained the LPAT sorting-signals but utilized different electrophilic warheads (diazoketone, chloroketone or vinyl sulfone). Compared to the parent compound **1**, these warheads were 150–5000-fold less reactive (k_{inact} = 0.0002 s^{-1} 6.6·10 ^{6} s^{-1}), however, the vinyl sulfone was shown to gain significant reactivity above pH 8.00 due to the deprotonation of Cys126 (pK_a = 9.4[48]). Since the peptidoglycan is slightly acidic[49] and several Gram-positive bacteria have trained themselves by evolution for survival in low-pH environment,[50] we raised the hypothesis that inhibitors with an optimum effect at pH 8.00 or above are unsuitable to target SrtA *in cellulo*. To investigate the pH-dependence of the novel disulfanylbenzamide warhead in comparison to a common Michael-acceptor warhead, we designed sorting-signal derived leucine-proline dipeptide inhibitors, with disulfanylbenzamide (**16a**) and monomaleamide (**16b**) warheads and characterized their inhibition kinetics and pH-dependence as presented in table 1 and figure 3.

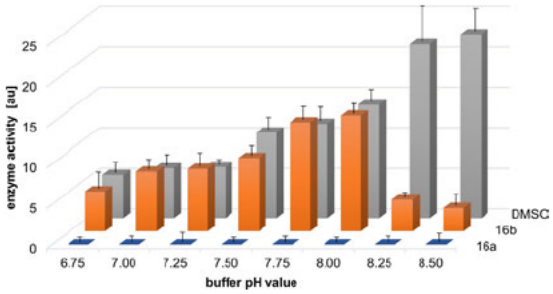

Figure 3. pH dependency on the inhibition potency of the disulfide inhibitor **16a** and the monomaleamide inhibitor **16b** at a final inhibitor concentration of 20 μM. The residual enzymatic activity was assessed from the initial slope of the substrate conversion plots. For the inhibitors, no preincubation was used. All results include the mean and standard deviations from triplicate measurements.

Disulfanylbenzamide inhibitor **16a** showed irreversible inhibition, with a twofold increased affinity compared to the parent compound **1** (K_i: 34.2 vs. 16.6 μM), but its overall inhibition potency (k_{2nd}) was threefold lower, mainly due to its reduced inactivation rate constant (k_{inact} = 0.0044 s^{-1}). The dipeptide monomaleamide **16b** did not show significant inhibition in the standard fluorometric assay, but a two-hour pre-incubation of the enzyme and inhibitor prior to substrate addition led to an IC_{50} = 20.4 μM. We hypothesized a covalent inhibition mode of **16b** with very slow inactivation kinetics due to the poor nucleophilicity of Cys126. We measured the pH-dependence of SrtA inactivation by **16a** and **16b** at eight different pH-values (6.75–8.50). As shown in figure 3, the general enzymatic activity increased with higher pH-values, which is in coherence with the reported enzyme optimum at pH 8.80.[51] The inhibition potency of the monomaleamide **16b** was overall low but increased significantly above pH 8.00 either due to the deprotonation of the Cys126 or *in situ* conversion of **16b** to a more electrophilic maleic isoimide, maleimide or pyridazinedione.[52–54]

In contrast, the disulfide inhibitor **16a** showed strong and pH-independent inhibition, indicating that either a negatively charged thiolate as a nucleophile is not required for the reaction with disulfanylbenzamides or that an inhibitor binding-induced zwitterion formation might occur.[55] Besides the classical S_N2-mechanism involving a thiolate,[56] thiol-disulfide conversion was reported to proceed via oxidative and radical-mediated pathways, which might be relevant for the action of disulfanylbenzamides on SrtA.[57–60] We could also show the inhibition by **16a** was completely reversible by the addition of 1 mM reducing agents such as DTT or TCEP. Thus, we postulate that covalent targeting of the SrtA Cys126 under physiological conditions was much more effective by disulfanylbenzamides and should be optimized for potency and selectivity (see next chapter).

Structure-activity relationship

A broad series of disulfanylbenzamides was synthesized to derive structure-activity-relationship (SAR). In fact, 26 out of 32

ChemMedChem
Full Papers
doi.org/10.1002/cmdc.201900687
Chemistry Europe
European Chemical Societies Publishing

Table 2. Inhibition constant values (K_i, k_{inact}, k_{2nd}) of the compounds **7a–ζ** and **12a,b** for *S. aureus* SrtA.

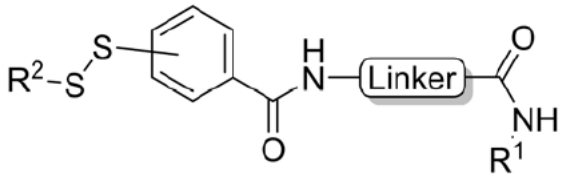

Cpd.	R^1	HN-linker-C (O)	R^2	K_i [μM]	k_{inact} [s^{-1}]	k_{2nd} [$M^{-1}min^{-1}$]
12a	3-PhOPh	(*R*)-aspartic acid	Et (*ortho*)	10.3 ± 2.30	0.0141 ± 0.0007	82136 ± 15136
7a	3-PhOPh	glycine	Et (*ortho*)	11.1 ± 2.15	0.0134 ± 0.0009	72432 ± 9581
7b	1-cyclohexanemethyl	glycine	Et (*ortho*)	12.6 ± 2.34	0.0151 ± 0.0010	71339 ± 8765
7c	*N,N*-dicyclohexyl	glycine	Et (*ortho*)	8.32 ± 1.31	0.0094 ± 0.0005	63873 ± 6238
7d	4-fluorophenyl	glycine	Et (*ortho*)	12.7 ± 2.73	0.0130 ± 0.0010	61417 ± 8957
7e	1-adamantyl	glycine	Me (*ortho*)	16.2 ± 2.87	0.0160 ± 0.0012	59259 ± 6283
7f	1-adamantyl	glycine	Et (*ortho*)	14.3 ± 2.87	0.0138 ± 0.0011	57902 ± 7348
7g	1-adamantyl	(*S*)-proline	Me (*ortho*)	17.0 ± 3.04	0.0163 ± 0.0012	57529 ± 6285
7h	1-adamantyl	sarcosine	Et (*ortho*)	20.5 ± 3.53	0.0174 ± 0.0013	50927 ± 5414
7i	4-cyclohexanephenyl	glycine	Et (*ortho*)	1.88 ± 0.32	0.0013 ± 0.0001	41489 ± 4005
7j	1-napthyl	glycine	Et (*ortho*)	10.0 ± 1.87	0.0066 ± 0.0004	39600 ± 5217
7k	1-(thiophene-2-methyl)	glycine	Et (*ortho*)	10.9 ± 1.91	0.0068 ± 0.0004	37431 ± 4518
7l	2-adamantyl	glycine	Et (*ortho*)	14.4 ± 2.31	0.0089 ± 0.0005	37083 ± 3985
7m	1-adamantyl	glycine	*t*Bu (*ortho*)	6.40 ± 0.84	0.0039 ± 0.0002	36563 ± 2984
7n	isobutyl	glycine	Et (*ortho*)	13.5 ± 3.47	0.0082 ± 0.0011	36444 ± 4848
7o	1-adamantyl	glycine	*i*Pr (*ortho*)	8.24 ± 1.12	0.0044 ± 0.0002	32039 ± 2962
7p	1-adamantyl	(*R*)-phenylalanine	Et (*ortho*)	2.72 ± 0.43	0.0013 ± 0.0001	28676 ± 2397
7q	1-adamantyl	β-alanine	Et (*ortho*)	9.60 ± 1.93	0.0028 ± 0.0002	17500 ± 2380
7r	1-adamantyl	(*R*)-proline	Et (*ortho*)	5.37 ± 0.83	0.0015 ± 0.0001	16760 ± 1515
7s	1-adamantyl	glycine	EtPh (*ortho*)	21.6 ± 3.75	0.0059 ± 0.0005	16389 ± 1509
7t	1-adamantyl	isonipecotic acid	Et (*ortho*)	11.0 ± 2.05	0.0026 ± 0.0001	14182 ± 2186
12b	1-adamantyl	(*S*)-aspartic acid	Me (*ortho*)	40.2 ± 8.73	0.0092 ± 0.0011	13731 ± 1418
7u	1-adamantyl	glycine	Et (*meta*)	24.1 ± 5.94	0.0031 ± 0.0003	7718 ± 1242
7v	1-adamantyl	(*S*)-asparagine	Et (*ortho*)	25.3 ± 5.81	0.0029 ± 0.0003	6877 ± 924
7w	1-adamantyl	(*S*)-alanine	Et (*ortho*)	13.8 ± 3.68	0.0014 ± 0.0001	6087 ± 1294
7α	1-adamantyl	glycine	Et (*para*)	n.d.	n.d.	n.d.
7β	1-adamantyl	glycine	see Scheme 1	n.d.	n.d.	n.d.
7γ	1-adamantyl	(*S*)-phenylalanine	Et (*ortho*)	n.d.	n.d.	n.d.
7δ	2-phenylethyl	glycine	Et (*ortho*)	n.d.	n.d.	n.d.
7ε	1-adamantyl	(*R*)-leucine	Et (*ortho*)	n.d.	n.d.	n.d.
7ζ	1-adamantyl	(*S*)-terleucine	Et (*ortho*)	n.d.	n.d.	n.d.

n.d. < 30% inhibition after 30 min at 50 μM of final compound concentration. All results include the mean value and standard deviations from triplicate measurements.

analogs (**7a–w**, **12a,b** and **16a**) did inhibit SrtA in the fluorometric enzyme assay, but with varying potency. Based on the k_{2nd} values, eight compounds (**12a**, **7a–g**) appeared to be more potent than parent compound **1**, while all investigated disulfanylbenzamides exhibited at least twofold reduced k_{inact} values ranging from 0.0013 s^{-1} to 0.0174 s^{-1} (Table 2). Strikingly, we observed a drop in SrtA inhibition for most modifications on the glycine amino acid linker. This finding suggested that substitution at this position is not well tolerated, except for (*R*)-aspartic acid in inhibitor **12a**, which we hypothesized to interact with Arg139 (Figure 6). Considering the k_{2nd} value, **12a** was the most potent irreversible inhibitor (82,136 $M^{-1}min^{-1}$). Compounds **7α–ζ** were found to be non-binders displaying < 30% inhibition at 50 μM. Interestingly, the (*R*)-phenylalanine derivate **7p** which showed one of the highest binding affinities (K_i = 2.72 μM) had very low inactivation kinetics (k_{inact} = 0.0013 s^{-1}). The (*S*)-phenylalanine enantiomer **7γ**, however, did not show any inhibition. No significant loss in activity was observed upon amide-methylation of glycine (**7f**) to sarcosine (**7h**), demonstrating that the activity is not mediated by an *in situ* activation to benzisothiazolinones. More pronounced effects could be associated with the replacement of the amide substituent (R^1), but no clear structural trend was identified. It should be noted that the two most potent compounds identified here (**12a**, **7a**) incorporated a 3-phenoxyaniline substituent (R^1). Intriguingly, the change of the disulfide warhead (R^2) affected both, affinity (K_i) and reactivity (k_{inact}). The *ortho*-configuration (**7f**) seemed to be strongly preferred over *meta* (**7u**) and *para* (**7α**). The alkyl group (R^2) followed the trend: Me ~ Et > *i*Pr ~ *t*Bu > EtPh. A methyldisulfanyl- (**7e**) to methoxy-(**7β**) exchange led to a complete loss of inhibition. We concluded from these findings that both, the warhead's positioning and the steric demand were likely to influence the inhibitor's potency.

ChemMedChem
Full Papers
doi.org/10.1002/cmdc.201900687
Chemistry Europe
European Chemical Societies Publishing

Characterization of covalent protein adducts

For asymmetric disulfanylbenzamides, two covalent protein adducts are principally possible: the transfer of a thioethyl fragment (+60.0 Da) or the transfer of the thiosalicylamide subunit (+356.2 Da). By using mass spectrometry, we aimed to determine the mode of inhibitor action (Figure 4). The site-specific modification of Cys126 was investigated using trypsin digestion and followed by LC-MS/MS analysis of the tryptic peptides. Three samples were analyzed: the native SrtA and the inhibitor-labeled protein either with **7h** or with **16b**.

For labeling with disulfanylbenzamide **7h**, the measurement was in agreement with the predicted tryptic peptide QLTLITC (SS Et)DDYNEK (*m/z* 808.41), encompassing a thioethylated Cys126 (Figure 4A). MS/MS fragmentation confirmed the correct peptide sequence (Figure S3). In contrast, the untreated protein sample was lacking this type of modification (Figure 4B). The transfer of a thioethyl fragment (+60.0 Da) seems to be the predominant mode of action, but minor modifications with the thiosalicylamide subunit (+356.2 Da) cannot be completely excluded since corresponding adducts may be below the detection limit or show poor ionization. Thiosalicylamide-protein adducts from benzisothiazolinones were previously linked to haptenization and allergic contact dermatitis,[61,62] thus, we evaluate the absence of this adduct form as potentially beneficial. The MS/MS analysis for the monomaleamide inhibitor **16b** (Figure S2) indicated that the inhibition became irreversible due to slow covalent modification of the Cys126 even at physiological pH. However, from labeling with 400 μM inhibitor, we observed only 27% modified peptide masses, supporting the fluorometric assay results (Figure 3), which showed that this reaction is not very efficient at pH 7.50.

In addition to the mass spectrometric analysis, differential scanning fluorimetry (DSF) was used to characterize covalently labeled SrtA proteins (Figure 5A).[63] The native SrtA unfolding temperature was determined to be 50.5 °C in absence of any ligand. By reaction with the benzisothiazolinone compound **1**, the equilibrium was pulled toward the unfolded complex and the protein was destabilized to a lower melting point (47.1 °C). This agreed with the previously solved NMR structure (PDB: 2MLM) showing a higher degree of disorder upon covalent complex formation ($RMSD_{mean}$: 1.57 Å vs 3.12 Å; Figure 5B). From a thermodynamic point of view, the loss of the most energetically favorable fold might be compensated here by the released enthalpy of the warhead reaction.

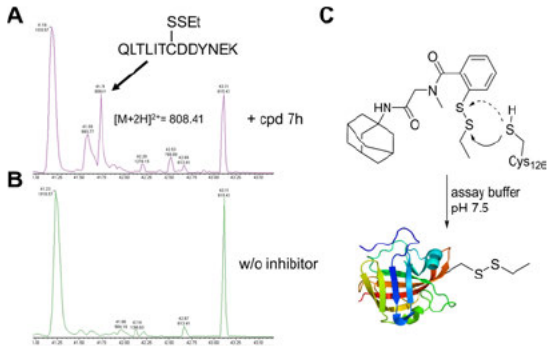

Figure 4. Mass spectrometric analysis of SrtA labeled with compound **7h** revealed the mode of inhibition for disulfanylbenzamides. A) TIC chromatogram of the labeled SrtA showed the distinct modification of the active-site Cys126. The peak at *m/z* 808.41 in the TIC chromatogram (t_R 41.7 min) corresponds to the thioethylated peptide QLTLITC(SS–Et)DDYNEK. B) Native SrtA did not show this modification. C) The predominant mode of SrtA inhibition was the transfer of the thioethyl fragment to Cys126.

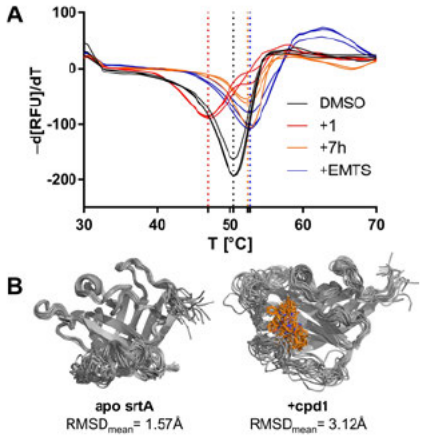

Figure 5. Differential scanning fluorimetry to characterize labeled SrtA proteins. A) Derivative –d(RFU)/dT of the protein-denaturing curves to determine the melting temperature (native SrtA: 50.5 °C, + cpd **1**: 47.1 °C, + cpd **7h**: 52.4 °C, + EMTS: 52.7 °C). B) Structural super-positioning of the NMR structures PDB: 1IJA (apo SrtA) and PDB: 2MLM (+ cpd **1**) showing differences in overall disorder.

Treatment of sortases with *S*-alkyl methanethiosulfonates led to the quantitative formation of thioalkylated sortase proteins.[64,65] Labeling of SrtA with *S*-ethyl methanethiosulfonate (EMTS) was performed to generate a purely thioethylated SrtA protein, which was found to melt slightly higher than the native SrtA protein (52.7 °C). The protein melt analysis of **7h**-labeled SrtA showed a similar melting point (52.4 °C), thus, these results are strengthening the hypothesis of a thioethyl fragment transfer.

Molecular modeling of the ligand-binding

Molecular docking studies were performed by FlexX docking within the LeadIT work suite. The docking of the noncovalently bound inhibitors resulted in a conformation that aligned well with the benzisothiazolinone inhibitor of the NMR structure PDB: 2MLM (Figure 6). When docked into the active site of SrtA **12a** inserted its space-filling 3-phenoxyaniline moiety into the lipophilic sub-pocket generated by the side chains of Thr122, Ile124 and the hydrophobic stretch of the β6/7-loop (Val108-Leu111). This might explain why altering the 3-phenoxyaniline fragment to smaller or less hydrophobic moieties, such as isobutylamine at the R^1 position, reducing the potency up to

ChemMedChem
Full Papers
doi.org/10.1002/cmdc.201900687
Chemistry Europe
European Chemical Societies Publishing

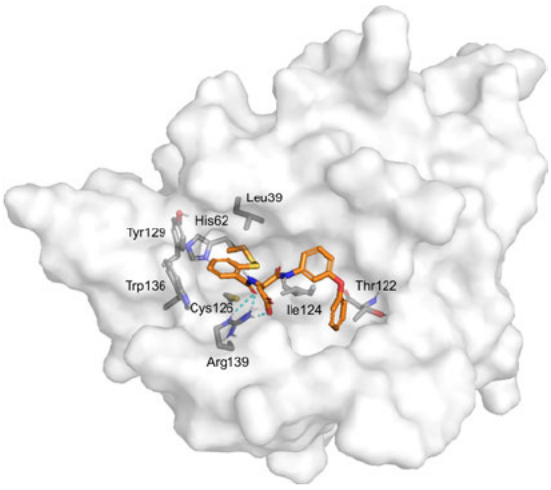

Figure 6. Docking pose of inhibitor **12a** in complex with the NMR structure (PDB: 2MLM) highlighting the proposed interaction features upon non-covalent binding.

threefold. However, the flexible β6/7-loop was previously shown to adapt to substrate/inhibitor binding, and hence, it was difficult to predict the optimal R^1 substituent *ab initio* by molecular modeling.[66]

On the amino acid linker, both the carbonyl oxygen and the aspartic acid side chain group were positioned towards the highly conserved side chain of Arg139, suggesting a potential hydrogen-bonding network. This could explain the observed reduction in activity when nonpolar functional groups were introduced to the amino acid position of the inhibitor scaffold. The disulfanylbenzamide aromatic system was enclosed by π–π interactions in a sub-pocket comprising His62, Tyr129 and Trp136 positioning the disulfide warhead towards the targeted Cys126. With *meta* or *para*-substituted inhibitors (**7u** and **7α**), no reasonable docking pose could be generated explaining their low inhibitory activity. Furthermore, we found the alkyl sulfur atom at a distance of 3.53 Å from the Cys126, whereas the aromatic sulfur atom had a distance of 3.90 Å. The closer proximity of the alkyl sulfur atom supported the findings that most likely the thioethyl fragment was transferred. The docking calculations suggested the dithioethyl group to be the largest tolerated R^2 substituent due to the gatekeeping Leu39 residue. Correspondingly, larger alkyl substituents such as *i*Pr, *t*Bu, EtPh led to a substantial decrease in inhibition.

Effect on fibrinogen-mediated adherence of S. *aureus*

To determine the effect of SrtA inhibitors on living bacterial cells we studied the ability of various *S. aureus* strains to adhere to fibrinogen-coated surfaces, a prerequisite mechanism for biofilm formation and the pathogenesis of bloodstream infections.[67] The treatment of the *S. aureus* SA113 strain with a set of selected disulfanylbenzamides efficiently reduced staphylococcal binding to fibrinogen (Figure 7). Here, we identified compound **7g** as the most potent adherence inhibitor with 66% adherence reduction at a concentration of 10 μM. The monomaleamide **16b** did not show a significant reduction of adherence. In contrast to the efficient reduction of adherence in SA113 cells, we did not observe significant effects in *S. aureus* USA300 cells at final inhibitor concentrations of 10 μM (data not shown).

Inhibition of synthetic substrate incorporation in *S. aureus*

The activity of SrtA on the surface of *S. aureus* was determined by employing a fluorescein-conjugate of the LPXTG-substrate (FAM GSLPETGGS NH_2). When added to the cell culture, the fluorescence label is incorporated into the cell wall, and thus, SrtA activity can be measured by fluorescence quantification.[25,68] **7f** was selected as the model compound because it showed one of the best potencies in both the fluorometric assay and the adherence assays. **7f** inhibited the incorporation of the substrate in a concentration-dependent manner in SA113 cells (Figure 8). For the USA300 strain, however, only weak inhibition (17% at 100 μM of **7f**) was detected; this agrees with the results of the fibrinogen adherence assays.

The combined data suggest interesting strain-specific effects of disulfanylbenzamides. Of note, the USA300 strain was described before as less susceptible to SrtA-targeting compounds. Thus, rhodanines (which are known as covalent modifiers of SrtA[30]) were found to be 40-fold weaker biofilm inhibitors in USA300 compared to SA113.[69] Our data suggest that this insusceptibility of USA300 might also hold true for the disulfanylbenzamides tested in this study. The reasons for these differences remain unknown, but it is conceivable that the two strains might differ regarding their overall cell wall composition, and that the inhibitors are therefore unable to reach the SrtA

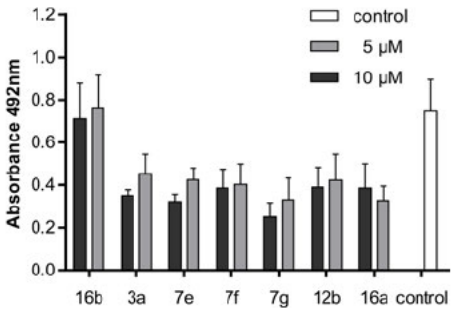

Figure 7. Analysis of fibrinogen-mediated adherence inhibition of *S. aureus* SA113. Different concentrations (5 and 10 μM) of the various inhibitors were added to the bacterial inoculum, and the biofilm was allowed to form overnight by static grow at 30 °C. The total biofilm was determined. Untreated bacteria served as control. Graphs represent the results of four independent biological replicates. Error bars indicate the mean value with the standard deviation.

ChemMedChem
Full Papers
doi.org/10.1002/cmdc.201900687
Chemistry Europe
European Chemical Societies Publishing

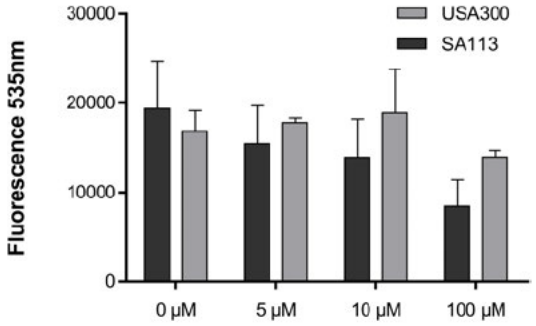

Figure 8. Inhibition of SrtA-mediated incorporation of a synthetic fluorescence substrate into the cell wall of *S. aureus* SA113 and USA300. Different concentrations of compound **7f** (5, 10 and 100 μM) were added to the bacterial inoculum containing 0.3 mM FAM–GSLPETGGS–NH_2, and cells were grown overnight. After washing and the removal of noncovalently bound FAM-substrate, the fluorescence was measured. Graphs represent the results of three independent biological replicates, and error bars indicate the mean with the standard deviation.

Table 3. The minimal inhibitory concentration of representative compounds on two strains of *S. aureus* and one *E. coli* strain.

Cpd.	Structure	MIC [μM] SA113	USA300	*E. coli*
7e	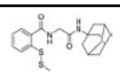	16.0	16.0	>500
7f	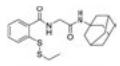	7.74	15.4	>500
7g		116	464	>500
12b	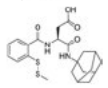	222	222	>500
16a	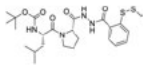	381	381	>500

All results include the median value from three biological replicates with two technical replicates each.

protein in the cell wall of USA300. However, at the present stage the issue needs further investigation.

Growth inhibition of bacterial cells

To test the bacterial growth inhibition by the compounds, we determined the minimum inhibitory concentration (MIC) by a microbroth dilution assay. The inhibitors which showed effective adherence reduction (**7e**, **7f**, **7g**, **12b**, and **16a**) were tested for growth inhibition in two strains of *S. aureus* (SA113 and USA300) and one *E. coli* strain (Table 3). Unlike parent compound **1**, which rapidly killed *Staphylococci* (MIC = 2.92 μM[32]), the addition of most disulfanylbenzamides to staphylococcal cultures had no measurable effect on the growth of *S. aureus* strains at effective adherence inhibition concentrations (5–10 μM).

While the inhibitors **7e** and **7f** showed medium cell growth inhibition at higher concentrations (MIC = 7–16 μM), all other inhibitors did not exhibit any effect at < 100 μM. The MIC for all inhibitors tested on *E. coli* was higher than the upper test limit of 200 mg/L, indicating that these compounds only affect Gram-positive bacteria. These results indicate that most disulfanylbenzamides selectively inhibit SrtA activity and do not function as antibiotics for *S. aureus* strains.

Table 4. Protease inhibition selectivity of a representative compound set. Compounds were tested with 20 μM of inhibitor.

Cpd.	Structure	Inhibition [%] at 20 μM Cathepsin B	Cathepsin L	NS2B/NS3 (ZIKV)
1	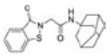	98% ± 0.4%	79% ± 2.2%	n.i.
3a		100% ± 0.5%	93% ± 5.6%	n.i.
7a	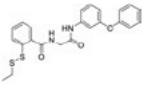	98% ± 0.1%	14% ± 8.9%	18% ± 1.1%
7f	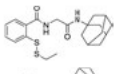	60% ± 0.5%	n.i.	12% ± 3.1%
7g		18% ± 3.9%	n.i.	17% ± 7.7%
7h	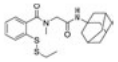	69% ± 1.7%	23% ± 11%	13% ± 8.0%
12a	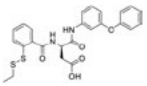	90% ± 0.5%	n.i.	15% ± 5.7%

n.i. no inhibition at 20 μM compound concentration. All results include the mean value and standard deviations from triplicate measurements.

Protease inhibition selectivity

Mammalian cathepsin B, L and SrtA are all structurally related to papain-like proteases, thus, we used their relatedness to study the selectivity of our inhibitors.[70] In fact, disulfides and isothiazolinones are known inhibitors of the cathepsin family.[71–73] In line with previous cytotoxicity studies,[74,75] parent compound **1** and the fragment-based inhibitor **3a** showed the weakest selectivity and up to 100% inhibition at 20 μM on both cathepsins (Table 4). However, most disulfanylbenzamides displayed no inhibition of cathepsin L and only moderate inhibition of cathepsin B, indicating a favorable shift of selectivity.

As endopeptidases, both cathepsins prefer large hydrophobic amino acids in the P2 site.[76] This might explain why the 3-phenoxyaniline inhibitors (**7a** and **12a**) showed the highest cathepsin inhibition (90–98%) among all disulfanylbenzamides. The exopeptidase activity makes cathepsin B unique among

ChemMedChem
Full Papers
doi.org/10.1002/cmdc.201900687
Chemistry Europe
European Chemical Societies Publishing

Table 5. Cytotoxicity (CC_{50}) toward HeLa cells and srtA inhibition constant values (K_i) of representative compounds.

Cpd.	Structure	CC_{50} [μM]	K_i [μM]
1	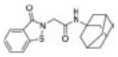	87 ± 2.8	34.2 ± 5.87
3a		409 ± 3.9	367 ± 24.4
7e	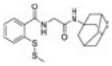	316 ± 31	16.2 ± 2.87
7f	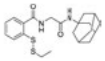	156 ± 8.5	14.3 ± 2.87
7g		253 ± 67	17.0 ± 3.04
7h	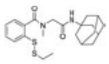	> 1000	20.5 ± 3.53
7m	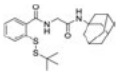	> 1000	6.40 ± 0.84
7o	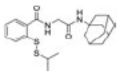	762 ± 137	8.24 ± 1.12
12a	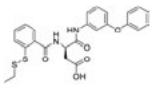	331 ± 36	10.3 ± 2.3

All results include the mean value and standard deviations from triplicate measurements.

cysteine cathepsins, thus, we hypothesized this could cause the selectivity of our inhibitors within the cathepsin family and might favor the binding of the carboxylic acid **12a** to the histidine-rich occluding loop of cathepsin B.[77] The ZIKV NS2B/NS3 protease is a serine protease and contains only two noncatalytic cysteine residues, thus as expected, only minimal inhibition by all of our thiol-reactive compounds was observed.[78] Compound **7g** showed neither relevant inhibition of cathepsins nor the NS2B/NS3 protease, while it was the most potent inhibitor in the fibrinogen adherence assay on *S. aureus* (Figure 7). This is a remarkable improvement compared to the weak selectivity of parent compound **1**.

Cytotoxicity on HeLa cells

In vitro cytotoxicity assessment of disulfanylbenzamides was accomplished on HeLa cells using the MTT-assay. The results demonstrated the nontoxic properties of disulfanylbenzamides at relevant treatment concentrations (Table 5). While the parent compound **1** displayed a CC_{50} of 87 μM, the cytotoxicity of the disulfanylbenzamides was between 156 μM and > 1000 μM. (Tables 5).[79]

Compounds **7f** and **7h** differed only by the N-methylation of the amide bond. The affinity (K_i) and reactivity (k_{inact}) of both inhibitors did not deviate significantly, but the methylated substance **7h** showed reduced cytotoxicity by a factor of > 8. The metabolic conversion of substituted disulfanylbenzamides to benzisothiazolinones could be a cause for this different cytotoxicity behavior (Scheme 4).[80,81]

In this case, the N-methylation of **7h** prevented the conversion to the benzisothiazolinone **1** (Scheme 4b). A recent metabolism study suggested the thermodynamics of 2-sulfanylbenzamides' metabolism having a strong effect on its biological activity.[81] A metabolic involvement is supported by the fact that only prolonged cellular incubation times (48 h) with all disulfanylbenzamides lead to significant cytotoxic effects.

Conclusions

Based on a warhead chemotype transformation strategy, we discovered a novel class of small-molecule SrtA inhibitors. We established the structure-activity relationship of a broad series of substituted disulfanylbenzamides and defined the structural requirements for efficient SrtA inhibition. The choice of a warhead for irreversible inhibitors was guided by the particular biochemical properties of the catalytic Cys126. We concluded from our findings that covalent targeting is much more effective by disulfanylbenzamides than by conventional Michael-acceptor warheads. The pH-independent transfer of a thioethyl fragment (+60.0 Da) was found to be the predominant mode of action for SrtA inhibition. While showing low mammalian cytotoxicity (CC_{50} = 253 μM), weak bacterial growth inhibition (MIC = 116 μM), and low off-target protease inhibition, compound **7g** was the most effective inhibitor in diminishing *S. aureus* fibrinogen adherence (66% at 10 μM). Therefore, we concluded that, as a lead structure, compound **7g** should be investigated in further studies. The selectivity differences in adherence inhibition between the *S. aureus* strains SA113 and USA300 should also be addressed in further studies, just as the potential of any bacterial resistance development towards disulfanylbenzamides.

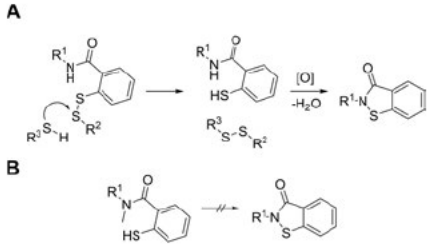

Scheme 4. Hypothesis for a proposed metabolic conversion of disulfanylbenzamides to benzisothiazolinones adapted fromNikolayevskiy *et al.*[81] A) Transfer of the thioalkyl fragment (R^2) to cellular thiols (R^3) leaves the 2-mercaptobenzamide, which can be metabolized to benzisothiazolinones. B) This metabolic conversion is blocked by N-methylation.

ChemMedChem
Full Papers
doi.org/10.1002/cmdc.201900687
Chemistry Europe
European Chemical Societies Publishing

Experimental Section

Synthesis: Protocols for the synthesis of all final products and intermediates with their respective analytical data can be found in the Supporting Information.

Protein expression and purification: Expression of the *S. aureus* SrtA was performed as described previously.[41] *E. coli* strain BL21-Gold (DE3) cells (Agilent Technologies, Santa Clara, California) were transformed with a pET23b expression construct and grown in LB medium containing 100 μM ampicillin at 37 °C to an OD_{600} of ~0.7. Expression was induced with 1 mM isopropyl-D-thiogalactoside (IPTG) for 16 h at 20 °C. After harvesting, cells were resuspended in lysis buffer (20 mM Tris HCl, pH 6.9, 300 mM NaCl, 0.1% Triton X-100, RNase, DNase, lysozyme) and lysed by sonication (Sonoplus, Bandelin, Berlin, Germany). The lysate was cleared by centrifugation (45 min at 15 krpm) and the protein was purified from the supernatant by IMAC (HisTrap HP 5 mL column, GE Healthcare, Chicago, Illinois). Eluted proteins were subsequently subjected to a gel-filtration step (HiLoad 16/60 Superdex 200 column, GE Healthcare) and eluted in the storage buffer (20 mM Tris-HCl, pH 7.50, 150 mM NaCl, 5 mM $CaCl_2$). Purified proteins were concentrated, shock frozen in liquid nitrogen and stored at −80 °C until further usage. Throughout all steps, protein concentrations were measured via absorbance at 280 nm and sample purity was assessed via SDS-PAGE.

Inhibition of sortase A: Inhibition of SrtA-catalyzed *in vitro* transpeptidation was performed as described previously.[20,82] Briefly, the recombinantly expressed SrtA (final concentration: 1 μM) was incubated in assay buffer (50 mM Tris, 150 mM NaCl, 5 mM $CaCl_2$, pH 7.50) with 25 μM of the FRET-pair substrate Abz-LPETG-Dap (Dnp)-OH (Genscript, Piscataway, New Jersey) and 0.5 mM triglycine (Sigma Aldrich, St. Louis, Missouri). Inhibitors were added from DMSO stocks. Negative inhibition control was performed by mock treatment with DMSO. Reactions were initiated by addition of SrtA and monitored for 30 min at 25 °C in an Infinite M200 Pro plate reader with λ_{ex} 320 nm/λ_{em} 430 nm (Tecan, Männedorf, Switzerland). Three technical replicates were carried out for each inhibitor in black flat-bottom 96-well plates (Greiner bio-one, Kremsmünster, Austria). The enzyme kinetics were analyzed as described previously.[83] To determine first-order inactivation rate constants (k_{obs}) for the irreversible inhibition, progress curves were analyzed by nonlinear regression analysis (t = 0–10 min) using the equation: $F = [P]^{\infty}(1 - e^{-k_{obs} \cdot t}) + offset$. Fitting of the k_{obs} values against the inhibitor concentrations to the hyperbolic equation $k_{obs} = (k_{inact}[I])/(K_{iapp} + [I])$ gave the individual values of K_{iapp} and k_{inact}. Progress curves and k_{obs} vs [I] plots of all active compounds can be found in figures S5–S7. K_{iapp} values were corrected to the zero-substrate concentration by the Cheng-Prusoff equation $K_i = K_{iapp}/(1 + \frac{[S]}{K_M})$. For $[S] \ll K_M$ we assumed $K_{iapp} = K_i$.

Protease inhibition selectivity: Fluorometric assays of the ZIKV NS2B/NS3 protease were performed as described previously.[84] The assay was carried out in triplicates at 25 °C in assay buffer (50 mM Tris, pH 9.0, 20% glycerol and 1 mM CHAPS). 100 μM Boc GRR AMC (Bachem, Bubendorf, Switzerland) was used as a substrate on a Tecan Infinite M200 Pro plate reader (λ_{ex} 380 nm/λ_{em} 460 nm). Fluorometric assays for cathepsin B and cathepsin L (Calbiochem, Merck Millipore, Burlington, Massachusetts) were performed as described previously.[85] Cbz Phe Arg AMC was used as substrate (80 μM for cathepsin B, 5 μM for cathepsin L) in assay buffer (20 mM Tris, pH 6.0, 5 mM EDTA, 200 mM NaCl, 0.005% Brij).

Protein mass spectrometry: An *S. aureus* SrtA stock solution (3.8 μL, 760 μM) was diluted in 500 μL enzyme dilution buffer (50 mM Tris, 150 mM NaCl, 5 mM $CaCl_2$, pH 7.50). The compounds **7h** and **16b** were dissolved in DMSO to generate stock solutions. Inhibitors were added to SrtA at a final concentration of 400 μM and were allowed to react for 1 h at room temperature. Samples were stored until MS analysis at −20 °C. The detailed procedure for the proteolytic digestion and the LC/MS can be found in the Supporting Information.

Differential scanning fluorimetry: Thermal shift assays were conducted in triplicate using a C1000/CFX384 qPCR system (Bio-Rad, Hercules, California) using the FRET channel and contained SrtA (2.2 μg), the respective test compound (50 μM) and Sypro Orange (5×) in 25 μL of assay buffer (50 mM Tris, 150 mM NaCl, 5 mM $CaCl_2$, pH 7.50). The samples were heated at 0.5 °C/s, from 25 to 75 °C. The fluorescence intensity was plotted as a function of the temperature. The melting point was given by the inflection point of the fluorescence curve as calculated by the High-Precision-Melt software (Bio-Rad).

Cell viability assay (HeLa Cells): Cell culturing was performed in a humidified incubator at 37 °C with 5% CO_2 atmosphere. HeLa cells were grown in cell culture flasks according to standard protocols (Dulbecco's modified Eagle medium [DMEM], 10% (v/v) fetal calf serum, 1% pyruvate, and 1% penicillin-streptomycin) and seeded to 96-well microplates at a concentration of 15,000 cells in a volume of 100 μL of DMEM. Inhibitors were dissolved at a concentration of 7.8–250 μg/mL in DMEM containing DMSO (0.08%–2.5%) and added in triplicates to the HeLa cells. Negative inhibition control was performed by mock treatment with DMEM with DMSO in the same concentration as the compound solutions were used. After an incubation time of 48 h (37 °C, 5% CO_2) a solution of 3-(4,5-dimethyl-2-thiazolyl)-2,5-diphenyl-2*H*-tetrazolium bromide (MTT) in DMEM (40 μL, 3.0 mg/mL) was added directly to each well and the plate was incubated for additional 20 min. The medium was aspirated and replaced by 200 μL of DMSO and 25 μL of glycine buffer (0.1 M glycine, 0.1 M NaCl, pH 10.5). After shaking for 20 min, the absorbance was measured at 595 nm using an Infinite M200 Pro plate reader (Tecan). The background at 670 nm and the absorbance of the compounds at the same wavelength was subtracted from the data obtained from the first readout. Cell viability was normalized to the absorbance measured from DMSO-DMEM threated cells.

Bacterial growth inhibition: The MIC of different inhibitors was determined against *S. aureus* USA300,[86] SA113[87] and a laboratory strain of *E. coli* using the microbroth dilution assay according to standard protocols in 96-well, polystyrene tissue culture plates (Greiner Bio-One, Cellstar, F-form). The MIC was determined as the concentration of the inhibitor where the lowest OD_{595} values were recorded with a Tecan Infinite 200Pro (Tecan).

***S. aureus* adherence assay:** *S. aureus* adherence was tested in 96-well, polystyrene tissue culture plates (Greiner Bio-One, Cellstar, F-form) as previously described[88] with the following modifications. Before starting the experiment, the plates were coated with fibrinogen.[89] Fibrinogen from human plasma (Sigma Aldrich) was dissolved in NaCl solution (0.9%) to 10 mg/mL. A fibrinogen solution of 100 μg/mL was prepared in PBS and 100 μL were dispensed into each well of the plate. After sealing, the plate was incubated at 4 °C overnight to allow fibrinogen coating of the well. The next day, the fibrinogen solution was aspirated. Bacterial strains (OD_{600} ~0.05 in tryptic soy broth) were incubated under static conditions in the presence of different dilutions of inhibitors in 1.6% DMSO at 30 °C for 18 h. The next day, the planktonic bacteria were discarded, the plates were rinsed twice with PBS (1×) and the biofilm was heat-fixed at 65 °C for 1 h. Plates were stained with 10 mg/mL crystal violet for 2 min, washed twice with double-distilled water before measuring the absorbance at OD_{492} with an ELISA plate reader (Multiskan Ascent, Thermo Fisher Scientific, Waltham, Massachusetts).

ChemMedChem | Full Papers doi.org/10.1002/cmdc.201900687 | Chemistry Europe European Chemical Societies Publishing

Incorporation of synthetic SrtA substrates on *S. aureus*: The FAM-GSLPETGGS-NH_2 substrate was synthesized using a 3D-printed solid-phase peptide synthesizer[90] (detailed procedure in the Supporting Information). The incorporation of a synthetic substrate on the *S. aureus* cell wall was conducted as described previously with minor modifications.[25] USA300 and SA113 were grown in tryptic soy broth medium in the presence of 0.3 mM FAM-GSLPETGGS-NH_2 and different concentrations of compound **7f**. After 15 h, cells (OD_{600} ~ 8) were harvested from all cultures in a final volume of 500 μL and washed with cold PBS (1×). Noncovalently bound substrate was removed by treatment with 5% SDS for 5 min at 60 °C. Cells were washed twice with cold PBS and then suspended in 200 μL PBS. The fluorescence of incorporated substrate was measured with an Infinite M200 Pro plate reader (λ_{ex} 485 nm/λ_{em} 535 nm).

Molecular modeling: A FlexX-algorithm docking protocol was conducted within the LeadIT-2.3.2 work suite.[91] The NMR structure 2MLM (frame 18) was downloaded from the Protein Databank (PDB). Prior to docking, the benzisothiazolinone-modified active-site Cys126 was untethered and reprotonated with MOE2019.01.[92] Receptor preparation was performed using the automated binding site and protonation detection routine within LeadIT. Ligands were energy minimized using the MMFF94 force field within MOE. The docking protocol was performed under default parameters using the hybrid approach (enthalpy/entropy) for ligand placement.

Acknowledgments

Work of the Ziebuhr laboratory was supported by the German Research Council (DFG) through grant Zl665/3-1 as well as by the German Federal Ministry of Education and Research (BMBF), grant number 01KI1727E.

Conflict of Interest

The authors declare no conflict of interest.

Keywords: Antibiotics · biofilm · drug design · sortase A · *Staphylococcus aureus*

[1] S. W. Dickey, G. Y. C. Cheung, M. Otto, *Nat. Rev. Drug Discovery* **2017**, *16*, 457–471.
[2] G. Michaud, R. Visini, M. Bergmann, G. Salerno, R. Bosco, E. Gillon, B. Richichi, C. Nativi, A. Imberty, A. Stocker, T. Darbre, J.-L. Reymond, *Chem. Sci.* **2016**, *7*, 166–182.
[3] W. J. Weiss, E. Lenoy, T. Murphy, L. Tardio, P. Burgio, S. J. Projan, O. Schneewind, L. Alksne, *J. Antimicrob. Chemother.* **2004**, *53*, 480–486.
[4] S. K. Mazmanian, G. Liu, E. R. Jensen, E. Lenoy, O. Schneewind, *Proc. Mont. Acad. Sci.* **2000**, *97*, 5510–5515.
[5] A. W. Maresso, O. Schneewind, *Pharmacol. Rev.* **2008**, *60*, 128–141.
[6] S. K. Mazmanian, G. Liu, H. Ton-That, O. Schneewind, *Science* **1999**, *285*, 760–763.
[7] J. Zhang, H. Liu, K. Zhu, S. Gong, S. Dramsi, Y.-T. Wang, J. Li, F. Chen, R. Zhang, L. Zhou, L. Lan, H. Jiang, O. Schneewind, C. Luo, C.-G. Yang, *Proc. Natl. Acad. Sci.* **2014**, *111*, 13517–13522.
[8] S. Cascioferro, M. Totsika, D. Schillaci, *Microb. Pathog.* **2014**, *77*, 105–112.
[9] D. Mu, H. Xiang, H. Dong, D. Wang, T. Wang, *J. Microbiol. Biotechnol.* **2018**, *28*, 7.
[10] W. W. Navarre, O. Schneewind, *Microbiol. Mol. Biol. Rev.* **1999**, *63*, 174–229.
[11] N. Suree, C. K. Liew, V. A. Villareal, W. Thieu, E. A. Fadeev, J. J. Clemens, M. E. Jung, R. T. Clubb, *J. Biol. Chem.* **2009**, *284*, 24465–24477.
[12] A. M. Perry, H. Ton-That, S. K. Mazmanian, O. Schneewind, *J. Biol. Chem.* **2002**, *277*, 16241–16248.
[13] E. Tsompanidou, E. L. Denham, M. J. J. B. Sibbald, X. Yang, J. Seinen, A. W. Friedrich, G. Buist, J. M. van Dijl, *PLoS One* **2012**, *7*, e44646.
[14] O. Schneewind, D. Missiakas, *Protein Secretion Pathways Bact.* **2019**, 173–188.
[15] K. W. Clancy, J. A. Melvin, D. G. McCafferty, *Pept. Sci.* **2010**, *94*, 385–396.
[16] U. Ilangovan, H. Ton-That, J. Iwahara, O. Schneewind, R. T. Clubb, *Proc. Mont. Acad. Sci.* **2001**, *98*, 6056–6061.
[17] W. van 't Hof, S. H. Mañásková, E. C. I. Veerman, J. G. M. Bolscher, *Biol. Chem.* **2015**, *396*, 283–293.
[18] K. Kappel, J. Wereszczynski, R. T. Clubb, J. A. McCammon, *Protein Sci.* **2012**, *21*, 1858–1871.
[19] J. Zhu, L. Xiang, F. Jiang, Z. J. Zhang, *Exp. Biol. Med. (Maywood NJ U. S.)* **2016**, *241*, 90–100.
[20] R. G. Kruger, P. Dostal, D. G. McCafferty, *Anal. Biochem.* **2004**, *326*, 42–48.
[21] J. A. Melvin, C. F. Murphy, L. G. Dubois, J. W. Thompson, M. A. Moseley, D. G. McCafferty, *Biochemistry* **2011**, *50*, 7591–7599.
[22] B. C. Chenna, J. R. King, B. A. Shinkre, A. L. Glover, A. L. Lucius, S. E. Velu, *Eur. J. Med. Chem.* **2010**, *45*, 3752–3761.
[23] P. M. Wehrli, I. Uzelac, T. Olsson, T. Jacso, D. Tietze, J. Gottfries, *Bioorg. Med. Chem.* **2019**, 115043.
[24] S. Oniga, C. Araniciu, M. Palage, M. Popa, M.-C. Chifiriuc, G. Marc, A. Pirnau, C. Stoica, I. Lagoudis, T. Dragoumis, O. Oniga, *Molecules* **2017**, *22*, 1827.
[25] I. Rentero Rebollo, S. McCallin, D. Bertoldo, J. M. Entenza, P. Moreillon, C. Heinis, *ACS Med. Chem. Lett.* **2016**, *7*, 606–611.
[26] Y. Zhang, J. Bao, X.-X. Deng, W. He, J.-J. Fan, F.-Q. Jiang, L. Fu, *Bioorg. Med. Chem. Lett.* **2016**, *26*, 4081–4085.
[27] S. Cascioferro, D. Raffa, B. Maggio, M. V. Raimondi, D. Schillaci, G. Daidone, *J. Med. Chem.* **2015**, *58*, 9108–9123.
[28] G. Nitulescu, A. Zanfirescu, O. T. Olaru, I. M. Nicorescu, G. M. Nitulescu, D. Margina, *Molecules* **2016**, *21*, 1591.
[29] A. W. Maresso, R. Wu, J. W. Kern, R. Zhang, D. Janik, D. M. Missiakas, M.-E. Duban, A. Joachimiak, O. Schneewind, *J. Biol. Chem.* **2007**, *282*, 23129–23139.
[30] N. Suree, S. W. Yi, W. Thieu, M. Marohn, R. Damoiseaux, A. Chan, M. E. Jung, R. T. Clubb, *Bioorg. Med. Chem.* **2009**, *17*, 7174–7185.
[31] A. H. Chan, S. W. Yi, E. M. Weiner, B. R. Amer, C. K. Sue, J. Wereszczynski, C. A. Dillen, S. Senese, J. Z. Torres, J. A. McCammon, L. S. Miller, M. E. Jung, R. T. Clubb, *Chem. Biol. Drug Des.* **2017**, *90*, 327–344.
[32] D. Zhulenkovs, Z. Rudevica, K. Jaudzems, M. Turks, A. Leonchiks, *Bioorg. Med. Chem.* **2014**, *22*, 5988–6003.
[33] K. Jaudzems, V. Kurbatska, A. Jēkabsons, R. Bobrovs, Z. Rudevica, A. Leonciks, *ACS Infect. Dis.* **2019**, acsinfecdis.9b00265.
[34] G. Nitulescu, D. P. Mihai, I. M. Nicorescu, O. T. Olaru, A. Ungurianu, A. Zanfirescu, G. M. Nitulescu, D. Margina, *Drug Dev. Res.* **2019**, ddr.21599.
[35] B. Evans, E. Shaw, *J. Biol. Chem.* **1983**, *258*, 10227–10232.
[36] T. Waag, C. Gelhaus, J. Rath, A. Stich, M. Leippe, T. Schirmeister, *Bioorg. Med. Chem. Lett.* **2010**, *20*, 5541–5543.
[37] C. S. I. Nobel, M. Kimland, D. W. Nicholson, S. Orrenius, A. F. G. Slater, *Chem. Res. Toxicol.* **1997**, *10*, 1319–1324.
[38] F. Yang, W. Wang, K. Li, W. Zhao, X. Dong, *Tetrahedron Lett.* **2017**, *58*, 218–222.
[39] S. Kusaka, R. Matsuda, S. Kitagawa, *Chem. Commun.* **2018**, *54*, 4782–4785.
[40] M. R. James, *Process for the Preparation of 1,2-Benzisothiazolin-3-Ones*, **2004**, KR100429082B1.
[41] L. Schmohl, J. Bierlmeier, F. Gerth, C. Freund, D. Schwarzer, *J. Pept. Sci.* **2017**, *23*, 631–635.
[42] B.-F. Krippendorff, R. Neuhaus, P. Lienau, A. Reichel, W. Huisinga, *J. Biomol. Screening* **2009**, *14*, 913–923.
[43] J. M. Strelow, *SLAS Discovery* **2017**, *22*, 3–20.
[44] M. Gehringer, S. A. Laufer, *J. Med. Chem.* **2019**, *62*, 5673–5724.
[45] J. B. Baell, J. W. M. Nissink, *ACS Chem. Biol.* **2018**, *13*, 36–44.
[46] C. J. Scott, A. McDowell, S. L. Martin, J. F. Lynas, K. Vandenbroeck, B. Walker, *Biochem. J.* **2002**, *366*, 953–958.
[47] K. M. Connolly, B. T. Smith, R. Pilpa, U. Ilangovan, M. E. Jung, R. T. Clubb, *J. Biol. Chem.* **2003**, *278*, 34061–34065.
[48] B. A. Frankel, R. G. Kruger, D. E. Robinson, N. L. Kelleher, D. G. McCafferty, *Biochemistry* **2005**, *44*, 11188–11200.
[49] A. C. C. Plette, W. H. van Riemsdijk, M. F. Benedetti, A. van der Wal, *J. Colloid Interface Sci.* **1995**, *173*, 354–363.
[50] P. D. Cotter, C. Hill, *Microbiol. Mol. Biol. Rev.* **2003**, *67*, 429–453.

ChemMedChem | Full Papers doi.org/10.1002/cmdc.201900687 | Chemistry Europe European Chemical Societies Publishing

[51] L. Schmohl, F. R. Wagner, M. Schümann, E. Krause, D. Schwarzer, *Bioorg. Med. Chem.* **2015**, *23*, 2883–2889.
[52] I. Klimenkovs, E. Bakis, A. Priksane, *Synth. Commun.* **2013**, *43*, 2634–2640.
[53] U. Bhatt, B. C. Duffy, P. R. Guzzo, L. Cheng, T. Elebring, *Synth. Commun.* **2007**, *37*, 2793–2806.
[54] H. Feuer, E. H. White, J. E. Wyman, *J. Am. Chem. Soc.* **1958**, *80*, 3790–3792.
[55] A. Paasche, A. Zipper, S. Schäfer, J. Ziebuhr, T. Schirmeister, B. Engels, *Biochemistry* **2014**, *53*, 5930–5946.
[56] R. D. Bach, O. Dmitrenko, C. Thorpe, *J. Org. Chem.* **2008**, *73*, 12–21.
[57] R. E. Benesch, R. Benesch, *J. Am. Chem. Soc.* **1958**, *80*, 1666–1669.
[58] G. I. Giles, C. Jacob, *Biol. Chem.* **2002**, *383*, 375–388.
[59] A. P. Ryle, F. Sanger, *Biochem. J.* **1955**, *60*, 535–540.
[60] P. Nagy, *Antioxid. Redox Signaling* **2013**, *18*, 1623–1641.
[61] R. Alvarez-Sánchez, D. Basketter, C. Pease, J.-P. Lepoittevin, *Bioorg. Med. Chem. Lett.* **2004**, *14*, 365–368.
[62] M.-A. Morren, A. Dooms-Goossens, J. Delabie, C. D. Wolf-Peeters, K. Marien, H. Degreef, *Dermatology* **1992**, *184*, 260–264.
[63] B. M. Dorr, H. O. Ham, C. An, E. L. Chaikof, D. R. Liu, *Proc. Mont. Acad. Sci.* **2014**, 201411179.
[64] D. J. Smith, E. T. Miggio, G. L. Kenyon, *Biochemistry* **1975**, *14*, 766–771.
[65] Y. Zong, S. K. Mazmanian, O. Schneewind, S. V. L. Narayana, *Structure* **2004**, *12*, 105–112.
[66] C. Gao, I. Uzelac, J. Gottfries, L. A. Eriksson, *Sci. Rep.* **2016**, *6*, 20413.
[67] M. McAdow, H. K. Kim, A. C. DeDent, A. P. A. Hendrickx, O. Schneewind, D. M. Missiakas, *PLoS Pathog.* **2011**, *7*, e1002307.
[68] S. H. Mañásková, K. Nazmi, W. van 't Hof, A. van Belkum, N. I. Martin, F. J. Bikker, W. J. B. van Wamel, E. C. I. Veerman, *PLoS One* **2016**, *11*, e0147401.
[69] T. J. Opperman, S. M. Kwasny, J. D. Williams, A. R. Khan, N. P. Peet, D. T. Moir, T. L. Bowlin, *Antimicrob. Agents Chemother.* **2009**, *53*, 4357–4367.
[70] W. J. Bradshaw, A. H. Davies, C. J. Chambers, A. K. Roberts, C. C. Shone, K. R. Acharya, *FEBS J.* **2015**, *282*, 2097–2114.
[71] T. Bratkovič, M. Lunder, T. Popovič, S. Kreft, B. Turk, B. Štrukelj, U. Urleb, *Biochem. Biophys. Res. Commun.* **2005**, *332*, 897–903.
[72] R. Wisastra, M. Ghizzoni, H. Maarsingh, A. J. Minnaard, H. J. Haisma, F. J. Dekker, *Org. Biomol. Chem.* **2011**, *9*, 1817–1822.
[73] C. L. Cywin, R. A. Firestone, D. W. McNeil, C. A. Grygon, K. M. Crane, D. M. White, P. R. Kinkade, J. L. Hopkins, W. Davidson, M. E. Labadia, J. Wildeson, M. M. Morelock, J. D. Peterson, E. L. Raymond, M. L. Brown, D. M. Spero, *Bioorg. Med. Chem.* **2003**, *11*, 733–740.
[74] K. Hu, H.-R. Li, R.-J. Ou, C.-Z. Li, X.-L. Yang, *Environ. Toxicol. Pharmacol.* **2014**, *37*, 529–535.
[75] E. Turos, K. D. Revell, P. Ramaraju, D. A. Gergeres, K. Greenhalgh, A. Young, N. Sathyanarayan, S. Dickey, D. Lim, M. M. Alhamadsheh, *Bioorg. Med. Chem.* **2008**, *16*, 6501–6508.
[76] Y. Choe, F. Leonetti, D. C. Greenbaum, F. Lecaille, M. Bogyo, D. Brömme, J. A. Ellman, C. S. Craik, *J. Biol. Chem.* **2006**, *281*, 12824–12832.
[77] M. H. S. Cezari, L. Puzer, M. A. Juliano, A. K. Carmona, L. Juliano, *Biochem. J.* **2002**, *368*, 365–369.
[78] Y. Li, W. W. Phoo, Y. R. Loh, Z. Zhang, E. Y. Ng, W. Wang, T. H. Keller, D. Luo, C. Kang, *FEBS Lett.* **2017**, *591*, 2338–2347.
[79] W. G. E. J. Schoonen, W. M. A. Westerink, J. A. D. M. de Roos, E. Débiton, *Toxicol. in Vitro* **2005**, *19*, 505–516.
[80] P. J. Tummino, P. J. Harvey, T. McQuade, J. Domagala, R. Gogliotti, J. Sanchez, Y. Song, D. Hupe, *Antimicrob. Agents Chemother.* **1997**, *41*, 394–400.
[81] H. Nikolayevskiy, M. Robello, M. T. Scerba, E. H. Pasternak, M. Saha, T. L. Hartman, C. A. Buchholz, R. W. Buckheit, S. R. Durell, D. H. Appella, *Eur. J. Med. Chem.* **2019**, *178*, 818–837.
[82] L. Schmohl, J. Bierlmeier, N. von Kügelgen, L. Kurz, P. Reis, F. Barthels, P. Mach, M. Schutkowski, C. Freund, D. Schwarzer, *Bioorg. Med. Chem.* **2017**, *25*, 5002–5007.
[83] T. Schirmeister, J. Kesselring, S. Jung, T. H. Schneider, A. Weickert, J. Becker, W. Lee, D. Bamberger, P. R. Wich, U. Distler, S. Tenzer, P. Johe, U. A. Hellmich, B. Engels, *J. Am. Chem. Soc.* **2016**, *138*, 8332–8335.
[84] F. von Hammerstein, L. M. Lauth, S. Hammerschmidt, A. Wagner, T. Schirmeister, U. A. Hellmich, *FEBS Lett.* **2019**, *593*, 2204–2213.
[85] R. Ettari, E. Nizi, M. E. Di Francesco, M.-A. Dude, G. Pradel, R. Vičík, T. Schirmeister, N. Micale, S. Grasso, M. Zappalà, *J. Med. Chem.* **2008**, *51*, 988–996.
[86] B. A. Diep, S. R. Gill, R. F. Chang, T. H. Phan, J. H. Chen, M. G. Davidson, F. Lin, J. Lin, H. A. Carleton, E. F. Mongodin, G. F. Sensabaugh, F. Perdreau-Remington, *Lancet* **2006**, *367*, 9.
[87] S. Iordanescu, M. Surdeanu, *Microbiology* **1976**, *96*, 277–281.
[88] M. F. Lerch, S. M. Schoenfelder, G. Marincola, F. D. Wencker, M. Eckart, K. U. Förstner, C. M. Sharma, K. M. Thormann, M. Kucklick, S. Engelmann, *Mol. Microbiol.* **2019**, *111*, 1571–1591.
[89] C. Colomer-Winter, J. A. Lemos, A. L. Flores-Mireles, *Bio-Protoc.* **2019**, *9*.
[90] F. Barthels, U. Barthels, M. Schwickert, T. Schirmeister, *SLAS Technol.* **2019**, 2472630319877374.
[91] B. Kramer, M. Rarey, T. Lengauer, *Proteins Struct. Funct. Bioinf.* **1999**, *37*, 228–241.
[92] V. Moe, *Quebec: Montreal* **2006**..

Manuscript received: December 9, 2019
Revised manuscript received: February 7, 2020
Version of record online: March 25, 2020

ChemMedChem

Supporting Information

Asymmetric Disulfanylbenzamides as Irreversible and Selective Inhibitors of *Staphylococcus aureus* Sortase A

Fabian Barthels, Gabriella Marincola, Tessa Marciniak, Matthias Konhäuser, Stefan Hammerschmidt, Jan Bierlmeier, Ute Distler, Peter R. Wich, Stefan Tenzer, Dirk Schwarzer, Wilma Ziebuhr, and Tanja Schirmeister*

Protein mass spectrometry

Proteolytic digestion

For LC-MS analysis, samples (corresponding to 2 µg) were diluted with 50 mM NH_4HCO_3 buffer to a final volume of 50 µL and denatured at 80 °C in the presence of the acid-labile detergent RapiGest (0.1% w/v) for 15 min. Afterwards, SrtA was digested overnight at 37 °C using either a mix of trypsin/LysC (1:25 w/w) in case of **16b** or trypsin (1:25 w/w) in case of **7h**. Unlabeled SrtA served as control. After overnight digestion of proteins, RapiGest was hydrolyzed by the addition of HCl. Generated peptides were desalted using SepPak tC18 microelution plates according to manufacturer's instructions (Waters Corporation, Milford, Massachusetts). Purified peptides were lyophilized and reconstituted in 0.1% (v/v) formic acid for LC-MS analysis.

Liquid Chromatography-Mass Spectrometry (LC-MS)

LC separation of peptides was performed using a nanoAcquity UPLC system (Waters Corporation) equipped with a 75 µm×250 mm C18 HSS-T3 1.8 µm reverse-phase column. Peptides were loaded onto the column using direct injection mode. For reverse-phase separation of peptides, two mobile phases were used. Mobile phase A contained 0.1% (v/v) formic acid, 3% (v/v) DMSO in water and mobile phase B 0.1% (v/v) formic acid, 3% (v/v) DMSO in acetonitrile. Peptides were separated at 55 °C running a gradient of 5–40% mobile phase B over 90 min at a flow rate of 300 nL/min.

LC-MS data were collected in data-dependent acquisition (DDA) mode using a Synapt G2-S QTOF mass spectrometer (Waters Corporation), operated with a typical resolving power of R = 25,000. All analyses were performed in positive mode ESI. After the acquisition, LC-MS/MS data were processed and searched using PEAKS version 8.5 (Bioinformatics Solutions, Waterloo, Canada). Protein identifications were assigned by searching a custom compiled database containing all protein sequences from *E. coli* and known poss ble contaminants (e.g., human keratins). Sequence information of SrtA was added to the database. For database search the following parameters were used: i) maximum precursor delta mass: 15 ppm, ii) maximum fragment delta mass: 0.03 Da, iii) maximum number of missed cleavages: 2, iv) allowed variable modifications: carbamidomethylation (Cys); deamidation (Asn, Gln); oxidation (Met) and covalent modifications (Cys) with the inh bitors **7h** and **16b**. The false discovery rate (FDR) for peptide and protein identification was evaluated searching a reversed database and set to 1% for database search in PEAKS.

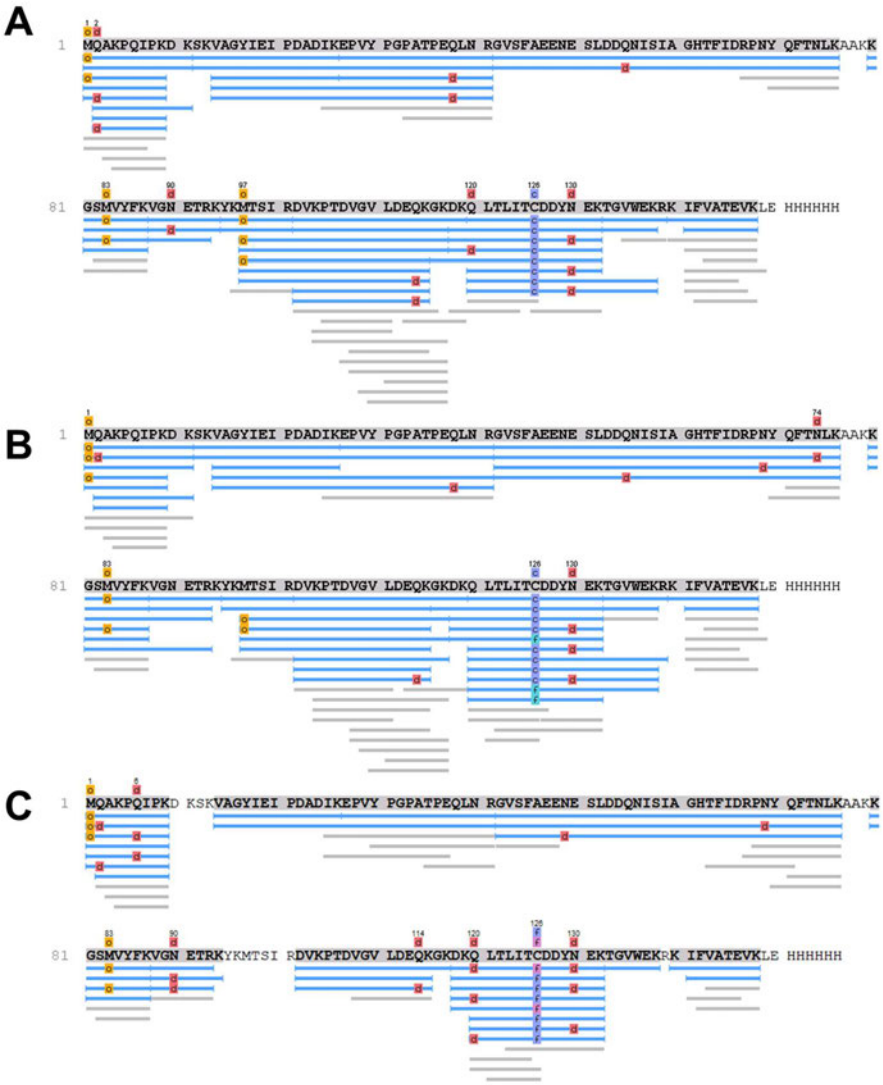

Figure 1: Sequence coverage of SrtA constructs after LC-MS analysis. A) In the absence of covalent inhibitors. B) After incubation with compound **16b**. C) After incubation with compound **7h**. [c: carbamidomethyl cysteine, d: deamidation, o: oxidation of methionine, f: modification with the respective covalent modifier]. The analysis confirmed covalent modification of the active site cysteine residue of sortase A by both **16b** (mass shift: +440.23 Da) and compound **7h** (mass shift: +60.00 Da).

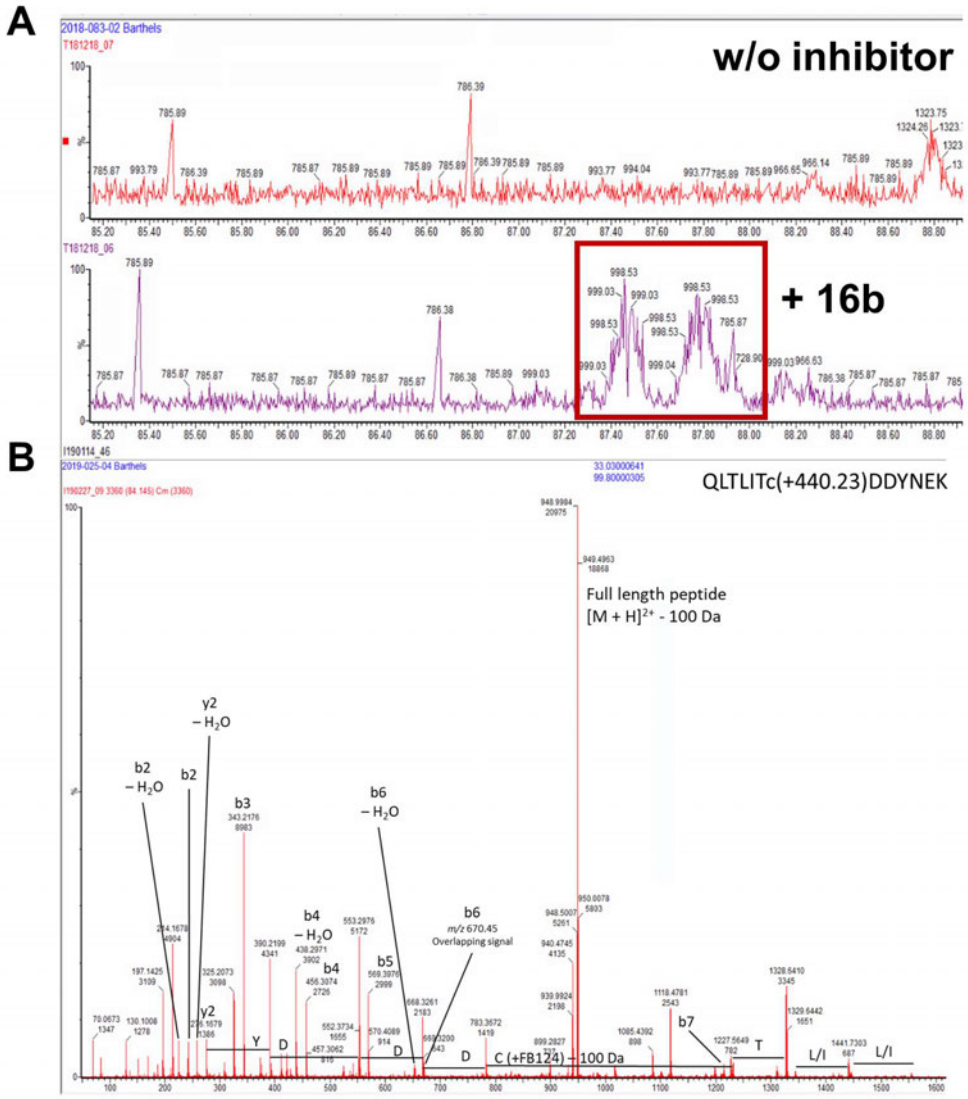

Figure 2: Protein adduct with mono-maleamide **16b** observed by mass spectrometry. A) The signal at *m/z*=998.53 corresponds to the inhibitor-bound peptide QLTLITCDDYNEK and was not observed in the control (SrtA without inhibitor) proving covalent attachment of **16b**. B) Fragmentation of the precursor ion (at *m/z*=998.53) revealed the correct peptide sequence and the characteristic loss of the *tert*-butyloxycarbonyl group (–100 Da).

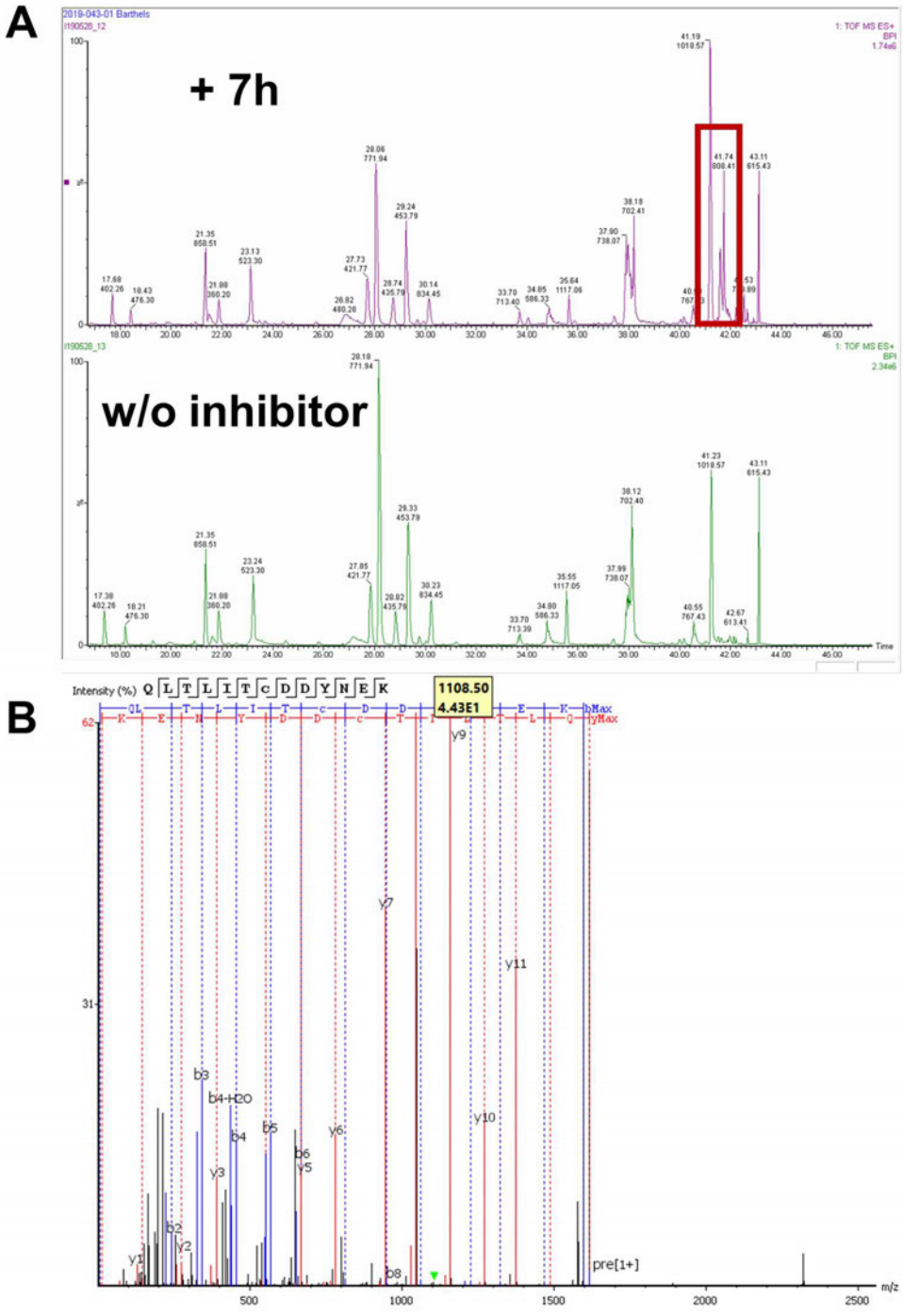

Figure 3: Thioethyl cysteine adduct from SrtA and compound **7h** observed by mass spectrometry. A) The peak *m/z*=808.41 in the TIC chromatogram (R_t= 41.7 min) corresponds to the thioethylated peptide QLTLITC(SS-Et)DDYNEK, which was confirmed by the fragmentation (B) of the precursor ion (*m/z*=808.41).

Syntheses procedures

All reactions were carried out in oven-dried glassware and dry solvents were used. Fine chemicals were purchased from commercial suppliers (Sigma Aldrich, Chempur, Fisher Scientific, TCI, Carbolution) and used without further purification unless otherwise noted. Solvents were used in technical quality but redistilled before usage. Reaction progress and composition homogeneity were monitored by thin-layer chromatography using Machery-Nagel Alugram Xtra F_{254} silica plates for UV-detection at 254 nm. Chemical staining of thin-layer chromatography plates was done using ninhydrin solution. Purification of intermediary and final products was conducted by either flash chromatography with self-packed columns (Machery-Nagel silica gel 0.030–0.063 mm) and UV-detection (Knauer K-2001 detector) or by preparative HPLC using a Varian ProStar 210 system with an Agilent Zorbax XDB-C18 column (21.2×150 mm, 5 µm). ^{1}H and ^{13}C NMR spectra were acquired on a Bruker Fourier 300 (300 MHz) spectrometer at room temperature in DMSO-d_6, $CDCl_3$ or CD_2Cl_2 (Deutero GmbH). Chemical shifts are given in ppm relative to the respective undeuterated solvent peak. If necessary, DEPT, HSQC and HMBC experiments were used for the number of nuclei assignment in the carbon spectra. Variable temperature proton spectra (VT-NMR) over the range of 25−60 °C were used to resolve multiplets due to restricted rotation at room temperature. Identity and purity were assessed by combined HPLC/ESI-MS analysis using an Agilent 1100 series HPLC system with an Agilent Poroshell 120 EC-C18 column (150×2.10 mm, 4 µm; mobile phase: ACN/H_2O 45:55 +0.1% formic acid; flow rate: 0.4 mL/min). Tested compounds possessed a purity of >95% confirmed via analytical HPLC (254 nm). Mass detection was done by electron spray ionization with the Agilent 1100 series LC/MSD Trap in positive ionization mode. Melting points (uncorrected) were determined by a Krüss KSPIN in semi-open capillaries. The specific rotation was measured on a P3000 polarimeter from Krüss and was reported in $cm^3g^{-1}dm^{-1}$. Fourier-transformed ATR-corrected IR spectra were obtained on a ThermoNicolet Avatar 330 single crystal spectrometer from neat material. Background spectra were recorded from air prior to sample loading to yield IR transmission spectra.

3a 2-(Methyldisulfanyl)benzoic acid

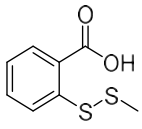

2-(Methyldisulfanyl)benzoic acid (**3a**) was synthesized by a procedure according to Kusaka *et al*.[1] Thiosalicylic acid (355 mg, 2.30 mmol) and *S*-methyl methanethiosulfonate (364 mg, 2.30 mmol) were dissolved in methanol (20 mL) and the reaction was stirred for 16 h at room temperature. The solvent was evaporated *in vacuo* and the crude product was purified by column chromatography (CH/EA 5:1 + 1% TFA) to yield **3a** as a colourless solid (400 mg, 86%). mp: 170 °C; ^{1}H NMR (300 MHz, DMSO-d_6) δ= 8.10 – 8.04 (m, 1H), 7.98 (d, *J* = 7.7 Hz, 1H), 7.69 (t, *J* = 8.3 Hz, 1H), 7.41 – 7.24 (m, 1H), 2.39 (s, 3H); ^{13}C NMR (75 MHz, DMSO-d_6) δ= 167.9, 140.4, 133.5, 131.9, 128.0, 125.9, 125.1, 22.0; FT-IR (neat): ṽ [cm^{-1}]= 693, 742, 798, 907, 1038, 1257, 1312, 1416, 1460, 1559, 1585, 1673; ESI-MS *m/z*: $[M\text{-}SCH_3+H]^+$ 153.12 (100%), 154.08 (10.7%), 156.19 (0.6%); purity (HPLC)= 99%.

General procedure (I) to synthesize asymmetric disulfanylbenzoic acids (3b–3g)

A method reported by Yang *et al*.[2] was used to synthesize the disulfanylbenzoic acids (**3b–3g**). Trichloroisocyanuric acid (156 mg, 0.67 mmol) was solved in anhydrous acetonitrile (10 mL) and cooled to –50 °C. The corresponding mercaptobenzoic acid (**2a–c**, 2.00 mmol) was added as a suspension in acetonitrile (10 mL) over 5 minutes. The reaction was warmed to –20 °C and the respective alkylthiole (2.00 mmol) in acetonitrile (3 mL) was added dropwise. The mixture was warmed to room temperature and stirred for additional 10 min. The reaction was quenched with NH_3 (100 µL, 25% aqueous), evaporated *in vacuo* and extracted from a mixture of HCl (1M, 20 mL) and ethyl acetate (20 mL). The organic phase was evaporated and purified by column chromatography (CH/EA 3:1 + 1% TFA) to provide the corresponding disulfanylbenzoic acids (**3b–3g**).

3b 3-(Ethyldisulfanyl)benzoic acid

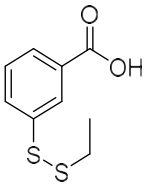

The title compound was synthesized by the general procedure (I) to give **3b** as a colourless solid (294 mg, 68%). mp: 68 °C; ^{1}H NMR (300 MHz, DMSO-d_6) δ= 13.20 (s, 1H), 8.09 (s, 1H), 7.81 (d, *J* = 7.7 Hz, 1H), 7.76 (d, *J* = 7.7 Hz, 1H), 7.51 (t, *J* = 7.7 Hz, 1H), 2.80 (q, *J* = 7.3 Hz, 2H), 1.24 (t, *J* = 7.3 Hz, 3H); ^{13}C NMR (75 MHz, DMSO-d_6) δ= 167.1, 138.0, 132.3, 131.3, 130.0, 128.1, 127.3, 32.5, 14.5; FT-IR (neat): ṽ [cm^{-1}]= 655, 673, 714, 746, 808, 848, 897, 935, 1070, 1259, 1305, 1411, 1441, 1570, 1679.

3c 4-(Ethyldisulfanyl)benzoic acid

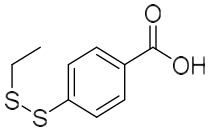

The title compound was synthesized by the general procedure (I) to give **3c** as a beige solid (297 mg, 69%). mp: 143 °C; ^{1}H NMR (300 MHz, DMSO-d_6) δ= 12.98 (s, 1H), 8.05 – 7.75 (m, 2H), 7.80 – 7.46 (m, 2H), 2.82 (q, *J* = 7.3 Hz, 2H), 1.24 (t, *J* = 7.3 Hz, 3H); ^{13}C NMR (75 MHz, DMSO-d_6) δ= 167.2, 143.2, 130.5 (2C), 129.2, 126.0 (2C), 32.5, 14.5; FT-IR (neat): ṽ [cm^{-1}]= 687, 762, 816, 847, 949, 1013, 1112, 1129, 1175, 1292, 1307, 1396, 1421, 1588, 1674.

3d 2-(Ethyldisulfanyl)benzoic acid

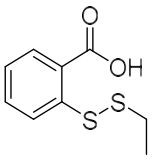

The title compound was synthesized by the general procedure (I) to give **3d** as a beige solid (265 mg, 61%). mp: 130 °C; ^{1}H NMR (300 MHz, $CDCl_3$) δ= 8.26 (d, *J* = 8.1 Hz, 1H), 8.18 (d, *J* = 7.7 Hz, 1H), 7.65 (t, *J* = 7.7 Hz, 1H), 7.39 – 7.22 (m, 1H), 2.76 (q, *J* = 7.2 Hz, 2H), 1.36 (t, *J* = 7.2 Hz, 3H); ^{13}C NMR (75 MHz, $CDCl_3$) δ= 168.5, 143.2, 133.5, 132.5, 125.8, 125.7, 125.1, 32.2, 14.3; FT-IR (neat): ṽ [cm^{-1}]= 692, 743, 797, 890, 1040, 1053, 1155, 1257, 1268, 1314, 1414, 1436, 1460, 1560, 1585, 1675.

3e 2-(Propan-2-yldisulfanyl)benzoic acid

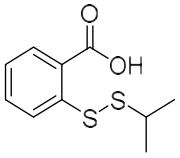

The title compound was synthesized by the general procedure (I) to give **3e** as a beige solid (259 mg, 56%). mp: 117 °C; ^{1}H NMR (300 MHz, DMSO-d_6) δ= 13.78 (s, 1H), 8.53 (d, *J* = 8.3 Hz, 1H), 8.38 (d, *J* = 7.8 Hz, 1H), 8.07 (dd, *J* = 8.3, 7.4 Hz, 1H), 7.73 (t, *J* = 7.4 Hz, 1H), 3.49 (hept, *J* = 6.7 Hz, 1H), 1.67 (d, *J* = 6.7 Hz, 6H); ^{13}C NMR (75 MHz, DMSO-d_6) δ= 167.9, 141.5, 133.2, 131.7, 128.1, 126.8, 125.8, 40.9, 22.7 (2C); FT-IR (neat): ṽ [cm^{-1}]= 693, 744, 806, 912, 1038, 1154, 1257, 1270, 1316, 1377, 1417, 1437, 1459, 1558, 1666, 2963.

3f 2-(*tert*-Butyldisulfanyl)benzoic acid

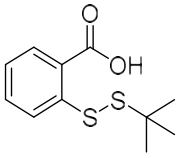

The title compound was synthesized by the general procedure (I) to give **3f** as a beige solid (285 mg, 58%). mp: 162 °C; ^{1}H NMR (300 MHz, DMSO-d_6) δ= 13.34 (s, 1H), 8.15 (d, *J* = 8.3 Hz, 1H), 7.93 (d, *J* = 7.7, Hz, 1H), 7.62 (dd, *J* = 8.3, 7.4 Hz, 1H), 7.29 (d, *J* = 7.4 Hz, 1H), 1.27 (s, 9H); ^{13}C NMR (75 MHz, DMSO-d_6) δ= 167.9, 141.8, 132.9, 131.5, 128.2, 126.2, 125.8, 49.50, 29.9 (3C); FT-IR (neat): ṽ [cm^{-1}]= 693, 744, 903, 1037, 1153, 1259, 1272, 1316, 1361, 1419, 1437, 1461, 1561, 1668, 2955.

3g 2-[(2-Phenylethyl)disulfanyl]benzoic acid

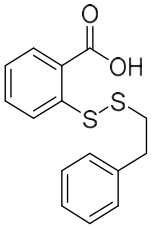

The title compound was synthesized by the general procedure (I) to give **3g** as a colourless solid (350 mg, 60%). mp: 106 °C; ^{1}H NMR (300 MHz, DMSO-d_6) δ= 13.39 (s, 1H), 8.03 (d, J = 8.3 Hz, 1H), 7.97 (d, J = 7.7 Hz, 1H), 7.63 (dd, J = 8.3, 7.3 Hz, 1H), 7.37 – 7.15 (m, 6H), 3.05 – 2.95 (m, 2H), 2.95 – 2.85 (m, 2H); ^{13}C NMR (75 MHz, DMSO-d_6) δ= 167.9, 140.9, 140.0, 133.4, 131.7, 129.0 (2C), 128.8 (2C), 128.1, 126.8, 125.9, 125.6, 39.0, 34.9; FT-IR (neat): ṽ [cm^{-1}]= 693, 705, 737, 811, 895, 1038, 1055, 1173, 1222, 1260, 1289, 1314, 1413, 1461, 1563, 1586, 1667.

General procedure (II) to synthesize Boc/Cbz-protected amides (5a–v, 9a,b & 14)

Boc/Cbz-protected amino acids **4a–l** or **8a–b** (2.00 mmol), the corresponding amine component (2.00 mmol), TBTU (642 mg, 2.00 mmol) and DIPEA (1.39 mL, 8.00 mmol) were suspended in ethyl acetate (20 mL) and stirred for 72 h at room temperature. The organic phase was extracted with $NaHCO_3$ sat., HCl (1 M) and filtered through a pad of silica. Evaporation of the solvent yielded the corresponding Boc-protected amides (**5a–v, 9a,b & 14**), which were used without further purification.

5a *tert*-Butyl *N*-{[(adamantan-1-yl)carbamoyl]methyl}carbamate

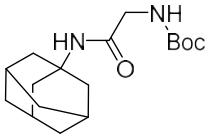

The title compound was synthesized by the general procedure (II) to give **5a** as a colourless solid (530 mg, 85%). mp: 120 °C; ^{1}H NMR (300 MHz, $CDCl_3$) δ= 5.77 (s, 1H), 5.24 (s, 1H), 3.70 (s, 2H), 2.14 – 2.05 (m, 3H), 2.01 (d, J = 3.0 Hz, 6H), 1.70 (t, J = 3.0 Hz, 6H), 1.48 (s, 9H); ^{13}C NMR (75 MHz, $CDCl_3$) δ= 168.4, 156.2, 80.1, 52.1, 44.9, 41.5 (3C), 36.2 (3C), 29.4 (3C), 28.3 (3C); FT-IR (neat): ṽ [cm^{-1}]= 781, 865, 943, 1028, 1049, 1094, 1165, 1245, 1272, 1344, 1364, 1454, 1520, 1658, 2850, 2906, 3314.

5b *tert*-Butyl (2*S*)-2-[(adamantan-1-yl)carbamoyl]pyrrolidine-1-carboxylate

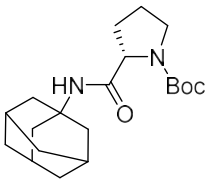

The title compound was synthesized by the general procedure (II) to give **5b** as a colourless solid (635 mg, 91%). mp: 152 °C; $[\alpha]_{D23}$=−95 °(c=10 in chloroform); ^{1}H NMR (300 MHz, $CDCl_3$) δ= 5.69 (s, 1H), 4.15 (q, J = 7.2 Hz, 1H), 3.45 (s, 2H), 2.03 – 2.16 (m, 4H), 2.00 (d, J = 3.0 Hz, 6H), 1.87 (s, 3H), 1.70 (t, J = 3.0 Hz, 6H), 1.50 (s, 9H); ^{13}C NMR (75 MHz, $CDCl_3$) δ= 171.3, 154.9, 80.7, 61.8, 51.5, 47.0, 41.6 (3C), 36.3 (3C), 29.4 (3C), 29.1, 28.4 (3C), 28.0; FT-IR (neat): ṽ [cm^{-1}]= 773, 882, 1089, 1121, 1166, 1225, 1270, 1345, 1364, 1392, 1454, 1478, 1525, 1668, 2851, 2909, 3335.

5c *tert*-Butyl *N*-[(1*S*)-1-[(adamantan-1-yl)carbamoyl]-2-phenylethyl]carbamate

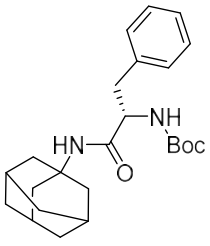

The title compound was synthesized by the general procedure (II) to give **5c** as a colourless solid (680 mg, 85%). mp: 85 °C; $[\alpha]_{D23}$=−75 °(c=10 in chloroform); ^{1}H NMR (300 MHz, DMSO-d_6) δ= 7.33 – 7.11 (m, 6H), 6.68 (d, J = 8.7 Hz, 1H), 4.18 – 3.93 (m, 1H), 2.95 – 2.60 (m, 2H), 2.14 – 2.05 (m, 3H), 1.88 (d, J = 3.0 Hz, 6H), 1.61 (t, J = 3.0 Hz, 6H), 1.30 (s, 9H); ^{13}C NMR (75 MHz, DMSO-d_6) δ= 171.0, 155.5, 138.5, 129.7 (2C), 128.3 (2C), 126.5, 78.3, 56.3, 51.1, 41.3 (3C), 38.4, 36.4 (3C), 29.2 (3C), 28.5 (3C); FT-IR (neat): ṽ [cm^{-1}]= 697, 728, 862, 1022, 1049, 1094, 1168, 1237, 1272, 1364, 1454, 1533, 1652, 2850, 2906, 3293.

5d *tert*-Butyl (2*R*)-2-[(adamantan-1-yl)carbamoyl]pyrrolidine-1-carboxylate

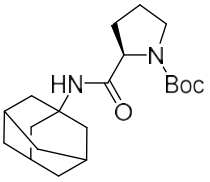

The title compound was synthesized by the general procedure (II) to give **5d** as a colourless solid (672 mg, 96%). mp: 153 °C; $[\alpha]_{D23}$=+96 °(*c*=10 in chloroform); ^{1}H NMR (300 MHz, DMSO-d_6) δ= 7.31 – 7.14 (m, 1H), 4.12 – 3.85 (m, 1H), 3.33 (s, 2H), 1.99 (s, 4H), 1.98 – 1.81 (m, 6H), 1.86 – 1.62 (m, 3H), 1.60 (t, *J* = 3.0 Hz, 6H), 1.36 (s, 9H); ^{13}C NMR (75 MHz, DMSO-d_6) δ= 172.0, 153.8, 78.6, 60.0, 50.9, 46.9, 41.4 (3C), 36.5 (3C), 29.2 (3C), 28.9, 28.5 (3C), 28.3; FT-IR (neat): ṽ [cm^{-1}]= 773, 882, 920, 995, 1089, 1122, 1166, 1226, 1270, 1345, 1363, 1393, 1455, 1477, 1525, 1669, 2851, 2909, 3332.

5e *tert*-Butyl *N*-{2-[(adamantan-1-yl)carbamoyl]ethyl}carbamate

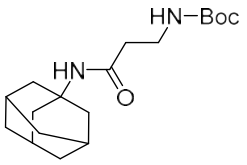

The title compound was synthesized by the general procedure (II) to give **5e** as a colourless solid (580 mg, 89%). mp: 126 °C; ^{1}H NMR (300 MHz, DMSO-d_6) δ= 7.27 (s, 1H), 6.66 (t, *J* = 5.7 Hz, 1H), 3.06 (td, *J* = 7.5, 5.7 Hz, 2H), 2.15 (t, *J* = 7.5 Hz, 2H), 1.98 (s, 3H), 1.89 (d, *J* = 3.0 Hz, 6H), 1.60 (t, *J* = 3.0 Hz, 6H), 1.36 (s, 9H); ^{13}C NMR (75 MHz, DMSO-d_6) δ= 170.1, 155.8, 77.9, 51.0, 41.4 (3C), 37.2, 36.9, 36.5 (3C), 29.2 (3C), 28.6 (3C); FT-IR (neat): ṽ [cm^{-1}]= 861, 966, 1001, 1066, 1094, 1161, 1266, 1364, 1451, 1490, 1516, 1543, 1644, 1665, 1689, 1719, 2850, 2905, 3316.

5f *tert*-Butyl 4-[(adamantan-1-yl)carbamoyl]piperidine-1-carboxylate

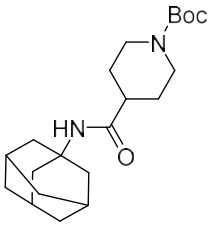

The title compound was synthesized by the general procedure (II) to give **5f** as a colourless solid (624 mg, 86%). mp: 174 °C; ^{1}H NMR (300 MHz, DMSO-d_6) δ= 7.22 (s, 1H), 4.05 – 3.82 (m, 4H), 2.69 (s, 1H), 2.03 – 1.93 (m, 3H), 1.88 (d, *J* = 3.0 Hz, 6H), 1.59 (t, *J* = 3.0 Hz, 6H), 1.54 (s, 4H), 1.38 (s, 9H); ^{13}C NMR (75 MHz, DMSO-d_6) δ= 173.9, 154.3, 78.9, 50.1, 42.5 (2C), 41.4 (3C), 40.8, 36.5 (3C), 29.2 (3C), 29.0 (2C), 28.5 (3C); FT-IR (neat): ṽ [cm^{-1}]= 860, 966, 1000, 1066, 1094, 1161, 1266, 1364, 1450, 1490, 1517, 1543, 1644, 1665, 1689, 1719, 2850, 2905, 3317.

5g *tert*-Butyl *N*-{[(adamantan-1-yl)carbamoyl]methyl}-*N*-methylcarbamate

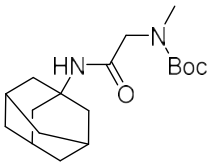

The title compound was synthesized by the general procedure (II) to give **5g** as a colourless solid (595 mg, 92%). mp: 114 °C; ^{1}H NMR (300 MHz, DMSO-d_6) δ= 7.81 – 7.58 (s, 1H), 4.04 (s, 2H), 3.73 (s, 3H), 2.39 (s, 3H), 2.31 (d, *J* = 3.0 Hz, 6H), 2.00 (t, *J* = 3.0 Hz, 6H), 1.76 (s, 9H); ^{13}C NMR (75 MHz, DMSO-d_6) δ= 168.1, 155.7, 78.7, 51.3, 51.1, 41.5 (3C), 36.4 (3C), 36.2, 29.2 (3C), 28.4 (3C); FT-IR (neat): ṽ [cm^{-1}]= 692, 744, 910, 1038, 1150, 1172, 1257, 1269, 1316, 1362, 1377, 1416, 1436, 1458, 1558, 1659, 2919.

5h *tert*-Butyl *N*-[(1*S*)-1-[(adamantan-1-yl)carbamoyl]-2-carbamoylethyl]carbamate

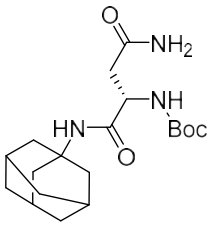

The title compound was synthesized by the general procedure (II) to give **5h** as a colourless solid (181 mg, 24%). mp: 69 °C; $[\alpha]_{D23}$=−20 °(*c*=10 in chloroform); ^{1}H NMR (300 MHz, DMSO-d_6) δ= 7.43 (s, 1H), 7.09 (d, *J* = 8.5 Hz, 1H), 4.21 (td, *J* = 8.5, 5.5 Hz, 1H), 2.84 – 2.61 (m, 2H), 2.04 – 1.93 (m, 3H), 1.94 – 1.84 (m, 6H), 1.60 (t, *J* = 3.1 Hz, 6H), 1.39 (s, 9H); ^{13}C NMR (75 MHz, DMSO-d_6) δ= 168.3, 156.3, 118.5, 79.1, 52.8, 51.0, 41.2 (3C), 39.1, 36.9 (3C), 29.2 (3C), 28.5 (3C); FT-IR (neat): ṽ [cm^{-1}]= 861, 966, 1000, 1066, 1162, 1266, 1364, 1451, 1490, 1517, 1543, 1644, 1664, 1689, 1719, 2850, 2905, 3317.

5i *tert*-Butyl *N*-[(1*S*)-1-[(adamantan-1-yl)carbamoyl]ethyl]carbamate

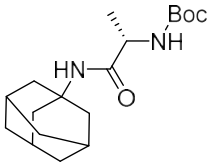

The title compound was synthesized by the general procedure (II) to give **5i** as a colourless solid (525 mg, 81%). mp: 109 °C; $[\alpha]_{D23}$=−6 °(*c*=10 in chloroform); ^{1}H NMR (300 MHz, DMSO-d_6) δ= 7.11 (s, 1H), 6.66 (d, *J* = 7.6 Hz, 1H), 3.88 (t, *J* = 7.6 Hz, 1H), 2.03 – 1.95 (m, 3H), 1.89 (d, *J* = 3.0 Hz, 6H), 1.61 (t, *J* = 3.0 Hz, 6H), 1.37 (s, 9H), 1.11 (d, *J* = 7.0 Hz, 3H); ^{13}C NMR (75 MHz, DMSO-d_6) δ= 171.4, 155.3, 78.4, 50.9, 50.3, 41.4 (3C), 36.4 (3C), 29.2 (3C), 28.6 (3C), 19.1; FT-IR (neat): ṽ [cm^{-1}]= 758, 862, 1024, 1046, 1070, 1168, 1240, 1312, 1364, 1454, 1525, 1650, 1683, 2909, 3292.

5j *tert*-Butyl *N*-[(1*S*)-1-[(adamantan-1-yl)carbamoyl]-2,2-dimethylpropyl]carbamate

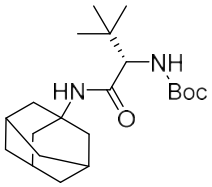

The title compound was synthesized by the general procedure (II) to give **5j** as a colourless solid (625 mg, 85%). mp: 178 °C; $[\alpha]_{D23}$=−13 °(*c*=10 in chloroform); ^{1}H NMR (300 MHz, DMSO-d_6) δ= 7.32 (s, 1H), 6.15 (d, *J* = 9.7 Hz, 1H), 3.81 (d, *J* = 9.7 Hz, 1H), 1.99 (d, *J* = 3.0 Hz, 3H), 1.92 (d, *J* = 3.0 Hz, 6H), 1.60 (t, *J* = 3.0 Hz, 6H), 1.38 (s, 9H), 0.87 (s, 9H); ^{13}C NMR (75 MHz, DMSO-d_6) δ= 169.8, 155.5, 78.4, 61.9, 51.4, 41.3 (3C), 36.4 (3C), 34.7, 29.2 (3C), 28.6 (3C), 27.1 (3C); FT-IR (neat): ṽ [cm^{-1}]= 788, 865, 1008, 1064, 1093, 1173, 1236, 1322, 1365, 1454, 1513, 1647, 1690, 2852, 2906, 3315.

5k *tert*-Butyl *N*-[(1*R*)-1-[(adamantan-1-yl)carbamoyl]-3-methylbutyl]carbamate

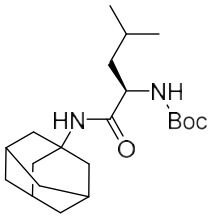

The title compound was synthesized by the general procedure (II) to give **5k** as a colourless solid (555 mg, 76%). mp: 183 °C; $[\alpha]_{D23}$=+11 °(*c*=10 in chloroform); ^{1}H NMR (300 MHz, DMSO-d_6) δ= 7.01 (s, 1H), 6.53 (d, *J* = 8.7 Hz, 1H), 3.87 (q, *J* = 7.8 Hz, 1H), 1.98 (s, 3H), 1.93 – 1.86 (m, 6H), 1.64 – 1.51 (m, 7H), 1.37 (s, 11H), 0.85 (t, *J* = 6.2 Hz, 6H); ^{13}C NMR (75 MHz, DMSO-d_6) δ= 172.1, 155.5, 79.7, 53.7, 51.1, 41.7, 41.3 (3C), 36.4 (3C), 29.2 (3C), 28.6 (3C), 24.7, 23.4, 22.2; FT-IR (neat): ṽ [cm^{-1}]= 668, 1022, 1047, 1170, 1238, 1273, 1364, 1390, 1532, 1655, 1685, 2907.

5l *tert*-Butyl *N*-[(1*R*)-1-[(adamantan-1-yl)carbamoyl]-2-phenylethyl]carbamate

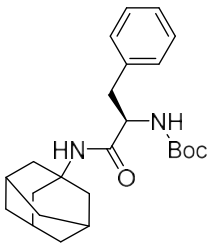

The title compound was synthesized by the general procedure (II) to give **5l** as a colourless solid (749 mg, 94%). mp: 86 °C; $[\alpha]_{D23}$=+72 °(*c*=10 in chloroform); ^{1}H NMR (300 MHz, DMSO-d_6) δ= 7.31 – 7.12 (m, 6H), 6.68 (d, *J* = 8.7 Hz, 1H), 4.18 – 4.06 (m, 1H), 2.96 – 2.62 (m, 2H), 1.99 (s, 3H), 1.88 (d, *J* = 3.0 Hz, 6H), 1.61 (t, *J* = 3.0 Hz, 6H), 1.30 (s, 9H); ^{13}C NMR (75 MHz, DMSO-d_6) δ= 171.0, 155.5, 138.5, 129.7 (2C), 128.3 (2C), 126.5, 78.3, 56.3, 51.1, 41.3 (3C), 38.4, 36.4 (3C), 29.2 (3C), 28.5 (3C); FT-IR (neat): ṽ [cm^{-1}]= 668, 697, 728, 1021, 1032, 1049, 1094, 1168, 1237, 1271, 1364, 1390, 1454, 1497, 1534, 1654, 1686, 2850, 2907.

5m *tert*-Butyl *N*-{[(4-fluorophenyl)carbamoyl]methyl}carbamate

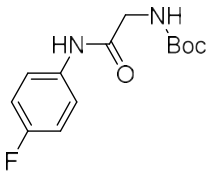

The title compound was synthesized by the general procedure (II) to give **5m** as a colourless solid (420 mg, 78%). mp: 140 °C; ^{1}H NMR (300 MHz, DMSO-d_6) δ= 9.97 (s, 1H), 7.64 – 7.54 (m, 2H), 7.20 – 7.11 (m, 2H), 7.05 (t, *J* = 6.0 Hz, 1H), 3.70 (d, *J* = 6.0 Hz, 2H), 1.39 (s, 9H); ^{13}C NMR (75 MHz, DMSO-d_6) δ= 175.4, 161.7 (d, 1C, J_{CF} = 62 Hz), 156.8, 132.4, 121.2 (d, 2C, J_{CF} = 6.0 Hz), 115.6 (d, 2C, J_{CF} = 27 Hz), 78.5, 44.0, 28.6 (3C); FT-IR (neat): ṽ [cm^{-1}]= 710, 784, 836, 936, 1049, 1153, 1210, 1250, 1289, 1364, 1391, 1507, 1618, 1671, 2901.

5n *tert*-Butyl *N*-{[(2-phenylethyl)carbamoyl]methyl}carbamate

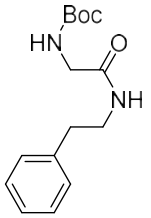

The title compound was synthesized by the general procedure (II) to give **5n** as a colourless oil (528 mg, 94%). ^{1}H NMR (300 MHz, DMSO-d_6) δ= 7.83 (t, J = 5.7 Hz, 1H), 7.28 (dd, J = 8.0, 6.7 Hz, 2H), 7.24 – 7.13 (m, 3H), 6.91 (t, J = 6.1 Hz, 1H), 3.49 (d, J = 6.1 Hz, 2H), 3.34 – 3.21 (m, 2H), 2.70 (t, J = 7.4 Hz, 2H), 1.38 (s, 9H); ^{13}C NMR (75 MHz, DMSO-d_6) δ= 169.6, 156.2, 139.8, 129.0 (2C), 128.7 (2C), 126.5, 78.4, 43.7, 40.6, 35.6, 28.6 (3C); FT-IR (neat): ṽ [cm^{-1}]= 699, 751, 947, 1022, 1162, 1247, 1281, 1365, 1454, 1515, 1667, 1713.

5o *tert*-Butyl *N*-{[(cyclohexylmethyl)carbamoyl]methyl}carbamate

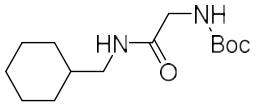

The title compound was synthesized by the general procedure (II) to give **5o** as a colourless oil (250 mg, 46%). ^{1}H NMR (300 MHz, DMSO-d_6) δ= 7.67 (d, J = 5.5 Hz, 1H), 6.89 (t, J = 6.0 Hz, 1H), 3.48 (d, J = 6.0 Hz, 2H), 2.89 (t, J = 6.4 Hz, 2H), 1.99 (s, 1H), 1.69 – 1.58 (m, 6H), 1.37 (s, 9H), 1.23 – 1.04 (m, 4H); ^{13}C NMR (75 MHz, DMSO-d_6) δ= 170.1, 157.1, 79.1, 46.8, 44.5, 36.8, 30.7 (2C), 28.6 (3C), 26.4, 25.8 (2C); FT-IR (neat): ṽ [cm^{-1}]= 743, 782, 864, 942, 1052, 1170, 1240, 1295, 1365, 1391, 1450, 1500, 1542, 1652, 1681, 1729, 2853, 2924, 3302.

5p *tert*-Butyl *N*-{[(2-methylpropyl)carbamoyl]methyl}carbamate

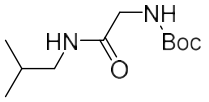

The title compound was synthesized by the general procedure (II) to give **5p** as a colourless oil (344 mg, 74%). ^{1}H NMR (300 MHz, DMSO-d_6) δ= 7.69 (d, J = 5.5 Hz, 1H), 6.90 (t, J = 6.1 Hz, 1H), 3.49 (d, J = 6.1 Hz, 2H), 2.87 (t, J = 6.7 Hz, 2H), 1.66 (dt, J = 13.4, 6.7 Hz, 1H), 1.37 (s, 9H), 0.82 (d, J = 6.7 Hz, 6H); ^{13}C NMR (75 MHz, DMSO-d_6) δ= 169.5, 156.2, 78.4, 46.3, 43.7, 28.6 (3C), 28.5, 20.4 (2C); FT-IR (neat): ṽ [cm^{-1}]= 729, 865, 942, 1049, 1087, 1152, 1254, 1278, 1298, 1369, 1394, 1426, 1471, 1527, 1645, 1674, 2959, 3292.

5q *tert*-Butyl *N*-{[(3-phenoxyphenyl)carbamoyl]methyl}carbamate

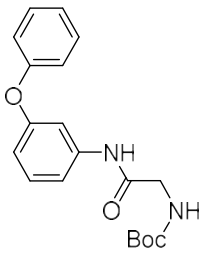

The title compound was synthesized by the general procedure (II) to give **5q** as a colourless solid (509 mg, 74%). mp: 122 °C; ^{1}H NMR (300 MHz, DMSO-d_6) δ= 9.99 (s, 1H), 7.46 – 7.35 (m, 2H), 7.35 – 7.24 (m, 3H), 7.20 – 7.10 (m, 1H), 7.07 – 6.95 (m, 3H), 6.75 – 6.64 (m, 1H), 3.68 (d, J = 6.1 Hz, 2H), 1.37 (s, 9H); ^{13}C NMR (75 MHz, DMSO-d_6) δ= 168.8, 157.5, 156.8, 156.3, 140.9, 130.5, 130.5 (2C), 124.0, 119.3 (2C), 114.2, 113.6, 109.3, 78.5, 44.2, 28.6 (3C); FT-IR (neat): ṽ [cm^{-1}]= 687, 757, 861, 896, 954, 1057, 1159, 1220, 1285, 1366, 1440, 1485, 1533, 1589, 1671.

5r *tert*-Butyl *N*-{[(4-cyclohexylphenyl)carbamoyl]methyl}carbamate

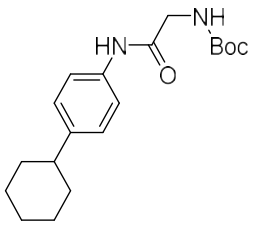

The title compound was synthesized by the general procedure (II) to give **5r** as a colourless solid (623 mg, 93%). mp: 145 °C; ^{1}H NMR (300 MHz, DMSO-d_6) δ= 9.81 (s, 1H), 7.45 (d, J = 8.3 Hz, 2H), 7.13 (d, J = 8.3 Hz, 2H), 7.00 (t, J = 6.1 Hz, 1H), 3.68 (d, J = 6.1 Hz, 2H), 3.54 – 3.47 (m, 1H), 2.42 (s, 2H), 1.84 – 1.58 (m, 5H), 1.38 (s, 9H), 1.37 – 1.23 (m, 3H); ^{13}C NMR (75 MHz, DMSO-d_6) δ= 168.4, 156.3, 142.9, 137.1, 127.2 (2C), 119.6 (2C), 78.5, 44.1, 43.6, 34.5 (2C), 28.6 (3C), 26.8 (2C), 26.0; FT-IR (neat): ṽ [cm^{-1}]= 756, 829, 863, 956, 1026, 1055, 1161, 1252, 1281, 1366, 1391, 1412, 1447, 1492, 1514, 1546, 1605, 1671, 1686, 2851, 2927.

5s *tert*-Butyl *N*-{[(naphthalen-1-yl)carbamoyl]methyl}carbamate

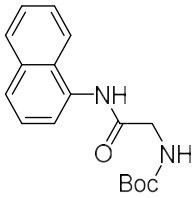

The title compound was synthesized by the general procedure (II) to give **5s** as a colourless solid (460 mg, 76%). mp: 158 °C; ^{1}H NMR (300 MHz, DMSO-d_6) δ= 9.89 (s, 1H), 8.11 – 8.00 (m, 1H), 7.98 – 7.89 (m, 1H), 7.77 (d, *J* = 8.2 Hz, 1H), 7.66 (d, *J* = 7.4 Hz, 1H), 7.61 – 7.43 (m, 3H), 7.14 (t, *J* = 6.1 Hz, 1H), 3.89 (d, *J* = 6.1 Hz, 2H), 1.41 (s, 9H); ^{13}C NMR (75 MHz, DMSO-d_6) δ= 169.5, 156.5, 134.1, 133.7, 128.5, 128.2, 126.5, 126.2, 126.0, 125.7, 123.1, 122.0, 78.6, 44.2, 28.6 (3C); FT-IR (neat): ṽ [cm^{-1}]= 727, 775, 796, 857, 939, 1045, 1153, 1213, 1248, 1285, 1344, 1364, 1408, 1424, 1505, 1546, 1660, 1686, 3344.

5t *tert*-Butyl *N*-({[(thiophen-2-yl)methyl]carbamoyl}methyl)carbamate

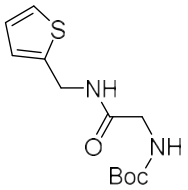

The title compound was synthesized by the general procedure (II) to give **5t** as a colourless oil (502 mg, 92%). ^{1}H NMR (300 MHz, DMSO-d_6) δ=8.37 (t, *J* = 6.0 Hz, 1H), 7.36 (d, *J* = 4.8 Hz, 1H), 7.00 – 6.89 (m, 3H), 4.42 (d, *J* = 6.0 Hz, 2H), 3.53 (d, *J* = 6.0 Hz, 2H), 1.37 (s, 9H); ^{13}C NMR (75 MHz, DMSO-d_6) δ= 169.7, 156.2, 142.6, 127.0, 125.8, 125.4, 78.5, 43.6, 37.5, 28.6 (3C); FT-IR (neat): ṽ [cm^{-1}]= 694, 782, 853, 942, 1044, 1161, 1240, 1365, 1391, 1503, 1655, 3303.

5u *tert*-Butyl *N*-{[(adamantan-2-yl)carbamoyl]methyl}carbamate

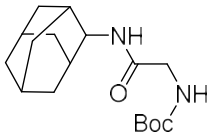

The title compound was synthesized by the general procedure (II) to give **5u** as a colourless solid (443 mg, 70%). mp: 71 °C; ^{1}H NMR (300 MHz, DMSO-d_6) δ= 7.51 (d, *J* = 7.6 Hz, 1H), 6.94 (t, *J* = 6.1 Hz, 1H), 3.82 (d, *J* = 7.6 Hz, 1H), 3.56 (d, *J* = 6.1 Hz, 2H), 2.06 – 1.86 (m, 2H), 1.83 – 1.66 (m, 10H), 1.56 – 1.45 (m, 2H), 1.38 (s, 9H); ^{13}C NMR (75 MHz, DMSO-d_6) δ= 169.2, 156.6, 78.8, 53.6, 37.8, 37.5, 32.2 (4C), 31.7 (2C), 28.9 (3C), 27.5 (2C); FT-IR (neat): ṽ [cm^{-1}]= 865, 942, 1048, 1110, 1165, 1247, 1365, 1391, 1453, 1525, 1654, 2852, 2905, 3323.

5v *tert*-Butyl *N*-[(dicyclohexylcarbamoyl)methyl]carbamate

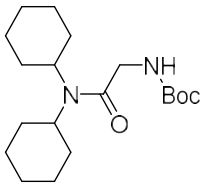

The title compound was synthesized by the general procedure (II) to give **5v** as a colourless oil (392 mg, 57%). ^{1}H NMR (300 MHz, DMSO-d_6) δ= 6.52 (t, *J* = 5.6 Hz, 1H), 3.74 (d, *J* = 5.6 Hz, 2H), 2.42 – 2.19 (m, 2H), 1.79 – 1.41 (m, 9H), 1.39 – 1.35 (m, 12H), 1.31 – 0.99 (m, 8H); ^{13}C NMR (75 MHz, DMSO-d_6) δ= 167.2, 155.9, 73.7, 55.1 (2C), 45.7, 30.9 (2C), 30.1 (4C), 28.6 (3C), 26.3 (4C); FT-IR (neat): ṽ [cm^{-1}]= 742, 780, 873, 895, 996, 1046, 1126, 1169, 1238, 1304, 1366, 1439, 1644, 1704, 2856, 2931.

9a *tert*-Butyl (3*R*)-3-{[(benzyloxy)carbonyl]amino}-3-[(3-phenoxyphenyl)carbamoyl]propanoate

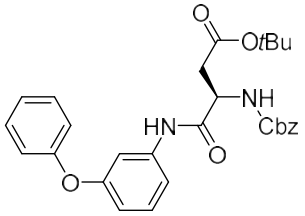

The title compound was synthesized by the general procedure (II) to give **9a** as a colourless oil (669 mg, 68%). [α]$_{D23}$=+103 °(*c*=10 in chloroform); ^{1}H NMR (300 MHz, DMSO-d_6) δ= 10.17 (s, 1H), 7.69 (d, *J* = 8.1 Hz, 1H), 7.46 – 7.22 (m, 10H), 7.19 – 7.10 (m, 1H), 7.10 – 6.92 (m, 2H), 6.76 – 6.68 (m, 1H), 5.13 – 4.96 (m, 2H), 4.51 (td, *J* = 8.3, 5.9 Hz, 1H), 2.80 – 2.41 (m, 2H), 1.35 (s, 9H); ^{13}C NMR (75 MHz, DMSO-d_6) δ= 169.9, 169.5, 157.4, 156.8, 156.2, 140.8, 137.3, 130.4 (3C), 128.7 (2C), 128.2, 128.1 (2C), 124.0, 119.3 (2C), 114.6, 113.9, 109.7, 80.7, 66.0, 52.6, 38.0, 28.1 (3C); FT-IR (neat): ṽ [cm^{-1}]= 688, 748, 794, 845, 878, 972, 1024, 1074, 1140, 1218, 1250, 1367, 1438, 1487, 1514, 1586, 1671, 1711, 3272.

9b *tert*-Butyl (3*S*)-3-[(adamantan-1-yl)carbamoyl]-3-{[(benzyloxy)carbonyl]amino}propanoate

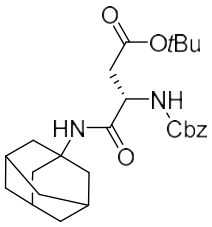

The title compound was synthesized by the general procedure (II) to give **9b** as a colourless solid (880 mg, 96%). mp: 56 °C; $[\alpha]_{D23}$=−84 °(*c*=10 in chloroform); ^{1}H NMR (300 MHz, $CDCl_3$) δ= 7.41 – 7.30 (m, 5H), 6.15 (s, 1H), 5.91 (d, *J* = 6.3 Hz, 1H), 5.11 (d, *J* = 3.2 Hz, 2H), 4.40 (d, *J* = 6.3 Hz, 1H), 3.07 – 2.36 (m, 2H), 2.09 – 2.00 (m, 3H), 1.98 – 1.89 (m, 6H), 1.70 – 1.60 (m, 6H), 1.43 (s, 9H); ^{13}C NMR (75 MHz, $CDCl_3$) δ= 171.3, 169.1, 155.9, 136.2, 128.5 (2C), 128.2, 128.1 (2C), 81.7, 67.0, 52.0, 51.4, 41.3 (3C), 37.8, 36.2 (3C) , 29.3 (3C), 28.0 (3C); FT-IR (neat): ṽ [cm^{-1}]= 700, 755, 848, 907, 950, 1019, 1160, 1217, 1247, 1282, 1369, 1409, 1447, 1515, 1668, 1715, 2912, 3390.

14 Benzyl (2*S*)-1-[(2*S*)-2-{[(*tert*-butoxy)carbonyl]amino}-4-methylpentanoyl]pyrrolidine-2-carboxylate

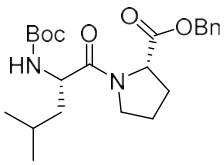

The title compound was synthesized by the general procedure (II) to give **14** as a colourless oil (1184 mg, 56%). $[\alpha]_{D23}$=−64 °(*c*=10 in chloroform); ^{1}H NMR (300 MHz, DMSO-*d*$_6$) δ= 7.44 – 7.26 (m, 5H), 6.96 (d, *J* = 8.1 Hz, 1H), 5.08 (d, *J* = 2.2 Hz, 2H), 4.39 (dd, *J* = 8.6, 4.8 Hz, 1H), 4.27 – 4.14 (m, 1H), 3.58 (s, 2H), 2.29 – 2.11 (m, 1H), 1.99 – 1.75 (m, 3H), 1.49 – 1.28 (m, 12H), 0.83 (t, *J* = 6.7 Hz, 6H); ^{13}C NMR (75 MHz, DMSO-*d*$_6$) δ= 172.1, 171.6, 155.8, 136.3, 128.8 (2C), 128.4, 128.2 (2C), 78.3, 66.3, 59.0, 50.6, 46.7, 40.7, 28.9, 28.6 (3C), 25.1, 23.5, 21.7 (2C); FT-IR (neat): ṽ [cm^{-1}]= 698, 738, 870, 1021, 1044, 1163, 1245, 1366, 1427, 1499, 1645, 1705, 1740, 2957.

General procedure (III) to deprotect Boc-amines (6a–v)

Boc-protected amides **5a–v** (0.50 mmol) were dissolved in tetrahydrofuran (5 mL). Concentrated hydrochloric acid (5 mL) was added dropwise and the mixture was stirred for 1 h at room temperature. The solvent was evaporated, and the residual was lyophilized from ACN/H_2O (1:1, 5 mL) to give the amine hydrochlorides (**6a–v**).

6a [(Adamantan-1-yl)carbamoyl]methanaminium chloride

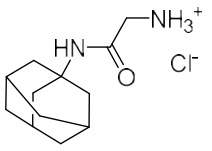

According to the general procedure (III), amine hydrochloride **6a** was obtained from **5a** as a colourless solid (106 mg, 86%). mp: 238 °C; ^{1}H NMR (300 MHz, DMSO-*d*$_6$) δ= 8.07 (s, 3H), 7.98 (s, 1H), 3.46 (s, 2H), 2.01 (s, 3H), 1.93 (s, 6H), 1.62 (s, 6H); ^{13}C NMR (75 MHz, DMSO-*d*$_6$) δ= 165.1, 51.7, 41.3 (3C), 40.7, 36.3 (3C), 29.2 (3C); FT-IR (neat): ṽ [cm^{-1}]= 901, 1096, 1113, 1252, 1286, 1297, 1344, 1363, 1430, 1454, 1479, 1546, 1677, 2851, 2897, 3009, 3277.

6b (2*S*)-2-[(Adamantan-1-yl)carbamoyl]pyrrolidin-1-ium chloride

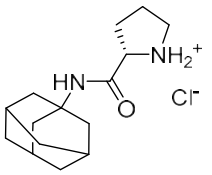

According to the general procedure (III), amine hydrochloride **6b** was obtained from **5b** as a colourless solid (106 mg, 74%). mp: 240 °C; $[\alpha]_{D23}$=−74 °(*c*=10 in DMSO); ^{1}H NMR (300 MHz, DMSO-*d*$_6$) δ= 10.33 – 9.91 (m, 1H), 8.42 – 8.26 (m, 1H), 8.18 (s, 1H), 4.16 – 3.93 (m, 1H), 3.24 – 3.07 (m, 2H), 2.36 – 2.19 (m, 1H), 2.05 – 1.97 (m, 3H), 1.93 (s, 6H), 1.89 – 1.65 (m, 3H), 1.61 (s, 6H); ^{13}C NMR (75 MHz, DMSO-*d*$_6$) δ= 167.6, 59.3, 51.9, 46.0, 41.2 (3C), 36.3 (3C), 30.7, 29.1 (3C), 24.1; FT-IR (neat): ṽ [cm^{-1}]= 815, 1009, 1041, 1097, 1127, 1240, 1312, 1343, 1360, 1394, 1453, 1551, 1649, 1673, 2848, 2903, 3216.

6c (1*S*)-1-[(Adamantan-1-yl)carbamoyl]-2-phenylethan-1-aminium chloride

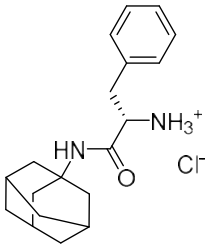

According to the general procedure (III), amine hydrochloride **6c** was obtained from **5c** as a colourless solid (150 mg, 88%). mp: 219 °C; $[\alpha]_{D23}$=−88 °(*c*=10 in DMSO); ^{1}H NMR (300 MHz, DMSO-d_6) δ= 8.29 (s, 3H), 7.88 (s, 1H), 7.37 – 7.19 (m, 5H), 3. 97 (s, 1H), 3.10 – 2.90 (m, 2H), 2.01 – 1.93 (m, 3H), 1.84 – 1.77 (m, 6H), 1.66 – 1.48 (m, 6H); ^{13}C NMR (75 MHz, DMSO-d_6) δ= 167.0, 135.5, 130.1 (2C), 128.7 (2C), 127.4, 53.8, 51.7, 41.1 (3C), 37.5, 36.3 (3C), 29.1 (3C); FT-IR (neat): ῡ [cm^{-1}]= 699, 745, 1092, 1455, 1497, 1570, 1683, 2849, 2905.

6d (2*R*)-2-[(Adamantan-1-yl)carbamoyl]pyrrolidin-1-ium chloride

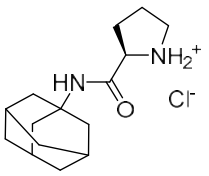

According to the general procedure (III), amine hydrochloride **6d** was obtained from **5d** as a colourless solid (122 mg, 85%). mp: 238 °C; $[\alpha]_{D23}$=+72 °(*c*=10 in DMSO); ^{1}H NMR (300 MHz, DMSO-d_6) δ= 10.06 (s, 1H), 8.35 (s, 1H), 8.15 (s, 1H), 4.13 – 4.05 (m, 1H), 3.19 – 3.11 (m, 2H), 2.36 – 2.19 (m, 1H), 2.06 – 1.98 (m, 3H), 1.93 (s, 6H), 1.89 – 1.67 (m, 3H), 1.62 (s, 6H); ^{13}C NMR (75 MHz, DMSO-d_6) δ= 167.6, 59.3, 51.9, 46.0, 41.2 (3C), 36.3 (3C), 30.7, 29.1 (3C), 24.1; FT-IR (neat): ῡ [cm^{-1}]= 1097, 1240, 1313, 1343, 1360, 1453, 1552, 1573, 1648, 1673, 2847, 2904.

6e 2-[(Adamantan-1-yl)carbamoyl]ethan-1-aminium chloride

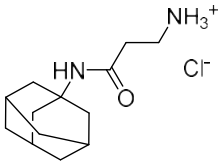

According to the general procedure (III), amine hydrochloride **6e** was obtained from **5e** as a colourless solid (124 mg, 95%). mp: 253 °C; ^{1}H NMR (300 MHz, DMSO-d_6) δ= 8.02 (s, 3H), 7.64 (s, 1H), 2.95 – 2.82 (m, 2H), 2.50 – 2.39 (m, 2H), 2.03 – 1.95 (m, 3H), 1.91 (s, 6H), 1.60 (s, 6H); ^{13}C NMR (75 MHz, DMSO-d_6) δ= 169.1, 51.3, 41.4 (3C), 36.4 (3C), 35.7, 32.9, 29.2 (3C); FT-IR (neat): ῡ [cm^{-1}]= 683, 809, 853, 875, 1044, 1105, 1127, 1243, 1280, 1293, 1311, 1319, 1343, 1365, 1378, 1449, 1541, 1598, 1647, 2850, 2907, 3255.

6f 4-[(Adamantan-1-yl)carbamoyl]piperidin-1-ium chloride

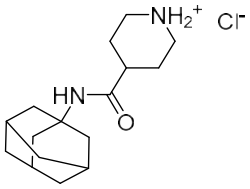

According to the general procedure (III), amine hydrochloride **6f** was obtained from **5f** as a colourless solid (131 mg, 87%). mp: 307 °C; ^{1}H NMR (300 MHz, DMSO-d_6) δ= 9.14 (s, 1H), 8.72 (s, 1H), 7.38 (s, 1H), 3.22 (d, *J* = 12.3 Hz, 2H), 2.77 (q, *J* = 12.3 Hz, 2H), 2.43 – 2.27 (m, 1H), 2.02 – 1.94 (m, 3H), 1.89 (s, 6H), 1.83 – 1.63 (m, 4H), 1.60 (s, 6H); ^{13}C NMR (75 MHz, DMSO-d_6) δ= 172.9, 50.9, 42.8 (2C), 41.4 (3C), 40.2, 36.4 (3C), 29.2 (3C), 25.7 (2C); FT-IR (neat): ῡ [cm^{-1}]= 669, 704, 961, 1237, 1307, 1360, 1393, 1453, 1567, 1599, 1644, 2801, 2848, 2903.

6g {[(Adamantan-1-yl)carbamoyl]methyl}(methyl)azanium chloride

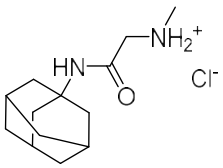

According to the general procedure (III), amine hydrochloride **6g** was obtained from **5g** as a colourless solid (125 mg, 96%). mp: 268 °C; ^{1}H NMR (300 MHz, DMSO-d_6) δ= 8.93 (s, 2H), 8.31 – 7.85 (m, 1H), 3.58 (s, 2H), 2.50 (s, 3H), 2.11 – 1.97 (m, 3H), 1.93 (s, 6H), 1.62 (s, 6H); ^{13}C NMR (75 MHz, DMSO-d_6) δ= 164.3, 49.7, 51.8, 41.3 (3C), 36.3 (3C), 32.9, 29.1 (3C); FT-IR (neat): ῡ [cm^{-1}]= 798, 1096, 1248, 1294, 1343, 1363, 1431, 1457, 1546, 1673, 2852, 2905, 2921, 3264.

6h (1*S*)-1-[(Adamantan-1-yl)carbamoyl]-2-carbamoylethan-1-aminium chloride

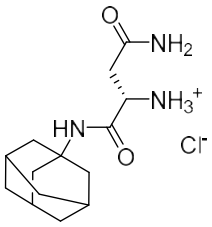

According to the general procedure (III), amine hydrochloride **6h** was obtained from **5h** as a colourless solid (112 mg, 74%). mp: 204 °C; $[\alpha]_{D23}$=−3 °(*c*=10 in DMSO); ^{1}H NMR (300 MHz, DMSO-d_6) δ= 9.50 (s, 2H), 8.83 – 8.53 (m, 3H), 8.39 (s, 1H), 4.08 (s, 1H), 3.18 (dd, *J* = 17.3, 5.9 Hz, 2H), 2.09 – 1.98 (m, 3H), 1.97 – 1.87 (m, 6H), 1.65 – 1.55 (m, 6H); ^{13}C NMR (75 MHz, DMSO-d_6) δ= 171.3, 165.1, 52.1, 48.7, 41.2, 41.1 (3C), 36.3 (3C), 29.1 (3C); FT-IR (neat): ṽ [cm^{-1}]= 1092, 1301, 1362, 1456, 1479, 1558, 1683, 2849, 2908.

6i (1*S*)-1-[(Adamantan-1-yl)carbamoyl]ethan-1-aminium chloride

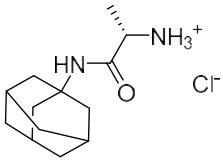

According to the general procedure (III), amine hydrochloride **6i** was obtained from **5i** as a colourless solid (98 mg, 75%). mp: 233 °C; $[\alpha]_{D23}$=−7 °(*c*=10 in DMSO); ^{1}H NMR (300 MHz, DMSO-d_6) δ= 8.22 (s, 3H), 8.04 (s, 1H), 3.84 – 3.69 (m, 1H), 2.04 – 1.96 (m, 3H), 1.96 – 1.88 (m, 6H), 1.61 (s, 6H), 1.31 (d, *J* = 6.8 Hz, 3H); ^{13}C NMR (75 MHz, DMSO-d_6) δ= 169.0, 51.6, 48.7, 41.2 (3C), 36.3 (3C), 29.2 (3C), 18.1; FT-IR (neat): ṽ [cm^{-1}]= 1102, 1241, 1280, 1292, 1343, 1360, 1454, 1495, 1542, 1574, 1650, 1677, 2848, 2904.

6j (1*S*)-1-[(Adamantan-1-yl)carbamoyl]-2,2-dimethylpropan-1-aminium chloride

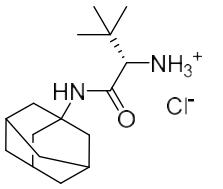

According to the general procedure (III), amine hydrochloride **6j** was obtained from **5j** as a colourless solid (150 mg, 99%). mp: 294 °C; $[\alpha]_{D23}$=−40 °(*c*=10 in DMSO); ^{1}H NMR (300 MHz, DMSO-d_6) δ= 8.22 – 8.09 (m, 3H), 8.02 (s, 1H), 3.57 (d, *J* = 5.3 Hz, 1H), 2.00 (s, 3H), 1.98 – 1.89 (m, 6H), 1.61 (s, 6H), 0.98 (s, 9H); ^{13}C NMR (75 MHz, DMSO-d_6) δ= 166.6, 60.5, 51.9, 41.2 (3C), 40.2, 36.4 (3C), 33.2, 29.1 (3C), 26.8 (3C); FT-IR (neat): ṽ [cm^{-1}]= 675, 737, 1278, 1334, 1360, 1405, 1455, 1474, 1509, 1567, 1642, 1682, 2848, 2900, 3073.

6k (1*R*)-1-[(Adamantan-1-yl)carbamoyl]-3-methylbutan-1-aminium chloride

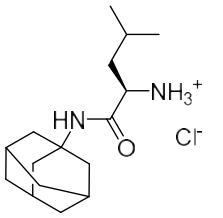

According to the general procedure (III), amine hydrochloride **6k** was obtained from **5k** as a colourless solid (134 mg, 89%). mp: 244 °C; $[\alpha]_{D23}$=+23 °(*c*=10 in DMSO); ^{1}H NMR (300 MHz, DMSO-d_6) δ= 8.29 (s, 3H), 8.14 (s, 1H), 3.87 – 3.58 (m, 1H), 2.04 – 1.96 (m, 3H), 1.96 – 1.89 (m, 6H), 1.67 – 1.56 (m, 7H), 1.56 – 1.46 (m, 2H), 0.88 (t, *J* = 6.6 Hz, 6H); ^{13}C NMR (75 MHz, DMSO-d_6) δ= 168.3, 51.8, 51.6, 41.2 (3C), 40.7, 36.3 (3C), 29.1 (3C), 24.2, 23.0, 22.9; FT-IR (neat): ṽ [cm^{-1}]= 700, 743, 1092, 1243, 1277, 1360, 1455, 1496, 1542, 1684, 2849, 2905.

6l (1*R*)-1-[(Adamantan-1-yl)carbamoyl]-2-phenylethan-1-aminium chloride

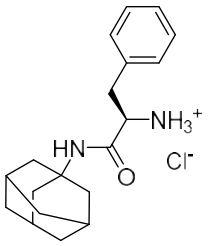

According to the general procedure (III), amine hydrochloride **6l** was obtained from **5l** as a colourless solid (147 mg, 87%). mp: 221 °C; $[\alpha]_{D23}$=+85 °(*c*=10 in DMSO); ^{1}H NMR (300 MHz, DMSO-d_6) δ= 8.48 – 8.27 (m, 3H), 7.97 (s, 1H), 7.36 – 7.15 (m, 5H), 4.11 – 3.89 (m, 1H), 3.16 – 2.86 (m, 2H), 2.00 – 1.92 (m, 3H), 1.80 (s, 6H), 1.56 (s, 6H); ^{13}C NMR (75 MHz, DMSO-d_6) δ= 167.0, 135.6, 130.1 (2C), 128.6 (2C), 127.3, 53.8, 51.7, 41.1 (3C), 37.4, 36.3 (3C), 29.1 (3C); FT-IR (neat): ṽ [cm^{-1}]= 700, 743, 1092, 1243, 1277, 1293, 1310, 1344, 1360, 1455, 1496, 1542, 1684, 2849, 2905.

6m [(4-Fluorophenyl)carbamoyl]methanaminium chloride

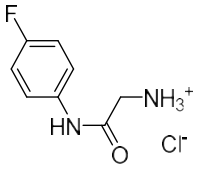

According to the general procedure (III), amine hydrochloride **6m** was obtained from **5m** as a colourless solid (100 mg, 97%). mp: 140 °C; ^{1}H NMR (300 MHz, DMSO-d_6) δ= 11.05 (s, 1H), 8.35 (s, 3H), 7.80 – 7.50 (m, 2H), 7.17 (t, J = 8.9 Hz, 2H), 3.90 – 3.70 (m, 2H); ^{13}C NMR (75 MHz, DMSO-d_6) δ= 165.1, 158.64 (d, 1C, J_{CF} = 240 Hz), 135.2 (d, 1C, J_{CF} = 2.7 Hz), 121.3 (d, 2C, J_{CF} = 7.8 Hz), 115.9 (d, 2C, J_{CF} = 22.3 Hz), 41.3; FT-IR (neat): ṽ [cm^{-1}]= 777, 833, 906, 1108, 1121, 1220, 1311, 1402, 1423, 1464, 1505, 1557, 1617, 1677, 2849, 2916, 2956.

6n [(2-Phenylethyl)carbamoyl]methanaminium chloride

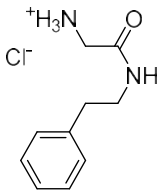

According to the general procedure (III), amine hydrochloride **6n** was obtained from **5n** as a colourless solid (106 mg, 98%). mp: 165 °C; ^{1}H NMR (300 MHz, DMSO-d_6) δ= 8.75 (t, J = 5.6 Hz, 1H), 8.29 (s, 3H), 7.34 – 7.15 (m, 5H), 3.50 (s, 2H), 3.39 – 3.24 (m, 2H), 2.73 (t, J = 7.4 Hz, 2H); ^{13}C NMR (75 MHz, DMSO-d_6) δ= 166.6, 140.0, 129.5 (2C), 129.2 (2C), 127.1, 41.2, 40.6, 35.8; FT-IR (neat): ṽ [cm^{-1}]= 698, 748, 894, 910, 1077, 1124, 1203, 1265, 1432, 1455, 1494, 1573, 1660, 1694, 2870, 2957.

6o [(Cyclohexylmethyl)carbamoyl]methanaminium chloride

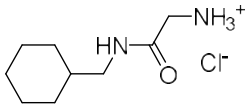

According to the general procedure (III), amine hydrochloride **6o** was obtained from **5o** as a colourless solid (89 mg, 86%). mp: 174 °C; ^{1}H NMR (300 MHz, DMSO-d_6) δ= 8.56 (t, J = 5.8 Hz, 1H), 8.24 (d, J = 6.1 Hz, 3H), 3.51 (q, J = 5.8 Hz, 2H), 2.94 (t, J = 6.1 Hz, 2H), 1.77 – 1.49 (m, 5H), 1.47 – 1.26 (m, 1H), 1.25 – 0.99 (m, 3H), 0.98 – 0.72 (m, 2H); ^{13}C NMR (75 MHz, DMSO-d_6) δ= 166.1, 45.3, 40.4, 37.7, 30.7 (2C), 26.4, 25.8 (2C); FT-IR (neat): ṽ [cm^{-1}]= 765, 918, 973, 1066, 1153, 1270, 1281, 1394, 1428, 1448, 1515, 1578, 1610, 1645, 2631, 2713, 2851, 2923, 3065.

6p [(2-Methylpropyl)carbamoyl]methanaminium chloride

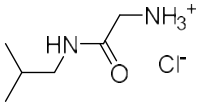

According to the general procedure (III), amine hydrochloride **6p** was obtained from **5p** as a colourless solid (83 mg, 99%). mp: 32 °C; ^{1}H NMR (300 MHz, DMSO-d_6) δ= 9.10 (t, J = 5.8 Hz, 1H), 9.00 – 8.51 (m, 3H), 4.01 (q, J = 5.8 Hz, 2H), 3.39 (t, J = 6.2 Hz, 2H), 2.25 – 2.06 (m, J = 6.7 Hz, 1H), 1.31 (d, J = 6.7 Hz, 6H); ^{13}C NMR (75 MHz, DMSO-d_6) δ= 166.1, 46.5, 40.4, 28.3, 20.5 (2C); FT-IR (neat): ṽ [cm^{-1}]= 712, 767, 914, 966, 1072, 1108, 1196, 1268, 1439, 1469, 1644, 1680, 3261, 3413.

6q [(3-Phenoxyphenyl)carbamoyl]methanaminium chloride

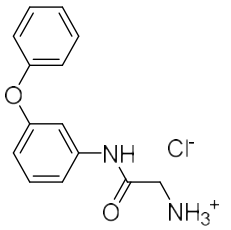

According to the general procedure (III), amine hydrochloride **6q** was obtained from **5q** as a colourless solid (112 mg, 80%). mp: 235 °C; ^{1}H NMR (300 MHz, DMSO-d_6) δ= 10.83 (s, 1H), 8.55 – 8.01 (m, 3H), 7.47 – 7.27 (m, 5H), 7.16 (t, J = 7.4 Hz, 1H), 7.03 (d, J = 8.0 Hz, 2H), 6.79 – 6.70 (m, 1H), 3.75 (q, J = 5.5 Hz, 2H); ^{13}C NMR (75 MHz, DMSO-d_6) δ= 165.3, 157.7, 156.6, 140.2, 130.7, 130.5 (2C), 124.2, 119.5 (2C), 114.2, 114.0, 109.2, 41.4; FT-IR (neat): ṽ [cm^{-1}]= 688, 743, 768, 790, 818, 882, 895, 938, 967, 1130, 1165, 1211, 1246, 1286, 1445, 1478, 1557, 1594, 1679, 2832, 3040.

6r [(4-Cyclohexylphenyl)carbamoyl]methanaminium chloride

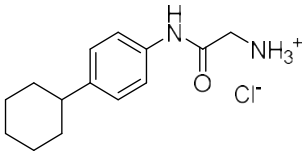

According to the general procedure (III), amine hydrochloride **6r** was obtained from **5r** as a colourless solid (124 mg, 92%). mp: 242 °C; ^{1}H NMR (300 MHz, DMSO-d_6) δ= 10.70 (s, 1H), 8.55 – 8.03 (m, 3H), 7.51 (d, J = 8.2 Hz, 2H), 7.17 (d, J = 8.2 Hz, 2H), 3.77 (d, J = 5.7 Hz, 2H), 2.48 – 2.36 (m, 1H), 1.88 – 1.58 (m, 6H), 1.42 – 1.28 (m, 4H); ^{13}C NMR (75 MHz, DMSO-d_6) δ= 164.9, 143.5, 136.5 (2C), 127.4 (2C), 119.6, 43.6, 41.3, 34.4 (2C), 26.8 (2C), 26.0; FT-IR (neat): ṽ [cm^{-1}]= 827, 894, 939, 1258, 1316, 1416, 1447, 1511, 1549, 1605, 1681, 2849, 2921.

6s [(Naphthalen-1-yl)carbamoyl]methanaminium chloride

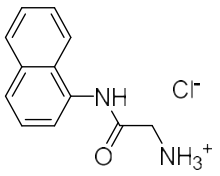

According to the general procedure (III), amine hydrochloride **6s** was obtained from **5s** as a colourless solid (104 mg, 87%). mp: 245 °C; ^{1}H NMR (300 MHz, DMSO-d_6) δ= 10.71 (s, 1H), 8.40 (s, 3H), 8.25 – 8.11 (m, 1H), 8.00 – 7.87 (m, 1H), 7.80 (d, J = 8.1 Hz, 1H), 7.71 (d, J = 7.4 Hz, 1H), 7.62 – 7.45 (m, 3H), 4.00 (s, 2H); ^{13}C NMR (75 MHz, DMSO-d_6) δ= 166.2, 134.1, 133.1, 128.5, 128.0, 126.6, 126.4, 126.2, 126.0, 123.4, 121.9, 41.3; FT-IR (neat): ṽ [cm^{-1}]= 771, 798, 890, 959, 1251, 1272, 1395, 1465, 1508, 1541, 1599, 1669, 3000.

6t {[(Thiophen-2-yl)methyl]carbamoyl}methanaminium chloride

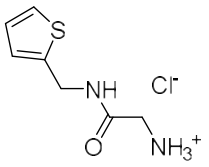

According to the general procedure (III), amine hydrochloride **6t** was obtained from **5t** as a colourless solid (101 mg, 97%). mp: 203 °C; ^{1}H NMR (300 MHz, DMSO-d_6) δ= 9.15 (t, J = 5.9 Hz, 1H), 8.30 (d, J = 7.6 Hz, 3H), 7.41 (dd, J = 5.1 Hz, 1H), 7.02 (d, J = 3.3 Hz, 1H), 6.96 (dd, J = 5.1, 3.3 Hz, 1H), 4.48 (d, J = 5.9 Hz, 2H), 3.55 (q, J = 5.9 Hz, 2H); ^{13}C NMR (75 MHz, DMSO-d_6) δ= 166.1, 141.7, 127.2, 126.4, 125.7, 40.7, 37.6; FT-IR (neat): ṽ [cm^{-1}]= 682, 700, 713, 748, 845, 915, 988, 1064, 1138, 1158, 1216, 1266, 1394, 1424, 1495, 1556, 1650, 2612, 2708, 2798, 3117.

6u [(Adamantan-2-yl)carbamoyl]methanaminium chloride

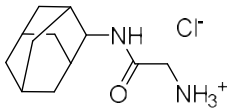

According to the general procedure (III), amine hydrochloride **6u** was obtained from **5u** as a colourless solid (120 mg, 98%). mp: 190 °C; ^{1}H NMR (300 MHz, DMSO-d_6) δ= 8.38 (d, J = 7.5 Hz, 1H), 8.16 (s, 3H), 3.89 (d, J = 7.5 Hz, 1H), 3.72 – 3.50 (m, 2H), 2.01 (d, J = 12.8 Hz, 2H), 1.88 – 1.60 (m, 10H), 1.49 (d, J = 12.8 Hz, 2H); ^{13}C NMR (75 MHz, DMSO-d_6) δ= 166.0, 54.2, 37.9, 37.5 (2C), 32.3 (4C), 31.7 (2C), 27.5; FT-IR (neat): ṽ [cm^{-1}]= 931, 943, 1105, 1266, 1296, 1453, 1497, 1552, 1652, 1670, 2904.

6v (Dicyclohexylcarbamoyl)methanaminium chloride

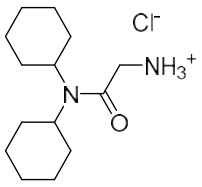

According to the general procedure (III), amine hydrochloride **6v** was obtained from **5v** as a colourless solid (125 mg, 91%). mp: 181 °C; ^{1}H NMR (300 MHz, DMSO-d_6) δ= 8.18 (s, 3H), 3.92 – 3.71 (m, 2H), 3.55 – 3.16 (m, 2H), 1.82 – 0.93 (m, 20H); ^{13}C NMR (75 MHz, DMSO-d_6) δ= 164.9, 56.5, 55.3 (2C), 30.5 (2C), 30.0 (2C), 26.2 (2C), 25.6 (2C), 24.9 (2C); FT-IR (neat): ṽ [cm^{-1}]= 763, 824, 895, 995, 1126, 1182, 1245, 1271, 1307, 1381, 1446, 1645, 2845, 2928.

General procedure (IV) to deprotect Cbz-amines (10a,b)

To a solution of the Cbz-protected amines **9a,b** (0.50 mmol) in MeOH (20 mL) Pd/C (20 mg) was added. The reaction mixture was stirred for 16 h under H_2-atmosphere (60 psi) at room temperature. Subsequentially, the catalyst was filtered off and the solvent was removed *in vacuo* to afford **10a** and **10b** as colourless oils.

10a *tert*-Butyl (*R*)-3-amino-3-[(3-phenoxyphenyl)carbamoyl]propanoate

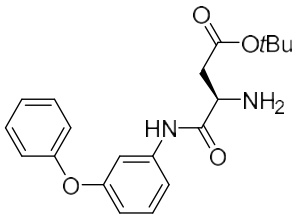

According to the general procedure (IV), amine **10a** was obtained from **9a** as a colourless oil (165 mg, 92%). $[\alpha]_{D23}$=+72 °(*c*=10 in chloroform); ^{1}H NMR (300 MHz, DMSO-d_6) δ= 10.03 (s, 1H), 7.45 – 7.33 (m, 4H), 7.30 (t, *J* = 8.0 Hz, 1H), 7.19 – 7.09 (m, 1H), 7.04 – 6.98 (m, 2H), 6.75 – 6.64 (m, 1H), 3.66 – 3.55 (m, 1H), 2.65 – 2.33 (m, 2H), 1.36 (s, 9H); ^{13}C NMR (75 MHz, DMSO-d_6) δ= 173.8, 171.0, 157.8, 157.3, 141.3, 130.8 (2C), 130.2, 124.3, 119.6 (2C), 114.8, 114.1, 109.9, 81.2, 51.8, 39.5, 27.8 (3C); FT-IR (neat): ṽ [cm^{-1}]= 688, 748, 794, 845, 878, 1140, 1218, 1250, 1367, 1438, 1487, 1514, 1586, 1671, 1711.

10b *tert*-Butyl (*S*)-3-[(adamantan-1-yl)carbamoyl]-3-aminopropanoate

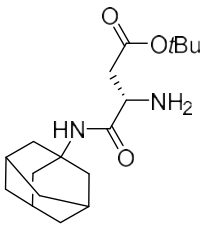

According to the general procedure (IV), amine **10b** was obtained from **9b** as a colourless oil (160 mg, 99%). $[\alpha]_{D23}$=−52 °(*c*=10 in chloroform); ^{1}H NMR (300 MHz, DMSO-d_6) δ= 7.72 – 7.22 (m, 1H), 3.42 – 3.30 (m, 1H), 2.47 – 2.06 (m, 2H), 2.00 (s, 3H), 1.90 (s, 6H), 1.60 (s, 6H), 1.39 (s, 9H); ^{13}C NMR (75 MHz, DMSO-d_6) δ= 173.1, 172.5, 77.3, 50.7, 49.0, 41.3 (3C), 40.7, 36.4 (3C), 29.2 (3C), 28.2 (3C); FT-IR (neat): ṽ [cm^{-1}]= 726, 813, 842, 1038, 1146, 1257, 1310, 1359, 1392, 1454, 1522, 1655, 1679, 1730, 2905.

1 *N*-(Adamantan-1-yl)-2-(3-oxobenzo[*d*]isothiazol-2(3*H*)-yl) acetamide

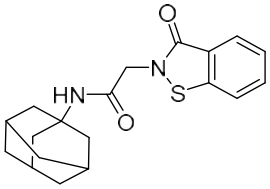

A solution of **3a** (80 mg, 0.40 mmol), **6a** (73 mg, 0.30 mmol), TBTU (128 mg, 0.40 mmol), DIPEA (0.28 mL, 1.60 mmol) in dimethylformamide (1 mL) was stirred 16 h at room temperature. LiOH (958 mg, 40.0 mmol) in water (10 mL) was added and the reaction was stirred for 4 h at 60 °C. The reaction was cooled to 0 °C and the precipitate was isolated by filtration. Purification by column chromatography (CH/EA 3:1) afforded the title compound **1** as a colourless solid (77 mg, 75%).[3] mp: 205 °C; ^{1}H NMR (300 MHz, DMSO-d_6) δ= 7.95 (d, *J* = 7.9 Hz, 1H), 7.87 (d, *J* = 7.9 Hz, 1H), 7.77 (s, 1H), 7.74 – 7.62 (m, 1H), 7.43 (t, *J* = 7.5 Hz, 1H), 4.38 (s, 2H), 2.01 (s, 3H), 1.93 (s, 6H), 1.61 (s, 6H); ^{13}C NMR (75 MHz, DMSO-d_6) δ= 165.8, 165.2, 141.9, 132.3, 126.0, 125.7, 123.9, 122.0, 51.6, 46.3, 41.4 (3C), 36.4 (3C), 29.2 (3C); FT-IR (neat): ṽ [cm^{-1}]= 702, 738, 998, 1035, 1237, 1293, 1359, 1432, 1536, 1626, 2904, 3280; ESI-MS *m/z*: $[M+H]^+$ 343.16 (100%), 344.12 (20.7%), 345.16 (7.0%); purity (HPLC)= 95%.

15 *tert*-Butyl *N*-[(2*S*)-1-[(2*S*)-2-(hydrazinecarbonyl)pyrrolidin-1-yl]-4-methyl-1-oxopentan-2-yl]carbamate

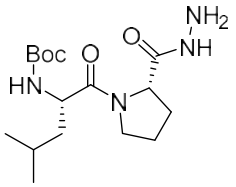

To a solution of **14** (982 mg, 2.35 mmol) in methanol (5 mL) hydrazine hydrate (0.63 mL, 20.0 mmol) was added and the mixture was stirred for 16 h at room temperature. The solvent was evaporated, and the residual was purified by silica column chromatography (CH/EA/MeOH 10:10:1) to afford **15** as a colourless solid (600 mg, 74%). mp: 51 °C; $[\alpha]_{D23}$=−43 °(*c*=10 in chloroform); ^{1}H NMR (300 MHz, DMSO-d_6) δ= 9.02 – 8.90 (m, 1H), 7.38 – 7.27 (m, 3H), 4.28 – 4.16 (m, 2H), 3.68 – 3.48 (m, 2H), 2.07 – 1.81 (m, 2H), 1.80 – 1.46 (m, 5H), 1.35 (s, 9H), 0.88 (d, *J* = 6.6 Hz, 6H); ^{13}C NMR (75 MHz, DMSO-d_6) δ= 171.6, 171.3, 155.9, 142.9, 78.3, 63.3, 58.6, 50.7, 29.6, 28.6 (3C), 25.0, 24.5, 23.7 (2C); FT-IR (neat): ṽ [cm^{-1}]= 875, 920, 1022, 1045, 1164, 1248, 1366, 1435, 1521, 1633, 2957, 3288.

16b (2*Z*)-4-{[(2*S*)-1-[(2*S*)-4-Methyl-2-(methylamino)pentanoyl]pyrrolidin-2-yl]formohydrazido}-4-oxobut-2-enoic acid

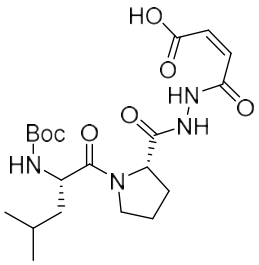

To a solution of **15** (77 mg, 0.3 mmol) in glacial acetic acid (1.0 mL) maleic anhydride (29 mg, 0.3 mmol) was added, and the reaction was stirred for 16 h at room temperature. The crude product was filtered off, purified by preparative HPLC (ACN/H_2O 30:70) and lyophilized to afford **16b** as colourless solid (84 mg, 79%). mp: 167 °C; $[\alpha]_{D23}$=−102 °(*c*=10 in chloroform); ^{1}H NMR (300 MHz, DMSO-d_6) δ= 13.36 (s, 1H), 10.64 (s, 1H), 10.21 (s, 1H), 6.89 (d, *J* = 8.1 Hz, 1H), 6.36 (d, *J* = 12.2 Hz, 1H), 6.26 (d, *J* = 12.2 Hz, 1H), 4.45 – 4.32 (m, 1H), 4.30 – 4.11 (m, 1H), 3.74 – 3.43 (m, 2H), 2.19 – 1.77 (m, 3H), 1.75 – 1.51 (m, 1H), 1.36 (s, 12H), 0.88 (d, *J* = 6.5 Hz, 6H); ^{13}C NMR (75 MHz, DMSO-d_6) δ= 171.4, 170.6, 167.2, 162.8, 155.9, 133.4, 127.3, 78.3, 58.2, 50.7, 46.7, 41.5, 29.5, 28.6 (3C), 25.0, 24.5, 23.7 (2C); FT-IR (neat): ṽ [cm^{-1}]= 668, 848, 1046, 1162, 1248, 1367, 1392, 1451, 1506, 1625, 1704; ESI-MS *m/z*: [M+Na]$^+$ 463.20 (100%), 464.20 (25.4%), 465.20 (4.35%); purity (HPLC)= 98%.

General procedure (V) to synthesize asymmetric disulfanylbenzamides (7a–ζ, 11a,b & 16a)

Disulfanylbenzoic acid **3a–g** (0.30 mmol), the corresponding amine component (**6a–v, 10a,b & 15**) (0.30 mmol), TBTU (96 mg, 0.30 mmol) and DIPEA (0.21 mL, 1.20 mmol) were suspended in ethyl acetate (10 mL) and stirred for 16 h at room temperature. The organic phase was extracted with $NaHCO_3$ sat., HCl (1 M) and purified by silica column chromatography (isocratic, CH/EA 5:1–1:2). Evaporation of the solvent and lyophilization from ACN/H_2O (1:1) yielded the corresponding asymmetric disulfanylbenzamides (**7a–ζ, 11a,b & 16a**).

7a 2-{[2-(Ethyldisulfanyl)phenyl]formamido}-*N*-(3-phenoxyphenyl)acetamide

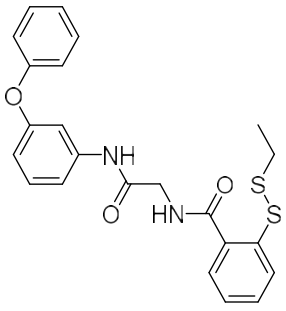

According to the general procedure (V), disulfanylbenzamide **7a** was obtained from **3d** and **6q** as a colourless solid (57 mg, 43%). mp: 125 °C; ^{1}H NMR (300 MHz, DMSO-d_6) δ= 10.16 (s, 1H), 8.84 (t, *J* = 5.9 Hz, 1H), 8.01 (d, *J* = 8.1 Hz, 1H), 7.71 (d, *J* = 7.7 Hz, 1H), 7.57 (t, *J* = 7.7 Hz, 1H), 7.45 – 7.27 (m, 6H), 7.20 – 7.09 (m, 1H), 7.09 – 6.96 (m, 2H), 6.77 – 6.66 (m, 1H), 4.02 (d, *J* = 5.9 Hz, 2H), 2.72 (q, *J* = 7.3 Hz, 2H), 1.20 (t, *J* = 7.3 Hz, 3H); ^{13}C NMR (75 MHz, DMSO-d_6) δ= 168.5, 168.1, 157.9, 157.2, 141.3, 138.9, 133.6, 132.0, 131.0, 130.9 (2C), 129.0, 126.9, 126.4, 124.4, 119.7 (2C), 114.72, 114.15, 109.76, 43.98, 32.28, 14.94; FT-IR (neat): ṽ [cm^{-1}]= 690, 738, 870, 939, 993, 1145, 1162, 1217, 1257, 1292, 1314, 1431, 1443, 1456, 1485, 1533, 1557, 1588, 1622, 1677; ESI-MS *m/z*: [M+H]$^+$ 439.15 (100%), 440.16 (25.3%), 441.16 (11.3%); purity (HPLC)= 99%.

7b *N*-(Cyclohexylmethyl)-2-{[2-(ethyldisulfanyl)phenyl]formamido}acetamide

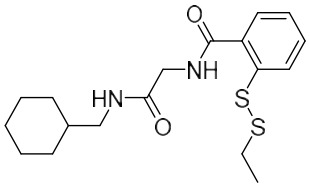

According to the general procedure (V), disulfanylbenzamide **7b** was obtained from **3d** and **6o** as a colourless solid (64 mg, 58%). mp: 104 °C; ^{1}H NMR (300 MHz, DMSO-d_6) δ= 8.72 (t, J = 5.9 Hz, 1H), 8.00 (d, J = 8.0 Hz, 1H), 7.83 (t, J = 6.0 Hz, 1H), 7.70 (d, J = 8.0 Hz, 1H), 7.56 (t, J = 7.5 Hz, 1H), 7.31 (t, J = 7.5 Hz, 1H), 3.83 (d, J = 5.9 Hz, 2H), 2.93 (t, J = 6.3 Hz, 2H), 2.72 (q, J = 7.3 Hz, 2H), 1.79 – 1.50 (m, 5H), 1.50 – 1.29 (m, 1H), 1.21 (t, J = 7.3 Hz, 3H), 1.17 – 1.06 (m, 3H), 0.98 – 0.73 (m, 2H); ^{13}C NMR (75 MHz, DMSO-d_6) δ= 168.9, 167.5, 138.4, 133.5, 131.5, 128.6, 126.4, 125.9, 45.2, 42.9, 37.9, 31.8, 30.8 (2C), 26.5, 25.9 (2C), 14.5; FT-IR (neat): ṽ [cm^{-1}]= 698, 728, 752, 996, 1032, 1244, 1277, 1338, 1363, 1375, 1416, 1435, 1453, 1523, 1539, 1557, 1586, 1620, 1660, 1682, 2924, 3266; ESI-MS *m/z*: [M+H]$^{+}$ 367.21 (100%), 368.21 (23.7%), 369.20 (10.5%); purity (HPLC)= 99%.

7c *N*,*N*-Dicyclohexyl-2-{[2-(ethyldisulfanyl)phenyl]formamido}acetamide

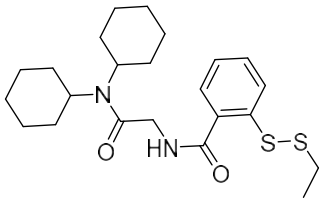

According to the general procedure (V), disulfanylbenzamide **7c** was obtained from **3d** and **6v** as a colourless solid (43 mg, 33%). mp: 91 °C; ^{1}H NMR (300 MHz, DMSO-d_6) δ= 8.43 (t, J = 5.5 Hz, 1H), 8.04 – 7.95 (m, 1H), 7.70 (d, J = 7.7 Hz, 1H), 7.56 (t, J = 7.7 Hz, 1H), 7.31 (t, J = 7.5 Hz, 1H), 4.10 (d, J = 5.5 Hz, 2H), 3.64 – 3.39 (m, 1H), 3.16 – 2.86 (m, 1H), 2.72 (q, J = 7.3 Hz, 2H), 2.43 – 2.17 (m, 2H), 1.84 – 1.25 (m, 11H), 1.21 (t, J = 7.3 Hz, 3H), 1.17 – 0.87 (m, 7H); ^{13}C NMR (75 MHz, DMSO-d_6) δ= 172.4, 167.1, 138.3, 133.6, 131.4, 128.5, 126.4, 126.0, 56.3, 55.2, 42.5, 31.9, 31.0 (2C), 30.2 (2C), 26.8 (2C), 26.3, 25.1 (2C), 21.5, 14.5; FT-IR (neat): ṽ [cm^{-1}]= 668, 684, 718, 743, 781, 835, 1214, 1304, 1509, 1541, 1636, 1672, 2342, 2363, 3279; ESI-MS *m/z*: [M+H]$^{+}$ 435.31 (100%), 436.31 (24.9%), 437.31 (12.2%); purity (HPLC)= 96%.

7d 2-{[2-(Ethyldisulfanyl)phenyl]formamido}-*N*-(4-fluorophenyl)acetamide

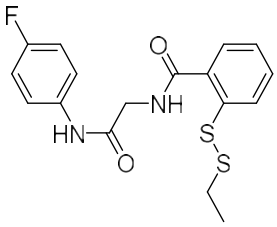

According to the general procedure (V), disulfanylbenzamide **7d** was obtained from **3d** and **6m** as a colourless solid (52 mg, 47%). mp: 144 °C; ^{1}H NMR (300 MHz, DMSO-d_6) δ= 10.73 (s, 1H), 9.47 (t, J = 5.8 Hz, 1H), 8.65 – 8.58 (m, 1H), 8.33 (d, J = 7.8 Hz, 1H), 8.28 – 8.10 (m, 3H), 7.93 (t, J = 7.5 Hz, 1H), 7.75 (t, J = 8.9 Hz, 2H), 4.69 – 4.56 (m, 2H), 3.40 – 3.27 (m, 2H), 1.88 – 1.75 (m, 3H); ^{13}C NMR (75 MHz, DMSO-d_6) δ= 172.4, 167.8, 167.7, 138.5, 135.7, 133.3, 131.6, 128.6, 126.5, 126.0, 121.3 (d, 2C, J_{CF} = 8.1 Hz), 115.7 (d, 2C, J_{CF} = 22.4 Hz), 43.5, 31.8, 21.5; FT-IR (neat): ṽ [cm^{-1}]= 668, 684, 718, 743, 781, 835, 1214, 1304, 1509, 1541, 1636, 1672, 3279; ESI-MS *m/z*: [M+Na]$^{+}$ 387.15 (100%), 388.15 (16.6%), 389.15 (7.4%); purity (HPLC)= 99%.

7e *N*-(Adamantan-1-yl)-2-{[2-(methyldisulfanyl)phenyl]formamido}acetamide

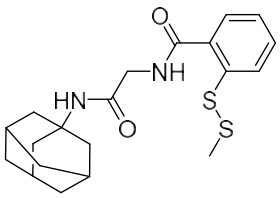

According to the general procedure (V), disulfanylbenzamide **7e** was obtained from **3a** and **6a** as a colourless solid (71 mg, 60%). mp: 112 °C; ^{1}H NMR (300 MHz, DMSO-d_6) δ= 7.96 (t, J = 8.6 Hz, 1H), 7.86 (d, J = 7.8 Hz, 1H), 7.76 (s, 1H), 7.71 – 7.65 (m, 1H), 7.43 (t, J = 7.5 Hz, 1H), 7.34 (d, J = 6.7 Hz, 1H), 4.37 (s, 2H), 3.29 (s, 3H), 1.99 (d, J = 5.6 Hz, 3H), 1.93 (s, 6H), 1.61 (s, 6H); ^{13}C NMR (75 MHz, DMSO-d_6) δ= 168.8, 165.8, 142.7, 137.5, 133.6, 126.1, 124.4, 122.2, 51.6, 46.2, 41.4 (3C), 40.9, 36.4 (3C), 29.2 (3C); FT-IR (neat): ṽ [cm^{-1}]= 669, 684, 739, 784, 1100, 1196, 1236, 1276, 1293, 1343, 1359, 1417, 1448, 1548, 1593, 1644, 1675, 2851, 2882, 2919, 3291; ESI-MS *m/z*: [M+H]$^{+}$ 391.14 (100%), 392.11 (22.8%), 393.15 (10.4%); purity (HPLC)= 95%.

7f *N*-(Adamantan-1-yl)-2-{[2-(ethyldisulfanyl)phenyl]formamido}acetamide

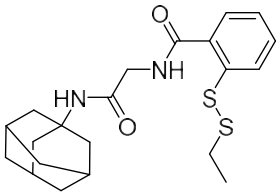

According to the general procedure (V), disulfanylbenzamide **7f** was obtained from **3d** and **6a** as a colourless solid (108 mg, 89%). mp: 121 °C; ^{1}H NMR (300 MHz, DMSO-d_6) δ= 8.60 (t, J = 5.9 Hz, 1H), 7.98 (d, J = 8.1 Hz, 1H), 7.64 (d, J = 7.6 Hz, 1H), 7.61 – 7.50 (m, 1H), 7.38 – 7.22 (m, 2H), 3.78 (d, J = 5.9 Hz, 2H), 2.73 (q, J = 7.3 Hz, 2H), 2.01 (s, 3H), 1.97 – 1.90 (m, 6H), 1.66 – 1.57 (m, 6H), 1.21 (t, J = 7.3 Hz, 3H); ^{13}C NMR (75 MHz, DMSO-d_6) δ= 167.9, 167.5, 138.1, 133.8, 131.4, 128.5, 126.5, 126.1, 51.3, 43.1, 41.5 (3C), 36.4 (3C), 31.9, 29.2 (3C), 14.5; FT-IR (neat): ṽ [cm^{-1}]= 703, 734, 990, 1000, 1240, 1259, 1295, 1313, 1330, 1360, 1412, 1432, 1448, 1541, 1591, 1627, 1668, 2849, 2907; ESI-MS *m/z*: [M+H]$^+$ 405.13 (100%), 406.11 (22.3%), 407.13 (11.6%); purity (HPLC)= 98%.

7g (2*S*)-*N*-(Adamantan-1-yl)-1-[2-(methyldisulfanyl)benzoyl]pyrrolidine-2-carboxamide

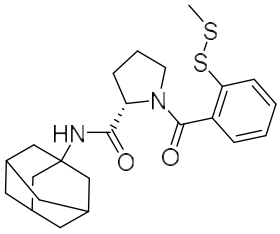

According to the general procedure (V), disulfanylbenzamide **7g** was obtained from **3a** and **6b** as a colourless solid (60 mg, 46%). mp: 78 °C; [α]$_{D23}$=−78 °(c=10 in chloroform); ^{1}H NMR (300 MHz, DMSO-d_6) δ= 7.86 – 7.71 (m, 1H), 7.55 – 7.43 (m, 1H), 7.42 – 7.00 (m, 3H), 4.51 – 3.86 (m, 1H), 3.64 – 3.43 (m, 1H), 3.28 – 2.93 (m, 1H), 2.46 (s, 3H), 2.15 – 1.46 (m, 16H), 1.39 – 1.03 (m, 3H); ^{13}C NMR (75 MHz, DMSO-d_6) δ= 170.5, 170.0, 166.6, 137.2, 136.9, 133.3, 133.1, 130.0, 129.6, 128.2, 127.6, 127.3, 126.9, 126.7, 59.6, 58.1, 50.7, 50.2, 48.9, 47.3, 36.0, 35.9, 32.1, 31.6, 29.4, 28.8, 28.6, 24.4, 22.6; FT-IR (neat): ṽ [cm^{-1}]= 690, 747, 768, 953, 1034, 1094, 1233, 1292, 1311, 1343, 1359, 1415, 1538, 1586, 1620, 2848, 2905; ESI-MS *m/z*: [M+H]$^+$ 431.18 (100%), 432.13 (28.6%), 433.18 (10.6%); purity (HPLC)= 99%.

7h *N*-(Adamantan-1-yl)-2-{1-[2-(ethyldisulfanyl)phenyl]-*N*-methylformamido}acetamide

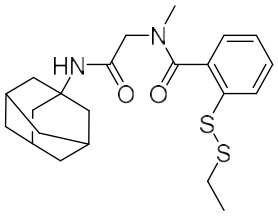

According to the general procedure (V), disulfanylbenzamide **7h** was obtained from **3d** and **6g** as a colourless solid (82 mg, 65%). mp: 73 °C; ^{1}H NMR (300 MHz, DMSO-d_6) δ= 7.80 (t, J = 8.3 Hz, 1H), 7.55 – 7.41 (m, 1H), 7.41 – 7.11 (m, 3H), 4.02 (s, 1H), 3.61 (s, 1H), 3.34 (s, 3H), 2.86 – 2.69 (m, 2H), 2.11 – 1.89 (m, 6H), 1.88 – 1.81 (m, 3H), 1.61 (d, J = 12.0 Hz, 6H), 1.23 (t, J = 7.3 Hz, 3H); ^{13}C NMR (75 MHz, DMSO-d_6) δ= 169.1, 166.9, 136.6, 134.3, 130.1, 128.4, 127.6, 127.2, 51.4, 50.7, 41.3 (3C), 36.4 (3C), 34.0, 31.6, 29.2 (3C), 14.4; FT-IR (neat): ṽ [cm^{-1}]= 668, 688, 747, 996, 1033, 1049, 1084, 1093, 1233, 1273, 1292, 1343, 1359, 1398, 1449, 1540, 1586, 1622, 1681, 2849, 2906; ESI-MS *m/z*: [M+H]$^+$ 419.13 (100%), 420.13 (28.2%), 421.12 (10.2%); purity (HPLC)= 98%.

7i *N*-(4-Cyclohexylphenyl)-2-{[2-(ethyldisulfanyl)phenyl]formamido}acetamide

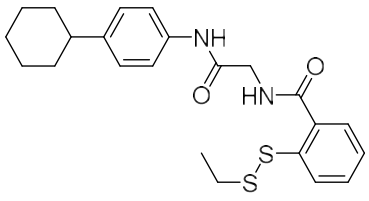

According to the general procedure (V), disulfanylbenzamide **7i** was obtained from **3d** and **6r** as a colourless solid (69 mg, 53%). mp: 136 °C; ^{1}H NMR (300 MHz, DMSO-d_6) δ= 9.97 (s, 1H), 8.84 (t, J = 5.8 Hz, 1H), 8.01 (d, J = 8.1 Hz, 1H), 7.73 (d, J = 7.8 Hz, 1H), 7.63 – 7.53 (m, 1H), 7.50 (d, J = 8.3 Hz, 2H), 7.33 (t, J = 7.5 Hz, 1H), 7.15 (d, J = 8.3 Hz, 2H), 4.03 (d, J = 5.8 Hz, 2H), 2.72 (q, J = 7.3 Hz, 2H), 2.49 – 2.35 (m, 1H), 1.88 – 1.60 (m, 5H), 1.47 – 1.24 (m, 5H), 1.21 (t, J = 7.3 Hz, 3H); ^{13}C NMR (75 MHz, DMSO-d_6) δ= 167.7, 167.6, 143.0, 138.5, 137.1, 133.4, 131.5, 128.6, 127.2, 126.5 (2C), 126.0, 119.6 (2C), 43.6, 43.5, 34.5 (2C), 31.9, 26.8 (2C), 26.0, 14.5; FT-IR (neat): ṽ [cm^{-1}]= 698, 735, 990, 1000, 1033, 1240, 1262, 1295, 1312, 1333, 1360, 1412, 1432, 1454, 1497, 1540, 1591, 1624, 1668, 2850, 2905; ESI-MS *m/z*: [M+H]$^+$ 429.41 (100%), 430.41 (2.9%), 431.41 (11.5%); purity (HPLC)= 98%.

7j 2-{[2-(Ethyldisulfanyl)phenyl]formamido}-*N*-(naphthalen-1-yl)acetamide

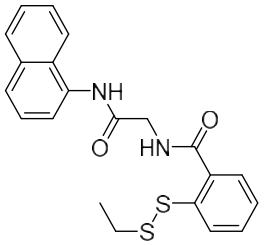

According to the general procedure (V), disulfanylbenzamide **7j** was obtained from **3d** and **6s** as a colourless solid (29 mg, 24%). mp: 99 °C; ^{1}H NMR (300 MHz, DMSO-d_6) δ= 10.05 (s, 1H), 8.97 (t, *J* = 5.8 Hz, 1H), 8.20 – 8.10 (m, 1H), 8.03 (d, *J* = 8.1 Hz, 1H), 7.99 – 7.89 (m, 1H), 7.78 (dd, *J* = 8.1, 5.0 Hz, 2H), 7.69 (d, *J* = 7.4 Hz, 1H), 7.64 – 7.44 (m, 4H), 7.34 (t, *J* = 7.4 Hz, 1H), 4.22 (d, *J* = 5.8 Hz, 2H), 2.73 (q, *J* = 7.4 Hz, 2H), 1.21 (t, *J* = 7.4 Hz, 3H); ^{13}C NMR (75 MHz, DMSO-d_6) δ= 169.3, 168.4, 139.1, 134.7, 134.3, 133.9, 132.1, 129.2, 129.0, 128.8, 127.0, 126.8, 126.5 (2C), 126.4, 125.0, 123.9, 122.6, 44.1, 32.4, 15.0; FT-IR (neat): ṽ [cm^{-1}]= 688, 704, 741, 763, 780, 791, 798, 1256, 1274, 1389, 1433, 1503, 1535, 1622, 1656, 3266; ESI-MS *m/z*: [M+H]$^{+}$ 397.12 (100%), 398.12 (29.5%), 399.09 (11.9%); purity (HPLC)= 98%.

7k 2-{[2-(Ethyldisulfanyl)phenyl]formamido}-*N*-[(thiophen-2-yl)methyl]acetamide

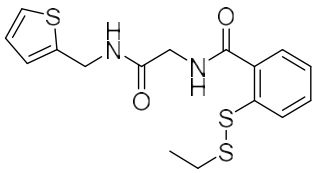

According to the general procedure (V), disulfanylbenzamide **7k** was obtained from **3d** and **6t** as a colourless solid (42 mg, 38%). mp: 83 °C; ^{1}H NMR (300 MHz, DMSO-d_6) δ= 8.79 (t, *J* = 6.0 Hz, 1H), 8.53 (t, *J* = 5.9 Hz, 1H), 8.01 (d, *J* = 8.1 Hz, 1H), 7.74 (d, *J* = 7.8 Hz, 1H), 7.64 – 7.50 (m, 1H), 7.38 (d, *J* = 5.0 Hz, 1H), 7.32 (t, *J* = 7.5 Hz, 1H), 7.03 – 6.90 (m, 2H), 4.46 (d, *J* = 5.9 Hz, 2H), 3.87 (d, *J* = 5.9 Hz, 2H), 2.72 (q, *J* = 7.3 Hz, 2H), 1.21 (t, *J* = 7.3 Hz, 3H); ^{13}C NMR (75 MHz, DMSO-d_6) δ= 168.9, 167.6, 142.6, 138.5, 133.3, 131.5, 128.7, 127.0, 126.4, 125.9 (2C), 125.4, 42.9, 37.6, 31.8, 14.5; FT-IR (neat): ṽ [cm^{-1}]= 695, 728, 758, 789, 850, 1039, 1224, 1250, 1367, 1433, 1529, 1585, 1619, 1682, 3278, 3331; ESI-MS *m/z*: [M+H]$^{+}$ 367.09 (100%), 368.09 (20.6%), 369.09 (14.8%); purity (HPLC)= 99%.

7l *N*-(Adamantan-2-yl)-2-{[2-(ethyldisulfanyl)phenyl]formamido}acetamide

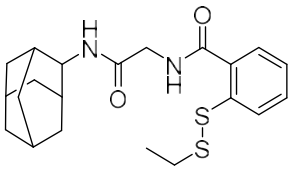

According to the general procedure (V), disulfany benzamide **7l** was obtained from **3d** and **6u** as a colourless solid (48 mg, 39%). mp: 97 °C; ^{1}H NMR (300 MHz, DMSO-d_6) δ= 8.70 (t, *J* = 6.0 Hz, 1H), 7.99 (d, *J* = 8.1 Hz, 1H), 7.72 – 7.61 (m, 2H), 7.60 – 7.51 (m, 1H), 7.31 (t, *J* = 7.5 Hz, 1H), 3.95 – 3.79 (m, 3H), 2.73 (q, *J* = 7.3 Hz, 2H), 2.03 – 1.90 (m, 2H), 1.86 – 1.72 (m, 8H), 1.69 (s, 2H), 1.51 (d, *J* = 12.7 Hz, 2H), 1.21 (t, *J* = 7.3 Hz, 3H); ^{13}C NMR (75 MHz, DMSO-d_6) δ= 168.3, 167.7, 138.1, 133.8, 131.5, 128.5, 126.6, 126.1, 53.5, 43.1, 37.5, 37.2, 31.9 (4C), 31.4 (2C), 27.2 (2C), 14.5; FT-IR (neat): ṽ [cm^{-1}]= 699, 736, 991, 1000, 1033, 1239, 1295, 1330, 1360, 1412, 1432, 1455, 1497, 1537, 1590, 1626, 1668, 2850, 2905; ESI-MS *m/z*: [M+H]$^{+}$ 405.26 (100%), 406.26 (24.0%), 407.26 (10.4%); purity (HPLC)= 99%.

7m *N*-(Adamantan-1-yl)-2-{[2-(*tert*-butyldisulfanyl)phenyl]formamido}acetamide

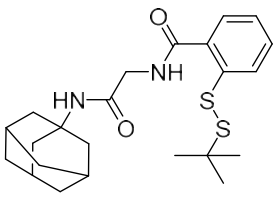

According to the general procedure (V), disulfanylbenzamide **7m** was obtained from **3f** and **6a** as a colourless solid (83 mg, 63%). mp: 128 °C; ^{1}H NMR (300 MHz, DMSO-d_6) δ= 8.61 (t, *J* = 6.0 Hz, 1H), 8.01 (d, *J* = 8.1 Hz, 1H), 7.59 (d, *J* = 7.6 Hz, 1H), 7.56 – 7.44 (m, 1H), 7.33 – 7.23 (m, 2H), 3.79 (d, *J* = 6.0 Hz, 2H), 2.09 – 1.97 (m, 3H), 1.97 – 1.87 (m, 6H), 1.66 – 1.54 (m, 6H), 1.25 (s, 9H); ^{13}C NMR (75 MHz, DMSO-d_6) δ= 167.9, 167.6, 138.7, 134.0, 131.0, 128.3, 126.9, 126.0, 51.2, 49.3, 43.3, 41.5 (3C), 36.4 (3C), 29.9 (3C), 29.2 (3C); FT-IR (neat): ṽ [cm^{-1}]= 702, 733, 989, 1000, 1165, 1240, 1261, 1295, 1330, 1360, 1411, 1431, 1456, 1545, 1591, 1625, 1667, 2850, 2911, 3347; ESI-MS *m/z*: [M+H]$^{+}$ 433.17 (100%), 434.15 (28.1%), 435.16 (12.9%); purity (HPLC)= 97%.

7n 2-{[2-(Ethyldisulfanyl)phenyl]formamido}-*N*-(2-methylpropyl)acetamide

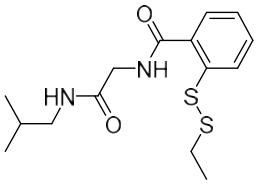

According to the general procedure (V), disulfanylbenzamide **7n** was obtained from **3d** and **6p** as a colourless solid (46 mg, 47%). mp: 74 °C; ^{1}H NMR (300 MHz, DMSO-d_6) δ= 8.72 (t, *J* = 5.9 Hz, 1H), 8.00 (d, *J* = 8.0 Hz, 1H), 7.86 (t, *J* = 6.1 Hz, 1H), 7.71 (d, *J* = 7.7 Hz, 1H), 7.56 (t, *J* = 7.7 Hz, 1H), 7.31 (t, *J* = 7.5 Hz, 1H), 3.84 (d, *J* = 5.9 Hz, 2H), 2.92 (t, *J* = 6.4 Hz, 2H), 2.72 (q, *J* = 7.3 Hz, 2H), 1.70 (hept, *J* = 6.7 Hz, 1H), 1.21 (t, *J* = 7.3 Hz, 3H), 0.84 (d, *J* = 6.7 Hz, 6H); ^{13}C NMR (75 MHz, DMSO-d_6) δ= 168.9, 167.5, 138.4, 133.5, 131.5, 128.6, 126.4, 125.9, 46.5, 42.9, 31.8, 28.5, 20.5 (2C), 14.5; FT-IR (neat): ṽ [cm^{-1}]= 700, 1035, 1132, 1165, 1236, 1280, 1332, 1368, 1387, 1411, 1431, 1458, 1524, 1590, 1629, 1656, 2923, 2952; ESI-MS *m/z*: [M+H]$^{+}$ 327.12 (100%), 328.12 (21.3%), 329.22 (9.7%); purity (HPLC)= 99%.

7o *N*-(Adamantan-1-yl)-2-{[2-(propan-2-yldisulfanyl)phenyl]formamido}acetamide

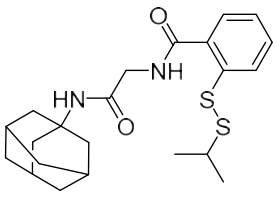

According to the general procedure (V), disulfanylbenzamide **7o** was obtained from **3e** and **6a** as a colourless solid (75 mg, 59%). mp: 107 °C; ^{1}H NMR (300 MHz, DMSO-d_6) δ= 8.60 (t, *J* = 6.0 Hz, 1H), 7.98 (d, *J* = 8.2 Hz, 1H), 7.63 (d, *J* = 7.7 Hz, 1H), 7.59 – 7.48 (m, 1H), 7.35 – 7.08 (m, 2H), 3.78 (d, *J* = 6.0 Hz, 2H), 3.05 (hept, *J* = 6.8 Hz, 1H), 2.07 – 1.97 (m, 3H), 1.96 – 1.84 (m, 6H), 1.61 (s, 6H), 1.23 (d, *J* = 6.8 Hz, 6H); ^{13}C NMR (75 MHz, DMSO-d_6) δ= 167.9, 167.5, 138.4, 133.8, 131.3, 128.4, 126.7, 126.0, 51.2, 43.2, 41.5, 41.0 (3C), 36.4 (3C), 29.2 (3C), 22.7 (2C); FT-IR (neat): ṽ [cm^{-1}]= 701, 734, 989, 999, 1033, 1095, 1240, 1261, 1296, 1312, 1332, 1360, 1411, 1431, 1453, 1542, 1591, 1625, 1668, 2849, 2906; ESI-MS *m/z*: [M+H]$^{+}$ 419.15 (100%), 420.15 (27.1%), 421.15 (11.6%); purity (HPLC)= 99%.

7p (2*R*)-*N*-(Adamantan-1-yl)-2-{[2-(ethyldisulfanyl)phenyl]formamido}-3-phenylpropanamide

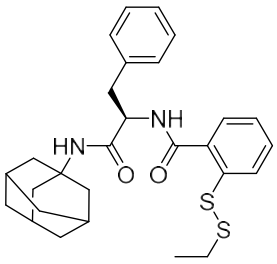

According to the general procedure (V), disulfanylbenzamide **7p** was obtained from **3d** and **6l** as a colourless solid (65 mg, 43%). mp: 161 °C; [α]$_{D23}$=+18 °(*c*=10 in chloroform); ^{1}H NMR (300 MHz, DMSO-d_6) δ= 8.52 (d, *J* = 8.5 Hz, 1H), 7.92 (d, *J* = 8.1 Hz, 1H), 7.57 – 7.47 (m, 1H), 7.45 – 7.38 (m, 2H), 7.35 – 7.21 (m, 5H), 7.22 – 7.12 (m, 1H), 4.77 – 4.32 (m, 1H), 3.10 – 2.83 (m, 2H), 2.68 (q, *J* = 7.3 Hz, 2H), 2.01 (s, 3H), 1.97 – 1.84 (m, 6H), 1.70 – 1.49 (m, 6H), 1.18 (t, *J* = 7.3 Hz, 3H); ^{13}C NMR (75 MHz, DMSO-d_6) δ= 170.4, 167.1, 138.5, 137.9, 134.2, 131.3, 129.7 (2C), 128.4 (3C), 126.6 (2C), 126.0, 55.3, 51.3, 41.3 (3C), 36.4 (3C), 31.8, 29.2 (3C), 26.8, 14.5; FT-IR (neat): ṽ [cm^{-1}]= 697, 737, 1032, 1097, 1256, 1292, 1360, 1454, 1538, 1587, 1624, 2848, 2905; ESI-MS *m/z*: [M+H]$^{+}$ 495.34 (100%), 496.38 (29.1%), 497.34 (10.4%); purity (HPLC)= 97%.

7q *N*-(Adamantan-1-yl)-3-{[2-(ethyldisulfanyl)phenyl]formamido}propenamide

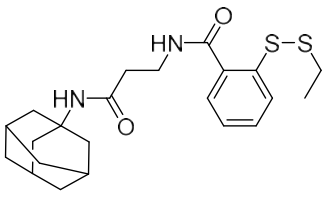

According to the general procedure (V), disulfanylbenzamide **7q** was obtained from **3d** and **6e** as a colourless solid (82 mg, 65%). mp: 154 °C; ^{1}H NMR (300 MHz, DMSO-d_6) δ= 8.46 (t, *J* = 5.6 Hz, 1H), 8.02 – 7.89 (m, 1H), 7.59 – 7.49 (m, 2H), 7.36 (s, 1H), 7.32 – 7.24 (m, 1H), 3.43 – 3.34 (m, 2H), 2.72 (q, *J* = 7.3 Hz, 2H), 2.31 (t, *J* = 7.3 Hz, 2H), 2.03 – 1.95 (m, 3H), 1.95 – 1.88 (m, 6H), 1.64 – 1.56 (m, 6H), 1.21 (t, *J* = 7.3 Hz, 3H); ^{13}C NMR (75 MHz, DMSO-d_6) δ= 169.9, 167.2, 137.8, 134.6, 131.1, 128.2, 126.6, 126.0, 51.1, 41.7, 41.4 (3C), 36.5 (3C), 31.2, 29.5 (3C), 29.2, 14.5; FT-IR (neat): ṽ [cm^{-1}]= 686, 747, 1066, 1094, 1131, 1244, 1292, 1311, 1344, 1361, 1450, 1534, 1585, 1634, 2846, 2904, 3303; ESI-MS *m/z*: [M+H]$^{+}$ 419.19 (100%), 420.17 (25.7%), 421.17 (12.0%); purity (HPLC)= 97%.

7r (2*R*)-*N*-(Adamantan-1-yl)-1-[2-(ethyldisulfanyl)benzoyl]pyrrolidine-2-carboxamide

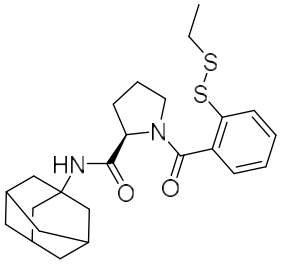

According to the general procedure (V), disulfanylbenzamide **7r** was obtained from **3d** and **6d** as a colourless solid (82 mg, 61%). mp: 80 °C; $[\alpha]_{D23}$=+72 °(*c*=10 in chloroform); ^{1}H NMR (300 MHz, DMSO-d_6) δ= 7.80 (dd, *J* = 15.3, 8.0 Hz, 1H), 7.55 – 7.41 (m, 1H), 7.41 – 7.19 (m, 2H), 7.17 – 7.01 (m, 1H), 4.55 – 3.82 (m, 1H), 3.56 (t, *J* = 6.9 Hz, 1H), 3.31 – 2.99 (m, 1H), 2.86 – 2.65 (m, 2H), 2.19 – 1.44 (m, 19H), 1.33 – 1.11 (m, 3H); ^{13}C NMR (75 MHz, DMSO-d_6) δ= 170.2, 169.7, 166.4, 136.7, 136.5, 134.0, 133.3, 129.6, 129.2, 127.7, 127.4, 126.8, 126.5, 126.3, 60.9, 59.3, 50.5, 50.2, 48.7, 40.7, 40.3, 35.7, 35.6, 31.9, 31.6, 31.4, 29.1, 28.5, 28.4, 24.2, 22.0, 13.7; FT-IR (neat): ṽ [cm^{-1}]= 694, 716, 750, 877, 1000, 1056, 1094, 1207, 1248, 1310, 1342, 1362, 1428, 1473, 1557, 1587, 1609, 1665, 2845, 2904, 3260, 3442; ESI-MS *m/z*: [M+H]$^+$ 445.18 (100%), 446.14 (26.2%), 447.17 (15.4%); purity (HPLC)= 99%.

7s *N*-(Adamantan-1-yl)-2-({2-[(2-phenylethyl)disulfanyl]phenyl}formamido)acetamide

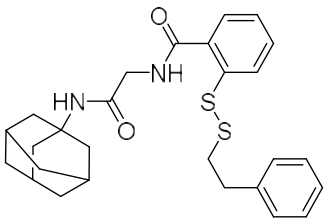

According to the general procedure (V), disulfanylbenzamide **7s** was obtained from **3g** and **6a** as a colourless solid (75 mg, 52%). mp: 132 °C; ^{1}H NMR (300 MHz, DMSO-d_6) δ= 8.64 (t, *J* = 5.9 Hz, 1H), 7.94 (d, *J* = 8.1 Hz, 1H), 7.66 (d, *J* = 7.7 Hz, 1H), 7.52 (t, *J* = 7.7 Hz, 1H), 7.35 – 7.18 (m, 7H), 3.81 (d, *J* = 5.9 Hz, 2H), 3.05 – 2.82 (m, 4H), 2.02 – 1.97 (m, 3H), 1.96 – 1.91 (m, 6H), 1.68 – 1.53 (m, 6H); ^{13}C NMR (75 MHz, DMSO-d_6) δ= 167.9, 167.5, 140.0, 137.9, 134.1, 131.4, 129.0 (2C), 128.7 (2C), 128.4, 126.9, 126.7, 126.2, 51.3, 43.2, 41.5 (3C), 39.1, 36.4 (3C), 34.9, 29.2 (3C); FT-IR (neat): ṽ [cm^{-1}]= 699, 734, 990, 1000, 1095, 1239, 1295, 1332, 1359, 1411, 1431, 1453, 1541, 1591, 1626, 1667, 2849, 2905; ESI-MS *m/z*: [M+H]$^+$ 481.17 (100%), 482.14 (33.6%), 483.14 (14.8%); purity (HPLC)= 97%.

7t *N*-(Adamantan-1-yl)-1-[2-(ethyldisulfanyl)benzoyl]piperidine-4-carboxamide

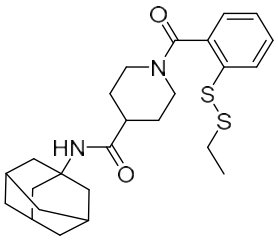

According to the general procedure (V), disulfanylbenzamide **7t** was obtained from **3d** and **6f** as a colourless solid (82 mg, 59%). mp: 94 °C; ^{1}H NMR (300 MHz, DMSO-d_6) δ= 7.81 (d, *J* = 8.0 Hz, 1H), 7.48 (t, *J* = 7.7 Hz, 1H), 7.33 (t, *J* = 7.4 Hz, 1H), 7.28 – 7.17 (m, 2H), 4.49 (d, *J* = 12.9 Hz, 1H), 3.28 (s, 1H), 2.95 (t, *J* = 11.4 Hz, 1H), 2.77 (q, *J* = 7.3 Hz, 2H), 2.42 – 2.25 (m, 1H), 2.02 – 1.94 (m, 3H), 1.92 – 1.84 (m, 6H), 1.64 – 1.54 (m, 6H), 1.57 – 1.35 (m, 5H), 1.22 (t, *J* = 7.3 Hz, 3H); ^{13}C NMR (75 MHz, DMSO-d_6) δ= 173.5, 166.8, 136.8, 134.3, 130.1, 128.4, 127.5, 126.9, 50.8, 46.6, 42.4 (2C), 41.4 (3C), 36.5 (3C), 32.4 (2C), 29.2 (3C), 28.7, 14.5; FT-IR (neat): ṽ [cm^{-1}]= 696, 741, 773, 1032, 1261, 1284, 1310, 1344, 1359, 1437, 1586, 1622, 2848, 2905; ESI-MS *m/z*: [M+H]$^+$ 459.32 (100%), 460.23 (27.1%), 461.23 (12.6%); purity (HPLC)= 97%.

7u *N*-(Adamantan-1-yl)-2-{[3-(ethyldisulfanyl)phenyl]formamido}acetamide

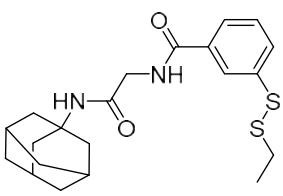

According to the general procedure (V), disulfanylbenzamide **7u** was obtained from **3b** and **6a** as a colourless solid (72 mg, 59%). mp: 143 °C; ^{1}H NMR (300 MHz, DMSO-d_6) δ= 8.67 (t, *J* = 5.9 Hz, 1H), 8.01 (s, 1H), 7.80 – 7.63 (m, 2H), 7.49 (t, *J* = 7.8 Hz, 1H), 7.38 (s, 1H), 3.81 (d, *J* = 5.9 Hz, 2H), 2.81 (q, *J* = 7.3 Hz, 2H), 2.00 (s, 3H), 1.97 – 1.80 (m, 6H), 1.66 – 1.52 (m, 6H), 1.24 (t, *J* = 7.3 Hz, 3H); ^{13}C NMR (75 MHz, DMSO-d_6) δ= 168.0, 166.0, 137.7, 135.6, 130.0, 129.7, 126.2, 126.2, 51.2, 43.1, 41.5 (3C), 36.4 (3C), 32.5, 29.2 (3C), 14.5; FT-IR (neat): ṽ [cm^{-1}]= 679, 735, 998, 1097, 1227, 1252, 1309, 1358, 1431, 1466, 1510, 1547, 1565, 1644, 2848, 2905, 3315; ESI-MS *m/z*: [M+H]$^+$ 405.13 (100%), 406.1 (23.4%), 407.11 (12.1%); purity (HPLC)= 99%.

7v (2*S*)-*N*-(Adamantan-1-yl)-2-{[2-(ethyldisulfanyl)phenyl]formamido}butanediamide

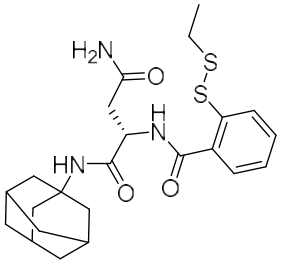

According to the general procedure (V), disulfanylbenzamide **7v** was obtained from **3d** and **6h** as a colourless solid (46 mg, 49%). mp: 85 °C; $[\alpha]_{D23}$=−18 °(*c*=10 in chloroform); ^{1}H NMR (300 MHz, DMSO-d_6) δ= 8.88 (d, *J* = 8.1 Hz, 1H), 7.98 (d, *J* = 8.1 Hz, 1H), 7.67 – 7.48 (m, 3H), 7.34 (t, *J* = 7.5 Hz, 1H), 4.81 – 4.53 (m, 1H), 3.02 – 2.80 (m, 2H), 2.73 (q, *J* = 7.3 Hz, 2H), 2.08 – 1.97 (m, 3H), 1.96 – 1.84 (m, 6H), 1.69 – 1.54 (m, 6H), 1.21 (t, *J* = 7.3 Hz, 3H); ^{13}C NMR (75 MHz, DMSO-d_6) δ= 168.2, 167.8, 138.4, 134.0, 132.1, 129.0, 127.2, 126.6, 118.9, 52.0, 49.6, 41.6 (3C), 37.7 (3C), 32.3, 30.3 (3C), 27.1, 14.2; FT-IR (neat): ῡ [cm^{-1}]= 689, 747, 1095, 1255, 1294, 1312, 1360, 1452, 1536, 1586, 1636, 2849, 2906, 3301; ESI-MS *m/z*: [M+H]$^+$ 444.27 (100%), 445.27 (27.3%), 446.27 (12.9%); purity (HPLC)= 95%.

7w (2*S*)-*N*-(Adamantan-1-yl)-2-{[2-(ethyldisulfanyl)phenyl]formamido}propenamide

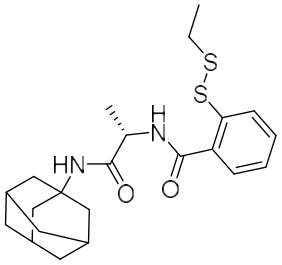

According to the general procedure (V), disulfanylbenzamide **7w** was obtained from **3d** and **6i** as a colourless solid (63 mg, 50%). mp: 83 °C; $[\alpha]_{D23}$=−28 °(*c*=10 in chloroform); ^{1}H NMR (300 MHz, DMSO-d_6) δ= 8.45 (d, *J* = 7.6 Hz, 1H), 7.95 (d, *J* = 8.1 Hz, 1H), 7.61 (d, *J* = 7.6 Hz, 1H), 7.58 – 7.50 (m, 1H), 7.32 (d, *J* = 7.6 Hz, 1H), 7.30 – 7.22 (m, 1H), 4.37 (p, *J* = 7.2 Hz, 1H), 2.73 (q, *J* = 7.3 Hz, 2H), 2.01 (s, 3H), 1.97 – 1.86 (m, 6H), 1.67 – 1.52 (m, 6H), 1.32 – 1.13 (m, 6H); ^{13}C NMR (75 MHz, DMSO-d_6) δ= 172.3, 167.6, 165.3, 155.5, 137.7, 134.4, 133.1, 126.2, 51.1, 49.7, 41.4 (3C), 36.4 (3C), 31.9, 29.2 (3C), 18.5, 14.5; FT-IR (neat): ῡ [cm^{-1}]= 742, 867, 1041, 1103, 1253, 1290, 1310, 1360, 1447, 1506, 1633, 1680, 2848, 2905, 3291; ESI-MS *m/z*: [M+H]$^+$ 419.26 (100%), 420.24 (26.5%), 421.26 (11.9%); purity (HPLC)= 98%.

7α *N*-(Adamantan-1-yl)-2-{[4-(ethyldisulfanyl)phenyl]formamido}acetamide

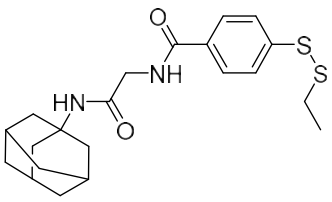

According to the general procedure (V), disulfanylbenzamide **7α** was obtained from **3c** and **6a** as a colourless solid (72 mg, 59%). mp: 81 °C; ^{1}H NMR (300 MHz, DMSO-d_6) δ= 8.59 (t, *J* = 5.9 Hz, 1H), 7.96 – 7.74 (m, 2H), 7.67 – 7.49 (m, 2H), 7.36 (s, 1H), 3.80 (d, *J* = 5.9 Hz, 2H), 2.82 (q, *J* = 7.3 Hz, 2H), 2.06 – 1.96 (m, 3H), 1.96 – 1.85 (m, 6H), 1.68 – 1.52 (m, 6H), 1.24 (t, *J* = 7.3 Hz, 3H); ^{13}C NMR (75 MHz, DMSO-d_6) δ= 168.1, 166.0, 141.1, 132.8, 128.5 (2C), 126.2 (2C), 51.2, 43.1, 41.5 (3C), 36.4 (3C), 32.5, 29.2 (3C), 14.5; FT-IR (neat): ῡ [cm^{-1}]= 753, 843, 1000, 1096, 1237, 1272, 1317, 1360, 1450, 1486, 1541, 1593, 1629, 1677, 2848, 2907, 3268; ESI-MS *m/z*: [M+H]$^+$ 405.14 (100%), 406.13 (23.8%), 407.15 (12.2%); purity (HPLC)= 98%.

7β *N*-(Adamantan-1-yl)-2-[(2-methoxyphenyl)formamido]acetamide

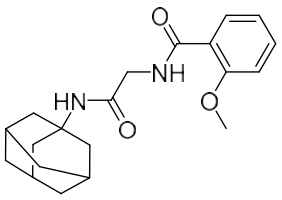

According to the general procedure (V), disulfanylbenzamide **7β** was obtained from *o*-anisic acid and **6a** as a colourless solid (85 mg, 82%). mp: 190 °C; ^{1}H NMR (300 MHz, DMSO-d_6) δ= 8.51 (t, *J* = 5.0 Hz, 1H), 7.87 (d, *J* = 7.7 Hz, 1H), 7.56 – 7.39 (m, 2H), 7.18 (d, *J* = 8.3 Hz, 1H), 7.11 – 6.98 (m, 1H), 3.93 (s, 3H), 3.87 (d, *J* = 5.1 Hz, 2H), 2.01 (s, 3H), 1.98 – 1.86 (m, 6H), 1.70 – 1.53 (m, 6H); ^{13}C NMR (75 MHz, DMSO-d_6) δ= 167.8, 164.6, 161.8, 135.7, 133.2, 122.0, 121.0, 112.6, 52.6, 51.2, 43.5, 41.4 (3C), 36.4 (3C), 29.2 (3C); FT-IR (neat): ῡ [cm^{-1}]= 754, 999, 1022, 1097, 1159, 1244, 1273, 1361, 1434, 1451, 1482, 1514, 1556, 1597, 1634, 1682, 2899, 3304, 3370; ESI-MS *m/z*: [M+H]$^+$ 343.18 (100%), 344.16 (20.0%), 345.15 (2.1%); purity (HPLC)= 99%.

7γ (2*S*)-*N*-(Adamantan-1-yl)-2-{[2-(ethyldisulfanyl)phenyl]formamido}-3-phenylpropanamide

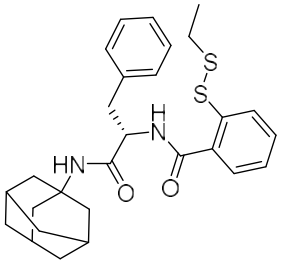

According to the general procedure (V), disulfanylbenzamide **7γ** was obtained from **3d** and **6c** as a colourless solid (56 mg, 37%). mp: 162 °C; $[\alpha]_{D23}$=−16 °(*c*=10 in chloroform); ^{1}H NMR (300 MHz, DMSO-*d*$_6$) δ= 8.53 (d, *J* = 8.4 Hz, 1H), 7.92 (d, *J* = 8.0 Hz, 1H), 7.51 (t, *J* = 7.7 Hz, 1H), 7.43 (d, *J* = 7.7 Hz, 2H), 7.37 – 7.12 (m, 6H), 4.83 – 4.49 (m, 1H), 3.11 – 2.84 (m, 2H), 2.67 (q, *J* = 7.3 Hz, 2H), 2.08 – 1.96 (m, 3H), 1.97 – 1.87 (m, 6H), 1.69 – 1.53 (m, 6H), 1.17 (t, *J* = 7.3 Hz, 3H); ^{13}C NMR (75 MHz, DMSO-*d*$_6$) δ= 170.5, 167.1, 138.5, 137.9, 134.2, 131.3, 129.7 (2C), 128.4 (3C), 126.6 (2C), 126.0, 55.3, 51.3, 41.3 (3C), 36.4 (3C), 31.8, 29.2 (3C), 26.8, 14.5; FT-IR (neat): ῡ [cm^{-1}]= 698, 735, 1000, 1033, 1095, 1239, 1295, 1331, 1360, 1454, 1539, 1590, 1625, 1667, 2849, 2905; ESI-MS *m/z*: [M+H]$^+$ 495.19 (100%), 496.17 (31.4%), 497.15 (12.4%); purity (HPLC)= 96%.

7δ 2-{[2-(Ethyldisulfanyl)phenyl]formamido}-*N*-(2-phenylethyl)acetamide

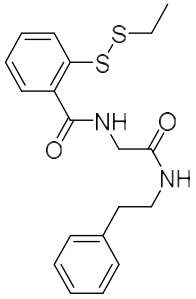

According to the general procedure (V), disulfanylbenzamide **7δ** was obtained from **3d** and **6n** as a colourless solid (70 mg, 62%). mp: 150 °C; ^{1}H NMR (300 MHz, DMSO-*d*$_6$) δ= 8.73 (t, *J* = 5.9 Hz, 1H), 8.06 – 7.89 (m, 2H), 7.72 (d, *J* = 7.6 Hz, 1H), 7.57 (t, *J* = 8.2 Hz, 1H), 7.36 – 7.11 (m, 6H), 4.02 (q, *J* = 7.2, Hz, 2H), 3.83 (d, *J* = 5.9 Hz, 2H), 3.40 – 3.23 (m, 2H), 2.79 – 2.63 (m, 2H), 1.19 (t, *J* = 7.2 Hz, 3H); ^{13}C NMR (75 MHz, DMSO-*d*$_6$) δ= 172.4, 168.9, 139.8, 138.5, 133.3, 131.5, 129.0 (2C), 128.7 (2C), 128.7, 126.5, 126.4, 125.9, 42.9, 35.6, 31.8, 21.4, 14.5; FT-IR (neat): ῡ [cm^{-1}]= 700, 729, 996, 1046, 1235, 1335, 1414, 1435, 1454, 1468, 1496, 1540, 1593, 1622, 1662, 3260; ESI-MS *m/z*: [M+H]$^+$ 375.18 (100%), 376.16 (22.5%), 377.17 (12.3%); purity (HPLC)= 99%.

7ε (2*R*)-*N*-(Adamantan-1-yl)-2-{[2-(ethyldisulfanyl)phenyl]formamido}-4-methylpentanamide

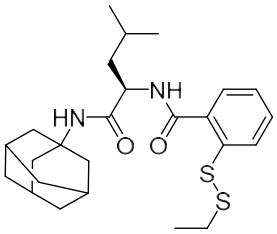

According to the general procedure (V), disulfanylbenzamide **7ε** was obtained from **3d** and **6k** as a colourless solid (32 mg, 23%). mp: 89 °C; $[\alpha]_{D23}$=+25 °(*c*=10 in chloroform); ^{1}H NMR (300 MHz, $CDCl_3$) δ= 7.92 (d, *J* = 8.2 Hz, 1H), 7.47 – 7.33 (m, 2H), 7.20 – 7.06 (m, 1H), 6.65 (d, *J* = 8.2 Hz, 1H), 5.98 (s, 1H), 4.58 – 4.44 (m, 1H), 2.66 (q, *J* = 7.3 Hz, 2H), 1.99 (s, 3H), 1.96 – 1.91 (m, 6H), 1.74 – 1.50 (m, 9H), 1.23 (t, *J* = 7.3 Hz, 3H), 0.95 – 0.86 (m, 6H);^{13}C NMR (75 MHz, $CDCl_3$) δ= 170.9, 167.7, 138.0, 133.6, 131.0, 127.8, 127.5, 126.0, 52.7, 41.4 (3C), 36.3 (3C), 32.3, 29.4 (3C), 26.9 (2C), 24.9, 23.0, 22.4, 14.2; FT-IR (neat): ῡ [cm^{-1}]= 697, 738, 868, 1032, 1096, 1255, 1292, 1360, 1454, 1539, 1587, 1624, 2848, 2906, 3279; ESI-MS *m/z*: [M+H]$^+$ 461.29 (100%), 462.28 (27.8%), 463.27 (11.9%); purity (HPLC)= 99%.

7ζ (2*S*)-*N*-(Adamantan-1-yl)-2-{[2-(ethyldisulfanyl)phenyl]formamido}-3,3-dimethylbutanamide

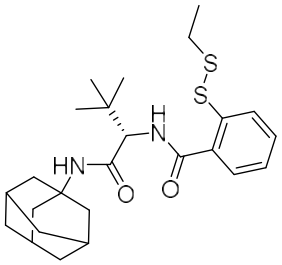

According to the general procedure (V), disulfany benzamide **7ζ** was obtained from **3d** and **6j** as a colourless solid (56 mg, 40%). mp: 92 °C; $[\alpha]_{D23}$=−36 °(*c*=10 in chloroform); ^{1}H NMR (300 MHz, $CDCl_3$) δ= 8.09 – 7.98 (m, 1H), 7.60 – 7.52 (m, 1H), 7.52 – 7.42 (m, 1H), 7.33 – 7.17 (m, 1H), 6.88 (d, *J* = 9.0 Hz, 1H), 5.65 (s, 1H), 4.39 (d, *J* = 9.0 Hz, 1H), 2.76 (q, *J* = 7.3 Hz, 2H), 2.12 – 2.06 (m, 3H), 2.06 – 1.99 (m, 6H), 1.79 – 1.58 (m, 6H), 1.33 (t, *J* = 7.3 Hz, 3H), 1.11 (s, 9H); ^{13}C NMR (75 MHz, $CDCl_3$) δ= 169.0, 167.5, 138.0, 134.0, 130.9, 127.7, 127.4, 125.9, 61.4, 51.2, 42.0 (3C), 37.0 (3C), 34.5, 31.8, 29.4 (3C), 26.9 (3C), 14.9; FT-IR (neat): ῡ [cm^{-1}]= 695, 744, 869, 1038, 1096, 1237, 1311, 1361, 1454, 1587, 1626, 2849, 2905, 3296; ESI-MS *m/z*: [M+H]$^+$ 461.30 (100%), 462.29 (29.4%), 463.28 (11.7%); purity (HPLC)= 95%.

11a *tert*-Butyl (3*R*)-3-{[2-(ethyldisulfanyl)phenyl]formamido}-3-[(3-phenoxyphenyl)carbamoyl] propanoate

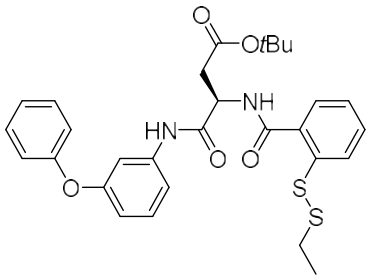

According to the general procedure (V), disulfanylbenzamide **11a** was obtained from **3d** and **10a** as a colourless oil (132 mg, 79%). $[\alpha]_{D23}$=+43 °(*c*=10 in chloroform); ^{1}H NMR (300 MHz, DMSO-d_6) δ= 10.59 (s, 1H), 9.23 (d, *J* = 7.7 Hz, 1H), 8.45 – 8.26 (m, 1H), 8.01 (d, *J* = 7.7 Hz, 1H), 7.93 (t, *J* = 7.7 Hz, 2H), 7.82 – 7.60 (m, 5H), 7.51 (t, *J* = 7.3 Hz, 1H), 7.44 – 7.32 (m, 2H), 7.18 – 7.00 (m, 1H), 5.25 (t, *J* = 8.0 Hz, 1H), 3.25 – 2.95 (m, 4H), 1.74 (s, 9H), 1.55 (t, *J* = 7.3 Hz, 3H); ^{13}C NMR (75 MHz, DMSO-d_6) δ= 169.9, 167.7, 164.6, 157.8, 157.2, 141.2, 138.7, 133.9, 131.9, 130.8 (2C), 129.2, 127.0, 126.3, 124.4, 119.7 (2C), 115.0, 114.3, 110.1, 107.1, 81.1, 55.7, 51.8, 32.3, 28.5 (3C), 14.8; FT-IR (neat): ῡ [cm^{-1}]= 683, 758, 848, 1151, 1216, 1268, 1367, 1439, 1486, 1545, 1591, 1731.

11b *tert*-Butyl (3*S*)-3-[(adamantan-1-yl)carbamoyl]-3-{[2-(methyldisulfanyl)phenyl]formamido} propanoate

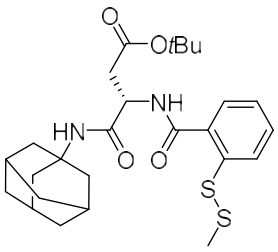

According to the general procedure (V), disulfany benzamide **11b** was obtained from **3a** and **10b** as a colourless solid (126 mg, 83%). mp: 66 °C; $[\alpha]_{D23}$=−46 °(*c*=10 in chloroform); ^{1}H NMR (300 MHz, DMSO-d_6) δ= 8.27 (d, *J* = 8.1 Hz, 1H), 7.87 – 7.67 (m, 1H), 7.61 – 7.46 (m, 2H), 7.37 (dd, *J* = 7.5, 6.2 Hz, 1H), 6.84 (s, 1H), 4.93 (t, *J* = 8.2, Hz, 1H), 2.94 – 164 (m, 2H), 2.17 – 2.09 (m, 3H), 2.08 – 1.96 (m, 3H), 1.97 – 1.87 (m, 6H), 1.69 – 1.53 (m, 6H), 1.37 (s, 9H); ^{13}C NMR (75 MHz, DMSO-d_6) δ= 170.1, 169.3, 168.5, 138.9, 135.7, 130.1, 129.3, 128.0, 127.9, 84.3, 50.5, 48.3, 41.4 (3C), 36.3 (3C), 35.4, 29.8 (3C), 28.6 (3C), 20.6; FT-IR (neat): ῡ [cm^{-1}]= 803, 898, 966, 990, 1024, 1072, 1226, 1257, 1342, 1376, 1414, 1433, 1519, 1604, 1645, 1709, 3283, 3332.

16a *tert*-Butyl *N*-[(2*S*)-4-methyl-1-[(2*S*)-2-({[2-(methyldisulfanyl)phenyl]formohydrazido} carbonyl)pyrrolidin-1-yl]-1-oxopentan-2-yl]carbamate

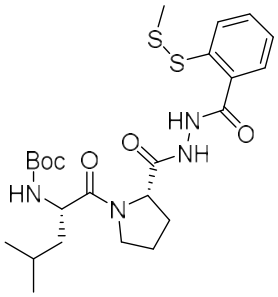

According to the general procedure (V), disulfanylbenzamide **16a** was obtained from **3a** and **15** as a colourless solid (25 mg, 16%). mp: 195 °C; $[\alpha]_{D23}$=−107 °(*c*=10 in chloroform); ^{1}H NMR (300 MHz, CD_2Cl_2) δ= 8.67 (s, 1H), 8.02 (d, *J* = 8.1 Hz, 1H), 7.62 (d, *J* = 7.7 Hz, 1H), 7.52 (t, *J* = 7.8 Hz, 1H), 7.26 (t, *J* = 7.5 Hz, 1H), 5.24 (d, *J* = 8.9 Hz, 1H), 4.73 – 4.58 (m, 1H), 4.56 – 4.35 (m, 1H), 3.83 – 3.48 (m, 2H), 2.40 (s, 3H), 2.36 – 2.26 (m, 1H), 2.21 – 1.93 (m, 4H), 1.84 – 1.65 (m, 1H), 1.56 – 1.45 (m, 1H), 1.42 (s, 9H), 1.36 (s, 1H), 0.95 (dd, *J* = 12.2, 6.6 Hz, 6H); ^{13}C NMR (75 MHz, CD_2Cl_2) δ= 174.1, 165.0, 156.1, 143.3, 138.8, 132.3, 131.5, 128.8, 127.7, 126.6, 79.9, 58.9, 51.1, 47.9, 42.4, 28.6 (3C), 27.4, 25.7, 25.2, 23.7, 22.8, 21.9; FT-IR (neat): ῡ [cm^{-1}]= 668, 712, 802, 1060, 1202, 1305, 1423, 1489, 1509, 1577, 1648, 2872, 3363; ESI-MS *m/z*: $[M+Na]^+$ 547.21 (100%), 548.22 (15.0%), 549.21 (6.7%); purity (HPLC)= 96%.

General procedure (VI) to deprotect *tert*-butyl ester (12a,b)

The *tert*-butyl esters **11a,b** (0.18 mmol) were suspended in DCM (5 mL). Subsequently, trifluoracetic acid (2.5 mL) was added and the reaction was stirred for 4 h at room temperature. Evaporation of the solvent and lyophilization from ACN/H_2O (1:1) yielded the corresponding asymmetric disulfanylbenzamides (**12a,b**) as colourless solids.

12a (3*R*)-3-{[2-(Ethyldisulfanyl)phenyl]formamido}-3-[(3-phenoxyphenyl)carbamoyl]propanoic acid

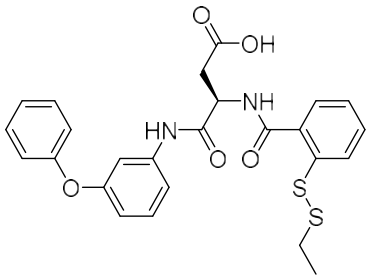

According to the general procedure (VI), **12a** was obtained from **11a** as a colourless solid (82 mg, 91%). mp: 103 °C; $[\alpha]_{D23}$=+35 °(*c*=10 in chloroform); ^{1}H NMR (300 MHz, DMSO-d_6) δ= 10.24 (d, *J* = 16.8 Hz, 1H), 8.87 (d, *J* = 7.3 Hz, 1H), 7.98 (d, *J* = 8.1 Hz, 1H), 7.71 – 7.61 (m, 1H), 7.61 – 7.50 (m, 1H), 7.50 – 7.24 (m, 6H), 7.20 – 7.09 (m, 1H), 7.08 – 6.93 (m, 3H), 4.98 – 4.73 (m, 1H), 2.89 – 2.60 (m, 4H), 1.19 (t, *J* = 7.3 Hz, 3H); ^{13}C NMR (75 MHz, DMSO-d_6) δ= 172.0, 169.8, 167.4, 157.5, 156.8, 140.9, 138.4, 133.4, 131.6, 130.5 (2C), 128.9, 126.6, 125.9, 124.0, 119.3 (2C), 114.6, 113.9, 109.6, 66.8, 51.5, 36.2, 31.9, 14.5; FT-IR (neat): ṽ [cm^{-1}]= 687, 747, 869, 966, 1160, 1211, 1434, 1485, 1520, 1587, 1642, 1710, 2979; ESI-MS *m/z*: $[M+Na]^+$ 519.24 (100%), 520.27 (35.8%), 521.21 (8.1%); purity (HPLC)= 98%.

12b (3*S*)-3-[(Adamantan-1-yl)carbamoyl]-3-{[2-(methyldisulfanyl)phenyl]formamido}propanoic acid

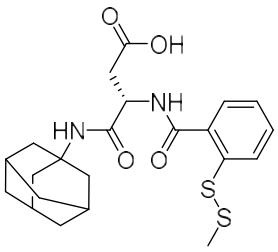

According to the general procedure (VI), **12b** was obtained from **11b** as a colourless solid (89 mg, 99%). mp: 101 °C; $[\alpha]_{D23}$=−39 °(*c*=10 in chloroform); ^{1}H NMR (300 MHz, DMSO-d_6) δ= 8.87 – 8.65 (m, 1H), 8.10 – 7.82 (m, 2H), 7.73 – 7.53 (m, 1H), 7.49 – 7.18 (m, 2H), 4.72 – 4.56 (m, 1H), 2.87 – 2.54 (m, 2H), 2.40 (s, 3H), 2.00 (s, 3H), 1.94 – 1.89 (m, 6H), 1.69 – 1.54 (m, 6H); ^{13}C NMR (75 MHz, DMSO-d_6) δ= 172.2, 169.8, 167.4, 137.4, 134.0, 128.4, 126.4, 126.2, 122.6, 97.4, 66.8, 51.3, 41.3 (3C), 35.3 (3C), 28.6 (3C), 22.4; FT-IR (neat): ṽ [cm^{-1}]= 673, 742, 872, 1041, 1102, 1187, 1253, 1305, 1359, 1454, 1538, 1634, 1708, 2849, 2907; ESI-MS *m/z*: $[M+H]^+$ 449.13 (100%), 450.13 (25.9%), 451.13 (12.4%); purity (HPLC)= 98%.

Synthesis of the FAM-GSLPETGGS-NH_2 substrate peptide

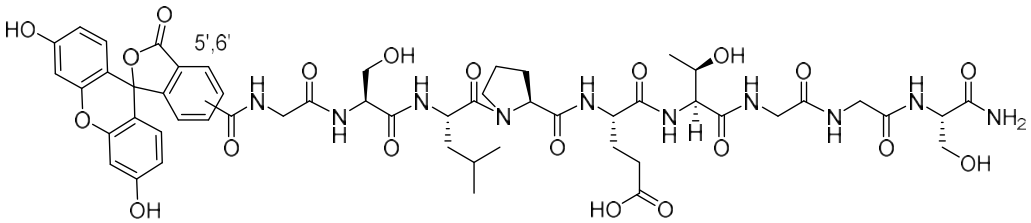

The FAM-GSLPETGGS-NH_2 substrate peptide was synthesized by Fmoc-based solid-phase peptide chemistry using the peptide synthesis module of a homemade 3D-printed liquid handling workstation.[4] The synthesis was performed on NovelGel Rink amide resin (0.71 mmol/g) and a standard TBTU coupling protocol on a 0.142 mmol scale.[5] Each amino acid was coupled in a threefold molar excess for 60 min. Coupling reactions were performed by 2-(1*H*-benzotriazole-1-yl)-1,1,3,3-tetramethyluronium-hexafluorophosphate (TBTU) and *N*-methylmorpholine (NMM). Removal of the Fmoc-group was done twice with 40% piperidine in DMF for 10 min and 20 min. The N-terminal carboxamidofluorescein moiety was coupled in a 1.5-fold molar excess of 5,6-carboxyfluorescein and TBTU/NMM for 6 h. The peptide was deprotected and cleaved from the resin with TFA/TIPS/water (90:5:5) for 3 h, precipitated by –80 °C cold ether, isolated by centrifugation and lyophilized from water/acetonitrile (1:1). The crude peptide was purified twice by preparative HPLC (gradient: 0–15% ACN:H_2O + 0.1% TFA). Lyophilization of the product containing fractions yielded the substrate peptide as a yellow solid (68 mg; 41%); ESI-MS *m/z*: $[M+2H]^{2+}$ 581.27 (100%), $[M+H]^+$ 1161.40 (13.4%), purity (HPLC)= 96%.

VT-NMR spectra

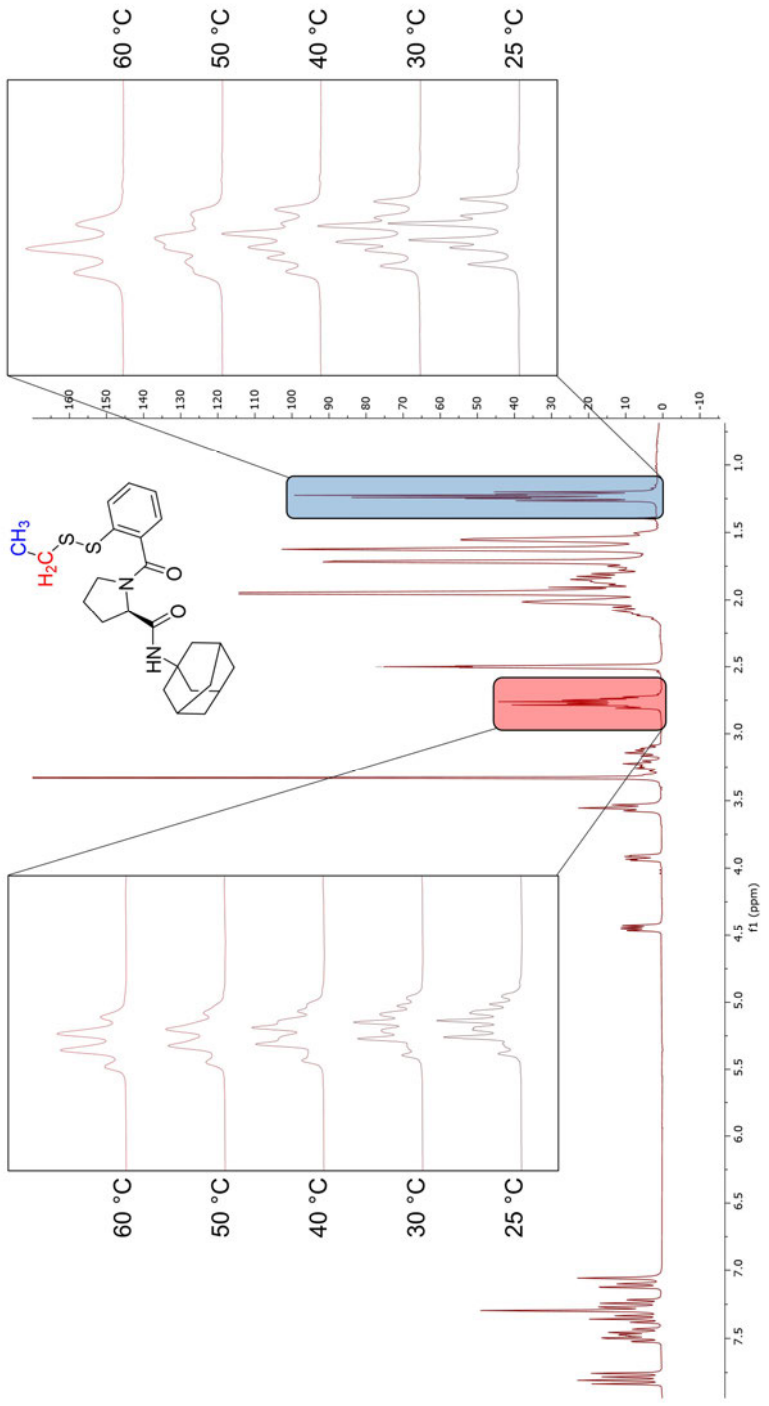

Figure 4: VT-NMR of compound **7r** (25–60 °C). Duplication of the NMR signal set (25 °C) was due to different energetic states (rotamers). The resolution of the ethyl group to a single signal set (quartet & triplet) at higher temperatures is exemplified.

Fluorometric enzyme kinetics

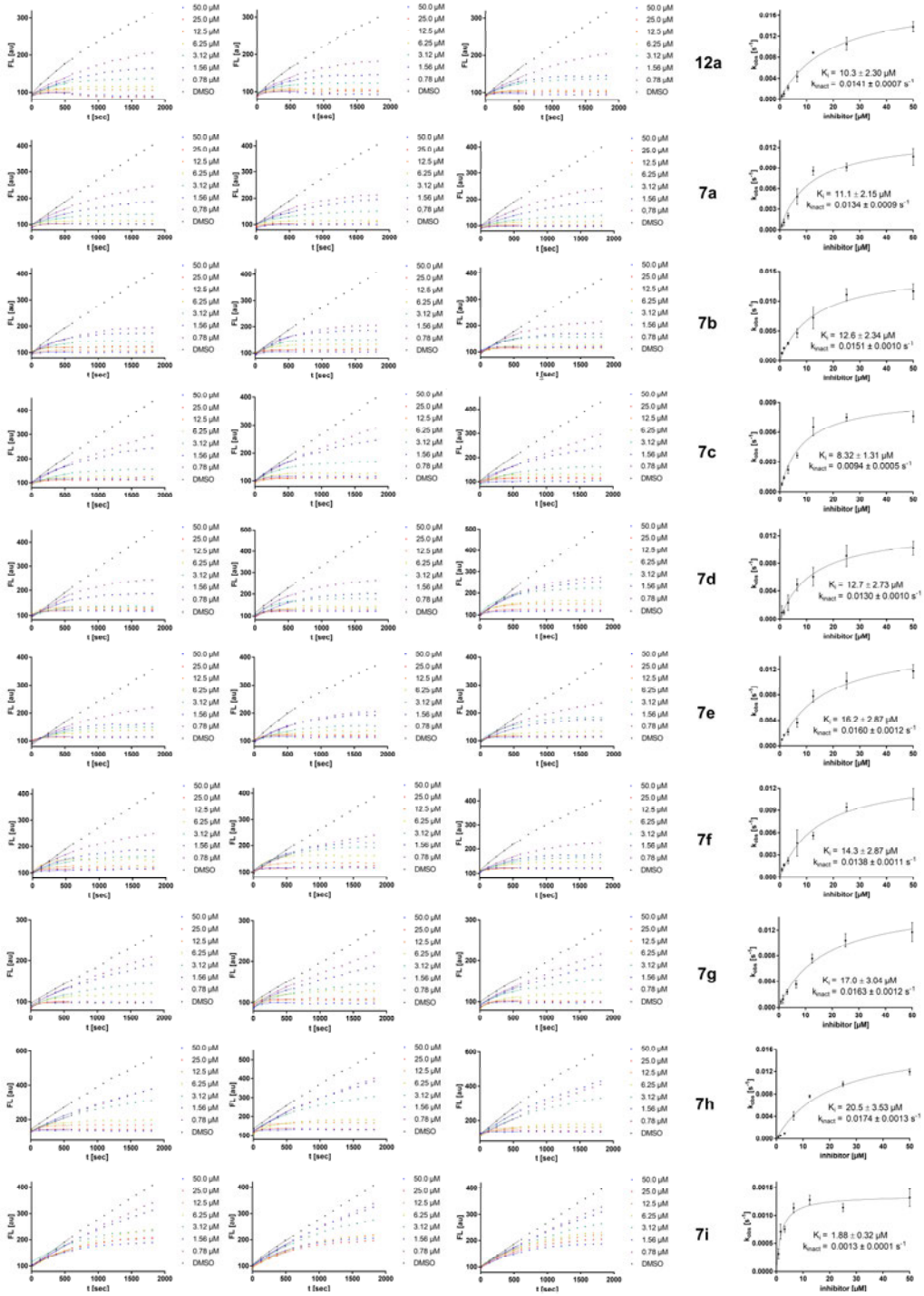

Figure 5: (left) Fluorescence progress curves (triplicates) for **7a–i** and **12a**. The fluorescence was recorded for 30 min every 30 s. For clarity, only every fourth fluorescence data point is shown. Lines represent non-linear fits for determining the k_{obs} values (t=0–10 min); (right) k_{obs} vs. [I] plots showing the respective K_i and k_{inact} values from hyperbolic fits.

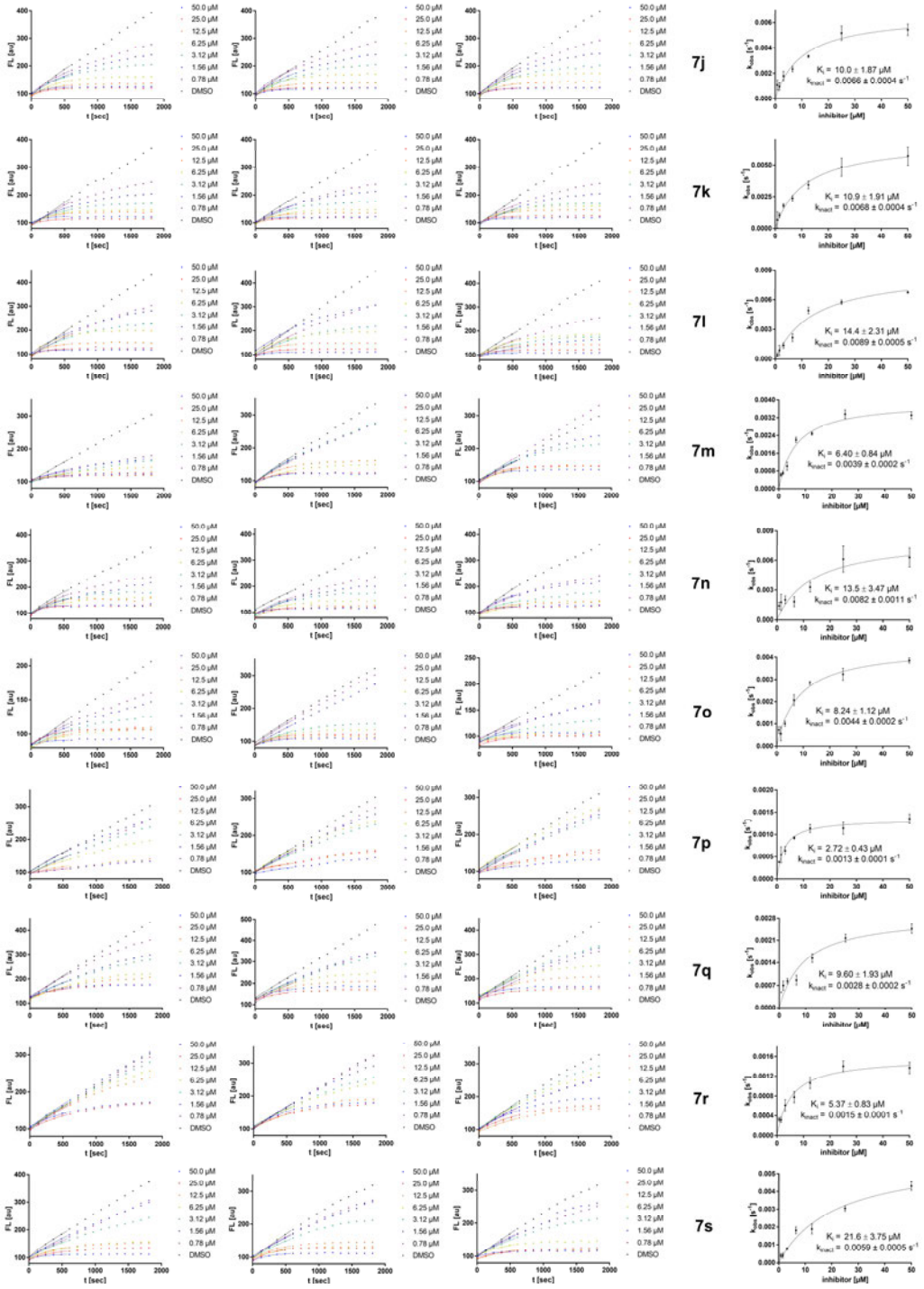

Figure 6: (left) Fluorescence progress curves (triplicates) for **7j–s**. The fluorescence was recorded for 30 min every 30 s. For clarity, only every fourth fluorescence data point is shown. Lines represent non-linear fits for determining the k_{obs} values (t=0–10 min); (right) k_{obs} vs. [I] plots showing the respective K_i and k_{inact} values from hyperbolic fits.

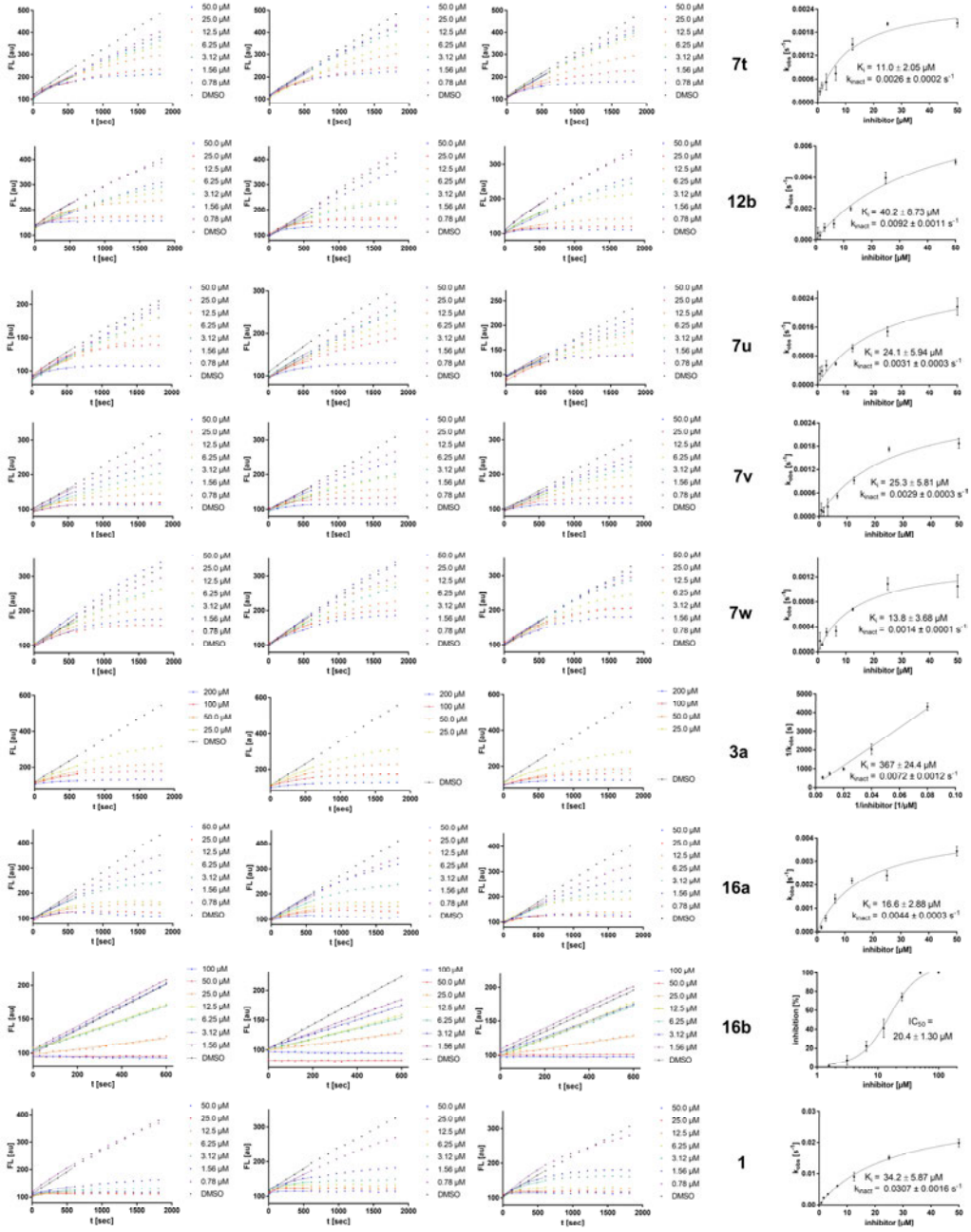

Figure 7: (left) Fluorescence progress curves (triplicates) for **1**, **3a**, **7t–w**, **12b** and **16a,b**. The fluorescence was recorded for 30 min every 30 s. For clarity, only every fourth fluorescence data point is shown. Lines represent non-linear fits for determining the k_{obs} values (t=0–10 min); (right) k_{obs} vs. [I] plots showing the respective K_i and k_{inact} values from hyperbolic fits. For **3a** no k_{obs} saturation was observed, thus, a Lineweaver-Burk linearization ($\frac{1}{k_{obs}} = \frac{K_{Iapp}}{k_{inact}}\frac{1}{[I]} + \frac{1}{k_{inact}}$) was employed to obtain K_i and k_{inact} values. For **16b** no time-dependence was found, thus, the IC_{50} value was determined using the slope of the fluorescence progress curves and a 4-parameter logistic model ($\frac{v_i}{v_0} = max\frac{min - max}{1+(\frac{[I]}{IC_{50}})^b}$).

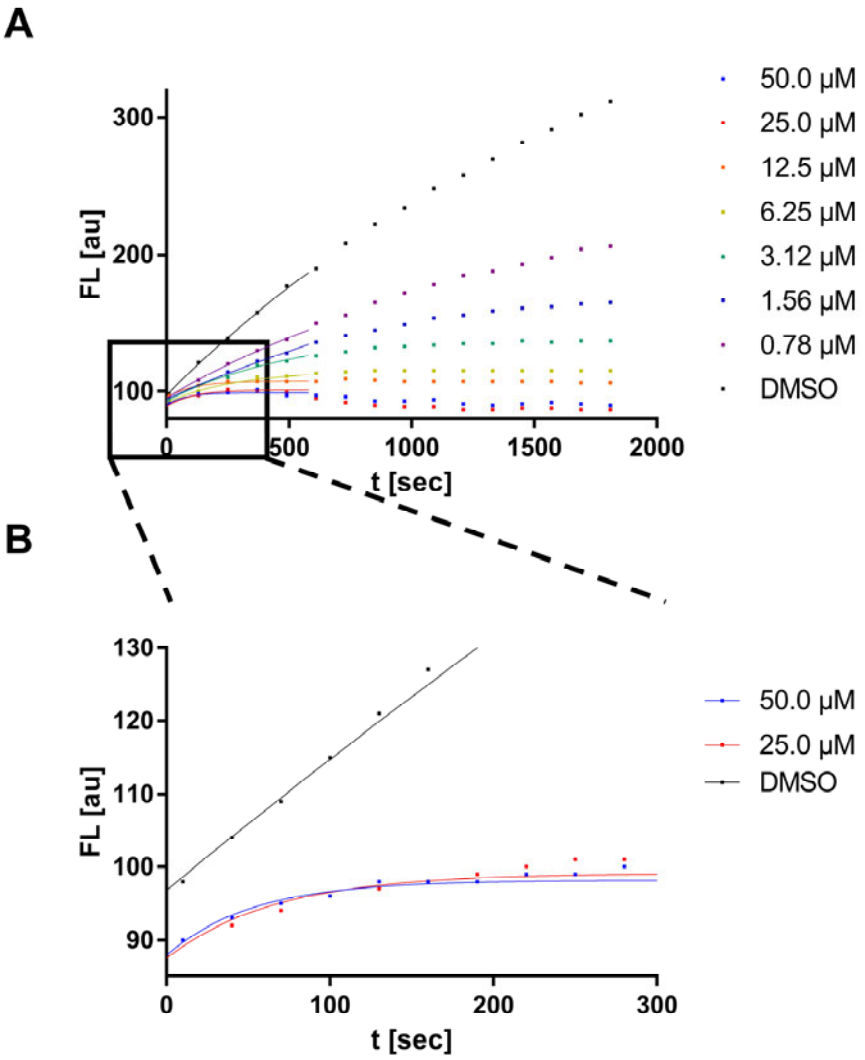

Figure 8: A) First replicate of the fluorescence progress curves for **12a**. The fluorescence was recorded for 30 min every 30 s. For clarity, only every fourth fluorescence data point is shown. Lines represent non-linear fits for determining the k_{obs} values (t=0–10 min); B) Magnification of the initial phase in the fluorescence progress curves (25 µM, 50 µM) with all data points showing rapid plateau formation after t=100 s.

References

[1] S. Kusaka, R. Matsuda, S. Kitagawa, *Chem. Commun.* **2018**, *54*, 4782–4785.
[2] F. Yang, W. Wang, K. Li, W. Zhao, X. Dong, *Tetrahedron Lett.* **2017**, *58*, 218–222.
[3] M. R. James, *Process for the Preparation of 1,2-Benzisothiazolin-3-ones*, **2004**, KR100429082B1.
[4] F. Barthels, U. Barthels, M. Schwickert, T. Schirmeister, *SLAS Technol. Transl. Life Sci. Innov.* **2019**, 2472630319877374.
[5] I. Rentero Rebollo, S. McCallin, D. Bertoldo, J. M. Entenza, P. Moreillon, C. Heinis, *ACS Med. Chem. Lett.* **2016**, *7*, 606–611.

“

4 Covalent Inhibitors of Rhodesain

4.1 Naphthoquinones as Covalent Reversible Inhibitors of Cysteine Proteases — Studies on Inhibition Mechanism and Kinetics

4.1.1 Context, Project Summary, and own Contribution

In this study, chloro- and nitrile-substituted peptidyl 1,4-naphthoquinones were evaluated for their potential to inhibit *Trypanosoma brucei rhodesiense* cathepsin L (rhodesain). The inhibitors consisted of a conserved recognition sequence (H_2N-L-Phe-L-Leu-OR) with a 1,4-naphthoquinone warhead at its N-terminus and were synthesized by the group of [redacted]. Substituted naphthoquinones have rarely been studied as warheads for papain-like cysteine protease,[302] but these are interesting multifunctional chemotypes due to multiple electrophilic centers which can undergo Michael-type additions, substitution reactions, and in the case of a nitrile substituent addition to the same is conceivable.

Eight different inhibitors were synthesized, with the most potent inhibitor showing sub-nanomolar affinity (K_I=0.15 nM) and a time-dependent, covalent-reversible mode of inhibition. Subsequently, detailed enzyme inhibition assays, native ESI mass spectrometry, and quantum chemical calculations were performed to elucidate the mode of inhibitor action. By kinetic separation of the covalent and non-covalent inhibition terms, it was possible to determine the half-life of the complex $t_{1/2}$=570 s which corresponds to a typical residence time for covalent-reversible inhibitors. From the biphasic substrate-turnover plots, it was also possible to determine the reaction energy of the covalent warhead reaction (ΔE_{reac}=–1.5 kcal/mol) which is very low, emphasizing the reversible nature of covalent inhibition (for irreversible inhibition of vinyl sulfone K11777 ΔE_{reac}=–23 kcal/mol was calculated).[116] Native ESI mass spectrometry of rhodesain showed the formation of a defined adduct upon treatment with the inhibitors which, however, did not correspond to the mass difference of a possible warhead reaction but could be attributed to the Michael addition and additional loss of the benzyl ester group of the inhibitor.

Further mass spectrometric and UV/Vis spectroscopic hydrolysis assays showed that rhodesain acts as a moonlighting esterase and cleaves the benzyl ester prodrug yielding the free carboxylic acid which represents the active inhibitor species. Molecular docking and quantum chemical calculations supported this mode of inhibition: first, the ester is cleaved by rhodesain, and subsequently, the reversible attack of the Cys25 thiolate on the α-position of the naphthoquinone olefin leads to a reversible Michael adduct. With an EC_{50}=0.12 µM, the benzyl ester prodrug exhibited potent anti-trypanosomal in cellular assays, indicating this type of warhead has potential for future covalent-reversible inhibitor design.

Own contributions: Rhodesain inhibition assays, Dialysis assays, Dilution assays, Protease selectivity assays, Hydrolysis LC/MS assays, Hydrolysis UV/Vis assays & Writing parts of the manuscript.

Contributions from other authors: Synthesis and characterization of the inhibitors, Thiol reactivity experiments, Protein expression and purification, Protein mass spectrometry, Parts of the rhodesain inhibition assays, *T. brucei* cell assays & Quantum chemical investigations.

This work has been published in: Molecules (impact factor: 4.41).

The 'Supporting Information' can be accessed online at doi: 10.3390/molecules25092064.

4.1.2 Publication

The following publication quoted (within “”) from page 149 to page 170 is exactly the same as the manuscript cited on page 148:”

molecules

MDPI

Article

Naphthoquinones as Covalent Reversible Inhibitors of Cysteine Proteases—Studies on Inhibition Mechanism and Kinetics

Philipp Klein [1], Fabian Barthels [2], Patrick Johe [2], Annika Wagner [3], Stefan Tenzer [4], Ute Distler [4], Thien Anh Le [5], Paul Schmid [5], Volker Engel [5], Bernd Engels [5], Ute A. Hellmich [3,6], Till Opatz [1,*] and Tanja Schirmeister [2,*]

1 Department of Chemistry, Organic Chemistry Section, Johannes Gutenberg-Universität, Duesbergweg 10-14, 55128 Mainz, Germany; klein@uni-mainz.de
2 Institute of Pharmaceutical and Biomedical Sciences, Johannes Gutenberg-Universität, Staudingerweg 5, 55128 Mainz, Germany; barthels@uni-mainz.de (F.B.); pajohe@uni-mainz.de (P.J.)
3 Department of Chemistry, Biochemistry Section, Johannes Gutenberg-Universität, Johann-Joachim Becherweg 30, 55128 Mainz, Germany; a.wagner@uni-mainz.de (A.W.); u.hellmich@uni-mainz.de (U.A.H.)
4 Institute of Immunology, University Medical Center, Johannes Gutenberg-Universität Mainz, Langenbeckstr. 1, 55131 Mainz, Germany; tenzer@uni-mainz.de (S.T.); ute.distler@uni-mainz.de (U.D.)
5 Institute of Physical and Theoretical Chemistry, Universität Würzburg, Emil-Fischer-Straße 42, 97074 Würzburg, Germany; thien_anh.le@physik.uni-wuerzburg.de (T.A.L.); paul.schmid@uni-wuerzburg.de (P.S.); volker.engel@uni-wuerzburg.de (V.E.); bernd.engels@uni-wuerzburg.de (B.E.)
6 Centre for Biomolecular Magnetic Resonance (BMRZ), Goethe-University Frankfurt, 60323 Frankfurt, Germany
* Correspondence: opatz@uni-mainz.de (T.O.); schirmei@uni-mainz.de (T.S.); Tel.: +49-(0)6131-39-22272 (T.O.); +49-(0)6131-39-25742 (T.S.)

Received: 31 March 2020; Accepted: 21 April 2020; Published: 28 April 2020

check for updates

Abstract: The facile synthesis and detailed investigation of a class of highly potent protease inhibitors based on 1,4-naphthoquinones with a dipeptidic recognition motif (HN-L-Phe-L-Leu-OR) in the 2-position and an electron-withdrawing group (EWG) in the 3-position is presented. One of the compound representatives, namely the acid with EWG = CN and with R = H proved to be a highly potent rhodesain inhibitor with nanomolar affinity. The respective benzyl ester (R = Bn) was found to be hydrolyzed by the target enzyme itself yielding the free acid. Detailed kinetic and mass spectrometry studies revealed a reversible covalent binding mode. Theoretical calculations with different density functionals (DFT) as well as wavefunction-based approaches were performed to elucidate the mode of action.

Keywords: protease; rhodesain; covalent reversible inhibition; 1,4-naphthoquinone; nucleophilic addition; prodrug

1. Introduction

Covalently acting drugs have traditionally been considered as problematic due to their potential to elicit off-target effects. In the last years, however, such compounds have received increasing attention in drug development due to several advantages including longer target residence times, higher potency and ligand efficiency. It has been recognized that the benefits of such inhibitors can be additionally enhanced by careful tuning of their reactivity, i.e., by switching the covalent inhibition mode from covalent irreversible to covalent reversible [1–8].

In general, covalent inhibitors consist of two parts, namely a recognition unit fitting into the substrate binding pockets, and an electrophilic functional group. In the case of protease inhibitors, the recognition unit is typically a peptidic or peptidomimetic fragment. Covalent inhibitors also contain an electrophilic functional group (the so-called "warhead"), which can undergo a chemical reaction with a nucleophilic amino acid in the vicinity. In most cases, Cys, Ser or Thr side chains are addressed. A large fraction of the known types of warheads targeting Cys residues is based on activated double bonds (Michael acceptors) [9] comprising, e.g., vinyl sulfones [10–12], α,β-unsaturated esters, nitriles and ketones [13–16]. Depending on the substitution pattern of the double bond, the inhibition of the target enzyme can either be covalent reversible or irreversible [17]. Heterocyclic or peptide-derived nitriles constitute another important substance class of protease inhibitors, which inhibit cysteine and serine proteases in a covalent reversible manner via the formation of a (thio) imidate [18–21].

In the present study, we compared chloro- and nitrile-substituted peptidyl 1,4-naphthoquinones with respect to their inhibition properties. In principle, such multifunctional warheads [22] could undergo either Michael-type additions or substitution reactions or—in case of the nitrile derivative—also reversible addition to the nitrile group.

We explored the potential of such groups as new warheads for cysteine proteases of the papain family, namely the human cathepsins L and B (Cath. L and Cath. B), and the cathepsin L-like *Trypanosoma* protease rhodesain (Rhod.). The human enzymes of this family play crucial roles in, e.g., tumor metastasis [23,24]. Rhodesain from *Trypanosoma brucei rhodesiense*, the parasite causing human African trypanosomiasis (HAT), is essential for the parasite's survival as it is involved in several host invasion processes [25,26]. In order to check the selectivity, the inhibition potencies of the new inhibitors were also tested for the serine protease of the Dengue virus (DENV PR) [27,28].

Since we were interested in the inhibition properties of the two warheads, we used the same recognition unit, the dipeptide sequence H_2N-L-Phe-L-Leu-OBn and attached the 1,4-naphthoquinone unit to its N-terminus. This dipeptide sequence was chosen since it was previously shown to be an appropriate recognition unit for cathepsin-like cysteine proteases [29,30]. Moreover, as opposed to amino acids with functionalized side chains, no additional protection/deprotection steps are necessary during synthesis. We previously observed that rhodesain is able to hydrolyze compounds with the dipeptidic H_2N-L-Phe-L-Leu-OBn recognition unit [30]. In agreement with these findings, we also observed the protease-mediated hydrolysis of the benzyl ester moieties of the naphthoquinone-modified inhibitors to yield the free acids (see Sections 2.4 and 2.6). We therefore additionally compared the free acids as well as the respective methyl and *tert*-butyl esters of our current molecules for their ability to inhibit rhodesain.

Mass spectrometry revealed the formation of a covalent bond between the inhibitors and rhodesain. We therefore also computed the thermodynamics of possible inhibition reactions to gain insights into the energetics of the various possible covalent inhibition mechanisms. The chemical properties of such groups are strongly influenced by their degree of aromatic stabilization, which is often overestimated by standard density functional approaches [31]. To evaluate which theoretical approaches are sufficiently reliable to predict the inhibition mechanisms and potencies of such groups, a benchmark study employing various wave functions as well as density-based approaches were performed.

2. Results

2.1. Syntheses

The dipeptide product H_2N-L-Phe-L-Leu-OBn was synthesized as reported previously [30]. The potential inhibitors were synthesized by an addition/elimination reaction on the naphthoquinone unit carrying two potential leaving groups (Scheme 1).

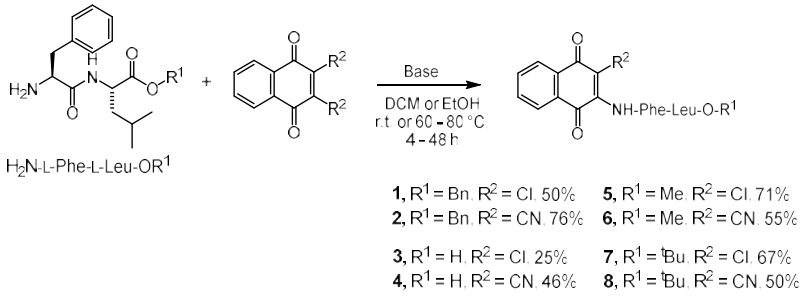

Scheme 1. Syntheses of potential protease inhibitors with naphthoquinone units as the reactive group.

The respective methyl and *tert*-butyl esters **5**–**8** were synthesized accordingly. To further investigate whether the hydrolysis products of the benzyl esters **1** and **2** are the active compounds as indicated by the MS and hydrolysis studies (see Sections 2.4 and 2.6), the corresponding free acids **3** and **4** were also synthesized

2.2. Enzyme Assays

Enzyme inhibition by the benzyl esters **1** and **2** was tested with the fluorogenic substrate Cbz-Phe-Arg-AMC as described previously [18,30]. First, assays with 20 µM inhibitor concentration were performed. For compounds displaying > 60% inhibition at that concentration, concentration-dependent assays were performed and IC_{50} values as well as detailed kinetic constants (K_i, K_i^* and $k_{3/4}$) were determined (Tables 1 and 2). The IC_{50} values (In case of time-dependent inhibition, the steady-state residual enzyme activities (vS) were used for determination of the IC50 values) were determined at different substrate concentrations in order to check for competitive or non-competitive inhibition [32,33]. The values were found to increase linearly with increasing substrate concentrations, indicating competitive inhibition (see exemplarily Figure 1 for inhibition of cathepsin L by benzyl esters **1** and **2**). The respective $K_i^{(*)}$ values (Table 1) were determined from plots of the IC_{50} values against the substrate concentration according to the Cheng–Prusoff relationship (Figure 1) [34].

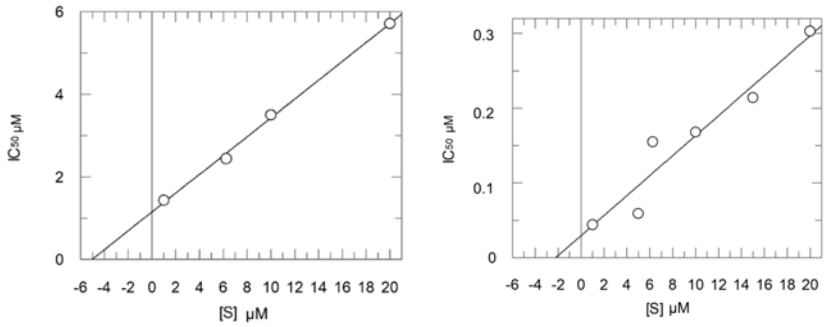

Figure 1. Dependence of inhibition potency (IC_{50} values) from substrate concentration for inhibition of cathepsin L by compounds **a** (left) and **b** (right). Increasing IC_{50} values at increasing substrate concentrations prove competitive inhibition; the $K_i^{(*)}$ value (corresponding to the IC_{50} value at zero substrate concentration) is obtained as the intercept of the regression line with the *y*-axis (**a**: K_i = 1.14 µM and **b**: K_i^* = 0.030 µM).

In order to check the cross-reactivity against serine proteases, we determined the potency of the compounds to inhibit the NS3/NS2B protease of the Dengue virus (DENV PR) [27,28].

Table 1. Inhibition data for 1,4-naphthoquinone (NQ)-derived inhibitors of the general structure NQ-NH-L-Phe-L-Leu-OR, % inhibition at 20 μM or $K_i^{(*)}$ (nM) [1].

Cpd.	Cath. L % inh.	Cath. L $K_i^{(*)}$	Cath. B % inh	Cath. B $K_i^{(*)}$	Rhod. % inh.	Rhod. $K_i^{(*)}$	DENV PR % inh.	DENV PR $K_i^{(*)}$
1		1140	53%			2900	41%	Nd
2		33 [3]		1900		180		41,000 [2]
3		57 [3]	25%	Nd		24 [3]	43%	Nd
4		17 [3]	45%	Nd		0.15 [3]	38%	Nd
5	45%	Nd	Nd	Nd	48%	Nd	Nd	Nd
6	40%	Nd	Nd	Nd		1235	Nd	Nd
7	38%	Nd	Nd	Nd	51%	Nd	Nd	Nd
8	21%	Nd	Nd	Nd	38%	Nd	Nd	Nd

[1] All values are from at least three independent measurements; standard deviations are 15% or less in case of K_i values and 5% or less in case of % inhibition @ 20 μM; IC_{50} values and $K_i^{(*)}$ values were determined for compounds displaying > 60% inhibition at 20 μM; [2] IC_{50} value in nM at [S] = 100 μM (Boc-Gly Arg Arg-AMC); [3] reversible, time-dependent inhibition; the K_i^* values for the final high-affinity complexes are given as mean values from method 1 and method 2 (see Section 2.2); for more detailed inhibition constants see Table 2. Cpd., compound; Cath. L, cathepsin L; Cath. B, cathepsin B; Rhod., rhodesain; DENV PR, Dengue virus protease. Nd, not determined.

For the two benzyl esters **1** and **2** the highest inhibition was found for cathepsin L with the nitrile substituted quinone **2** (K_i^* ca. 30 nM). Both esters also inhibited cathepsin B and rhodesain however with lower inhibitory potencies compared to cathepsin L. Still, the nitrile derivative **2** exhibited the higher inhibition efficiency. Very low inhibition was found for the DENV PR.

The progress curves for inhibition of cathepsin L were found to be non-linear in case of the nitrile-substituted benzyl ester **2**, i e , time dependent inhibition was observed (see Figure 2).

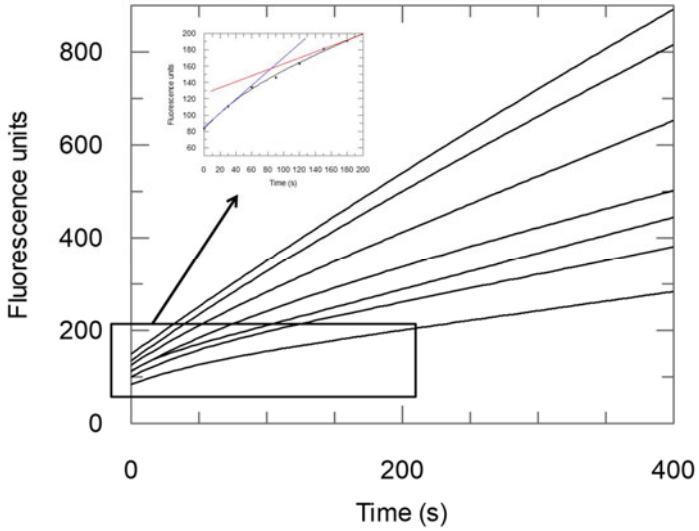

Figure 2. Progress curves for inhibition of cathepsin L by compound **2**. The following inhibitor concentrations were tested (from top to bottom): 0.01–0.05–0.1–0.25–0.5–1.0–2.5 μM. For clarity, the residual initial (v_i, blue) and the residual steady-state (v_S, red) velocities are shown exemplarily for the progress curve at [I] = 2.5 μM.

Non-linear progress curves indicate a covalent inhibition mechanism (resulting either from covalent reversible or covalent irreversible inhibition), or indicate a slow/tight-binding non-covalent reversible inhibition. In case of an irreversible inhibition, the progress curves should reach a plateau value with the terminal residual enzyme activity, i.e., the steady-state velocity of substrate turnover

in the presence of the nhibitor, $v_S = 0$ In the case of reversible inhibition, the progress curves may also reflect a time-dependent inhibition if a two-step mechanism of inhibition occurs. In these cases, the second step reflects the reversible covalent reaction between a nucleophilic amino acid of the enzyme and the electrophilic warhead of the inhibitor or it reflects the inhibition due to a non-covalent high-affinity complex, e.g., resulting from large conformational changes. In such cases, the progress curves display a biphasic behavior with the terminal residual enzyme activity in the presence of the inhibitor $v_S \neq 0$, but with $v_S < v_i$ (with v_i being the initial residual enzyme activity in the presence of the inhibitor, Figure 2). The two scenarios, i.e., irreversible and reversible two-step mechanism, may not be distinguished easily when only the progress curves are regarded, requiring additional investigations of the (ir)reversibility of the inhibition, e.g., by dialysis or dilution assays [35].

In order to verify the (ir)reversibility of inhibition, we thus performed dilution assays with cathepsin L and both inhibitors **1** and **2**, as well with rhodesain and chloro-derivative **1**. These assays showed full reactivation of the enzyme activity in the case of cathepsin L for both inhibitors **1** and **2** (see Figure 3) but only partial reactivation (40–50%) in the case of rhodesain and the chloro-derivative **1** (data not shown).

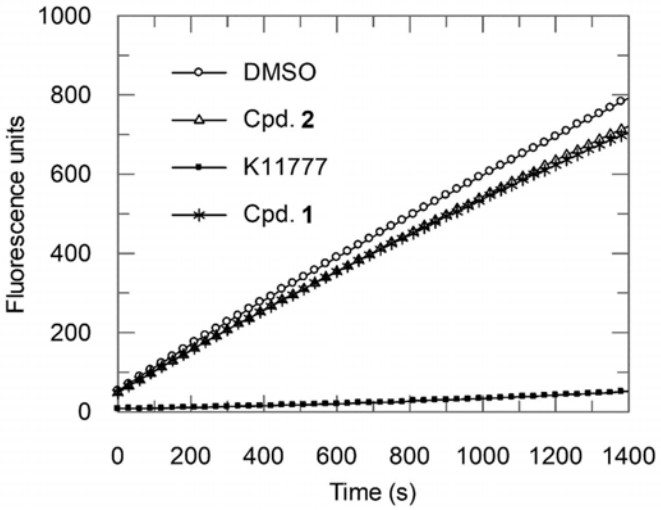

Figure 3. Dilution assays to prove reversible inhibition. Cathepsin L was incubated (15 min) with an excess of inhibitor **1** or **2**, respectively (five times the IC_{50} concentration) to ensure full inhibition. Then, the mixture was diluted by 50-fold to yield a final inhibitor concentration of 10% of the IC_{50} concentration. The enzyme activity, measured through addition of the substrate, nearly fully recovered in case of inhibitors **1** and **2**, whereas in case of the irreversible inhibitor K11777, a well-known vinyl sulfone [36], no recovery was observed.

The biphasic behavior observed in the progress curves for inhibition of cathepsin L by compound **2** (Figure 2) with the steady-state velocity of substrate turnover $v_S \neq 0$, indicates a reversible two-step mechanism, which was supported by the dilution assays. We calculated the dissociation constants of the initial non-covalent enzyme-inhibitor complex K_i ($=\frac{k_2}{k_1}$) and of the final, high-affinity complex K_i^*.

$$\underbrace{\underbrace{E + I \underset{k_2}{\overset{k_1}{\rightleftharpoons}} E{-}{-}{-}I}_{k_i} \underset{k_4}{\overset{k_3}{\rightleftharpoons}} E - I}_{K_i^*}$$

To this end, we determined the initial and steady-state velocities (v_i and v_S) in the presence of the inhibitor (Figure 2) as well as the pseudo-first order rate constants k_{obs} of inhibition for seven different inhibitor concentrations [I] by fitting the progress curves (Figure 2) to Equation (1) [37,38]:

$$[P] = v_s * t + \frac{v_i - v_s}{k_{obs}}[1 - \exp(-k_{obs} * t)] + offset \quad (1)$$

The k_{obs} values were fitted against the inhibitor concentrations [I] (Figure 4) with Equation (2) [37]:

$$k_{obs} = k_4 + (\frac{k_3 * [I]}{K_i^{app} + [I]}) \quad (2)$$

to yield the apparent dissociation constant K_i^{app} of the initial enzyme–inhibitor complex, as well as the rate constants k_3 and k_4 of the second inhibition step (method 1).

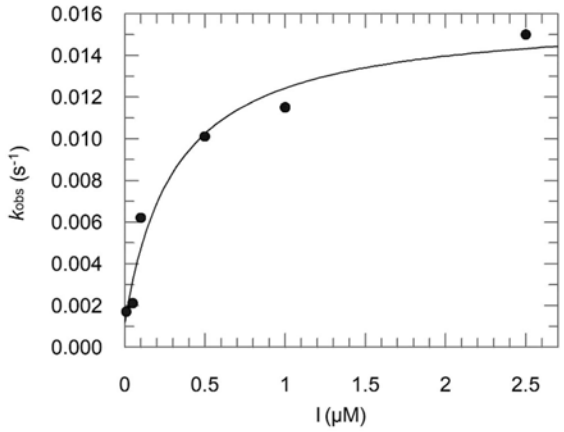

Figure 4. Example of a replot of the k_{obs} values for the progress curves from Figure 2 as a function of inhibitor concentration. The intercept with the *y*-axis provides an estimate of k_4, while the maximum value of k_{obs} at infinite inhibitor concentration reflects the sum of k_3 and k_4. The concentration of inhibitor yielding a half-maximal value of k_{obs} is equal to K_i^{app}.

Since the compound displays competitive inhibition with respect to the substrate (see Figure 1), the K_i^{app} value could be converted to K_i for the initial inhibitor encounter complex with the Cheng–Prusoff equation (Equation (3)) [34]:

$$K_i = \frac{K_i^{app}}{1 + \frac{[S]}{K_m}} \quad (3)$$

The K_i^* value as the dissociation constant of the final high-affinity complex was calculated from Equation (4):

$$K_i^* = \frac{K_i}{1 + (\frac{k_3}{k_4})} \quad (4)$$

Both dissociation constants, K_i and K_i^*, were also obtained (method 2) by fitting the initial (v_i) and steady-state (v_S) velocities, respectively, against the inhibitor concentrations using the Dixon equation (Equation (5)) [32,33]:

$$\frac{v_{i,s}}{v_0} = \frac{[I]}{1 + (\frac{[I]}{K_i^{(*)app}})} \quad (5)$$

In order to obtain K_i^{app} (from fitting v_i against [I]) and K_i^{*app} (from fitting vs. against [I]) with v_0 as the substrate turnover velocity in the absence of the inhibitor. The apparent dissociation constants were again converted into the true dissociation constant using the Cheng–Prusoff equation (Equation (3)).

The following results were obtained:

Method 1: K_i = 0.16 μM; K_i^* = 0.012 μM; k_3 = 0.0148 s^{-1}; k_4 = 0.0012 s^{-1};
Method 2: K_i = 0.30 μM; K_i^* = 0.054 μM.

The results show, that there is good conformity between the two methods for determination of K_i and K_i^* values. The data show that compound **2** displays a two-step inhibition mechanism on cathepsin L with a high affinity (0.012 μM (method 1)/0.054 μM (method 2); i.e., ca. 0.03 μM as mean value) of the final complex and a half-life $t_{1/2}$ of ca. 570 s, i.e., around 10 min(calculated by $t_{1/2} = \frac{0.693}{k_4}$).

Assuming that the forward and the backward reaction proceed along the same reaction path and that their kinetic prefactors are equal, the quotient of k_3 and k_4 can be used to estimate the reaction energy ΔE_{reac} of the second inhibition step by Equation (7), which is derived from Equation (6):

$$\frac{k_3}{k_4} = \frac{A_3 \exp\left(-\frac{\Delta E_3^A}{RT}\right)}{A_4 \exp\left(-\frac{\Delta E_4^A}{RT}\right)} = \exp\left(\frac{\Delta E_4^A - \Delta E_3^A}{RT}\right) = \exp\left(\frac{\Delta E_{reac}}{RT}\right) \quad (6)$$

$$\Delta E_{reac} = ln\left(\frac{k_3}{k_4}\right)RT \quad (7)$$

In Equation (6), ΔE_3^A and ΔE_4^A are the corresponding reaction barriers of the second inhibition step; their difference corresponds to the reaction energy ΔE_{reac} of this step. Using the k_3 and k_4 values measured for **2**, a reaction energy ΔE_{reac} of about −1.5 kcal/mol was obtained.

Table 2. Detailed inhibition data for the time-dependent inhibition of cathepsin L and rhodesain by 1,4-naphthoquinone (NQ)-derived inhibitors of the general structure NQ-NH-L-Phe-L-Leu-OR [1].

Cpd.	Cath. L				Rhod.			
	K_i/K_i^* Method 1	K_i/K_i^* Method 2	k_3/k_4	$t_{1/2}$/ ΔE_{reac}	K_i/K_i^* Method 1	K_i/K_i^* Method 2	k_3/k_4	$t_{1/2}$/ ΔE_{reac}
2	160/12	300/54	0.0148/0.0012	570/ −1.5	Nd	Nd	Nd	Nd
3	443/53	345/61	0.0052/ 0.0007	990/ −1.2	57/11	63/36	0.0025/ 0.0006	1155/−0.85
4	129/19	91/15	0.0051/ 0.0009	770/ −1.1	0.47/0.10	0.32/0.20	0.0027/ 0.0006	1155/−0.89

[1] $K_i^{(*)}$ values in nM; k_3, k_4 in 1/s, $t_{1/2}$ in s, ΔE_{reac} in kcal/mol; values are mean values from at least five independent measurements with standard deviations 15% or less. Nd, not determined.

*2.3. Mass Spectrometry with Benzyl Esters **1** and **2***

To further characterize the interaction between rhodesain and the two benzyl ester-based inhibitors **1** and **2**, we performed a liquid-chromatography–mass spectrometric (LC–MS) analysis of rhodesain that had been incubated with the compounds. Rhodesain without an inhibitor served as a control. Both compounds reacted with rhodesain (Figure 5).

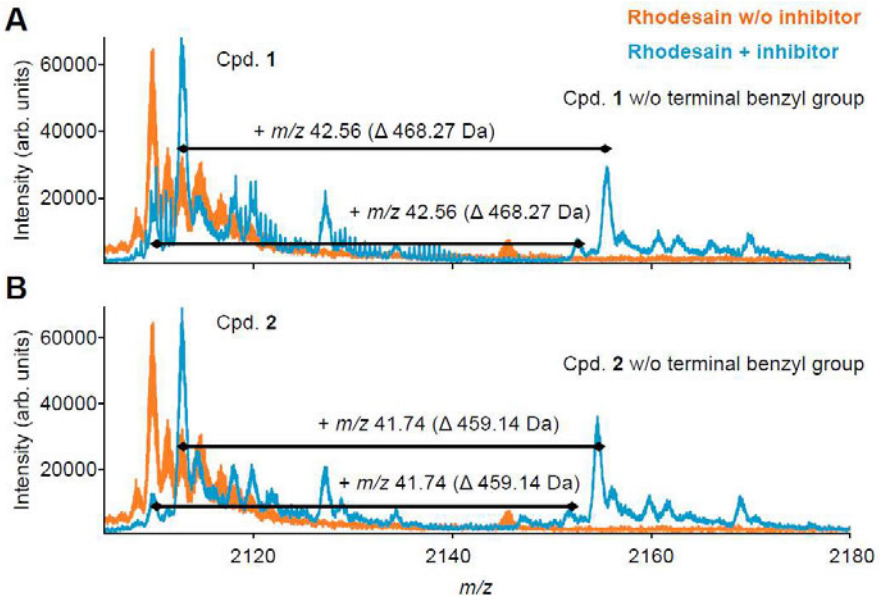

Figure 5. ESI–MS (electrospray ionization) mass spectra (MS) of rhodesain ($[M + 11\ H]^{11+}$ at *m/z* 2109.9 ± 20 ppm) in the absence (orange) or presence (blue) of compounds **1** (**A**) and **2** (**B**). The addition of compounds **1** and **2** resulted in mass shifts of (**A**) *m/z* 42.56 (corresponding to 468.27 Da) and (**B**) *m/z* 41.74 (corresponding to 459.14 Da), in both cases indicating the formation of an adduct between rhodesain and the hydrolysis product (i.e., the acid) of the respective compound.

Interestingly, for both investigated compounds we found that rhodesain catalyzed the hydrolysis of the benzyl ester of the dipeptide recognition unit to the corresponding acid, indicated by a mass shift of 90 Da corresponding to the loss of the terminal benzyl group (Figure 5). Notably, only adducts of the hydrolysis products (i.e., the acids) with rhodesain were detectable by LC–MS analysis. This is in full agreement with previous results, which also revealed enzyme-catalyzed hydrolysis of peptidic benzyl esters with electrophilic warhead by rhodesain yielding free acids as highly active inhibitors [30].

*2.4. Enyzme Assays with Acids **3** and **4**, and Esters **5**–**8***

In order to investigate whether this inhibition mode is also found for other esters, we synthesized and tested the respective methyl and *tert*-butyl esters **5**–**8**. None of these compounds was found to significantly inhibit either cathepsin L or rhodesain at 20 μM.

The free acids **3** and **4**, which were identified via mass spectrometry as rhodesain inhibitors emerging through hydrolysis of the benzyl esters by the target enzyme, were synthesized and tested. While in the case of cathepsin L, we observed a 20-fold improvement for the chloro-derivative **3** compared to the ester **1** (1140 vs. 57 nM), the nitrile-substituted acid **4** turned out to be comparable in potency to its benzyl ester **2** (33 vs. 17 nM). In agreement with previous findings [30], the inhibition of rhodesain was extraordinarily improved with the two acid derivatives **3** and **4** (with 2900 vs. 24 nM ca. 120-fold for the chloro-derivative **3** compared to the ester **1**, with 180 vs. 0.15 nM ca. 1200-fold for the nitrile derivative **4** compared to the ester **2**). For cathepsin B and the DENV PR no improvement in inhibition was observed.

Dilution assays with the five-fold IC_{50} concentrations and 50-fold dilution for the carboxylic acid inhibitors **3** and **4** were performed on both, cathepsin L and rhodesain. These assays showed full reactivation of the enzyme activity for both inhibitors on both enzymes (data not shown). To strengthen the statement of reversible inhibition, we performed dialysis assays with the 20-fold concentration

of the IC_{50} of inhibitor **3** or **4** and rhodesain (Figure 6). For both compounds, **3** and **4**, the enzymatic activity was restored by dialyzing the inhibitor from he reaction vessel. In the case of compound **4**, i.e., the highly potent nitrile-derivative, only slow rea tivation was observed. In the case of the known irreversible inhibitor K11777 [36,39], the enzyme activity could not be recovered.

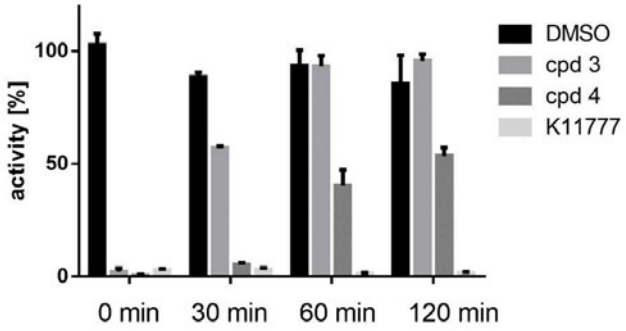

Figure 6. Dialysis assay to investigate the reversibility of the inhibition. Rhodesain was preincubated (30 min) with inhibitor **3**, **4** or K11777, respectively, (20 times the IC_{50} concentration). Then, the mixture was dialyzed in a self-made dialysis chamber [35]. The enzyme activity of all samples was determined relatively to the DMSO treated sample (0 min) by a fluorometric enzyme assay.

Both acids were found to inhibit both enzymes, cathepsin L and rhodesain, reversibly (Figure 6), but time-dependently (Figure 7A,C,E; see Tables 1 and 2 for detailed kinetic data). Dissociation constants K_i and K_i^*, the rate constants k_3 and k_4 and the half-lives $t_{1/2}$ and reaction energies ΔE_{reac} were obtained as described above (see Table 2, see exemplarily Figure 7 for inhibition of cathepsin L by compound **4**, and rhodesain by compounds **3** and **4**).

The detailed kinetic data for the two acid derivatives show that the k_3 and k_4 values, and as a consequence also $t_{1/2}$ and ΔE_{reac} were in the same range for all tested systems. In general, the high overall inhibition exhibited by the compounds was mainly due to very low off-rates k_4 leading to relatively long half-lives (770–1155 s, i.e., 10–20 min). The differences in the overall inhibition potencies of the two acid derivatives against the two enzymes (represented by the K_i^* values) mainly originated from the different stabilities of the initial non-covalent complexes [E−−−I], represented by the K_i values (ca. 400 nM for **3**-CathL; ca. 100 nM for **4**-CathL; ca. 60 nM for **3**-Rhod and ca. 0.4 nM for **4**-Rhod). Thus, the different overall potencies were mainly due to the non-covalent interactions and not to the covalent second inhibition steps. This is especially apparent for the very strong inhibition of rhodesain by compound **4**: the k_3 and k_4 values for the second, covalent step were similar to those of the other enzyme-inhibitor pairs, but the dissociation constant for the initial inhibition step was much lower (K_i ca. 0.4 nM) than those of the others indicating an extremely stable initial non-covalent complex [E−−−I] finally leading to an extraordinarily strong overall inhibition (K_i^* ca. 0.15 nM).

2.5. Hydrolysis Assays with Benzyl, Methyl and tert-Butyl Esters

As reported previously for benzyl esters of the tested dipeptide sequence [30], we raised the hypothesis also in the current case, that the observed ester cleavage of the rhodesain–inhibitor adduct (Figure 5) might occur by rhodesain-catalyzed enzymatic hydrolysis. To verify this hypothesis, we incubated compounds **1**, **2** (benzyl esters), compound **6** (methyl ester) and compound **8** (*tert*-butyl ester) for 24 h with rhodesain. The reaction mixtures were subsequently analyzed by LC–MS.

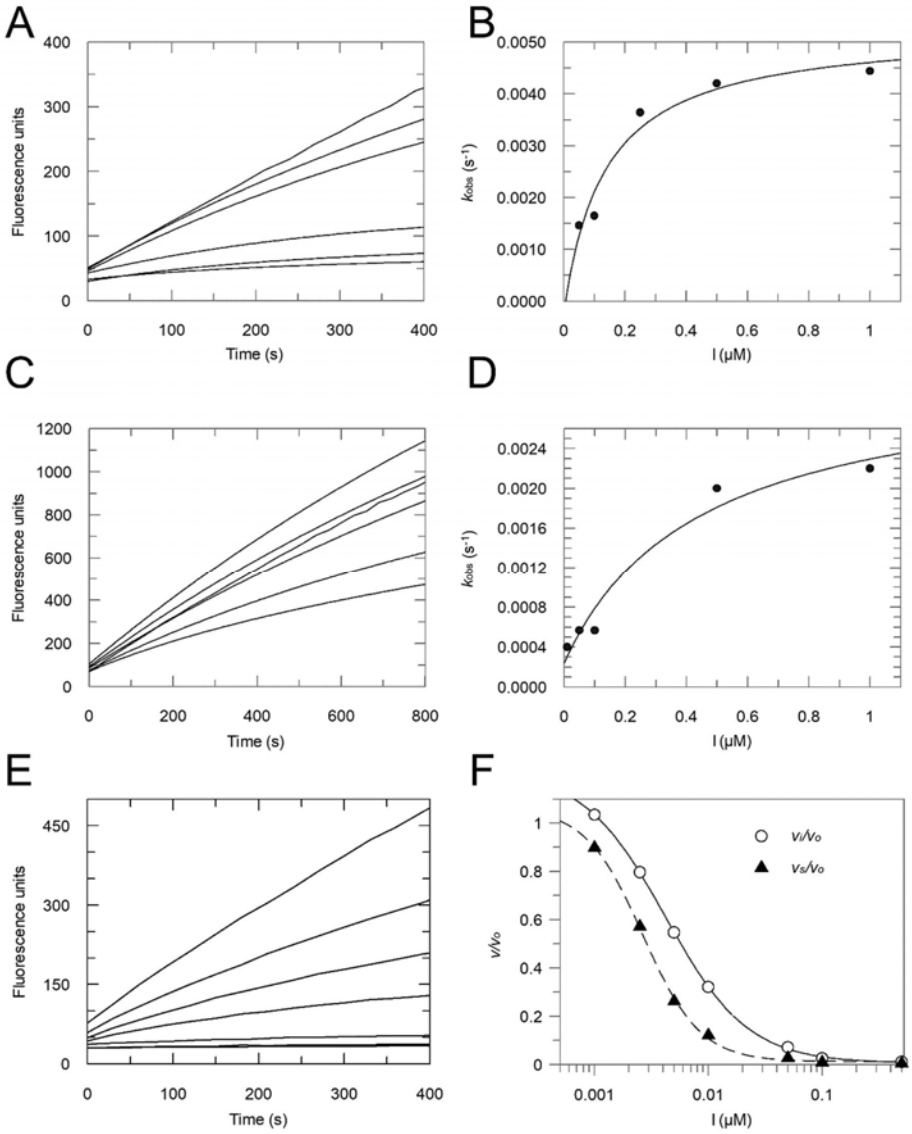

Figure 7. Inhibition of cathepsin L by compound **4** (**A**,**B**), rhodesain by compound **3** (**C**,**D**) and rhodesain by compound **4** (**E**,**F**). **A**,**C**,**E**: Progress curves with the following inhibitor concentrations (each from top to bottom): 0–0.05–0.1–0.25–0.5–1.0 μM (**A**); 0–0.01–0.05–0.1–0.5–1.0 μM (**C**) and 0.001–0.0025–0.005–0.01–0.05–0.1–0.5 μM (**E**). **B, D:** Replots of the k_{obs} values for the progress curves from Figure **7A** (→**B**) and **7C** (→**D**) as a function of inhibitor concentrations. The intercept with the *y*-axis provides an estimate of k_4, while the maximum value of k_{obs} at infinite inhibitor concentration reflects the sum of k_3 and k_4. The concentration of inhibitor yielding a half-maximal value of k_{obs} is equal to K_i^{app}. **F**: Plot of the v_i/v_o and v_S/v_o values obtained from the progress curves of plot E as a function of inhibitor concentrations to yield K_i^{app} and K_i^{*app}, respectively.

In fact, we found ester hydrolysis for the benzyl and methyl esters, but not for the *tert*-butyl ester. Negative controls without rhodesain showed that the esters were not hydrolyzed by the reaction buffer. Exemplarily, the LC–MS analysis of compound **1** is shown in Figure 8. The unconverted ester **1**

was eluted at t_R = 3.19 min. Upon incubation with rhodesain, a peak at t_R = 1.03 min was observed matching the retention time of the reference acid **3**. The detected masses matched the theoretical 90 Da loss of a benzyl group ([cpd**1** + H]$^+$ = 559.2 m/z; [cpd**3** + H]$^+$ = 469.2 m/z) and the isotopic pattern for the chlorine substituent demonstrating the rhodesain-catalyzed ester hydrolysis.

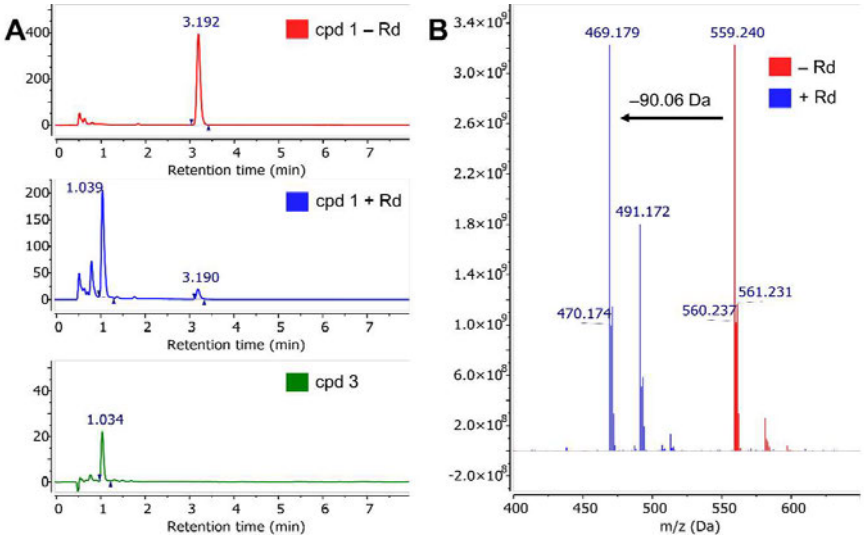

Figure 8. Hydrolysis assay to investigate the ester hydrolysis prodrug concept. (**A**) Exemplarily, the chromatograms for cpd. **1** are shown. Cpd. **1** hydrolyzed with rhodesain (blue, t_R = 1.03 min) shows the same retention time as the reference cpd. **3** (green, t_R = 1.03 min). The negative control incubated without rhodesain shows only the educt peak of cpd. **1** (red, t_R = 3.19 min). (**B**) Analysis of the mass spectrum reveals the loss of a 90 Da fragment, matching the mass and isotopic distribution of the predicted enzymatic benzyl ester hydrolysis ([cpd**1** + H]$^+$ = 559.2 m/z; [cpd**3** + H]$^+$ = 469.2 m/z).

These findings again support our previous identification of the benzyl ester prodrug concept for rhodesain inhibitors [30]: dipeptide-derived benzyl esters containing an electrophilic building block were hydrolyzed by the target enzyme itself to yield the free acids as highly potent inhibitors. According to the MS data, which show the *m/z* peak of the adduct of the enzyme and the complete free acid, the inhibition proceeds via a nucleophilic addition reaction rather than a combined addition/elimination (i.e., a substitution) reaction under the loss of chloride or cyanide. This is in agreement with previous studies on halogen-substituted Michael-acceptors, which showed slow elimination of the halide only in the case of bromine [17].

In order to determine whether the differences in activity between the benzyl esters and the methyl ester are due to different rates of hydrolysis catalyzed by rhodesain yielding the acid as much more potent inhibitor, we followed the reactions spectrophotometrically. Since the esters and the free carboxylic acid have different UV-Vis characteristics, we recorded time-dependent absorbance spectra at 400 nm (Figure 9). Plots of absorbance at 400 nm vs. time showed hyperbolic turnover curves for the benzyl ester (cpd. **2**) and the methyl ester (cpd. **6**), but not for the *tert*-butyl ester (cpd. **8**) or the free carboxylic acid (cpd. **4**) We were able to show that the benzyl ester ($t_{1/2}$ = 3.41 min) was hydrolyzed about three times faster than the methyl ester ($t_{1/2}$ = 10.2 min), which supports the hypothesis that in-situ hydrolysis of the benzyl ester to the more active acid may in parts also be responsible for its inhibitory activity.

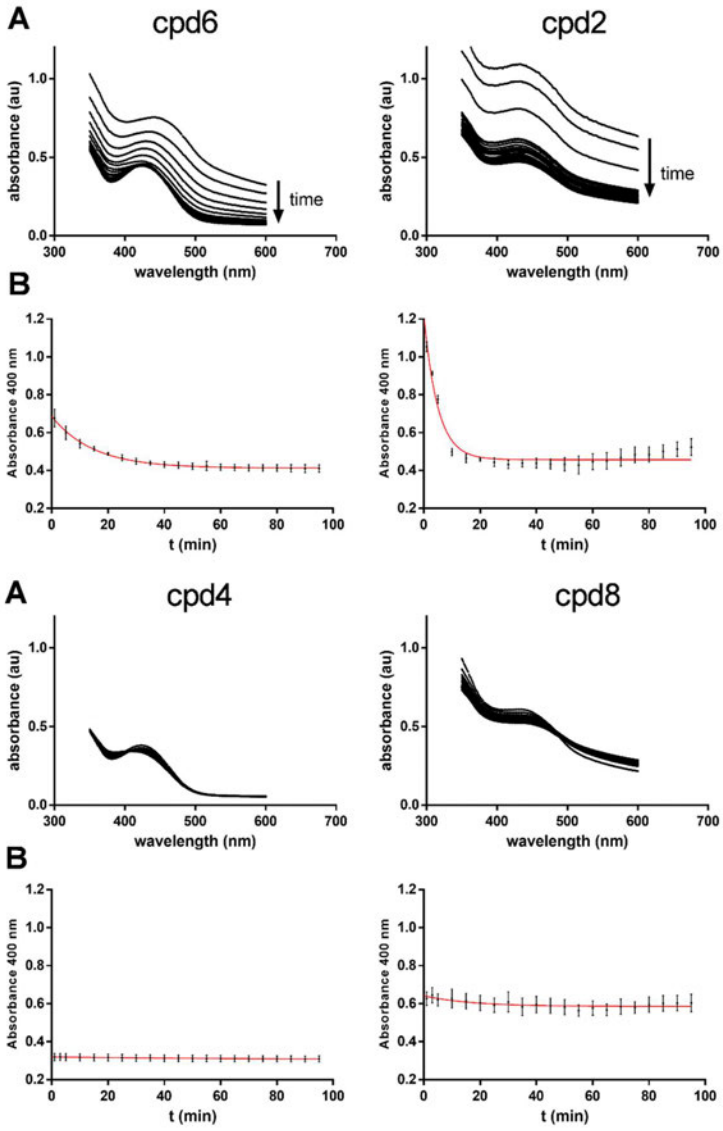

Figure 9. Kinetic analysis of the ester hydrolysis by rhodesain. (**A**) Time-dependent measurement of absorbance spectra (λ = 350–600 nm) of the respective compounds treated with rhodesain; (**B**) Plot of absorbance at 400 nm versus time showed hyperbolic turnover curves for the methyl ester (cpd. **6**, $t_{1/2}$ = 10.2 min) and the benzyl ester (cpd. **2**, $t_{1/2}$ = 3.41 min) but not for the free acid (cpd. **4**) and the *tert*-butyl ester (cpd. **8**).

*2.6. Reaction of Benzyl Esters **1** and **2** with a Low Molecular Weight Thiol*

To further investigate the interaction between the inhibitors and a low molecular weight thiol (LMW thiol), the reactions of the esters **1** and **2** with 2-phenylethanethiol in the presence of a base in ethanol were carried out. It is worth mentioning that, with excess thiol and triethylamine at 80 °C, inhibitor **1** gave the substitution product **9** (Scheme 2) with thiol, which—from a chemical point of view—could be expected (yield 83%), while inhibitor **2** did not react with the thiol at all under the

same reaction conditions. These results were in contrast to the reactions of the inhibitors within the enzyme, which yielded the addition products with the chloro- and the nitrile-substituted inhibitor, but not the substitution products (see below).

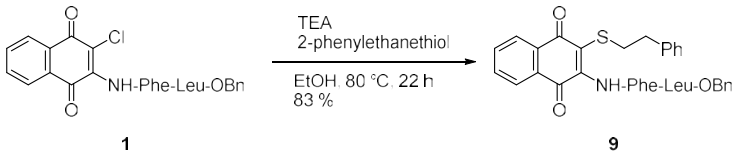

1 **9**

Scheme 2. Substitution reaction with 2-phenylethanethiol.

2.7. Quantum-Mechanical Computations

All tested compounds contain an activated double bond that could undergo a nucleophilic addition or substitution reaction at one of the C-atoms of the α,β-unsaturated carbonyl function with the Cys residue of the active site of cysteine proteases. According to the MS studies, an addition reaction is displayed by both acids **3** and **4**. For unsubstituted naphthoquinones [22], the attack at the β-C atom was proposed. It is known from kinase inhibitors [40] and also from cysteine protease inhibitors [17] that Michael-acceptor systems can be switched from irreversible nucleophilic addition to reversible addition by introduction of an electron-withdrawing group X (X = halogen, nitrile) at the α-position [41]. A reversible addition is also observed for the inhibitors presented herein. As discussed above, in some cases (X = Br), slow irreversible inactivation was found with such inhibitors due to release of the halide anion [17]. On the other hand, nitrile groups are well-known to undergo covalent reversible addition reactions with the active site Cys or Ser residues of cysteine and serine proteases to yield a thioimidate and imidate, respectively [18–21]. Taken together, the structures of the compounds provide several possibilities (Scheme 3) for reactions with the nucleophilic active site Cys residue: reversible nucleophilic attack at one of the carbonyl carbon atoms (Scheme 3: **I a,b**), reversible attack at the nitrile group (**II**) or attack at one of the C-atoms of the double bond (**III, IV**). From the reversible attack at the nitrile group, compound **II** results after protonation. In the case of the β-attack (**III**), the reaction should be reversible since an *S*,*N*-acetal is produced and elimination of the amino group (yielding **III b**) should not be favored, even after its protonation. In case of the α-attack (**IV**), the addition reaction could be either reversible or irreversible (**IV a**). If an elimination of cyanide (or chloride, not shown in the Scheme 3) occurs (**IV b**) the reaction will become irreversible. For the chloro-derivatives, the corresponding products, except **II**, should be possible. According to the MS studies, addition reactions take place within the enzyme for both, the nitrile- and the chloro-substituted compounds. However, the obvious differences between the reaction with an LMW thiol in solution and the reaction within the enzyme have to be considered: with an LMW thiol, the substitution reaction takes place with the chloro-substituted ester (path **IV b**), while the nitrile compound is virtually unreactive.

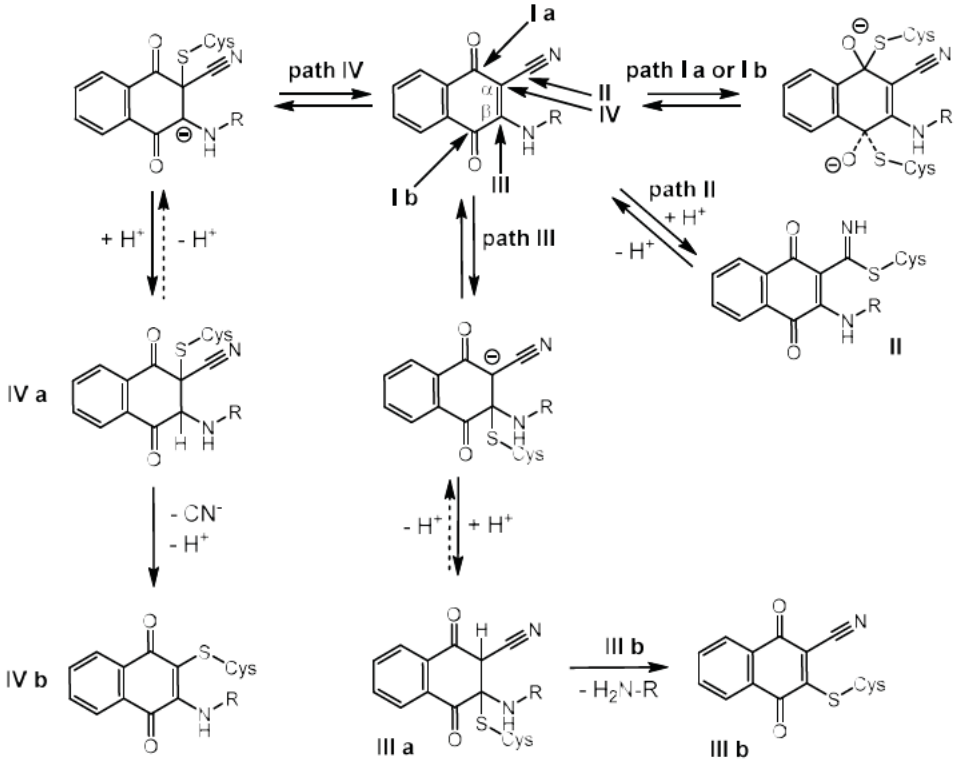

Scheme 3. Possible reaction mechanisms of the 1,4-naphthoquinones with the active-site cysteinate residue, elucidated by quantum-chemical computations. For chloro-substituted compounds, the same pathways and products, except **II**, should be possible.

In order to shed some light on possible inhibition mechanisms, we performed quantum-mechanical (QM) computations of the reaction energies of all possible reactions. In these simulations, the HN-Phe-Leu-OR/OH group was replaced by $HNCH_3$ and the attacking cysteine group was mimicked by methanethiol. In the computations, the influence of water was taken into account through the conductor-like polarizable continuum model (C-PCM) approach [42]. The calculations were performed with the Gaussian 16 program packages [43]. Our computations only focus on reaction energies of the reactions in solvents, i.e., kinetic effects, the influence of the enzyme environment and entropy effects are neglected, which all may influence which reaction path is taken. However, comparable calculations were previously successfully employed to get insights into the inhibition mechanisms of various electrophilic warheads such as three-membered heterocycles [44–46] and Michael-systems [47]. Additionally, more detailed simulations that compute the whole reaction path, take the molecular nature of the enzyme environment and entropy effects into account and thus can provide quantitative predictions about the kinetics of the reactions [48,49] are hardly feasible in the present case because experimental information about the orientation of the inhibitor within the active site of the enzymes are missing. Table 3 shows possible products and intermediates resulting from the various reaction paths given in Scheme 3. Please note that **III a 1** and **III a 4** are enantiomers. The same holds for **III a 2** and **III a 3**; **IV a 1** and **IV a 4** as well as **IV a 2** and **IV a 3**. Nevertheless, we present all data to show that our computations indeed found the same conformers in each case. To ensure that we computed the lowest conformers we characterized various additional conformers, which were all higher in energy.

Table 3 Reactants and products of the reaction of methanethiol with the 1,4-naphthoquinones The corresponding products (except **II**) for the chloro-derivatives are obtained by replacing CN by Cl.

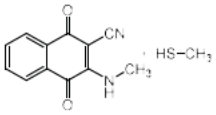			
reactants			
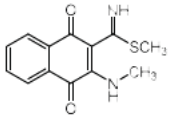			
II			
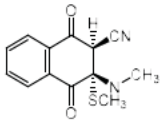	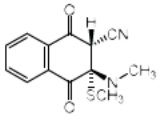	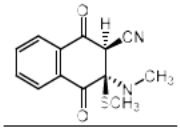	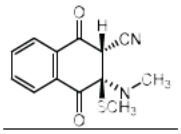
III a 1	**III a 2**	**III a 3**	**III a 4**
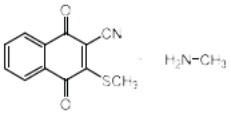			
III b			
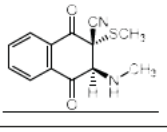	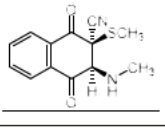	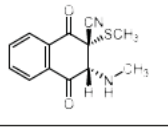	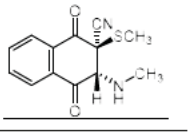
IV a 1	**IV a 2**	**IV a 3**	**IV a 4**
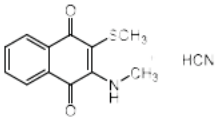			
IV b			

The experimentally determined reversibility of the inhibition for both, the benzyl esters and the acids is in line with a reversible addition to the double bond because backward reactions from the intermediates **I**, **III a** and **IV a** are possible if the exothermicity of the addition reaction is small. The same holds true for the formation of **II**, which represents the product of the addition to the CN group. Such a reaction is also known to be reversible. In contrast, backward reactions from the intermediates **III b** and **IV b** are unlikely because the corresponding leaving groups cyanide (CN^-), chloride (Cl^-) or H_2N-R are not expected to reattack the double bond. Their reactivity is low and they will diffuse away from the reaction site after the bond dissociation. Hence, the reaction paths **III b** and **IV b** would not be in line with the experimental findings concerning the reaction within the enzyme, which neither yielded substitution products with the enzyme for the chloro- nor for the nitrile-substituted derivatives. However, such a reaction path is found for the chloro-derivative in reaction with a low molecular weight thiol. Thus, these steps should be included in the simulation because an insight into the relative energetics of all reaction paths answers the question if the inhibition mechanism might be steered by substituent effects.

The computed data for the nitrile are summarized in Table 4 (C-PCM with ε = 78.36). DFT approaches are known to overestimate stabilization effects in delocalized systems. Consequently, DFT might considerably overestimate the stability of the reactants and of **II**, **III b** and **IV b** with respect to the intermediates **III a 1-4** and **IV a 1-4**, i.e., addition-elimination mechanisms would be erroneously favored with respect to simple addition reactions. Hence, to obtain insights into the applicability of DFT functionals we compared the predictions of B3LYP-D [50,51], CAM-B3LYP, CAM-B3LYP-D [52], M06, M06-2X [53] and ωB97-XD [54] with the computed values of the spin component scaled Møller–Plesset perturbation theory second order (SCS-MP2) approach [55,56]. For the present model computations, we focus on reaction energies (ΔE_{reac}) rather than on free reaction energies (ΔG_{reac}) since the entropy effects are more important for the formation of the non-covalent reversible enzyme-inhibitor complex, which represents a bimolecular reaction. The chemical reaction between inhibitor and enzyme, which will take place after the formation of this complex, represents a unimolecular reaction, i.e., entropy effects are expected to be small within this step.

Table 4. Summary of the reaction energies (ΔE_{reac}) of possible reaction products for the reaction of the nitrile derivative with methanethiol (Scheme 3, Table 3). All calculations were performed with 6-311++G(d,p) basis sets [57] in combination with the C-PCM approach (solvent = water) to mimic environmental effects. The structures were previously optimized with ωB97-XD/6-311G(d,p) [58]. All energy values in kcal/mol.

Method	SCS-MP2	B3LYP-D	CAM-B3LYP	CAM-B3LYP-D	M06	M06-2X	ωB97-XD
II	−1.8	−2.8	−0.1	−3.7	−4.5	−4.7	−4.9
III a 1	−8.5	5.5	8.2	2.1	1.1	−1.8	1.2
III a 2	−6.2	6.5	8.9	2.8	1.6	−1.3	2.1
III a 3	−6.2	6.5	8.9	2.8	1.6	−1.3	2.1
III a 4	−8.5	5.5	8.2	2.1	1.1	−1.8	1.2
III b	9.4	15.7	17.3	17.2	15.1	15.2	16.9
IV a 1	−5.2	9.8	12.0	6.3	6.0	2.8	5.6
IV a 2	−1.6	14.0	15.6	10.4	10.3	6.4	9.3
IV a 3	−1.6	14.0	15.6	10.4	10.3	6.4	9.3
IV a 4	−5.2	9.8	12.0	6.3	6.0	2.8	5.6
IV b	8.8	14.0	15.2	13.8	13.7	11.5	13.9
MAE [1]		**11.6**	**13.5**	**9.2**	**8.6**	**6.1**	**8.6**

[1] Mean average error with respect to SCS-MP2 averaged of all compounds.

According to the presumably most accurate SCS-MP2 approach, the formation of **III a 1** and its enantiomeric form **III a 4** were mostly exothermic (ΔE_{reac} = −8.5 kcal/mol). **III a 2** and its enantiomeric form **III a 3** were predicted to be less stable. For the attack to the nitrile group (formation of **II**), a reaction energy of −1.8 kcal/mol was computed. The most stable isomers of compounds **IV a** were **IV a 1** and **IV a 4** with about −5 kcal/mol. The compounds from which no back-reaction was expected (**III b**, **IV b**) were computed to be very unstable (+9.4 kcal/mol and +8.8 kcal/mol, respectively). DFT calculations came to different conclusions: All functionals predicted compound **II** to be lower in energy than the addition products connected with **III a** or **IV a**. The computed stabilities of **II** with respect to the reactants varied between −0.1 kcal/mol (CAM-B3LYP) and about −5 kcal/mol (ωB97-XD). Products resulting from the addition of methanethiol to the activated double bond were computed to be considerably less stable, in some cases the corresponding reaction was computed to be endothermic. The difference between the wave function and the DFT-based approaches might result because many DFT functionals often overestimate stabilities of delocalized systems. Such effects stabilized the reactants, **II**, **III b** and **IV b** with respect to **III a** and **IV b**. This again underlines that the DFT-based predictions about the reaction mechanisms of warheads have to be regarded with care if compounds with different degrees of delocalization are involved.

The computations provided insights into the thermodynamics of the possible reaction mechanisms, however effects arising from the enzyme environments were neglected. Endothermic mechanisms

were not expected to take place. However, the computations could not predict which of the exothermic reactions did actually take place since this is also dependent on the environment within the enzyme and the geometry of the non-covalent enzyme-inhibitor complex. Computations that take these influences into account, e.g., QM/MM or even QM/MM/MD computations, are only possible when the necessary crystallographic information of the enzyme–inhibitor complex are available, which was not the case for the systems presented herein.

The reaction energies obtained from the measured k_3 and k_4 values for the nitrile-compounds **2** and **4** were between −0.89 and −1.5 kcal/mol. These values fit best to the value for the attack at the nitrile group computed with SCS-MP2 but the formation of **III a** or **IV a** were predicted to be more exothermic, i.e., they should be formed. However, within an enzyme environment they might become less favored due to two reasons. Firstly, the orientation of the inhibitor within the active site might only allow an attack at the nitrile. Additionally, the formation of **III** or **IV** might be hampered by steric effects because the flat sp^2 hybridized inhibitor is transformed into a considerably more bulky form due to the formation of two sp^3 centers. Nevertheless, the computations definitely excluded the formation of intermediates, which should lead to an irreversible enzyme inhibition. This was in line with the experimental results. It is also important to note that the formation of **IV b,** which was not observed in the solvent experiment, was definitively excluded by our computations.

The differences between SCS-MP2 and DFT approaches were even more obvious for the chloro-substituted 1,4-naphthoquinone (Table 5). As for the nitrile compound, SCS-MP2 predicts that the formation of compounds **III a 1** and its enantiomer **III a 4** were most favorable (ΔE_{reac} = −17.3 kcal/mol). Additionally, as computed for the nitrile compound, other compounds could be formed because their reactions energies differed only slightly from those of the formation of **III a 1** and **III a 4**. However, the products that indicate an irreversible substitution reaction (**III b** and **IV b**), were again too high in energy to be formed. In contrast, most DFT functionals predicted the formation of compound **IV b**, i.e., the addition to the double bond followed by the elimination of HCl (H^+ + Cl^-). Since the elimination product (i.e., chloride) is expected to diffuse away and because it is not sufficiently reactive for a reverse reaction, most functionals predicted an irreversible reaction. This was in agreement with the experimental findings for the reaction of the chloro-derivative with excess LMW thiol in solution in the presence of a base. The product of this solution reaction corresponds to product **IV b** in which the chloride was substituted by the attacking thiol group. Does this result indicate that the DFT functionals are right while SCS-MP2 is wrong? This is not the case. For **III a 1**, SCS-MP2 predicted a reversible reaction, i.e., reactants and products were in equilibrium. The formation of **IV b** was also predicted to be exothermic, i.e., this reaction would also take place. Due to the difference in the exothermicity, **IV b** was formed to a lower extent, but because this reaction is irreversible while the formation of **III a 1** is reversible, finally only the product of the irreversible reaction would be found. For the enzyme environment, both reactions can be expected to be in equilibrium because the chloride as elimination product will be formed within the active site of the enzyme, i.e., its diffusion will be strongly hindered. In this case, the formation of e.g., **III a 1** would be considerably favored so that the irreversible reaction will be suppressed. It is also important to note that our computations are in line with the experimental observation that in the solvent reaction of an LMW thiol with the chloro-substituted compound the elimination product **IV b** was formed while it was not formed for the CN-substituted one.

For the chloro-substituted compound, the experimental and computed reaction energies differed considerably. This may be owed to the fact that the computations neglected steric as well as electronic effects arose from the enzyme environment.

According to the QM computations, for both compound classes, namely the chloro and the nitrile derivatives, the reversible attack of the thiolate at the α- or β-position of the double bond (yielding products **III a** or **IV a**) should be possible. The reaction with a LMW thiol took place at the α-C atom in case of the chloro derivative (yielding **IV b**). The experimentally determined ΔE_{reac} values for both the chloro and the nitrile derivatives (**2**–**4**) were in the same range for both enzymes (−0.85 to −1.5 kcal/mol, see Table 2). Taken together, it may be hypothesized that for at least the

chloro-substituted acid, the second covalent inhibition step is the reversible addition of the active-site Cys residue at the α-position, and furthermore, that this inhibition mechanism might also hold true for the nitrile-substituted derivatives.

Table 5. Summary of the relative energies of possible reaction products for the reaction of the chloro-derivative with methanethiol (Scheme 3, Table 3). All calculations were performed with 6-311++G(d,p) basis sets in combination with the C-PCM approach (solvent = water) to mimic environmental effects. The structures were previously optimized with ωB97-XD/6-311G(d,p). All energy values were in kcal/mol.

Method	SCS-MP2	B3LYP-D	CAM-B3LYP	CAM-B3LYP-D	M06	M06-2X	ωB97-XD
III a 1	−17.3	−4.6	−1.3	−7.8	−9.0	−11.4	−8.3
III a 2	−13.2	−1.0	1.4	−4.7	−5.7	−8.7	−5.3
III a 3	−13.2	−1.0	1.4	−4.7	−5.7	−8.7	−5.3
III a 4	−17.3	−4.6	−1.3	−7.8	−9.0	−11.4	−8.3
III b	3.8	11.6	12.4	12.3	10.9	9.9	11.7
IV a 1	−13.6	0.8	3.2	−2.6	−3.4	−6.4	−3.6
IV a 2	−11.4	2.6	4.5	−1.1	−1.3	−4.5	−1.6
IV a 3	−11.4	2.6	4.5	−1.1	−1.3	−4.5	−1.6
IV a 4	−13.6	0.8	3.2	−2.6	−3.4	−6.4	−3.6
IV b	−8.2	−5.8	−5.0	−6.3	−5.3	−6.9	−6.6
MAE [1]		**11.7**	**13.8**	**8.9**	**8.2**	**5.6**	**8.3**

[1] Mean average error with respect to SCS-MP2 averaged of all compounds.

2.8. T. b. brucei Cell Survival Assay

Benzyl ester **2** was tested for its antitrypanosomal activity as described previously [59]. With an EC_{50} value of 0.12 (±0.013) μM (48 h), the compound was found to exhibit very high antitrypanosomal activity. This finding is in agreement with previous investigations, which yielded benzyl esters of the same dipeptidic recognition unit as highly active antitrypanosomal compounds [30]. Again, our results underlined the hypotheses that the benzyl ester **2** is a prodrug with good cell permeability properties that is hydrolyzed by its target enzyme yielding the free acid as highly active rhodesain inhibitor.

3. Discussion

In summary, we presented the facile synthesis and detailed investigation of a class of highly potent protease inhibitors based on 1,4-naphthoquinones carrying a peptidic recognition motif in the 2-position and an electron-withdrawing substituent in the 3-position. A member of this class, namely the nitrile-substituted compound containing the dipeptide sequence NH-L-Phe-L-Leu-OH, was shown to be a highly potent inhibitor of rhodesain, an essential protease of a human-pathogenic parasite, with subnanomolar affinity. To investigate the exact mode of inhibition exerted by this compound class, detailed kinetic and mass spectrometry studies were used and revealed a time-dependent, reversible-covalent binding mode. This particular mode is highly attractive in providing long residence times while at the same time suppressing undesired off-target activity. As found in our previous studies, which reported inhibitors with the same peptidic recognition unit [30], the respective benzyl ester is hydrolyzed by the target enzyme itself yielding the free acid. To better understand the physicochemical basis of the involved processes, we performed calculations with different DFT functionals as well as wave function-based approaches. These were compared in an extensive analysis in which the SCS-MP2 method, but not the investigated density functional turned out to provide reliable estimates for the energetics of the possible individual reaction steps. The knowledge gained in this multifaceted study provides an early step towards the goal of the rational design of new covalent-reversible electrophilic warheads for enzyme inhibitors. The latter ideally provide desirable pharmacokinetic parameters and may even confer resistance-breaking properties as already demonstrated for “simple” covalent kinase inhibitors applied in human oncotherapy.

4. Materials and Methods

See Supplementary Materials.

Supplementary Materials: The following are available online at http://www.mdpi.com/1420-3049/25/9/2064/s1: Syntheses and analytical data of the compounds; Crystallographic data for cpd. **1**; Mass spectrometry; Enzyme assays and hydrolysis assays; *T. b. brucei* cell survival assay; NMR spectra.

Author Contributions: Conceptualization, T.S.; T.O.; P.K.; B.E.; methodology, P.K.; P.J.; F.B.; A.W.; S.T.; U.D.; T.A.L.; P.S.; U.A.H.; investigation, P.K.; P.J.; F.B.; A.W.; S.T.; U.D.; P.S.; U.A.H.; writing—original draft preparation, T.S.; writing—review and editing, T.S.; T.O.; V.E.; B.E.; U.A.H.; supervision, T.S.; T.O.; V.E.; B.E.; U.A.H.; project administration, T.S.; T.O.; funding acquisition, T.O.; U.A.H. All authors have read and agreed to the published version of the manuscript.

Funding: T.O.: Financial support by the Carl Zeiss foundation (project ChemBioMed) is gratefully acknowledged. U.A.H. acknowledges support by the Carl Zeiss Foundation and the Centre for Biomolecular Magnetic Resonance (BMRZ), University of Frankfurt, funded by the state of Hesse.

Acknowledgments: We thank J. C. Liermann (Mainz) for NMR spectroscopy of the compounds, and N. Hanold (Mainz) for mass spectrometry of the compounds.

Conflicts of Interest: The authors declare no conflict of interest.

References

1. Bauer, R.A. Covalent inhibitors in drug discovery: From accidental discoveries to avoided liabilities and designed therapies. *Drug Discov. Today* **2015**, *20*, 1061–1073. [CrossRef] [PubMed]
2. Singh, J.; Petter, R.C.; Kluge, A.F. Targeted covalent drugs of the kinase family. *Curr. Opin. Chem. Biol.* **2010**, *14*, 475–480. [CrossRef] [PubMed]
3. Singh, J.; Petter, R.C.; Baillie, T.A.; Whitty, A. The resurgence of covalent drugs. *Nat. Rev. Drug Discov.* **2011**, *10*, 307–317. [CrossRef] [PubMed]
4. Johnson, D.S.; Weerapana, E.; Cravatt, B.F. Strategies for discovering and derisking covalent, irreversible enzyme inhibitors. *Future Med. Chem.* **2010**, *2*, 949–964. [CrossRef] [PubMed]
5. Potashman, M.H.; Duggan, M.E. Covalent modifiers: An orthogonal approach to drug design. *J. Med. Chem.* **2009**, *52*, 1231–1246. [CrossRef] [PubMed]
6. Mah, R.; Thomas, J.R.; Shafer, C.M. Drug discovery considerations in the development of covalent inhibitors. *Bioorg. Med. Chem. Lett.* **2014**, *24*, 33–39. [CrossRef] [PubMed]
7. Baillie, T.A. Targeted covalent inhibitors for drug design. *Angew. Chem. Int. Ed.* **2016**, *55*, 13408–13421. [CrossRef]
8. De Cesco, S.; Kurian, J.; Dufresne, C.; Mittermaier, A.K.; Moitessier, N. Covalent inhibitors design and discovery. *Eur. J. Med. Chem.* **2017**, *10*, 96–114. [CrossRef]
9. Johansson, M.H. Reversible Michael additions: Covalent inhibitors and prodrugs. *Mini Rev. Med. Chem.* **2012**, *12*, 1330–1344.
10. Palmer, J.T.; Rasnick, D.; Klaus, J.L.; Broemme, D. Vinyl sulfones as mechanism-based cysteine protease inhibitors. *J. Med. Chem.* **1995**, *38*, 3193–3196. [CrossRef]
11. Ettari, R.; Nizi, E.; Di Francesco, M.E.; Dude, M.-A.; Pradel, G.; Vicik, R.; Schirmeister, T.; Micale, N.; Grasso, S.; Zappala, M. Development of peptidomimetics with a vinyl sulfone warhead as irreversible falcipain-2 inhibitors. *J. Med. Chem.* **2008**, *51*, 988–996. [CrossRef] [PubMed]
12. Ettari, R.; Bonaccorso, C.; Micale, N.; Heindl, C.; Schirmeister, T.; Calabro, M.L.; Grasso, S.; Zappala, M. Development of novel peptidomimetics containing a vinyl sulfone moiety as proteasome inhibitors. *ChemMedChem* **2011**, *6*, 1228–1237. [CrossRef] [PubMed]
13. Ettari, R.; Cosconati, S.; Amendola, G.; Chouchene, K.; Wagner, A.; Hellmich, U.A.; Ulrich, K.; Krauth-Siegel, R.L.; Wich, P.R. Development of novel peptide-based Michael acceptors targeting rhodesain and falcipain-2 for the treatment of Neglected Tropical Diseases (NTDs). *J. Med. Chem.* **2017**, *60*, 6911–6923.
14. Breuning, A.; Degel, B.; Schulz, F.; Büchold, C.; Stempka, M.; Machon, U.; Gelhaus, C.; Leippe, M.; Leyh, M.; Kisker, C.; et al. Michael acceptor based antiplasmodial and antitrypanosomal cysteine protease inhibitors with unusual amino acids. *J. Med. Chem.* **2010**, *53*, 1951–1963. [CrossRef]

15. Machon, U.; Büchold, C.; Stempka, M.; Schirmeister, T.; Gelhaus, C.; Leippe, M.; Gut, J.; Rosenthal, P.J.; Kisker, C.; Leyh, M.; et al. On-bead screening of a combinatorial fumaric acid derived peptide library yields antiplasmodial cysteine protease inhibitors with unusual peptide sequences. *J. Med. Chem.* **2009**, *52*, 5662–5672. [CrossRef]
16. Ettari, R.; Micale, N.; Schirmeister, T.; Gelhaus, C.; Leippe, M.; Nizi, E.; Di Francesco, M.E.; Grasso, S.; Zappala, M. Novel peptidomimetics containing a vinyl ester moiety as highly potent and selective falcipain-2 inhibitors. *J. Med. Chem.* **2009**, *52*, 2157–2160. [CrossRef]
17. Schirmeister, T.; Kesselring, J.; Jung, S.; Schneider, T.H.; Weickert, A.; Becker, J.; Lee, W.; Bamberger, D.; Wich, P.R.; Distler, U.; Tenzer, S.; et al. Quantum chemical-based protocol for the rational design of covalent inhibitors. *J. Am. Chem. Soc.* **2016**, *138*, 8332–8335. [CrossRef]
18. Ehmke, V.; Quinsaat, J.E.; Rivera-Fuentes, P.; Heindl, C.; Schirmeister, T.; Diederich, F. Tuning and predicting biological affinity: Aryl nitriles as cysteine protease inhibitors. *Org. Biomol. Chem.* **2012**, *10*, 5764–5768. [CrossRef]
19. Ehmke, V.; Winkler, E.; Banner, D.W.; Haap, W.; Schweizer, W.B.; Rottmann, M.; Kaiser, M.; Freymond, C.; Brun, R.; Schirmeister, T.; et al. Optimization of triazine nitriles as rhodesain inhibitors: Structure-activity relationships, bioisosteric imidazopyridine nitriles, and X-ray crystal structure analysis with human cathepsin L. *ChemMedChem* **2013**, *8*, 967–975. [CrossRef]
20. Schirmeister, T.; Schmitz, J.; Jung, S.; Schmenger, T.; Krauth-Siegel, R.L.; Gütschow, M. Evaluation of dipeptide nitriles as inhibitors of rhodesain, a major cysteine protease of *Trypanosoma brucei*. *Bioorg. Med. Chem. Lett.* **2016**, *27*, 45–50. [CrossRef]
21. Giroud, M.; Ivkovic, J.; Martignoni, M.; Fleuti, M.; Trapp, N.; Haap, W.; Kuglstatter, A.; Benz, J.; Kuhn, B.; Schirmeister, T.; et al. Inhibition of the cysteine protease human cathepsin L by triazine nitriles: Amide·heteroarene π-stacking interactions and chalcogen bonding in the S3 pocket. *ChemMedChem* **2017**, *12*, 257–270. [CrossRef]
22. Valente, C.; Moreira, R.; Guedes, R.C.; Iley, J.; Jaffar, M.; Douglas, K.T. The 1,4-naphthoquinone scaffold in the design of cysteine protease inhibitors. *Bioorg. Med. Chem. Lett.* **2007**, *15*, 5340–5350. [CrossRef] [PubMed]
23. Olson, O.C. Cysteine cathepsin proteases: Regulators of cancer progression and therapeutic response. *Nat. Rev. Cancer* **2015**, *15*, 712–729. [CrossRef] [PubMed]
24. Mohamed, M.M. Cysteine cathepsins: Multifunctional enzymes in cancer. *Nat. Rev. Cancer* **2006**, *6*, 764–775. [CrossRef] [PubMed]
25. Ettari, R.; Previti, S.; Tamborini, L.; Cullia, G.; Grasso, S.; Zappala, M. The inhibition of cysteine proteases rhodesain and TbCatB: A valuable approach to treat Human African Trypanosomiasis. *Mini Rev. Med. Chem.* **2016**, *16*, 1374–1391. [CrossRef] [PubMed]
26. Ferreira, L.G.; Andricopulo, A.D. Targeting cysteine proteases in trypanosomatid disease drug discovery. *Pharmacol. Ther.* **2017**, *180*, 49–61. [CrossRef] [PubMed]
27. Nitsche, C.; Holloway, S.; Schirmeister, T.; Klein, C.D. Biochemistry and medicinal chemistry of the Dengue virus protease. *Chem. Rev.* **2014**, *114*, 11348–11381. [CrossRef] [PubMed]
28. Millies, B.; Hammerstein, V.F.; Gellert, A.; Hammerschmidt, S.; Barthels, F.; Göppel, U.; Immerheiser, M.; Elgner, F.; Jung, N.; Basic, M.; et al. Proline-based allosteric inhibitors of Zika and Dengue virus NS2B/NS3 proteases. *J. Med. Chem.* **2019**, *62*, 11359–11382. [CrossRef]
29. Vicik, R.; Busemann, M.; Gelhaus, C.; Stiefl, N.; Scheiber, J.; Schmitz, W.; Schulz, F.; Mladenovic, M.; Engels, B.; Leippe, M.; et al. Aziridide-based inhibitors of cathepsin L: Synthesis, inhibition activity, and docking studies. *ChemMedChem* **2006**, *1*, 1126–1141. [CrossRef]
30. Klein, P.; Johe, P.; Wagner, A.; Jung, S.; Kühlborn, J.; Tenzer, S.; Distler, U.; Waigel, W.; Engels, B.; Hellmich, U.A.; et al. New cysteine protease inhibitors: Electrophilic (het)arenes and unexpected prodrug identification for the *Trypanosoma* protease rhodesain. *Molecules* **2020**, *25*, 1451. [CrossRef]
31. Autschbach, J.; Srebro, M. Delocalization Error and "Functional Tuning" in Kohn–Sham Calculations of Molecular Properties. *Acc. Chem. Res.* **2014**, *47*, 2592–2602. [CrossRef] [PubMed]
32. Dixon, M. The determination of enzyme inhibitor constants. *Biochem. J.* **1953**, *55*, 170–171. [CrossRef] [PubMed]
33. Dixon, M. The graphical determination of K_m and K_i. *Biochem. J.* **1972**, *129*, 197–202. [CrossRef] [PubMed]

34. Cheng, Y.-C.; Prusoff, W.H. Relationship between the inhibition constant (K_i) and the concentration of inhibitor which causes 50 percent inhibition (I_{50}) of an enzymatic reaction. *Biochem. Pharmacol.* **1973**, *22*, 3099–3108.
35. Ludewig, S.; Kossner, M.; Schiller, M.; Baumann, K.; Schirmeister, T. Enzyme kinetics and hit validation in fluorometric enzyme assays. *Curr. Top. Med. Chem.* **2010**, *10*, 368–382. [CrossRef]
36. Kerr, I.D.; Lee, J.H.; Farady, C.J.; Marion, R.; Rickert, M.; Sajid, M.; Pandey, K.C.; Caffrey, C.R.; Legac, J.; Hansell, E.; et al. Vinyl sulfones as antiparasitic agents and a structural basis for drug design. *J. Biol. Chem.* **2009**, *284*, 25697–25703. [CrossRef]
37. Purich, D.L. *Enzyme Kinetics, Catalysis and Control: A reference of Theory and Best-Practice Methods*; Elsevier: San Diego, CA, USA, 2010; pp. 531–533, ISBN 9780123809247.
38. Copeland, R.A. *Evaluation of Enzyme Inhibitors in Drug Discovery: A Guide for Medicinal Chemists and Pharmacologists*; Wiley: Hoboken, NJ, USA, 2005.
39. Yang, P.-Y.; Wang, M.; He, C.Y.; Yao, S.Q. Proteomic profiling and potential cellular target identification of K11777, a clinical cysteine protease inhibitor, in *Trypanosoma brucei*. *Chem. Commun.* **2012**, *48*, 835–837. [CrossRef]
40. Smith, S.; Keul, M.; Engel, J.; Basu, D.; Eppmann, S.; Rauh, D. Characterization of covalent-reversible EGFR inhibitors. *ACS Omega* **2017**, *2*, 1563–1575. [CrossRef]
41. Lee, C.-U.; Grossmann, T.N. Reversible covalent inhibition of a protein target. *Angew. Chem. Int. Ed. Engl.* **2012**, *51*, 8699–8700. [CrossRef] [PubMed]
42. Cossi, M.; Rega, N.; Scalmani, G.; Barone, V. Energies, structures, and electronic properties of molecules in solution with the C-PCM solvation model. *J. Comput. Chem.* **2003**, *24*, 669–681. [CrossRef]
43. Frisch, M.J.; Trucks, G.W.; Schlegel, H.B.; Scuseria, G.E.; Robb, M.A.; Cheeseman, J.R.; Scalmani, G.; Barone, V.; Petersson, G.A.; Nakatsuji, H.; et al. *Gaussian 16 revision B.01*; Gaussian: Wallingford, CT, USA, 2016.
44. Helten, H.; Schirmeister, T.; Engels, B. Model calculations about the influence of protic environments on the alkylation step of epoxide, aziridine and thiirane based cysteine protease inhibitors. *J. Phys. Chem. A* **2004**, *108*, 7691–7701. [CrossRef]
45. Vicik, R.; Helten, H.; Schirmeister, T.; Engels, B. Rational design of aziridine containing cysteine protease inhibitors with improved potency—Studies on inhibition mechanism. *ChemMedChem* **2006**, *1*, 1021–1028. [CrossRef] [PubMed]
46. Helten, H.; Schirmeister, T.; Engels, B. Theoretical studies about the influence of different ring substituents on the nucleophilic ring opening of three-membered heterocycles and possible implications for the mechanisms of cysteine protease inhibitors. *J. Org. Chem.* **2005**, *70*, 233–237. [CrossRef] [PubMed]
47. Paasche, A.; Schiller, M.; Mladenovic, M.; Schirmeister, T.; Engels, B. Mechanistic study about the reaction of thiol-containing enzymes with α,β-unsaturated carbonyl substrates by computations and chemoassays. *ChemMedChem* **2010**, *5*, 869–880. [CrossRef]
48. Mladenovic, M.; Junold, K.; Fink, R.F.; Thiel, W.; Schirmeister, T.; Engels, B. Atomistic insights into the inhibition of cysteine proteases: First QM/MM calculations clarifying the regiospecificity and the inhibition potency of epoxide- and aziridine-based inhibitors. *J. Phys. Chem. B* **2008**, *112*, 5458–5469. [CrossRef]
49. Mladenovic, M.; Fink, R.F.; Thiel, W.; Schirmeister, T.; Engels, B. Atomistic insights into the inhibition of cysteine proteases: First QM/MM calculations clarifying the stereoselectivity of epoxide-based inhibitors. *J. Phys. Chem. B* **2008**, *112*, 11798–11808. [CrossRef]
50. Becke, A.D. Density-Functional Thermochemistry. III. The Role of Exact Exchange. *J. Chem. Phys.* **1993**, *98*, 5648–5652. [CrossRef]
51. Grimme, S.; Antony, J.; Ehrlich, S.; Krieg, H. A Consistent and accurate ab initio parameterization of density functional dispersion correction (DFT-D) for the 94 elements H-Pu. *J. Chem. Phys.* **2010**, *132*, 154104. [CrossRef]
52. Yanai, T.; Tew, D.P.; Handy, N.C. A new hybrid exchange–correlation functional using the Coulomb-attenuating method (CAM-B3LYP). *Chem. Phys. Lett.* **2004**, *393*, 51–57. [CrossRef]
53. Zhao, Y.; Truhlar, D.G. The M06 suite of density functionals for main group thermochemistry, thermochemical kinetics, noncovalent interactions, excited states, and transition elements: Two new functionals and systematic testing of four M06-class functionals and 12 other functionals. *Theor. Chem. Acc.* **2008**, *120*, 215–241.
54. Chai, J.-D.; Head-Gordon, M. Long-range corrected hybrid density functionals with damped atom-atom dispersion corrections. *Phys. Chem. Chem. Phys.* **2008**, *10*, 6615–6620. [CrossRef] [PubMed]

55. Grimme, S. Improved second-order Møller−Plesset perturbation theory by separate scaling of parallel- and antiparallel-spin pair correlation energies. *J. Chem. Phys.* **2003**, *118*, 9095–9102. [CrossRef]
56. Head-Gordon, M.; Pople, J.A.; Frisch, M.J. MP2 energy evaluation by direct methods. *Chem. Phys. Lett.* **1988**, *153*, 503–506. [CrossRef]
57. Clark, T.; Chandrasekhar, J.; Spitznagel, G.W.; Schleyer, P.V.R. Efficient diffuse function-augmented basis-sets for anion calculations. III.* The 3-21+G basis set for first-row elements, Li-F. *J. Comp. Chem.* **1983**, *4*, 294–301. [CrossRef]
58. Krishnan, R.; Binkley, J.S.; Seeger, R.; Pople, J.A. Self-consistent molecular orbital methods. XX. A basis set for correlated wave functions. *J. Chem. Phys.* **1980**, *72*, 650–654. [CrossRef]
59. Wagner, A.; Le, T.A.; Brennich, M.; Klein, P.; Bader, N.; Diehl, E.; Paszek, D.; Weickhmann, A.K.; Dirdjaja, N.; Krauth-Siegel, R.L.; et al. Inhibitor-induced dimerization of an essential oxidoreductase from African trypanosomes. *Angew. Chem. Int. Ed.* **2019**, *58*, 3640–3644. [CrossRef]

“

4.2 New Cysteine Protease Inhibitors: Electrophilic (Het)Arenes and Unexpected Prodrug Identification for the Trypanosoma Protease Rhodesain

4.2.1 Context, Project Summary, and own Contribution

Nucleophilic aromatic substitution (S_NAr) reactions have rarely been used for enzyme inhibiting warheads.[121] In this study, fluorine and chlorine substituted (hetero)aromatic warheads were investigated for their ability to inhibit rhodesain. The reactivity of (hetero)arenes in S_NAr reaction increases with the electron deficiency of the aromatic system and is therefore finely modulable, making S_NAr warheads potentially versatile chemotypes for medicinal chemical applications.[303] The eight inhibitors of this study consisted of a conserved recognition sequence (H_2N-L-Phe-L-Leu-OBn) with an S_NAr warhead at its N-terminus and were synthesized by the group of [redacted].

Kinetic enzyme assays revealed a potent fluorodinitroarene inhibitor with nanomolar affinity (K_I=4 nM) and a reversible course of inhibition. Selectivity studies with human cathepsins B and L indicated that this novel inhibitor chemotype has excellent selectivity for the trypanosomal rhodesain (S.I.>375). Subsequent NMR spectroscopy, mass spectrometry, and theoretical investigations unraveled an unexpected mode of inhibitor action: There was no elimination of the fluorine atom during the warhead reaction with the catalytic Cys25 which would have resulted in covalent bonding and an irreversible inhibition course. Instead, an S_NAr-type intermediate (σ, π, or Meisenheimer complex) was stabilized which could be detected in both NMR and mass spectrometric investigations. The inhibition kinetics showed the characteristics of non-covalently reversible inhibition, highlighting the borderline character of this warhead reactivity.

Hydrolysis assays similar to those performed in chapter 4.1 showed the loss of the benzyl ester group of the inhibitor upon treatment with rhodesain.[6] Subsequent ESI mass spectrometry of the intact protein-inhibitor complex was used to confirm this “on-target” prodrug concept. MD and QM/MM simulations of the rhodesain inhibitor complex proposed that after cleavage of the ester, the carboxylic acid leaves the substrate-binding pocket and rebinds in an inverted orientation, forming a very stable non-covalent π-complex between the inhibitor and the catalytic Cys25. The benzyl ester prodrug of the fluorodinitroarene inhibitor showed an EC_{50}=95 nM, making the compound one of the most potent known anti-trypanosomal inhibitors.[261]

Own contributions: Protease selectivity assays & Minor parts of the rhodesain inhibition assays.

Contributions from other authors: Synthesis and characterization of the inhibitors, Thiol reactivity experiments, Protein expression and purification, Protein mass spectrometry, ^{19}F-NMR spectrometry, Major parts of the rhodesain inhibition assays, *T. brucei* cell assays, Molecular modeling & Quantum chemical investigations.

This work has been published in: Molecules (impact factor: 4.41).

The 'Supporting Information' can be accessed online at doi: 10.3390/molecules25061451.

4.2.2 Publication

The following publication quoted (within "") from page 173 to page 194 is exactly the same as the manuscript cited on page 172:"

molecules

MDPI

Article

New Cysteine Protease Inhibitors: Electrophilic (Het)arenes and Unexpected Prodrug Identification for the *Trypanosoma* Protease Rhodesain

Philipp Klein [1,†], Patrick Johe [2,†], Annika Wagner [3], Sascha Jung [2,4], Jonas Kühlborn [1], Fabian Barthels [2], Stefan Tenzer [5], Ute Distler [5], Waldemar Waigel [6], Bernd Engels [6], Ute A. Hellmich [3,7], Till Opatz [1,*] and Tanja Schirmeister [2,*]

1 Department of Chemistry, Organic Chemistry Section, Johannes Gutenberg-Universität, 55128 Mainz, Germany; klein@uni-mainz.de (P.K.); jokuehlb@uni-mainz.de (J.K.)
2 Institute of Pharmaceutical and Biomedical Sciences, Johannes Gutenberg-Universität, 55128 Main, Germany; pajohe@uni-mainz.de (P.J.); sascha.jung@tu-dortmund.de (S.J.); barthels@uni-mainz.de (F.B.)
3 Department of Chemistry, Biochemistry Section, Johannes Gutenberg-Universität, 55128 Mainz, Germany; a.wagner@uni-mainz.de (A.W.); u.hellmich@uni-mainz.de (U.A.H.)
4 Present address: Faculty of Chemistry and Chemical Biology, TU Dortmund University, 44227 Dortmund, Germany
5 Institute of Immunology, University Medical Center, Johannes Gutenberg-Universität Mainz, 55131 Mainz, Germany; tenzer@uni-mainz.de (S.T.); ute.distler@uni-mainz.de (U.D.)
6 Institute of Physical and Theoretical Chemistry, Universität Würzburg, 97074 Würzburg, Germany; waldemar.waigel@uni-wuerzburg.de (W.W.); bernd.engels@uni-wuerzburg.de (B.E.)
7 Centre for Biomolecular Magnetic Resonance (BMRZ), Goethe-University Frankfurt, 60323 Frankfurt, Germany
* Correspondence: opatz@uni-mainz.de (T.O.); schirmei@uni-mainz.de (T.S.); Tel.: +49-(0)6131-39-22272 (T.O.); +49-(0)6131-39-25742 (T.S.)
† Both authors contributed equally.

Received: 11 February 2020; Accepted: 13 March 2020; Published: 23 March 2020

check for updates

Abstract: Electrophilic (het)arenes can undergo reactions with nucleophiles yielding π- or Meisenheimer (σ-) complexes or the products of the S_NAr addition/elimination reactions. Such building blocks have only rarely been employed for the design of enzyme inhibitors. Herein, we demonstrate the combination of a peptidic recognition sequence with such electrophilic (het)arenes to generate highly active inhibitors of disease-relevant proteases. We further elucidate an unexpected mode of action for the trypanosomal protease rhodesain using NMR spectroscopy and mass spectrometry, enzyme kinetics and various types of simulations. After hydrolysis of an ester function in the recognition sequence of a weakly active prodrug inhibitor, the liberated carboxylic acid represents a highly potent inhibitor of rhodesain (K_i = 4.0 nM). The simulations indicate that, after the cleavage of the ester, the carboxylic acid leaves the active site and re-binds to the enzyme in an orientation that allows the formation of a very stable π-complex between the catalytic dyad (Cys-25/His-162) of rhodesain and the electrophilic aromatic moiety. The reversible inhibition mode results because the S_NAr reaction, which is found in an alkaline solvent containing a low molecular weight thiol, is hindered within the enzyme due to the presence of the positively charged imidazolium ring of His-162. Comparisons between measured and calculated NMR shifts support this interpretation.

Keywords: cysteine protease; rhodesain; electrophilic (het)arene; nucleophilic aromatic substitution; Meisenheimer complex; π-complex; prodrug

1. Introduction

Inhibition of enzymes may occur either reversibly or irreversibly. In the case of irreversible inhibition, a covalent reaction between a nucleophilic amino acid (in most cases, an activated Cys, Ser or Thr side chain), either of the active or an allosteric site, reacts with an electrophilic functional group of the inhibitor, the so-called "warhead". Besides this reactive building block, enzyme inhibitors also contain a recognition unit fitting into the substrate binding pockets. In the case of protease inhibitors these are mainly peptidic or peptidomimetic sequences. However, not all covalent reactions of enzyme and inhibitor lead to irreversible inhibition, and this has received increasing attention in drug development in the last years to design covalent, but reversible inhibitors due to several advantages over non-covalent inhibitors such as longer target residence times or higher potency and ligand efficiency (for reviews on this topic see [1–8]).

In contrast to classical electrophilic building blocks like Michael-acceptor systems [9–17], nitriles [18–21], aldehydes, ketones [22–24], three-membered heterocycles [25–28] or a iodoacetic acid moiety [29,30], (hetero)aromatic electrophiles, which can react via nucleophilic addition (yielding π- or σ-complexes) or substitution reactions (S_NAr) have only rarely been employed [31–35]. Such aromatic moieties have also seldom been investigated as non-covalently binding parts of the recognition units of enzyme inhibitors [36,37].

We therefore aimed to explore the potential of such groups as new building blocks for cysteine proteases of the papain family, specifically the human cathepsins B and L, and the *Trypanosoma* protease rhodesain. The human enzymes of this family play crucial roles in tumor diseases [38,39]. The cathepsin L-like protease rhodesain from *Trypanosoma brucei rhodesiense*, the parasite causing human African trypanosomiasis (HAT), is essential for the parasite's survival, since it is involved in several pathological processes in the host. These include, e.g., the crossing of the parasite through the blood–brain barrier as well as the turnover of variant surface glycoproteins (VSGs), and degradation of host immunoglobulins [40,41].

In the current proof-of-principle study, we tested the overall potency of (hetero)aromatics as building blocks for peptidic protease inhibitors. Since we were interested in the inhibition properties of the (hetero)aromatic moiety, we used the same recognition unit, the dipeptide sequence H_2N-L-Phe-L-Leu-OBn, and attached various (hetero)aromatic electrophiles to its N-terminus. This dipeptide was chosen for two reasons: (1) It was previously shown to be an appropriate recognition unit for cathepsin L-like cysteine proteases supposed to bind into the substrate-binding pockets in an anti-substrate orientation [14,15,42]; (2) In contrast to amino acids with functionalized side chains, no additional protection/deprotection steps are necessary during synthesis.

For one inhibitor, we observed that the benzyl ester of the recognition unit was hydrolyzed by the target proteases. Intriguingly, the resulting free acid (with HN-L-Phe-L-Leu-OH moiety) represents a nanomolar inhibitor against rhodesain.

The inhibition potencies of the new inhibitors were tested on the human cathepsins B and L (cath. B, cath. L), the cathepsin L-like protease rhodesain (rhod.) from *T. b. rhodesiense*, and, in order to check their selectivity and to exclude promiscuous inhibition, on the *Staphylococcus aureus* cysteine protease and transpeptidase sortase A with a "reversely protonated" catalytic cysteine residue [43], as well as on the serine protease of the Dengue virus (DENV PR), which shares the P1 specificity for Arg with cathepsins.

The formation of a complex between inhibitor and the target protease rhodesain was indicated by mass spectrometry and NMR spectroscopy. Possible binding modes of selected inhibitors were analyzed by docking, followed by subsequent molecular dynamics (MD) simulations. Additionally, we performed quantum mechanical (QM) computations for model systems and quantum mechanics / molecular mechanics (QM/MM) simulations, which include the enzyme environment.

2. Results

.1. Syntheses

The synthesis of the new inhibitors started from commercially available L-leucine benzyl ester *p* oluenesulfonate and Boc-protec ed L-phenylalanine, which were coupled by carbodiimide chemistry. The dipeptide product was easily purified by recrystallization (Scheme 1). Deprotection with either hydrochloric acid in dioxane (4 M) or trifluoro-acetic acid (TFA) in dichloromethane (DCM)(40%) afforded the ammonium salt, which was directly used in the subsequent steps.

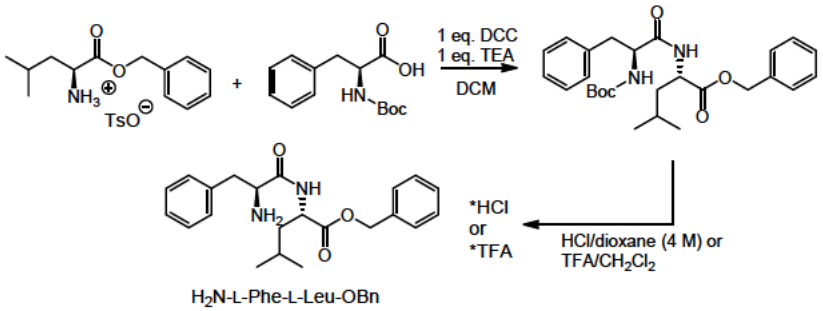

Scheme 1. Synthesis of the dipeptide sequence of new protease inhibitors.

The potential inhibitors were synthesized either by S_NAr reaction on a (hetero)aromatic unit carrying two potential leaving groups (compounds **2**, **3**, and **7**) or by reaction with an electrophilic group attached to the ring system (e.g., acid chloride, isocyanate and compounds **1**, **4**, **5**, and **6**, Scheme 2).

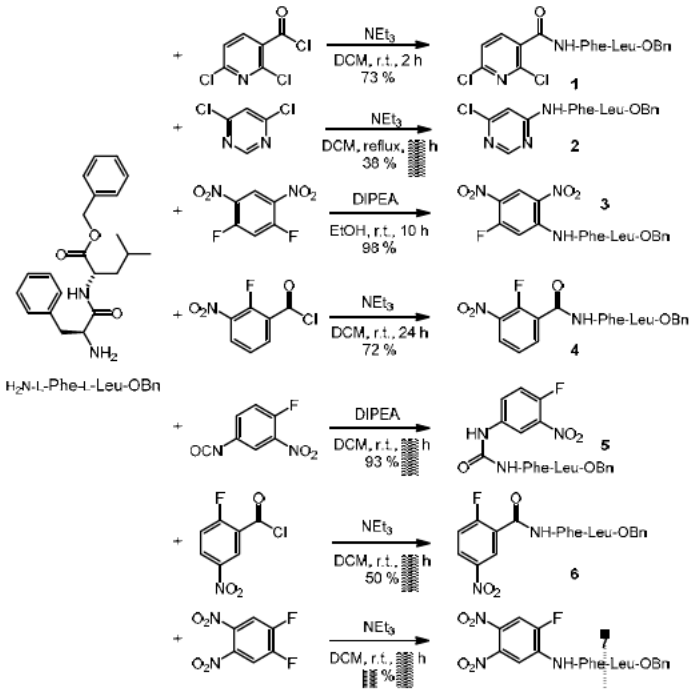

Scheme 2. Syntheses of potential protease inhibitors of the general structure R-NH-L-Phe-L-Leu-OBn with (hetero)aromatic units (R).

To further investigate whether the hydrolysis product of compound **7** is the active compound as indicated by MS, NMR and hydrolysis studies (see Sections 2.3–2.5), the corresponding free acid **8** was also synthesized (Scheme 3). First attempts to cleave the benzyl ester of compound **7** with PPL (porcine pancreatic lipase) were unsuccessful. The compound was synthesized starting from the fully protected dipeptide Boc-NH-L-Phe-L-Leu-OBn. In a first step, the benzyl ester was removed by hydrogenolysis. A short filtration over celite yielded a crude material that was subjected to acidolytic removal of the Boc-protecting group with trifluoroacetic acid (TFA). The solvent was removed to perform the reaction with the warhead (1,2-difluoro-4,5-dinitrobenzene) in ethanol in the presence of triethylamine. After 21 h at 80 °C, the desired acid **8** was obtained after purification by preparative high-performance liquid chromatography (HPLC).

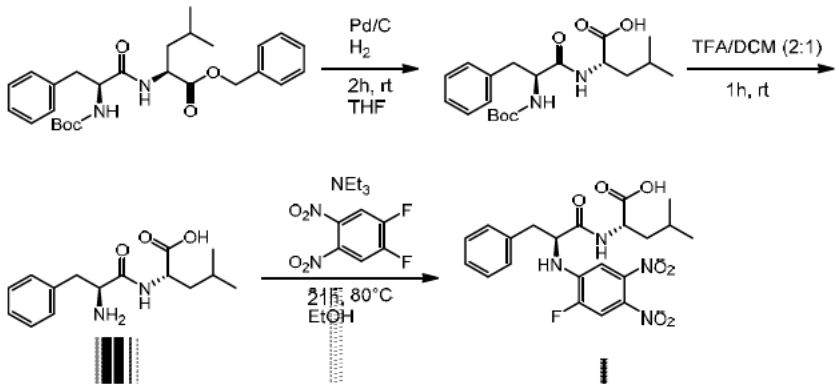

Scheme 3. Synthesis of acid **8** (R-NH-L-Phe-L-Leu-OH).

2.2. Enzyme Assays

Inhibition of cathepsins and rhodesain was tested with the fluorogenic substrate Cbz-Phe-Arg-AMC as described previously [19]. First, a screening at 20 µM inhibitor concentration was performed. For compounds showing >60% inhibition at this concentration, the IC_{50} values were determined. For the most active compounds, namely **4** and **7**, the IC_{50} values were determined at different substrate concentrations in order to check for competitive or non-competitive inhibition [44,45]. IC_{50} values were found to increase linearly with increasing substrate concentrations in both cases, indicating competitive inhibition (see exemplarily Figure 1 for compound **7**). The respective K_i values (Table 1) were determined from plots of the IC_{50} values against substrate concentration according to the Cheng–Prusoff relationship [46].

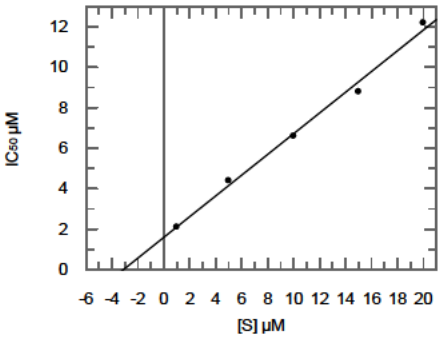

Figure 1. Dependence of inhibition potency (IC_{50} values) on substrate concentration for inhibition of cathepsin L by compound **7**. Increasing IC_{50} values at increasing substrate concentrations indicate a competitive inhibition mode.

Table 1. Inhibition data for inhibitors of the general structure R-NH-L-Phe-L-Leu-OBn, % inhibition at 20 μM and K_i [μM] [1].

Cpd.	Cath. L	Cath. B	Rhod.	DENV PR	Sortase A
	% inh./K_i	% inh./K_i	% inh./K_i	% inh./K_i	% inh./K_i
1	57/nd	16/nd	nd/nd	19/nd	nd/nd
2	56/nd	33/nd	nd/nd	24/nd	nd/nd
3	60/nd	22/nd	nd/nd	28/nd	nd/nd
4	99/0.66	20/nd	75/0.29	10/nd	11/nd
5	8/nd	10/nd	nd/nd	11/nd	nd/nd
6	50/nd	21/nd	nd/nd	12/nd	nd/nd
7	98/1.6	63/4.4	45/nd	31/nd	16/nd

[1] All values are from at least three independent measurements; standard deviations are 10% or less; nd, not determined; cpd., compound; Cath. L, cathepsin L; Cath. B, cathepsin B; Rhod.; rhodesain, DENV PR, Dengue virus protease

The progress curves for inhibition of cathepsins and rhodesain by the compounds were found to be linear in all cases, i.e., no time-dependent inhibition was observed, pointing to fast reversible inhibition

The highest inhibition of cathepsin L was found with the benzoic acid amide **4** (K_i = 0.66 μM) and the amine **7** (K_i = 1.6 μM)**.** The latter also turned out to be the best inhibitor of cathepsin B and the Dengue virus (DENV) protease [47,48], however with lower inhibitory potency (Cath. B: K_i = 4.4 μM; DENV PR: 31% at 20 μM). These two compounds were also tested for inhibition of the cathepsin L-like parasitic protease rhodesain. While only a weak inhibitory potency (45% inhibition at 20 μM) was detected for compound **7**, the amide **4** displayed a K_i value of 0.29 μM.

The benzyl ester **7** was found to be hydrolyzed, yielding the free acid **8** (see Sections 2.3–2.5). Thus, the enzyme assays were also performed with the acid **8**. K_i values of 3.0 ± 0.9 μM for cathepsin L (n = 10), 1.50 ± 0 29 μM for cathepsin B (n = 6) and, most interestingly, 4.0 ± 1.3 nM (n = 14) for rhodesain, were determined (Figure 2). This indicates that acid **8** and ester **7** are similarly active on cathepsins L and B, whereas in the case of rhodesain, an enormous increase in inhibition potency was observed comparing the benzyl ester **7** and the respective free acid **8**.

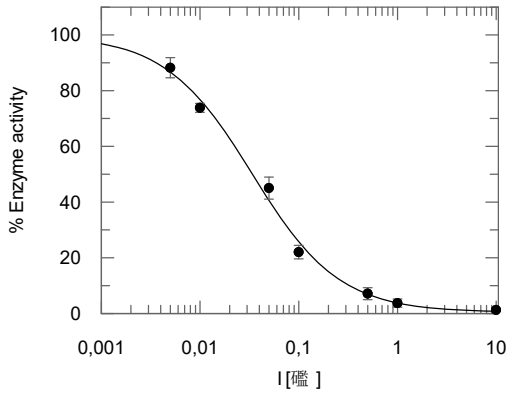

Figure 2. Inhibition of rhodesain by compound **8**.

To investigate the inhibitory effects against a cysteine protease with a protonated thiol instead of an imidazolium/thiolate dyad, compounds **4**, **7** and **8** were tested for inhibition of the *S. aureus* sortase A. None of the inhibitors showed significant inhibition at a final inhibitor concentration of 20 μM (compound **4**: 11%; compound **7**: 16%; compound **8**: 0%), indicating selectivity for cysteine proteases from the CA-clan (cathepsins and rhodesain) over the CL-clan sortase A [49].

The progress curves for inhibition of cathepsins L and B and rhodesain by compound **8** did not clearly show time-dependent behavior Since the inhibition mechanism (reversible vs irreversible) can unequivocally not be deduced from the progress urves, we also used other meth ds to ascertain the (ir)reversibility of the inhibition: (A) The IC_{50} values for inhibition of rhodesain were determined in dependence of incubation time of enzyme and inhibitor prior to substrate addition (10 min vs. 45 min). No differences were observed indicating reversible inhibition; (B) Furthermore, dilution assays were performed with rhodesain. To this end, the enzyme was completely inhibited by an inhibitor concentration 100 fold higher than the IC_{50} value. After dilution of the enzyme-inhibitor mixture with a buffer by a factor of 100, slow and time-dependent reactivation of the enzyme was observed, finally proving the reversibility of inhibition (see Supplementary Material).

2.3. ^{19}F NMR Spectroscopy

The interaction of the fluorinated inhibitors **7** and **8** with rhodesain was probed via ^{19}F NMR spectroscopy (Figure 3). Compound **7** displayed some solubility issues apparent from the observed turbidity of the sample and the reduced signal-to-noise ratio in the spectrum (Figure 3a). To probe the rhodesain-mediated turnover of **7** into **8**, we recorded time-resolved ^{19}F NMR spectra of **7** (800 µM) in the presence of 4 µM rhodesain (Figure 3b). During the measurement, the solution became clear and a dramatic difference in the chemical shift occurred to values identical to those observed for compound **8**. The reaction was subsequently analyzed by MS (see Section 2 4), which confirmed the formation of the free acid **8**.

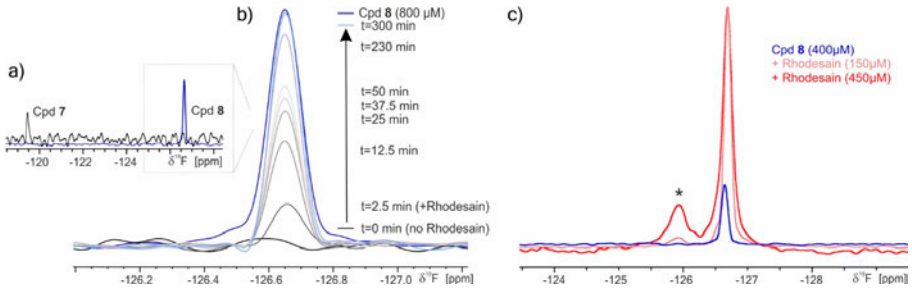

Figure 3. ^{19}F NMR spectra: (**a**) Ester **7** and acid **8** are readily distinguishable by their chemical shifts. (**b**) Time-resolved ^{19}F NMR shows rhodesain-dependent turnover of **7** into **8**. As a control, a separate spectrum of the expected amount of compound **8** that should have formed from **7** in the NMR-based enzymatic assay is recorded (blue trace). Due to the poor solubility of compound **7** (compare (a)), no peak was observed within the 128 scans run for each time-trace. Upon addition of rhodesain, the turbid sample gradually turned clear and the resonance for compound **8** appeared. Therefore, the spectral region has been confined to that displaying the chemical shift for compound **8**. (**c**) Acid **8** forms a stable complex (asterisk) with rhodesain. The peak intensity depends on the amount of protein. For reference, the spectrum of free compound **8** (blue) is included (as shown in (**a**)).

To observe the chemical shift of the rhodesain-bound reaction product, a higher concentration of rhodesain (150 or 450 µM) was incubated with **8**. Indeed, a new, broad peak (Figure 3c, asterisk) was observed, which probably results from an enzyme-inhibitor adduct (see Sections 2.6 and 2.7).

2.4. Mass Spectrometry

To further characterize the interaction between rhodesain and the different inhibitors, we performed a liquid chromatography-mass spectrometric (LC–MS coupled to nano-ESI-Q-TOF) analysis of rhodesain that had been incubated with compounds **4** or **7**. Samples were analyzed in positive ion mode on a quadrupole time-of-flight mass spectrometer (Synapt G2-S HDMS, Waters Corporation) using electrospray ionization (ESI). Rhodesain without inhibitor served as a control. Both compounds

reacted with rhodesain (Figure 4). Interestingly, we found that rhodesain catalyzes the hydrolysis of the benzyl esters of the dipeptide recognition units to the corresponding acids, indicated by a mass shift of 90 Da corresponding to the loss of the terminal benzyl group (Figure 4). Notably, only reaction products of the hydrolyzed compounds with rhodesain were detectable by LC–MS analysis. Since the NMR experiments also showed conversion of ester **7** into the acid **8** catalyzed by rhodesain, the LC–MS analyses were repeated with the acid **8**. These experiments revealed the formation of an adduct with rhodesain for both acid **8** and ester **7** showing exactly the same pattern (Figure 4). These data are in line with the previous NMR spectroscopic observation that the benzyl ester of the dipeptide recognition unit is first hydrolyzed by rhodesain, which subsequently forms a very stable complex with the hydrolysis product. This may also hold true for inhibitor **4**. Since the complex formation is reversible—as shown by the enzyme assays discussed above—and the mass spectra show the mass of the adduct of enzyme and acid **8** and not the mass of an adduct resulting from nucleophilic substitution of either the fluoride or a nitro group, the S_NAr reaction cannot be completed. Hence, the data are only consistent with a π- or a Meisenheimer (σ-) complex.

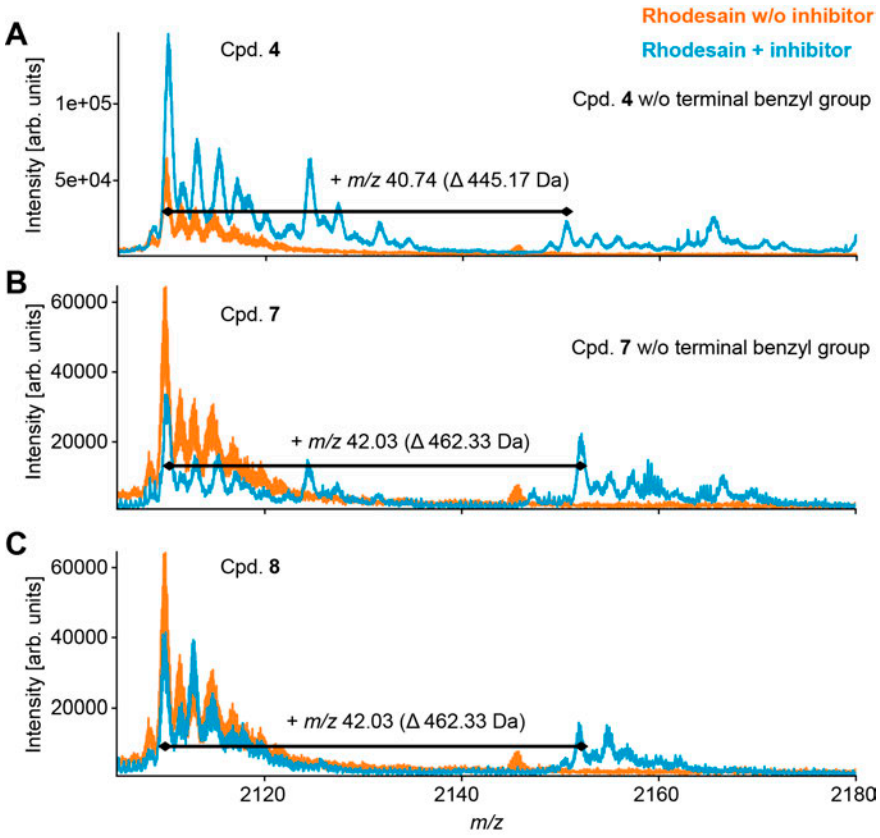

Figure 4. ESI-MS mass spectra of rhodesain ($[M + 11\ H]^{11+}$ at *m/z* 2109.9 +/– 20 ppm) in the absence (orange) or presence (blue) of compounds **4** (**A**), **7** (**B**) and **8** (**C**).

2.5. Hydrolysis of Ester 7 by Rhodesain

In order to verify that the ester cleavage of compound **7** indeed occurs by enzymatic hydrolysis catalyzed by the target protease rhodesain, the compound was incubated with: (a) catalytically active rhodesain; (b) reaction buffer; or (c) rhodesain inactivated by the vinyl sulfone K11777 [50]. The reaction mixtures were subsequently analyzed by LC–MS. Unconverted ester **7** and acid **8** were eluted at t(**8**) =

0.9 min and t(**7**) = 2.1 min. The detected masses matched the theoretical values ([**7** + H^+] = 553.3 m/z, [**7** + Na^+] = 575.4 m/z, [**8** + H^+] = 463.3 m/z and [**8** + Na^+] = 485.3 m/z). A complete conversion of the ester **7** into acid **8** was observed in the case of catalytically active rhodesain (a) (Figure 5), but not with the irreversibly inactivated enzyme (c). A control showed that the ester was not hydrolyzed by the reaction buffer (b) (Figure 5).

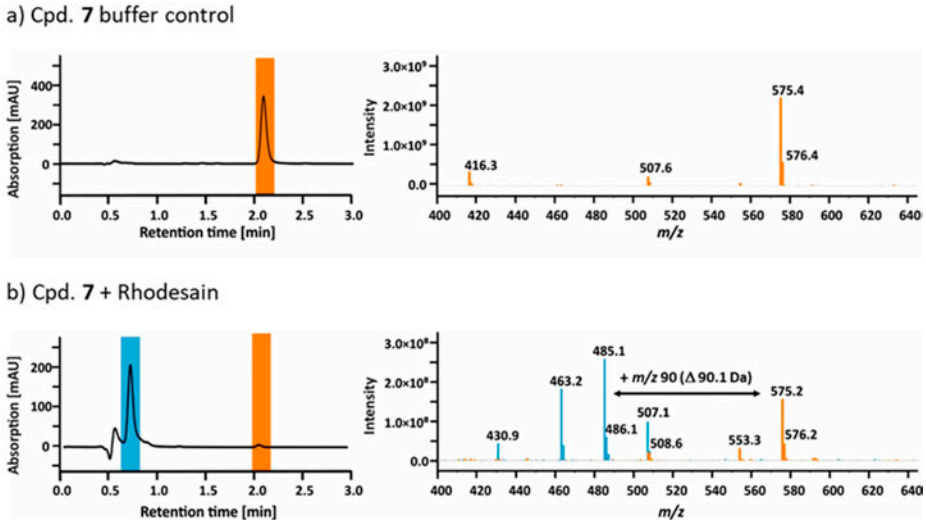

Figure 5. Chromatograms and mass spectra of the LC–MS runs of compound **7** preincubated with (**a**) buffer or (**b**) buffer and catalytically active rhodesain. The elution peaks and mass signals of the unconverted ester **7** are presented in orange, the signals of the resulting acid **8** are highlighted in blue.

2.6. Reaction of Inhibitor 7 with a Low Molecular Weight Thiol

Since cathepsins and rhodesain are cysteine proteases, we also investigated the interaction between the inhibitor **7** and a low molecular weight thiol (LMW thiol). The reaction of compound **7** was carried out with 2-phenylethanethiol (**9**) in the presence of a base in ethanol (Scheme 4). All three possible reaction products resulting from substitution of the nitro- (**10**), fluoro- (**11**) and of both groups (**12**) were obtained in the experiments, in which the reaction temperature (rt or 80 °C), the amounts of thiol and base (excess or two equivalents each) and the reaction time (4 h, 16 h, 28 h) were varied. The main product (ca. 60–70%) detected in the 16 h reaction at 80 °C with a large excess of thiol and triethylamine was the double-substitution product (**12**) accompanied by small amounts of **10** and **11**. At rt with two eq. base and thiol, ca. 70–80% unreacted starting material, accompanied by small amounts of all three reaction products (**10**–**12**), was detected. After 28 h at rt (2 eq. base and thiol), the amount of starting material decreased (to ca. 40%) and the amounts of the three substitution products (**10**–**12**) increased (to ca. 15–25% each). These reactions show that the chosen electrophilic aromatic moiety is indeed competent to undergo nucleophilic aromatic substitutions.

The regiochemistry of the substitution in product **12** could not be unequivocally determined by the usual 2D NMR methods, so that DFT calculations and a DP4-probability analysis were performed. The observed NMR chemical shifts were compared with those of values for both possible regioisomers computed by DFT calculations. Conformational analyses were performed on a PM6 (Parametric Method 6) [51] or MMFF (Merck Molecular Force Field) [52] level of theory and the geometries of all conformers found were subsequently reoptimized [B3LYP/6-31G(d)] [53–59]. For the calculation of the NMR shielding tensors, the *m*PW1PW91 [60] functional was used in combination with the 6-31 + G(d,p) [57–59] basis set and the gauge-independent atomic orbital (GIAO) method [61]. For this computation, undirected solvent effects were taken into account using the integral equation formalism

polarizable continuum model (IEFPCM) [62]. After Boltzmann weighting, the DP4+ probabilities [63] (see Supplementary Material) were calculated, which unambiguously show that the most likely regioisomer is the one with both thioether moieties in *para*-position to each other (**12**).

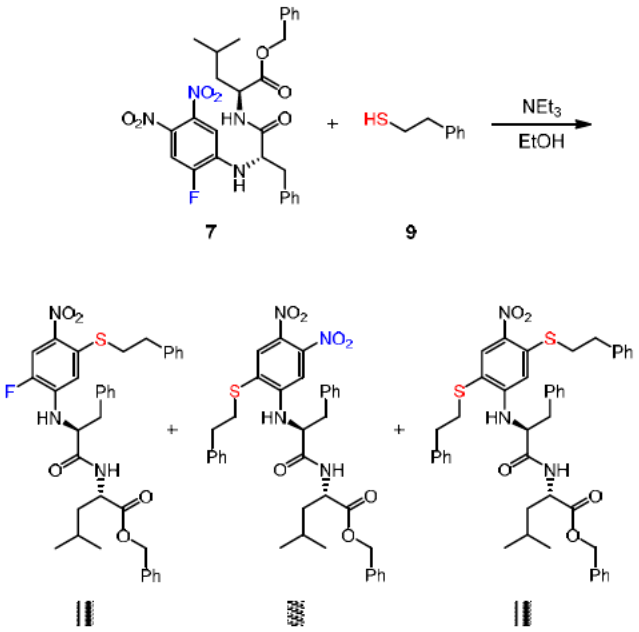

Scheme 4. Reaction of compound **7** with 2-phenylethanethiol and observed products.

High level quantum chemical calculations for appropriate model systems are often very helpful to understand the situation in an enzyme [28,64–66]. Hence, to shed some light on possible reaction intermediates, we also computed the relative stabilities of the involved Meisenheimer complexes in a polar solvent. To mimic the polar environment, we used the IEFPCM approach for a water environment [62]. To obtain information about the influence of the employed theoretical approach, we used density functional (ωB97XD [67]/6-31 + G* [59]) as well as the more reliable 2nd order perturbation theory without and with the SCS (spin-component-scaled) [68] approximation. For these computations we also employed the 6-31 + G* basis set. All computations were performed with the GAUSSIAN program package [69]. The data are summarized in Table 2. The computed structures are depicted in Figure 6. In all model systems, the inhibitor was approximated by the substituted benzene ring.

Table 2. Stabilities (only thiolate/thiolate and imidazolium: full optimization/thiolate and imidazolium: R(S-CX) fixed at 1.9 Å) of the Meisenheimer complexes in a polar solvent [in kcal/mol]. For all calculations the 6-31 + G* basis sets were employed. For further information see main text and Figure 6.

Structure	ωB97XD	MP2	SCS-MP2
Pre-complex	–8.8/–9.0/	–12.3/–16.0/-	–10.3/–12.8/
S-CH	+0.8/–11.5/–6.8	–6.6/–16.0/–12.8	–4.1/–12.9/–9.3
S-CF	–3.3/–13.1/–3.1	–13.2/–20.3/–12.5	–11.1/–16.5/–10.1
S-NO_2	–2.7/–9.3/+3.3	–11.9/–17.0/–5.3	–9.1/–13.3/–2.9

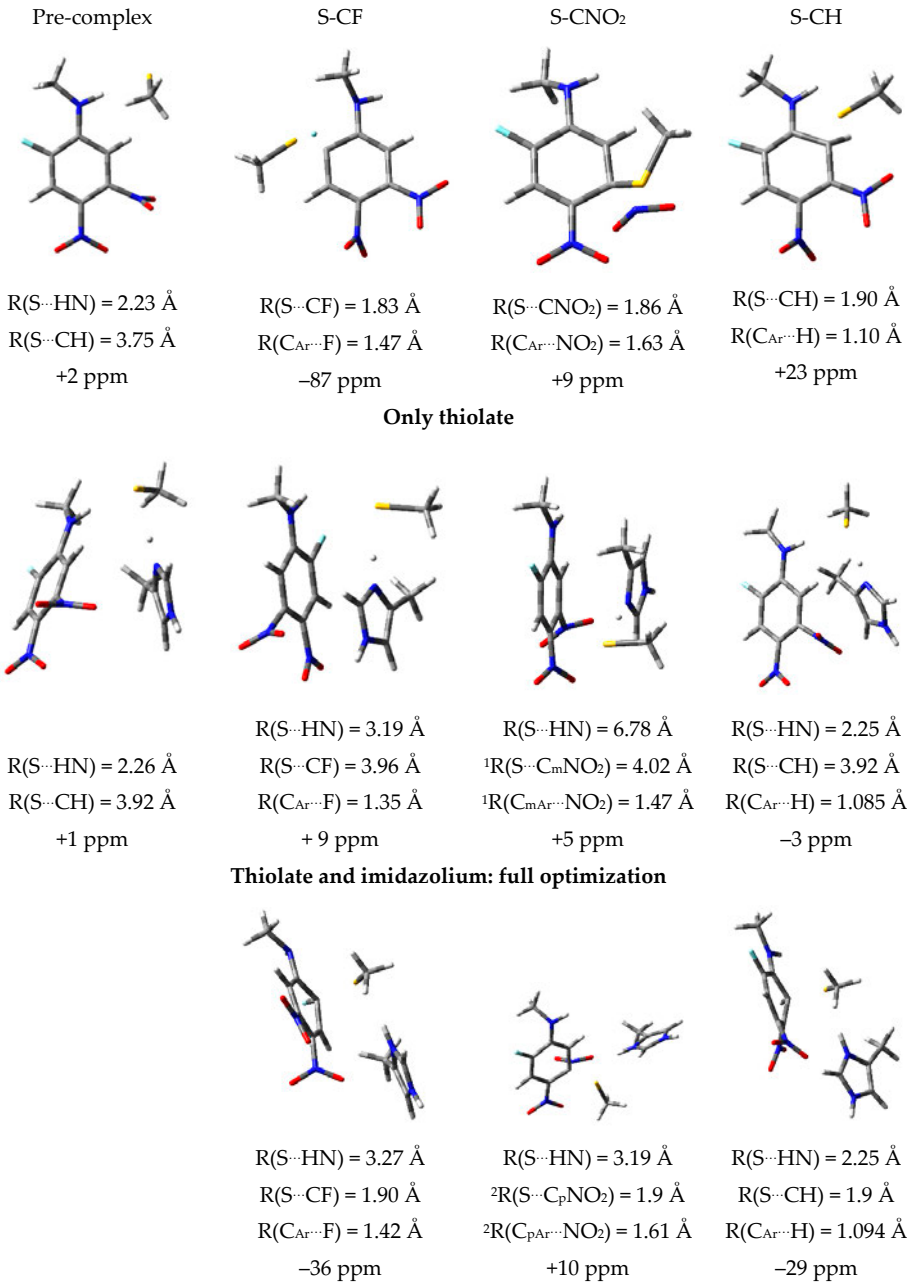

Figure 6. Computed structures and ^{19}F shifts relative to the ^{19}F shift of the free inhibitor for the different model systems. For the undistorted inhibitor the following distances are obtained: R(CAr$\cdots$F) = 1.35 Å, R(CAr$\cdots$NO$_2$) = 1.47 Å and R(CAr$\cdots$H) = 1.085 Å. For further explanation see main text; [1] with respect to the NO$_2$ group in meta-position to F; [2] with respect to the NO$_2$ group in *para*-position to F. MP2, second-order Møller–Plesset perturbation theory.

The model system without an imidazole ring mimics the situation of the reaction with 2-phenylethanethiol (**9**) in the presence of a base in ethanol, in which the reaction can be viewed as a simple thiolate attack at the substituted ring. The corresponding complexes are depicted in Figure 6 in the row "only thiolate". They were obtained by a full geometry optimization starting with a S···CX distance (X = F, NO_2, H) of 1.9 Å. The resulting complexes represent Meisenheimer complexes as can be deduced from the distances: the distances R(S···CX) remain at about 1.9 Å and the distances R(C_{Ar}···X) are already considerably elongated. According to the more accurate MP2 or SCS-MP2 computations, the Meisenheimer complexes represent stable minima on the hypersurface, which lie about 4–13 kcal/mol lower than the reactants. The computations also indicate a stable pre-complex stabilized by a hydrogen bond between the NH group and the attacking thiolate, which according to the more accurate MP2- and SCS-MP2-calculations, is similarly stable as the Meisenheimer complexes. It should be noted that wB97XD considerably underestimates the stability of the Meisenheimer complexes. The computations are in good agreement with the experiment, which finds S_NAr reactions between 2-phenylethanethiol (**9**) in the presence of a base in ethanol at rt. Figure 6 also contains the ^{19}F NMR shifts relative to the value computed for the inhibitor. The computed variation upon the formation of the Meisenheimer complexes are magnitudes larger than the variation found experimentally for a possible inhibitor-enzyme complex (≈ 1 ppm).

Possible reactions between the substituted aromatic ring and the catalytic dyad of the enzyme differ from the solvent reaction in several ways. Besides steric restrictions, the thiolate group of the active-site cysteine residue is always stabilized by a strong salt bridge to the positively charged imidazolium ring of the active-site histidine residue, which might reduce the thiolate reactivity. To mimic this situation, we added a positively charged imidazolium ring to the model system. In the first calculation, we put the thiolate at a distance of about 1.9 Å from the attacked carbon center of the aromatic ring and performed a full geometry optimization. The resulting complexes are depicted in Figure 6 as "thiolate and imidazolium: full optimization". The more reliable MP2- or SCS-MP2-computations predict that the resulting complexes are stable with respect to the fragmentation into the inhibitor and thiolate/imidazolium complex. The computed complexes, however, are not Meisenheimer complexes as found for the situation without the imidazolium (only thiolate). The R(S···CX) distances are about 3.9–4.0 Å and the R(C_{Ar}···X) are not elongated. Nevertheless, the stability of this complex upon fragmentation into inhibitor and thiolate/imidazolium complex is about 20 kcal/mol, i.e., they are even more stable than the Meisenheimer complexes found for the "only thiolate" situation. It should be noted that the situation found for the attack at C−NO_2 does not reflect the situation in the enzyme, because the thiolate and the imidazolium ring interchange their positions during the full optimization to maximize the interaction energy. The same holds true for the attack at C−F due to the orientation of the substituted ring. Both the pre-complex and the situation found for the attack at the CH group of the ring could also take place in the enzyme (see Section 2.7). To get more insights, we also built a complex in which we fixed the S–CX bond lengths to about 1.9 Å, i.e., we enforced a kind of Meisenheimer complex in which the positively charged imidazolium is present. According to MP2 or SCS-MP2, the resulting complexes (Figure 6: thiolate and imidazolium: R(S−CX fixed at 1.9 Å)) are 4–10 kcal/mol less stable than the complex obtained by the full optimization. This indicates that a thiolate/imidazolium complex should not be able to form a Meisenheimer complex. Again, the ^{19}F NMR shifts were computed. Their variations with respect to the ^{19}F NMR shift of the pure inhibitor are also given in Figure 6. It can be seen that the NMR shift variations found for the complexes are considerably smaller than those found for the corresponding Meisenheimer complexes. Furthermore, they are of similar size as the experimental shift difference. The comparison between the employed theoretical approaches clearly shows that the DFT functional ωB97XD underestimates the stability of the complexes by up to 10 kcal/mol.

Our model calculations indicate that the catalytic dyad of the enzyme, mimicked by a thiolate/imidazolium complex, behaves differently than a single attacking thiolate. Consequently, the formation of a Meisenheimer complex would not be expected for the enzyme, but instead, the

formation of a quite stable complex with larger distances between the catalytic dyad and the substituted aromatic ring would be expected. From the orientation of the fragments, it resembles a π-complex. Despite this relatively long distance, the complex is quite stable. The magnitudes of the computed NMR shifts also indicate that a π- instead of a Meisenheimer complex is formed.

2.7. Theoretical Investigations of the Enzyme-Inhibitor Complex

Docking studies using the crystal structure of rhodesain (pdb 2p7u) were performed with acid **8** and its benzyl ester **7** to understand the molecular basis of the observed enzyme inhibition by acid **8** and of the observed enzymatic hydrolysis of ester **7** in more detail. Docking was performed with the FlexX/LeadIT 2.3.2 software suite [70]. The detailed procedure is given in the Supplementary Material.

For the benzyl ester **7**, three different kinds of poses were found. In the highest ranked pose (i.e., the pose with the most negative score of –20.56), the electrophilic aromatic ring binds to the S1′ pocket and is not close to the cysteine (see Figure S3 in the Supplementary Material for more details). In various other highly stable poses, this inhibitor moiety sits in the active site and hence is close to the active site cysteine (score –18.26, see Figure S4 in the Supplementary Material for more details). Additionally, multiple poses with a substrate-like orientation of compound **7** were predicted with the benzyl ester being in a position close to the cysteine (distance 3.2 Å, score –13.77, Figure 7). In this orientation, the ester carbonyl carbon atom is in a suitable position for nucleophilic attack initiating the hydrolysis of the ester.

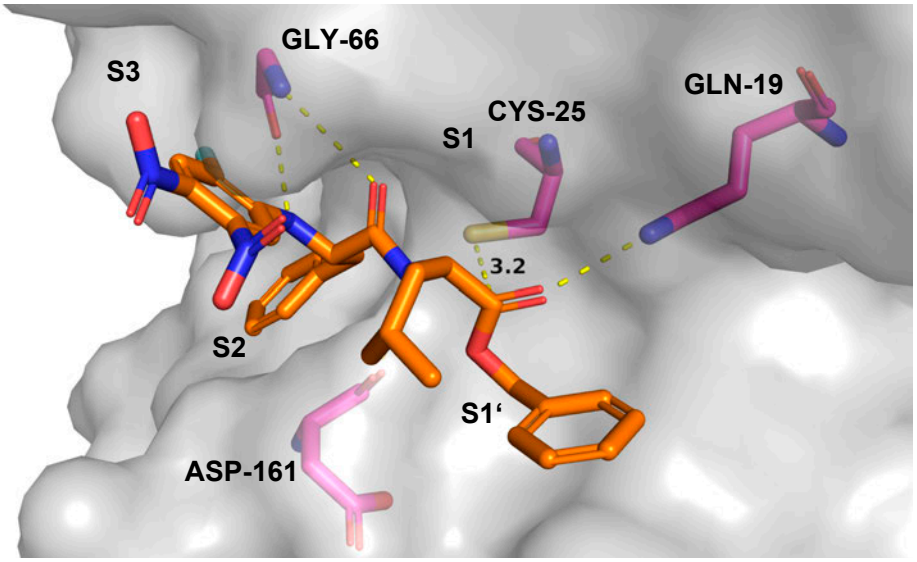

Figure 7. Substrate-like binding mode of ester **7**. Light grey: solvent accessible surface of rhodesain; magenta: carbon atoms of rhodesain amino acid residues; orange: carbon atoms of ester **7**; blue: nitrogen; red: oxygen; yellow: sulfur; cyan: fluorine.

In this reverse, i.e., substrate-like orientation, the carbonyl oxygen of the ester group points towards Gln-19. The benzyl group extends into the S1′ pocket and the leucine residue is located in the S1 pocket. The phenylalanine side chain occupies the S2 pocket, and the aromatic ring is placed in the S3 pocket.

To investigate the stability of the poses in more detail, three MD simulations for each pose were performed. The poses in which the electrophilic aromatic ring sits in the active site were found to be quite stable, although in some cases parts of the inhibitor left the enzyme. However, the enzyme-inhibitor complex never split up completely. Furthermore, the distances between the cysteine

moiety and the aromatic ring remained at distances above 4.5 Å, i.e., for these poses, an attack at the substituted aromatic ring is unlikely.

MD simulations were also performed for the reverse, i.e., substrate-like binding mode given in Figure 7. These simulations indicate a moderately stable complex. However, as shown in Figure 8a, the distance between the cysteine moiety and the ester group increases along the simulation time. Nevertheless, the ester may remain sufficiently long within the active site for an attack at the carbonyl carbon followed by ester hydrolysis. To investigate possible differences between the ester and the acid we performed an MD simulation starting from the pose given in Figure 7, but replaced the ester group by the corresponding acid group. Figure 8b shows that in this case, the inhibitor leaves the enzyme rapidly and the enzyme-inhibitor complex splits up completely. The behavior may result from the repulsion between the negatively charged carboxylate and the negatively charged thiolate moiety of Cys-25.

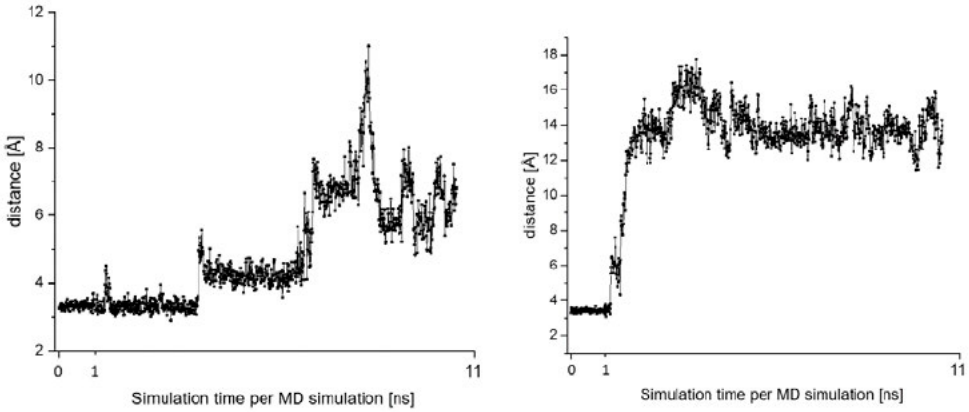

(a) Ester: distance Cys-S···COOR (b) Acid: distance Cys-S···COOH

Figure 8. Fluctuations in the distance between the sulfur center of Cys-25 and (**a**) the carbon center of the ester group of compound **7** and (**b**) the carbon center of the acid group. The simulations were started from the pose given in Figure 7.

For acid **8** in the highest ranked docking pose, the electrophilic aromatic ring was found to be located close to the nucleophilic cysteine (distance 2.7 Å, score –18.03, Figure 9). The peptide backbone has interactions with Asp-161 and Gly-66, while the phenylalanine side chain occupies the hydrophobic S2 pocket. The leucine side-chain and the carboxylic acid group reside in the S3 pocket. One nitro group forms hydrogen bonds to Gln-19. To investigate the stability of the binding pose, we performed various MD simulations, which indicated a very stable complex. The corresponding fluctuations in the distances between the thiolate moiety and the CH- and CNO_2-groups of the aromatic ring are depicted in Figure 10a,b, respectively.

Our model computations indicate a stable pre-complex that is stabilized by a strong hydrogen bond between the thiolate and the NH substituent of the aromatic ring. To investigate whether this hydrogen bond is also important for the enzyme-inhibitor complex, we analyzed the distance Cys-S···H-N between the sulfur center of Cys-25 and the proton of the NH substituent along our MD simulations. The corresponding fluctuations are given in Figure 10c,d for two MD simulations, which reflect the two different conformations that are adopted along these MD simulations. Both conformations are depicted in Figure 11.

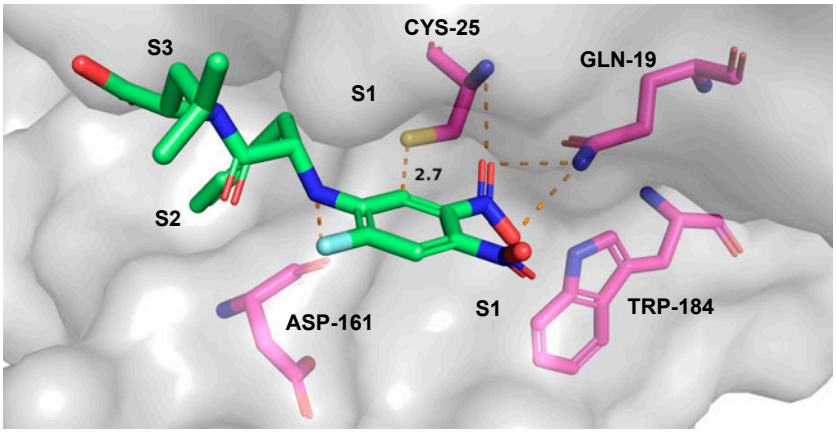

Figure 9. Predicted binding mode of acid **8**. Light grey: solvent accessible surface of rhodesain; magenta: carbon atoms of rhodesain amino acid residues; green: carbon atoms of acid **8**; blue: nitrogen; red: oxygen; yellow: sulfur; cyan: fluorine.

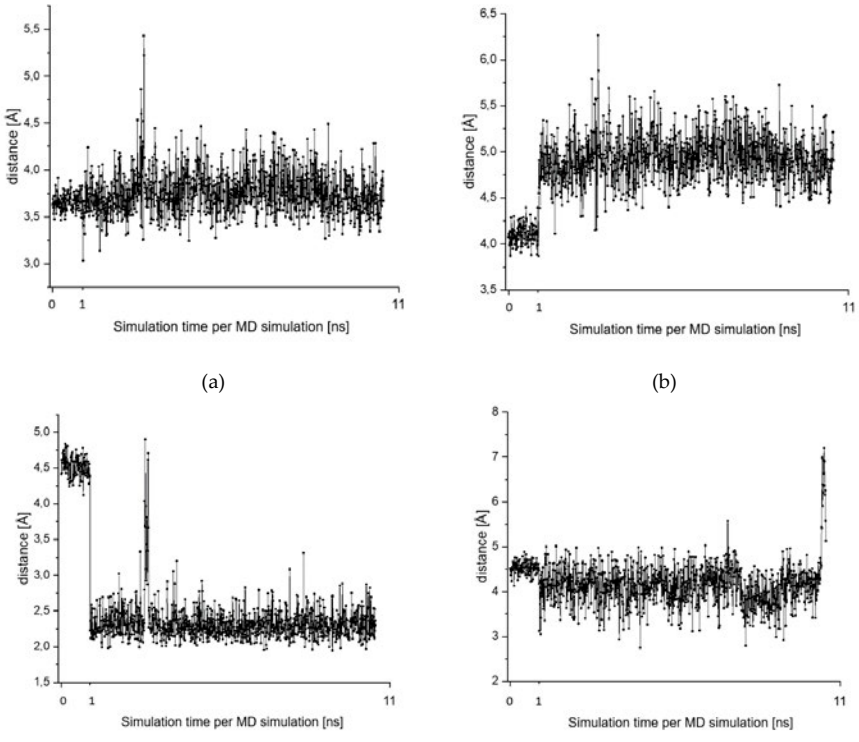

Figure 10. Charts (**a**,**b**) present the fluctuation of the distances between the sulfur center of Cys-25 and the carbon centers (CX) of the aromatic ring: (**a**) = distance S···CH; (**b**) = S···CNO_2. (**c**,**d**) give the fluctuation in the distance of the Cys-S···H-N hydrogen bond along MD 5 (**c**) and MD 6 (**d**). All simulations start from the pose in Figure 9.

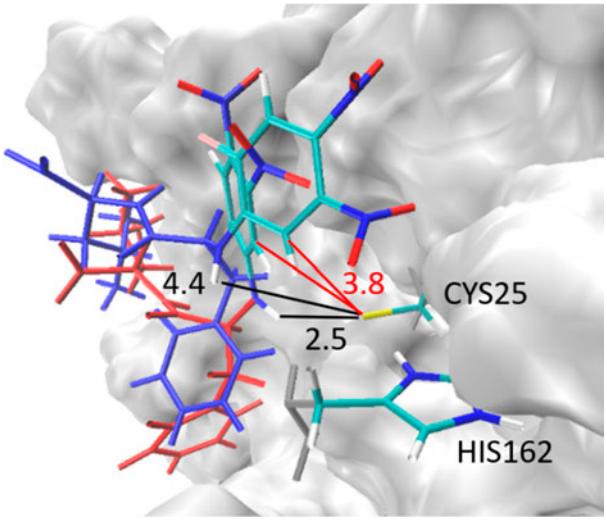

Figure 11. Sketch of the two principle conformations of acid **8** taken along the molecular dynamics (MD) simulations starting from the pose depicted in Figure 9. The electrophilic aromatic ring is given in atomic color while the rest of the inhibitor is given in blue or red. The distances between the S-center of Cys-25 and the NH group (Cys-S···H-N) are given in black, while the distances to the CH group of the aromatic ring (Cys-S···H-C) are given in red. For more information, see main text.

Within the pose depicted in Figure 9, the Cys-S···H-N distance is around 4.5 Å, i.e., all MD simulations started from that distance. For some MDs this conformation was kept for the whole simulation (Figure 10d, Figure 11 conformation with Cys-S···H-N = 4.4 Å). In other cases (Figure 10c, Figure 11 conformation with Cys-S···H-N = 2.5 Å), a presumably more stable conformation is adopted in which the Cys-S···H-N distance decreases strongly and fluctuates around 2.2 Å, indicating a strong hydrogen bond. While the distance Cys-S···H-N strongly differs between both conformations, the distances between the sulfur center of Cys-25 and the CH group of the substituted aromatic ring (Cys-S···H-C) remains constant. The latter indicates a strong interaction between the catalytic dyad Cys-25/His-162 and the electrophilic aromatic ring, which was also found for the model system (see Section 2.6). It is worth noting that for poses of the ester **7** in which the electrophilic aromatic ring was also in the vicinity of Cys-25 such a conformational change was not found. In the case of the ester, all poses stayed in conformations with quite long Cys-S···H-N distances. This indicates that the formation of the Cys-S···H-N bond is one reason for the strong inhibition potency of the acid, while the corresponding ester does not show a comparably strong inhibition.

A complete nucleophilic substitution reaction would lead to an irreversible inhibition because the eliminated group would diffuse away. Consequently, for a reversible inhibition the reaction must get trapped in a minimum from which the elimination of the leaving group cannot happen. This minimum cannot be a Meisenheimer complex as found for the model system with a single attacking thiolate because in this complex, the bonds to the leaving groups are already elongated, i.e., an elimination could occur. The π-complex found for the model system consisting of a thiolate/imidazolium unit instead of a single thiolate represents such a trap. It is more stable than the reactants and a further approach of the thiolate towards the inhibitor, which is necessary for an S_NAr reaction, cannot take place because the underlying potential is repulsive. The question remains whether a similar situation exists for the enzyme.

In many cases the enzyme environment strongly influences the reactivity of a given inhibitor [71–73]. To investigate the situation for the present question, possible reaction paths of the addition step of the thiolate moiety to the aromatic ring including the influence of the enzyme environment were computed.

For this instance, hybrid QM/MM computations were performed in which the most important part is described quantum-mechanically (QM) while the influence of the rest is taken into account by force field approaches (MM) using the ONIOM (own n-layered integrated molecular orbital and molecular mechanics) approach implemented in GAUSSIAN16 [69]. Within these computations, the QM part consisted of 35 atoms. It was described by SCS-MP2/6-31 + G* because the ωB97XD values underestimated the effects in the model computation. The influence of the rest of the enzyme (more than 5200 atoms) was included into the MM part, which was described by the AMBER16 force field. The electrostatic embedding was employed to include possible polarization effects. For the calculations, some frames of the MD simulation performed for the complex of compound **8** and rhodesain were selected, and a full geometry optimization was conducted using QM/MM. The resulting geometry represents the starting point for a possible addition of the thiolate to the substituted aromatic ring as the first step of the S_NAr reaction. We computed the minimal energy path of the addition by decreasing the distance between the thiolate and the two reachable carbon centers (C–H and C–NO_2). For each distance all other geometrical degrees of freedom were optimized. The results are depicted in Table 3.

Table 3. Shapes of various addition–reaction pathways of the Cys moiety to the substituted aromatic rings. Relative energies [kcal/mol] are given with respect to the full geometry optimization. The full optimization started from the indicated MD frame.

Starting Structure	R(S-CNO_2)	R(S-CH)	ΔE
MD 6 Frame 963 conformer with short Cys-S···H-N distance		3.7	0.0
		3.3	1.4
		3.1	1.7
		2.9	2.5
MD 6 Frame 1096 conformer with short Cys-S···H-N distance		3.7	0.0
		3.3	0.7
		3.1	0.8
		2.9	2.6
MD 6 Frame 542 conformer with short Cys-S···H-N distance	4.9		0.0
	4.5		1.2
	4.1		3.4
	3.9		0.4
	3.5		5.3

Table 3 indeed indicates small minima in the reaction path. They appear at distances for R(S-CH) of about 3.1–3.3 Å or for R(S-CNO_2) of about 3.9 Å, i.e., in the range of the complex of the model "thiolate and imidazolium: full optimization" (Figure 6). They seem to be shallower than in the corresponding model system. However, we expect that parts of the attractive forces between the catalytic dyad and the substituted ring are already taken into account by the force field used for the MD simulations or in the subsequent QM/MM geometry optimization, i.e., they already stabilize the minimum from which the computation of the reaction paths started. Additionally, steric interactions may counteract. Nevertheless, beside the indicated strong Cys-S···H-N hydrogen bond (see above), the underlying interactions will contribute to the high inhibition potency of the acid **8** for rhodesain. The specific nature and the interplay of the various interactions still have to be deciphered. As for the model system, the computations for the enzyme environment also find a repulsive reaction path, so that a Meisenheimer complex cannot be formed. As a consequence, a complete substitution reaction cannot take place in the enzyme.

In summary, our QM/MM computations indicate that acid **8** and rhodesain form a very stable π-complex, which can explain the high inhibition potency of **8**. Because the reaction path of the formation of a Meisenheimer complex is repulsive, a S_NAr reaction as found for the reaction of 2-phenylethanethiol with the ester **7** in the presence of a base in ethanol cannot take place in the enzyme. This explains why acid **8** is a reversible inhibitor. The lower inhibitory potency of ester **7**

is a consequence of the non-covalent interactions between inhibitor and enzyme, which prevent the formation of such a strong complex.

2.8 T. b. brucei Cell Survival Assay

Ester **7** and acid **8** were tested for their anti-trypanosomal activity against *T. brucei brucei* using the ATPlite assay according to previously published procedures [74]. After 24 h, EC_{50} values of 0.0953 (±0.0402) µM for the ester **7** and 18.5 (±4.97) µM for the acid **8** were found (Figure 12). The differences in anti-protease and anti-trypanosomal activity between the lipophilic ester **7** and the more hydrophilic acid **8** might be due to different cell permeabilities of the compounds. With the acid **8** being the active protease inhibitor and the more lipophilic benzyl ester **7** being the better anti-trypanosomal compound that is converted to the active protease inhibitor **8** by the target enzyme itself, we presumably have discovered a new prodrug concept for anti-trypanosomal compounds targeting the major trypanosomal cysteine protease rhodesain. These results are in agreement with previous findings [75], which showed that especially rhodesain inhibitors with benzyl ester moieties display high anti-trypanosomal activity.

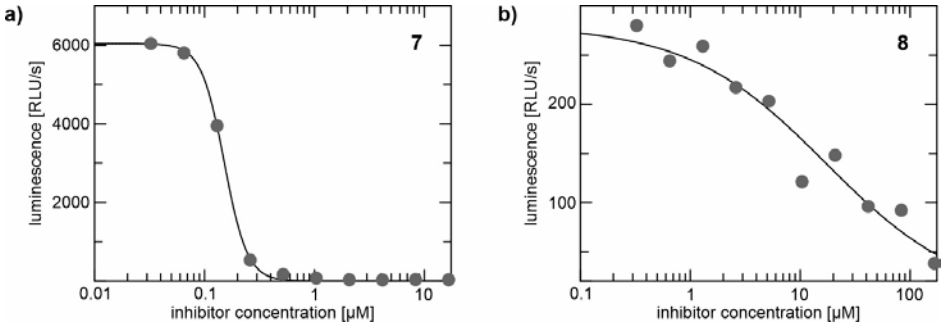

Figure 12. Anti-trypanosomal activity of the (**a**) benzyl ester **7** and (**b**) acid **8** measured by the ATPlite assay. Shown is luminescence (RLU/s = relative light unit per second) in dependence of compound concentration.

3. Discussion

The realm of potentially S_NAr-reactive units as building blocks for protease inhibitors is still largely unexplored and as stated in the introduction part, only very few steps have been undertaken in this direction. The evaluation of (hetero)aromatic electrophiles as possible inhibitory fragments or warheads for peptidic cysteine protease inhibitors is a first important step. Among the inhibitors presented herein, which contain the dipeptide HN-L-Phe-L-Leu-OBn as the recognition unit for cathepsin L-like proteases, the 2-fluoro-3-nitro-substituted benzoic acid amide **4** and the 2-fluoro-4,5-dinitro-substituted aniline derivative **7** were discovered as very potent cathepsin L inhibitors. Amide **4** additionally inhibits the trypanosomal cathepsin L-like protease rhodesain. The compounds were found to exhibit a competitive and reversible mode of inhibition. As shown by NMR spectroscopy, mass spectrometry and hydrolysis assays, the benzyl ester **7** was found to be hydrolyzed to the free acid **8** by rhodesain to yield a highly potent reversible rhodesain inhibitor (K_i = 4.0 nM). Thus, with the benzyl ester **7**, we identified an unexpected prodrug that is converted into the active protease inhibitor by the target enzyme itself. This is supported by the *T. b. brucei* cell survival assays, which revealed the benzyl ester **7** as a compound with significantly enhanced anti-trypanosomal activity. The serendipitous discovery of the dual mode of action of compound **8** implies that other ester- or even amide-type inhibitors may also react similarly. The ester **7** performed S_NAr reactions with 2-phenylethanethiol in ethanol in the presence of a base. Such a reaction is also expected for **8** because both possess the same substituted aromatic ring. However, because **8** acts as a reversible inhibitor, such a reaction cannot be the inhibition mechanism of rhodesain.

To investigate possible inhibition mechanisms, QM computations for relevant model systems were performed. Docking and MD simulation were conducted to detect and investigate possible inhibitor-enzyme complexes of the compounds **7** and **8**. Finally, QM/MM computations were carried out to get some insights into possible reactions between **8** and rhodesain.

The model calculations show that a single attacking thiolate behaves completely different than a dyad consisting of a thiolate and a positively charged imidazolium ring. The former is a model for the reaction of phenylethanethiol in ethanol in the presence of a base, while the latter mimics the catalytic dyad of the protease. For a single thiolate, the computations predict stable Meisenheimer complexes, which is in line with the observed S_NAr reactions. By contrast, for a thiolate/imidazolium dyad, a stable π-complex is found. The reaction potential of a further approach towards a Meisenheimer complex is repulsive, i.e., the reaction cannot take place. Consequently, while an irreversible reaction is predicted for a single thiolate, a reversible formation of a stable π-complex is computed for the thiolate/imidazolium dyad. Subsequent QM/MM computations simulating the reaction of **8** with rhodesain indicate a similar situation. Hence, we expect that an S_NAr reaction of acid **8** with rhodesain does not take place because the reaction is trapped in a very stable π-complex. The complex seems to receive additional stability through a strong hydrogen bridge between the thiolate group of Cys-25 and the NH-substituent of the aromatic ring.

The conducted docking and MD simulations reveal several stable complexes between ester **7** and rhodesain, in which the substituted aromatic ring sits in the active site, i.e., in close vicinity to the reactive dyad. Nevertheless, reactions are not expected because MD simulations show that the distances are still too large. Additionally, no indication for the formation of a stable π-complex or the thiolate-NH bridge is seen. Hence, we expect that these complexes are less stable, which nicely explains the lower inhibitory potency of ester **7** compared to acid **8**. Docking also predicts a reverse, substrate-like binding pose, which is ideal for the hydrolysis of the ester through rhodesain. MD simulations find this pose to be reasonably stable. For the acid **8** in rhodesain, docking and MD find very stable complexes in which the substituted aromatic ring and the catalytic Cys-25/His-162 dyad are sufficiently close. However, as described above, the reaction path towards the Meisenheimer complex only exhibits shallow minima for large distances (R(S-CH) or R(S-CNO_2) $\approx$ 3.1 – 4.0 Å) while it is repulsive for a further approach. This finding is in line with the reversible inhibition of rhodesain by acid **8**.

In summary, with the benzyl ester **7**, we present an efficient prodrug that has a strong anti-trypanosomal effect and inhibits the trypanosomal protease rhodesain in vitro via the hydrolysis and subsequent reversible binding of the hydrolysis product **8** via a π-complex. In future studies, we will address the question if esters other than benzyl can also be used as prodrugs.

4. Materials and Methods

See Supplementary Materials.

Supplementary Materials: The following are available online at http://www.mdpi.com/1420-3049/25/6/1451/s1: Syntheses and analytical data of the compounds; Analysis of the reaction products of the reaction with low-molecular weight thiol; Calculation of the chemical shifts/determination of the regiochemistry of the addition products; Mass spectrometry; NMR material and methods; Enzyme and hydrolysis assays; *T. b. brucei* cell survival assay; Docking procedures; NMR spectra of the compounds.

Author Contributions: Conceptualization, T.S., T.O., P.K., P.J. and B.E.; methodology, P.K., P.J., A.W., S.J., J.K., F.B., S.T., U.D., W.W. and U.A.H.; investigation, P.K., P.J., A.W., S.J., J.K., F.B., S.T., U.D., W.W. and U.A.H.; writing—original draft preparation, T.S.; writing—review and editing, T.S., T.O., U.A.H. and B.E.; supervision, T.S., T.O., B.E. and U.A.H.; project administration, T.S. and T.O.; funding acquisition, T.O. and U.A.H. All authors have read and agreed to the published version of the manuscript.

Funding: T.O.: Financial support by the Carl Zeiss foundation (project ChemBioMed) is gratefully acknowledged. U.A.H. acknowledges support by the Carl Zeiss Foundation, the Center for Biomolecular Magnetic Resonance (BMRZ), the University of Frankfurt, funded by the state of Hesse, and the DFG (INST 161/916-1 FUGG).

Acknowledgments: We thank J. C. Liermann (Mainz) for NMR spectroscopy of the compounds, and N. Hanold (Mainz) and C. Kampf (Mainz) for mass spectrometry of the compounds. Furthermore, the authors are grateful to the Zentrum für Datenverarbeitung (ZDV) of the JGU Mainz for access to the MOGON HPC-Cluster and for the computer and data resources of the Leibniz-Rechenzentrum of the Bayerischen Akademie der Wissenschaften.

Conflicts of Interest: The authors declare no conflict of interest.

References

1. Bauer, R.A. Covalent inhibitors in drug discovery: From accidental discoveries to avoided liabilities and designed therapies. *Drug Discov. Today* **2015**, *20*, 1061–1073. [CrossRef] [PubMed]
2. Singh, J.; Petter, R.C.; Kluge, A.F. Targeted covalent drugs of the kinase family. *Curr. Opin. Chem. Biol.* **2010**, *14*, 475–480. [CrossRef] [PubMed]
3. Singh, J.; Petter, R.C.; Baillie, T.A.; Whitty, A. The resurgence of covalent drugs. *Nat. Rev. Drug Discovery* **2011**, *10*, 307–317. [CrossRef] [PubMed]
4. Johnson, D.S.; Weerapana, E.; Cravatt, B.F. Strategies for discovering and derisking covalent, irreversible enzyme inhibitors. *Future Med. Chem.* **2010**, *2*, 949–964. [CrossRef] [PubMed]
5. Potashman, M.H.; Duggan, M.E. Covalent modifiers: An orthogonal approach to drug design. *J. Med. Chem.* **2009**, *52*, 1231–1246. [CrossRef] [PubMed]
6. Mah, R.; Thomas, J.R.; Shafer, C.M. Drug discovery considerations in the development of covalent inhibitors. *Bioorg. Med. Chem. Lett.* **2014**, *24*, 33–39. [CrossRef]
7. Baillie, T.A. Targeted covalent inhibitors for drug design. *Angew. Chem. Int. Ed.* **2016**, *55*, 13408–13421. [CrossRef]
8. De Cesco, S.; Kurian, J.; Dufresne, C.; Mittermaier, A.K.; Moitessier, N. Covalent inhibitors design and discovery. *Eur. J. Med. Chem.* **2017**, *10*, 96–114. [CrossRef]
9. Johansson, M.H. Reversible Michael additions: Covalent inhibitors and prodrugs. *Mini Rev. Med. Chem.* **2012**, *12*, 1330.
10. Palmer, J.T.; Rasnick, D.; Klaus, J.L.; Broemme, D. Vinyl sulfones as mechanism-based cysteine protease inhibitors. *J. Med. Chem.* **1995**, *38*, 3193–3196. [CrossRef]
11. Ettari, R.; Nizi, E.; Di Francesco, M.E.; Dude, M.-A.; Pradel, G.; Vicik, R.; Schirmeister, T.; Micale, N.; Grasso, S.; Zappala, M. Development of peptidomimetics with a vinyl sulfone warhead as irreversible falcipain-2 inhibitors. *J. Med. Chem.* **2008**, *51*, 988–996. [CrossRef] [PubMed]
12. Ettari, R.; Bonaccorso, C.; Micale, N.; Heindl, C.; Schirmeister, T.; Calabro, M.L.; Grasso, S.; Zappala, M. Development of novel peptidomimetics containing a vinyl sulfone moiety as proteasome inhibitors. *ChemMedChem* **2011**, *6*, 1228–1237. [CrossRef] [PubMed]
13. Ettari, R.; Cosconati, S.; Amendola, G.; Chouchene, K.; Wagner, A.; Hellmich, U.A.; Ulrich, K.; Krauth-Siegel, R.L.; Wich, P.R.; Schmid, I.; et al. Development of novel peptide-based Michael acceptors targeting rhodesain and falcipain-2 for the treatment of Neglected Tropical Diseases (NTDs). *J. Med. Chem.* **2017**, *60*, 6911–6923.
14. Breuning, A.; Degel, B.; Schulz, F.; Büchold, C.; Stempka, M.; Machon, U.; Gelhaus, C.; Leippe, M.; Leyh, M.; Kisker, C.; et al. Michael acceptor based antiplasmodial and antitrypanosomal cysteine protease inhibitors with unusual amino acids. *J. Med. Chem.* **2010**, *53*, 1951–1963. [CrossRef] [PubMed]
15. Machon, U.; Büchold, C.; Stempka, M.; Schirmeister, T.; Gelhaus, C.; Leippe, M.; Gut, J.; Rosenthal, P.J.; Kisker, C.; Leyh, M.; et al. On-bead screening of a combinatorial fumaric acid derived peptide library yields antiplasmodial cysteine protease inhibitors with unusual peptide sequences. *J. Med. Chem.* **2009**, *52*, 5662–5672. [CrossRef] [PubMed]
16. Ettari, R.; Micale, N.; Schirmeister, T.; Gelhaus, C.; Leippe, M.; Nizi, E.; Di Francesco, M.E.; Grasso, S.; Zappala, M. Novel peptidomimetics containing a vinyl ester moiety as highly potent and selective falcipain-2 inhibitors. *J. Med. Chem.* **2009**, *52*, 2157–2160. [CrossRef] [PubMed]
17. Schirmeister, T.; Kesselring, J.; Jung, S.; Schneider, T.H.; Weickert, A.; Becker, J.; Lee, W.; Bamberger, D.; Wich, P.R.; Distler, U.; et al. Quantum chemical-based protocol for the rational design of covalent inhibitors. *J. Am. Chem. Soc.* **2016**, *138*, 8332–8335. [CrossRef]
18. Ehmke, V.; Quinsaat, J.E.; Rivera-Fuentes, P.; Heindl, C.; Schirmeister, T.; Diederich, F. Tuning and predicting biological affinity: Aryl nitriles as cysteine protease inhibitors. *Org. Biomol. Chem.* **2012**, *10*, 5764–5768. [CrossRef]

19. Ehmke, V.; Winkler, E.; Banner, D.W.; Haap, W.; Schweizer, W.B.; Rottmann, M.; Kaiser, M.; Freymond, C.; Brun, R.; Schirmeister, T.; et al. Optimization of triazine nitriles as rhodesain inhibitors: Structure-activity relationships, bioisosteric imidazopyridine nitriles, and X-ray crystal structure analysis with human cathepsin L. *ChemMedChem* **2013**, *8*, 967–975. [CrossRef]
20. Schirmeister, T.; Schmitz, J.; Jung, S.; Schmenger, T.; Krauth-Siegel, R.L.; Gütschow, M. Evaluation of dipeptide nitriles as inhibitors of rhodesain, a major cysteine protease of Trypanosoma brucei. *Bioorg. Med. Chem. Lett.* **2016**, *27*, 45–50. [CrossRef]
21. Giroud, M.; Ivkovic, J.; Martignoni, M.; Fleuti, M.; Trapp, N.; Haap, W.; Kuglstatter, A.; Benz, J.; Kuhn, B.; Schirmeister, T.; et al. Inhibition of the cysteine protease human cathepsin L by triazine nitriles: Amide···heteroarene π-stacking interactions and chalcogen bonding in the S3 pocket. *ChemMedChem* **2017**, *12*, 257–270. [CrossRef] [PubMed]
22. Walker, B.; Lynas, J.F. Strategies for the inhibition of serine proteases. *CMLS Cell. Mol. Life Sci.* **2001**, *58*, 596–624. [CrossRef] [PubMed]
23. Siklos, M.; BenAissa, M.; Thatcher, G.R.J. Cysteine proteases as therapeutic targets: Does selectivity matter? A systematic review of calpain and cathepsin inhibitors. *Acta Pharm. Sin. B* **2015**, *5*, 506–519. [CrossRef] [PubMed]
24. Ettari, R.; Zappala, M.; Evers, A.; Gelhaus, C.; Leippe, M.; Schirmeister, T.; Micale, N.; Grasso, S. Synthesis of novel peptidomimetics as inhibitors of protozoan cysteine proteases falcipain-2 and rhodesain. *Eur. J. Med. Chem.* **2010**, *45*, 3228–3233. [CrossRef]
25. Otto, H.-H.; Schirmeister, T. Cysteine proteases and their inhibitors. *Chem. Rev.* **1997**, *97*, 133–171. [CrossRef]
26. Powers, J.C.; Asgian, J.L.; Ekici, O.D.; James, K.E. Irreversible inhibitors of serine, cysteine, and threonine proteases. *Chem. Rev.* **2002**, *102*, 4639–4750. [CrossRef]
27. Schirmeister, T.; Klockow, A. Cysteine protease inhibitors containing small rings. *Mini Rev. Med. Chem.* **2003**, *3*, 585–596. [CrossRef]
28. Vicik, R.; Helten, H.; Schirmeister, T.; Engels, B. Rational design of aziridine containing cysteine protease inhibitors with improved potency - Studies on inhibition mechanism. *ChemMedChem* **2006**, *1*, 1021–1028. [CrossRef]
29. Park, T.; Yang, C.; Yu, Z. Specific inhibitors of lysozyme and peptidases inhibit the growth of the rumen protozoan Entodinium caudatum without decreasing feed digestion or fermentation in vitro. *J. Appl. Microbiol.* **2019**, *127*, 670–682. [CrossRef]
30. Hartmann, K.; Mielczarek, P.; Silberring, J. Synthesis of the novel covalent cysteine proteases inhibitor with iodacetic functional group. *Molecules* **2020**, *25*, 813. [CrossRef]
31. Shannon, D.A.; Banerjee, R.; Webster, E.R.; Bak, D.W.; Wang, C.; Weerapana, E. Investigating the proteome reactivity and selectivity of aryl halides. *J. Am. Chem. Soc.* **2014**, *136*, 3330–3333. [CrossRef] [PubMed]
32. Leesnitzer, L.M.; Parks, D.J.; Bledsoe, R.K.; Cobb, J.E.; Collins, J.L.; Consler, T.G.; Davis, R.G.; Hull-Ryde, E.A.; Lenhard, J.M.; Patel, L.; et al. Functional consequences of cysteine modification in the ligand binding sites of peroxisome proliferator activated receptors by GW9662. *Biochemistry* **2002**, *41*, 6640–6650. [CrossRef] [PubMed]
33. Gehringer, M.; Laufer, S.A. Emerging and re-emerging warheads for Targeted Covalent Inhibitors: Applications in medicinal chemistry and chemical biology. *J. Med. Chem.* **2019**, *62*, 5673–5724. [CrossRef] [PubMed]
34. Spokoyny, A.M.; Zou, Y.; Ling, J.J.; Yu, H.; Lin, Y.-S.; Pentelute, B.L.J. A perfluoroaryl-cysteine SNAr chemistry approach to unprotected peptide stapling. *J. Am. Chem. Soc.* **2013**, *135*, 5946–5949. [CrossRef]
35. Dolle, R.A.; Hoyer, D.; Rinker, J.M.; Ross, T.M.; Schmidt, S.J.; Helaszek, C.T.; Ator, M.A. 3-Chloro-4-carboxamido-6-arylpyridazines as non-peptide class of interleukin-1β converting enzyme inhibitor. *Bioorg. Med. Chem. Lett.* **1997**, *7*, 1003–1006. [CrossRef]
36. Shie, J.-J.; Fang, J.-M.; Kuo, C.-J.; Kuo, T.-H.; Liang, P.-H.; Huang, H.-J.; Yang, W.-B.; Lin, C.-H.; Chen, J.-L.; Wu, Y.-T.; et al. Discovery of potent anilide inhibitors against the Severe Acute Respiratory Syndrome 3CL protease. *J. Med. Chem.* **2005**, *48*, 4469–4473. [CrossRef]
37. Li, Z.; Brecher, M.; Deng, Y.-Q.; Zhang, J.; Sakamuru, S.; Liu, B.; Huang, R.; Koetzner, C.A.; Allen, C.A.; Jones, S.A.; et al. Existing drugs as broad-spectrum and potent inhibitors for Zika virus by targeting NS2B-NS3 interaction. *Cell Res.* **2017**, *27*, 1046–1064. [CrossRef]

38. Olson, O.C. Cysteine cathepsin proteases: Regulators of cancer progression and therapeutic response. *Nat. Rev. Cancer* **2015**, *15*, 712–729. [CrossRef]
39. Mohamed, M.M. Cysteine cathepsins: Multifunctional enzymes in cancer. *Nat. Rev. Cancer* **2006**, *6*, 764–775. [CrossRef]
40. Ferreira, L.G.; Andricopulo, A.D. Targeting cysteine proteases in trypanosomatid disease drug discovery. *Pharmacol. Ther.* **2017**, *180*, 49–61. [CrossRef]
41. Ettari, R.; Previti, S.; Tamborini, L.; Cullia, G.; Grasso, S.; Zappala, M. The inhibition of cysteine proteases rhodesain and TbCatB: A valuable approach to treat Human African Trypanosomiasis. *Mini Rev. Med. Chem.* **2016**, *16*, 1374–1391. [CrossRef] [PubMed]
42. Vicik, R.; Busemann, M.; Gelhaus, C.; Stiefl, N.; Scheiber, J.; Schmitz, W.; Schulz, F.; Mladenovic, M.; Engels, B.; Leippe, M.; et al. Aziridide-based inhibitors of cathepsin L: Synthesis, inhibition activity, and docking studies. *ChemMedChem* **2006**, *1*, 1126–1141. [CrossRef] [PubMed]
43. Barthels, F.; Marincola, G.; Marciniak, T.; Konhäuser, M.; Hammerschmidt, S.; Bierlmeier, J.; Distler, U.; Wich, P.R.; Tenzer, S.; Schwarzer, D.; et al. Asymmetric disulfanylbenzamides as irreversible and selective inhibitors of Staphylococcus aureus sortase A. *ChemMedChem* **2020**. accepted. [CrossRef] [PubMed]
44. Dixon, M. The determination of enzyme inhibitor constants. *Biochem. J.* **1953**, *55*, 170–171. [CrossRef]
45. Dixon, M. The graphical determination of Km and Ki. *Biochem. J.* **1972**, *129*, 197–202. [CrossRef]
46. Cheng, Y.-C.; Prusoff, W.H. Relationship between the inhibition constant (Ki) and the concentration of inhibitor which causes 50 percent inhibition (I50) of an enzymatic reaction. *Biochem. Pharmacol.* **1973**, *22*, 3099–3108.
47. Nitsche, C.; Holloway, S.; Schirmeister, T.; Klein, C.D. Biochemistry and medicinal chemistry of the Dengue virus protease. *Chem. Rev.* **2014**, *114*, 11348–11381. [CrossRef]
48. Millies, B.; Hammerstein, v.F.; Gellert, A.; Hammerschmidt, S.; Barthels, F.; Göppel, U.; Immerheiser, M.; Elgner, F.; Jung, N.; Basic, M.; et al. Proline-based allosteric inhibitors of Zika and Dengue virus NS2B/NS3 proteases. *J. Med. Chem.* **2019**, *62*, 11359–11382. [CrossRef]
49. Barrett, A.J.; Woessner, J.F.; Rawlings, N.D. (Eds.) *Handbook of Proteolytic Enzymes*; Elsevier: London, UK, 2012; Volume 2, 984p, Available online: https://www.sciencedirect.com/book/9780120796113/handbook-of-proteolytic-enzymes (accessed on 23 March 2020).
50. Kerr, I.D.; Lee, J.H.; Farady, C.J.; Marion, R.; Rickert, M.; Sajid, M.; Pandey, K.C.; Caffrey, C.R.; Legac, J.; Hansell, E.; et al. Vinyl sulfones as antiparasitic agents and a structural basis for drug design. *J. Biol. Chem.* **2009**, *284*, 25697–25703. [CrossRef]
51. Stewart, J.J.P. Optimization of parameters for semiempirical methods V: Modification of NDDO approximations and application to 70 elements. *J. Mol. Model.* **2007**, *13*, 1173–1213. [CrossRef]
52. Halgren, T.A. Merck molecular force field. I. Basis, form, scope, parameterization and performance of MMFF94. *J. Comput. Chem.* **1996**, *17*, 490–519.
53. Vosko, S.H.; Wilk, L.; Nusair, M. Accurate spin-dependent electron liquid correlation energies for local spin density calculations: A critical analysis. *Can. J. Phys.* **1980**, *58*, 1200–1211. [CrossRef]
54. Lee, C.; Yang, W.; Parr, R.G. Development of the Colle-Salvetti correlation-energy formula into a functional of the electron density. *Phys. Rev. B* **1988**, *37*, 785–789. [CrossRef] [PubMed]
55. Becke, A.D. Density-functional thermochemistry. III. The role of exact exchange. *J. Chem. Phys.* **1993**, *98*, 5648–5652. [CrossRef]
56. Stephens, P.J.; Devlin, F.J.; Chabalowski, C.F.; Frisch, M.J. Ab initio calculation of vibrational absorption and circular dichroism spectra using density functional force fields. *J. Phys. Chem.* **1994**, *98*, 11623–11627. [CrossRef]
57. Krishnan, R.; Binkley, J.S.; Seeger, R.; Pople, J.A. Self-consistent molecular orbital methods. XX. A basis set for correlated wave functions. *J. Chem. Phys.* **1980**, *72*, 650–654. [CrossRef]
58. Clark, T.; Chandrasekhar, J.; Spitznagel, G.W.; Schleyer, P.v.R. Efficient diffuse function-augmented basis-sets for anion calculations. 3. The 3-21+G basis set for 1st-row elements, Li-F. *J. Comput. Chem.* **1983**, *4*, 294–301.
59. Frisch, M.J.; Pople, J.A.; Binkley, J.S. Self-consistent molecular orbital methods 25. Supplementary functions for Gaussian basis sets. *J. Chem. Phys.* **1984**, *80*, 3265–3269. [CrossRef]
60. Adamo, C.; Barone, V. Exchange functionals with improved long-range behavior and adiabatic connection methods without adjustable parameters: The mPW and mPW1PW models. *J. Chem. Phys.* **1998**, *108*, 664–675. [CrossRef]

61. Ditchfield, R. Self-consistent perturbation theory of diamagnetism. *Mol. Physics* **1974**, *27*, 789–807. [CrossRef]
62. Tomasi, J.; Mennucci, B.; Cancès, E. The IEF version of the PCM solvation method: An overview of a new method addressed to study molecular solutes at the QM ab initio level. *J. Mol. Struct.: Theochem* **1999**, *464*, 211–226. [CrossRef]
63. Grimblat, N.; Zanardi, M.M.; Sarotti, A.M. Beyond DP4: An improved probability for the stereochemical assignment of isomeric compounds using quantum chemical calculations of NMR shifts. *J. Org. Chem.* **2015**, *80*, 12526–12534. [CrossRef] [PubMed]
64. Helten, H.; Schirmeister, T.; Engels, B. Theoretical studies about the influence of different ring substituents on the nucleophilic ring opening of three-membered heterocycles and possible implications for the mechanisms of cysteine protease inhibitors. *J. Org. Chem.* **2005**, *70*, 233–237. [CrossRef] [PubMed]
65. Helten, H.; Schirmeister, T.; Engels, B. Model calculations about the influence of protic environments on the alkylation step of epoxide, aziridine, and thiirane based cysteine protease inhibitors. *J. Phys. Chem. A* **2004**, *108*, 7691–7701. [CrossRef]
66. Buback, V.; Mladenovic, M.; Engels, B.; Schirmeister, T. Rational design of improved aziridine-based inhibitors of cysteine proteases. *J. Phys. Chem. B* **2009**, *113*, 5282–5289. [CrossRef]
67. Chai, J.-D.; Head-Gordon, M. Long-Range Corrected Hybrid Density Functionals with Damped Atom−Atom Dispersion Corrections. *Phys. Chem. Chem. Phys.* **2008**, *10*, 6615–6621. [CrossRef]
68. Grimme, S. Improved second-order Moller-Plesset perturbation theory by separate scaling of parallel- and antiparallel-spin pair correlation energies. *J. Phys. Chem.* **2003**, *118*, 9095–9102. [CrossRef]
69. *Gaussian 16, Revision A.03*; Gaussian, Inc.: Wallingford, CT, USA, 2016.
70. LeadIT/FlexX. *Version 2.3.2*; BioSolveIT GmbH: St. Augustin, Germany, 2018.
71. Mladenovic, M.; Junold, K.; Fink, R.F.; Thiel, W.; Schirmeister, T.; Engels, B. Atomistic insights into the inhibition of cysteine proteases: First QM/MM calculations clarifying the regiospecificity and the inhibition potency of epoxide- and aziridine-based inhibitors. *J. Phys. Chem. B* **2008**, *112*, 5458–5469. [CrossRef]
72. Mladenovic, M.; Schirmeister, T.; Thiel, S.; Thiel, W.; Engels, B. The importance of the active site histidine for the activity of epoxide- or aziridine-based inhibitors of cysteine proteases. *ChemMedChem* **2007**, *2*, 120–128. [CrossRef]
73. Mladenovic, M.; Ansorg, K.; Fink, R.F.; Thiel, W.; Schirmeister, T.; Engels, B. Atomistic Insights into the Inhibition of Cysteine Proteases: First QM/MM Calculations Clarifying the Stereoselectivity of Epoxide-Based Inhibitors. *J. Phys. Chem. B* **2008**, *112*, 11798–11808. [CrossRef]
74. Wagner, A.; Le, T.A.; Brennich, M.; Klein, P.; Bader, N.; Diehl, E.; Paszek, D.; Weickhmann, A.K.; Dirdjaja, N.; Krauth-Siegel, R.L.; et al. Inhibitor-induced dimerization of an essential oxidoreductase from African trypanosomes. *Angew. Chem. Int. Ed.* **2019**, *58*, 3640–3644. [CrossRef] [PubMed]
75. Vicik, R.; Hoerr, V.; Glaser, M.; Schultheis, M.; Hansell, E.; McKerrow, J.H.; Holzgrabe, U.; Caffrey, C.R.; Ponte-Sucre, A.; Moll, H.; et al. Aziridine-2,3-dicarboxylate inhibitors targeting the major cysteine protease of Trypanosoma brucei as lead trypanocidal agents. *Bioorg. Med. Chem. Lett.* **2006**, *16*, 2753–2757. [CrossRef] [PubMed]

Sample Availability: Samples of the compounds are available from the authors.

4.3 Fluorovinyl sulfones and -Sulfonates as Potent Covalent Reversible Inhibitors of the Trypanosomal Cysteine Protease Rhodesain: Structure–Activity Relationship, Inhibition Mechanism, Metabolism, and In Vivo Studies

4.3.1 Context, Project Summary, and own Contribution

The vinyl sulfone-based cysteine protease inhibitor K11777 provides a suitable starting point for the structure-based development of anti-trypanosomal agents, as it showed efficient growth inhibition of trypanosomes and the elucidated crystal structure of the covalent inhibitor complex provides a basis for rational optimization.[231,239] Early ventures in the 2000s attempted to optimize the vinyl sulfone warhead by substituting the Michael acceptor system. In this regard, STEERT et al. found only weak inhibitors of the Leishmanial cathepsin B-like protease by α-fluorination of the olefin and therefore concluded that "α-fluorine in a Michael acceptor enzyme inhibitor does not afford biologically interesting compounds".[304] SCHIRMEISTER et al. disproved this in 2016 by QM/MM-based rational design of novel rhodesain inhibitors.[116] Here, fluorovinyl sulfones were characterized as very potent and covalent-reversible rhodesain inhibitors, mitigating potential off-target reactivity and toxicity risks (see chapter 1.1.4).

In this study led by [redacted] and [redacted], 33 fluorovinyl sulfones and -sulfonates were systematically optimized by SAR studies, resulting in a potent rhodesain inhibitor (K_I=3 nM) which showed good selectivity against mammalian cathepsin B and L (S.I.=32). The covalent-reversible mode of inhibition was confirmed and rationalized by adduct identification using ESI-MS and MALDI-TOF as well as QM/MM calculations. In comparison to the mass spectrometric study of fluorodinitroarenes from chapter 4.2, using acidic MALDI matrices, it was shown that the differentiation between non-covalent and covalent-reversible rhodesain inhibitors is gradual.[5] Fluorodinitroarenes do not form a chemical bond to the catalytic Cys25, whereas for fluorovinyl sulfones the reversible formation of a Michael adduct is certain.

The identified inhibitors showed a promising pharmacodynamic profile with anti-trypanosomal EC_{50} values comparable to those of K11777 but without toxicity deficits against mammalian cells (CC_{50}>100 μM). Metabolism and biodistribution studies in mice showed that the investigated fluorovinyl sulfones accumulate in the brain tissue of mice, which in summary indicates a good pharmacokinetic profile as well.

Own contributions: Conceptualization of protein MALDI-TOF mass spectrometry experiments, Execution of MALDI-TOF experiments with rhodesain and fluorodinitroarenes & Parts of the protease selectivity assays.

Contributions from other authors: Synthesis and characterization of the inhibitors, Rhodesain inhibition assays, Protein expression and purification, Protein ESI mass spectrometry, MALDI-TOF experiments with fluorovinyl sulfones, *T. brucei* cell assays, In vitro metabolism experiments, In vivo distribution studies, Molecular modeling & Quantum chemical investigations.

This work has been published in: Journal of Medicinal Chemistry (impact factor: 7.44).

The 'Supporting Information' can be accessed online at doi: 10.1021/acs.jmedchem.1c01002.

4.3.2 Publication

The following publication quoted (within “”) from page 197 to page 233 is exactly the same as the manuscript cited on page 196:”

Journal of Medicinal Chemistry

pubs.acs.org/jmc Article

Fluorovinylsulfones and -Sulfonates as Potent Covalent Reversible Inhibitors of the Trypanosomal Cysteine Protease Rhodesain: Structure−Activity Relationship, Inhibition Mechanism, Metabolism, and In Vivo Studies

Sascha Jung,[‡‡] Natalie Fuchs,[‡‡] Patrick Johe, Annika Wagner, Erika Diehl, Tri Yuliani, Collin Zimmer, Fabian Barthels, Robert A. Zimmermann, Philipp Klein, Waldemar Waigel, Jessica Meyr, Till Opatz, Stefan Tenzer, Ute Distler, Hans-Joachim Räder, Christian Kersten, Bernd Engels, Ute A. Hellmich, Jochen Klein, and Tanja Schirmeister*

Cite This: *J. Med. Chem.* 2021, 64, 12322 12358 Read Online

ACCESS | Metrics & More | Article Recommendations | Supporting Information

ABSTRACT: Rhodesain is a major cysteine protease of *Trypanosoma brucei rhodesiense*, a pathogen causing Human African Trypanosomiasis, and a validated drug target. Recently, we reported the development of α-halovinylsulfones as a new class of covalent reversible cysteine protease inhibitors. Here, α-fluorovinylsulfones/-sulfonates were optimized for rhodesain based on molecular modeling approaches. **2d**, the most potent and selective inhibitor in the series, shows a single-digit nanomolar affinity and high selectivity toward mammalian cathepsins B and L. Enzymatic dilution assays and MS experiments indicate that **2d** is a slow-tight binder (K_i = 3 nM). Furthermore, the nonfluorinated **2d-(H)** shows favorable metabolism and biodistribution by accumulation in mice brain tissue after intraperitoneal and oral administration. The highest antitrypanosomal activity was observed for inhibitors with an N-terminal 2,3-dihydrobenzo[*b*][1,4]dioxine group and a 4-Me-Phe residue in P2 (**2e**/**4e**) with nanomolar EC_{50} values (0.14/0.80 μM). The different mechanisms of reversible and irreversible inhibitors were explained using QM/MM calculations and MD simulations.

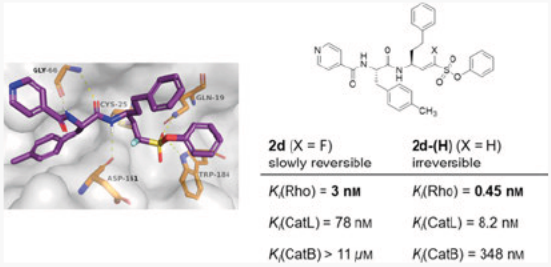

■ INTRODUCTION

Human African Trypanosomiasis (HAT, sleeping sickness) is a severe disease classified as a neglected tropical disease (NTD).[1] HAT is caused by the protozoan parasite *Trypanosoma brucei* (*T. brucei*), which is transmitted to humans via the bite of the Tsetse fly.[2] Sleeping sickness is fatal if left untreated. Pentamidine and suramin are used to treat the early, hemolymphatic stage of the disease, while eflornithine and melarsoprol and the combination therapy nifurtimox-eflornithine target the late, neurological stage of the disease.[3] Recently, the nitroimidazole fexinidazole was introduced as the first oral treatment of both, stage-1 and stage-2 *T. b. gambiense* HAT.[4] However, most available drugs show severe toxicity, poor bioavailability, and need long-time administration due to their lack of efficiency.[5] Therefore, there is an urgent need to develop new therapies against this disease and, in addition, *T. brucei* can serve as a valuable model organism for other pathogenic kinetoplastid diseases. The cysteine protease rhodesain (*Tb*CatL) is essential for the development of the parasite and for the progression of the disease.[6,7] Inhibition of the parasitic cysteine protease activity has been validated as a drug target in vitro and in vivo.[8] Consequently, rhodesain represents a promising target for the development of safer drugs against HAT.

Rhodesain belongs to the papain family of cysteine proteases and shares high structural similarity with the human cathepsins, especially cathepsin L (CatL; sequence identity 44.7%, similarity 59.1%, C_α-RMSD 1.35 Å).[9,10] A prominent inhibitor of papain-family cysteine proteases is **K11777**, a peptide-based vinyl-sulfone that mimics the autoinhibition of prorhodesain and that reacts in a Michael-type addition with the active-site cysteine (Figure 1).[10,11] The arising carbanion is protonated, resulting in the irreversible formation of the covalent enzyme inhibitor complex. Substitution of the hydrogen at the α-position of the

Received: June 3, 2021
Published: August 11, 2021

https://doi.org/10.1021/acs.jmedchem.1c01002
J. Med. Chem. 2021, 64, 12322 12358

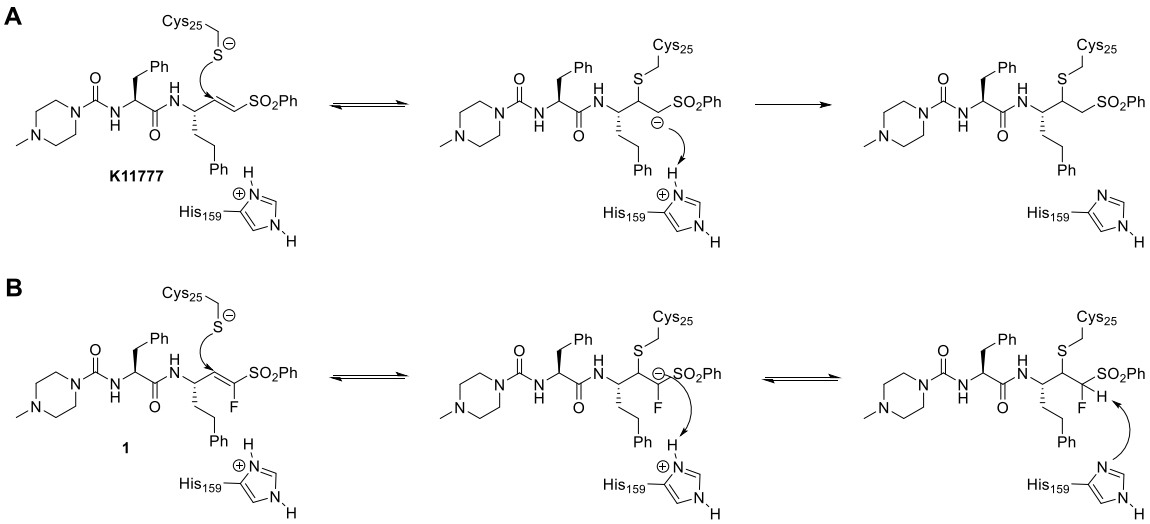

Figure 1. Structures and inhibition mechanisms of irreversible (**K11777**; A) and covalent reversible (**1**; B) peptide-based vinylsulfones.

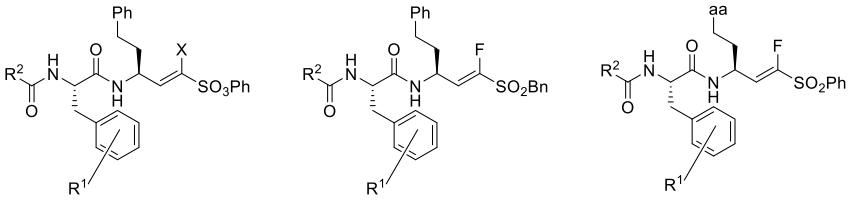

2a	R^1 = H, R^2 = 4-Pyr, X = F	**3a**	R^1 = H, R^2 = 4-Pyr	**4a**	R^1 = H, R^2 = 4-Pyr, aa = hPhe
2a-(*Z*)	R^1 = H, R^2 = 4-Pyr, X = F	**3b**	R^1 = H, R^2 = DHBD	**4b**	R^1 = H, R^2 = DHBD, aa = hPhe
2b	R^1 = H, R^2 = DHBD, X = F	**3c**	R^1 = H, R^2 = 3,5-DiFPh	**4c**	R^1 = H, R^2 = 3,5-DiFPh, aa = hPhe
2d	R^1 = 4-Me, R^2 = 4-Pyr, X = F	**3d**	R^1 = 4-Me, R^2 = 4-Pyr	**4d**	R^1 = 4-Me, R^2 = 4-Pyr, aa = hPhe
2d-(H)	R^1 = 4-Me, R^2 = 4-Pyr, X = H	**3e**	R^1 = 4-Me, R^2 = DHBD	**4e**	R^1 = 4-Me, R^2 = DHBD, aa = hPhe
2e	R^1 = 4-Me, R^2 = DHBD, X = F	**3f**	R^1 = 4-Me, R^2 = 3,5-DiFPh	**4f**	R^1 = 4-Me, R^2 = 3,5-DiFPh, aa = hPhe
2f	R^1 = 4-Me, R^2 = 3,5-DiFPh, X = F	**3g**	R^1 = 3-Me, R^2 = 4-Pyr	**4g**	R^1 = 3-Me, R^2 = 4-Pyr, aa = hPhe
2g	R^1 = 3-Me, R^2 = 4-Pyr, X = F	**3h**	R^1 = 3-Me, R^2 = DHBD	**4h**	R^1 = 3-Me, R^2 = DHBD, aa = hPhe
2h	R^1 = 3-Me, R^2 = DHBD, X = F	**3i**	R^1 = 3-Me, R^2 = 3,5-DiFPh	**4i**	R^1 = 3-Me, R^2 = 3,5-DiFPh, aa = hPhe
2i	R^1 = 3-Me, R^2 = 3,5-DiFPh, X = F			**4j**	R^1 = H, R^2 = *N*-MePip, aa = Met
2j	R^1 = H, R^2 = OBn, X = F			**4k**	R^1 = H, R^2 = 4-Pyr, aa = Met
2k	R^1 = H, R^2 = *N*-MePip, X = F			**4l**	R^1 = H, R^2 = *N*-MePip, aa = Cys(Bn)

Figure 2. Structures of compounds **2a** **4l**.

double bond by fluorine (compound **1**) generates an α-fluorovinylsulfone, which can undergo a reversible Michael-type addition with thiols (Figure 1).[12]

The development of covalent inhibitors has seen a resurgence in academia as well as in the industry during the past decade.[13] There is much debate on the advantages and disadvantages of covalent inhibition, especially concerning reversible covalent inhibition mechanisms.[14] On the one hand, covalent reversible inhibitors alleviate some of the concerns arising from covalent irreversible protein modifications, such as toxicity emerging from off-target effects,[15] idiosyncratic toxicity,[16] and haptenization,[17] but maintain benefits such as enhanced potency and prolonged residence times.[18,19] In recent studies with reversible fluorinated vinylsulfones and their irreversible counterparts, it was shown that the electrophilic group, the so-called warhead, and not the binding of the peptidic recognition unit limits the kinetics of inhibition of the protease and that the fluorinated vinylsulfone warhead reduces the rate constant of binding.[20,21]

https://doi.org/10.1021/acs.jmedchem.1c01002
J. Med. Chem. 2021, 64, 12322 12358

Scheme 1. Synthesis of Building Blocks 13 17[a]

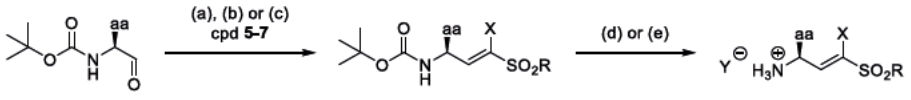

VI aa = hPhe
VII aa = Met
VIII aa = Cys(Bn)

(a) 8 R = Ph, X = F, aa = hPhe
9 R = OPh, X = F, aa = Met
(Z)-9 R = OPh, X = F, aa = Cys(Bn)
(b) 10 R = Bn, X = F, aa = hPhe
(c) 9-(H) R = OPh, X = H, aa = hPhe
11 R = Ph, X = F, aa = Met
12 R = Ph, X = F, aa = Cys(Bn)

(d) 13 Y = Cl, R = Ph, X = F, aa = hPhe
14 Y = Cl, R = OPh, X = F, aa = hPhe
(Z)-14 Y = Cl, R = OPh, X = F, aa = hPhe
14-(H) Y = Cl, R = OPh, X = H, aa = hPhe
15 Y = Cl, R = Bn, X = F, aa = hPhe
(e) 16 Y = TFA, R = Ph, X = F, aa = Met
17 Y = TFA, R = Ph, X = F, aa = Cys(Bn)

[a]Reagents and conditions: aa = amino acid side chain; (a) NaH, THF, 0 °C, 1 h, 22 43%; (b) KHMDS, THF, 78 °C for 20 min, 1 h at rt, 47%; (c) LHMDS, THF, 78 °C for 30 min, 12 h at rt, 54 75%; (d) 4 M HCl in dioxane, rt, 30 min, quant.; and (e) TFA, DCM, 0 °C, 1 h, quant.

Scheme 2. Preparation of Phosphonates 5 7[a]

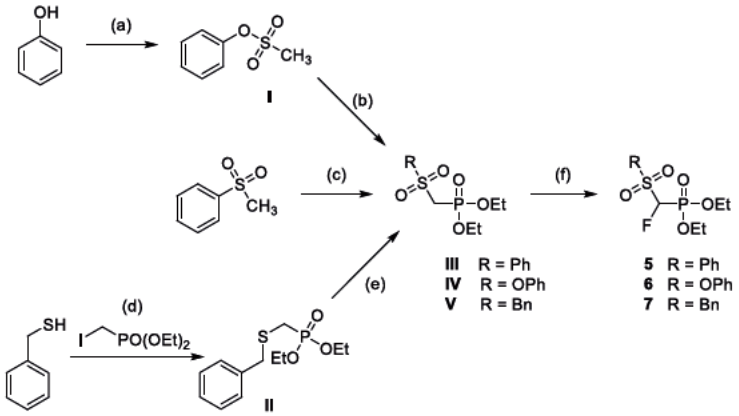

III R = Ph
IV R = OPh
V R = Bn

5 R = Ph
6 R = OPh
7 R = Bn

[a]Reagents and conditions: (a) Ms-Cl, TEA, EtOAc, 0 °C to rt, 30 min, 92%; (b) diethyl chlorophosphite (DECP), KHMDS, THF, 78 to 60 °C, 1 h, 74%; (c) DECP, *n*-BuLi, THF, 0 °C, 1 h, 52%; (d) NaH, THF, 0 °C to rt, 4 h, 84%; (e) *m*CPBA, DCM, 0 °C to rt, 12 h, 99%; and (f) Selectfluor, KHMDS, THF/DMF, 78 °C to rt, 3 h, 48 62%.

Based on the previously reported structure of the covalent reversible inhibitor **1**,[12] in the present study we performed structure activity relationship (SAR) studies to optimize inhibition potency for rhodesain and selectivity against human cathepsins B and L using molecular docking approaches. Additionally, quantum chemical-based computations were performed to get further information about the differences in the inhibition mechanisms of **K11777** and its fluorinated counterpart **1**. These studies were performed because in our previous study, the computed reaction energies for X = F and X = H in the α-position of the warhead (Figure 1) did not differ significantly. Thus, the transition from irreversible to reversible inhibition by exchange of hydrogen by fluorine could not be explained conclusively. The covalent behavior of the compounds was experimentally evaluated with MS studies, and reversibility was demonstrated with enzymatic dilution and dialysis assays.

Furthermore, the ADME parameters of compound **1** and the optimized inhibitor **2d-(H)** were investigated via in vitro metabolism studies and in vivo mouse studies in order to determine their organ distribution and their accumulation in brain tissue, thus evaluating their potential as candidates for the treatment of stage-2 HAT.

RESULTS AND DISCUSSION

Design of Inhibitors. Structural variations of the fluorinated vinylsulfone **1** (Figure 1B) were inspired by peptide-based inhibitors of rhodesain, which contain structural elements at the P3, P2, and P1′ positions[21] that are known to either enhance potency against rhodesain and/or increase selectivity against CatL and CatB.[22−25] For the P3 position, introduction of aromatic and heteroaromatic systems was reported to favor inhibition of rhodesain over CatL and CatB.[22−24] Introduction of an additional methyl group to the 3- or 4-position of the phenylalanine aromatic ring at the P2 position can improve potency and selectivity for rhodesain.[22] Additionally, the extension of the phenyl ring at the warhead into the S1′ pocket via linker atoms increases potency for rhodesain.[25] Based on these observations, a virtual library of 511 modified compounds was generated. These compounds were docked at rhodesain (crystal structure of rhodesain bound to **K11777**, protein databank (PDB) 2p7u[11]) using FlexX[26] and DOCKTITE,[27] as reported previously (Table S1).[12] The noncovalent enzyme inhibitor complex was generated with FlexX, and the scores reflect whether the designed compounds have an improved noncovalent affinity compared to the starting vinylsulfone **1**. Only compounds with a comparable or higher score were selected for synthesis. In addition, the covalent complex was modeled with DOCKTITE.[27] In this case, the scores (Table S1)

https://doi.org/10.1021/acs.jmedchem.1c01002
J. Med. Chem. 2021, 64, 12322 12358

Scheme 3. Synthesis of Compounds 2a 4l from Building Blocks 13 17[a]

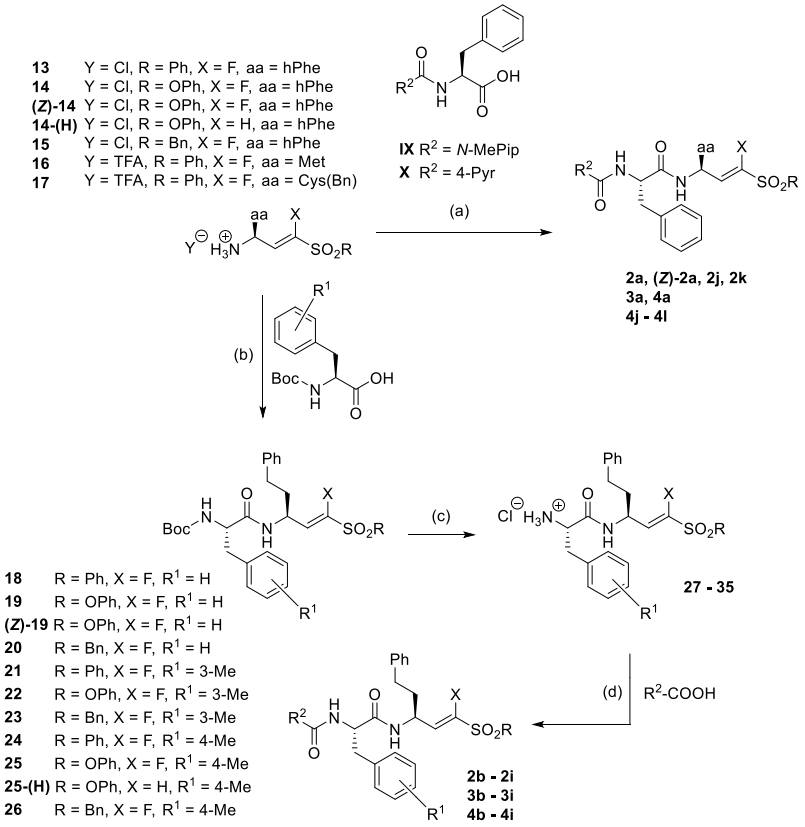

[a]Reagents and conditions: (a) TBTU, HOBt, DIEA, DMF, 0 °C to rt, 12 h, 59 81%; (b) TBTU, HOBt, DIEA, DCM, 0 °C to rt, 12 h, 69 83%; (c) 4 M HCl in dioxane, rt, 30 min, quant.; and (d) TBTU, DIEA, DCM, 0 °C to rt, 12 h, 62 84%.

may be interpreted in terms of stability of the protein-bound state.

Based on the results obtained from docking, a series of compounds (**2a** **4i**) were selected for synthesis and subsequent evaluation of SAR (Figure 2). For all selected compounds, scores obtained from both docking approaches were generally higher when compared to starting compound **1** (Table S1). Depending on the substitution pattern of the warhead at the P1′ position, compounds can be subdivided into aromatic fluorovinylsulfones (phenyl substituent at P1′, cpds **4a** **4i**), aliphatic fluorovinylsulfones (benzyl group at P1′, cpds **3a** **3i**), and fluorovinylsulfonates (phenol ester at P1′, cpds **2a** **2k**).

Based on noncovalent docking (Table S1), compounds (**4j** **4l**) with methionine and *S*-benzylcysteine at P1 were suggested to show a comparable (yet slightly lower) affinity to the respective molecules with a homophenylalanine residue. Therefore, these compounds were included in the present study and investigated for their potency.

Chemistry. Compounds **2a** **4l** (Figure 2) were synthesized using Horner Wadsworth Emmons (HWE) chemistry as the key step (Scheme 1). The required boc-protected amino-aldehydes (**VI** **VIII**) were prepared using Weinreb chemistry. The appropriate phosphonates (**5** **7**) were synthesized in three different ways (Scheme 2). The preparation of phosphonate **5** has been published previously.[12] Phosphonates **6** and **7** were obtained by fluorination of the respective nonhalogenated precursors (**IV**, **V**) with Selectfluor in the presence of KHMDS. The nonhalogenated precursors (**III** **V**) were synthesized according to literature procedures.[28]

HWE olefination of the aldehydes (**VI** **VII**) with the respective phosphonates (**5** **7**) provided the corresponding boc-protected vinylsulfones (**8** **12**) as mixtures of (*E*)/(*Z*)-isomers (Scheme 1), whereby the (*E*)-isomer was generally favored under the employed conditions. Overall yields ranged from 59 to 75%. The (*E*)-isomers were isolated by column chromatography in acceptable yields (41 63%) and used for the next steps. In the case of vinylsulfonate **9**, the (*Z*)-isomer was also isolated ((*Z*)-**9**, yield 22%). In the next step, the boc-group was removed using standard protocols, either 4 M HCl in dioxane or TFA in DCM, giving the amine building blocks **13** **17** in quantitative yields (Scheme 2). These building blocks were subjected to peptide chemistry based on the boc strategy with TBTU/HOBt as the coupling reagent (Scheme 3). The desired compounds (**2a** **4l**) were obtained after one or two coupling and deprotection steps.

The metabolites of compounds **1** and **2d**-(**H**), namely **1a**, **1b**, and **2l**, were synthesized using similar procedures to that described above. For the *N*-demethylated metabolite **1a** (Scheme 4), vinylsulfone **13** was coupled with **XIII**. After removal of the boc group, **1a** was obtained with a yield of 93%.

https://doi.org/10.1021/acs.jmedchem.1c01002
J. Med. Chem. 2021, 64, 12322 12358

Scheme 4. Synthesis of the *N*-Demethylated Metabolite 1a[a]

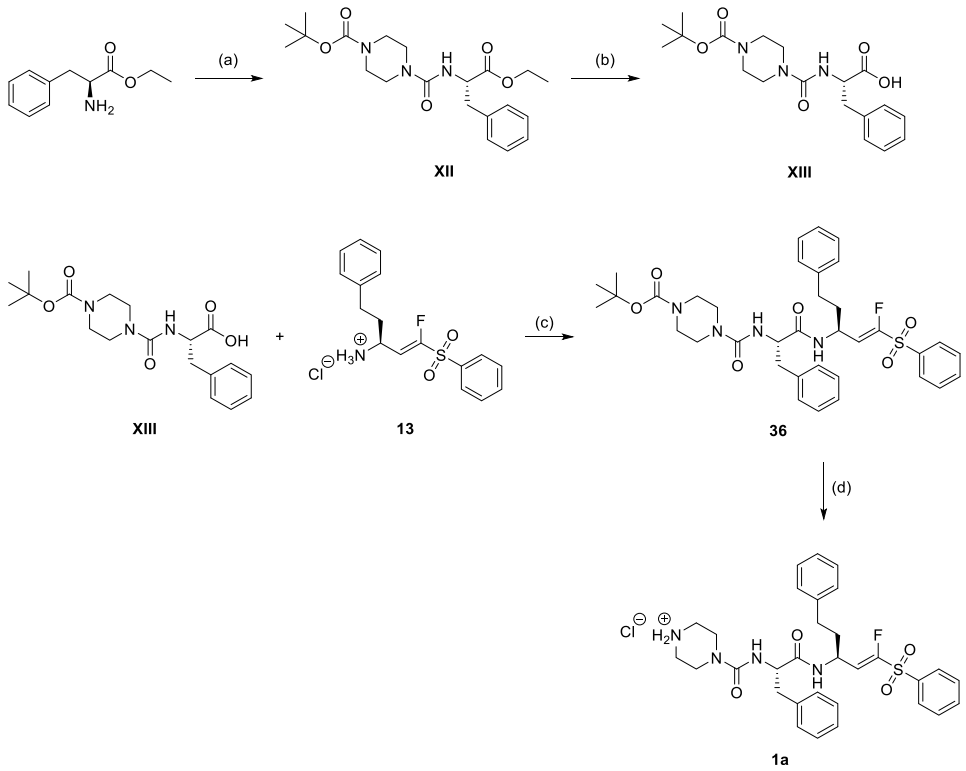

[a]Reagents and conditions: (a) (1) triphosgene, DCM, 0 °C, 1 h, 85%. (2) 1-Boc piperazine, THF, rt, 18 h, 50%, (b) LiOH, THF, 0 °C to rt, 3 h, 74%, (c) HOBt, TBTU, DIEA, DCM, 0 °C to rt, 12 h, 45%, and (d) 4 M HCl in dioxane, rt, 1 h, 93%.

Scheme 5. Synthesis of the *N*-Oxidized Metabolite 1b[a]

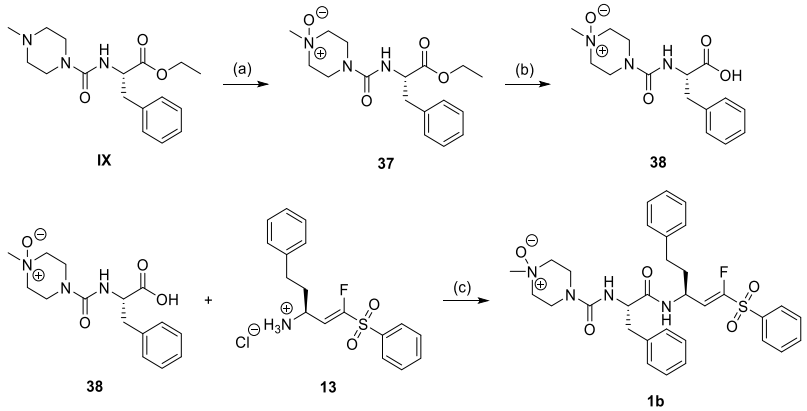

[a]Reagents and conditions: (a) *m*CPBA, DCM, 0 °C, 16 h, 52%; (b) LiOH, THF, 0 °C to rt, 3 h, 53%; and (c) HOBt, TBTU, DIEA, DCM/DMF, 0 °C to rt, 24 h, 23%.

In Scheme 5, the preparation of the metabolite **1b**, the *N*-oxide of compound **1**, is described. The synthesis started with compound **IX**, which was oxidized with *m*CPBA,[29] resulting in ester **37**, which was hydrolyzed with LiOH. Compound **38** was then coupled with vinylsulfone **13**, yielding compound **1b**.

The *N*-oxidized metabolite **2l** of compound **2d-(H)** was prepared as shown in Scheme 6. Isonicotinic acid was esterified and then oxidized with *m*CPBA.[29] The resulting compound **40** was hydrolyzed to **41** and then coupled with **34-(H)**, yielding the *N*-oxide **2l**.

https://doi.org/10.1021/acs.jmedchem.1c01002
J. Med. Chem. 2021, 64, 12322 12358

Scheme 6. Synthesis of the N-Oxidized Metabolite 2l of Compound 2d-(H)[a]

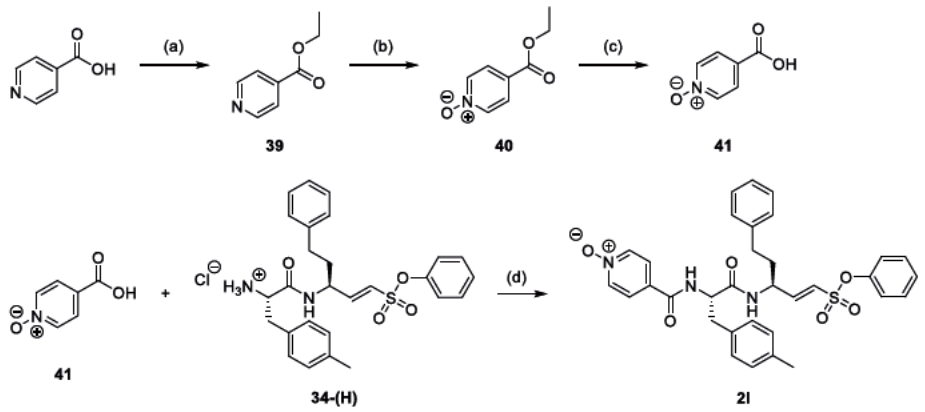

[a]Reagents and conditions: (a) ethanol, H_2SO_4, reflux, 24 h, 73%; (b) *m*CPBA, DCM, 0 °C, 16 h, 29%; (c) LiOH, THF, 0 °C to rt, 3 h, 90%; and (d) HOBt, TBTU, DIEA, DCM, 0 °C to rt, 24 h, 13%.

Table 1. Inhibition Data for Compounds 2a 2k[a]

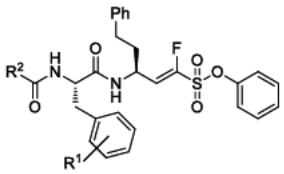

	substitution		rhodesain		CatL			CatB
Cpd	R^1	R^2	$K_i/\mu M$[b]	$K_i^*/\mu M$[b]	$K_i/\mu M$[c]	$K_i^*/\mu M$[c]	SI[d]	$K_i/\mu M$
2a	H	4-Pyr	0.098[g]	0.015[g]	0.258[g]	0.060[g]	4	1.7
(Z)-2a	H	4-Pyr	0.525[e,g]		n.d.		n.d.	n.d.
2b	H	DHBD	0.045[g]	0.009[g]	n.d.	n.d.	n.d.	n.d.
2d	4-Me	4-Pyr	0.024[g]	0.003[g]	0.313[g]	0.078[g]	26	38%[f]
2e	4-Me	DHBD	0.098[g]	0.007[g]	0.348[g]	0.039[g]	6	14%[f]
2f	4-Me	3,5-F_2Ph	0.034[g]	0.005[g]	n.d.	n.d.	n.d.	n.d.
2g	3-Me	4-Pyr	0.094[g]	0.007[g]	0.266[g]	0.030[g]	4	50%[f]
2h	3-Me	DHBD	0.059[g]	0.010[g]	n.d.	n.d.	n.d.	n.d.
2i	3-Me	3,5-F_2Ph	0.152[g]	0.021[g]	n.d.	n.d.	n.d.	n.d.
2j	H	OBn	0.158[e,g]		n.d.		n.d.	n.d.
2k	H	*N*-MePip	0.108[e]		n.d.		n.d.	n.d.

[a]K_i^* denotes the dissociation constant of the high-affinity complex in the case of biphasic, time-dependent inhibition. [b]Calculated with method 1 (see the text). [c]Calculated with method 2 (Dixon equation).[31] [d]K_i^*(CatL)/K_i^*(rhodesain). [e]Calculated from IC_{50} value with the Cheng Prusoff equation.[32] [f]% inhibition at 11 μM inhibitor concentration (single measurement). [g]Mean value of three independent assays; standard deviations less than 10%.

Enzyme Assays. Inhibition of rhodesain was tested with the fluorogenic substrate Cbz-Phe-Arg-AMC as described previously.[12,30] For the three series of compounds, the results from the fluorometric enzyme assays with rhodesain and the related mammalian enzymes cathepsin L and B are summarized in Tables 1 3.

For benzyl and phenyl fluorovinylsulfones (cpds 3a 3i, 4a 4l), the progress curves for inhibition of rhodesain were found to be linear in all cases, indicating a fast reversible inhibition (exemplarily shown for compound 3d in Figure 3A and for 4a in Figure 3B). In order to confirm the competitive behavior of these compounds, IC_{50} values were measured at seven different substrate concentrations. IC_{50} values were found to increase linearly with ascending substrate concentration, showing competitive inhibition (Figure 3C,D). This was assumed to be the case for all compounds of the series. Consequently, IC_{50} values were converted to K_i values using the Cheng Prusoff relationship (Tables 2 and 3).[32]

Reversibility was confirmed by dilution assays, that is, the enzyme was incubated with an excess of inhibitor (10-fold the IC_{50} concentration) to ensure full inhibition. Then, the mixture was diluted 100-fold to yield an inhibitor concentration of 0.1-fold the IC_{50} concentration. In the case of reversible inhibition, the enzyme activity should recover, whereas in the case of irreversible inhibition, it should not. For both compounds (3d, 4a), enzyme activity recovers after dilution, whereas for the irreversible inhibitor K11777 used as a control, enzyme activity does not recover (Figure 4A).

For vinylsulfonates (2a 2k), the progress curves for inhibition of rhodesain were not linear for most of the

https://doi.org/10.1021/acs.jmedchem.1c01002
J. Med. Chem. 2021, 64, 12322 12358

Table 2. Inhibition Data for Compounds 3a 3i

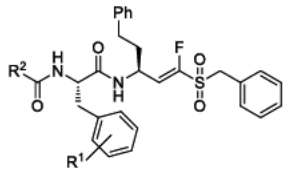

	substitution		rhodesain	CatL		CatB
cpd	R^1	R^2	K_i/μM	K_i/μM	SI[a]	K_i/μM
3a	H	4-Pyr	0.053[d]	0.226[d]	4	44%[b]
3b	H	DHBD	0.046[d]	n.d.	n.d.	n.d.
3c	H	3,5-F_2Ph	0.124[d]	n.d.	n.d.	n.d.
3d	4-Me	4-Pyr	0.015[d]	0.181[d]	12	35%[b]
3e	4-Me	DHBD	0.014[d]	0.076[d]	6	8%[b]
3f	4-Me	3,5-F_2Ph	0.029[d]	n.d.	n.d.	n.d.
3g	3-Me	4-Pyr	0.061[d]	0.122[d]	2	1.7[c]
3h	3-Me	DHBD	0.092[d]	n.d.	n.d.	n.d.
3i	3-Me	3,5-F_2Ph	0.380[d]	n.d.	n.d.	n.d.

[a]K_i(CatL)/K_i(rhodesain). [b]% inhibition at 11 μM (single measurement). [c]Single measurement. [d]Mean value of three independent assays; standard deviations less than 10%.

compounds (**2a** **2i**), but showed time-dependency (exemplified for **2d** in Figure 5A). Inhibition by all vinylsulfonates was found to be competitive with respect to the substrate (Figure 5B). Time-dependent inhibition is typical for irreversible inhibitors but may also be observed for covalent reversible inhibition. In the case of irreversible inhibition, the progress curves reach a plateau value with the terminal enzyme activity, that is, the steady-state velocity of substrate turnover in the presence of the inhibitor, $v_s = 0$. For covalent reversible inhibition, time-dependent progress curves reflect a biphasic behavior with the terminal enzyme activity in the presence of the inhibitor $v_s \neq 0$, but with $v_s < v_i$ (v_i = the initial enzyme activity in the presence of the inhibitor). To distinguish between these two scenarios, dilution assays were performed (see above), exemplarily shown for inhibitor **2d** (Figure 4A). The results clearly indicate that vinylsulfonate **2d** is a reversible inhibitor, but dissociates significantly slower compared to compounds **4a** and **3d**, indicating a tight covalent reversible inhibition according to the following inhibition mechanism, with $K_i = k_2/k_1$ as the dissociation constant of the initial noncovalent enzyme inhibitor (E···I) complex and K_i^* as the dissociation constant of the final covalent, high-affinity complex (E I)[33]

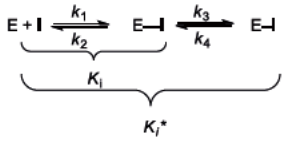

For these inhibitors, the initial (v_i) and steady-state (v_s) velocities in the presence of the inhibitor as well as the pseudo-first order rate constants k_{obs} were determined for the different inhibitor concentrations by fitting the progress curves (shown for cpd **2d** in Figure 5A) to the slow-binding equation (off = offset)[33]

$$[P] = v_s \times t + \frac{v_i - v_s}{k_{obs}}[1 - \exp(-k_{obs} \times t)] + \text{off}$$

The k_{obs} values were replotted against the inhibitor concentrations [I] (Figure 5C) with the equation[33]

$$k_{obs} = k_4 + \left(\frac{k_3 \times [I]}{K_i^{app} + [I]}\right)$$

to yield the apparent dissociation constant K_i^{app} of the initial enzyme inhibitor complex, as well as the rate constants k_3 and k_4 of the second inhibition step (Method 1). Because the compounds display competitive inhibition with respect to the substrate (Figure 5B), the K_i^{app} value was converted to K_i for the

Table 3. Inhibition Data for Compounds 4a 4l

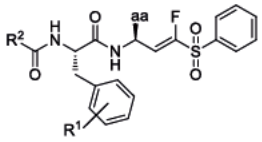

	substitution			rhodesain	CatL		CatB
cpd	R^1	R^2	aa	K_i/μM	K_i/μM	SI[a]	K_i/μM
1	H	*N*-MePip	hPhe	0.190[c,e]	0.023[e]	0.1	0.47[d]
4a	H	4-Pyr	hPhe	0.032[c,e]	0.110[e]	3	3.13[d]
4b	H	DHBD	hPhe	0.012[e]	0.033[e]	3	4.81[d]
4c	H	3,5-F_2Ph	hPhe	0.035[e]	n.d.	n.d.	n.d.
4d	4-Me	4-Pyr	hPhe	0.008[e]	0.115[e]	14	2.08[d]
4e	4-Me	DHBD	hPhe	0.005[e]	0.023[e]	5	34%[b]
4f	4-Me	3,5-F_2Ph	hPhe	0.010[e]	n.d.	n.d.	n.d.
4g	3-Me	4-Pyr	hPhe	0.025[e]	0.049[e]	2	0.35[d]
4h	3-Me	DHBD	hPhe	0.035[e]	n.d.	n.d.	n.d.
4i	3-Me	3,5-F_2Ph	hPhe	0.329[e]	n.d.	n.d.	n.d.
4j	H	*N*-MePip	Met	0.360[e]	0.173[e]	0.5	1.20[d]
4k	H	4-Pyr	Met	0.056[e]	0.577[e]	10	6.17[d]
4l	H	*N*-MePip	Cys(Bn)	0.630[e]	0.628[e]	1	8.62[d]

[a]K_i(CatL)/K_i(rhodesain). [b]% inhibition at 11 μM. [c]Ref 12 ; n.d.: not determined. [d]Single measurement. [e]Mean value of three independent assays; standard deviations less than 10%.

https://doi.org/10.1021/acs.jmedchem.1c01002
J. Med. Chem. 2021, 64, 12322 12358

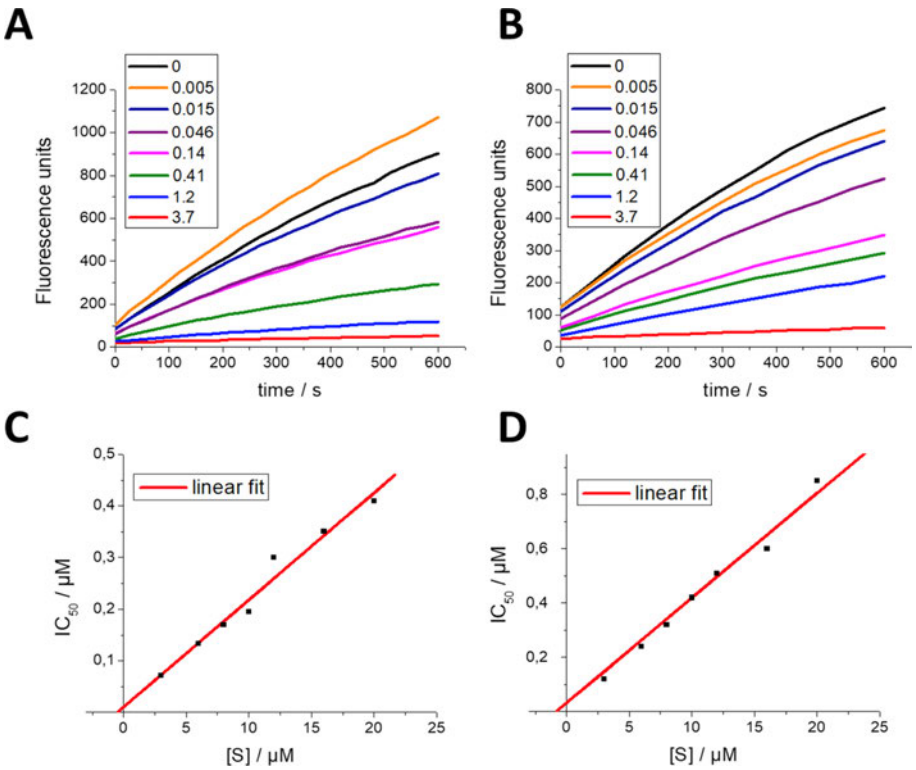

Figure 3. (A) Example for progress curves for inhibition of rhodesain by compound **3d**. Inhibitor concentrations in μM. (B) Example for progress curves for inhibition of rhodesain by compound **4a**. Inhibitor concentrations in μM. (C) Dependence of inhibition potency (IC_{50} values) on substrate concentration for inhibition of rhodesain by compound **3d**. Increasing IC_{50} values at ascending substrate concentrations show competitive inhibition. The K_i value is obtained as the intercept of the regression line with the y-axis (K_i = 25 nM). (D) Dependence of inhibition potency (IC_{50} values) on the substrate concentration for inhibition of rhodesain by compound **4a**. Increasing IC_{50} values at ascending substrate concentrations prove competitive inhibition. The K_i value is obtained as the intercept of the regression line with the y-axis (K_i = 47 nM).

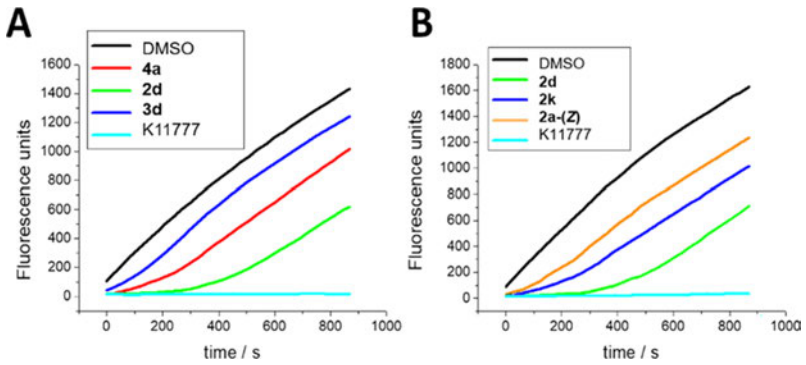

Figure 4. (A) Dilution assays show reversible inhibition of rhodesain (see the text). For all compounds, enzyme activity did recover after dilution, except for the irreversible vinylsulfone **K11777** (control). Compound **3d** showed faster reversibility than compound **4a**. Vinylsulfonate **2d** can be considered a tight-binding, slowly reversible inhibitor. (B) Dilution assays of several compounds of the series of vinylsulfonates. In the case of compound **2d**, which showed two-step inhibition in the enzyme assay, enzymatic activity recovers slower compared to vinylsulfonates **2k** and **2a**-(*Z*), which did not show biphasic behavior. The irreversible inhibitor **K11777** was used as a control.

initial inhibitor complex with the Cheng Prusoff equation.[32]

$$K_i^* = \frac{K_i}{1 + \left(\frac{k_3}{k_4}\right)}$$

The K_i^* value as the dissociation constant of the final complex was calculated from

https://doi.org/10.1021/acs.jmedchem.1c01002
J. Med. Chem. 2021, 64, 12322 12358

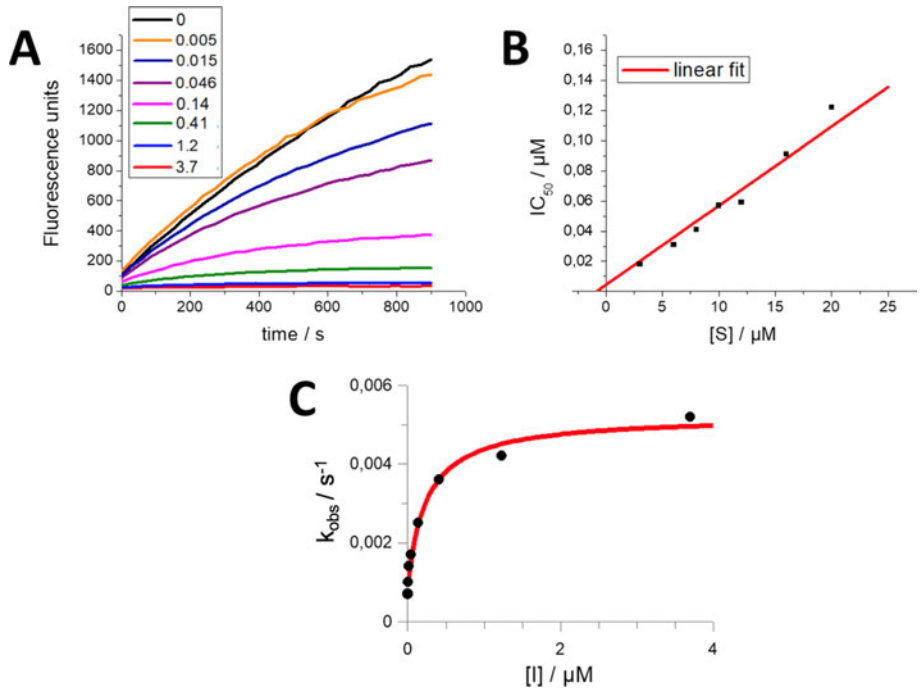

Figure 5. (A) Example for progress curves for inhibition of rhodesain by compound **2d**. Curve shape indicates time-dependent inhibition. Inhibitor concentrations in μM. (B) Dependence of inhibition potency (IC_{50} values) from the substrate concentration for inhibition of rhodesain by compound **2d**. Increasing IC_{50} values at ascending substrate concentrations show competitive inhibition. The K_i value is obtained as the intercept of the regression line with the *y*-axis (K_i = 19 nM). (C) Plot of the rate constants k_{obs} for the progress curves of compound **2d** from Figure 5A as a function of the inhibitor concentration. k_4 is obtained from the intercept of the regression curve with the *y*-axis. The maximum value of k_{obs} at infinite inhibitor concentration provides the sum of k_3 and k_4. The concentration of inhibitor yielding a half-maximal value of k_{obs} is equal to K_i^{app}.

Both dissociation constants, K_i and K_i^*, were also calculated by fitting the initial (v_i) and steady-state (v_s) velocities, respectively, against the inhibitor concentrations using the Dixon equation (Method 2)[31]

$$\frac{v_{i,s}}{v_0} = \frac{[I]}{1 + \left(\frac{[I]}{K_i^{(*)app}}\right)}$$

K_i^{app} was obtained from fitting v_i against [I] and $K_i^{(*)app}$ from fitting v_s against [I] (v_0 is the substrate turnover velocity in the absence of the inhibitor), and both constants were converted into K_i and K_i^* with the Cheng Prusoff equation.[32]

A comparison of the dissociation constants for inhibition of rhodesain by inhibitors **2a** **2i** obtained by both methods is shown in Table 4.

The data show that both methods yield similar dissociation constants for the initial low-affinity as well as for the final high-affinity complex proving that both methods are reliable. For all compounds, the rate constant of dissociation of the final complex (k_4) was found to be slower than the rate constant of association (k_3), indicating tight binding of these inhibitors. Interestingly, vinylsulfonates (*Z*)-**2a**, **2k**, and **2j** did not show time dependency of inhibition, but linear progress curves similar to the benzyl and phenyl vinylsulfones. Dilution assays for these three vinylsulfonates [(*Z*)-**2a**, **2k**, and **2j**] indicated a significantly faster recovery of the enzyme activity compared to the time-dependent inhibitor **2d** [shown for compound (*Z*)-**2a** and **2k** in Figure 4B].

Table 4. Inhibition Data and Kinetic Parameters k_3 and k_4 for Time-Dependent Inhibition of Rhodesain by Compounds 2a 2i

	method 1 (slow-binding equation)[a]				method 2 (Dixon equation)[b]	
Cpd	K_i/μM	K_i^*/μM	k_3/s^{-1}	k_4/s^{-1}	K_i/μM	K_i^*/μM
2a	0.098	0.015	0.055	0.010	0.110	0.008
2b	0.045	0.009	0.045	0.011	0.060	0.005
2d	0.024	0.003	0.075	0.010	0.022	0.002
2e	0.098	0.007	0.065	0.005	0.124	0.002
2f	0.034	0.005	0.049	0.009	0.052	0.004
2g	0.094	0.007	0.062	0.005	0.089	0.004
2h	0.059	0.010	0.074	0.015	0.068	0.006
2i	0.152	0.021	0.055	0.010	0.155	0.024

[a]Calculated with slow-binding equation (see the text). [b]Calculated with the Dixon equation (see the text).[31] Mean values of three independent assays, standard deviations less than 10%.

To further quantify the degree of reversibility for the different warheads, compounds **2d**, **3d**, and **4d** with identical recognition units were subjected to a dialysis experiment.[12] Here, rhodesain was incubated with an excess of inhibitor (10-fold the IC_{50} concentration) to ensure full inhibition. Then, the mixture was dialyzed against a continuous flow of enzyme buffer using a 3.5 kDa cut-off dialysis tubing.[34] Samples were taken after 10, 30, 60, and 120 min and analyzed for their residual enzyme activity with the standard fluorometric assay. The results are presented as the

https://doi.org/10.1021/acs.jmedchem.1c01002
J. Med. Chem. 2021, 64, 12322 12358

fractional activity of uninhibited rhodesain, which was subjected to dialysis in the same experiment (Figure 6). Compound **3d**

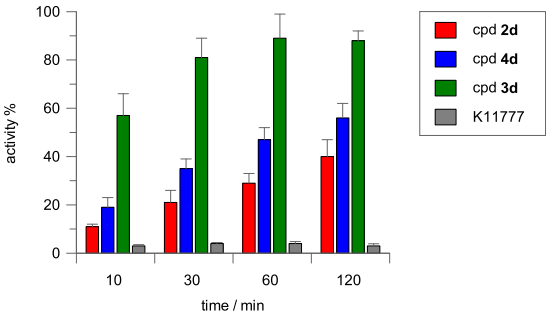

Figure 6. Dialysis experiment for compounds **2d**, **3d**, **4d**, and **K11777**. Rhodesain was incubated with the inhibitors at a concentration of 10-fold the respective IC_{50} value. The mixture was dialyzed against a continuous flow of buffer. Samples were taken after 10, 30, 60, and 120 min and the substrate was added to measure the residual enzyme activity. **K11777** was used as an irreversible control.

showed the fastest reversibility (89% recovery after 1 h), which is in accordance with findings from the dilution assay. Compound **4d** dissociated significantly slower (47% recovery after 1 h). Vinylsulfonate **2d** displayed the slowest reversibility (29% after 1 h), which supports the tight-binding nature of the inhibition with the formation of a very stable high-affinity complex. **K11777** was used as an irreversible control, showing no recovery of the enzymatic activity.

The most potent compounds of each series were also tested against the human enzymes CatL and CatB. For the tested vinylsulfonates (**2a**, **2d**, **2e**, and **2g**), a biphasic behavior was also observed for inhibition of CatL. In these cases, K_i and K_i^* values were calculated with the Dixon equation (Table 2).[31] For inhibition of CatB, no biphasic behavior was observed for these compounds (**2a**, **2d**, **2e**, and **2g**). This can be explained with the low affinity of the compounds for CatB. Notably, compounds **2d**, **2e**, and **2g** showed only very weak inhibition at concentrations of up to 11 μM.

Discussion of SAR. Comparison of the K_i values for rhodesain of the starting compound **1** (K_i = 190 nM) with the P3-modified analogues **4a** **4c** demonstrates that the exchange of *N*-methyl piperazine against aromatic residues with no or only limited basicity significantly enhances inhibition potency (e.g., cpd **4b** with K_i = 12 nM). This is also reflected by the scores obtained from docking for these compounds, for example, for **4b** noncovalent affinity as well as the stability of the covalent complex are predicted to be higher (Table S1). Additionally, compounds **4a** **4c** show improved selectivity for rhodesain over the human cathepsins. Lead compound **1** shows a higher affinity for human CatL (K_i = 23 nM) than for rhodesain (K_i = 190 nM), while P3-modified compounds **4a** and **4b** slightly favor inhibition of rhodesain (3-fold). Furthermore, selectivity for rhodesain over CatB is dramatically enhanced by these structural variations. This is a remarkable improvement (2-fold) compared to the weak selectivity of starting compound **1**. A further increase in potency for rhodesain is observed for compounds with an additional 4-methyl substituent at the phenylalanine aromatic ring (**4d** **4f**), with compound **4e** (K_i = 5 nM) being the most potent inhibitor in the series of phenyl vinylsulfones. As suggested from noncovalent docking, this increase in potency may be directly attributed to additional hydrophobic interactions of the 4-methyl group with lipophilic residues lining the S2 pocket (Ala208, Leu160, Figure 7), which is also reflected in

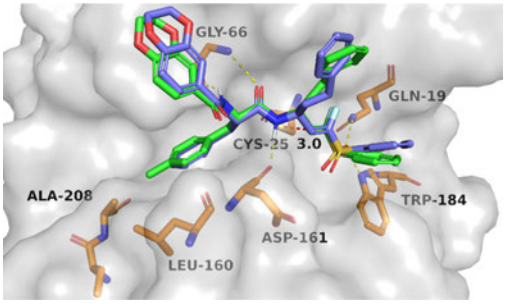

Figure 7. Noncovalent binding mode of compound **4b** (light blue, FlexX score: 31.2, Hyde score: 10.0 kcal mol ^{1}) and **4e** (green, FlexX score: 32.5, Hyde score: 11.7 kcal mol ^{1}) as predicted by FlexX. The electrophilic β-carbon of the fluorovinylsulfone warhead comes in close proximity to the nucleophilic sulfur of Cys25 (3.0 Å). The sulfone group forms hydrogen bonds with Gln19 and Trp184. The recognition unit forms hydrogen bonds to Gly66 and Asp161. The additional 4-methyl group of **4e** at the phenylalanine aromatic ring points into a hydrophobic cavity between Ala208 and Leu160, resulting in additional lipophilic interactions compared to compound **4b**.

higher scores compared to compounds **4a** **4c** (Table S1). Additionally, introduction of the 4-methyl substituent further increases selectivity against CatL (14-fold for **4d**). In contrast, incorporation of a 3-methyl substituent (**4g** **4i**) does reduce potency and selectivity compared to compounds **4a** **4c**. In particular, the combination of the 3-methyl substituent and the 3,5-difluorophenyl moiety (**4i**) is not advantageous: compound **4i** displayed significantly reduced potency (K_i = 329 nM). The considerable difference compared to compound **4e** with a 4-methyl substituent (K_i = 10 nM) cannot be explained exclusively with the slightly reduced docking scores (Table S1).

Within the set of benzyl vinylsulfones (**3a** **3i**), the SAR relationships are very similar compared to phenyl vinylsulfones (**4a** **4i**). Consequently, compounds **3d** and **3e** with a 4-methyl substituent and a 4-pyridyl or DHBD moiety, respectively, are the most potent and most selective inhibitors (**3d**: K_i = 15 nM, 12-fold selectivity over CatL). Remarkably, compound **3d** showed even lower activity against CatB (35% inhibition at 11 μM) compared with its counterpart **4d**. Again, compound **3i** with a 3-methyl substituent and 3,5-difluorophenyl residue shows noticeably lower potency (K_i = 380 nM). Comparison of inhibitory potency for benzyl and phenyl vinylsulfones with the same recognition unit (e.g., **3a** vs **4a**) reveals that the benzyl substituent at the warhead has a negative influence on inhibition potency. In general, benzyl vinylsulfones have slightly increased K_i values compared to their phenyl counterparts.

These findings cannot be correlated with scores from docking, which generally predicted a higher affinity for compounds with a benzyl group at P1′. Computational conclusions to explain these differences between theory and experiment would be desirable, but are difficult because the differences in K_i values result from an increase in binding energy of less than 1 kcal mol^{-1} (e.g., **3d** K_i = 0.015 μM, i.e., ΔG = 11.10 kcal mol^{-1} vs **4d** K_i = 0.008 μM, i.e., ΔG = 11.49 kcal mol^{-1}), which is out of the scope of even high-level quantum chemical computations. Possibly, entropic

https://doi.org/10.1021/acs.jmedchem.1c01002
J. Med. Chem. 2021, 64, 12322 12358

effects due to the higher flexibility of the benzyl group in the noncovalent enzyme inhibitor complex may contribute.

The results from dilution and dialysis assays revealed that benzyl vinylsulfones are faster reversible than their phenyl counterparts, which may be explained with a lower reaction energy for the covalent bond-forming step, resulting in a weaker covalent bond.

Comparison of the K_i values of starting compound **1** (K_i = 190 nM) and the corresponding vinylsulfonate **2k** (K_i = 108 nM) demonstrates a nearly 2-fold improvement in affinity for rhodesain. The increase in potency may be partly attributed to the enlarged substituent at P1′. The results from noncovalent docking suggest that the vinylsulfonate moiety extends further into the S1′ pocket and forms nonpolar interactions with Trp184 (Figure 8), which is also reflected by the slightly

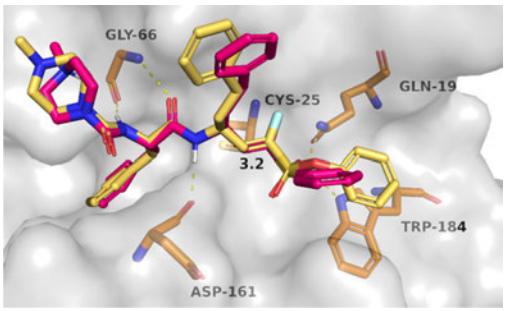

Figure 8. Overlay of noncovalent docking poses of compound **1** (magenta, FlexX score: 27.9, Hyde score: 6.2 kcal mol ^{1}) and compound **2k** (gold, FlexX score: 28.4, Hyde score: 8.8 kcal mol ^{1}). The enlarged vinylsulfonate moiety of compound **2k** extends further into the S1′ pocket and the aromatic ring can form additional hydrophobic interactions with Trp184 (π π-stacking interactions).

enhanced scores. Again, substitution of the *N*-methyl piperazine against aromatic residues (cpds **2a** **2i**) further improves affinity for rhodesain. Additionally, and in contrast to compound **2k**, compounds **2a** **2i** show a biphasic, time-dependent inhibition mechanism.

Dilution and dialysis experiments demonstrated reversibility for compound **2d** (Figures 4 and 6), which is, however, significantly slower compared to vinylsulfonate **2k**, which supports the tight-binding properties of **2d**. The related vinylsufones (**3d** and **4d**) do not show two-step inhibition, indicating that a combination of the properties of the fluorovinylsulfonate warhead with appropriate noncovalent interactions is required for tight binding. This is further supported by vinylsulfonate **2j** with a Cbz group at P3, which also does not show time-dependent inhibition. Among the tight-binding compounds, **2d** shows the highest potency for rhodesain with a dissociation constant of the initial encounter complex K_i = 24 nM, and with a high-affinity complex formed in the second step (K_i^* = 3 nM). Especially, the covalent complex is predicted to be very stable (Figure 9B). This is in excellent accordance with the high scores obtained from both docking approaches for compound **2d** (Table S1). Notably, compound **2d** showed good selectivity over the human cathepsins, with 26-fold selectivity against CatL and virtually no activity against CatB (38% at 11 μM), which is a significant improvement compared to the starting compound **1**.

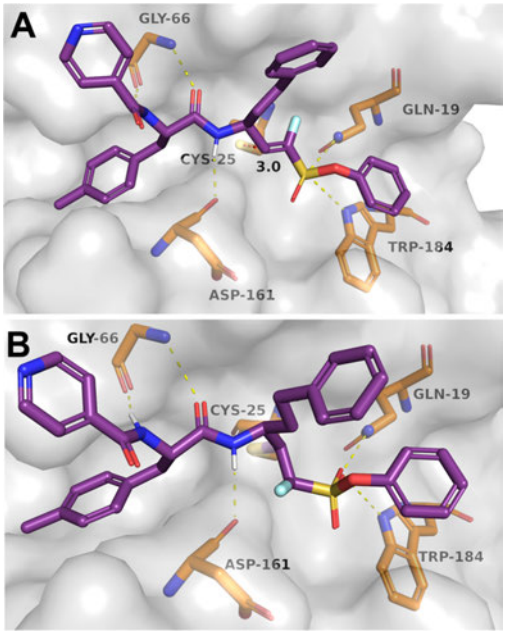

Figure 9. (A) Non-covalent docking pose of compound **2d** predicted with FlexX (FlexX score: 34.3, Hyde score: 38). (B) Geometry of the covalent complex between rhodesain and compound **2d** as predicted with DOCKTITE [score (affinity ΔG, kcal mol ^{1}): 6.2, DSX score: 195.5]. The combination of the vinylsulfonate aromatic ring extending further into the S1′ pocket and forming lipophilic interactions with Trp184, additional hydrophobic interactions of the 4-methyl group at phenylalanine aromatic ring with the S2 pocket and the preferred 4-pyridyl group at P3 results in a high affinity of compound **2d** for the binding site. This is reflected from higher scores obtained from both docking approaches compared to its analogues (Table S1).

Assuming that inhibitor binding to CatL and CatB is similar to rhodesain binding and that the binding mode is not largely altered for the compounds presented herein compared to **K11777**, which is also suggested by the docking (Figures 7 9), the underlying molecular mechanisms for selectivity can be explained by analysis of the known X-ray structures. Rhodesain shares an overall sequence identity of 44.7% and similarity of 59.1% with CatL and 27.9% identity and 47.4% similarity with CatB, as well as a highly similar fold with an C_α-RMSD of 1.35 and 2.15 Å, respectively, known from crystal structures available in the PDB[35] (entries, rhodesain: 2p7u,[11] CatL: 2xu1,[36] and CatB: 3ai8).[37] For residues forming the binding site (defined as all amino acids within 6 Å of reference ligand **K11777**) identity/similarity even increase to 59.1%/70.2% for CatL and 40.4%/49.1% for CatB. Nevertheless, slight structural differences of residues forming the S1 S3 sites can be observed, explaining the selectivity profile of the compounds under investigation. Additionally, CatB, divergent from CatL and rhodesain, contains a so-called occluding loop (residues 104 124), which is crucial for this enzyme's exopeptidase activity.[38] This loop structure closes upon the S′ sites. Neither phenyl- nor benzylfluorovinylsulfone nor fluorovinylsulfonate moieties of the compounds within this study reach far enough toward this sites to form interactions, but in contrast may even cause clashes with the residues of CatB (Figure 10A). Further focusing on the S1 site reveals one residue of the CatB occluding loop, which provides

https://doi.org/10.1021/acs.jmedchem.1c01002
J. Med. Chem. 2021, 64, 12322 12358

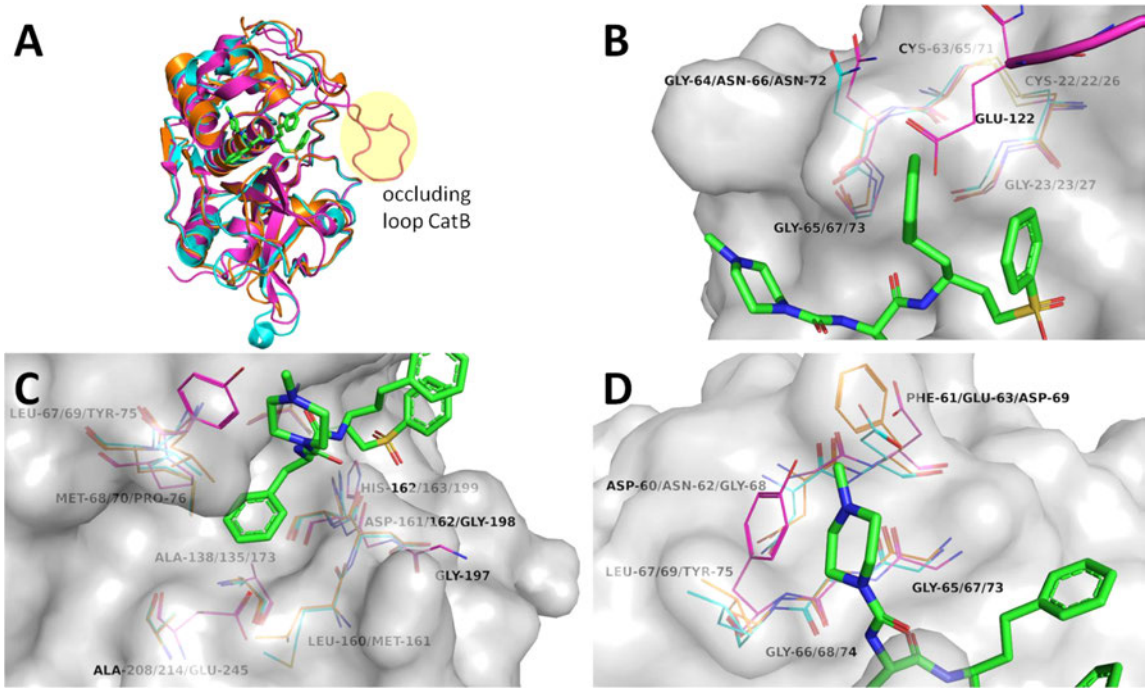

Figure 10. Structure comparison of rhodesain (orange carbon atoms, pdb entry 2p7u), CatL (cyan carbon atoms, pdb entry 2xu1), and CatB (magenta carbon atoms, pdb entry 3ai8) with inhibitor **K11777** shown with green carbon atoms. Residue enumeration is rhodesain/CatL/CatB. For (B D), the rhodesain surface is shown in gray for orientation. (A) Whole protease structures depicted as cartoons with the CatB occluding loop highlighted. (B) Close view of S1 site residues. CatB-unique occluding loop shown in the upper right with Glu122 as a selectivity determining feature over CatB. (C) Close view of S2 site residues. (D) Close view of S3 site residues reveals acidic Glu63 and Asp69 in cathepsins to form ionic interactions with the basic center of compound **K11777**, which is absent in compounds with more favorable selectivity profiles.

an explanation for selectivity (Figure 10B). Glu122 reaches toward the S1 pocket, not only making this site more polar, but also narrower, clashing with the homophenylalanine moiety of the inhibitors and thereby causing selectivity over CatB. Within the S2 pocket, the largest differences were found for CatB as well (Figure 10C). CatB Gly197 shows a different orientation than the corresponding residues Leu160 in rhodesain and Met161 in CatL. Additionally, Ala208/214 (enumeration is rhodesain/CatL) is exchanged to Glu246, Met69/70 to Pro76, and Leu67/69 to Tyr75. These differences all together result in a more open and polar pocket within CatB, which leads to a higher affinity for rhodesain and CatL for inhibitors carrying (3- or 4-methyl)-phenylalanine moieties. Additionally, the selectivity for rhodesain over CatL introduced by the 4-methyl substitution (compounds **2d**, **3d**, and **4d**) is likely to be caused by non-polar interactions with Leu160 being more favorable compared to the CatL Met161, which is slightly more distant and potentially impaired in its flexibility upon binding. The most significant improvement in selectivity was the displacement of *N*-methyl piperazine by 4-pyridine or less pronounced by DHDB (compounds **2d**, **2e**, **3d**, **3e**, **4d**, and **4e**). Within the S3 site, acidic amino acids Glu63 and Asp69 are found in CatL and CatB, respectively, while in rhodesain Phe61 sits at the corresponding position (Figure 1D). By the removal of the positively charged *N*-methyl piperazine, the loss of potential ionic interactions only with the off-target cathepsins is, therefore, likely to improve the selectivity profile of these compounds. Additionally, the Tyr75 residue in CatB compared to Leu in rhodesain and CatL results in a smaller S3 pocket and an enhanced selectivity over CatB, too.

In contrast to all other compounds in this study, the geometry of the double bond of compound (**Z**)-**2a** has a (*Z*)-configuration. Because (*Z*)-isomers are obtained as side products from HWE olefination, it was obvious to explore the influence of the geometry of the double bond on inhibitory potency. Compared to the (*E*)-isomer **2a** (K_i^* = 15 nM), compound (**Z**)-**2a** (K_i = 525 nM) shows markedly reduced potency and forms no high-affinity complex, indicating that the (*Z*)-configuration of the double bond is not favorable.

Compounds with a modified P1 residue (**4j** **4l**) showed reduced potency for rhodesain compared to the counterparts with homophenylalanine, which was already anticipated from non-covalent docking scores. Nevertheless, compound **4k**, with methionine at P1 and the 4-pyridyl moiety at P3, is still a potent inhibitor of rhodesain (K_i = 56 nM).

MS Analysis. Covalent protein ligand interactions were verified by ESI MS for compounds **2a**, (**Z**)-**2a**, and **2j** and MALDI-TOF MS for **K11777**, **1**, **2a**, **2j**, and **2k**.

In all three cases (**2a**, (**Z**)-**2a**, and **2j**), the protein ligand adduct resulting from Michael addition was detected in the ESI mass spectra. The observed mass shift corresponds to the mass of the inhibitor [exemplified for compound **2a** in Figure 11; for compounds (**Z**)-**2a** and **2j**, see Figure S2], which shows covalent bond formation.

To further elucidate possible differences in binding mode related to compound variability, especially to confirm the

https://doi.org/10.1021/acs.jmedchem.1c01002
J. Med. Chem. 2021, 64, 12322 12358

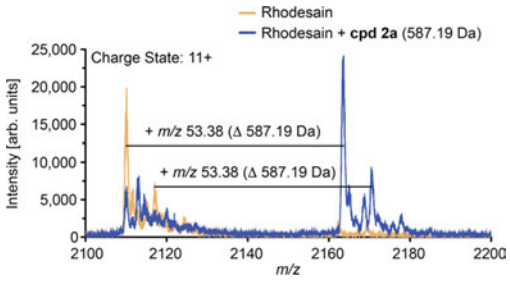

Figure 11. Intact protein ligand adducts obtained by mass spectrometry for compound **2a**. The observed shift corresponds to the mass of the inhibitor considering the charge state of the protein ($m/z = 11^+$).

covalent inhibition, a representative subset of compounds covering the majority of synthesized modifications was selected and analyzed by MALDI-TOF MS. The aim here was to analyze whether these modifications impede covalent bond formation between the catalytic thiolate and the vinyl moiety. ESI MS is a softer method in terms of transition to the gas phase, where non-covalent adducts can be found as well as covalent adducts. Depending on the matrix, MALDI-TOF MS can discriminate between covalent and non-covalent binding: the formation of non-covalent adducts can be suppressed by using an acidic matrix, which was attributed to the disruption of salt bridges and the subsequent destabilization of the non-covalent protein ligand complex.[39−41] Therefore, MALDI-TOF MS was applied to further investigate the binding mode.[40,42,43]

In terms of warhead modification, vinyl sulfone **K11777**, α-fluorovinylsulfone **1**, and α-fluorovinylsulfonates **2a**, **2j**, and **2k** were evaluated. Furthermore, the selected subset differed in their substituents in the P3 position, namely isonicotinyl amide (**2a**), benzylcarbamate (**2j**), and 4-methylpiperazine-1-carboxamide (**K11777**, **1**, and **2k**), while sharing the preceding PhehPhe motif in P2 and P1, respectively. **K11777** was used as a known, structurally equivalent control compound for its analogous, though covalent irreversible binding mode. A non-covalent inhibitor of rhodesain (**42**) carrying a fluorodinitrobenzene moiety as an aromatic electrophile was chosen as a control substance for its different inhibition mode (Figure 12) compared to the vinylsulfones. The compound forms a tight π-complex with the catalytic thiolate, the adduct mass of which was detectable in ESI MS experiments with rhodesain.[44]

For all evaluated α-fluorovinyl analogues (**1**, **2a**, **2j**, and **2k**), covalent adducts with rhodesain were observed by MALDI-TOF MS. The resulting spectra consisted of a broad peak corresponding to the protein (ca. 23.3 kDa),[45−47] and a second peak corresponding to the covalent protein inhibitor adduct (ca. 23.8 kDa) that shows a mass shift corresponding to the mass of the respective compound (Figure 12). The observed multiplicity of the peaks was attributed to additions of matrix molecules [m(sinapinic acid) = 224 Da] to rhodesain, as similar phenomena are described in the literature.[47] The four fluorovinyl derivatives (**1**, **2a**, **2j**, and **2k**) behaved like the irreversible control substance **K11777**, while the non-covalent inhibitor (**42**) did not show any detectable adduct signals under the evaluated conditions. Apart from that, an adduct of **42** was found with ESI MS as published previously.[39,40,44] The identical behavior of **K11777** and the α-fluorovinylsulfones/-sulfonates in the MALDI-TOF MS experiments could be observed using two different matrices, sinapinic acid and a mixture of α-cyano-4-hydroxycinnamic acid and 2,5-dihydroxybenzoic acid,[43] respectively, the latter data are shown in the Figure S1. These findings, combined with the results from ESI MS and the dialysis

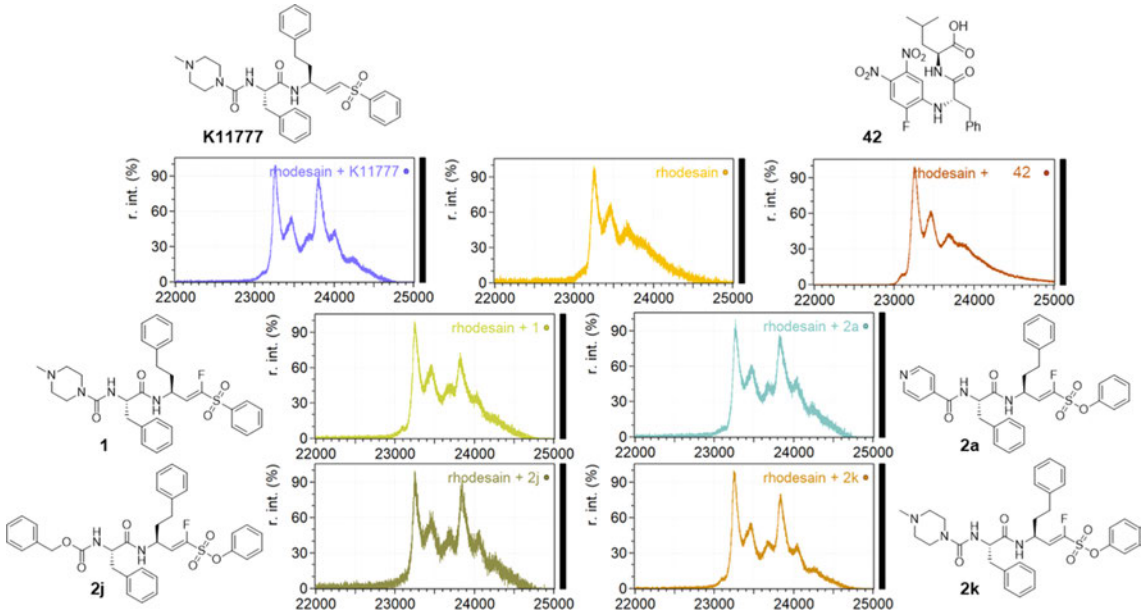

Figure 12. MALDI-TOF mass spectra of rhodesain (ca. 23 kDa) in the presence of different inhibitors (10-fold molar excess of inhibitor to protein). Sinapinic acid was used as the matrix substance. The figures show the relevant range of the spectrum to display $[M + H]^+$, which were baseline corrected.

https://doi.org/10.1021/acs.jmedchem.1c01002
J. Med. Chem. 2021, 64, 12322 12358

and dilution assays, clearly show that the α-fluorovinylsulfones and -sulfonates are indeed covalent reversible inhibitors of rhodesain.

Comparison of the Inhibition Mechanisms of K11777 and 1 by QM/MM Modeling. In our previous study,[12] the computed reaction energies of **K11777** and **1** differed only marginally so that the computational results could hardly explain the transition from irreversible to reversible inhibition. In that study, both reaction pathways had been calculated starting from the X-ray structure of the covalent enzyme inhibitor complex of K1177 with rhodesain (PDB: 2p7u) going backwards from the covalent toward the non-covalent complex. To generate the reaction path for **1**, the hydrogen atom had been substituted for fluorine in the X-ray structure. It had been necessary to start the computations from the X-ray structure of the covalent complex because no experimental information on the non-covalent complex was available. Moreover, such procedures had been very successful to explain the stereo- and regioselectivity of various epoxide- and aziridine-based inhibitors and to predict improved inhibitors.[48−50] However, such approaches can be error-prone in cases when the geometries of the covalent and non-covalent enzyme inhibitor complexes differ largely, especially when substitution leads to large differences in the non-covalent complex.

To obtain more reliable insights into possible differences between the non-covalent enzyme-inhibitor complexes of **K11777** and **1**, at first, non-covalent structures starting from the X-ray structure of **K11777** with rhodesain (PDB: 2p7u) were calculated. For **1**, the hydrogen atom in the α-position was substituted by fluorine. These structures then were used as starting points for MD simulations (10 times 10 ns sequences for each compound). Exemplarily, Figure 13 presents the

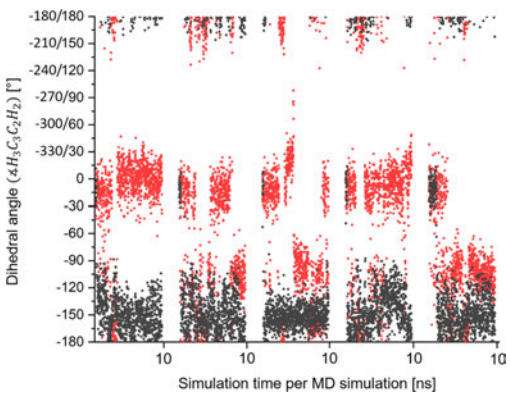

Figure 13. Variation of the dihedral angle $\angle H^3C^3C^2H^2$ along the MD simulations (sequences of 10.0 ns, respectively) for **K11777** with X = H (in red) and the fluorinated vinylsulfone with X = F (in black). Figure 13 defines the dihedral angle and gives the corresponding orientation of the warhead in the active site. Please note that $\angle H^3C^3C^2H^2 = 150°$ is equal to $\angle H^3C^3C^2H^2 = -210°$.

fluctuations in the dihedral angle $\angle H^3C^3C^2H^2$ (see Figure 14 for definition) for five different MD samplings. A variation of $\angle H^3C^3C^2H^2$ from 0 to ±180° describes the rotation of the inhibitor around the C^3C^2 single bond, adjacent to the double bond. Due to this rotation, the C^1X bond (X = H1, F) moves from the Gly23-oriented side to the opposite side (Figure 14). For **K11777**, mainly values between −40 and 40° (−320°) were found for the $\angle H^3C^3C^2H^2$ angle. In the following, we denominate alignments with $-40° < \angle H^3C^3C^2H^2 < 40°$ (Figure 14) as "H-orientation". For **1**, $\angle H^3C^3C^2H^2$ adopted values between −120 and −190° (170°), that is, the warhead of the compound oscillates around a position, where the F-atom is oriented toward the backbone NH groups of Cys25, Ser24, and the side-chain NH_2 group of Gln19 (Figure 14b), but mainly adopts positions with $\angle H^3C^3C^2H^2 > -180°$. In the following, geometries with $-190° < \angle H^3C^3C^2H^2 < -120°$ are denominated "F-orientation".

During the MD simulation, **K11777** populated both H- (≈80%) and F-orientation (≈20%) indicating that both alignments are energetically quite similar. In contrast, **1** predominantly adopted the F-orientation due to attractive interactions with the NH backbone group of Cys25, the side chain NH_2 group of Gln19 (known as the oxyanion hole of rhodesain), and the NH backbone group of Ser24. Similar variations in the structures upon fluorination were reported in the literature).[51,52]

While the orientation of the recognition unit (in Figure 14 given in purple) remained fixed in the torsional motion around $\angle H^3C^3C^2H^2$, the relative positions between the attacked double bond of the inhibitor and the involved side chains of Cys25 and His162 changed drastically as shown in Figure 15. In both cases, a syn-addition takes place because the thiolate group of Cys25 and the protonated imidazole ring of His162 are found to be on the same side of the double bond (Figure 15), but for the H-orientation, the CS bond of the Cys25 side chain is orthogonally oriented with respect to the C^1C^2 double bond while it is oriented in parallel for the F-orientation. The position of the protonated imidazole ring of His162 also changed accordingly.

To calculate the influence of the different orientation of the warhead of **K11777** and **1** on the inhibition mechanism (Figure 1), the corresponding reaction paths were computed. However, due to the large number of local minima for the non-covalent complex (the reactant) and the covalent complex (the product) in combination with the roughness of the underlying potential energy surface (PES), the appropriate picture of the inhibition reaction is not that of a single reaction path with one starting point, one transition state, and one product, but that of a very rough PES with various energetically similar pathways starting from and ending at slightly different reactants and products. To achieve representative pathways, we performed geometry optimizations starting from two selected snapshots of the MD simulation for each inhibitor and computed the reaction paths starting from the obtained minima. The geometrical parameters of the respective minima are given in Table S2.

To characterize the reaction mechanism, we first computed two-dimensional scans using the distances $R(S_{cys}\ C_2)$ and $R(H_{His}\ C_1)$ as main reaction parameters (Figure 14). The resulting transition states served as starting points for subsequent IRC (intrinsic reaction paths) simulations,[53] the course of which generally gives good insights into the reaction mechanism (reaction barrier, reaction energy, and structural changes in the course of the reaction). More details are given in the Experimental Section. In Figure 15, representative IRCs for **K11777** starting from the H-orientation and **1** starting from the F-orientation are compared. Figure 16 also sketches the geometry variations along the IRCs. Further information on the geometries is given in Table S3. Additional paths starting from other reactant minima showing similar shapes can also be found in the Supporting Information (Figures S4 and S7).

https://doi.org/10.1021/acs.jmedchem.1c01002
J. Med. Chem. 2021, 64, 12322 12358

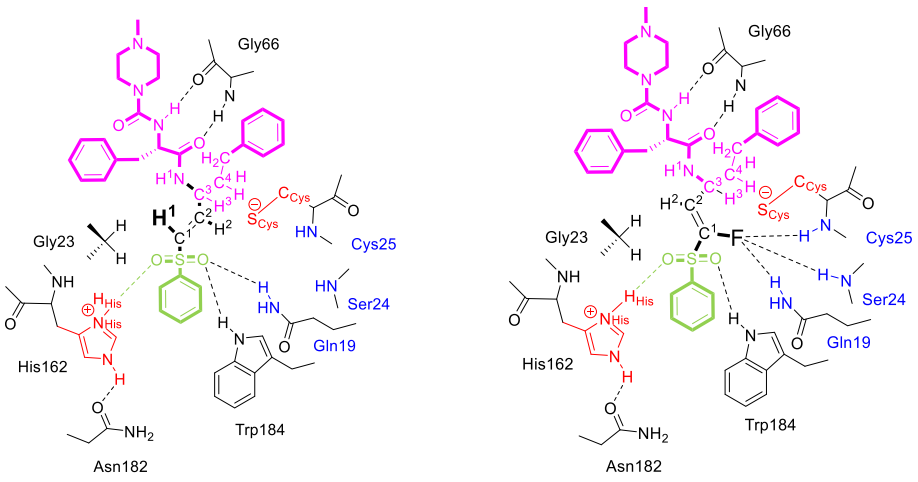

Figure 14. Sketch of the predominant orientation of the warheads (bold) in the active site during the MD simulations given in Figure 13. (a) H-orientation: predominant conformations of **K11777** (X = H) with $40° \leq \angle H^3C^3C^2H^2 \leq 40°$ (b) F-orientation: predominant conformations for the fluorinated vinylsulfone **1**, with $190° \leq \angle H^3C^3C^2H^2 \leq 120°$. For more information, see the text.

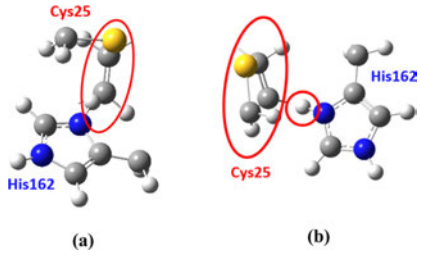

Figure 15. Relative orientation of Cys25 and His162 moieties with respect to the double bond of the vinylsulfone group attacked by Cys25, (a) for **K11777** (X = H) in the H-orientation, and (b) for the fluorinated vinylsulfone (X = F) in the F-orientation.

Figure 16 shows considerable differences in the IRCs of both compounds. While the reaction pathway for the inhibition of rhodesain by **K11777** passes over a barrier of about 12 kcal mol^{-1} and has an exothermic reaction energy of about 20 kcal mol^{-1}, we predict a thermoneutral reaction for the inhibition reaction of **1** with a very high barrier of 25 kcal mol^{-1}. The small reaction barrier and the strong exothermicity nicely explain why **K11777** is an efficient irreversible inhibitor.

The different shapes of the reaction pathways presented in Figure 16 may result from the different orientation of the olefin in the active site or from changes in the electronic structure due to the fluorine substitution in **1**. To obtain more insights, the reaction of **K11777** from the F-orientation was computed. For this purpose, we first computed the energy profile of the torsional motion of the C^1C^2 double bond around the dihedral angle $\angle H^3C^3C^2H^2$ (Figure S3). As expected from the MD simulations, for **K11777**, the energy difference between the H- and the F-orientation was found to be small (1 2 kcal mol^{-1}) so that the reaction could take place from both orientations. However, the two-dimensional scan starting from the F-orientation predicted barriers of about 33 kcal mol^{-1} and nearly isothermal reactions (ΔE_{reac} = 3 kcal mol^{-1}). This indicates that the different starting orientations are leading forces for the observed differences. Attempts to generate IRCs failed, possibly because the paths energetically lie above the path given in Figure 15a.

This finding could also indicate that a reaction of **1** starting from the H-orientation is more favorable. To answer this question, we calculated a two-step mechanism for inhibitor **1**. In the first step, **1** was found to twist from the F- into the H-orientation (variation of $\angle H^3C^3C^2H^2$). Starting from the obtained local minimum, we then calculated the course of inhibition by compound **1** starting from the H-orientation as the second step of the overall inhibition reaction. The result of this two-step inhibition reaction is shown in Figure 17.

Figure 17 indicates that the shape of the reaction path of **1**, if it starts from the H-orientation, resembles the path found for **K11777** (Figure 16). Starting from the H-orientation (Figure 17, structure 3), the reaction proceeds over a barrier of about 18 kcal mol^{-1} and has a reaction energy of about 12 kcal mol^{-1}. However, the exothermicity of the whole reaction drops to only 4 kcal mol^{-1}, due to the previously necessary transition from the F- to the H-orientation. Other reaction courses given in the Supporting Information provide a similar picture (Figures S8 S10).

Our investigation revealed that the differences between **K11777** and **1** are mainly due to the interaction between the fluorine atom and the oxyanion hole of rhodesain, which induces a flip of the olefin group of the warhead within the active site. This change in the orientation significantly complicates the further course of the inhibition reaction. As a result, for inhibitor **1**, a two-step mechanism becomes more favorable, which contains a torsional movement from the F- to the H-orientation before the actual covalent Michael-type reaction can take place leading to a considerably reduced exothermicity. These differences nicely explain the switch from the irreversible (**K11777**) to the reversible (**1**) inhibition mode and are in line with all experimental data, which indicate a covalent, but reversible bond formation for various fluorinated inhibitors.

https://doi.org/10.1021/acs.jmedchem.1c01002
J. Med. Chem. 2021, 64, 12322 12358

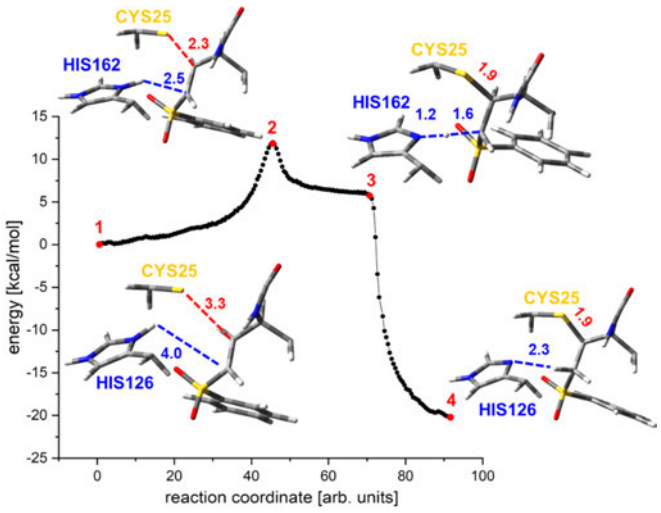

Figure 16. Representative intrinsic reaction coordinate (IRC) simulation of the inhibition reaction of **K11777** (a) and **1** (b). Selected geometrical parameters of the indicated structures are summarized in Table S3.

Antitrypanosomal Activity and Toxicity. Selected compounds were tested for antitrypanosomal activity and cytotoxicity (Table 5). Trypanocidal activity was measured against *T. brucei brucei* TC211[54,55] or *T. brucei brucei* BS449, as described previously.[56,57] Cytotoxicity was measured for selected compounds in the macrophage cell line J774.1 and in HeLa cells as described before.[12,55] Most inhibitors tested showed significantly improved antitrypanosomal activity compared to starting compound **1**. This correlates very well with the higher inhibitory potency of the compounds for rhodesain. The compounds also displayed an improved safety profile by showing no relevant cytotoxicity in HeLa cells or in the J774.1 macrophage cell line. Most interestingly, from the hPhe series, the compounds with N-terminal DHBD group and 4-Me-Phe residue at the P2 position (**2e**, **4e**) exhibited highest antitrypanosomal potency with the sulfonate **2e** being the most potent compound (EC_{50} = 0.14 μM), similarly active to the irreversible **K11777**. Also, within the 4-Pyr series, the compounds with 4-Me-Phe residue (**2d**, **3d**, and **4d**) are more potent than those with Phe at P2 position (**2a**, **4a**). Probably, the higher lipophilicity and thus better membrane permeability of these compounds contribute to their better antitrypanosomal activity. No differences are observed between the various warheads (phenyl vinylsulfonate **2d**, benzyl vinylsulfone **3d**, and phenyl vinylsulfone **4d**). Within the *N* Me-Pip series (**1**, **4j**, and **4l**), the compound with Cys(Bn) in the P1 position (**4l**) is most active (3.0 μM) despite being a much less-potent inhibitor of rhodesain. This observation may be explained with the relatively high toxicity of the compound, which seems to be also

https://doi.org/10.1021/acs.jmedchem.1c01002
J. Med. Chem. 2021, 64, 12322 12358

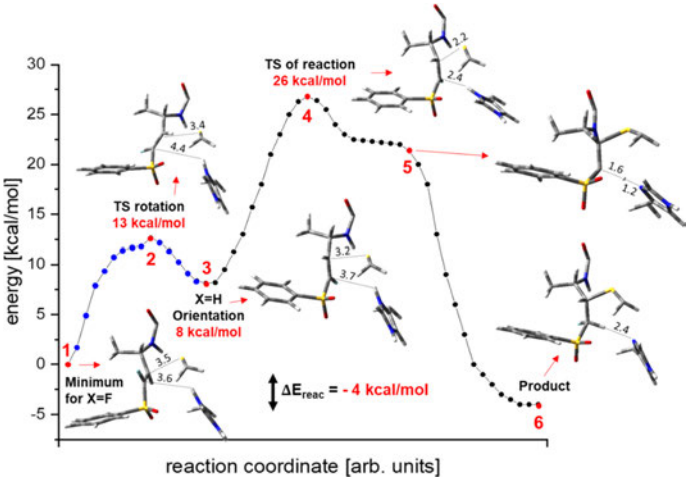

Figure 17. Reaction profile of the two-step inhibition reaction of **1**. The rotation about $\angle H^3C^3C^2H^2$ is given in blue. Please note that the reaction path is put together from several IRCs. Selected geometrical parameters of the indicated structures are summarized in Table S3. See also Figure S6.

Table 5. Antitrypanosomal Activity and Cytotoxicity of Selected Compounds[a]

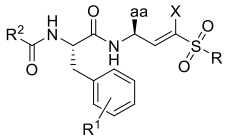

	substitution					*T. b. b.* $EC_{50}/\mu M$	cytotoxicity $CC_{50}/\mu M$	
cpd	R	R^1	R^2	aa	X	48 h	J774.1	HeLa
K11777	Ph	H	*N*-MePip	hPhe	H	0.18 ± 0.03[b,c]	41[b]	>10[d]
1	Ph	H	*N*-MePip	hPhe	F	12.5 ± 0.4[c]	38	10 ± 2
2a	OPh	H	4-Pyr	hPhe	F	4.8 ± 0.9[c]	n.d.	>100
2d	OPh	4-Me	4-Pyr	hPhe	F	1.9 ± 1.8[e]	n.d.	>100
2e	OPh	4-Me	DHBD	hPhe	F	0.14 ± 0.05[e]	n.d.	>100
3d	Bn	4-Me	4-Pyr	hPhe	F	1.4 ± 0.9[e]	n.d.	>100
4a	Ph	H	4-Pyr	hPhe	F	3.0 ± 0.4[c]	>100	>100
4d	Ph	4-Me	4-Pyr	hPhe	F	1.9 ± 1.2[e]	n.d.	>100
4e	Ph	4-Me	DHBD	hPhe	F	0.80 ± 0.5[e]	n.d.	>100
4j	Ph	H	*N*-MePip	Met	F	14.1 ± 0.6[c]	43	77 ± 8
4l	Ph	H	*N*-MePip	Cys(Bn)	F	3.0 ± 0.1[c]	8.7	8 ± 0.4

[a]n.d. not determined. [b]See ref 12. [c]*T. brucei brucei* TC211. [d]See ref 58. [e]*T. brucei brucei* BS449.

connected to the *N*-Me-Pip moiety (compounds **K11777**, **1**, **4j**, and **4l**).

Selectivity over Serine and Threonine Proteases. For selected compounds, inhibitory potency against other proteases (the threonine protease 20S proteasome and the serine protease NS2B/NS3 of the Dengue virus) was tested (Table 6). The activity of the compounds against the different catalytically active subunits of the proteasome (trypsin-like, caspase-like, and α-chymotrypsin-like) was tested separately by the use of specific fluorogenic substrates (see Experimental Section). Most compounds showed no relevant inhibition (less than 50%) at concentrations of 11 μM. Highest percentage inhibition was observed in the case of the caspase-like activity for compounds **2d** (44%) and **4a** (41%). Inhibitor **4l** was the only compound that showed relevant inhibition of the α-chymotrypsin-like activity of the proteasome (71% at 11 μM).

In Vitro Metabolism. The metabolism of compounds **1** and **2d-(H)** was investigated using rat liver microsomes and an NADPH-generating system. The covalent cysteine protease inhibitor **K11777** was used as a control. Previous in vitro metabolism studies by Jacobsen and co-workers revealed three metabolites of **K11777** depicted in Figure 18.[59]

Compound **1** (fluorinated **K11777**) also showed N-demethylation (**1a**) and N-oxidation (**1b**) as shown in Figure S13. The metabolites were analyzed via LC MS fragmentation. Additionally, the potential metabolites were synthesized as described in the Chemistry section, and their fragments and retention times were compared to those found in the metabolism studies to ensure the identity of the metabolites. In contrast to the reported metabolism of **K11777**, the β-hydroxy homophenylalanine derivative[32] did not occur, neither in the experiments with compound **1** nor in those with **K11777**.

https://doi.org/10.1021/acs.jmedchem.1c01002
J. Med. Chem. 2021, 64, 12322 12358

Table 6. Inhibition Data for 20S Proteasome and Dengue NS2B/NS3 Protease for Selected Compounds

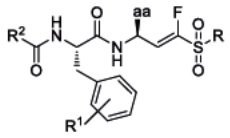

	substitution				human 20S proteasome/%[a]			dengue
cpd	R	R^1	R^2	aa	trypsin	caspase	α-chymotrps.	NS2B/NS3%[a]
1	Ph	H	*N*-MePip	hPhe	n.i.	16	13	n.i.
2a	OPh	H	4-Pyr	hPhe	n.i.	22	11	n.i.
2d	OPh	4-Me	4-Pyr	hPhe	10	44	20	n.i.
2e	OPh	4-Me	DHBD	hPhe	n.i.	31	22	11
3d	Bn	4-Me	4-Pyr	hPhe	n.i.	n.i.	n.i.	n.i.
4a	Ph	H	4-Pyr	hPhe	n.i.	41	10	n.i.
4b	Ph	H	DHBD	hPhe	n.i.	26	n.i.	n.d.
4d	Ph	4-Me	4-Pyr	hPhe	12	28	13	n.d.
4j	Ph	H	*N*-MePip	Met	n.i.	18	n.i.	n.d.
4l	Ph	H	*N*-MePip	Cys(Bn)	14	n.i.	71	13

[a]% inhibition at inhibitor concentrations of 11 μM; n.i. = <10% inhibition at 11 μM; and n.d. = not determined.

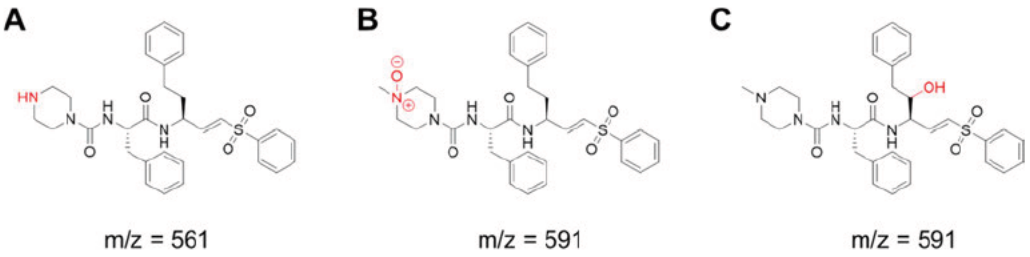

Figure 18. Metabolites of K11777 as published by Jacobsen and co-workers.[59] N-Demethylation at the *N*-methyl piperazine moiety (A) and N-oxidation (B) are the major metabolic reactions. Additionally, a β-hydroxy homophenylalanine metabolite was found (C).

Table 7. Assay Results of the Metabolites

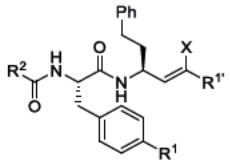

	substitution				rhodesain		
cpd	R^1	R^2	$R^{1'}$	X	K_i/nm	k_i/s^{-1}	$k_{2nd}/M^{-1} s^{-1}$
1	H	*N*-MePip	SO_2Ph	F	190[a,b]	n.a.	n.a.
1a	H	Pip	SO_2Ph	F	192 ± 40[b]	n.a.	n.a.
2d-(H)	Me	4-Pyr	SO_3Ph	H	0.45 ± 0.06	0.020	46×10^6
2l	Me	4-Pyr-*N*-oxide	SO_3Ph	H	1.50 ± 0.46	0.018	12×10^6

[a]See ref 12. [b]K_i calculated from the Cheng Prusoff equation;[32] n.a. not applicable.

The metabolism studies of **2d-(H)** only resulted in a single metabolite, the N-oxidized derivative **2l** as shown in Figure S14. In order to verify the structure, the metabolite was synthesized as described in the Chemistry section and retention times and fragments were compared as described above.

The synthesized metabolites were also tested in the fluorometric enzyme assay in order to determine their K_i values. The assays were performed as described in the Enzyme assays section and the results are shown in Table 7.

The demethylation of compound **1** to its metabolite **1a** does not decrease its inhibitory activity significantly. Both, compound **2d-(H)** and its metabolite **2l**, show a good inhibition of rhodesain in the low nanomolar range. Therefore, it can be concluded that the metabolites retain most of the inhibitory potency of the parent drug.

In Vivo Distribution. Compound **1** as an example for a covalent reversible and compound **2d-(H)** as an example for a covalent irreversible inhibitor were tested for their biodistribution in vivo in wild type CD1 mice. Their biodistribution after oral (p.o.) or intraperitoneal (i.p.) application was investigated by LC MS analysis of plasma samples and brain tissues to determine the ability of the compounds to cross the blood

https://doi.org/10.1021/acs.jmedchem.1c01002
J. Med. Chem. 2021, 64, 12322 12358

brain barrier. The compounds were chosen for the in vivo assays based on their differences in the mode of inhibition (covalent reversible vs irreversible) and based on their physicochemical properties (Table 8), which are similar for compound **2d-(H)** and its fluorinated counterpart **2d**.

Table 8. Comparison of 1, 2d, and 2d-(H) in Terms of Physicochemical Properties and the Mechanism of Inhibition

cpd	inhibition mode	SlogP (calc.)[a]	TPSA [Å^2] (calc.)[a]
1	covalent reversible	3.96	98.82
2d	covalent reversible	5.07	114.46
2d-(H)	covalent irreversible	4.77	114.46

[a]Calculated using MOE.[60]

Compound **1** was found in plasma samples but not in the brain homogenate, whereas compound **2d-(H)** could be found in both, plasma and brain tissue after i.p. and p.o. administration, respectively (Figures 19, S15, and S16). Therefore, it can be concluded that **2d-(H)** is able to cross the blood brain barrier due to its higher lipophilicity. An accumulation of this compound was also suggested because of a higher AUC after multiple oral administration compared to a single dose i.p. administration, thus making it a possible candidate for the treatment of stage-2 HAT.

Furthermore, the distribution of the compounds in the brain extracellular space was also investigated via microdialysis. Only compound **2d-(H)** could be found in the dialysate with recovery rates from the plasma concentration between 0.8 and 6% of plasma values after i.p. injection. This indicates that the lipophilic compound **2d-(H)** reaches higher concentrations intracellularly than in the extracellular fluid.

Notably, the mice treated with the compounds did not show any signs of toxification.

It can be concluded that the optimization of compound **1** through SAR studies not only enhanced the inhibitory potency against rhodesain and the selectivity over CatB and CatL but also resulted in a potential drug candidate for stage-2 HAT with a higher lipophilicity (calc. *S* log *P* = 4.77 compared to 3.96 for **1**) that is able to cross the blood brain barrier and accumulate in brain tissue.

CONCLUSIONS

In this study, compound **1** (K_i = 190 nM, EC_{50} (*T. brucei*) = 12.5 μM), which was recently identified as a covalent reversible cysteine protease inhibitor by the application of a quantum-chemical-based design protocol,[12] was optimized in terms of inhibitory potency and selectivity for rhodesain. Based on the results obtained from molecular docking and MD simulations, a series of compounds with a modified recognition unit and an altered substitution pattern of the warhead were synthesized. Introduction of aromatic residues at P3 significantly enhanced the potency for rhodesain (**4b**: K_i = 12 nM) and increased the trypanocidal activity against *T. brucei* [**4a**: EC_{50} (*T. brucei*) = 3.0 μM]. Incorporation of a 4-methyl substituent at the phenylalanine aromatic ring additionally improved selectivity against human cathepsins (**4d**: K_i = 8 nM, 12-fold selectivity over CatL, more than 200-fold selectivity over CatB). By alteration of the substitution pattern of the warhead, two new classes of covalent reversible cysteine protease inhibitors with distinct properties were obtained. The compounds from the series of benzyl fluorovinylsulfones (cpds **3a** **3i**) showed a similar potency compared to the respective analogues with phenyl substituents (**4a** **4i**) but were significantly more rapidly reversible in dilution and dialysis assays. Several compounds in the series of fluorovinylsulfonates (**2a** **2i**) showed a biphasic inhibition mechanism, with the formation of a single digit nanomolar, high-affinity complex in the second step (**2d**: K_i^* = 3 nM). This complex was shown to dissociate markedly slower in dialysis experiments for compound **2d**. Therefore, compound **2d** represents a potent, tight binding, and slowly reversible inhibitor of rhodesain. Furthermore, compound **2d** shows selectivity over CatL (26-fold) and is only a weak inhibitor of CatB (38% at 11 μM). In addition, no relevant off-target activity against threonine and serine proteases was observed and the cytotoxicity profile improved considerably. Compounds with a DHBD moiety at the N-terminus and 4-Me-Phe in the P2 position (**2e**, **4e**) are not only nanomolar inhibitors of rhodesain, but are most promising with regard to their the antitrypanosomal activity and cytotoxicity profile, with EC_{50} values comparable to those of the irreversible inhibitor **K11777** (EC_{50} = 0.14 0.80 μM) and no cytotoxic effects against HeLa cells (EC_{50} > 100 μM).

Microsomal stability assays revealed N-oxidation of the 4-Pyr substituent in the P3 position of **2d-(H)**. However, this does not seem to reduce the inhibitory potency. Moreover, the

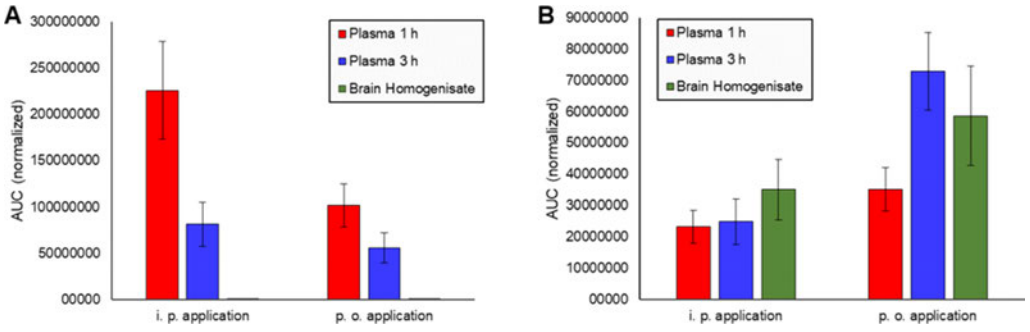

Figure 19. (A) Compound **1** was found in mouse plasma after 1 and 3 h, but not in the brain homogenate after i.p. and p.o. administration, respectively. (B) Compound **2d-(H)** showed plasma levels and distribution in brain tissue after both i.p. and p.o. administration. Both diagrams show the average AUC values of all tested mice (five for each compound and route of administration).

https://doi.org/10.1021/acs.jmedchem.1c01002
J. Med. Chem. 2021, 64, 12322 12358

accumulation of **2d-(H)** in mouse brain tissue, which did not occur with **1**, indicates a correlation of CNS permeation with the physicochemical properties of the tested inhibitors, such as SlogP values. These findings confirm that the optimized covalent reversible fluorovinylsulfonates should be further investigated as possible candidates for the treatment of both stage-1 and -2 HAT.

Based on these features, the high-affinity, lipophilic, and selective reversible α-fluorovinylsulfones and sulfonates as inhibitors of rhodesain may serve as a basis for the future development of effective and non-toxic drugs for the treatment of HAT.

In addition, we used mass spectrometry to demonstrate the formation of a covalent bond. Using QM/MM and MD computations, we could attribute the differences in inhibition mechanisms between **K11777** (irreversible) and **1** (reversible) to the interaction between the fluorine atom and the oxyanion hole of rhodesain. Due to this interaction, the olefin group of the warhead flips in the active site significantly complicating the further course of the inhibition reaction and leading to a considerably reduced exothermicity and thus a reversible inhibition.

EXPERIMENTAL SECTION

Syntheses. *General.* All reagents and solvents were of analytical grade quality and purchased from Sigma-Aldrich, Alfa Aesar, Acros, or TCI. Chemicals were used without further purification. Solvents were purified by distillation and desiccated by standard methods if necessary. ^{1}H and ^{13}C spectra were recorded on a Bruker Fourier 300 using DMSO-d_6, $CDCl_3$, or CD_2Cl_2 as a solvent. Chemical shifts δ are given in parts per million (ppm) using residual proton peaks of the solvent as the internal standard (^{1}H/^{13}C: DMSO: 2.50/39.52 ppm, $CHCl_3$: 7.26/77.16 ppm, CH_2Cl_2: 5.32/54.00 ppm). The purity of the compounds was determined via HPLC-MS (δ = 254 nm). All compounds are >95% pure according to HPLC analysis. High-resolution mass spectra were obtained on a Waters Q-TOF-Ultima 3-instrument. Alternatively, the mass spectra were obtained from an LC MS system consisting of a 1100 series HPLC system from Agilent with an Agilent Poroshell 120 EC-C_{18} 150 × 2.10 mm, 4 μm column. The mobile phase was 80% acetonitrile, 10% H_2O, and 10% of a 0.1% solution of formic acid in water. Detection wavelength was 254 nm. The molecular mass was detected using an Agilent 1100 series LC/MSD Trap with electron spray ionization (ESI) in positive mode. Purification with a preparative HPLC system was performed with a Varian PrepStar system (model 218) with an Agilent Zorbax XDB-C18 21.2 × 150 mm, 5 μm column. Column chromatography was performed with silica gel (0.06 0.02 mm or 0.040 0.063 mm) obtained from Carl Roth. All reactions were monitored by thin-layer chromatography using Macherey-Nagel ALUGRAM Xtra SIL G/UV254 silica gel 60 plates for detection at 254 nm. Melting points were determined in open capillaries using a Stuart SMP10-instrument. Optical rotation $[\alpha]_D^{22}$ was measured on an P3000 polarimeter from Krüss at 22 °C and is reported in cm^3 g ^{1} dm ^{1}.

Synthesis of Starting Materials. Phenyl Methanesulfonate[61] (I). Phenol (2.35 g, 1.0 equiv) was dissolved in EtOAc and cooled to 0 °C. TEA (6.93 mL, 2.0 equiv) and methanesulfonyl chloride (2.52 mL, 1.3 equiv) were added successively and the mixture was allowed to warm to rt. After stirring for 30 min, the solution was washed with water (3×) and brine (1×) and was dried with Na_2SO_4. Evaporation of the solvent yielded phenyl methanesulfonate (**I**) as a colorless powder (3.95 g, 92%). Spectral data matched those reported in the literature.[28]

Diethyl((benzylthio)methyl)phosphonate[28] (II). Benzyl mercaptan (0.84 mL, 1.0 equiv) was dissolved in THF and cooled to 0 °C. NaH (60% in mineral oil, 0.32 g, 1.0 equiv) was added in portions and the mixture was stirred for 15 min. Diethyl iodomethylphosphonate (1.24 mL, 1.0 equiv) was added dropwise and the mixture was stirred for 3.5 h at rt. THF was removed in vacuo and EtOAc was added. The organic phase was washed with water (2×) and brine (1×) and dried with Na_2SO_4. After evaporation of the solvent, the residue was purified by column chromatography (petroleum ether/EtOAc 1:1), yielding the title compound as a colorless liquid. Yield: 1.66 g (84%). ^{1}H NMR (300 MHz, $CDCl_3$): δ 7.43 7.21 (m, 5H), 4.25 4.08 (m, 4H), 3.90 (s, 2H), 2.54 (d, $J_{H\ P}$ = 12.9 Hz, 2H), 1.34 (t, J = 7.1 Hz, 6H). ^{13}C NMR (75 MHz, $CDCl_3$): δ 137.3, 129.4, 128.7, 127.4, 62.7 (d, $J_{C\ P}$ = 6.7 Hz), 37.0 ($J_{C\ P}$ = 2.9 Hz), 23.8 ($J_{C\ P}$ = 150 Hz), 16.6 ($J_{C\ P}$ = 6.0 Hz). ^{1}H NMR data are consistent with the literature.[12]

Diethyl((phenylsulfonyl)methyl)phosphonate[12] (III). To a solution of methyl phenyl sulfone (3.81 g, 24 mmol) in dry THF, *n*-BuLi (2.5 M in hexane, 21.5 mL, 60 mmol) was added at 0 °C with stirring. After 30 min, diethyl chlorophosphate was added dropwise and the reaction mixture was stirred at 0 °C for 1 h. 25 mL of a saturated solution of ammonium chloride was added and the volatiles were evaporated. The residue was extracted with DCM and the combined extracts were washed with brine, dried with sodium sulfate, concentrated under reduced pressure, and purified by column chromatography (light petroleum/EtOAc 1:5) to afford the title compound as a colorless oil, which solidified upon standing (4.11 g, 52%). NMR data were consistent with the literature.[28,62]

Phenyl(diethoxyphosphoryl)methanesulfonate (IV). Phenyl methanesulfonate (I, 2.5 g, 1.0 equiv) was dissolved in THF and cooled to 78 °C. KHMDS (1.0 M in THF, 15 mL. 1.1 equiv) was added dropwise and the mixture was stirred for an additional 15 min. Diethyl chlorophosphate (1.5 mL, 0.7 equiv) was added slowly and stirred for 1 h at 60 °C. The reaction was quenched by addition of glacial AcOH (1 mL) and then allowed to warm to rt. THF was removed in vacuo and EtOAc was added to the residue. The solution was washed with water (2×) and brine (1×) and then dried with Na_2SO_4. Evaporation of the solvent gave a crude product, which was purified by column chromatography (petroleum ether/EtOAc 1:1 to 1:3), yielding the title compound as a colorless liquid (3.3 g, 74%). ^{1}H NMR (300 MHz, $CDCl_3$): δ 7.52 7.29 (m, 5H), 4.36 4.20 (m, 4H), 3.81 (d, $J_{H\ P}$ = 17 Hz, 2H), 1.44 1.31 (m, 6H). ^{13}C NMR (75 MHz, $CDCl_3$): δ 149.4, 130.2, 127.8, 122.3, 64.2 (d, $J_{C\ P}$ = 6.5 Hz), 47.3 (d, $J_{C\ P}$ = 139 Hz), 16.4 (d, $J_{C\ P}$ = 6.3 Hz).

Diethyl((benzylsulfonyl)methyl)phosphonate[28] (V). Compound **II** (2.55 g, 1.0 equiv) was dissolved in DCM and cooled to 0 °C. Subsequently, *m*CPBA (77%, 5.8 g, 3.0 equiv) was added in portions and the mixture was stirred for 12 h at rt. Then, the solution was filtered and washed with 1 M NaOH (4×), water (1×), and brine (1×) and dried with Na_2SO_4. After evaporation of the solvent, the title compound was obtained as a colorless oil. Yield: 2.82 g (99%). ^{1}H NMR (300 MHz, $CDCl_3$): δ 7.57 7.47 (m, 2H), 7.44 7.34 (m, 3H), 4.60 (s, 2H), 4.24 (dq, J = 8.1, 7.1 Hz, 4H), 3.36 (d, J = 16 Hz, 2H), 1.37 (dt, J = 7.1, 0.4 Hz, 6H). ^{13}C NMR (75 MHz, $CDCl_3$): δ 131.2, 129.3, 129.2, 128.2, 63.9 (d, $J_{C\ P}$ = 6.5 Hz), 60.4, 48.0 (d, $J_{C\ P}$ = 140 Hz), 16.50 (d, $J_{C\ P}$ = 6.4 Hz). Spectral data are consistent with the literature.[12,63]

(S) tert Butyl(1 oxo 4 phenylbutan 2 yl)carbamate (VI). L-Homophenylalanine (5.0 g, 28 mmol) was dissolved in THF (15 mL) and a solution of Na_2CO_3 (3 g, 28 mmol) in 100 mL of water was added followed by di-*tert*-butyl dicarbonate (31 mmol) in 75 mL THF. The mixture was stirred overnight, diluted with water (100 mL), and extracted with CH_2Cl_2. The aqueous layer was acidified with $KHSO_4$ to pH 3 and extracted with CH_2Cl_2. The combined organic extracts were dried with sodium sulfate and concentrated under reduced pressure to give crude boc-L-homophenylalanine (7.0 g, 89%). This crude material (4.91 g, 18 mmol) was dissolved in DCM (100 mL) and cooled to 0 °C. EDC HCl (4.05 g, 21 mmol), HOBt (3.23 g, 21 mmol), and DIEA (13.5 mL, 78 mmol) were added and the mixture was stirred for 15 min before *N*,*O*-dimethylhydroxylamine hydrochloride (2.06 g, 21 mmol) was added. The mixture was allowed to warm to rt and was stirred for 18 h. DCM was removed under reduced pressure, water (60 mL) was added, and the suspension was extracted with EtOAc. The combined organic extracts were washed with saturated aq $NaHCO_3$ (5×) and brine, dried with sodium sulfate, and concentrated under reduced pressure to give *tert*-butyl (*S*)-(1-(methoxy(methyl)amino)-1-oxo-4-phenylbutan-2-yl)carbamate as a crude yellow oil (5.64 g, 99%), which was used in the next step without further purification. ^{1}H NMR (300 MHz, DMSO-d_6): δ 7.46 7.18 (m, 5H), 5.28 (d, J = 9.3 Hz, 1H), 4.73

https://doi.org/10.1021/acs.jmedchem.1c01002
J. Med. Chem. 2021, 64, 12322 12358

(s, 1H), 3.67 (s, 3H), 3.21 (s, 3H), 2.88 2.61 (m, 2H), 2.18 1.79 (m, 2H), 1.52 (s, 9H). The crude oil (4.05 g, 12.5 mmol) was dissolved in dry diethyl ether (130 mL) and cooled to 0 °C. $LiAlH_4$ (0.59 g, 15.7 mmol) was added portion wise. The mixture was stirred for 30 min and subsequently quenched by addition of aqueous $KHSO_4$ (0.33 M, 65 mL). The organic phase was separated, and the aqueous phase was extracted with diethyl ether. The combined organic extracts were washed with 3 M HCl, saturated aq $NaHCO_3$, and brine, dried with sodium sulfate, concentrated under reduced pressure, and purified by column chromatography (light petroleum/EtOAc 3:1), yielding the title compound as a colorless solid (2.44 g, 74%). ^{1}H NMR (300 MHz, $CDCl_3$): δ 9.55 (s, 1H), 7.40 7.13 (m, 5H), 5.08 (d, J = 4.1 Hz, 1H), 4.26 (q, J = 5.9 Hz, 1H), 2.87 2.63 (m, 2H), 2.35 2.06 (m, 1H), 2.02 1.77 (m, 2H), 1.47 (s, 9H). ^{13}C NMR (75 MHz, $CDCl_3$): δ 199.6, 155.6, 140.7, 128.8, 128.7, 126.5, 80.4, 59.7, 31.6, 31.2, 28.4. NMR data are consistent with the literature.[64]

(S) tert Butyl(4 (methylthio) 1 oxobutan 2 yl)carbamate ***(VII).*** Boc-L-Met-OH (2.43 g, 1.0 equiv) was dissolved in DCM and cooled to 0 °C. HOBt (1.49 g, 1.0 equiv) and DIEA (5.0 mL, 3.0 equiv) were added successively, and the mixture was stirred until all materials were solubilized. To this mixture, TBTU (3.12 g, 1.0 equiv) was added in one portion and then stirred for 15 min at 0 °C. *N*,*O*-Dimethylhydroxylamine hydrochloride (1.0 g, 1.1 equiv) was added in one portion and the mixture was stirred for 12 h at rt. DCM was removed in vacuo, and the residue was diluted with EtOAc. The organic layer was washed with water (5×), conc. $NaHCO_3$ (2×), and 1 M aq HCl (2×) and dried with Na_2SO_4. After evaporation of the solvent, the residue was purified by column chromatography (petroleum ether/EtOAc 2:1), yielding *tert*-butyl (*S*)-(1-methoxy(methyl)amino)-4-(methylthio)-1-oxobutan-2-yl)carbamate as a colorless oil (2.42 g, 85%). ^{1}H NMR (300 MHz, $CDCl_3$): δ 5.23 (d, J = 7.7 Hz, 1H), 4.78 (s, 1H), 3.77 (s, 3H), 3.20 (s, 3H), 2.68 2.42 (m, 2H), 2.08 (s, 3H), 2.05 1.92 (m, 1H), 1.89 1.71 (m, 1H), 1.42 (s, 9H). ^{13}C NMR (75 MHz, $CDCl_3$): δ 172.7, 155.7, 79.9, 61.8, 50.0, 32.6, 32.3, 30.3, 28.5, 15.6. This material (2.42 g, 1.0 equiv) was dissolved in THF and cooled to 0 °C. $LiAlH_4$ (0.41 g, 1.3 equiv) was added in portions and stirred for 30 min. The mixture was diluted with 50 mL diethyl ether and then 1 M $KHSO_4$ (50 mL) was added carefully. The layers were separated, and the aqueous phase was extracted twice with diethyl ether. The combined organic layers were washed with 1 M HCl (2×), saturated aq $NaHCO_3$, and brine, and then dried with Na_2SO_4. After evaporation of the solvent, the residue was purified by column chromatography (petroleum ether/EtOAc 2:1) to give the title compound as a colorless solid (1.49 g, 77%). ^{1}H NMR (300 MHz, $CDCl_3$): δ 9.63 (s, 1H), 5.21 (s, 1H), 4.39 4.11 (m, 1H), 2.56 (t, J = 7.2 Hz, 2H), 2.34 2.13 (m, 1H), 2.07 (s, 3H), 1.99 1.83 (m, 1H), 1.44 (s, 9H). ^{13}C NMR (75 MHz, $CDCl_3$): δ 199.2, 155.6, 80.4, 59.1, 29.9, 28.8, 28.4, 15.5. NMR data are consistent with the literature.[65]

(R) tert Butyl(1 (benzylthio) 3 oxopropan 2 yl)carbamate ***(VIII).*** L-Cysteine hydrochloride (5.20 g, 1.0 equiv) was dissolved in 60 mL 2 M NaOH and 150 mL EtOH. To the mixture, 5.64 g (3.92 mL, 1.0 equiv) benzyl bromide is added dropwise. After stirring for 1 h, the mixture is neutralized by addition of conc. HCl. The precipitate is collected by filtration and washed with water, diethyl ether, and ethanol. *S*-Benzyl L-cysteine is obtained as a colorless solid and directly used for the next step (6.4 g. 91%). ^{1}H NMR (300 MHz, D_2O): δ 7.50 7.24 (m, 5H), 4.17 (q, J = 6.5 Hz, 1H), 3.88 3.71 (s, 2H), 3.09 2.87 (m, 2H). ^{13}C NMR (75 MHz, D_2O): δ 171.7, 138.2, 129.3, 129.1, 127.8, 51.8, 35.5, 30.7. *S*-Benzyl L-cysteine (3.0 g, 1.0 equiv) was dissolved in THF (50 mL), and K_2CO_3 (2.94 g, 1.5 equiv) and water (50 mL) were added. Di-*tert*-butyl-dicarbonate (3.25 g, 1.05 equiv) dissolved in 50 mL THF was added dropwise and stirred for 12 h at rt. THF was removed in vacuo and the residue was extracted twice with DCM. The aqueous layer was acidified to pH 3 by addition of 1 M $KHSO_4$ and extracted with DCM (3×). The combined organic layers were washed with brine (2×), dried with Na_2SO_4, and evaporated under reduced pressure to give crude boc-*S*-benzyl L-cysteine as a colorless oil (3.05 g, 69%). ^{1}H NMR (300 MHz, DMSO-d_6): δ 7.38 7.03 (m, 5H), 4.14 4.02 (m, 1H), 3.71 (s, 2H), 2.67 (m, 2H), 1.35 (s, 9H). ^{13}C NMR (75 MHz, DMSO-d_6): δ 172.6, 155.4, 138.3, 128.9, 128.4, 126.9, 78.3, 53.2, 39.5, 35.2, 32.4, 28.2. This material (3.05 g, 1.0 equiv) was dissolved in DCM and cooled to 0 °C. HOBt (1.49 g, 1.0 equiv) and DIEA (5.0 mL, 3.0 equiv) were added successively, and the mixture was stirred until all materials were solubilized. To this mixture, TBTU (3.40 g, 1.0 equiv) was added in one portion and then stirred for 15 min at 0 °C. *N*,*O*-Dimethylhydroxylamine hydrochloride (1.0 g, 1.1 equiv) was added in one portion and the mixture was stirred for 12 h at rt. DCM was removed in vacuo, and the residue was diluted with EtOAc. The organic layer was washed with water (5×), conc. $NaHCO_3$ (2×), and 1 M aq HCl (2×) and dried with Na_2SO_4. After evaporation of the solvent, the residue was purified by column chromatography (petroleum ether/EtOAc 2:1), yielding (*R*)-*tert*-butyl (3-(benzylthio)-1-(methoxy-(methyl)amino)-1-oxopropan-2-yl)carbamate as a colorless oil (3.25 g, 95%). ^{1}H NMR (300 MHz, $CDCl_3$): δ 7.42 7.15 (m, 5H), 5.28 (d, J = 8.6 Hz, 1H), 4.84 4.59 (m, 1H), 3.67 (s, 3H), 3.21 (s, 3H), 2.83 2.54 (m, 2H), 2.15 1.77 (m, 2H), 1.50 (s, 9H). ^{13}C NMR (75 MHz, $CDCl_3$): δ 173.2, 155.7, 141.3, 128.7, 128.5, 126.1, 61.6, 50.2, 38.8, 34.7, 31.8, 28.5. The above compound (3.0 g, 1.0 equiv) was dissolved in diethyl ether and cooled to 0 °C. $LiAlH_4$ (0.42 g, 1.3 equiv) was added in portions and stirred for 30 min. The mixture was diluted with 50 mL diethyl ether and then 1 M $KHSO_4$ (50 mL) was added carefully. The layers were separated, and the aqueous phase was extracted twice with diethyl ether. The combined organic layers were washed with 1 M HCl (2×), saturated aq $NaHCO_3$, and brine, and then dried with Na_2SO_4. After evaporation of the solvent, the residue was purified by column chromatography (petroleum ether/EtOAc 2:1) to give the title compound as a colorless solid (1.70 g, 68%). ^{1}H NMR (300 MHz, $CDCl_3$): δ 9.46 (s, 2H), 7.32 7.21 (m, 13H), 5.29 (d, J = 21.5 Hz, 2H), 4.32 4.16 (m, 2H), 3.67 (s, 5H), 2.86 2.70 (m, 5H), 1.39 (s, 24H). ^{13}C NMR (75 MHz, $CDCl_3$): δ 198.8, 137.7, 129.1, 128.8, 127.3, 80.6, 77.2, 59.3, 37.1, 30.8, 28.4. NMR data are consistent with the literature.[12]

(S) 2 (4 Methylpiperazin 1 ium 1 carboxamido) 3 phenylpropanoate[72] ***(IX).*** L-Phenylalanine methyl ester hydrochloride (2.0 g, 1.0 equiv) was suspended in CH_2Cl_2 and 25 mL of a saturated aqueous solution of $NaHCO_3$ was added. At 0 °C, triphosgene (0.92 g, 0.3 equiv) was added and the mixture was allowed to stir for 30 min at this temperature. Subsequently, the organic phase was separated, and the aqueous phase was extracted with three portions of DCM. The combined organic extracts were washed with brine, dried with Na_2SO_4, and concentrated under reduced pressure. The residue was dissolved in THF and cooled to 0 °C. *N*-Methyl piperazine (0.93 g, 1.03 mL, 1.0 equiv) was added dropwise. After stirring for 1 h, THF was removed under reduced pressure and the residue was diluted with EtOAc. Aqueous work-up was performed with water (1×), saturated aq $NaHCO_3$ (1×), and brine (1×). The organic layer was dried with Na_2SO_4 and evaporated. The crude product was purified by column chromatography (CH_2Cl_2/MeOH 9:1), giving methyl (4-methylpiperazine-1-carbonyl)-L-phenylalaninate as a colorless oil. Yield: ^{1}H NMR (300 MHz, $CDCl_2$): δ 7.30 7.10 (m, 3H), 7.04 (d, J = 7.3 Hz, 2H), 4.77 (d, J = 7.3 Hz, 1H), 4.61 (m, 1H), 3.61 (s, 3H), 3.29 3.11 (m, 4H), 3.00 (m, 2H), 2.22 (t, J = 5.0 Hz, 4H), 2.16 (s, 3H). This material (3.0 g, 9.4 mmol) was dissolved in THF (20 mL) and LiOH (1.4 g, 33.4 mmol) in 10 mL water was added. The mixture was stirred for 18 h at rt and the volatiles were removed under reduced pressure. Water was added to the residue and the pH was adjusted to 2 with 1 M aq HCl. The title compound was crystallized at 4 °C along with some LiCl and collected by filtration. Recrystallization from methanol gave the pure compound as a colorless powder. ^{1}H NMR (300 MHz, DMSO-d_6): δ 7.33 7.05 (m, 5H), 6.68 (d, J = 7.9 Hz, 1H), 4.28 4.09 (m, 1H), 3.50 3.16 (m, 4H), 2.98 (m, 2H), 2.46 2.30 (m, 4H), 2.25 (s, 3H). ^{13}C NMR (75 MHz, DMSO-d_6): δ 174.6, 157.1, 139.0, 129.4, 128.0, 126.1, 56.0, 53.1, 44.8, 42.7, 39.5, 36.9.

Isonicotinoyl L phenylalanine[66] ***(X).*** To a solution of L-phenylalanine ethyl ester hydrochloride (2.50 g, 10.88 mmol) and TEA (4.5 mL, 32.65 mmol) in DCM, isonicotinoyl chloride hydrochloride (1.93 g, 10.88 mmol) was added in small portions. The mixture was stirred for 3 h, washed with a saturated solution of $NaHCO_3$, dried with Na_2SO_4, and concentrated under reduced pressure. Ethyl isonicotinoyl-L-phenylalaninate (2.84 g, yield 87%) was obtained as a yellowish oil,

https://doi.org/10.1021/acs.jmedchem.1c01002
J. Med. Chem. 2021, 64, 12322 12358

which crystallized upon standing and was used in the next step without further purification. ^{1}H NMR (300 MHz, DMSO-d_6): δ 9.18 (d, J = 7.7 Hz, 1H), 8.73 (d, J = 5.2 Hz, 2H), 7.69 (d, J = 5.2 Hz, 2H), 7.37 7.12 (m, 5H), 4.75 4.57 (m, 1H), 4.10 (q, J = 7.1 Hz, 2H), 3.05 3.21 (m, 2H), 1.14 (t, J = 7.1 Hz, 3H). ^{13}C NMR (75 MHz, DMSO-d_6): δ 171.3, 165.0, 150.3, 140.6, 137.4, 129.1, 128.3, 126.6, 121.3, 60.7, 54.4, 45.7, 39.5, 36.2, 14.0. The above compound (2.84 g, 9.53 mmol) was dissolved in water (30 mL) and THF (30 mL), then LiOH (1.20 g, 28.6 mmol) was added. The mixture was stirred for 2 h before the organic solvent was removed under reduced pressure and the aqueous residue was neutralized with 1 M aq HCl. The title compound was crystallized at 4 °C along with LiCl. Recrystallization from methanol gave the pure product as a colorless powder (1.59 g, 62%). ^{1}H NMR (300 MHz, DMSO-d_6): δ 8.76 8.57 (m, 2H), 8.22 (d, J = 7.3 Hz, 1H), 7.71 7.57 (m, 2H), 7.25 6.99 (m, 5H), 4.26 (td, J = 7.4, 4.6 Hz, 1H), 3.27 2.95 (m, 3H). ^{13}C NMR (75 MHz, DMSO-d_6): δ 171.9, 163.4, 150.2, 142.1, 139.5, 129.4, 127.7, 125.6, 121.0, 56.1, 37.2.

*11 (Tritylthio)undecanoic Acid (**XI**).* Triphenylmethyl chloride (0.63 g, 1.0 equiv) was dissolved in DCM (5 mL). Thereto, a solution of 11-mercaptoundecanoic acid (MUA) (0.5 g, 1.0 equiv) in DCM (15 mL) was added dropwise. The mixture was stirred for 2 h at rt. DCM was removed by distillation, and the residue was purified by column chromatography (petroleum ether/EtOAc 2:1). ^{1}H NMR (300 MHz, $CDCl_3$): δ 7.40 (d, J = 7.6 Hz, 6H), 7.31 7.09 (m, 9H), 2.32 (t, J = 7.1 Hz, 2H), 2.11 (t, J = 7.3 Hz, 2H), 1.60 (q, J = 7.4 Hz, 2H), 1.46 0.95 (m, 14H). ^{13}C NMR (75 MHz, $CDCl_3$): δ 179.7, 145.2, 129.8, 127.9, 126.6, 66.5, 34.1, 32.2, 29.5, 29.32, 29.27, 29.16, 29.12, 28.7, 24.8. NMR data are consistent with the literature.[12]

*tert Butyl (S) 4 ((1 Ethoxy 1 oxo 3 phenylpropan 2 yl) carbamoyl)piperazine 1 carboxylate (**XII**).* To a stirred solution of 0.798 g 1-boc piperazine in THF, a suspension of 0.860 g (*S*)-ethyl-2-isocyanate-3-phenylpropanoate in THF was added dropwise. The mixture was stirred for 18 h and the solvent was removed under reduced pressure. The residue was extracted with EtOAc and the combined extracts were washed with a saturated solution of $NaHCO_3$ and brine, dried with Na_2SO_4, and concentrated under reduced pressure, resulting in a colorless oil (0.81 g, 50%). ^{1}H NMR (300 MHz, $CDCl_3$): δ 7.49 7.33 (m, 3H), 7.29 7.18 (m, 2H), 5.10 4.83 (m, 1H), 4.28 (dq, J = 15.5, 7.2 Hz, 2H), 3.70 3.57 (m, 1H), 3.57 3.48 (m, 4H), 3.48 3.35 (m, 4H), 3.29 3.22 (m, 2H), 1.60 (s, 9H), 1.39 (td, J = 7.1, 3.3 Hz, 3H). ^{13}C NMR (75 MHz, $CDCl_3$): δ 172.6, 156.5, 154.6, 136.3, 129.3, 128.5, 127.0, 80.2, 61.4, 60.4, 54.37, 43.9, 38.4, 28.4, 21.1, 14.2.

*(4 (tert Butoxycarbonyl)piperazine 1 carbonyl) L phenylalanine (**XIII**).* 0.81 g of compound **XII** was dissolved in THF and cooled to 0 °C. A solution of 0.29 g LiOH in water was added dropwise and the mixture was stirred for 3 h at room temperature. The solvent was removed under reduced pressure and the pH of the residue was adjusted to 2 with 1 M HCl. The residue was extracted with ethyl acetate and the combined extracts were washed with brine, dried with Na_2SO_4, and concentrated under reduced pressure. The crude product was dissolved in diethyl ether, *n*-pentane was added, and the product was crystallized at 4 °C, giving a colorless solid (0.56 g, 74%). ^{1}H NMR (300 MHz, $CDCl_3$): δ 9.39 (s, 1H), 7.25 7.14 (m, 3H), 7.14 7.04 (m, 2H), 5.05 (d, J = 7.1 Hz, NH), 4.61 (q, J = 6.2 Hz, 1H), 3.30 (dd, J = 7.9, 4.0 Hz, 4H), 3.24 3.09 (m, 4H), 3.04 (dd, J = 14.0, 6.8 Hz, 2H), 1.39 (s, 9H). ^{13}C NMR (75 MHz, $CDCl_3$): δ 174.7, 157.5, 154.8, 136.4, 129.5, 128.7, 127.2, 80.6, 54.9, 43.7, 37.5, 28.5.

*Preparation of Phosphonates **5** **7**. Diethyl(fluoro (phenylsulfonyl)methyl)phosphonate[12,67] (**5**).* To a stirred solution of phosphonate **III** (1.54 g, 1.0 equiv) in THF, KHMDS (1 M in THF, 6.59 mL, 1.25 equiv) was added dropwise at 80 °C. After 30 min at this temperature, Selectfluor (2.80 g, 1.5 equiv) in 10 mL DMF was added and the reaction mixture was stirred for 3 h, slowly warming to 0 °C. 15 mL of a saturated solution of ammonium chloride was added and the volatiles were evaporated. The residue was extracted with DCM and the combined extracts were washed with a saturated solution of $NaHCO_3$ and brine, dried with Na_2SO_4, concentrated under reduced pressure, and purified by column chromatography (light petroleum/EtOAc 1:6) to afford the title compound as a colorless solid. Yield: 1.0 g (62%). ^{1}H NMR (300 MHz, $CDCl_3$): δ 8.01 (d, J = 7.5 Hz, 2H), 7.74 (t, J = 7.4 Hz, 1H), 7.61 (t, J = 7.7 Hz, 2H), 5.38 (dd, $J_{H\ F}$ = 45.5 Hz, $J_{H\ F}$ = 6.6 Hz, 1H), 4.40 4.18 (m, 4H), 1.35 (t, J = 7.1 Hz, 6H). NMR data were consistent with the literature.[12]

*Phenyl(diethoxyphosphoryl)fluoromethanesulfonate (**6**).* Phosphonate **IV** (1.73 g, 1.0 equiv) was dissolved in THF (15 mL) and cooled to 78 °C. KHMDS (1 M in THF, 7.0 mL, 1.25 equiv) was added dropwise and the mixture was stirred for an additional 30 min. Selectfluor (3.0 g, 1.5 equiv) was added in one portion and the mixture was stirred for 5 min. Then, DMF (12 mL) was added in one portion and the mixture was allowed to warm to 0 °C. After stirring for 3 h, the reaction was quenched with conc. aq NH_4Cl (5 mL) and THF was removed in vacuo. EtOAc was added and the organic phase was washed with water (3×) and brine (2×) and dried with Na_2SO_4. The solvent was removed under reduced pressure and the residue was purified by column chromatography (petroleum ether/EtOAc 1:1), yielding the title compound as a colorless oil (0.95 g, 52%). ^{1}H NMR (300 MHz, $CDCl_3$): δ 7.50 7.39 (m, 2H), 7.39 7.28 (m, 3H), 5.63 (dd, $J_{H\ F}$ = 45 Hz, $J_{H\ P}$ = 7.2 Hz, 1H), 4.45 4.25 (m, 4H), 1.39 (tdd, J = 7.1, 2.0, 0.7 Hz, 6H). ^{13}C NMR (75 MHz, $CDCl_3$): δ 149.6, 130.3, 128.0, 122.2, 93.4 (dd, $J_{C\ F}$ = 232 Hz, $J_{C\ P}$ = 162 Hz), 65.7 (dd, $J_{C\ P}$ = 10.7 Hz, $J_{C\ F}$ = 6.7 Hz), 16.44 (d, $J_{C\ P}$ = 5.8 Hz).

*Diethyl((benzylsulfonyl)fluoromethyl)phosphonate (**7**).* Phosphonate **V** (3.77 g, 1.0 equiv) was dissolved in THF (40 mL) and cooled to 78 °C. KHMDS (1 M in THF, 15.4 mL, 1.25 equiv) was added dropwise and the mixture was stirred for an additional 30 min. Selectfluor (6.55 g, 1.5 equiv) was added in one portion and the mixture was stirred for 5 min. Then, DMF (24 mL) was added in one portion and the mixture was allowed to warm to 0 °C. After stirring for 3 h, the reaction was quenched with conc. NH_4Cl (5 mL) and THF was removed in vacuo. EtOAc was added and the organic phase was washed with water (3×) and brine (2×) and dried with Na_2SO_4. The solvent was removed under reduced pressure and the residue was purified by column chromatography (DCM/EtOAc 9:1), yielding the title compound as a colorless oil (1.92 g, 48%). ^{1}H NMR (300 MHz, $CDCl_3$): δ 7.51 7.32 (m, 5H), 5.28 (dd, $J_{H\ F}$ = 45 Hz, $J_{H\ P}$ = 7.1 Hz, 1H), 4.67 4.49 (m, 2H), 4.42 4.21 (m, 4H), 1.39 (td, J = 7.1, 0.7 Hz, 6H). ^{13}C NMR (75 MHz, $CDCl_3$): δ 131.4, 129.5, 129.2, 125.8, 95.2 (dd, $J_{C\ F}$ = 228 Hz, $J_{C\ P}$ = 161 Hz), 65.4 (dd, $J_{C\ F}$ = 6.3 Hz, $J_{C\ P}$ = 6.2 Hz), 57.5, 16.5 (d, $J_{C\ P}$ = 5.8 Hz).

*HWE Olefination (Compounds **8** **12**). Procedure A.* The specified phosphonate (1.0 equiv) was dissolved in THF and cooled to 0 °C. NaH (60% in mineral oil, 1.1 equiv) was added in portions and the mixture was stirred for 15 min. The corresponding boc-protected aminoaldehyde (1.0 equiv) was added in one portion, and the mixture was allowed to warm to rt. After stirring for 1 h, EtOAc was added and the organic phase was extracted with water, saturated aq $NaHCO_3$, and brine and finally dried with Na_2SO_4. Evaporation of the solvent under reduced pressure provided the boc-protected vinylsulfones as a crude mixture of *E*/*Z* isomers. Purification and separation of the isomers were achieved by column chromatography. The products were obtained as colorless solids.

Procedure B. The specified phosphonate (1.0 equiv) was dissolved in THF and cooled to 78 °C. KHMDS (1 M in THF, 1.0 equiv) or LHMDS (1 M in THF, 1.0 equiv) was added dropwise and it was stirred for additional 20 min. The respective aldehyde (1.0 equiv) was added in one portion and the mixture was allowed to warm to rt over a period of 1 h. After stirring for an additional hour at rt, EtOAc was added and the organic phase was extracted with water (2×) and brine (1×). Evaporation of the solvent under reduced pressure gave the crude product as *E*/*Z* isomers. Purification by column chromatography allowed the isolation of the desired (*E*)-isomers. The products were obtained as colorless solids.

*tert Butyl (S,E) (1 Fluoro 5 phenyl 1 (phenylsulfonyl)pent 1 en 3 yl)carbamate[12] (**8**).* Prepared following procedure A using 0.35 g of phosphonate **5**, 0.3 g boc-homophenylalaninal or boc-homophenylalanine aldehyde or boc-hPhe-H (**VI**), and 0.05 g NaH in 6 mL THF. Column chromatography: petroleum ether/EtOAc 3:1. (*E*)-isomer: Yield 0.20 g (41%). ^{1}H NMR (300 MHz, $CDCl_3$): δ 7.95 (d, J = 7.6 Hz, 2H), 7.70 (t, J = 7.4 Hz, 1H), 7.58 (t, J = 7.6 Hz, 2H), 7.36 7.16 (m, 3H), 7.12 (d, J = 7.1 Hz, 2H), 6.19 (dd, $J_{H\ F}$ = 32.3 Hz, $J_{H\ H}$ = 7.1 Hz,

https://doi.org/10.1021/acs.jmedchem.1c01002
J. Med. Chem. 2021, 64, 12322 12358

1H), 4.61 (s, 1H), 4.46 (s, 1H), 2.74 2.52 (m, 2H), 2.00 1.77 (m, 2H), 1.39 (s, 9H). ^{13}C NMR (75 MHz, $CDCl_3$): δ 154.9, 154.7 (d, $J_{C\ F}$ = 300 Hz), 140.5, 137.2, 134.7, 129.61, 128.8, 128.7, 128.4, 126.4, 118.4 (d, $J_{C\ F}$ = 4.6 Hz), 80.3, 46.4 (d, $J_{C\ F}$ = 2.7 Hz), 36.2, 32.0, 28.3. (*Z*)-isomer: Yield 0.10 g (21%). ^{1}H NMR (300 MHz, $CDCl_3$): δ 8.09 (d, *J* = 4.2 Hz, 2H), 7.69 (t, *J* = 7.4 Hz, 1H), 7.57 (t, *J* = 7.7 Hz, 2H), 7.37 7.12 (m, 5H), 5.81 (dd, $J_{H\ F}$ = 21 Hz, $J_{H\ H}$ = 10 Hz, 1H), 5.35 5.18 (m, 1H), 4.70 (s, 1H), 2.89 2.62 (m, 2H), 2.14 1.86 (m, 2H), 1.46 (s, 9H). ^{13}C NMR (75 MHz, $CDCl_3$): δ 155.0, 152.7 (d, $J_{C\ F}$ = 293 Hz), 141.0, 137.7, 134.7, 129.5, 129.1, 128.7, 128.5, 126.3, 121.4 (d, $J_{C\ F}$ = 11 Hz), 80.0, 46.6 (d, $J_{C\ F}$ = 5 Hz), 37.3, 32.3, 28.5.

*Phenyl (S,E) 3 ((tert Butoxycarbonyl)amino) 1 fluoro 5 phenyl pent 1 ene 1 sulfonate (**9**).* Prepared following procedure A using 0.66 g of phosphonate **6**, 0.53 g boc-homophenylalaninal or boc-homophenylalanine aldehyde or boc-hPhe-H (**VI**), and 0.09 g NaH in 12 mL THF. Column chromatography: petroleum ether/EtOAc 5:1. (*E*)-isomer: Yield 0.38 g (43%). ^{1}H NMR (300 MHz, $CDCl_3$): δ 7.46 7.32 (m, 2H), 7.32 7.15 (m, 6H), 7.10 (d, *J* = 7.0 Hz, 2H), 5.91 (dd, $J_{H\ F}$ = 31.3 Hz, $J_{H\ H}$ = 8.6 Hz, 1H), 4.68 4.27 (m, 2H), 2.66 2.43 (m, 2H), 1.97 1.66 (m, 2H), 1.43 (s, 9H). ^{13}C NMR (75 MHz, $CDCl_3$): δ 154.8, 150.8, 148.9 (d, $J_{C\ F}$ = 296 Hz), 140.2, 130.2, 128.8, 128.4, 128.0, 126.5, 122.4 (d, $J_{C\ F}$ = 4.1 Hz), 122.3, 80.4, 46.3 (d, $J_{C\ F}$ = 2.1 Hz), 35.9, 31.9, 28.4. (*Z*)-isomer: yield 0.22 g (22%). ^{1}H NMR (300 MHz, $CDCl_3$): δ 7.44 7.32 (m, 2H), 7.32 7.13 (m, 6H), 7.04 (d, *J* = 7.2 Hz, 2H), 6.14 (br, 1H), 4.88 4.44 (br, 2H), 2.59 2.46 (m, 1H), 2.46 2.29 (m, 1H), 1.84 (br, 1H), 1.42 (br, 1H), 1.43 (s, 9H). ^{13}C NMR (75 MHz, $CDCl_3$): δ 154.8, 149.3, 147.5 (d, $J_{C\ F}$ = 296 Hz), 140.7, 130.1, 128.5, 128.4, 128.1, 126.3, 124.1 (d, $J_{C\ F}$ = 9.9 Hz), 122.4, 80.4, 47.1 (d, $J_{C\ F}$ = 3.6 Hz), 36.3, 32.0, 28.4.

*Phenyl (S,E) 3 ((tert Butoxycarbonyl)amino) 5 phenylpent 1 ene 1 sulfonate (**9 (H)**).* Prepared following procedure B using 1.45 g of phosphonate **IV**, 1.24 g boc-homophenylalaninal or boc-homophenylalanine aldehyde or boc-hPhe-H (**VI**), and 6.0 mL 1 M LHMDS in 25 mL THF. Column chromatography: cyclohexane/EtOAc 5:1. (*E*)-isomer: Yield 0.80 g (41%). ^{1}H NMR (300 MHz, $CDCl_3$): δ 7.43 7.35 (m, 2H), 7.35 7.27 (m, 3H), 7.27 7.20 (m, 3H), 7.18 7.10 (m, 2H), 6.76 (dd, *J* = 15.1, 5.1 Hz, 1H), 6.48 (dd, *J* = 15.1, 1.5 Hz, 1H), 4.58 (d, *J* = 8.2 Hz, 1H), 4.33 (s, 1H), 2.77 2.52 (m, 2H), 1.98 1.72 (m, 2H), 1.49 (s, 9H). ^{13}C NMR (75 MHz, $CDCl_3$): δ 154.9, 150.4, 149.6, 140.2, 130.0, 128.8, 128.4, 127.4, 126.6, 124.4, 122.6, 80.5, 51.0, 35.6, 32.0, 28.4.

*tert Butyl (S,E) (1 (Benzylsulfonyl) 1 fluoro 5 phenylpent 1 en 3 yl)carbamate (**10**).* Synthesized following procedure B using 0.92 g phosphonate **7**, 0.74 g boc-homophenylalaninal or boc-homophenylalanine aldehyde or boc-hPhe-H (**VI**), and 2.8 mL KHMDS (1 M in THF) in 14 mL THF. Column chromatography: DCM/EtOAc 100:1. (*E*)-isomer: yield: 0.57 g (47%). ^{1}H NMR (300 MHz, $CDCl_3$): δ 7.39 7.16 (m, 8H), 7.10 (d, *J* = 7.0 Hz, 2H), 5.76 (dd, $J_{H\ F}$ = 32.8 Hz, $J_{H\ H}$ = 8.1 Hz, 1H), 4.59 4.38 (m, 2H), 4.35 (s, 2H), 2.62 2.38 (m, 2H), 1.91 1.64 (m, 3H), 1.45 (s, 9H). ^{13}C NMR (75 MHz, $CDCl_3$): δ 154.8, 152.1 (d, $J_{C\ F}$ = 300 Hz), 140.5, 131.0, 129.5, 129.2, 128.7, 128.4, 126.8, 126.4, 120.9 (d, $J_{C\ F}$ = 3.1 Hz), 80.3, 58.9, 46.1, 36.2, 31.8, 28.5. The (*Z*)-isomer was not isolated.

*tert Butyl (S,E) (1 Fluoro 5 (methylthio) 1 (phenylsulfonyl)pent 1 en 3 yl)carbamate (**11**).* Synthesized following procedure B using 0.93 g phosphonate **5**, 0.75 g boc-Met-H, and 3.15 mL LHMDS (1 M in THF) in 20 mL THF. Column chromatography: Petroleum ether/EtOAc 3:1. (*E*)-isomer: Yield 0.88 g (75%). ^{1}H NMR (300 MHz, $CDCl_3$): δ 7.94 (d, *J* = 7.8 Hz, 2H), 7.70 (t, *J* = 7.3 Hz, 1H), 7.58 (t, *J* = 7.6 Hz, 2H), 6.21 (br d, $J_{H\ F}$ = 31.5 Hz, 1H), 4.74 (br s, 1H), 4.55 (br s, 1H), 2.57 2.40 (m, 2H), 2.07 (s, 3H), 2.00 1.78 (m, 2H), 1.37 (s, 9H). ^{13}C NMR (75 MHz, $CDCl_3$): δ 154.9, 154.7 (d, $J_{C\ F}$ = 300 Hz), 137.1, 134.7, 129.6, 128.8, 118.0 (d, $J_{C\ F}$ = 4.6 Hz), 80.4, 46.0 (d, $J_{C\ F}$ = 1.0 Hz), 33.8, 30.2, 28.3, 15.7. The (*Z*)-isomer was not further characterized.

*tert Butyl (R,E) (1 (Benzylthio) 4 fluoro 4 (phenylsulfonyl)but 3 en 2 yl)carbamate (**12**).* Synthesized following procedure B using 0.55 g phosphonate **5**, 0.55 g boc-L-Cys(Bn)-H, and 1.85 mL LHMDS (1 M in THF) in 10 mL THF. Column chromatography: Petroleum ether/EtOAc 3:1. (*E*)-isomer: yield 0.44 g (54%). ^{1}H NMR (300 MHz, $CDCl_3$): δ 8.00 7.92 (m, 3H), 7.75 7.53 (m, 5H), 7.30 7.27 (m, 3H), 6.23 (dd, $J_{H\ F}$ = 31.8 Hz, $J_{H\ H}$ = 8.5 Hz, 1H), 4.83 (s, 1H), 4.59 (s, 1H), 3.70 (s, 2H), 2.73 2.44 (m, 2H), 1.39 (s, 9H). ^{13}C NMR (75 MHz, $CDCl_3$): δ 156.9, 154.8, 137.5, 137.1, 135.0, 134.7, 129.7, 129.6, 129.2, 129.0, 128.9, 128.8, 127.5, 117.5, 80.5, 46.0, 36.7, 35.4, 28.4.

Peptide Chemistry. *Coupling Protocols. Procedure C.* The specified carboxylic acid (1.0 equiv) and HOBt (1.0 equiv) were dissolved in DCM (8 mL) and cooled to 0 °C. DIEA (3.0 equiv) was added slowly, and the mixture was stirred until all materials were solubilized. TBTU (1.0 equiv) was added in one portion and the mixture was stirred for 15 min at 0 °C. The specific amine (1.0 equiv) was dissolved in DCM and added dropwise to the reaction mixture. After stirring for 12 h at rt, DCM was removed in vacuo and the residue was dissolved in EtOAc. The organic phase was washed with water (5×), conc. $NaHCO_3$ (2×), and 1 M aq HCl (2×) and then dried with Na_2SO_4. Evaporation of the solvent gave the crude product, which was purified by column chromatography.

Procedure D. The specified carboxylic acid (1.0 equiv) and TBTU (1.0 equiv) were dissolved in DCM and cooled to 0 °C. DIEA (3.0 equiv) was added and the mixture was stirred for 15 min. The respective amine (1.0 equiv) was added in one portion. After stirring for 12 h at rt, DCM was removed in vacuo, and the residue was dissolved in EtOAc. The organic phase was washed with water (5×), conc. $NaHCO_3$ (2×), and 1 M aq HCl (2×) and then dried with Na_2SO_4. Evaporation of the solvent gave the crude product, which was purified by column chromatography.

Procedure E. The respective carboxylic acid (**IX** or **X**, 1.0 equiv) and HOBt (1.0 equiv) were dissolved in DMF (5 mL) and cooled to 0 °C. DIEA (3.0 equiv) was added and the mixture was stirred for 15 min. The respective amine (1.0 equiv) was added in one portion and the mixture was stirred for 12 h at rt. EtOAc was added and aqueous work-up was performed with 5% aq LiCl (5×), water (2×), and saturated aq $NaHCO_3$ (2×). After evaporation of the solvent, the residue was purified by column chromatography.

Removal of Boc Groups. Procedure F. Boc-protected compounds (**8** **10**) were dissolved in 4 M HCl/dioxane solution (5 10 mL). After stirring for 30 min at rt, dioxane was evaporated in vacuo and the residue was washed several times with diethyl ether. The precipitate was collected and dried under reduced pressure. The amines were obtained as hydrochloride salts and were sufficiently pure to be used in the next step without further purification.

Procedure G. Boc-protected compounds (**11** **12**) were dissolved in DCM (10 mL) and cooled to 0 °C. 1 mL TFA was added dropwise, and the resulting mixture was stirred for 1 h. After evaporation to dryness in high vacuum, the residue was washed with diethyl ether and collected by filtration. The amines were obtained as TFA salt and directly used for the next step.

*(S,E) 1 Fluoro 5 phenyl 1 (phenylsulfonyl)pent 1 en 3 amine Hydrochloride (**13**).* Prepared following procedure F using 0.60 g of compound **8** in 12 mL 4 M HCl/dioxane. Yield: 0.47 g (93%). ^{1}H NMR (300 MHz, DMSO-d_6): δ 8.65 (s, 3H), 8.03 (d, *J* = 7.8 Hz, 2H), 7.89 (t, *J* = 7.3 Hz, 1H), 7.77 (t, *J* = 7.6 Hz, 2H), 7.32 7.13 (m, 3H), 7.06 (d, *J* = 7.3 Hz, 2H), 6.54 (dd, $J_{H\ F}$ = 33 Hz, $J_{H\ H}$ = 9.8 Hz, 1H), 4.09 3.90 (m, 1H), 2.62 2.34 (m, 2H), 2.25 2.07 (m, 1H), 2.07 1.89 (m, 1H). ^{13}C NMR (75 MHz, DMSO-d_6): δ 155.2 (d, $J_{C\ F}$ = 301 Hz), 139.9, 135.9, 135.6, 130.2, 128.54, 128.45, 128.1, 126.2, 114.5 (d, $J_{C\ F}$ = 3.7 Hz), 45.0 (d, $J_{C\ F}$ = 2.7 Hz), 33.4 (d, $J_{C\ F}$ = 1.4 Hz), 30.5.

*Phenyl (S,E) 3 Amino 1 fluoro 5 phenylpent 1 ene 1 sulfonate Hydrochloride (**14**).* Prepared following procedure F using 0.3 g of compound **9** in 7 mL 4 M HCl/dioxane. Yield: 0.23 g (89%). ^{1}H NMR (300 MHz, DMSO-d_6): δ 8.72 (s, 3H), 7.56 7.47 (m, 2H), 7.47 7.37 (m, 3H), 7.31 (t, *J* = 7.2 Hz, 2H), 7.26 7.19 (m, 1H), 7.19 7.09 (m, 2H), 6.42 (dd, $J_{H\ F}$ = 32 Hz, $J_{H\ H}$ = 9.7 Hz, 1H), 4.15 (td, *J* = 9.2, 5.3 Hz, 1H), 2.48 2.32 (m, 2H), 2.19 2.01 (m, 1H), 2.00 1.81 (m, 1H). ^{13}C NMR (75 MHz, DMSO-d_6): δ 149.3 (d, $J_{C\ F}$ = 300 Hz), 148.6, 140.0, 130.6, 128.5, 128.4, 128.1, 126.3, 122.0, 118.4 (d, $J_{C\ F}$ = 3.2 Hz), 45.2 (d, $J_{C\ F}$ = 2.2 Hz), 40.4, 33.3, 30.4.

*Phenyl (S,Z) 3 Amino 1 fluoro 5 phenylpent 1 ene 1 sulfonate Hydrochloride (**14 (Z)**).* Prepared following procedure F using 0.2 g of compound **9**-(*Z*) in 7 mL 4 M HCl/dioxane. Yield: 0.16 g (93%). ^{1}H

https://doi.org/10.1021/acs.jmedchem.1c01002
J. Med. Chem. 2021, 64, 12322 12358

NMR (300 MHz, DMSO-d_6): δ 8.68 (s, 3H), 7.59 7.45 (m, 2H), 7.44 7.13 (m, 6H), 7.08 6.98 (m, 2H), 6.73 (dd, $J_{H\ F}$ = 21.2 Hz, $J_{H\ H}$ = 10.6 Hz, 1H), 4.27 (q, J = 7.8, 1H), 2.29 2.02 (m, 2H), 1.95 1.80 (m, 1H), 1.68 1.47 (m, 1H). ^{13}C NMR (75 MHz, DMSO-d_6): δ 148.3, 148.1 (d, $J_{C\ F}$ = 288 Hz), 140.1, 130.6, 128.7, 128.4, 128.0, 126.1, 122.1, 120.6 (d, J = 16 Hz), 45.9 (d, $J_{C\ F}$ = 6.7 Hz), 34.3, 30.2.

*Phenyl (S,E) 3 Amino 5 phenylpent 1 ene 1 sulfonate Hydro chloride (**14 (H)**).* Prepared following procedure F using 0.78 g of compound **9**-(**H**) in 14 mL 4 M HCl/dioxane. Yield: 0.34 g (51%). ^{1}H NMR (300 MHz, DMSO-d_6): δ 8.64 (s, 3H), 7.50 7.41 (m, 2H), 7.41 7.34 (m, 2H), 7.34 7.24 (m, 3H), 7.24 7.17 (m, 1H), 7.16 7.10 (m, 2H), 6.81 (dd, $J_{H\ H}$ = 15.3, 6.8 Hz, 1H), 4.15 3.95 (m, 1H), 2.61 2.38 (m, 2H), 2.10 1.84 (m, 2H). ^{13}C NMR (75 MHz, DMSO-d_6): δ 149.0, 145.3, 140.3, 130.1, 128.5, 128.2, 127.6, 127.6, 126.2, 122.6, 50.1, 33.3, 30.4.

*(S,E) 1 (Benzylsulfonyl) 1 fluoro 5 phenylpent 1 en 3 amine Hy drochloride (**15**).* Prepared following procedure F using 0.46 g of compound **10** in 10 mL 4 M HCl/dioxane. Yield: 0.37 g (95%). ^{1}H NMR (300 MHz, DMSO-d_6): δ 8.66 (s, 3H), 7.48 7.27 (m, 7H), 7.26 7.09 (m, 3H), 6.13 (dd, $J_{H\ F}$ = 33 Hz, $J_{H\ H}$ = 9.9 Hz, 1H), 4.87 (s, 2H), 4.04 (td, J = 9.3, 5.0 Hz, 1H), 2.39 (t, J = 8.1 Hz, 2H), 2.13 1.97 (m, 1H), 1.91 1.74 (m, 1H). ^{13}C NMR (75 MHz, DMSO-d_6): δ 154.1 (d, $J_{C\ F}$ = 304 Hz), 140.2, 131.2, 129.0, 128.7, 128.5, 128.2, 127.0, 126.2, 115.7 (d, $J_{C\ F}$ = 2.9 Hz), 57.6, 45.0 (d, $J_{C\ F}$ = 2.2 Hz), 33.5, 30.4.

*(S,E) 1 Fluoro 5 (methylthio) 1 (phenylsulfonyl)pent 1 en 3 aminium 2,2,2 Trifluoroacetate (**16**).* Prepared following procedure G with 0.88 g compound **11**. Yield: 0.60 g (65%). ^{1}H NMR (300 MHz, DMSO-d_6): δ 7.89 7.82 (m, 2H), 7.82 7.63 (m, 1H), 7.57 7.52 (m, 2H), 6.21 (d, $J_{H\ F}$ = 32 Hz, 1H), 4.46 (m, 1H), 2.69 2.41 (m, 2H), 2.06 (s, 3H), 2.05 1.75 (m, 2H).

*(R,E) 1 (Benzylthio) 4 fluoro 4 (phenylsulfonyl)but 3 en 2 ami nium 2,2,2 Trifluoroacetate (**17**).* Prepared following procedure G with 0.44 g compound **12**. Yield: 0.37 g (81%). ^{1}H NMR (300 MHz, DMSO-d_6): δ 8.04 (s, 3H), 7.95 7.84 (m, 2H), 7.77 7.55 (m, 4H), 7.25 7.19 (m, 4H), 6.44 (dd, $J_{H\ F}$ = 30 Hz, $J_{H\ H}$ = 9.1 Hz, 1H), 4.20 4.01 (m, 1H), 3.71 (s, 2H), 2.91 2.62 (m, 2H). ^{13}C NMR (75 MHz, DMSO-d_6): δ 161.4, 160.8, 155.5, 136.6, 135.5, 135.0, 129.9, 129.7, 129.2, 129.1, 128.9, 127.9, 117.3, 113.5, 111.1, 77.2, 46.2, 36.2, 33.3.

*tert Butyl ((S) 1 (((S,E) 1 Fluoro 5 phenyl 1 (phenylsulfonyl) pent 1 en 3 yl)amino) 1 oxo 3 phenylpropan 2 yl)carbamate (**18**).* Synthesized following procedure C with 0.180 g compound **13**, 0.135 g boc-L-Phe-OH, 0.162 g TBTU, 0.078 g HOBt, and 0.265 mL DIEA. Purification by column chromatography (petroleum ether/EtOAc 3:1). Yield: 0.21 g (73%). ^{1}H NMR (300 MHz, $CDCl_3$): δ 8.00 7.89 (m, 2H), 7.79 7.68 (m, 1H), 7.67 7.55 (m, 2H), 7.39 7.12 (m, 8H), 7.10 7.00 (m, 2H), 6.00 (dd, $J_{H\ F}$ = 32 Hz, $J_{H\ H}$ = 8.5 Hz, 1H), 5.82 (d, J = 8.0 Hz, 1H), 4.91 (s, 1H), 4.69 (quint, J = 7.7 Hz, 1H), 4.20 (q, J = 7.5 Hz, 1H), 3.04 (dd, J = 13.7, 6.6 Hz, 1H), 2.95 (dd, J = 13.7, 7.6 Hz, 1H), 2.52 (t, J = 7.2 Hz, 2H), 1.96 1.75 (m, 2H), 1.40 (s, 9H). ^{13}C NMR (75 MHz, $CDCl_3$): δ 170.8, 155.6, 154.8 (d, $J_{C\ F}$ = 301 Hz), 140.4, 137.1, 136.6, 134.8, 129.7, 129.4, 129.0, 128.8, 128.7, 128.4, 127.3, 126.4, 117.3 (d, $J_{C\ F}$ = 4.7 Hz), 80.6, 56.2, 45.0, 38.4, 35.7, 31.8, 28.4.

*Phenyl (S,E) 3 ((S) 2 ((tert Butoxycarbonyl)amino) 3 phenylpro panamido) 1 fluoro 5 phenylpent 1 Ene 1 sulfonate (**19**).* Synthesized following procedure C with 0.160 g compound **14**, 0.114 g boc-Phe-OH, 0.138 g TBTU, 0.066 g HOBt, and 0.225 mL DIEA. Purification by column chromatography (petroleum ether/EtOAc 3:1). Yield: 0.20 g (78%). ^{1}H NMR (300 MHz, $CDCl_3$): δ 7.47 7.35 (m, 2H), 7.35 7.10 (m, 9H), 7.08 6.95 (m, 4H), 5.65 (d, J = 7.9 Hz, 1H), 5.60 (dd, $J_{H\ F}$ = 32 Hz, $J_{H\ H}$ = 8.3 Hz, 1H), 5.02 (d, J = 7.1 Hz, 1H), 4.68 (q, J = 7.4 Hz, 1H), 4.18 (dd, J = 8.6, 5.6 Hz, 1H), 3.04 (dd, J = 13.4, 6.2 Hz, 1H), 2.85 (dd, J = 13.4, 8.4 Hz, 1H), 2.55 2.35 (m, 2H), 1.83 1.60 (m, 2H), 1.41 (s, 9H). ^{13}C NMR (75 MHz, $CDCl_3$): δ 170.8, 155.8, 149.4, 149.0 (d, $J_{C\ F}$ = 297 Hz), 147.0, 140.1, 136.5, 130.2, 129.3, 129.0, 128.8, 128.4, 128.0, 127.4, 126.6, 122.5, 121.3 (d, $J_{C\ F}$ = 5.1 Hz), 80.6, 56.2, 44.8, 38.7, 35.3, 31.7, 28.4.

*Phenyl (S,Z) 3 ((S) 2 ((tert Butoxycarbonyl)amino) 3 phenylpro panamido) 1 fluoro 5 phenylpent 1 ene 1 sulfonate (**19 (Z)**).* Synthesized following procedure C with 0.128 g compound **14**-(**Z**), 0.091 g boc-L-Phe-OH, 0.110 g TBTU, 0.053 g HOBt, and 0.204 mL DIEA. Purification by column chromatography (petroleum ether/EtOAc 3:1). Yield: 0.150 g (81%). ^{1}H NMR (300 MHz, $CDCl_3$): δ 7.46 7.08 (m, 13H), 6.97 (d, J = 6.8 Hz, 2H), 5.94 5.59 (m, 2H), 4.96 (s, 1H), 4.80 (q, J = 8.2 Hz, 1H), 4.25 4.11 (m, 1H), 3.14 2.87 (m, 2H), 2.44 2.17 (m, 2H), 1.82 1.61 (m, 1H), 1.53 1.42 (m, 1H), 1.41 (s, 9H). ^{13}C NMR (75 MHz, $CDCl_3$): δ 171.0, 155.6, 149.2, 148.0 (d, $J_{C\ F}$ = 289 Hz), 140.6, 136.7, 130.2, 129.5, 128.9, 128.6, 128.4, 128.1, 127.2, 126.3, 123.0, 123.0 (d, $J_{C\ F}$ = 12 Hz), 80.6, 56.1, 46.1 (d, $J_{C\ F}$ = 5.9 Hz), 38.5, 35.7, 31.8, 28.4.

*tert Butyl ((S) 1 (((S,E) 1 (Benzylsulfonyl) 1 fluoro 5 phenylpent 1 en 3 yl)amino) 1 oxo 3 phenylpropan 2 yl)carbamate (**20**).* Synthesized following procedure C with 0.230 g compound **15**, 0.165 g boc-L-Phe-OH, 0.200 g TBTU, 0.095 g HOBt, and 0.325 mL DIEA. Purification by column chromatography (petroleum ether/EtOAc 3:1). Yield: 0.30 g (85%). ^{1}H NMR (300 MHz, $CDCl_3$): δ 7.42 7.15 (m, 11H), 7.13 6.97 (m, 4H), 5.68 (d, J = 8.0 Hz, 1H), 5.53 (dd, $J_{H\ F}$ = 33 Hz, $J_{H\ H}$ = 8.9 Hz, 1H), 4.99 (br s, 1H), 4.68 (quint, J = 7.8 Hz, 1H), 4.35 (s, 2H), 4.18 (q, J = 7.9 Hz, 1H), 3.03 (dd, J = 13.5, 6.4 Hz, 1H), 2.91 (dd, J = 13.5, 8.0 Hz, 1H), 2.49 2.29 (m, 2H), 1.70 1.56 (m, 2H), 1.42 (s, 9H). ^{13}C NMR (75 MHz, $CDCl_3$): δ 170.6, 155.6, 152.3 (d, $J_{C\ F}$ = 301 Hz), 140.3, 136.6, 131.0, 129.5, 129.4, 129.2, 129.0, 128.7, 128.4, 127.3, 126.7, 126.5, 119.7 (d, $J_{C\ F}$ = 4.0 Hz), 80.6, 58.8, 56.2, 44.7 (d, $J_{C\ F}$ = 1.3 Hz), 38.6, 35.5 (d, $J_{C\ F}$ = 1.4 Hz), 31.7, 28.4.

*tert Butyl ((S) 1 (((S,E) 1 Fluoro 5 phenyl 1 (phenylsulfonyl) pent 1 en 3 yl)amino) 1 oxo 3 (m tolyl)propan 2 yl)carbamate (**21**).* Synthesized following procedure C with 0.220 g compound **13**, 0.173 g boc-L-Phe(3-Me)-OH, 0.198 g TBTU, 0.095 g HOBt, and 0.330 mL DIEA. Purification by column chromatography (petroleum ether/EtOAc 3:1). Yield: 0.28 g (77%). ^{1}H NMR (300 MHz, $CDCl_3$): δ 8.00 7.88 (m, 2H), 7.76 7.65 (m, 1H), 7.64 7.53 (m, 2H), 7.31 7.12 (m, 4H), 7.11 6.88 (m, 5H), 6.04 (dd, $J_{H\ F}$ = 32.1 Hz, $J_{H\ H}$ = 8.4 Hz, 1H), 5.93 (d, J = 8.0 Hz, 1H), 4.92 (s, 1H), 4.78 4.59 (m, 1H), 4.21 (q, J = 7.3 Hz, 1H), 3.01 (dd, J = 13.8, 6.6 Hz, 1H), 2.92 (dd, J = 13.8, 7.5 Hz, 1H), 2.58 2.46 (m, 2H), 2.31 (s, 3H), 1.93 1.77 (m, 2H), 1.41 (s, 9H). ^{13}C NMR (75 MHz, $CDCl_3$): δ 170.9, 155.62, 154.9 (d, $J_{C\ F}$ = 303 Hz), 140.4, 138.7, 137.1, 136.5, 134.8, 130.1, 129.7, 128.9, 128.8, 128.7, 128.4, 128.1, 126.4, 126.4, 117.4 (d, $J_{C\ F}$ = 3.6 Hz), 80.6, 56.2, 45.2, 38.2, 35.8, 31.8, 28.4, 21.5.

*Phenyl (S,E) 3 ((S) 2 ((tert Butoxycarbonyl)amino) 3 (m tolyl) propanamido) 1 fluoro 5 phenylpent 1 ene 1 sulfonate (**22**).* Synthesized following procedure C with 0.280 g compound **14**, 0.210 g boc-L-Phe(3-Me)-OH, 0.242 g TBTU, 0.115 g HOBt, and 0.40 mL DIEA. Purification by column chromatography (petroleum ether/EtOAc 3:1). Yield: 0.34 g (75%). ^{1}H NMR (300 MHz, $CDCl_3$): δ 7.40 (t, J = 7.3 Hz, 2H), 7.35 7.08 (m, 7H), 7.08 7.00 (m, 3H), 6.91 (s, 1H), 6.80 (d, J = 7.3 Hz, 1H), 5.78 (d, J = 7.7 Hz, 1H), 5.65 (dd, $J_{H\ F}$ = 31.4 Hz, $J_{H\ H}$ = 8.3 Hz, 1H), 5.04 (s, 1H), 4.70 (quint, J = 8.2, 7.0 Hz, 1H), 4.18 (quint, J = 8.7, 8.0 Hz, 1H), 3.01 (dd, J = 13.3, 6.1 Hz, 1H), 2.83 (dd, J = 13.3, 8.6 Hz, 1H), 2.55 2.37 (m, 2H), 2.28 (s, 3H), 1.81 1.65 (m, 2H), 1.42 (s, 9H). ^{13}C NMR (75 MHz, $CDCl_3$): δ 170.9, 155.6, 149.4, 149.0 (d, $J_{C\ F}$ = 297 Hz), 140.2, 138.7, 136.5, 130.2, 130.0, 128.9, 128.8, 128.4, 128.1, 128.0, 126.5, 126.4, 122.4, 121.3 (d, $J_{C\ F}$ = 4.9 Hz), 80.6, 56.2, 44.9 (d, $J_{C\ F}$ = 1.2 Hz), 38.5, 35.4 (d, $J_{C\ F}$ = 0.9 Hz), 31.7, 28.4, 21.4.

*tert Butyl ((S) 1 (((S,E) 1 (Benzylsulfonyl) 1 fluoro 5 phenylpent 1 en 3 yl)amino) 1 oxo 3 (m tolyl)propan 2 yl)carbamate (**23**).* Synthesized following procedure C with 0.230 g compound **15**, 0.174 g boc-L-Phe(3-Me)-OH, 0.200 g TBTU, 0.095 g HOBt, and 0.325 mL DIEA. Purification by column chromatography (petroleum ether/EtOAc 3:1). Yield: 0.28 g (69%). ^{1}H NMR (300 MHz, $CDCl_3$): δ 7.41 7.12 (m, 9H), 7.04 (d, J = 7.3 Hz, 3H), 6.94 (s, 1H), 6.85 (d, J = 7.3 Hz, 1H), 5.73 (d, J = 7.8 Hz, 1H), 5.56 (dd, $J_{H\ F}$ = 32.8 Hz, $J_{H\ H}$ = 8.8 Hz, 1H), 4.99 (s, 1H), 4.69 (quint, J = 8.3, 7.8 Hz, 1H), 4.34 (s, 2H), 4.18 (q, J = 8.7 Hz, 1H), 3.01 (dd, J = 13.6, 6.5 Hz, 1H), 2.87 (dd, J = 13.6, 7.9 Hz, 1H), 2.49 2.33 (m, 2H), 2.30 (s, 3H), 1.72 1.57 (m, 2H), 1.42 (s, 9H). ^{13}C NMR (75 MHz, $CDCl_3$): δ 170.7, 155.6, 152.3 (d, $J_{C\ F}$ = 301 Hz), 140.4, 138.7, 136.5, 131.1, 130.1, 129.5, 129.2, 128.9, 128.7, 128.4, 128.1, 126.7, 126.5, 119.8 (d, $J_{C\ F}$ = 4.2 Hz), 80.6, 58.8, 56.2, 44.8 (d, $J_{C\ F}$ = 1.3 Hz), 38.4, 35.6, 31.7, 28.4, 21.5.

https://doi.org/10.1021/acs.jmedchem.1c01002
J. Med. Chem. 2021, 64, 12322 12358

*tert Butyl ((S) 1 (((S,E) 1 Fluoro 5 phenyl 1 (phenylsulfonyl) pent 1 en 3 yl)amino) 1 oxo 3 (p tolyl)propan 2 yl)carbamate (**24**).* Synthesized following procedure C with 0.200 g compound **13**, 0.173 g boc-L-Phe(4-Me)-OH, 0.198 g TBTU, 0.095 g HOBt, and 0.30 mL DIEA. Purification by column chromatography (petroleum ether/EtOAc 3:1). Yield: 0.25 g (77%). ^{1}H NMR (300 MHz, $CDCl_3$): δ 7.94 (d, J = 7.8 Hz, 2H), 7.70 (t, J = 7.2 Hz, 1H), 7.59 (t, J = 7.6 Hz, 2H), 7.35 6.92 (m, 9H), 6.03 (dd, $J_{H\ F}$ = 32.0 Hz, $J_{H\ H}$ = 8.4 Hz, 1H), 5.89 (d, J = 8.0 Hz, 1H), 4.93 (s, 1H), 4.70 (quint, J = 7.4 Hz, 1H), 4.20 (q, J = 7.2 Hz, 1H), 3.01 (dd, J = 13.6, 6.4 Hz, 1H), 2.91 (dd, J = 13.6, 7.6 Hz, 1H), 2.52 (t, J = 7.5 Hz, 2H), 2.33 (s, 3H), 1.95 1.77 (m, 2H), 1.41 (s, 9H). ^{13}C NMR (75 MHz, $CDCl_3$): δ 170.9, 155.6, 154.8 (d, $J_{C\ F}$ = 301 Hz), 140.4, 137.2, 137.0, 134.7, 133.4, 129.70, 129.65, 129.3, 128.8, 128.7, 128.4, 126.4, 117.4 (d, $J_{C\ F}$ = 4.4 Hz), 80.5, 56.2, 45.0, 38.0, 35.8, 31.8, 28.4, 21.2.

*Phenyl (S,E) 3 ((S) 2 ((tert Butoxycarbonyl)amino) 3 (p tolyl) propanamido) 1 fluoro 5 phenylpent 1 ene 1 sulfonate (**25**).* Synthesized following procedure C with 0.292 g compound **14**, 0.220 g boc-L-Phe(4-Me)-OH, 0.252 g TBTU, 0.121 g HOBt, and 0.410 mL DIEA. Purification by column chromatography (petroleum ether/EtOAc 3:1). Yield: 0.39 g (83%). ^{1}H NMR (300 MHz, $CDCl_3$): δ 7.47 7.35 (m, 2H), 7.35 7.15 (m, 6H), 7.10 6.98 (m, 4H), 6.92 (d, J = 8.0 Hz, 2H), 5.75 (d, J = 7.9 Hz, 1H), 5.62 (dd, $J_{H\ F}$ = 31 Hz, $J_{H\ H}$ = 9.0 Hz, 1H), 5.05 (d, J = 7.8 Hz, 1H), 4.70 (quint, J = 7.7 Hz, 1H), 4.20 4.08 (m, 1H), 3.00 (dd, J = 13.5, 6.1 Hz, 1H), 2.81 (dd, J = 13.5, 8.3 Hz, 1H), 2.53 2.36 (m, 2H), 2.29 (s, 3H), 1.83 1.62 (m, 2H), 1.41 (s, 9H). ^{13}C NMR (75 MHz, $CDCl_3$): δ 170.9, 155.6, 149.4, 149.0 (d, $J_{C\ F}$ = 297 Hz), 140.2, 137.0, 133.3, 130.2, 129.7, 129.2, 128.8, 128.4, 128.0, 126.5, 122.4, 121.4, 121.3, 80.6, 56.3, 44.8 (d, $J_{C\ F}$ = 1.5 Hz), 38.3, 35.4, 31.7, 28.4, 21.1.

*Phenyl (S,E) 3 ((S) 2 ((tert Butoxycarbonyl)amino) 3 (p tolyl) propanamido) 5 phenylpent 1 ene 1 sulfonate (**25 (H)**).* Synthesized following procedure C with 0.34 g compound **14**-(**H**), 0.28 g boc-L-Phe(4-Me)-OH, 0.32 g TBTU, 0.14 g HOBt, and 0.70 mL DIEA. Purification by column chromatography (cyclohexane/EtOAc 4:1). Yield: 0.24 g (42%). ^{1}H NMR (300 MHz, $CDCl_3$): δ 7.42 7.32 (m, 2H), 7.31 7.02 (m, 12H), 6.52 (dd, $J_{H\ H}$ = 15.2, 4.6 Hz, 1H), 5.92 (dd, $J_{H\ H}$ = 37.5, 11.8 Hz, 2H), 5.00 (s, 1H), 4.63 4.47 (m, 1H), 4.31 4.18 (q, 1H), 3.08 2.89 (m, 2H), 2.62 2.42 (m, 2H), 2.31 (s, 3H), 1.88 1.60 (m, 2H), 1.43 (s, 9H). ^{13}C NMR (75 MHz, $CDCl_3$): δ 171.1, 149.5, 149.1, 140.1, 137.3, 133.0, 129.8 (d, J = 3.6 Hz), 129.1 (d, J = 6.7 Hz), 128.6, 128.3, 127.3, 126.4, 124.4, 122.6, 56.5, 49.2, 35.1, 31.7, 28.3, 21.0. mp 93 95 °C.

*tert Butyl ((S) 1 (((S,E) 1 (Benzylsulfonyl) 1 fluoro 5 phenylpent 1 en 3 yl)amino) 1 oxo 3 (p tolyl)propan 2 yl)carbamate (**26**).* Synthesized following procedure C with 0.230 g compound **15**, 0.174 g boc-L-Phe(4-Me)-OH, 0.200 g TBTU, 0.095 g HOBt, and 0.325 mL DIEA. Purification by column chromatography (petroleum ether/EtOAc 3:1). Yield: 0.290 g (79%). ^{1}H NMR (300 MHz, $CDCl_3$): δ 7.43 7.14 (m, 8H), 7.12 6.99 (m, 4H), 6.96 (d, J = 7.4 Hz, 2H), 5.66 (d, J = 7.8 Hz, 1H), 5.54 (dd, $J_{H\ F}$ = 32.9 Hz, $J_{H\ H}$ = 8.7 Hz, 1H), 4.98 (s, 1H), 4.69 (quint, J = 8.3 Hz, 1H), 4.34 (s, 2H), 4.15 (q, J = 7.8, 7.4 Hz, 1H), 3.01 (dd, J = 13.6, 5.9 Hz, 1H), 2.85 (dd, J = 13.6, 8.0 Hz, 1H), 2.54 2.33 (m, 2H), 2.30 (s, 3H), 1.70 1.55 (m, 3H), 1.42 (s, 9H). ^{13}C NMR (75 MHz, $CDCl_3$): δ 170.7, 155.6, 152.3 (d, $J_{C\ F}$ = 301 Hz), 140.4, 137.0, 133.4, 131.0, 129.7, 129.5, 129.3, 129.2, 128.7, 128.4, 126.7, 126.5, 119.8 (d, $J_{C\ F}$ = 4.0 Hz), 80.5, 58.8, 56.2, 44.7 (d, $J_{C\ F}$ = 1.6 Hz), 38.1, 35.6, 31.7, 28.4, 21.2.

*(S) 1 (((S,E) 1 Fluoro 5 phenyl 1 (phenylsulfonyl)pent 1 en 3 yl)amino) 1 oxo 3 phenylpropan 2 aminium Chloride (**27**).* Synthesized by following procedure F with 0.21 g of compound **18** in 10 mL 4 M HCl/dioxane. Yield: 0.19 g (99%) The crude product was used without further purification and characterization for the next step.

*(S) 1 (((S,E) 1 Fluoro 1 (phenoxysulfonyl) 5 phenylpent 1 en 3 yl)amino) 1 oxo 3 phenylpropan 2 aminium Chloride (**28**).* Synthesized by following procedure F with 0.20 g of compound **19** in 8 mL 4 M HCl/dioxane. Yield: 0.18 g (99%). The crude product was used without further purification and characterization for the next step.

*(S) 1 (((S,Z) 1 Fluoro 1 (phenoxysulfonyl) 5 phenylpent 1 en 3 yl)amino) 1 oxo 3 phenylpropan 2 aminium Chloride (**28 (Z)**).* Synthesized by following procedure F with 0.15 g of compound **19**-(**Z**) in 8 mL 4 M HCl/dioxane. Yield: 0.13 g (99%). The crude product was used without further purification and characterization for the next step.

*(S) 1 (((S,E) 1 (Benzylsulfonyl) 1 fluoro 5 phenylpent 1 en 3 yl) amino) 1 oxo 3 phenylpropan 2 aminium Chloride (**29**).* Synthesized by following procedure F with 0.30 g of compound **20** in 10 mL 4 M HCl/dioxane. Yield: 0.26 g (99%). The crude product was used without further purification and characterization for the next step.

*(S) 1 (((S,E) 1 Fluoro 5 phenyl 1 (phenylsulfonyl)pent 1 en 3 yl)amino) 1 oxo 3 (m tolyl)propan 2 aminium Chloride (**30**).* Synthesized by following procedure F with 0.28 g of compound **21** in 8 mL 4 M HCl/dioxane. Yield: 0.25 g (99%). The crude product was used without further purification and characterization for the next step.

*(S) 1 (((S,E) 1 Fluoro 1 (phenoxysulfonyl) 5 phenylpent 1 en 3 yl)amino) 1 oxo 3 (m tolyl)propan 2 aminium Chloride (**31**).* Synthesized by following procedure F with 0.34 g of compound **22** in 10 mL 4 M HCl/dioxane. Yield: 0.30 g (99%). The crude product was used without further purification and characterization for the next step.

*(S) 1 (((S,E) 1 (Benzylsulfonyl) 1 fluoro 5 phenylpent 1 en 3 yl) amino) 1 oxo 3 (m tolyl)propan 2 aminium Chloride (**32**).* Synthesized by following procedure F with 0.28 g of compound **23** in 8 mL 4 M HCl/dioxane. Yield: 0.25 g (99%). The crude product was used without further purification and characterization for the next step.

*(S) 1 (((S,E) 1 Fluoro 5 phenyl 1 (phenylsulfonyl)pent 1 en 3 yl)amino) 1 oxo 3 (p tolyl)propan 2 aminium Chloride (**33**).* Synthesized by following procedure F with 0.25 g of compound **24** in 8 mL 4 M HCl/dioxane. Yield: 0.22 g (99%). The crude product was used without further purification and characterization for the next step.

*(S) 1 (((S,E) 1 Fluoro 1 (phenoxysulfonyl) 5 phenylpent 1 en 3 yl)amino) 1 oxo 3 (p tolyl)propan 2 aminium Chloride (**34**).* Synthesized by following procedure F with 0.39 g of compound **25** in 10 mL 4 M HCl/dioxane. Yield: 0.34 g (99%). The crude product was used without further purification and characterization for the next step.

*(S) 1 Oxo 1 (((S,E) 1 (phenoxysulfonyl) 5 phenylpent 1 en 3 yl) amino) 3 (p tolyl)propan 2 aminium Chloride (**34 (H)**).* Synthesized by following procedure F with 0.20 g of compound **25**-(**H**) in 4 mL 4 M HCl/dioxane. Yield: 0.15 g (89%), colorless solid. ^{1}H NMR (300 MHz, DMSO-d_6): δ 9.06 (d, J = 8.4 Hz, 1H), 8.57 (s, 3H), 7.48 7.38 (m, 2H), 7.37 7.21 (m, 5H), 7.20 6.97 (m, 7H), 6.58 (dd, J = 15.3, 4.4 Hz, 1H), 6.21 (dt, J = 15.3, 2.1 Hz, 1H), 4.46 (s, 1H), 4.17 (s, 1H), 3.17 2.94 (m, 2H), 2.63 2.50 (m, 2H), 2.23 (d, J = 2.7 Hz, 3H), 1.82 1.62 (m, 2H). ^{13}C NMR (75 MHz, DMSO-d_6): δ 167.8, 150.5, 149.1, 141.1, 136.4, 131.7, 130.0, 129.2 (d, J = 5.5 Hz), 128.3 (d, J = 6.1 Hz), 127.4, 125.9, 123.4, 122.6, 53.5, 49.2, 34.3, 31.1, 20.7.

*(S) 1 (((S,E) 1 (Benzylsulfonyl) 1 fluoro 5 phenylpent 1 en 3 yl) amino) 1 oxo 3 (p tolyl)propan 2 aminium Chloride (**35**).* Synthesized by following procedure F with 0.29 g of compound **26** in 10 mL 4 M HCl/dioxane. Yield: 0.26 g (99%). The crude product was used without further purification and characterization for the next step.

*Phenyl (S,E) 1 Fluoro 3 ((S) 2 (isonicotinamido) 3 phenylpropa namido) 5 phenylpent 1 ene 1 sulfonate (**2a**).* Synthesized by following procedure E with 0.14 g of compound **14**, 0.10 g compound **X**, 0.13 g TBTU, 0.062 HOBt, and 0.21 mL DIEA. Column chromatography: petroleum ether/EtOAc 1:3 to 0:1. Yield: 0.16 g (73%), colorless solid. mp 71 73 °C. ^{1}H NMR (300 MHz, $CDCl_3$): δ 8.70 (d, J = 5.9 Hz, 2H), 7.64 (d, J = 6.0 Hz, 2H), 7.51 (d, J = 7.6 Hz, 1H), 7.45 7.34 (m, 2H), 7.34 7.11 (m, 9H), 7.12 7.02 (m, 2H), 6.97 (d, J = 6.6 Hz, 2H), 6.22 (d, J = 7.6 Hz, 1H), 5.61 (dd, $J_{H\ F}$ = 31.0 Hz, $J_{H\ H}$ = 9.2 Hz, 1H), 4.80 4.62 (m, 2H), 3.22 (dd, J = 13.3, 6.2 Hz, 1H), 2.96 (dd, J = 13.3, 9.0 Hz, 1H), 2.52 2.27 (m, 2H), 1.82 1.55 (m, 2H). ^{13}C NMR (75 MHz, $CDCl_3$): δ 170.2, 164.8, 149.3, 149.2 (d, $J_{C\ F}$ = 297 Hz), 147.2, 142.1, 139.9, 136.0, 130.3, 129.3, 129.1, 128.8, 128.3, 128.1, 127.7, 126.6, 122.4, 121.8, 120.94 (d, $J_{C\ F}$ = 4.8 Hz), 55.7, 44.9 (d, $J_{C\ F}$ = 1.9 Hz), 38.9, 35.3, 31.7. mp 71 73 °C. LC MS (ESI, m/z): $[M + H]^+$ calcd for $C_{32}H_{30}FN_3O_5S$, 588.20; found, 588.3. Purity: 97%. $[\alpha]_D^{22}$ 10° (c 0.5, $CHCl_3$).

*Phenyl (S,Z) 1 Fluoro 3 ((S) 2 (isonicotinamido) 3 phenylpropa namido) 5 phenylpent 1 ene 1 sulfonate (**2a (Z)**).* Synthesized by following procedure E with 0.10 g of compound **14**-(**Z**), 0.073 g compound **X**, 0.086 g TBTU, 0.041 g HOBt, and 0.14 mL DIEA. Column chromatography: petroleum ether/EtOAc 1:3. Yield: 0.12 g

https://doi.org/10.1021/acs.jmedchem.1c01002
J. Med. Chem. 2021, 64, 12322 12358

(79%), colorless solid. ^{1}H NMR (300 MHz, $CDCl_3$): δ 8.65 (d, J = 5.5 Hz, 2H), 7.85 (d, J = 7.4 Hz, 1H), 7.60 (d, J = 5.3 Hz, 2H), 7.44 7.07 (m, 14H), 6.98 6.83 (m, 2H), 6.38 (d, J = 7.2 Hz, 1H), 5.58 (dd, $J_{H\ F}$ = 20.5 Hz, $J_{H\ H}$ = 10.1 Hz, 1H), 4.96 (dt, J = 14.8, 6.6 Hz, 1H), 4.77 (q, J = 7.7 Hz, 1H), 3.24 (dd, J = 13.5, 6.6 Hz, 1H), 3.08 (dd, J = 13.4, 8.7 Hz, 1H), 2.37 2.22 (m, 1H), 2.20 2.08 (m, 1H), 1.69 1.52 (m, 1H), 1.43 1.32 (m, 1H). ^{13}C NMR (75 MHz, $CDCl_3$): δ 170.7, 164.9, 149.3, 149.1, 148.25 (d, $J_{C\ F}$ = 290 Hz), 141.9, 140.3, 136.4, 130.2, 129.5, 129.0, 128.6, 128.7, 128.2, 127.5, 126.4, 122.5 (d, $J_{C\ F}$ = 11.4 Hz), 122.3, 121.8, 55.8, 45.9 (d, $J_{C\ F}$ = 5.5 Hz), 38.6, 35.8 (d, $J_{C\ F}$ = 2.3 Hz), 31.6. mp 173 175 °C. LC MS (ESI, m/z): $[M + H]^+$ calcd for $C_{32}H_{30}FN_3O_5S$, 588.20; found, 588.3. Purity: 95%. $[\alpha]_D^{22}$ 13° (c 0.5, $CHCl_3$).

*Phenyl (S,E) 3 ((S) 2 (2,3 Dihydrobenzo[b][1,4]dioxine 6 carbox amido) 3 phenylpropanamido) 1 fluoro 5 phenylpent 1 ene 1 sulfonate (**2b**).* Synthesized by following procedure D with 0.10 g of compound **28**, 0.035 g 1,4-benzodioxane-6-carboxylic acid, 0.062 g TBTU, and 0.10 mL DIEA. Column chromatography: petroleum ether/EtOAc 2:1. Yield: 0.088 g (71%), colorless solid. ^{1}H NMR (300 MHz, $CDCl_3$): δ 7.46 7.35 (m, 2H), 7.35 7.10 (m, 11H), 7.04 (d, J = 6.5 Hz, 2H), 6.96 6.80 (m, 4H), 6.60 (d, J = 7.4 Hz, 1H), 5.60 (dd, $J_{H\ F}$ = 31.0 Hz, $J_{H\ H}$ = 9.0 Hz, 1H), 4.82 (q, J = 7.4 Hz, 1H), 4.67 (quint, J = 7.8 Hz, 1H), 4.34 4.19 (m, 4H), 3.17 (dd, J = 13.2, 6.2 Hz, 1H), 2.96 (dd, J = 13.2, 8.6 Hz, 1H), 2.45 2.26 (m, 2H), 1.72 1.52 (m, 2H). ^{13}C NMR (75 MHz, $CDCl_3$): δ 170.9, 167.0, 149.4, 149.0 (d, $J_{C\ F}$ = 297 Hz), 147.0, 143.6, 140.1, 136.3, 130.2, 129.4, 129.0, 128.6, 128.3, 128.0, 127.4, 126.4, 122.4, 121.4 (d, $J_{C\ F}$ = 4.4 Hz), 120.7, 117.5, 116.8, 64.7, 64.3, 55.2, 44.8 (d, $J_{C\ F}$ = 2.0 Hz), 38.9, 35.2 (d, $J_{C\ F}$ = 1.5 Hz), 31.6. mp 167 168 °C. LC MS (ESI, m/z): $[M + H]^+$ calcd for $C_{35}H_{33}FN_2O_7S$, 645.2; found, 645.3. Purity: 98%. $[\alpha]_D^{22}$ 12° (c 1, $CHCl_3$).

*Phenyl (S,E) 1 Fluoro 3 ((S) 2 (isonicotinamido) 3 (p tolyl) propanamido) 5 phenylpent 1 ene 1 sulfonate (**2d**).* Synthesized by following procedure D with 0.12 g of compound **34**, 0.028 g isonicotinic acid, 0.073 g TBTU, and 0.12 mL DIEA. Column chromatography: petroleum ether/EtOAc 1:3. Yield: 0.10 g (77%), colorless solid. ^{1}H NMR (300 MHz, $CDCl_3$): δ 8.69 (d, J = 3.5 Hz, 2H), 7.56 (d, J = 3.5 Hz, 2H), 7.44 7.36 (m, 3H), 7.36 7.12 (m, 7H), 7.06 (d, J = 7.7 Hz, 2H), 7.01 6.88 (m, 4H), 6.29 (d, J = 7.7 Hz, 1H), 5.62 (dd, $J_{H\ F}$ = 31.0 Hz, $J_{H\ H}$ = 9.1 Hz, 1H), 4.81 4.63 (m, 2H), 3.16 (dd, J = 13.4, 5.7 Hz, 1H), 2.92 (dd, J = 12.9, 9.6 Hz, 1H), 2.47 2.30 (m, 2H), 2.27 (s, 3H), 1.80 1.56 (m, 3H). ^{13}C NMR (75 MHz, $CDCl_3$): δ 170.3, 165.3, 150.4, 149.3, 149.2 (d, $J_{C\ F}$ = 297 Hz), 141.0, 139.9, 137.4, 132.8, 130.2, 129.8, 129.2, 128.8, 128.2, 128.1, 126.6, 122.4, 121.2, 120.9 (d, $J_{C\ F}$ = 5.2 Hz), 55.6, 44.8 (d, $J_{C\ F}$ = 1.6 Hz), 38.6, 35.4, 31.6, 21.1. mp 78 79 °C. LC MS (ESI, m/z): $[M + H]^+$ calcd for $C_{33}H_{32}FN_3O_5S$, 602.21; found, 602.3. Purity: 97%. $[\alpha]_D^{22}$ 8° (c 0.5, MeOH).

*Phenyl (S,E) 3 ((S) 2 (Isonicotinamido) 3 ((p tolyl) propanamido) 5 phenylpent 1 ene 1 sulfonate (**2d (H)**).* Synthesized by following procedure D with 0.21 g of compound **34**-(**H**), 0.054 g isonicotinic acid, 0.014 g TBTU, and 0.28 mL DIEA. Column chromatography: cyclohexane/EtOAc 1:3. Yield: 0.080 g (35%), colorless solid. ^{1}H NMR (300 MHz, $CDCl_3$): δ 8.71 (d, J = 13.0 Hz, 2H), 7.65 (d, J = 21.2 Hz, 2H), 7.52 7.41 (m, 1H), 7.42 7.32 (m, 1H), 7.32 7.23 (m, 3H), 7.22 7.15 (m, 4H), 7.15 7.03 (m, 2H), 7.02 6.90 (m, 2H), 6.71 6.59 (m, 1H), 6.51 (dd, J = 15.2, 5.1 Hz, 1H), 6.32 (d, J = 7.7 Hz, 1H), 5.99 (dd, J = 15.2, 1.5 Hz, 1H), 4.92 4.73 (m, 1H), 4.53 (s, 1H), 3.29 3.13 (m, 1H), 3.07 (dd, J = 13.5, 8.9 Hz, 1H), 2.60 2.40 (m, 2H), 2.32 (s, 3H), 1.83 1.58 (m, 3H). ^{13}C NMR (75 MHz, $CDCl_3$): δ 170.5, 164.5, 149.4, 148.7, 139.9, 137.6, 132.7, 129.9, 129.1, 128.7, 128.3, 127.4, 126.5, 124.6, 122.5, 126.6, 55.9, 49.6, 35.1, 31.7, 21.1. mp 84 86 °C. LC MS (ESI, m/z): $[M + H]^+$ calcd for $C_{33}H_{33}N_3O_5S$, 584.21; found, 584.3. Purity: 98%. $[\alpha]_D^{22}$ 11° (c 0.5, MeOH).

*Phenyl (S,E) 3 ((S) 2 (2,3 Dihydrobenzo[b][1,4]dioxine 6 carbox amido) 3 (p tolyl)propan amido) 1 fluoro 5 phenylpent 1 ene 1 sulfonate (**2e**).* Synthesized by following procedure D with 0.100 g of compound **34**, 0.034 g 1,4-benzodioxane-6-carboxylic acid, 0.060 g TBTU, and 0.10 mL DIEA. Column chromatography: petroleum ether/EtOAc 2:1. Yield: 0.094 g (78%), colorless solid. ^{1}H NMR (300 MHz, $CDCl_3$): δ 7.46 7.35 (m, 2H), 7.34 7.23 (m, 5H), 7.23 7.12 (m, 4H), 7.03 (d, J = 7.9 Hz, 2H), 6.97 6.88 (m, 4H), 6.88 6.78 (m, 2H), 6.58 (d, J = 7.7 Hz, 1H), 5.61 (dd, $J_{H\ F}$ = 31.2 Hz, $J_{H\ H}$ = 9.1 Hz, 1H), 4.85 4.60 (m, 2H), 4.34 4.20 (m, 4H), 3.12 (dd, J = 13.3, 6.1 Hz, 1H), 2.91 (dd, J = 13.3, 8.6 Hz, 1H), 2.44 2.30 (m, 2H), 2.26 (s, 3H), 1.72 1.55 (m, 2H). ^{13}C NMR (75 MHz, $CDCl_3$): δ 170.9, 166.8, 149.4, 148.9 (d, $J_{C\ F}$ = 296 Hz), 147.1, 143.6, 140.1, 137.1, 133.2, 130.2, 129.6, 129.3, 128.6, 128.3, 128.0, 126.4, 122.4, 121.5 (d, $J_{C\ F}$ = 4.6 Hz), 120.6, 117.5, 116.8, 64.7, 64.3, 55.3, 44.7 (d, $J_{C\ F}$ = 1.7 Hz), 38.5, 35.3, 31.6, 21.1. mp 92 93 °C. LC MS (ESI, m/z): $[M + H]^+$ calcd for $C_{36}H_{35}FN_2O_7S$, 659.22; found, 659.3. Purity: 95%. $[\alpha]_D^{22}$ 26° (c 1, MeOH).

*Phenyl (S,E) 3 ((S) 2 (3,5 Difluorobenzamido) 3 (p tolyl) propanamido) 1 fluoro 5 phenylpent 1 ene 1 sulfonate (**2f**).* Synthesized by following procedure D with 0.10 g of compound **34**, 0.030 g 3,5-difluorobenzoic acid, 0.060 g TBTU, and 0.10 mL DIEA. Column chromatography: petroleum ether/EtOAc 3:1. Yield: 0.097 g (81%), colorless solid. ^{1}H NMR (300 MHz, $CDCl_3$): δ 7.46 7.10 (m, 12H), 7.04 (d, J = 7.8 Hz, 2H), 6.99 6.84 (m, 5H), 6.23 (d, J = 7.7 Hz, 1H), 5.58 (dd, $J_{H\ F}$ = 31.0 Hz, $J_{H\ H}$ = 9.2 Hz, 1H), 4.80 4.60 (m, 2H), 3.15 (dd, J = 13.3, 6.0 Hz, 1H), 2.91 (dd, J = 13.3, 9.1 Hz, 1H), 2.49 2.31 (m, 2H), 2.26 (s, 3H), 1.73 1.56 (m, 2H). ^{13}C NMR (75 MHz, $CDCl_3$): δ 170.6, 164.9 (t, $J_{C\ F}$ = 2.6 Hz), 163.0 (dd, $J_{C\ F}$ = 251, 12 Hz), 149.3, 149.2 (d, $J_{C\ F}$ = 297 Hz), 140.0, 137.4, 136.8 (t, $J_{C\ F}$ = 8.5 Hz), 132.9, 130.2, 129.8, 129.2, 128.7, 128.3, 128.1, 126.6, 122.4, 121.0 (d, J = 5.0 Hz), 110.5 (dd, $J_{C\ F}$ = 26.2, 8.8 Hz), 107.4 (t, $J_{C\ F}$ = 25.4 Hz), 55.8, 44.9 (d, $J_{C\ F}$ = 2.4 Hz), 38.5, 35.4 (d, $J_{C\ F}$ = 1.6 Hz), 31.7, 21.1. mp 175 177 °C. LC MS (ESI, m/z): $[M + H]^+$ calcd for $C_{34}H_{31}F_3N_2O_5S$, 637.20; found, 637.2. Purity: >99%. $[\alpha]_D^{22}$ 7° (c 0.5, $CHCl_3$).

*Phenyl (S,E) 1 Fluoro 3 ((S) 2 (isonicotinamido) 3 (m tolyl) propanamido) 5 phenylpent 1 ene 1 sulfonate (**2g**).* Synthesized by following procedure D with 0.11 g of compound **31**, 0.026 g isonicotinic acid, 0.067 g TBTU, and 0.11 mL DIEA. Column chromatography: petroleum ether/EtOAc 1:3. Yield: 0.096 g (77%), colorless solid. ^{1}H NMR (300 MHz, $CDCl_3$): δ 8.62 (d, J = 4.6 Hz, 2H), 7.49 (d, J = 4.0 Hz, 2H), 7.39 7.03 (m, 11H), 6.97 (d, J = 7.3 Hz, 1H), 6.94 6.81 (m, 3H), 6.74 (d, J = 7.3 Hz, 1H), 6.10 (d, J = 7.5 Hz, 1H), 5.57 (dd, $J_{H\ F}$ = 31.0 Hz, $J_{H\ H}$ = 9.1 Hz, 1H), 4.74 4.50 (m, 2H), 3.11 (dd, J = 13.1, 5.7 Hz, 1H), 2.88 2.78 (m, 1H), 2.39 2.21 (m, 2H), 2.17 (s, 3H), 1.72 1.49 (m, 2H). ^{13}C NMR (75 MHz, $CDCl_3$): δ 170.2, 165.3, 150.3, 149.33, 149.25 (d, $J_{C\ F}$ = 297 Hz), 147.3, 141.2, 139.9, 138.9, 136.0, 130.2, 130.0, 129.0, 128.8, 128.5, 128.2, 128.1, 126.6, 126.4, 122.4, 121.2, 120.9 (d, $J_{C\ F}$ = 5.0 Hz), 55.5, 45.0 (d, $J_{C\ F}$ = 2.0 Hz), 38.9, 35.4, 31.6, 21.4. mp 67 68 °C. LC MS (ESI, m/z): $[M + H]^+$ calcd for $C_{33}H_{32}FN_3O_5S$, 602.21; found, 602.3. Purity: >99%. $[\alpha]_D^{22}$ 8° (c 0.5, $CHCl_3$).

*Phenyl (S,E) 3 ((S) 2 (2,3 Dihydrobenzo[b][1,4]dioxine 6 carbox amido) 3 (m tolyl)propanamido) 1 fluoro 5 phenylpent 1 ene 1 sulfonate (**2h**).* Synthesized by following procedure D with 0.10 g of compound **31**, 0.034 g 1,4-benzodioxane-6-carboxylic acid, 0.060 g TBTU, and 0.10 mL DIEA. Column chromatography: petroleum ether/EtOAc 2:1. Yield: 0.088 g (72%), colorless solid. ^{1}H NMR (300 MHz, $CDCl_3$): δ 7.37 7.27 (m, 2H), 7.27 6.99 (m, 10H), 6.94 (d, J = 7.7 Hz, 1H), 6.91 6.80 (m, 3H), 6.80 6.70 (m, 3H), 6.52 (d, J = 7.7 Hz, 1H), 5.57 (dd, $J_{H\ F}$ = 31.1 Hz, $J_{H\ F}$ = 9.1 Hz, 1H), 4.73 (q, J = 7.9 Hz, 1H), 4.59 (quint, J = 7.6 Hz, 1H), 4.26 4.09 (m, 4H), 3.07 (dd, J = 13.4, 6.3 Hz, 1H), 2.85 (dd, J = 13.4, 8.5 Hz, 1H), 2.38 2.19 (m, 2H), 2.15 (s, 3H), 1.65 1.46 (m, 2H). ^{13}C NMR (75 MHz, $CDCl_3$): δ 170.9, 166.9, 149.4, 149.0 (d, $J_{C\ F}$ = 297 Hz), 147.1, 143.6, 140.1, 138.7, 136.3, 130.2, 130.1, 128.8, 128.6, 128.3, 128.2, 128.0, 126.8, 126.5, 126.4, 122.4, 121.4 (d, $J_{C\ F}$ = 3.6 Hz), 120.6, 117.5, 116.8, 64.7, 64.3, 55.2, 44.9 (d, $J_{C\ F}$ = 1.1 Hz), 38.8, 35.3, 31.6, 21.4. mp 126 128 °C. LC MS (ESI, m/z): $[M + H]^+$ calcd for $C_{36}H_{35}FN_2O_7S$, 659.22; found, 659.3. Purity: 98%. $[\alpha]_D^{22}$ 3° (c 0.5, MeOH).

*Phenyl (S,E) 3 ((S) 2 (3,5 Difluorobenzamido) 3 (m tolyl) propanamido) 1 fluoro 5 phenylpent 1 ene 1 sulfonate (**2i**).* Synthesized by following procedure D with 0.10 g of compound **31**, 0.030 g 3,5-difluorobenzoic acid, 0.060 g TBTU, and 0.10 mL DIEA. Column

https://doi.org/10.1021/acs.jmedchem.1c01002
J. Med. Chem. 2021, 64, 12322 12358

chromatography: petroleum ether/EtOAc 3:1. Yield: 0.075 g (62%), colorless solid. ^{1}H NMR (300 MHz, $CDCl_3$): δ 7.36 7.27 (m, 2H), 7.28 7.03 (m, 10H), 7.03 6.94 (m, 2H), 6.94 6.80 (m, 4H), 6.74 (d, J = 7.4 Hz, 1H), 5.82 (d, J = 7.7 Hz, 1H), 5.54 (dd, $J_{H\ F}$ = 30.9 Hz, $J_{H\ H}$ = 9.1 Hz, 1H), 4.68 4.52 (m, 2H), 3.10 (dd, J = 13.4, 6.0 Hz, 1H), 2.80 (dd, J = 13.3, 9.1 Hz, 1H), 2.41 2.21 (m, J = 7.2 Hz, 2H), 2.19 (s, 3H), 1.68 1.57 (m, 2H). ^{13}C NMR (75 MHz, $CDCl_3$): δ 170.3, 165.0 (t, $J_{C\ F}$ = 2.7 Hz), 163.0 (dd, $J_{C\ F}$ = 251, 12 Hz), 149.4, 149.3 (d, $J_{C\ F}$ = 298 Hz), 139.9, 139.0, 137.0, 136.9, 136.8, 136.1, 130.2, 130.0, 129.1, 128.8, 128.5, 128.3, 128.1, 126.6, 126.4, 122.4, 120.9 (d, $J_{C\ F}$ = 5.0 Hz), 110.5 (dd, $J_{C\ F}$ = 26, 8.7 Hz), 107.5 (t, $J_{C\ F}$ = 25 Hz), 55.6, 45.0 (d, $J_{C\ F}$ = 2.3 Hz), 38.8, 35.4, 31.6, 21.4. mp 129 130 °C. LC MS (ESI, m/z): $[M + H]^+$ calcd for $C_{34}H_{31}F_3N_2O_5S$, 637.20; found, 637.3. Purity: 96%. $[\alpha]_D^{22}$ 9° (c 0.5, MeOH).

*Phenyl (S,E) 3 ((S) 2 (((Benzyloxy)carbonyl)amino) 3 phenylpropanamido) 1 fluoro 5 phenylpent 1 ene 1 sulfonate (**2j**).* Synthesized by following procedure E with 0.090 g of compound **14**, 0.076 g Cbz-L-Phe-OH, 0.082 g TBTU, 0.039 g HOBt, and 0.13 mL DIEA. Column chromatography: petroleum ether/EtOAc 2:1. Yield: 0.12 g (78%), colorless solid. ^{1}H NMR (300 MHz, $CDCl_3$): δ 7.48 7.14 (m, 17H), 7.06 6.92 (m, 4H), 5.56 (dd, $J_{H\ F}$ = 31.1 Hz, $J_{H\ H}$ = 9.0 Hz, 2H), 5.32 (d, J = 5.7 Hz, 1H), 5.06 (s, 2H), 4.68 (quint, J = 7.5 Hz, 1H), 4.22 (d, J = 6.6 Hz, 1H), 3.07 (dd, J = 13.4, 6.0 Hz, 1H), 2.83 (dd, J = 13.4, 8.6 Hz, 1H), 2.52 2.30 (m, 2H), 1.80 1.64 (m, 2H). ^{13}C NMR (75 MHz, $CDCl_3$): δ 170.3, 156.4, 149.4, 149.0 (d, $J_{C\ F}$ = 297 Hz), 140.1, 136.2, 136.1, 130.2, 129.3, 129.1, 128.8, 128.7, 128.5, 128.3, 128.2, 128.0, 127.5, 126.6, 122.5, 121.1 (d, $J_{C\ F}$ = 4.6 Hz), 67.4, 56.6, 44.9 (d, $J_{C\ F}$ = 1.1 Hz), 38.9, 35.2, 31.7. mp 127 128 °C. LC MS (ESI, m/z): $[M + H]^+$ calcd for $C_{34}H_{33}FN_2O_6S$, 617.21; found, 617.4. Purity: >99%. $[\alpha]_D^{22}$ 17° (c 0.5, $CHCl_3$).

*Phenyl (S,E) 1 Fluoro 3 ((S) 2 (4 methylpiperazine 1 carboxamido) 3 phenylpropanamido) 5 phenylpent 1 ene 1 sulfonate (**2k**).* Synthesized by following procedure E with 0.11 g of compound **14**, 0.086 g compound **IX**, 0.095 g TBTU, and 0.155 mL DIEA. Column chromatography: DCM/MeOH 95:5. Yield: 0.096 g (59%), colorless solid. ^{1}H NMR (300 MHz, $CDCl_3$): δ 7.45 7.35 (m, 2H), 7.35 7.14 (m, 10H), 7.06 6.93 (m, 4H), 6.62 (d, J = 7.6 Hz, 1H), 5.62 (dd, $J_{H\ F}$ = 31.2 Hz, $J_{H\ H}$ = 9.1 Hz, 1H), 5.21 (d, J = 7.6 Hz, 1H), 4.66 (quint, J = 7.7 Hz, 1H), 4.45 (q, J = 7.9 Hz, 1H), 3.42 3.24 (m, 4H), 3.05 (dd, J = 13.4, 6.5 Hz, 1H), 2.88 (dd, J = 13.4, 8.4 Hz, 1H), 2.49 2.33 (m, 6H), 2.31 (s, 3H), 1.78 1.52 (m, 3H). ^{13}C NMR (75 MHz, $CDCl_3$): δ 171.8, 156.9, 149.4, 148.9 (d, $J_{C\ F}$ = 297 Hz), 140.2, 136.8, 130.2, 129.4, 128.9, 128.7, 128.4, 128.0, 127.3, 126.5, 122.4, 121.5 (d, $J_{C\ F}$ = 5.1 Hz), 56.1, 54.4, 45.9, 44.7, 43.6, 39.1, 35.4, 31.6. mp 109 110 °C. LC MS (ESI, m/z): $[M + H]^+$ calcd for $C_{32}H_{37}FN_4O_5S$, 608.26; found, 609.3. Purity: >99%. $[\alpha]_D^{22}$ 10° (c 0.5, $CHCl_3$).

*N ((S) 1 (((S,E) 1 (Benzylsulfonyl) 1 fluoro 5 phenylpent 1 en 3 yl)amino) 1 oxo 3 phenylpropan 2 yl)isonicotinamide (**3a**).* Synthesized by following procedure E with 0.11 g of compound **15**, 0.080 g compound **X**, 0.095 g TBTU, 0.045 g HOBt, and 0.155 mL DIEA. Column chromatography: pure EtOAc. Yield: 0.14 g (81%), colorless solid. ^{1}H NMR (300 MHz, DMSO-d_6): δ 8.97 (d, J = 7.9 Hz, 1H), 8.71 (d, J = 4.4 Hz, 2H), 8.35 (d, J = 7.8 Hz, 1H), 7.70 (d, J = 4.4 Hz, 2H), 7.44 7.08 (m, 15H), 5.81 (dd, $J_{H\ F}$ = 34.1 Hz, $J_{H\ H}$ = 8.8 Hz, 1H), 4.75 (s, 2H), 4.70 4.50 (m, 2H), 3.19 2.87 (m, 2H), 2.49 2.39 (m, 3H), 1.86 1.56 (m, 2H). ^{13}C NMR (75 MHz, DMSO): δ 170.4, 164.8, 151.4 (d, $J_{C\ F}$ = 298 Hz), 150.2, 140.9, 140.9, 137.9, 131.0, 129.1, 128.8, 128.6, 128.30, 128.29, 128.1, 127.5, 126.4, 125.9, 121.4, 120.4 (d, $J_{C\ F}$ = 3.8 Hz), 57.6, 55.0, 43.7 (d, $J_{C\ F}$ = 2.0 Hz), 37.0, 35.0, 30.9. mp 169 171 °C. LC MS (ESI, m/z): $[M + H]^+$ calcd for $C_{33}H_{32}FN_3O_4S$, 586.22; found, 586.4. Purity: 96%. $[\alpha]_D^{22}$ 9° (c 0.5, MeOH).

*N ((S) 1 (((S,E) 1 (Benzylsulfonyl) 1 fluoro 5 phenylpent 1 en 3 yl)amino) 1 oxo 3 phenylpropan 2 yl) 2,3 dihydrobenzo[b][1,4] dioxine 6 carboxamide (**3b**).* Synthesized by following procedure D with 0.100 g of compound **29**, 0.036 g 1,4-benzodioxane-6-carboxylic acid, 0.064 g TBTU, and 0.104 mL DIEA. Column chromatography: petroleum ether/EtOAc 2:1 to pure EtOAc. Yield: 0.096 g (75%), colorless solid. ^{1}H NMR (300 MHz, DMSO-d_6): δ 8.44 (d, J = 8.1 Hz, 1H), 8.24 (d, J = 8.0 Hz, 1H), 7.45 7.09 (m, 17H), 6.89 (d, J = 8.3 Hz, 1H), 5.82 (dd, $J_{H\ F}$ = 34.2 Hz, $J_{H\ H}$ = 9.0 Hz, 1H), 4.74 (s, 2H), 4.65 4.47 (m, 2H), 4.34 4.16 (m, 4H), 3.11 2.91 (m, 2H), 2.48 2.35 (m, 2H), 1.87 1.54 (m, 2H). ^{13}C NMR (75 MHz, DMSO-d_6): δ 171.0, 165.4, 151.3 (d, $J_{C\ F}$ = 297 Hz), 146.1, 142.8, 140.9, 138.2, 131.0, 129.1, 128.7, 128.6, 128.3, 128.1, 127.5, 127.0, 126.2, 125.9, 120.9, 120.5 (d, $J_{C\ F}$ = 3.9 Hz), 116.6, 116.5, 64.3, 64.0, 57.6, 55.0, 43.6 (d, $J_{C\ F}$ = 2.4 Hz), 36.9, 35.0, 30.9. mp 204 206 °C (decomposition). LC MS (ESI, m/z): $[M + H]^+$ calcd for $C_{36}H_{35}FN_2O_6S$, 643.23; found, 643.3. Purity: >99%. $[\alpha]_D^{22}$ 7° (c 0.5, $CHCl_3$/MeOH 1:1).

*N ((S) 1 (((S,E) 1 (Benzylsulfonyl) 1 fluoro 5 phenylpent 1 en 3 yl)amino) 1 oxo 3 phenylpropan 2 yl) 3,5 difluorobenzamide (**3c**).* Synthesized by following procedure D with 0.120 g of compound **29**, 0.037 g 3,5-difluorobenzoic acid, 0.075 g TBTU, and 0.12 mL DIEA. Column chromatography: petroleum ether/EtOAc 3:1. Yield: 0.094 g (65%), colorless solid. ^{1}H NMR (300 MHz, DMSO-d_6): δ 8.86 (d, J = 8.2 Hz, 1H), 8.35 (d, J = 7.9 Hz, 1H), 7.56 7.41 (m, 3H), 7.41 7.10 (m, 16H), 5.81 (dd, $J_{H\ F}$ = 34.2 Hz, $J_{H\ H}$ = 9.1 Hz, 1H), 4.75 (s, 2H), 4.69 4.51 (m, 2H), 3.09 (dd, J = 13.7, 5.1 Hz, 1H), 2.97 (dd, J = 13.7, 10.1 Hz, 1H), 2.49 2.40 (m, 2H), 1.86 1.57 (m, 2H). ^{13}C NMR (75 MHz, DMSO-d_6): δ 170.48, 163.7 (t, $J_{C\ F}$ = 2.8 Hz), 162.2 (dd, $J_{C\ F}$ = 251, 12 Hz), 151.4 (d, $J_{C\ F}$ = 298 Hz), 140.9, 137.9, 137.4 (t, $J_{C\ F}$ = 8.5 Hz), 137.3, 131.0, 129.1, 128.8, 128.6, 128.3, 128.1, 127.5, 126.4, 126.0, 120.4 (d, $J_{C\ F}$ = 4.1 Hz), 110.8 (dd, $J_{C\ F}$ = 27, 8.7 Hz), 106.9 (t, $J_{C\ F}$ = 26 Hz), 57.6, 55.2, 43.7 (d, $J_{C\ F}$ = 2.3 Hz), 37.0, 35.0, 30.9. mp 194 196 °C (decomposition). LC MS (ESI, m/z): $[M + H]^+$ calcd for $C_{34}H_{31}F_3N_2O_4S$, 621.2; found, 621.3. Purity: >99%. $[\alpha]_D^{22}$ 6° (c 0.5, $CHCl_3$).

*N ((S) 1 (((S,E) 1 (Benzylsulfonyl) 1 fluoro 5 phenylpent 1 en 3 yl)amino) 1 oxo 3 (p tolyl)propan 2 yl)isonicotinamide (**3d**).* Synthesized by following procedure D with 0.11 g of compound **35**, 0.026 g isonicotinic acid, 0.067 g TBTU, and 0.11 mL DIEA. Column chromatography: petroleum ether/EtOAc 1:3. Yield: 0.091 g (73%), colorless solid. ^{1}H NMR (300 MHz, $CDCl_3$): δ 8.69 (d, J = 6.0 Hz, 2H), 7.61 7.53 (m, 2H), 7.43 7.28 (m, 6H), 7.25 7.14 (m, 3H), 7.07 (d, J = 7.8 Hz, 2H), 7.01 6.88 (m, 4H), 6.19 (d, J = 7.9 Hz, 1H), 5.55 (dd, $J_{H\ F}$ = 32.6 Hz, $J_{H\ H}$ = 9.2 Hz, 1H), 4.76 4.59 (m, 2H), 4.36 (s, 2H), 3.14 (dd, J = 13.5, 6.0 Hz, 1H), 2.93 (dd, J = 13.4, 8.6 Hz, 1H), 2.44 2.19 (m, 5H), 1.75 1.50 (m, 2H). ^{13}C NMR (75 MHz, $CDCl_3$): δ 170.2, 165.1, 152.5 (d, $J_{C\ F}$ = 301 Hz), 141.3, 140.1, 137.3, 132.8, 131.0, 129.8, 129.5, 129.3, 129.2, 128.7, 128.3, 126.7, 126.5, 121.3, 119.4 (d, $J_{C\ F}$ = 4.3 Hz), 58.7, 55.6, 44.7 (d, $J_{C\ F}$ = 2.2 Hz), 38.4, 35.6 (d, $J_{C\ F}$ = 1.6 Hz), 31.6, 21.2. mp 181 183 °C. LC MS (ESI, m/z): $[M + H]^+$ calcd for $C_{34}H_{34}FN_3O_4S$, 600.24; found, 600.4. Purity: 95%. $[\alpha]_D^{22}$ 13° (c 0.5, MeOH).

*N ((S) 1 (((S,E) 1 (Benzylsulfonyl) 1 fluoro 5 phenylpent 1 en 3 yl)amino) 1 oxo 3 (p tolyl)propan 2 yl) 2,3 dihydrobenzo[b][1,4] dioxine 6 carboxamide (**3e**).* Synthesized by following procedure D with 0.110 g of compound **35**, 0.037 g 1,4-benzodioxane-6-carboxylic acid, 0.067 g TBTU, and 0.108 mL DIEA. Column chromatography: petroleum ether/EtOAc 1:1 to 0:1. Yield: 0.10 g (76%), colorless solid. ^{1}H NMR (300 MHz, DMSO-d_6): δ 8.41 (d, J = 8.0 Hz, 1H), 8.23 (d, J = 8.0 Hz, 1H), 7.43 7.23 (m, 9H), 7.23 7.11 (m, 5H), 7.04 (d, J = 7.9 Hz, 2H), 6.89 (d, J = 8.4 Hz, 1H), 5.81 (dd, $J_{H\ F}$ = 34.3 Hz, $J_{H\ H}$ = 9.1 Hz, 1H), 4.74 (s, 2H), 4.63 4.47 (m, 2H), 4.32 4.18 (m, 4H), 3.05 2.87 (m, 2H), 2.49 2.39 (m, 2H), 2.22 (s, 3H), 1.86 1.57 (m, 2H). ^{13}C NMR (75 MHz, DMSO-d_6): δ 171.0, 165.4, 151.3 (d, $J_{C\ F}$ = 297 Hz), 146.0, 142.8, 140.9, 135.14, 135.10, 131.0, 129.0, 128.8, 128.7, 128.6, 128.3, 127.5, 127.0, 125.9, 121.0, 120.5 (d, $J_{C\ F}$ = 3.7 Hz), 116.6, 116.5, 64.3, 64.0, 57.6, 55.1, 43.6 (d, $J_{C\ F}$ = 1.6 Hz), 36.6, 35.0, 30.9, 20.6. mp 193 195 °C. LC MS (ESI, m/z): $[M + H]^+$ calcd for $C_{37}H_{37}FN_2O_6S$, 657.25; found, 657.4. Purity: 97%. $[\alpha]_D^{22}$ 8° (c 0.5, $CHCl_3$/MeOH 1:1).

*N ((S) 1 (((S,E) 1 (Benzylsulfonyl) 1 fluoro 5 phenylpent 1 en 3 yl)amino) 1 oxo 3 (p tolyl)propan 2 yl) 3,5 difluorobenzamide (**3f**).* Synthesized by following procedure D with 0.12 g of compound **35**, 0.036 g 3,5-difluorobenzoic acid, 0.073 g TBTU, and 0.12 mL DIEA. Column chromatography: petroleum ether/EtOAc 3:1 to pure EtOAc. Yield: 0.12 g (81%), colorless solid. ^{1}H NMR (300 MHz, DMSO-d_6): δ 8.82 (d, J = 8.1 Hz, 1H), 8.32 (d, J = 8.0 Hz, 1H), 7.61 7.40 (m, 3H), 7.40 7.23 (m, 8H), 7.23 7.10 (m, 5H), 7.05 (d, J = 7.9

https://doi.org/10.1021/acs.jmedchem.1c01002
J. Med. Chem. 2021, 64, 12322 12358

Hz, 2H), 5.79 (dd, $J_{H\ F}$ = 33.9 Hz, $J_{H\ H}$ = 9.3 Hz, 1H), 4.75 (s, 2H), 4.65 4.48 (m, 2H), 3.02 (dd, J = 13.5, 5.1 Hz, 1H), 2.92 (dd, J = 13.6, 10.0 Hz, 1H), 2.48 2.39 (m, 1H), 2.22 (s, 3H), 1.83 1.56 (m, 2H). ^{13}C NMR (75 MHz, DMSO-d_6): δ 170.5, 163.86, 163.7 (t, $J_{C\ F}$ = 2.6 Hz), 162.1 (dd, $J_{C\ F}$ = 251, 12 Hz), 151.3 (d, $J_{C\ F}$ = 298 Hz), 140.9, 137.4 (t, $J_{C\ F}$ = 8.4 Hz), 135.3, 134.8, 131.0, 129.0, 128.7, 128.6, 128.3, 127.5, 126.0, 120.4 (d, $J_{C\ F}$ = 4.0 Hz), 110.8 (dd, $J_{C\ F}$ = 26, 8.4 Hz), 106.9 (t, $J_{C\ F}$ = 25 Hz), 57.6, 55.3, 43.7 (d, $J_{C\ F}$ = 1.5 Hz), 36.6, 35.0, 30.9, 20.6. mp 196 198 °C (decomposition). LC MS (ESI, m/z): $[M + H]^+$ calcd for $C_{35}H_{33}F_3N_2O_4S$, 635.22; found, 635.3. Purity: 95%. $[\alpha]_D^{22}$ 9° (c 0.5, MeOH/$CHCl_3$ 1:1).

*Phenyl (S,E) 1 Fluoro 3 ((S) 2 (isonicotinamido) 3 (m tolyl) propanamido) 5 phenylpent 1 ene 1 sulfonate (**3g**).* Synthesized by following procedure D with 0.11 g of compound **32**, 0.026 g isonicotinic acid, 0.067 g TBTU, and 0.11 mL DIEA. Column chromatography: petroleum ether/EtOAc 1:3. Yield: 0.086 g (69%), colorless solid. ^{1}H NMR (300 MHz, $CDCl_3$): δ 8.68 (d, J = 4.7 Hz, 2H), 7.56 (d, J = 5.7 Hz, 2H), 7.40 (d, J = 7.6 Hz, 1H), 7.37 7.28 (m, 5H), 7.25 7.11 (m, 4H), 7.04 (d, J = 7.6 Hz, 1H), 6.99 6.90 (m, 3H), 6.84 (d, J = 7.5 Hz, 1H), 6.24 (d, J = 7.8 Hz, 1H), 5.57 (dd, $J_{H\ F}$ = 32.5 Hz, $J_{H\ H}$ = 9.1 Hz, 1H), 4.78 4.58 (m, 2H), 4.36 (s, 2H), 3.15 (dd, J = 13.4, 6.2 Hz, 1H), 2.93 (dd, J = 13.4, 8.5 Hz, 1H), 2.43 2.26 (m, 2H), 2.24 (s, 3H), 1.74 1.48 (m, 2H). ^{13}C NMR (75 MHz, $CDCl_3$): δ 170.2, 165.2, 152.5 (d, $J_{C\ F}$ = 301 Hz), 150.3, 141.2, 140.1, 138.8, 136.0, 131.0, 130.0, 129.5, 129.2, 129.0, 128.7, 128.4, 128.3, 126.7, 126.5, 126.5, 121.2, 119.4 (d, $J_{C\ F}$ = 4.1 Hz), 58.7, 55.5, 44.8 (d, $J_{C\ F}$ = 2.3 Hz), 38.7, 35.6, 35.7, 31.6, 21.4. mp 81 82 °C. LC MS (ESI, m/z): $[M + H]^+$ calcd for $C_{34}H_{34}FN_3O_4S$, 600.24; found, 600.4. Purity: 95%. $[\alpha]_D^{22}$ 7° (c 0.5, MeOH).

*N ((S) 1 (((S,E) 1 (Benzylsulfonyl) 1 fluoro 5 phenylpent 1 en 3 yl)amino) 1 oxo 3 (m tolyl)propan 2 yl) 2,3 dihydrobenzo[b][1,4] dioxine 6 carboxamide (**3h**).* Synthesized by following procedure D with 0.11 g of compound **32**, 0.037 g 1,4-benzodioxane-6-carboxylic acid, 0.067 g TBTU and 0.11 mL DIEA. Column chromatography: petroleum ether/EtOAc 2:1 to 0:1. Yield: 0.094 g (69%), colorless solid. ^{1}H NMR (300 MHz, DMSO-d_6): δ 8.43 (d, J = 8.1 Hz, 1H), 8.25 (d, J = 8.0 Hz, 1H), 7.46 7.23 (m, 9H), 7.23 7.03 (m, 6H), 6.97 (d, J = 7.2 Hz, 1H), 6.90 (d, J = 8.3 Hz, 1H), 5.83 (dd, $J_{H\ F}$ = 34.2 Hz, $J_{H\ H}$ = 9.0 Hz, 1H), 4.74 (s, 2H), 4.64 4.49 (m, 2H), 4.39 4.17 (m, 4H), 3.08 2.86 (m, 2H), 2.49 2.38 (m, 2H), 2.23 (s, 3H), 1.87 1.55 (m, 2H). ^{13}C NMR (75 MHz, DMSO-d_6): δ 171.0, 165.5, 151.3 (d, $J_{C\ F}$ = 298 Hz), 146.1, 142.8, 140.9, 138.2, 137.0, 131.0, 129.8, 128.7, 128.6, 128.3, 127.9, 127.5, 127.1, 126.9, 126.2, 125.9, 120.9, 120.5 (d, $J_{C\ F}$ = 4.2 Hz), 116.6, 116.5, 64.3, 64.0, 57.6, 55.0, 43.6 (d, $J_{C\ F}$ = 0.9 Hz), 36.9, 35.1, 30.9, 21.0. mp 188 190 °C. LC MS (ESI, m/z): $[M + H]^+$ calcd for $C_{37}H_{37}FN_2O_6S$, 657.25; found, 657.4. Purity >99%. $[\alpha]_D^{22}$ 11° (c 0.5, $CHCl_3$).

*N ((S) 1 (((S,E) 1 (Benzylsulfonyl) 1 fluoro 5 phenylpent 1 en 3 yl)amino) 1 oxo 3 (m tolyl)propan 2 yl) 3,5 difluorobenzamide (**3i**).* Synthesized by following procedure D with 0.12 g of compound **32**, 0.036 g 3,5-difluorobenzoic acid, 0.073 g TBTU, and 0.12 mL DIEA. Column chromatography: petroleum ether/EtOAc 2:1. Yield: 0.11 g (77%), colorless solid. ^{1}H NMR (300 MHz, DMSO-d_6): δ 8.83 (d, J = 8.1 Hz, 1H), 8.33 (d, J = 7.8 Hz, 1H), 7.61 7.02 (m, 17H), 6.98 (d, J = 7.1 Hz, 1H), 5.81 (dd, $J_{H\ F}$ = 34.1 Hz, $J_{H\ H}$ = 9.0 Hz, 1H), 4.74 (s, 2H), 4.67 4.46 (m, 2H), 3.04 (dd, J = 13.5, 4.7 Hz, 1H), 2.93 (dd, J = 13.5, 4.7 Hz, 1H), 2.48 2.39 (m, 2H), 2.23 (s, 3H), 1.83 1.59 (m, 2H). ^{13}C NMR (75 MHz, DMSO-d_6): δ 170.5, 163.8 (t, $J_{C\ F}$ = 2.7 Hz), 162.1 (dd, $J_{C\ F}$ = 247 Hz, 13 Hz), 151.3 (d, $J_{C\ F}$ = 298 Hz), 140.9, 137.9, 137.5 (t, $J_{C\ F}$ = 8.5 Hz), 137.1, 131.0, 129.8, 128.8, 128.6, 128.3, 128.0, 127.5, 127.0, 126.2, 126.0, 120.42 (d, $J_{C\ F}$ = 3.5 Hz), 110.8 (dd, $J_{C\ F}$ = 25 Hz, 8.6 Hz), 106.8 (t, $J_{C\ F}$ = 26 Hz), 57.6, 55.2, 43.7 (d, $J_{C\ F}$ = 2.0 Hz), 36.9, 35.0, 30.9, 21.0. mp 176 178 °C. LC MS (ESI, m/z): $[M + H]^+$ calcd for $C_{35}H_{33}F_3N_2O_4S$, 635.22; found, 635.3. Purity >99%. $[\alpha]_D^{22}$ 6° (c 0.5, $CHCl_3$).

*N ((S) 1 (((S,E) 1 Fluoro 5 phenyl 1 (phenylsulfonyl)pent 1 en 3 yl)amino) 1 oxo 3 phenylpropan 2 yl)isonicotinamide (**4a**).*[11] Synthesized by following procedure E with 0.14 g of compound **13**, 0.107 g compound **X**, 0.13 g TBTU, 0.062 g HOBt, and 0.21 mL DIEA. Column chromatography: DCM/MeOH 19:1. Yield: 0.17 g (75%), colorless solid. ^{1}H NMR (300 MHz, $CDCl_3$): δ 8.71 (br, 2H), 7.95 (d, J = 7.5 Hz, 2H), 7.76 7.54 (m, 5H), 7.50 (d, J = 7.4 Hz, 1H), 7.40 7.08 (m, 8H), 6.99 (d, J = 6.4 Hz, 2H), 6.40 (d, J = 7.7 Hz, 1H), 6.03 (dd, $J_{H\ F}$ = 31.9 Hz, $J_{H\ H}$ = 8.8 Hz, 1H), 4.87 4.60 (m, 2H), 3.21 (dd, J = 13.5, 6.3 Hz, 1H), 3.08 (dd, J = 13.5, 8.2 Hz, 1H), 2.49 (t, J = 7.4 Hz, 2H), 1.96 1.68 (m, 2H). ^{13}C NMR (75 MHz, $CDCl_3$): δ 170.3, 164.9, 155.1 (d, $J_{C\ F}$ = 301 Hz), 149.4, 142.1, 140.2, 137.1, 136.2, 134.9, 129.7, 129.4, 129.1, 128.8, 128.7, 128.3, 127.7, 126.50, 121.7, 117.0 (d, $J_{C\ F}$ = 5.3 Hz), 55.6, 45.1, 38.8, 35.7 (d, $J_{C\ F}$ = 1.9 Hz), 31.8. mp 184 187 °C. LC MS (ESI, m/z): $[M + H]^+$ calcd for $C_{32}H_{30}FN_3O_4S$, 572.20; found, 572.4. Purity: 95%. $[\alpha]_D^{22}$ 11° (c 0.5, $CHCl_3$).

*N ((S) 1 (((S,E) 1 Fluoro 5 phenyl 1 (phenylsulfonyl)pent 1 en 3 yl)amino) 1 oxo 3 phenylpropan 2 yl) 2,3 dihydrobenzo[b][1,4] dioxine 6 carboxamide (**4b**).* Synthesized by following procedure D with 0.100 g of compound **27**, 0.036 g 1,4-benzodioxane-6-carboxylic acid, 0.064 g TBTU, and 0.104 mL DIEA. Column chromatography: petroleum ether/EtOAc 1:1. Yield: 0.084 g (67%), colorless solid. ^{1}H NMR (300 MHz, DMSO-d_6): δ 8.43 (d, J = 8.0 Hz, 1H), 8.35 (d, J = 7.8 Hz, 1H), 7.94 (dt, J = 7.3, 1.7 Hz, 2H), 7.85 (tt, J = 7.3, 1.2 Hz, 1H), 7.73 (tt, J = 6.7, 1.1 Hz, 2H), 7.43 7.06 (m, 12H), 6.89 (d, J = 8.3 Hz, 1H), 6.30 (dd, $J_{H\ F}$ = 34.0 Hz, $J_{H\ H}$ = 8.9 Hz, 1H), 4.68 4.47 (m, 2H), 4.33 4.18 (m, 4H), 3.10 2.90 (m, 2H), 2.59 2.50 (m, 2H), 1.96 1.73 (m, 2H). ^{13}C NMR (75 MHz, DMSO-d_6): δ 171.0, 165.4, 153.0 (d, $J_{C\ F}$ = 296 Hz), 146.1, 142.8, 140.8, 138.2, 136.6, 135.2, 130.1, 129.1, 128.27, 128.26, 128.1, 128.0, 127.0, 126.3, 125.9, 120.9, 119.2 (d, $J_{C\ F}$ = 4.8 Hz), 116.6, 116.5, 64.3, 64.0, 54.9, 43.8 (d, $J_{C\ F}$ = 1.6 Hz), 36.9, 35.0 (d, $J_{C\ F}$ = 2.3 Hz), 31.0. mp 187 189 °C. LC MS (ESI, m/z): $[M + H]^+$ calcd for $C_{35}H_{33}FN_2O_6S$, 629.2; found, 629.3. Purity >99%. $[\alpha]_D^{22}$ 3° (c 0.5, $CHCl_3$).

*3,5 Difluoro N ((S) 1 (((S,E) 1 fluoro 5 phenyl 1 (phenylsulfonyl)pent 1 en 3 yl)amino) 1 oxo 3 phenylpropan 2 yl)benzamide (**4c**).* Synthesized by following procedure D with 0.124 g of compound **27**, 0.039 g 3,5-difluorobenzoic acid, 0.079 g TBTU, and 0.125 mL DIEA. Column chromatography: petroleum ether/EtOAc 2:1. Yield: 0.12 g (81%), colorless solid. ^{1}H NMR (300 MHz, $CDCl_3$): δ 7.99 7.90 (m, 2H), 7.73 7.63 (m, 1H), 7.57 (t, J = 7.6 Hz, 2H), 7.37 7.09 (m, 12H), 7.00 6.91 (m, 2H), 6.87 (tt, J = 8.5, 2.3 Hz, 1H), 6.37 (d, J = 7.7 Hz, 1H), 5.96 (dd, $J_{H\ F}$ = 31.8 Hz, $J_{H\ H}$ = 8.9 Hz, 1H), 4.82 4.61 (m, 2H), 3.14 (dd, J = 13.5, 6.4 Hz, 1H), 3.03 (dd, J = 13.5, 8.2 Hz, 1H), 2.45 (t, J = 7.7 Hz, 2H), 1.88 1.72 (m, 2H). ^{13}C NMR (75 MHz, $CDCl_3$): δ 170.6, 165.0 (t, $J_{C\ F}$ = 2.8 Hz), 163.0 (dd, $J_{C\ F}$ = 251, 12 Hz), 155.2 (d, $J_{C\ F}$ = 301 Hz), 140.2, 137.1, 136.8 (t, $J_{C\ F}$ = 8.3 Hz), 136.2, 134.8, 129.7, 129.4, 129.1, 128.8, 128.7, 128.3, 127.6, 126.5, 116.9 (d, $J_{C\ F}$ = 5.1 Hz), 110.5 (dd, $J_{C\ F}$ = 27, 8.7 Hz), 107.4 (t, $J_{C\ F}$ = 25 Hz), 55.7, 45.1 (d, $J_{C\ F}$ = 1.5 Hz), 38.7, 35.7, 31.8. mp 90 92 °C. LC MS (ESI, m/z): $[M + H]^+$ calcd for $C_{33}H_{29}F_3N_2O_4S$, 607.2; found, 607.3. Purity: 95%. $[\alpha]_D^{22}$ 5° (c 0.5, MeOH).

*N ((S) 1 (((S,E) 1 Fluoro 5 phenyl 1 (phenylsulfonyl)pent 1 en 3 yl)amino) 1 oxo 3 (p tolyl)propan 2 yl)isonicotinamide (**4d**).* Synthesized by following procedure D with 0.10 g of compound **33**, 0.024 g isonicotinic acid, 0.063 g TBTU, and 0.10 mL DIEA. Column chromatography: pure EtOAc. Yield: 0.094 g (83%), colorless solid. ^{1}H NMR (300 MHz, $CDCl_3$): δ 8.69 (d, J = 3.8 Hz, 2H), 7.95 (d, J = 7.7 Hz, 2H), 7.70 (t, J = 7.3 Hz, 1H), 7.65 7.46 (m, 4H), 7.30 7.23 (m, 1H), 7.23 7.01 (m, 7H), 6.96 (d, J = 6.8 Hz, 2H), 6.32 (d, J = 7.8 Hz, 1H), 6.01 (dd, $J_{H\ F}$ = 31.9 Hz, $J_{H\ H}$ = 8.8 Hz, 1H), 4.84 4.60 (m, 2H), 3.15 (dd, J = 13.6, 5.7 Hz, 1H), 3.01 (dd, J = 13.4, 8.2 Hz, 1H), 2.46 (t, J = 7.6 Hz, 2H), 2.32 (s, 3H), 1.90 1.73 (m, 2H). ^{13}C NMR (75 MHz, $CDCl_3$): δ 170.3, 165.4, 155.12 (d, $J_{C\ F}$ = 301 Hz), 150.7, 140.8, 140.1, 137.4, 137.1, 134.8, 132.9, 129.8, 129.7, 129.3, 128.8, 128.7, 128.3, 126.5, 121.0, 116.9 (d, $J_{C\ F}$ = 4.8 Hz), 55.4, 45.0 (d, $J_{C\ F}$ = 1.7 Hz), 38.4, 35.8, 31.8, 21.2. mp 84 86 °C. LC MS (ESI, m/z): $[M + H]^+$ calcd for $C_{33}H_{32}FN_3O_4S$, 586.22; found, 586.4. Purity: 96%. $[\alpha]_D^{22}$ 12° (c 0.5, MeOH).

*N ((S) 1 (((S,E) 1 Fluoro 5 phenyl 1 (phenylsulfonyl)pent 1 en 3 yl)amino) 1 oxo 3 (p tolyl)propan 2 yl) 2,3 dihydrobenzo[b] [1,4]dioxine 6 carboxamide (**4e**).* Synthesized by following procedure D with 0.065 g of compound **33**, 0.023 g 1,4-benzodioxane-6-carboxylic acid, 0.041 g TBTU, and 0.066 mL DIEA. Column chromatography: petroleum ether/EtOAc 2:1 to 1:1. Yield: 0.057 g (70%), colorless

https://doi.org/10.1021/acs.jmedchem.1c01002
J. Med. Chem. 2021, 64, 12322 12358

solid. ^{1}H NMR (300 MHz, $CDCl_3$): δ 8.00 7.90 (m, 2H), 7.75 7.65 (m, 1H), 7.64 7.53 (m, 2H), 7.26 (s, 1H), 7.23 7.03 (m, 8H), 6.93 (dd, J = 7.8, 1.5 Hz, 2H), 6.85 (d, J = 8.4 Hz, 1H), 6.79 (d, J = 7.7 Hz, 1H), 6.70 (d, J = 7.9 Hz, 1H), 6.02 (dd, $J_{H\ F}$ = 32.0 Hz, $J_{H\ H}$ = 8.7 Hz, 1H), 4.83 (q, J = 7.5 Hz, 1H), 4.68 (quint, J = 7.7 Hz, 1H), 4.34 4.21 (m, 4H), 3.13 (dd, J = 13.6, 6.3 Hz, 1H), 3.02 (dd, J = 13.6, 7.8 Hz, 1H), 2.54 2.38 (m, 2H), 2.31 (s, 3H), 1.87 1.69 (m, 2H). ^{13}C NMR (75 MHz, $CDCl_3$): δ 170.8, 166.8, 154.8 (d, $J_{C\ F}$ = 300 Hz), 147.0, 143.6, 140.3, 137.3, 137.0, 134.7, 133.3, 129.7, 129.6, 129.3, 128.8, 128.6, 128.4, 126.9, 126.3, 120.6, 117.62 (d, $J_{C\ F}$ = 5.1 Hz), 117.5, 116.8, 64.7, 64.3, 55.1, 44.9 (d, $J_{C\ F}$ = 1.7 Hz), 38.3, 35.7, 31.8, 21.2. mp 95 97 °C. LC MS (ESI, m/z): $[M + H]^+$ calcd for $C_{36}H_{35}FN_2O_6S$, 643.23; found, 643.3. Purity: 96%. $[\alpha]_D^{22}$ 13° (c 1, $CHCl_3$).

*3,5 Difluoro N ((S) 1 (((S,E) 1 fluoro 5 phenyl 1 (phenylsulfonyl)pent 1 en 3 yl)amino) 1 oxo 3 (p tolyl)propan 2 yl)benzamide (**4f**).* Synthesized by following procedure D with 0.065 g of compound **33**, 0.020 g 3,5-difluorobenzoic acid, 0.041 g TBTU, and 0.066 mL DIEA. Column chromatography: petroleum ether/EtOAc 3:1. Yield: 0.059 g (73%), colorless solid. ^{1}H NMR (300 MHz, $CDCl_3$): δ 8.00 7.91 (m, 2H), 7.74 7.63 (m, 1H), 7.62 7.53 (m, 2H), 7.31 (d, J = 7.6 Hz, 1H), 7.25 7.09 (m, 7H), 7.05 (d, J = 8.0 Hz, 2H), 6.97 6.82 (m, 3H), 6.39 (d, J = 7.7 Hz, 1H), 5.98 (dd, $J_{H\ F}$ = 31.9 Hz, $J_{H\ H}$ = 8.8 Hz, 1H), 4.83 4.60 (m, 2H), 3.11 (dd, J = 13.5, 6.3 Hz, 1H), 2.99 (dd, J = 13.5, 8.2 Hz, 1H), 2.52 2.40 (m, 2H), 2.31 (s, 3H), 1.90 1.74 (m, 2H). ^{13}C NMR (75 MHz, $CDCl_3$): δ 170.7, 164.95 (t, $J_{C\ F}$ = 2.9 Hz), 163.02 (dd, $J_{C\ F}$ = 251, 12 Hz), 155.12 (d, $J_{C\ F}$ = 301 Hz), 140.2, 137.3, 137.2, 136.9 (t, $J_{C\ F}$ = 8.3 Hz), 134.8, 133.0, 129.8, 129.7, 129.3, 128.8, 128.7, 128.3, 126.5, 117.05 (d, $J_{C\ F}$ = 4.8 Hz), 110.50 (dd, $J_{C\ F}$ = 27, 9.4 Hz), 107.37 (t, $J_{C\ F}$ = 25 Hz), 55.6, 45.1 (d, $J_{C\ F}$ = 1.6 Hz), 38.3, 35.7 (d, $J_{C\ F}$ = 1.5 Hz), 31.8, 21.2. mp 174 176 °C. LC MS (ESI, m/z): $[M + H]^+$ calcd for $C_{34}H_{31}F_3N_2O_4S$, 621.21; found, 621.3. Purity: 95%. $[\alpha]_D^{22}$ 9° (c 0.5, MeOH).

*N ((S) 1 (((S,E) 1 Fluoro 5 phenyl 1 (phenylsulfonyl)pent 1 en 3 yl)amino) 1 oxo 3 (m tolyl)propan 2 yl)isonicotinamide (**4g**).* Synthesized by following procedure D with 0.10 g of compound **30**, 0.024 g isonicotinic acid, 0.063 g TBTU, and 0.10 mL DIEA. Column chromatography: pure EtOAc. Yield: 0.071 g (63%), colorless solid. ^{1}H NMR (300 MHz, $CDCl_3$): δ 8.69 (d, J = 5.2 Hz, 2H), 7.94 (d, J = 7.5 Hz, 2H), 7.74 7.65 (m, 1H), 7.63 7.48 (m, 4H), 7.34 7.11 (m, 6H), 7.11 6.88 (m, 5H), 6.31 (d, J = 7.8 Hz, 1H), 6.01 (dd, $J_{H\ F}$ = 31.9 Hz, $J_{H\ H}$ = 8.8 Hz, 1H), 4.84 4.59 (m, 2H), 3.16 (dd, J = 13.5, 6.2 Hz, 1H), 3.00 (dd, J = 13.5, 8.4 Hz, 1H), 2.45 (t, J = 7.5 Hz, 2H), 2.29 (s, 3H), 1.89 1.73 (m, 2H). ^{13}C NMR (75 MHz, $CDCl_3$): δ 170.3, 165.4, 155.10 (d, $J_{C\ F}$ = 301 Hz), 150.6, 140.9, 140.1, 138.8, 137.0, 136.0, 134.7, 130.1, 129.7, 129.0, 128.8, 128.7, 128.4, 128.3, 126.5, 126.4, 121.1, 116.9 (d, $J_{C\ F}$ = 5.2 Hz), 55.4, 45.1 (d, $J_{C\ F}$ = 1.9 Hz), 38.7, 35.8 (d, $J_{C\ F}$ = 1.4 Hz), 31.8, 21.5. mp 182 184 °C. LC MS (ESI, m/z): $[M + H]^+$ calcd for $C_{33}H_{32}FN_3O_4S$, 586.22; found, 586.4. Purity: 95%. $[\alpha]_D^{22}$ 3° (c 0.5, $CHCl_3$).

*N ((S) 1 (((S,E) 1 Fluoro 5 phenyl 1 (phenylsulfonyl)pent 1 en 3 yl)amino) 1 oxo 3 (m tolyl)propan 2 yl) 2,3 dihydrobenzo[b] [1,4]dioxine 6 carboxamide (**4h**).* Synthesized by following procedure D with 0.10 g of compound **30**, 0.035 g 1,4-benzodioxane-6-carboxylic acid, 0.063 g TBTU, and 0.10 mL DIEA. Column chromatography: petroleum ether/EtOAc 1:1. Yield: 0.10 g (84%), colorless solid. ^{1}H NMR (300 MHz, DMSO-d_6): δ 8.44 (d, J = 8.1 Hz, 1H), 8.38 (d, J = 7.8 Hz, 1H), 7.94 (dt, J = 7.3, 1.5 Hz, 2H), 7.89 7.80 (m, 1H), 7.80 7.68 (m, 2H), 7.42 7.30 (m, 2H), 7.29 7.02 (m, 8H), 6.98 (d, J = 6.9 Hz, 1H), 6.90 (d, J = 8.3 Hz, 1H), 6.31 (dd, $J_{H\ F}$ = 34.0 Hz, $J_{H\ H}$ = 8.9 Hz, 1H), 4.65 4.46 (m, 2H), 4.27 (d, J = 5.4 Hz, 4H), 3.08 2.84 (m, 2H), 2.61 2.50 (m, 2H), 2.25 (s, 3H), 1.96 1.72 (m, 2H). ^{13}C NMR (75 MHz, DMSO-d_6): δ 171.1, 165.5, 152.9 (d, $J_{C\ F}$ = 295 Hz), 146.1, 142.8, 140.8, 138.1, 137.0, 136.6, 135.2, 130.1, 129.8, 128.3, 128.3, 128.2, 127.9, 127.0, 126.9, 126.2, 125.9, 121.0, 119.3 (d, $J_{C\ F}$ = 4.3 Hz), 116.6, 116.5, 64.3, 64.0, 55.0, 43.8 (d, $J_{C\ F}$ = 1.5 Hz), 36.8, 35.4, 31.0, 21.0. mp 186 188 °C. LC MS (ESI, m/z): $[M + H]^+$ calcd for $C_{36}H_{35}FN_2O_6S$, 643.23; found, 643.3. Purity: >99%. $[\alpha]_D^{22}$ 11° (c 1, $CHCl_3$).

*3,5 Difluoro N ((S) 1 (((S,E) 1 fluoro 5 phenyl 1 (phenylsulfonyl)pent 1 en 3 yl)amino) 1 oxo 3 (m tolyl)propan 2 yl)benzamide (**4i**).* Synthesized by following procedure D with 0.10 g of compound **30**, 0.031 g 3,5-difluorobenzoic acid, 0.063 g TBTU, and 0.10 mL DIEA. Column chromatography: petroleum ether/EtOAc 2:1. Yield: 0.075 g (62%), colorless solid. ^{1}H NMR (300 MHz, $CDCl_3$): δ 7.95 (d, J = 7.5 Hz, 2H), 7.72 7.64 (m, 1H), 7.57 (t, J = 7.6 Hz, 2H), 7.29 7.23 (m, 1H), 7.25 6.81 (m, 13H), 6.38 (d, J = 7.7 Hz, 1H), 6.01 (dd, $J_{H\ F}$ = 31.8 Hz, $J_{H\ H}$ = 8.8 Hz, 1H), 4.81 4.60 (m, 2H), 3.12 (dd, J = 13.5, 6.5 Hz, 1H), 2.98 (dd, J = 13.5, 8.1 Hz, 1H), 2.45 (t, J = 7.7 Hz, 2H), 2.28 (s, 3H), 1.88 1.74 (m, 2H). ^{13}C NMR (75 MHz, $CDCl_3$): δ 170.6, 165.02 (t, $J_{C\ F}$ = 2.4 Hz), 162.99 (dd, $J_{C\ F}$ = 251, 12 Hz), 155.14 (d, $J_{C\ F}$ = 301 Hz), 140.2, 138.8, 137.1, 136.8 (t, $J_{C\ F}$ = 8.4 Hz), 136.2, 134.8, 130.1, 129.7, 129.0, 128.8, 128.7, 128.4, 128.3, 126.5, 117.0 (d, $J_{C\ F}$ = 4.9 Hz), 110.5 (dd, $J_{C\ F}$ = 26, 8.7 Hz), 107.4 (t, $J_{C\ F}$ = 25 Hz), 55.6, 45.2 (d, $J_{C\ F}$ = 1.6 Hz), 38.5, 35.7, 31.8, 21.4. mp 176 178 °C. LC MS (ESI, m/z): $[M + H]^+$ calcd for $C_{34}H_{31}F3N_2O_4S$, 621.21; found, 621.3. Purity >99%. $[\alpha]_D^{22}$ 5° (c 0.5, MeOH/$CHCl_3$ 1:1).

*N ((S) 1 (((S,E) 1 Fluoro 5 (methylthio) 1 (phenylsulfonyl)pent 1 en 3 yl)amino) 1 oxo 3 phenylpropan 2 yl) 4 methylpiperazine 1 carboxamide (**4j**).* Synthesized by following procedure E with 0.11 g of compound **16**, 0.089 g compound **IX**, 0.088 g TBTU, 0.042 g HOBt, and 0.14 mL DIEA. Column chromatography: DCM/MeOH 19:1. Yield: 0.11 g (73%), colorless solid. (300 MHz, CD_2Cl_2): δ 7.85 (dd, J = 7.3, 1.7 Hz, 2H), 7.71 7.59 (m, 1H), 7.59 7.47 (m, 2H), 7.25 7.13 (m, 3H), 7.12 7.01 (m, 3H), 5.99 (dd, $J_{H\ F}$ = 32.4 Hz, $J_{H\ H}$ = 8.8 Hz, 1H), 5.06 (d, J = 7.7 Hz, 1H), 4.76 4.59 (m, 1H), 4.41 (q, J = 7.2 Hz, 1H), 3.21 (q, J = 4.5 Hz, 4H), 3.02 2.79 (m, 2H), 2.31 2.25 (m, 2H), 2.22 (t, J = 5.1 Hz, 4H), 2.16 (s, 3H), 1.90 (s, 3H), 1.82 1.60 (m, 2H). (75 MHz, CD2Cl2): δ 172.3, 157.5, 155.0 (d, $J_{C\ F}$ = 298 Hz), 137.6, 137.2, 135.2, 130.1, 129.9, 129.1, 127.4, 118.2 (d, $J_{C\ F}$ = 4.9 Hz), 56.3, 55.1, 54.0, 46.4, 44.7 (d, $J_{C\ F}$ = 1.8 Hz), 44.3, 39.0, 33.8, 30.4, 15.7. mp 110 112 °C. HR-MS (ESI, m/z): $[M + Na]^+$ calcd for $C_{27}H_{35}FN_4O_4S_2$, 585.1981; found, 585.1973. $[\alpha]_D^{22}$ 12° (c 1, $CHCl_3$).

*N ((S) 1 (((S,E) 1 Fluoro 5 (methylthio) 1 (phenylsulfonyl)pent 1 en 3 yl)amino) 1 oxo 3 phenylpropan 2 yl)isonicotinamide (**4k**).* Synthesized by following procedure E with 0.11 g of compound **16**, 0.074 g compound **X**, 0.088 g TBTU, 0.042 g HOBt, and 0.14 mL DIEA. Column chromatography: DCM/MeOH 95:5. Yield: 0.098 g (66%), colorless solid. (300 MHz, CD_2Cl_2): δ 8.70 (d, J = 4.5 Hz, 2H), 7.94 (d, J = 7.5 Hz, 2H), 7.76 7.53 (m, 5H), 7.44 7.15 (m, 9H), 7.07 (d, J = 7.3 Hz, 1H), 6.26 (d, J = 7.8 Hz, 1H), 6.04 (dd, $J_{H\ F}$ = 32.2 Hz, $J_{H\ H}$ = 8.8 Hz, 1H), 4.92 4.55 (m, 2H), 3.23 3.00 (m, 2H), 2.44 2.24 (m, 2H), 2.05 1.91 (m, 3H), 1.88 1.74 (m, 2H). (75 MHz, CD2Cl2): δ 170.0, 165.2, 151.4, 150.6, 140.7, 139.4, 137.0, 136.2, 134.8, 129.6, 129.3, 128.9, 128.6, 127.3, 120.8, 55.1, 45.3, 38.3, 29.8, 15.2. mp 64 66 °C. HR-MS (ESI, m/z): $[M + Na]^+$ calcd for $C_{27}H_{28}FN_3O_4S_2$, 564.1403; found, 564.1411. $[\alpha]_D^{22}$ 21° (c 1, $CHCl_3$).

*N ((S) 1 (((R,E) 1 (Benzylthio) 4 fluoro 4 (phenylsulfonyl)but 3 en 2 yl)amino) 1 oxo 3 phenylpropan 2 yl) 4 methylpiperazine 1 carboxamide (**4l**).* Synthesized by following procedure E with 0.11 g of compound **17**, 0.077 g compound **IX**, 0.076 g TBTU, 0.036 g HOBt, and 0.13 mL DIEA. Column chromatography: DCM/MeOH 9:1. Yield: 0.093 g (63%). (300 MHz, $CDCl_3$): δ 8.02 7.91 (m, 2H), 7.79 7.67 (m, 1H), 7.67 7.54 (m, 2H), 7.43 7.09 (m, 10H), 6.81 (dd, J = 47.2, 7.8 Hz, 1H), 6.16 (dd, J = 43.5, 31.8, 8.6 Hz, 1H), 5.15 (dd, J = 14.7, 7.4 Hz, 1H), 4.93 4.75 (m, 1H), 4.52 (m, 1H), 3.64 (s, 2H), 3.54 3.30 (m, 4H), 3.18 2.99 (m, 2H), 2.67 2.47 (m, 2H), 2.50 2.38 (m, 4H), 2.36 (s, 3H). (75 MHz, $CDCl_3$): δ 171.7, 156.9, 137.4, 137.4, 137.0, 136.93, 136.90, 136.87, 134.8, 129.7, 129.5, 129.4, 129.0, 128.9, 128.85, 128.76, 127.5, 127.3, 127.2, 116.6, 116.57, 116.5, 77.2, 55.9, 5588, 54.4, 54.4, 45.9, 45.8, 44.5, 44.3, 43.55, 38.8, 38.6, 36.5, 35.1, 35.0. mp 84 86 °C. HR-MS (ESI, m/z): $[M + Na]^+$ calcd for $C_{32}H_{37}FN_4O_4S_2$, 647.2138; found, 647.2152. $[\alpha]_D^{22}$ 13° (c 1, $CHCl_3$).

*Synthesis of the Metabolites. tert Butyl 4 (((S) 1 (((S,E) 1 Fluoro 5 phenyl 1 (phenylsulfonyl)pent 1 en 3 yl)amino) 1 oxo 3 phenyl propan 2 yl)carbamoyl)piperazine 1 carboxylate (**36**).* Compound **XIII** (0.31 g) was dissolved in DCM and cooled to 0 °C. 0.11 g HOBt, 0.26 g TBTU, and 0.42 mL DIEA were added and the mixture was stirred for 30 min. 0.24 g of compound **13** was added and the mixture was stirred for an additional 24 h at rt. The reaction was stopped with 7 equiv of water and the mixture was washed with a saturated solution of

https://doi.org/10.1021/acs.jmedchem.1c01002
J. Med. Chem. 2021, 64, 12322 12358

$NaHCO_3$ and brine, dried with Na_2SO_4, and the solvent was removed under reduced pressure. The crude product was purified by column chromatography (cyclohexane/EtOAc 1:1), resulting in a colorless oil (0.21 g, 45%). ^{1}H NMR (300 MHz, CDCl3): δ 7.97 7.88 (m, 2H), 7.74 7.65 (m, 1H), 7.63 7.53 (m, 2H, *H*-27), 7.35 7.11 (m, 8H), 7.02 (ddd, J = 7.8, 3.2, 1.5 Hz, 2H), 6.54 (d, J = 41.8 Hz, 1H), 5.99 (dd, J = 32.0, 8.7 Hz, 1H), 5.11 (d, J = 27.5 Hz, 1H), 4.71 4.56 (m, 1H), 4.47 (d, $J_{C\ F}$ = 10.3 Hz), 3.45 3.17 (m, 8H), 3.14 2.91 (m, 2H), 2.56 2.36 (m, 2H), 1.95 1.62 (m, 2H), 1.46 (s, 9H). ^{13}C NMR (75 MHz, CDCl3): δ 171.6, 157.0, 154.7, 140.4, 137.1 (d, J = 7.3 Hz), 136.8, 134.8, 129.7, 129.4, 128.9, 128.8, 128.7, 128.4, 127.3 (d, J = 5.1 Hz), 126.4, 117.4, 80.4, 56.1, 45.1, 43.7, 38.5, 35.8, 31.8, 28.5.

*(S) 4 ((1 Ethoxy 1 oxo 3 phenylpropan 2 yl)carbamoyl) 1 methylpiperazine 1 oxide (**28**).* Compound **IX** (1.3 g) was dissolved in DCM and cooled to 0 °C. 0.7 g of 3-chloroperbenzoic acid was added and the mixture was stirred for 16 h. Triphenylphosphine was added to stop the reaction. The solvent was removed under reduced pressure, giving the crude product as a colorless oil (0.82 g, 63%). ^{1}H NMR (300 MHz, methanol-d_4): δ 7.35 7.11 (m, 5H), 4.87 (t, J = 2.0 Hz, 4H), 4.49 (td, J = 5.9, 2.9 Hz, 1H), 4.22 4.03 (m, 2H), 3.47 3.40 (m, 1H), 3.23 2.87 (m, 4H), 2.39 (d, J = 2.9 Hz, 3H), 2.04 1.89 (m, 2H), 1.26 1.10 (m, 3H). ^{13}C NMR (75 MHz, methanol-d_4): δ 174.4, 159.3, 138.8, 130.2, 129.4, 127.8, 62.2, 57.0, 55.2, 45.6, 44.1, 38.5, 14.4.

*(S) 4 ((1 Carboxy 2 phenylethyl)carbamoyl) 1 methylpiperazine 1 oxide (**38**).* Compound **37** (0.65 g) was dissolved in THF and cooled to 0 °C, and 0.33 g of LiOH in water was added dropwise. The mixture was stirred for 3 h at room temperature. The product was isolated from the aqueous phase giving a colorless solid (0.31 g, 53%). ^{1}H NMR (300 MHz, DMSO-d_6): δ 11.49 (s, 1H), 7.39 6.82 (m, 5H), 4.15 3.96 (m, 1H), 3.96 3.67 (m, 1H), 3.16 2.68 (m, 8H), 2.50 (s, 2H), 2.33 (s, 3H). ^{13}C NMR (75 MHz, DMSO-d_6): δ 173.9, 157.1, 138.6, 129.3, 128.2, 126.4, 55.8, 51.9, 42.0, 40.8, 36.4.

*Ethyl Isonicotate (**39**).* Isonicotinic acid (2.46 g) was dissolved in 40 mL ethanol and 1 mL of concentrated H_2SO_4 was added dropwise. The mixture was refluxed for 24 h and the solvent was removed under reduced pressure. The residue was extracted with DCM and the combined extracts were washed with a saturated solution of $NaHCO_3$, resulting in a colorless oil (2.2 g, 73%). ^{1}H NMR (300 MHz, DMSO-d_6): δ 8.83 8.73 (m, 2H), 7.88 7.73 (m, 2H), 4.34 (q, J = 7.1 Hz, 2H), 1.32 (t, J = 7.1 Hz, 3H). ^{13}C NMR (75 MHz, DMSO-d_6): δ 164.8, 150.8, 137.2, 122.6, 61.7, 14.1.

*4 (Ethoxycarbonyl)pyridine 1 Oxide (**40**).* Compound **39** (1.51 g) was dissolved in DCM and cooled to 0 °C. 1.73 g of 3-chloroperbenzoic acid was added and the mixture was stirred for 16 h. Triphenylphosphine was added to stop the reaction. The solvent was removed under reduced pressure, giving the crude product that was further purified by column chromatography (cyclohexane/EtOAc 1:6), resulting in a colorless oil (0.24 g, 29%). ^{1}H NMR (300 MHz, DMSO-d_6): δ 8.43 8.19 (m, 2H), 7.97 7.77 (m, 2H), 4.31 (q, J = 7.1 Hz, 2H), 1.31 (t, J = 7.1 Hz, 3H). ^{13}C NMR (75 MHz, DMSO-d_6): δ 163.7, 139.9, 126.85, 125.7, 61.9, 14.5.

*4 Carboxypyridine 1 Oxide (**41**).* Compound **40** (0.20 g) was dissolved in THF and cooled to 0 °C. 0.20 g of LiOH was dissolved in water and added dropwise to the mixture, then stirred for 3 h at rt. The product was isolated from the aqueous phase giving a colorless solid (0.17 g, 100%). ^{1}H NMR (300 MHz, DMSO-d_6): δ 8.31 (d, J = 6.2 Hz, 2H), 7.82 (d, J = 6.2 Hz, 2H). ^{13}C NMR (75 MHz, DMSO-d_6): δ 165.00, 139.8, 127.5, 127.1.

*4 (((S) 1 (((S,E) 1 Fluoro 5 phenyl 1 (phenylsulfonyl)pent 1 en 3 yl)amino) 1 oxo 3 phenylpropan 2 yl)carbamoyl)piperazin 1 ium Chloride (**1a**).* A 4 M solution of HCl in dioxane (3 mL) was added to 0.208 g of compound **36**. The mixture was stirred for 12 h and the solvent was removed under reduced pressure. The residue was washed three times with diethyl ether in an ultrasonic bath and then lyophilized, resulting in a colorless solid (0.177 g, 93%). ^{1}H NMR (300 MHz, DMSO-d_6): δ 8.53 (s, 2H), 8.10 7.97 (m, 2H), 7.98 7.66 (m, 3H), 7.40 6.89 (m, 11H), 6.51 (dd, J = 32.7, 9.8 Hz, 1H), 4.58 4.40 (m, 1H), 4.33 3.93 (m, 1H), 3.61 3.44 (m, 8H), 3.09 2.83 (m, 4H), 2.34 1.78 (m, 2H). ^{13}C NMR (75 MHz, DMSO-d_6): δ 163.2, 157.2, 139.3, 136.6, 135.8, 132.6, 130.2, 129.1, 128.1, 126.1, 119.7, 117.8, 115.1, 57.2, 52.4, 46.0, 42.4, 42.4, 36.5, 35.2, 35.0, 33.3. mp 93 94 °C. LC MS (ESI, m/z): $[M + H]^+$ calcd for $C_{31}H_{35}FN_4O_4S$, 579.24; found, 579.3. Purity: 98%. $[\alpha]_D^{22}$ 10° (c 0.5, MeOH).

*4 (((S) 1 (((S,E) 1 Fluoro 5 phenyl 1 (phenylsulfonyl)pent 1 en 3 yl)amino) 1 oxo 3 phenylpropan 2 yl)carbamoyl) 1 methylpiperazine 1 oxide (**1b**).* Compound **38** (0.20 g) was dissolved in a 1:1 mixture of DCM/DMF and cooled to 0 °C. 0.05 g HOBt, 0.11 g TBTU, and 0.20 mL DIEA were added, and the mixture was stirred for 30 min until all components dissolved. 0.10 g of compound **13** were added, and the mixture was stirred for an additional 48 h at room temperature. The reaction was stopped by adding 7 equiv of water and the residue was extracted with EtOAc and washed with water (2×), $NaHCO_3$ (2×), 1 M HCl (2×), and brine (1×). The solvent was removed under reduced pressure and the crude product was purified by preparative HPLC and eluted with 70% water and 30% ACN, resulting in a colorless oil (0.04 g, 23%). ^{1}H NMR (300 MHz, DMSO-d_6): δ 10.13 (s, 1H), 8.43 7.45 (m, 10H), 7.33 7.03 (m, 5H), 6.33 6.26 (m, 1H), 5.81 (dd, J = 22.1, 10.2 Hz, 1H), 5.50 5.28 (m, 1H), 4.48 (q, J = 8.0 Hz, 1H), 4.36 4.20 (m, 2H), 3.71 3.12 (m, 8H), 2.50 (quint, J = 1.9 Hz, 3H), 2.06 (d, J = 43.8 Hz, 2H), 2.04 1.64 (m, 2H). ^{13}C NMR (300 MHz, DMSO-d_6): δ 172.0, 157.3, 142.4, 139.6, 136.9, 134.0, 129.8, 129.0, 128.9, 128.6, 128.2, 127.7, 126.0, 105.6, 60.2, 57.2, 50.4, 42.5, 36.9, 30.4. LC MS (ESI, m/z): $[M + H]^+$ calcd for $C_{32}H_{37}FN_4O_5S$, 609.25; found, 609.4. Purity: 99%. $[\alpha]_D^{22}$ 4° (c 0.5, MeOH).

*4 (((S) 1 Oxo 1 (((S,E) 1 (phenoxysulfonyl) 5 phenylpent 1 en 3 yl)amino) 3 (p tolyl)propan 2 yl)carbamoyl)pyridine 1 Oxide (**2l**).* Compound **41** (0.038 g) was dissolved in DCM and cooled to 0 °C. 0.036 g HOBt, 0.087 g TBTU, and 0.19 mL DIEA were added and the mixture was stirred for 30 min. Then, 0.14 g of compound **34**-(**H**) was added and the mixture was stirred for an additional 24 h at room temperature. The reaction was stopped by adding 7 equiv of water and the residue was extracted with DCM and washed with water (2×), $NaHCO_3$ (2×), 1 M HCl (2×), and brine (1×). The solvent was removed under reduced pressure and the product was further purified by column chromatography (EtOAc/MeOH 9:1), resulting in a colorless solid (0.021 g, 13%). ^{1}H NMR (300 MHz, DMSO-d_6): δ 9.11 8.90 (m, 1H), 8.51 8.39 (m, 1H), 8.36 8.20 (m, 2H), 7.91 7.78 (m, 2H), 7.52 7.38 (m, 2H), 7.37 7.29 (m, 2H), 7.27 7.18 (m, 6H), 7.15 7.00 (m, 4H), 6.68 (dt, J = 15.4, 4.0 Hz, 1H), 6.35 (dd, J = 15.4, 3.0 Hz, 1H), 4.72 (q, J = 10.1, 9.0 Hz, 1H), 4.41 (s, 1H), 3.13 2.92 (m, 2H), 2.66 2.46 (m, 2H), 2.22 (s, 3H), 1.27 1.09 (m, 2H). ^{13}C NMR (75 MHz, DMSO-d_6): δ 171.4, 163.6, 149.6, 141.4, 139.3, 136.0, 135.0, 130.4, 129.5, 129.3, 128.8 (d, J = 3.6 Hz), 127.9, 126.3, 125.5, 123.6, 123.0, 55.9, 49.4, 39.9 (m), 34.5, 31.6, 21.1. mp 112 114 °C. LC MS (ESI, m/z): $[M + H]^+$ calcd for $C_{33}H_{33}N_3O_6S$, 600.21; found, 600.3. Purity: 97%. $[\alpha]_D^{22}$ 6° (c 0.5, MeOH).

Enzyme Assays. *Fluorometric Assays.* Rhodesain was expressed as published previously.[34] The increase of fluorescence upon cleavage of the fluorogenic substrate Cbz-Phe-Arg-AMC (Bachem) by rhodesain, CatB, or CatL was monitored using a TECAN Infinite F200 Pro fluorimeter (δ excitation: 365 nm, δ emission: 460 nm). The enzymes were diluted from a stock solution (rhodesain: 4 mg/mL in 10 mM sodium citrate buffer, pH 5.5; CatB (human liver, Calbiochem): 0.532 mg/mL; CatL (human liver, Calbiochem): 0.266 mg/mL) with enzyme buffer (rhodesain: 50 mM sodium acetate pH 5.5, 5 mM EDTA, 200 mM NaCl and 2 mM DTT; CatB/CatL: 50 mM Tris HCl, 5 mM EDTA, 200 mM NaCl, 2 mM DTT, pH 6.5) and were incubated for 1 h at rt. Assays were performed in black, flat-bottom 96-well microtiter plates (Greiner bio-one) with a total volume of 200 μL at 37 °C. Inhibitors and the substrate were prepared as stock solutions in DMSO. Dilution series of inhibitors in DMSO with a minimum of seven different concentrations were prepared in duplicate at least. 180 μL assay buffer (rhodesain: 50 mM sodium acetate pH 5.5, 5 mM EDTA, 200 mM NaCl, and 0.005% Brij35; CatB/CatL: 50 mM Tris HCl, 5 mM EDTA, 200 mM NaCl, 0.005% Brij35, pH 6.5) was added to the 96-well plates, then 5 μL of the respective enzyme in enzyme buffer, followed by 10 μL DMSO with or without inhibitor and finally 5 μL substrate (final substrate concentrations for rhodesain 10 μM, for CatB 100 μM, and for CatL 6.5 μM). Fluorescence emission was monitored directly after addition of the substrate. The presented data

https://doi.org/10.1021/acs.jmedchem.1c01002
J. Med. Chem. 2021, 64, 12322 12358

are mean values of three independent measurements. Standard deviations are less than 10% unless otherwise depicted.

Screening of activity against the catalytically active subunits of the proteasome (commercially obtained from Enzo) and Dengue virus NS2/NS3 protease was performed with an inhibitor concentration of 11 μM in DMSO.[68] Human 20S proteasome (from human erythrocytes, 0.5 mg/mL) was diluted with enzyme buffer (for trypsin-like activity: 50 mM Tris HCl, 50 mM NaCl, 0.5 mM EDTA, pH 7.4; for α-chymotrypsin-/caspase-like activity: 50 mM Tris HCl, 25 mM KCl, 10 mM NaCl, 1 mM $MgCl_2$, 0.03% SDS, pH 7.5). Trypsin-like activity was measured with the fluorogenic substrate boc-Leu-Arg-Arg-AMC (Bachem), α-chymotrypsin-like activity with Succ-Leu-Leu-Val-Tyr-AMC (Bachem), and caspase-like activity with Cbz-Leu-Leu-Glu-AMC (Bachem). Measurements were conducted in in black, flat-bottom 96-well microtiter plates (Greiner bio-one) by successive addition of 180 μL enzyme buffer, 5 μL proteasome in enzyme buffer, 10 μL inhibitor (11 μM in DMSO) or 10 μL pure DMSO, and 5 μL of the respective substrate (final substrate concentrations for trypsin-like activity 85 μM, α-chymotrypsin-like activity 70 μM, and caspase-like activity 80 μM). Fluorescence emission was monitored directly after addition of the substrate. Dengue virus NS2B/NS3 protease was diluted from a stock solution (1 mg/mL) with enzyme buffer (50 mM Tris HCl, 1 mM Chaps, 20% glycerol).[68] Screening was performed with the substrate boc-Gly-Arg-Arg-AMC (Bachem) in black, flat-bottom 96-well microtiter plates (Greiner bio-one) by successive addition of 180 μL enzyme buffer, 5 μL Dengue protease in enzyme buffer, 10 μL inhibitor (11 μM in DMSO) or 10 μL pure DMSO, and 5 μL of the substrate (final substrate concentration 100 μM). Fluorescence emission was monitored directly after addition of the substrate.

The presented inhibition data for all enzymes are mean values of three independent measurements. Standard deviations are less than 10% unless otherwise depicted.

Calculations. The GraFit program (version 5.0.13, 2006, Erithacus Sofware Ltd., UK) was used for data analysis and non-linear regression.

For inhibitors showing time-independent inhibition (**2a-(*Z*)**, **2k**, **2j**, **3a** **3i**, and **4a** **4l**), the residual enzyme activity was plotted against the inhibitor concentration. IC_{50} values were obtained by non-linear regression using the equation

$$v_i = \frac{v_0}{1 + \left(\frac{[I]}{IC_{50}}\right)^S}$$

with v_0 = enzyme activity in the absence of inhibitor, v_i = enzyme activity in the presence of inhibitor, [I] = inhibitor concentration, and S = slope factor.

K_i values were obtained by correcting the IC_{50} values to zero substrate concentration using the Cheng Prusoff relationship[32]

$$K_i = \frac{IC_{50}}{1 + \frac{[S]}{K_M}}$$

Rhodesain: [S] = 10 μM, K_M = 0.8265 μM, CatL: [S] = 6.25 μM, K_M = 6.5 μM, CatB: [S] = 100 μM, and K_M = 150 μM.

Calculation for the inhibitors with slow, tight-binding properties (**2a** **2i**) is presented in the Results and Discussion section.

Dilution Assays. Rhodesain (5 μL from 4 mg/mL stock solution) in enzyme buffer (85 μL) was incubated for 30 min with inhibitors (10 μL in DMSO) at concentrations corresponding to 10-fold the IC_{50} value obtained from fluorometric enzyme assay to ensure complete inhibition. These mixtures (2 μL) were diluted 100-fold in assay buffer (198 μL) containing 5 μL substrate (400 μM) to give a final substrate concentration of 10 μM. Recovery of enzyme activity was measured immediately using a fluorescence readout. Rhodesain with DMSO and no inhibitor added was used as a reference while the irreversible inhibitor **K11777** was used as an irreversible control.

Dialysis Experiments. Dialysis experiments for rhodesain were performed in a custom-built dialysis chamber, allowing the parallel examination of five samples.[26] A 3.5 kDa MW cut-off dialysis tubing (Carl Roth, Zellutrans MWCO 3.5 kDa) was cut into half and placed in the instrument, separating a continuous flow of buffer from five cavities at the top of the instrument, where the samples (800 μL) were added. Therefore, 20 μL rhodesain in enzyme buffer was added to 740 μL assay buffer and 40 μL DMSO with or without inhibitor. Inhibitor concentrations of 10-fold the IC_{50} value were chosen in order to guarantee complete inhibition. After incubation for 30 min, the mixtures were transferred to the cavities in the instrument and dialyzed against a continuous flow of assay buffer containing 5% DMSO (300 mL/h). Samples (97.5 μL) were taken at different time points (10, 30, 60, and 120 min) and 2.5 μL of a substrate solution was added to give a final substrate concentration of 10 μM. Enzyme activity was determined by directly measuring the fluorescence emission. The results are given in fractional activity of uninhibited rhodesain used in the same experiment as positive control.

Docking Procedures. *Procedure for Non covalent Docking with FlexX/LeadIT (vs. 2.1.3).*[11] Non-covalent docking experiments were performed using the crystal structure of rhodesain with covalently bound inhibitor **K11777** (pdb entry 2p7u).[60] The binding site was defined as a 6.5 Å shell around **K11777**. Water molecules present in the crystal structure were omitted except HOH-512, which mediates hydrogen bonding between the inhibitor and the peptide backbone. Generation of 3D-coordinates and energy minimization of the ligands were accomplished with the Molecular Operating Environment (MOE2014.09) using the MMFF94x force field.[26] Docking calculations were executed with LeadIT version 2.1.3.[27] The results presented in Table 1 are those with the best HYDE score[69,70] selected from the 10 highest-priced solutions according to FlexX score (Table 7.1).

Procedure for Covalent Docking with DOCKTITE.[60] Covalent docking was performed with the DOCKTITE software implementation (version 1.2) for Molecular Operating Environment (MOE, 2014.09; Chemical Computing Group ULC, 1010 Sherbooke St. West, Suite #910, Montreal, QC, Canada, H3A 2R7, **2021**)[11,27] using the crystal structure of rhodesain with covalently bound inhibitor **K11777** (pdb entry 2p7u).[60] Energy minimization of the ligands was performed with MOE using the MMFF94x force field.[71] The different warheads were implemented into the DOCKTITE warhead filter file as described in the DOCKTITE manual. The standard DOCKTITE protocol was followed as described. The main pharmacophore docking step was performed without pharmacophore restriction for the nucleophilic sulfur of Cys25. The Amber12:EHT force field[72] was used for the pharmacophore docking step. Docking solutions were rescored with the MOE implemented scoring functions Affinity dG and additionally with the external empirical scoring function DSX.[73] The results shown in Table S1 are those with the best DSX scores.

Mass Spectrometry (MS). *ESI MS Analysis.* Lyophilized rhodesain was reconstituted at 4 mg/mL in 50 mM NaOAc, 200 mM NaCl, and 5 mM EDTA (pH 5.5). Prior to MS analysis, rhodesain was purified by weak anion exchange (WAX) chromatography using an *ÄKTA* protein purification system (GE Healthcare) equipped with a ProPac WAX-10G 4 × 50 mm guard and a ProPac WAX-10 4 × 250 mm analytical column (Thermo Fisher Scientific). 100 μL of rhodesain stock solution (4 mg/mL) was diluted in 20 mM imidazole, 1 mM DTT in water (pH 6.0) to a final volume of 1 mL, and separated running a gradient from 0 to 40% B in 40 min. Mobile phase A was 20 mM imidazole, 1 mM DTT in water (pH 6) and Solvent B 1 M NaCl, 20 mM imidazole, and 1 mM DTT in water (pH 6). Collected fractions were tested for activity.

For mass spectrometric analysis, the WAX fraction containing active rhodesain was further diluted in 50 mM NaOAc, 200 mM NaCl, 5 mM EDTA, and 5 mM DTT (pH 5.5) and incubated for 1 h at rt. After the addition of the inhibitors at a final concentration of 10 μM, samples were analyzed by LC MS using a nanoAcquity UPLC system (Waters Corporation) coupled to a nano-ESI-Q-TOF mass spectrometer (Synapt G2-S HDMS, Waters Corporation). Rhodesain without compound served as control. Protein drug complexes were loaded onto a 200 μm × 5 cm PepSwift Monolithic PS-DVB column from Dionex (Thermo Scientific) using direct injection mode. For LC separation, two mobile phases were used. Mobile phase A contained 0.1% formic acid (FA) and 3% DMSO in ultrapure water, whereas mobile phase B consisted of 0.1% FA and 3% DMSO in ACN. A gradient of 10 90% mobile phase B was run over 7 min at a flow rate of

https://doi.org/10.1021/acs.jmedchem.1c01002
J. Med. Chem. 2021, 64, 12322 12358

2000 nL/min. Column temperature was set to 45 °C. After separation, the column was rinsed with 90% of mobile phase B and re-equilibrated under initial conditions. All MS analyses were conducted in positive-mode ESI.

MALDI TOF MS Analysis. For this analysis, a recombinant rhodesain mutant expressed in *Pichia pastoris* was used as described in the enzyme assay section. The lyophilized protein was reconstituted in buffer A (pH 5.5, 50 mM NaOAc, 200 mM NaCl, 5 mM EDTA) at a concentration of 4 mg/mL (= 174 μM). This stock solution was diluted into buffer B (pH 5.5, 50 mM NaOAc, 200 mM NaCl, 5 mM EDTA, 5 mM DTT) to a final protein concentration of 1 or 10 μM and incubated for approximately 1 h, after which the compound of interest (4 mM stock in DMSO) was added at a final inhibitor concentration of 100 μM. Later, the analytes were desalted using Zeba Spin Desalting Columns (7 kDa MWCO, 0.5 mL; Thermo Fisher Scientific) in accordance with the manufacturer's instructions and afterward coprecipitated with a MALDI-matrix, utilizing two separate approaches: For the first method, a thin layer of sinapinic acid (saturated ethanolic solution) was prepared on the target, onto which, after film formation, a volumetric 3:1 mixture of matrix-solution to analyte solution was applied. For the second method, using a mixture of α-cyano-4-hydroxycinnamic acid and 2,5-dihydroxybenzoic acid,[40,44] the preparation of a basal matrix film was omitted and a volumetric 1:1 mixture of matrix-solution to analyte solution was prepared and applied to the target. After evaporation of the solvents (ca. 15 min), measurements were carried out on a rapifleX MALDI-TOF/TOF mass spectrometer (Bruker Daltonik GmbH, Bremen, Germany). The instrument is equipped with a scanning smartbeam 10 kHz Nd:YAG laser at a wavelength of 355 nm and a 10 bit 5 GHz digitizer. The acceleration voltage was set to 20 kV and the mass spectra were recorded in positive ion linear mode. Calibration was done with the Bruker protein calibration standard II in a mass range from 10 to 70 kDa. Samples were measured at a laser power of 100% (sinapinic acid) or 70% (matrix mixture), with random walk ionization across the sample spot. As control samples, rhodesain in buffer B with a DMSO concentration matching the samples, rhodesain incubated with a reportedly non-covalent inhibitor,[11] and a known covalent-irreversible inhibitor (**K11777**)[74] were used. Data analysis was performed using the open-source software mMass.[68]

QM/MM Computations. MD simulations were performed with the Amber program package (version 2018) in combination with the FF14SB force field. The unknown parameters for the ligand were calculated using GAFF.[75] The obtained enzymatic system was balanced with sodium ions. We added an octahedral water envelope of 10 Å consisting of TIP3P water molecules Figure S11).[76] All MD simulations were performed under periodic boundary conditions in three consecutive steps. In the first step, the cage of water molecules and then the whole system was minimized. In the next step, the system was heated in a controlled way from 0 to 300 K at 1 bar, using the SHAKE algorithm[77] employing the Langevin or Berendsen thermostat.[77,78] In the last step, the actual MD simulation with a duration of at least 10 ns was performed.

We used the subtractive QM/MM approach employing the electrostatic embedding scheme as implemented in the program package Gaussian (version 2016).[79] The QM part is specified in Figure S12. Please note that larger QM spaces did not lead to considerably changes (Table S4). For the QM part, we employed the ωB97XD functional in combination with the 6-31+G* basis sets.[80 82] The TAO-Toolkit was used.[83] For the intrinsic reaction coordinate (IRC) computations, the transition states were determined using the Berny-Algorithm.[84] All transition states were proved by frequency calculations.

The reaction paths were characterized by a two-step procedure. The covalent step of the inhibition mechanism first consists of the attack of the sulfur center of the thiolate group of Cys25 on the C_2 center of the alkene group. Additionally, a proton transfer from the protonated His152 moiety to the C_1 center occurs (Figure 1). Because it is unclear whether both steps proceed subsequently or simultaneously, we first computed two-dimensional scans selecting the distances R(S_{cys} C_2) and R(H_{His} C_1) as main reaction parameters (Figure 14). By varying the main reaction parameters and optimizing all other internal coordinates for each pair of main coordinates, a minimum energy path (MEP) from the reactant to the product is obtained, which gives the first information about the shape of the reaction path. Starting from the barriers obtained in these scans, we performed intrinsic reaction coordinate (IRC) simulations. Due to the roughness of the computed PES, often more than one transition state was found for the two-dimensional surface. In such cases, we started IRC from each TS to ensure that they lead to similar reactants and products. This was indeed the case. One example is shown in Figures S8 and S10 in which computations started from slightly different TS but yielded comparable shapes for the reaction paths. The same holds for the second step of the reaction path given in Figure 16. For this frame, we found four TS whose IRCs all lead to very similar results.

Antitrypanosomal Activity and Cytotoxicity. Antritrypanosomal activity of **2a**, **2d**, **2e**, **3d**, **4d**, and **4e** against the *T. brucei brucei* BS449 cell line, a descendant of the Lister 427 strain,[85,86] was determined using the ATPlite assay as described previously.[56,57,87] **2a**, **2d**, **2e**, **3d**, **4d**, and **4e** were prepared as 5 mM stock solutions in DMSO and diluted in HMI-9 medium in multiple steps (1:3, then 1:10, and subsequently in ten 1:2 dilution steps using separate microplates). In white 96-well microplates (PerkinElmer), 10 μL of the final 101 dilutions were added to 90 μL of a cell suspension containing 2500 cells/mL, leading to final concentrations of each tested compound from 16.67 μM to 32.55 nM in the microplates. As a negative control, 0.3% DMSO was added to the cell suspension corresponding to the highest DMSO concentration added by compound application. Addition of 10% DMSO served as a positive control because all cells die at this concentration. The plates were prepared as triplicates and incubated for 24 and 48 h at 37 °C and 5% CO_2. After the respective incubation time, 50 μL ATPlite 1 step solution (PerkinElmer) was added to each well. The plate was shaken orbitally for 2 min and luminescence was measured at room temperature with an Infinite M200 PRO plate reader (Tecan Trading AG). The measured luminescence was plotted against the compound concentration to obtain a dose response curve. The EC_{50} values were determined using GraFit version 5.013 (Erithacus Software Ltd.).

Antitrypanosomal activity of the compounds **1**, **4a**, **4j**, and **4l** was determined as described previously using the Alamar Blue assay.[54,55] Cytotoxicities against the macrophage cell line J774.1 and HeLa cells were investigated according to previously described methods.[12,88]

In Vitro Metabolism Studies. Rat liver microsomes were purchased from Sigma-Aldrich and characterized for cytochrome P450, cytochrome B5, and the activity of CYP1A, CYP3A, CYP2C, and cytochrome *c* reductase. The assay was performed as published previously.[68]

First, NADPH was generated by incubating potassium phosphate buffer (395 μL, 100 mM, pH 7.4), $MgCl_2$ (25 μL, 80 mM), glucose-6-phosphate (25 μL, 100 mM), NADP disodium salt (25 μL, 20 mM), and glucose-6-dehydrogenase (25 μL, 100 IU/mL, Sigma-Aldrich) at 37 °C for 10 min. After addition of the microsomes (25 μL, 20 mg/mL) and incubation (10 min) at 37 °C, the inhibitors (1 μL, 5.21 mM in acetonitrile) were added to the mixture and the incubation continued at 37 °C for 60 min. Aliquots of 50 μL were taken at 0, 15, 30, 45, and 60 min and added to 100 μL of ice-cold acetonitrile to stop the reaction. The samples were centrifuged at 4 °C, 10,000*g* for 10 min. The supernatant was analyzed by LC MS/MS using an Agilent Poroshell 120 EC-C18 150 × 2.10 mm 4 μm column; mobile phase: compound **1** (35% acetonitrile, 55% H_2O, 10% of a 0.1% solution of formic acid in water) and compound **2d**-(**H**) (55% acetonitrile, 35% H_2O, 10% of a 0.1% solution of formic acid in water). Ion chromatograms were obtained using electronic filters for the ions of interest. Control incubations were performed with potassium phosphate buffer instead of microsomes. The LC MS chromatograms and their corresponding mass spectra were analyzed using MestReNova (v. 12.0.4).[89]

In Vivo Distribution Studies. *Animals and Treatments.* 60 male and female CD1 mice of 35 45 g body weight (56 62 days of age) were purchased from Charles River Laboratories, Sulzfeld, Germany. Five mice per cage were housed in a controlled room (22 °C, 50 65% humidity; day/night cycle of 12/12 h) with free access to water and the standard laboratory diet (Altromin, Germany). After 7 days of

https://doi.org/10.1021/acs.jmedchem.1c01002
J. Med. Chem. 2021, 64, 12322 12358

acclimatization, they were randomly divided into eight groups in which each group received four different testing compounds (**1**, **2d-(H)**) at a dose of 25 mg/kg by i.p. injection or oral gavage (p.o.). Compound **1** was diluted in 1% DMSO, while **2d-(H)** was diluted in 2% DMSO. The i.p. injection was given once only while the p.o. administrations were given for 4 days, twice daily (8 doses in total) at 9 and 18 o'clock. The dose of 25 mg/kg was chosen based on preliminary tests. 60 min after the administration of the testing compounds, blood was collected (about 0.2 mL) from the facial vein using a lancet (Goldenrod animal lancet). At the end of the experiment (3 h after the last drug administration), the animals were sacrificed by decapitation under isoflurane anesthesia. Trunk blood was collected, and the brain was removed and homogenized. Experiments were carried out according to the German Law for Animal Protection and were registered with Regierungspräsidium Darmstadt (FR/1021). All efforts were made to minimize animal numbers and animal suffering.

Microdialysis Experiments. Mice were anesthetized with isoflurane (induction dose 5%, maintenance dose 1.5% v/v in synthetic air) (Air Liquide, Düsseldorf, Germany) and placed in a stereotaxic frame (Stoelting, Chicago, IL, USA). A Y-shaped, concentric microdialysis probe with a molecular weight cutoff of 30 kDa and an exchange area of 2 mm was manufactured as described previously.[90] The probe was implanted in the hippocampus with the following coordinates from bregma: AP 2.0 mm; *L* +2.0 mm; DV 2.3 mm.[91] The mice were allowed to recover overnight. On the next day, the probes were perfused (rate: 2 μL/min) with artificial cerebrospinal fluid (aCSF; 147 mM NaCl, 4 mM KCl, 1.2 mM $CaCl_2$, and 1.2 mM $MgCl_2$) for 4 h and dialysates were collected every 20 min. After dialysates were collected for 1 h for equilibration, the test compound was given as described above. A blood sample was collected 1 h after administration of the test compound. At the end of the experiment (3 h after the last drug administration), the animals were sacrificed by decapitation under isoflurane anesthesia. Trunk blood was collected, and the brain was removed and homogenized.

Sample Preparation and LC MS Analysis. The blood was centrifuged at 4 °C, 1500*g* for 20 min and the plasma supernatant was extracted with acetonitrile and centrifuged again at 4 °C, 10,000*g* for 10 min. The supernatant was analyzed by LC MS using an Agilent Poroshell 120 EC-C18 150 × 2.10 mm 4 μm column; mobile phase: compound **1** (35% acetonitrile, 55% H_2O, 10% of a 0.1% solution of formic acid in water) and compound **2d-(H)** (55% acetonitrile, 35% H_2O, 10% of a 0.1% solution of formic acid in water). Ion chromatograms were obtained using electronic filters for the ions of interest. The LC MS chromatograms and their corresponding mass spectra were analyzed using MestReNova (v. 12.0.4).[89]

The brain tissue was homogenized using a mixture of acetonitrile/MilliQ-water (ratio 2:1, 2 mL per 300 mg brain) in a tissue grinder (Potter S, B. Braun, Melsungen, Germany) at 1,500 rpm and 15 strokes. Afterward, the homogenate was centrifuged at 4 °C, 10,000*g* for 10 min and the supernatant was lyophilized. The lyophilizate was extracted with 400 μL acetonitrile and this extract was analyzed via LC MS as described above. The fractions of the microdialysate were used without further processing. The AUC that was obtained from the extracted ion chromatograms was normalized to a volume of 500 μL for the plasma samples or a weight of 450 mg for the brain homogenates. The average AUC for every sample was calculated from experiments performed in triplicate.

■ ASSOCIATED CONTENT

● Supporting Information

The Supporting Information is available free of charge at https://pubs.acs.org/doi/10.1021/acs.jmedchem.1c01002.

Scores for non-covalent (FlexX) and covalent docking (DOCKTITE); MALDI-TOF MS spectra of complexes of rhodesain with different inhibitors and different matrix substances; ESI MS spectra of complexes of rhodesain with inhibitors (**Z**)-**2a** and **2j**; additional data for the QM/MM computations; and ESI MS spectra of the in vitro metabolism and in vivo distribution studies of **1** and **2d-(H)** (PDF)

HPLC traces of lead compounds and molecular formula strings (CSV)

■ AUTHOR INFORMATION

Corresponding Author

Tanja Schirmeister *Institute of Pharmaceutical and Biomedical Sciences (IPBS), Johannes Gutenberg University, 55128 Mainz, Germany*; Email: schirmei@uni-mainz.de

Authors

Sascha Jung *Institute of Pharmaceutical and Biomedical Sciences (IPBS), Johannes Gutenberg University, 55128 Mainz, Germany*; Present Address: Faculty of Chemistry and Chemical Biology, TU Dortmund, Otto-Hahn-Str. 6, 44227 Dortmund, Germany

Natalie Fuchs *Institute of Pharmaceutical and Biomedical Sciences (IPBS), Johannes Gutenberg University, 55128 Mainz, Germany*; orcid.org/0000-0001-6404-676X

Patrick Johe *Institute of Pharmaceutical and Biomedical Sciences (IPBS), Johannes Gutenberg University, 55128 Mainz, Germany*

Annika Wagner *Department of Chemistry, Biochemistry Section, Johannes Gutenberg University, 55128 Mainz, Germany*; Present Address: Institute of Organic Chemistry & Macromolecular Chemistry (IOMC), Friedrich Schiller University, Humboldtstraße 10, 07743 Jena, Germany; Cluster of Excellence "Balance of the Microverse", Friedrich-Schiller-University Jena, Germany.

Erika Diehl *Department of Chemistry, Biochemistry Section, Johannes Gutenberg University, 55128 Mainz, Germany*

Tri Yuliani *Institute for Pharmacology and Clinical Pharmacy, Goethe University, 60439 Frankfurt, Germany*; Present Address: Research Center for Chemistry, Indonesian Institute of Sciences (LIPI), Gd. 452 Kawasan PUSPIPTEK, Tangerang Selatan, Indonesia.

Collin Zimmer *Institute of Pharmaceutical and Biomedical Sciences (IPBS), Johannes Gutenberg University, 55128 Mainz, Germany*

Fabian Barthels *Institute of Pharmaceutical and Biomedical Sciences (IPBS), Johannes Gutenberg University, 55128 Mainz, Germany*

Robert A. Zimmermann *Institute of Pharmaceutical and Biomedical Sciences (IPBS), Johannes Gutenberg University, 55128 Mainz, Germany*

Philipp Klein *Department of Chemistry, Organic Chemistry Section, Johannes Gutenberg University, 55128 Mainz, Germany*

Waldemar Waigel *Department of Physical and Theoretical Chemistry, Julius-Maximilians-University, 97074 Würzburg, Germany*

Jessica Meyr *Department of Physical and Theoretical Chemistry, Julius-Maximilians-University, 97074 Würzburg, Germany*

Till Opatz *Department of Chemistry, Organic Chemistry Section, Johannes Gutenberg University, 55128 Mainz, Germany*; orcid.org/0000-0002-3266-4050

Stefan Tenzer *Institute for Immunology, University Medical Center, Johannes Gutenberg University, 55131 Mainz, Germany*; orcid.org/0000-0003-3034-0017

https://doi.org/10.1021/acs.jmedchem.1c01002
J. Med. Chem. 2021, 64, 12322 12358

Ute Distler *Institute for Immunology, University Medical Center, Johannes Gutenberg University, 55131 Mainz, Germany;* orcid.org/0000-0002-8031-6384
Hans-Joachim Räder *Max Planck Institute for Polymer Research, 55128 Mainz, Germany;* orcid.org/0000-0002-7292-4013
Christian Kersten *Institute of Pharmaceutical and Biomedical Sciences (IPBS), Johannes Gutenberg University, 55128 Mainz, Germany*
Bernd Engels *Department of Physical and Theoretical Chemistry, Julius-Maximilians-University, 97074 Würzburg, Germany;* orcid.org/0000-0003-3057-389X
Ute A. Hellmich *Department of Chemistry, Biochemistry Section, Johannes Gutenberg University, 55128 Mainz, Germany; Center for Biomolecular Magnetic Resonance (BMRZ), Goethe University, 60438 Frankfurt, Germany;* Present Address: Institute of Organic Chemistry & Macromolecular Chemistry (IOMC), Friedrich Schiller University, Humboldtstraße 10, 07743 Jena, Germany; Cluster of Excellence "Balance of the Microverse", Friedrich-Schiller-University Jena, Germany.
Jochen Klein *Institute for Pharmacology and Clinical Pharmacy, Goethe University, 60439 Frankfurt, Germany*

Complete contact information is available at: https://pubs.acs.org/10.1021/acs.jmedchem.1c01002

Author Contributions

‡‡S.J. and N.F. contributed equally.

Funding

Financial support by the Rhine-Main Universities fund (RMU-Initiativfonds Forschung) is gratefully acknowledged. Funded by the Deutsche Forschungsgemeinschaft (DFG, German Research Foundation) under Germany's Excellence Strategy EXC 2051 Project ID390713860.

Notes

The authors declare no competing financial interest.

■ ACKNOWLEDGMENTS

E.D. acknowledges a PhD fellowship from the Sibylle Kalkhof-Rose-Stiftung.

■ ABBREVIATIONS

AcOH, acetic acid; aCSF, artificial cerebrospinal fluid; ADME, absorption, distribution, metabolism, excretion; AMC, 7-amido-4-methylcoumaryl; aq, aqueous; Arg, arginine; Asp, aspartate; AUC, area under the curve; Bn, benzyl; boc, *tert*-butyl carbonate; CatB, cathepsin B; CatL, cathepsin L; Cbz, carbobenzoxy; chymotrps., chymotrypsin; cpd, compound; Cys, cysteine; CYP, cytochrome P450; DCM, dichloromethane; DCTB, *trans*-2-[3-(4-*tert*-butylphenyl)-2-methyl-2-propenylidene]malononitrile; DECP, diethyl chlorophosphate; DIEA, *N*,*N*-diisopropylethylamine; DHBD, 2,3-dihydrobenzo-[*b*][1,4]dioxine; DMF, dimethyl formamide; DMSO, dimethyl sulfoxide; DTT, dithiothreitol; EDC, 1-ethyl-3-(3-dimethylaminopropyl)carbodiimide; EDTA, ethylenediamine tetraacetic acid; EtOAc, ethyl acetate; ESI, electrospray ionization; Glu, glutamate; Gly, glycine; HAT, Human African *Trypanosomiasis*; HeLa cells, Henrietta Lacks cells; HOBt, hydroxybenzotriazole; HPhe, homophenylalanine; HPLC, high-pressure liquid chromatography; HWE, Horner Wadsworth Emmons; i.p., intraperitoneal; KHMDS, potassium bis-(trimethylsilyl)amide; LC, liquid chromatography; Leu, leucin; LHMDS, lithium bis(trimethylsilyl)amide; MALDI, matrix-assisted laser desorption/ionization; *m*CPBA, *meta*-chloroperbenzoic acid; Me, methyl; Met, methionine; MM, molecular mechanics; MOE, molecular operating environment; MS, mass spectrometry; MS-Cl, mesyl chloride; mp, melting point; NADPH, nicotinamide adenine dinucleotide phosphate (reduced form); *n*-BuLi, *n*-butyllithium; n.d., not determined; NHS, *N*-hydroxysuccinimide; NMR, nuclear magnetic resonance; NTD, neglected tropical disease; PDB, Protein Database; Ph, phenyl; Phe, phenylalanine; Pip, piperazine; ppm, parts per million; Pyr, pyridine; QM, quantum mechanics; RMSD, root-mean-square deviation; rt, room temperature; SAR, structure activity relationship; SPR, surface plasmon resonance; Succ, *N*-succinyl; *T. b. gambiense*, *Trypanosoma brucei gambiense*; *T. b. rhodesiense*, *Trypanosoma brucei rhodesiense*; TBTU, 2-(1*H*-benzotriazole-1-yl)-1,1,3,3-tetramethyluronium tetrafluoroborate; TEA, triethyl amine; TFA, trifluoroacetic acid; THF, tetrahydrofuran; TLC, thin layer chromatography; TOF, time of flight; Tris, tris(hydroxymethyl)aminomethane; Trp, tryptophan; Tyr, tyrosine; UV, ultraviolet; val, valine; VS, vinyl sulfone; X-ray, energetic high-frequency electromagnetic radiation

■ REFERENCES

(1) Malvy, D.; Chappuis, F. Sleeping Sickness. *Clin. Microbiol. Infect.* **2011**, *17*, 986 995.
(2) Brun, R.; Blum, J.; Chappuis, F.; Burri, C. Human African Trypanosomiasis. *Lancet* **2010**, *375*, 148 159.
(3) Priotto, G.; Kasparian, S.; Mutombo, W.; Ngouama, D.; Ghorashian, S.; Arnold, U.; Ghabri, S.; Baudin, E.; Buard, V.; Kazadi-Kyanza, S.; Ilunga, M.; Mutangala, W.; Pohlig, G.; Schmid, C.; Karunakara, U.; Torreele, E.; Kande, V. Nifurtimox-Eflornithine Combination Therapy for Second-Stage African Trypanosoma Brucei Gambiense Trypanosomiasis: A Multicentre, Randomised, Phase III, Non-Inferiority Trial. *Lancet* **2009**, *374*, 56 64.
(4) Mesu, V. K. B. K.; Kalonji, W. M.; Bardonneau, C.; Mordt, O. V.; Blesson, S.; Simon, F.; Delhomme, S.; Bernhard, S.; Kuziena, W.; Lubaki, J.-P. F.; Vuvu, S. L.; Ngima, P. N.; Mbembo, H. M.; Ilunga, M.; Bonama, A. K.; Heradi, J. A.; Solomo, J. L. L.; Mandula, G.; Badibabi, L. K.; Dama, F. R.; Lukula, P. K.; Tete, D. N.; Lumbala, C.; Scherrer, B.; Strub-Wourgaft, N.; Tarral, A. Oral Fexinidazole for Late-Stage African Trypanosoma Brucei Gambiense Trypanosomiasis: A Pivotal Multicentre, Randomised, Non-Inferiority Trial. *Lancet* **2018**, *391*, 144 154.
(5) Fairlamb, A. H. Chemotherapy of Human African Trypanosomiasis: Current and Future Prospects. *Trends Parasitol.* **2003**, *19*, 488 494.
(6) Steverding, D.; Sexton, D. W.; Wang, X.; Gehrke, S. S.; Wagner, G. K.; Caffrey, C. R. Trypanosoma Brucei: Chemical Evidence That Cathepsin L Is Essential for Survival and a Relevant Drug Target. *Int. J. Parasitol.* **2012**, *42*, 481 488.
(7) Nikolskaia, O. v.; de A Lima, A. P. C.; Kim, Y. v.; Lonsdale-Eccles, J. D.; Fukuma, T.; Scharfstein, J.; Grab, D. J. Blood-Brain Barrier Traversal by African Trypanosomes Requires Calcium Signaling Induced by Parasite Cysteine Protease. *J. Clin. Invest.* **2006**, *116*, 2739 2747.
(8) Scory, S.; Caffrey, C. R.; Stierhof, Y.-D.; Ruppel, A.; Steverding, D. Trypanosoma Brucei: Killing of Bloodstream Formsin Vitroandin Vivo by the Cysteine Proteinase Inhibitor Z-Phe-Ala-CHN2. *Exp. Parasitol.* **1999**, *91*, 327 333.
(9) Kerr, I. D.; Wu, P.; Marion-Tsukamaki, R.; Mackey, Z. B.; Brinen, L. S. Crystal Structures of TbCatB and Rhodesain, Potential Chemotherapeutic Targets and Major Cysteine Proteases of Trypanosoma Brucei. *PLoS Neglected Trop. Dis.* **2010**, *4*, No. e701.
(10) Johé, P.; Jaenicke, E.; Neuweiler, H.; Schirmeister, T.; Kersten, C.; Hellmich, U. A. Structure, Interdomain Dynamics and PH-Dependent Autoactivation of pro-Rhodesain, the Main Lysosomal

Cysteine Protease from African Trypanosomes. *J. Biol. Chem.* **2021**, *296*, 100565.
(11) Kerr, I. D.; Lee, J. H.; Farady, C. J.; Marion, R.; Rickert, M.; Sajid, M.; Pandey, K. C.; Caffrey, C. R.; Legac, J.; Hansell, E.; Mckerrow, J. H.; Craik, C. S.; Rosenthal, P. J.; Brinen, L. S. Vinyl Sulfones as Antiparasitic Agents and a Structural Basis for Drug Design. *J. Biol. Chem.* **2009**, *284*, 25697 25703.
(12) Schirmeister, T.; Kesselring, J.; Jung, S.; Schneider, T. H.; Weickert, A.; Becker, J.; Lee, W.; Bamberger, D.; Wich, P. R.; Distler, U.; Tenzer, S.; Johé, P.; Hellmich, U. A.; Engels, B. Quantum Chemical-Based Protocol for the Rational Design of Covalent Inhibitors. *J. Am. Chem. Soc.* **2016**, *138*, 8332 8335.
(13) Singh, J.; Petter, R. C.; Baillie, T. A.; Whitty, A. The Resurgence of Covalent Drugs. *Nat. Rev. Drug Discovery* **2011**, *10*, 307 317.
(14) Bauer, R. A. Covalent Inhibitors in Drug Discovery: From Accidental Discoveries to Avoided Liabilities and Designed Therapies. *Drug Discovery Today* **2015**, *20*, 1061 1073.
(15) Kalgutkar, A. S.; Dalvie, D. K. Drug Discovery for a New Generation of Covalent Drugs. *Expert Opin. Drug Discovery* **2012**, *7*, 561 581.
(16) Lammert, C.; Einarsson, S.; Saha, C.; Niklasson, A.; Bjornsson, E.; Chalasani, N. Relationship between Daily Dose of Oral Medications and Idiosyncratic Drug-Induced Liver Injury: Search for Signals. *Hepatology* **2008**, *47*, 2003 2009.
(17) Lee, C.-U.; Grossmann, T. N. Reversible Covalent Inhibition of a Protein Target. *Angew. Chem., Int. Ed.* **2012**, *51*, 8699 8700.
(18) Copeland, R. A.; Pompliano, D. L.; Meek, T. D. Drug-Target Residence Time and Its Implications for Lead Optimization. *Nat. Rev. Drug Discovery* **2006**, *5*, 730 739.
(19) Bradshaw, J. M.; McFarland, J. M.; Paavilainen, V. O.; Bisconte, A.; Tam, D.; Phan, V. T.; Romanov, S.; Finkle, D.; Shu, J.; Patel, V.; Ton, T.; Li, X.; Loughhead, D. G.; Nunn, P. A.; Karr, D. E.; Gerritsen, M. E.; Funk, J. O.; Owens, T. D.; Verner, E.; Brameld, K. A.; Hill, R. J.; Goldstein, D. M.; Taunton, J. Prolonged and Tunable Residence Time Using Reversible Covalent Kinase Inhibitors. *Nat. Chem. Biol.* **2015**, *11*, 525 531.
(20) Johe, P.; Jung, S.; Endres, E.; Kersten, C.; Zimmer, C.; Ye, W.; Sönnichsen, C.; Hellmich, U. A.; Sotriffer, C.; Schirmeister, T.; Neuweiler, H. Warhead Reactivity Limits the Speed of Inhibition of the Cysteine Protease Rhodesain. *ACS Chem. Biol.* **2021**, *16*, 661 670.
(21) Schechter, I.; Berger, A. On the Size of the Active Site in Proteases. I. Papain. *Biochem. Biophys. Res. Commun.* **1967**, *27*, 157 162.
(22) Jaishankar, P.; Hansell, E.; Zhao, D.-M.; Doyle, P. S.; McKerrow, J. H.; Renslo, A. R. Potency and Selectivity of P2/P3-Modified Inhibitors of Cysteine Proteases from Trypanosomes. *Bioorg. Med. Chem. Lett.* **2008**, *18*, 624 628.
(23) Schirmeister, T.; Schmitz, J.; Jung, S.; Schmenger, T.; Krauth-Siegel, R. L.; Gütschow, M. Evaluation of Dipeptide Nitriles as Inhibitors of Rhodesain, a Major Cysteine Protease of Trypanosoma Brucei. *Bioorg. Med. Chem. Lett.* **2017**, *27*, 45 50.
(24) Yang, P.-Y.; Wang, M.; Li, L.; Wu, H.; He, C. Y.; Yao, S. Q. Design, Synthesis and Biological Evaluation of Potent Azadipeptide Nitrile Inhibitors and Activity-Based Probes as Promising Anti-*Trypanosoma Brucei* Agents. *Chem. Eur. J.* **2012**, *18*, 6528 6541.
(25) Caffrey, C. R.; Hansell, E.; Lucas, K. D.; Brinen, L. S.; Alvarez Hernandez, A.; Cheng, J.; Gwaltney, S. L.; Roush, W. R.; Stierhof, Y.-D.; Bogyo, M.; Steverding, D.; McKerrow, J. H. Active Site Mapping, Biochemical Properties and Subcellular Localization of Rhodesain, the Major Cysteine Protease of Trypanosoma Brucei Rhodesiense. *Mol. Biochem. Parasitol.* **2001**, *118*, 61 73.
(26) *LeadIT/FlexX*; BioSolveIT GmbH: St. Augustin, Germany 2012.
(27) Scholz, C.; Knorr, S.; Hamacher, K.; Schmidt, B. DOCKTITE-A Highly Versatile Step-by-Step Workflow for Covalent Docking and Virtual Screening in the Molecular Operating Environment. *J. Chem. Inf. Model.* **2015**, *55*, 398 406.
(28) Ng, S. L.; Yang, P.-Y.; Chen, K. Y.-T.; Srinivasan, R.; Yao, S. Q. "Click" Synthesis of Small-Molecule Inhibitors Targeting Caspases. *Org. Biomol. Chem.* **2008**, *6*, 844 847.
(29) Sun, A. C.; McClain, E. J.; Beatty, J. W.; Stephenson, C. R. J. Visible Light-Mediated Decarboxylative Alkylation of Pharmaceutically Relevant Heterocycles. *Org. Lett.* **2018**, *20*, 3487 3490.
(30) Ehmke, V.; Winkler, E.; Banner, D. W.; Haap, W.; Schweizer, W. B.; Rottmann, M.; Kaiser, M.; Freymond, C.; Schirmeister, T.; Diederich, F. Optimization of Triazine Nitriles as Rhodesain Inhibitors: Structure-Activity Relationships, Bioisosteric Imidazopyridine Nitriles, and X-Ray Crystal Structure Analysis with Human Cathepsin L. *ChemMedChem* **2013**, *8*, 967 975.
(31) DIXON, M. The Determination of Enzyme Inhibitor Constants. *Biochem. J.* **1953**, *55*, 170 171.
(32) Yung-Chi, C.; Prusoff, W. H. Relationship between the Inhibition Constant (KI) and the Concentration of Inhibitor Which Causes 50 per Cent Inhibition (I50) of an Enzymatic Reaction. *Biochem. Pharmacol.* **1973**, *22*, 3099 3108.
(33) Purich, D. L. *Enzyme Kinetics, Catalysis and Control, A Reference of Theory and Best-Practice Methods*; Elsevier, 2010.
(34) Ludewig, S.; Kossner, M.; Schiller, M.; Baumann, K.; Schirmeister, T. Enzyme Kinetics and Hit Validation in Fluorimetric Protease Assays. *Curr. Top. Med. Chem.* **2010**, *10*, 368 382.
(35) Berman, H. M.; Westbrook, J.; Feng, Z.; Gilliland, G.; Bhat, T. N.; Weissig, H.; Shindyalov, I. N.; Bourne, P. E. The Protein Data Bank. *Nucleic Acids Res.* **2000**, *28*, 235 242.
(36) Hardegger, L. A.; Kuhn, B.; Spinnler, B.; Anselm, L.; Ecabert, R.; Stihle, M.; Gsell, B.; Thoma, R.; Diez, J.; Benz, J.; Plancher, J. M.; Hartmann, G.; Banner, D. W.; Haap, W.; Diederich, F. Systematic Investigation of Halogen Bonding in Protein-Ligand Interactions. *Angew. Chem., Int. Ed.* **2011**, *50*, 314 318.
(37) Mirković, B.; Renko, M.; Turk, S.; Sosič, I.; Jevnikar, Z.; Obermajer, N.; Turk, D.; Gobec, S.; Kos, J. Novel Mechanism of Cathepsin B Inhibition by Antibiotic Nitroxoline and Related Compounds. *ChemMedChem* **2011**, *6*, 1351 1356.
(38) Illy, C.; Quraishi, O.; Wang, J.; Purisima, E.; Vernet, T.; Mort, J. S. Role of the Occluding Loop in Cathepsin B Activity. *J. Biol. Chem.* **1997**, *272*, 1197 1202.
(39) Zehl, M.; Allmaier, G. n. Investigation of Sample Preparation and Instrumental Parameters in the Matrix-Assisted Laser Desorption/Ionization Time-of-Flight Mass Spectrometry of Noncovalent Peptide/Peptide Complexes. *Rapid Commun. Mass Spectrom.* **2003**, *17*, 1931 1940.
(40) Salih, B.; Zenobi, R. MALDI Mass Spectrometry of Dye - Peptide and Dye - Protein Complexes. *Anal. Chem.* **1998**, *70*, 1536 1543.
(41) Woods, A. S.; Huestis, M. A. A Study of Peptide-Peptide Interaction by Matrix-Assisted Laser Desorption/Ionization. *J. Am. Soc. Mass Spectrom.* **2001**, *12*, 88 96.
(42) Heck, A. J. R.; van den Heuvel, R. H. H. Investigation of Intact Protein Complexes by Mass Spectrometry. *Mass Spectrom. Rev.* **2004**, *23*, 368 389.
(43) Laugesen, S.; Roepstorff, P. Combination of Two Matrices Results in Improved Performance of MALDI MS for Peptide Mass Mapping and Protein Analysis. *J. Am. Soc. Mass Spectrom.* **2003**, *14*, 992 1002.
(44) Klein, P.; Johe, P.; Wagner, A.; Jung, S.; Kühlborn, J.; Barthels, F.; Tenzer, S.; Distler, U.; Waigel, W.; Engels, B.; Hellmich, U. A.; Opatz, T.; Schirmeister, T. New Cysteine Protease Inhibitors: Electrophilic (Het)Arenes and Unexpected Prodrug Identification for the Trypanosoma Protease Rhodesain. *Molecules* **2020**, *25*, 1451.
(45) Whittal, R. M.; Li, L. High-Resolution Matrix-Assisted Laser Desorption/Ionization in a Linear Time-of-Flight Mass Spectrometer. *Anal. Chem.* **1995**, *67*, 1950 1954.
(46) Bahr, U.; Stahl-Zeng, J.; Gleitsmann, E.; Karas, M. Delayed Extraction Time-of-Flight MALDI Mass Spectrometry of Proteins above 25 000 Da. *J. Mass Spectrom.* **1997**, *32*, 1111 1116.
(47) Kollmeier, A. S.; de la Torre, X.; Müller, C.; Botrè, F.; Parr, M. K. In-Depth Gas Chromatography/Tandem Mass Spectrometry Fragmentation Analysis of Formestane and Evaluation of Mass Spectral Discrimination of Isomeric 3-Keto-4-Ene Hydroxy Steroids. *Rapid Commun. Mass Spectrom.* **2020**, *34*, No. e8937.

https://doi.org/10.1021/acs.jmedchem.1c01002
J. Med. Chem. 2021, 64, 12322 12358

(48) Mladenovic, M.; Ansorg, K.; Fink, R. F.; Thiel, W.; Schirmeister, T.; Engels, B. Atomistic Insights into the Inhibition of Cysteine Proteases: First QM/MM Calculations Clarifying the Stereoselectivity of Epoxide-Based Inhibitors. *J. Phys. Chem. B* **2008**, *112*, 11798 11808.
(49) Mladenovic, M.; Junold, K.; Fink, R. F.; Thiel, W.; Schirmeister, T.; Engels, B. Atomistic Insights into the Inhibition of Cysteine Proteases: First QM/MM Calculations Clarifying the Regiospecificity and the Inhibition Potency of Epoxide- and Aziridine-Based Inhibitors. *J. Phys. Chem. B* **2008**, *112*, 5458 5469.
(50) Vicik, R.; Busemann, M.; Gelhaus, C.; Stiefl, N.; Scheiber, J.; Schmitz, W.; Schulz, F.; Mladenovic, M.; Engels, B.; Leippe, M.; Baumann, K.; Schirmeister, T. Aziridide-Based Inhibitors of Cathepsin L: Synthesis, Inhibition Activity, and Docking Studies. *ChemMedChem* **2006**, *1*, 1126 1141.
(51) Müller, K.; Faeh, C.; Diederich, F. Fluorine in Pharmaceuticals: Looking beyond Intuition. *Science* **2007**, *317*, 1881 1886.
(52) Tosstorff, A.; Cole, J. C.; Taylor, R.; Harris, S. F.; Kuhn, B. Identification of Noncompetitive Protein-Ligand Interactions for Structural Optimization. *J. Chem. Inf. Model.* **2020**, *60*, 6595 6611.
(53) Maeda, S.; Harabuchi, Y.; Ono, Y.; Taketsugu, T.; Morokuma, K. Intrinsic Reaction Coordinate: Calculation, Bifurcation, and Automated Search. *Int. J. Quantum Chem.* **2015**, *115*, 258 269.
(54) Vicik, R.; Hoerr, V.; Glaser, M.; Schultheis, M.; Hansell, E.; McKerrow, J. H.; Holzgrabe, U.; Caffrey, C. R.; Ponte-Sucre, A.; Moll, H.; Stich, A.; Schirmeister, T. Aziridine-2,3-Dicarboxylate Inhibitors Targeting the Major Cysteine Protease of Trypanosoma Brucei as Lead Trypanocidal Agents. *Bioorg. Med. Chem. Lett.* **2006**, *16*, 2753 2757.
(55) Ettari, R.; Pinto, A.; Previti, S.; Tamborini, L.; Angelo, I. C.; la Pietra, V.; Marinelli, L.; Novellino, E.; Schirmeister, T.; Zappalà, M.; Grasso, S.; de Micheli, C.; Conti, P. Development of Novel Dipeptide-like Rhodesain Inhibitors Containing the 3-Bromoisoxazoline Warhead in a Constrained Conformation. *Bioorg. Med. Chem.* **2015**, *23*, 7053 7060.
(56) Wagner, A.; Le, T. A.; Brennich, M.; Klein, P.; Bader, N.; Diehl, E.; Paszek, D.; Weickhmann, A. K.; Dirdjaja, N.; Krauth-Siegel, R. L.; Engels, B.; Opatz, T.; Schindelin, H.; Hellmich, U. A. Inhibitor-Induced Dimerization of an Essential Oxidoreductase from African Trypanosomes. *Angew. Chem., Int. Ed.* **2019**, *58*, 3640 3644.
(57) Previti, S.; Ettari, R.; Cosconati, S.; Amendola, G.; Chouchene, K.; Wagner, A.; Hellmich, U. A.; Ulrich, K.; Krauth-Siegel, R. L.; Wich, P. R.; Schmid, I.; Schirmeister, T.; Gut, J.; Rosenthal, P. J.; Grasso, S.; Zappalà, M. Development of Novel Peptide-Based Michael Acceptors Targeting Rhodesain and Falcipain-2 for the Treatment of Neglected Tropical Diseases (NTDs). *J. Med. Chem.* **2017**, *60*, 6911 6923.
(58) Mellott, D. M.; Tseng, C.-T.; Drelich, A.; Fajtová, P.; Chenna, B. C.; Kostomiris, D. H.; Hsu, J.; Zhu, J.; Taylor, Z. W.; Kocurek, K. I.; Tat, V.; Katzfuss, A.; Li, L.; Giardini, M. A.; Skinner, D.; Hirata, K.; Yoon, M. C.; Beck, S.; Carlin, A. F.; Clark, A. E.; Beretta, L.; Maneval, D.; Hook, V.; Frueh, F.; Hurst, B. L.; Wang, H.; Raushel, F. M.; O'Donoghue, A. J.; de Siqueira-Neto, J. L.; Meek, T. D.; McKerrow, J. H. A Clinical-Stage Cysteine Protease Inhibitor Blocks SARS-CoV-2 Infection of Human and Monkey Cells. *ACS Chem. Biol.* **2021**, *16*, 642 650.
(59) Jacobsen, W.; Christians, U.; Benet, L. Z. In Vitro Evaluation of the Disposition of a Novel Cysteine Protease Inhibitor. *Drug Metab. Dispos.* **2000**, *28*, 1343 1351.
(60) *Molecular Operating Environment (MOE)|MOEsaic|PSILO*; Chemical Computing Group Inc.: Montreal, QC, Canada, 2014.
(61) Lei, X.; Jalla, A.; Abou Shama, M.; Stafford, J.; Cao, B. Chromatography-Free and Eco-Friendly Synthesis of Aryl Tosylates and Mesylates. *Synthesis* **2015**, *47*, 2578 2585.
(62) Stokes, B. J.; Liu, S.; Driver, T. G. Rh2(II)-Catalyzed Nitro-Group Migration Reactions: Selective Synthesis of 3-Nitroindoles from *β*-Nitro Styryl Azides. *J. Am. Chem. Soc.* **2011**, *133*, 4702 4705.
(63) Scheidt, K. A.; Roush, W. R.; McKerrow, J. H.; Selzer, P. M.; Hansell, E.; Rosenthal, P. J. Structure-Based Design, Synthesis and Evaluation of Conformationally Constrained Cysteine Protease Inhibitors. *Bioorg. Med. Chem.* **1998**, *6*, 2477 2494.
(64) Ivkovic, J.; Lembacher-Fadum, C.; Breinbauer, R. A Rapid and Efficient One-Pot Method for the Reduction of N-Protected *α*-Amino Acids to Chiral *α*-Amino Aldehydes Using CDI/DIBAL-H. *Org. Biomol. Chem.* **2015**, *13*, 10456 10460.
(65) White, J. D.; Xu, Q.; Lee, C.-S.; Valeriote, F. A. Total Synthesis and Biological Evaluation of (+)-Kalkitoxin, a Cytotoxic Metabolite of the Cyanobacterium Lyngbya Majuscula. *Org. Biomol. Chem.* **2004**, *2*, 2092 2102.
(66) Weissenborn, M. J.; Wehner, J. W.; Gray, C. J.; Šardzík, R.; Eyers, C. E.; Lindhorst, T. K.; Flitsch, S. L. Formation of Carbohydrate-Functionalised Polystyrene and Glass Slides and Their Analysis by MALDI-TOF MS. *Beilstein J. Org. Chem.* **2012**, *8*, 753 762.
(67) Andrei, D.; Wnuk, S. F. Synthesis of the Multisubstituted Halogenated Olefins via Cross-Coupling of Dihaloalkenes with Alkylzinc Bromides. *J. Org. Chem.* **2006**, *71*, 405 408.
(68) Millies, B.; von Hammerstein, F.; Gellert, A.; Hammerschmidt, S.; Barthels, F.; Göppel, U.; Immerheiser, M.; Elgner, F.; Jung, N.; Basic, M.; Kersten, C.; Kiefer, W.; Bodem, J.; Hildt, E.; Windbergs, M.; Hellmich, U. A.; Schirmeister, T. Proline-Based Allosteric Inhibitors of Zika and Dengue Virus NS2B/NS3 Proteases. *J. Med. Chem.* **2019**, *62*, 11359 11382.
(69) Schneider, N.; Lange, G.; Hindle, S.; Klein, R.; Rarey, M. A Consistent Description of HYdrogen Bond and DEhydration Energies in Protein-Ligand Complexes: Methods behind the HYDE Scoring Function. *J. Comput.-Aided Mol. Des.* **2013**, *27*, 15 29.
(70) Reulecke, I.; Lange, G.; Albrecht, J.; Klein, R.; Rarey, M. Towards an Integrated Description of Hydrogen Bonding and Dehydration: Decreasing False Positives in Virtual Screening with the HYDE Scoring Function. *ChemMedChem* **2008**, *3*, 885 897.
(71) Halgren, T. A. Merck Molecular Force Field. I. Basis, Form, Scope, Parameterization, and Performance of MMFF94. *J. Comput. Chem.* **1996**, *17*, 490 519.
(72) Maier, J. A.; Martinez, C.; Kasavajhala, K.; Wickstrom, L.; Hauser, K. E.; Simmerling, C. Ff14SB: Improving the Accuracy of Protein Side Chain and Backbone Parameters from Ff99SB. *J. Chem. Theory Comput.* **2015**, *11*, 3696 3713.
(73) Neudert, G.; Klebe, G. DSX: A Knowledge-Based Scoring Function for the Assessment of Protein-Ligand Complexes. *J. Chem. Inf. Model.* **2011**, *51*, 2731 2745.
(74) Marinas, M.; Sa, E.; Rojas, M. M.; Moalem, M.; Urbano, F. J.; Guillou, C.; Rallo, L. A Nuclear Magnetic Resonance (1 H and 13 C) and Isotope Ratio Mass Spectrometry (d 13 C , d 2 H and d 18 O) Study of Andalusian Olive Oils. *Rapid Commun. Mass Spectrom.* **2010**, *24*, 1457 1466.
(75) Wang, J.; Wolf, R. M.; Caldwell, J. W.; Kollman, P. A.; Case, D. A. Development and Testing of a General Amber Force Field. *J. Comput. Chem.* **2004**, *25*, 1157 1174.
(76) Jorgensen, W. L.; Chandrasekhar, J.; Madura, J. D.; Impey, R. W.; Klein, M. L. Comparison of Simple Potential Functions for Simulating Liquid Water. *J. Chem. Phys.* **1983**, *79*, 926 935.
(77) Ryckaert, J.-P.; Ciccotti, G.; Berendsen, H. J. C. Numerical Integration of the Cartesian Equations of Motion of a System with Constraints: Molecular Dynamics of n-Alkanes. *J. Comput. Phys.* **1977**, *23*, 327 341.
(78) Berendsen, H. J. C.; Postma, J. P. M.; van Gunsteren, W. F.; Dinola, A.; Haak, J. R. Molecular Dynamics with Coupling to an External Bath. *J. Chem. Phys.* **1984**, *81*, 3684 3690.
(79) Frisch, M. J.; Trucks, G. W.; Schlegel, H. B.; Scuseria, G. E.; Robb, M. A.; Cheeseman, J. R.; Scalmani, G.; Barone, V.; Petersson, G. A.; Nakatsuji, H.; Li, X.; Caricato, M.; Marenich, A. V.; Bloino, J.; Janesko, B. G.; Gomperts, R.; Mennucci, B.; Hratchian, H. P.; Ortiz, J. V.; Izmaylov, A. F.; Sonnenberg, J. L.; Ding, F.; Lipparini, F.; Egidi, F.; Goings, J.; Peng, B.; Petrone, A.; Henderson, T.; Ranasinghe, D.; Zakrzewski, V. G.; Gao, J.; Rega, N.; Zheng, G.; Liang, W.; Hada, M.; Ehara, M.; Fukuda, R.; Hasegawa, J.; Ishida, M.; Nakajima, T.; Honda, Y.; Kitao, O.; Nakai, H.; Vreven, T.; Throssell, K.; Montgomery, J. A., Jr.; Peralta, J. E.; Ogliaro, F.; Bearpark, M. J.; Heyd, J. J.; Brothers, E. N.; Kudin, K. N.; Staroverov, V. N.; Keith, T. A.; Kobayashi, R.; Normand, J.; Raghavachari, K.; Rendell, A. P.; Burant, J. C.; Iyengar, S. S.; Tomasi, J.; Cossi, M.; Millam, J. M.; Klene, M.; Adamo, C.; Cammi, R.; Ochterski, J. W.; Martin, R. L.; Morokuma, K.; Farkas, O.; Foresman, J.

https://doi.org/10.1021/acs.jmedchem.1c01002
J. Med. Chem. 2021, 64, 12322 12358

B.; Fox, D. J. *Gaussian 16*, Rev. C.01; Gaussian Inc., Wallingford, CT, 2016.
(80) Hariharan, P. C.; Pople, J. A. The Influence of Polarization Functions on Molecular Orbital Hydrogenation Energies. *Theor. Chim. Acta* **1973**, *28*, 213 222.
(81) Chai, J.-D.; Head-Gordon, M. Long-Range Corrected Hybrid Density Functionals with Damped Atom-Atom Dispersion Corrections. *Phys. Chem. Chem. Phys.* **2008**, *10*, 6615 6620.
(82) Ditchfield, R.; Hehre, W. J.; Pople, J. A. Self-Consistent Molecular-Orbital Methods. IX. An Extended Gaussian-Type Basis for Molecular-Orbital Studies of Organic Molecules. *J. Chem. Phys.* **1971**, *54*, 724.
(83) Tao, P.; Schlegel, H. B. A Toolkit to Assist ONIOM Calculations. *J. Comput. Chem.* **2010**, *31*, 2363 2369.
(84) Li, X.; Frisch, M. J. Energy-Represented Direct Inversion in the Iterative Subspace within a Hybrid Geometry Optimization Method. *J. Chem. Theory Comput.* **2006**, *2*, 835 839.
(85) Biebinger, S.; Elizabeth Wirtz, L.; Lorenz, P.; Christine Clayton, C. Vectors for Inducible Expression of Toxic Gene Products in Bloodstream and Procyclic Trypanosoma Brucei. *Mol. Biochem. Parasitol.* **1997**, *85*, 99 112.
(86) Cunningham, M. P.; Vickerman, K. Antigenic Analysis in the Trypanosoma Brucei Group, Using the Agglutination Reaction. *Trans. R. Soc. Trop. Med. Hyg.* **1962**, *56*, 48 59.
(87) Klein, P.; Barthels, F.; Johe, P.; Wagner, A.; Tenzer, S.; Distler, U.; Le, T. A.; Schmid, P.; Engel, V.; Engels, B.; Hellmich, U. A.; Opatz, T.; Schirmeister, T. Naphthoquinones as Covalent Reversible Inhibitors of Cysteine Proteases-Studies on Inhibition Mechanism and Kinetics. *Molecules* **2020**, *25*, 2064.
(88) Barthels, F.; Marincola, G.; Marciniak, T.; Konhäuser, M.; Hammerschmidt, S.; Bierlmeier, J.; Distler, U.; Wich, P. R.; Tenzer, S.; Schwarzer, D.; Ziebuhr, W.; Schirmeister, T. Asymmetric Disulfanylbenzamides as Irreversible and Selective Inhibitors of Staphylococcus Aureus Sortase A. *ChemMedChem* **2020**, *15* (10), 839 850.
(89) Mnova 12.0.4 Mestrelab. https://mestrelab.com/download_file/mnova-12-0-4/ (accessed May 3, 2021).
(90) Lietsche, J.; Gorka, J.; Hardt, S.; Karas, M.; Klein, J. Custom-Made Microdialysis Probe Design. *J. Visualized Exp.* **2015**, *2015*, 53048.
(91) Buttner-Ennever, J. *The Rat Brain in Stereotaxic Coordinates*, 3; Paxinos, G.; Watson, C.; Academic Press: San Diego, 1996; Journal of Anatomy 1997, Vol. *191* (2), pp 315 317.

https://doi.org/10.1021/acs.jmedchem.1c01002
J. Med. Chem. 2021, 64, 12322 12358

“

4.4 Modular Solid-Phase Synthesis of Antiprotozoal Barnesin Derivatives

4.4.1 Context, Project Summary, and own Contribution

Barnesin A is a lipodipeptide that has a rare form of a vinylogous arginine residue in the P1 position.[305] Besides barnesin A, only one other natural product, miraziridine A, has been reported with this type of modification.[306] This natural product was found to be a metabolite of non-ribosomal polyketide synthesis in epsilonproteobacteria (*Sulfurospirrilum barnesii*) by condensation of an acetate unit to a lipopeptide chain via the NRPS-PKS assembly line. Barnesin A showed efficient and irreversible inhibition of cathepsin B, making this vinylogous arginine warhead an interesting chemotype for rational inhibitor development.[305] However, barnesin derivatives are neither isolable in good yields nor easily accessible via synthesis. The first total synthesis of barnesin A was accomplished in a nine-step solution-based synthesis sequence (total yield: 0.8%).[305]

In this study, the group of [redacted] developed a new and efficient synthesis protocol of barnesin A and derivatives using solid-phase supported Horner-Wadsworth-Emmons reactions to synthesize a library of 17 natural product-like analogs. All synthesized compounds were evaluated for metabolic stability and inhibition towards human cathepsin L and rhodesain. One barnesin analog with a lysine residue in P1 and a tyrosine residue in P2 position showed the strongest overall irreversible inhibition of rhodesain (k_{2nd}=673,809$M^{-1}min^{-1}$), tenfold weaker inhibition of human cathepsin L, and complete stability in glutathione resp. liver microsome assays. Here, in summary, a novel promising Michael acceptor warhead for the development of cysteine protease inhibitors was characterized and made synthetically accessible.

Own contributions: Rhodesain inhibition assays & Cathepsin selectivity assays.

Contributions from other authors: Synthesis and characterization of the inhibitors, Microsome stability assays & Glutathione stability assays.

This work has been published in: Organic Letters (impact factor: 6.00).

The 'Supporting Information' can be accessed online at doi: 10.1021/acs.orglett.0c00723.

4.4.2 Publication

The following publication quoted (within “”) from page 236 to page 240 is exactly the same as the manuscript cited on page 235:”

OL | Organic Letters

pubs.acs.org/OrgLett Letter

Modular Solid-Phase Synthesis of Antiprotozoal Barnesin Derivatives

Dávid Roman, Luka Raguž, François Keiff, Florian Meyer, Fabian Barthels, Tanja Schirmeister, Florian Kloss, and Christine Beemelmanns*

Cite This: *Org. Lett.* 2020, 22, 3744 3748 Read Online

ACCESS | Metrics & More | Article Recommendations | Supporting Information

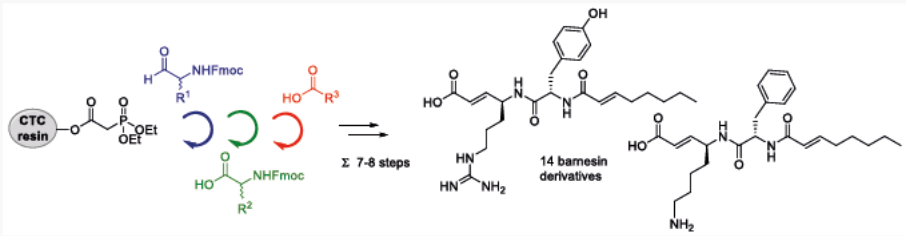

ABSTRACT: Here, we applied and optimized a solid support (SP)-based Horner Wadsworth Emmons reagent to prepare SP-bound vinylogous amino acids. Subsequent SP-based peptide synthesis, global deprotection, and chemical modifications yielded 14 lipodipeptides carrying vinylogous amino acids, including the natural product barnesin A (**1**). Biological evaluation revealed that several synthesized derivatives show micromolar to nanomolar inhibitory activity against papain-like cysteine proteases, human cathepsin L, and rhodesain.

Barnesin A (**1**) is the first metabolite reported from the bacterial class Epsilonproteobacterium (*Sulfurospirrilum barnesii*),[1,2] and also the first metabolite known from anaerobic bacteria biosynthesized by a nonribosomal peptide synthetase polyketide synthase (NRPS PKS) hybrid.[3] Barnesin A is a lipodipeptide containing a rare unnatural vinylogous arginine moiety, which is biosynthesized by condensation of an acetate unit and an activated lipopeptide chain via the NRPS PKS assembly line.[4] Such highly reactive vinylogous amino acids are rarely found in natural products. To date, only one other natural product containing a vinylogous arginine, miraziridine A (**2**), has been identified.[5−7] Most prominent and almost exclusive examples of structurally related natural products containing other vinylogous amino acids are syringolines[8] and glidobactins,[9] which contain vinyl-Val and vinyl-Tyr units, respectively.[10] The electrophilic nature of the α,β-unsaturated amide moiety (warhead) activates these natural products for conjugate addition reactions, a key reactivity of protease inhibitors.[11] As an example, pharmacological studies of syringolin A (**3**) disclosed that the molecule covalently targets the active site of proteasomes via a Michael addition reaction.[12] Similarly, first bioactivity studies of barnesin A (**1**) revealed selective nanomolar inhibitory activity (91.7 nM) against the cysteine protease cathepsin B,[13] and indicated inhibition mechanisms via a Michael-type addition reaction to the enzymatic target (Figure 1).[1]

The first total synthesis of barnesin A (**1**) was accomplished in nine steps (0.8% overall yield) using a solution-based approach commencing with readily available Fmoc-Arg(Boc)$_2$-OH.[1]

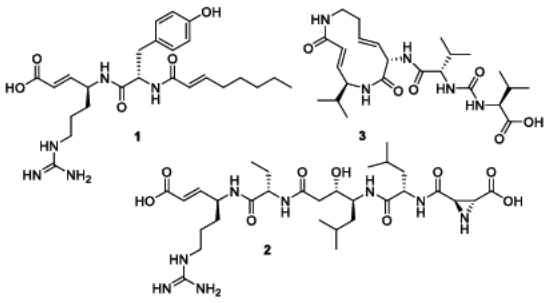

Figure 1. Structures of barnesin A (**1**), miraziridine A (**2**), and syringolin A (**3**).

Although the first-generation synthesis of barnesin allowed for the absolute structure confirmation and first bioactivity tests, a more efficient and modular synthetic approach was

Received: February 25, 2020
Published: March 26, 2020

https://dx.doi.org/10.1021/acs.orglett.0c00723
Org. Lett. 2020, 22, 3744 3748

Scheme 1. General Procedure for HWE-Based Solid-Phase Synthesis of Barnesin Derivatives

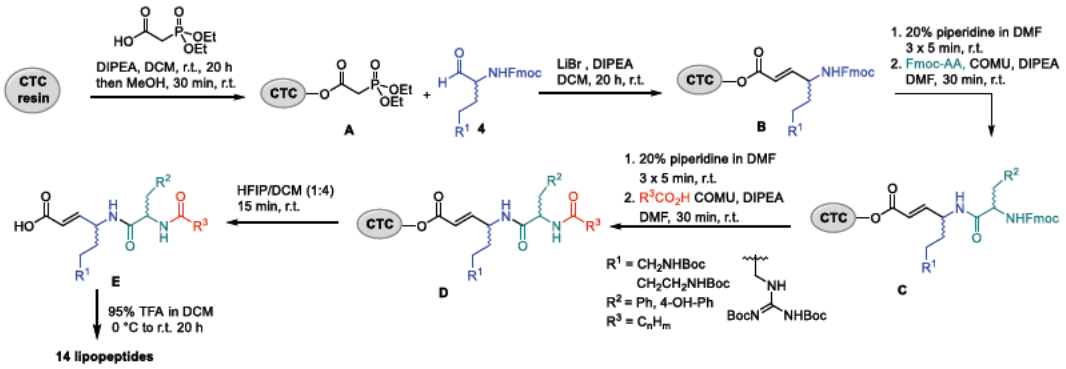

highly desirable to pursue more detailed structure activity studies.

Thus, we decided to combine the advantageous features of solid-phase peptide (SPP) synthesis (e.g., minimal amount of purification steps)[14,15] and Horner Wadsworth Emmons (HWE) reaction by coupling the carboxy terminus of HWE reagent to a resin.[16−18] This strategy would allow us to synthesize any required vinylogous amino acid on solid support and enable subsequent SPP-based peptide elongation steps.

As a first proof of principle, we aimed for the synthesis of barnesin A (**1**), followed by the synthesis of C4, C10-stereoisomers (**5**, **6**), acyl chain length derivatives (**7**–**10**), and derivatives containing different amino acids (**12**–**17**). To maintain the essential structural protease recognition features, we focused on the exchange of vinyl arginine against lysine, and phenylalanine against tyrosine. Fully reduced barnesin derivative **11** should be obtained by hydrogenationfrom **1** or **8**, respectively.

Among several possible resin candidates, we selected 2-chlorotrityl chloride resin (CTC resin) for subsequent studies as mild cleavage conditions are required to release the peptide scaffold carrying a vinylogous amino acid from the resin. The envisaged SPP based Horner Wadsworth Emmons (HWE) reaction required the preparation of phosphonate A loaded on to the solid-phase (CTC) (Scheme 1),[16−18] which was achieved using standard coupling conditions (theoretical loading of 0.8 mmol phosphonate per gram resin, Supporting Information). Here, it is worth noting that the newly formed resin could be stored for several months at 4 °C until further use. The synthesis of the resin-bound vinylogous arginine required the preparation of triple protected D- or L-Fmoc-Arg(Boc)$_2$-OMe, which was achieved according to a previously described four step synthesis starting from commercially available L- or D-ornithine hydrochloride.[1,19] The methyl ester was then reduced using a moderate excess of DIBAL(H) at −78 °C to ensure high conversion and minimal over reduction (Scheme 1, Supporting Information). For the preparation of vinylogous lysine derivatives commercially available *N*-Boc-Lys-Fmoc was transformed in an analogous fashion.

Due to their inherent instability amino acid aldehydes **4** were immediately subjected to modified HWE reaction conditions using resin-bound phosphonate A and reaction scales varied between 0.5 and 3.0 g of resin.[16−18] The resulting resin-bound alkene **B** was obtained with excellent *E*-selectivity (vide infra).[20]

The general strategy for subsequent peptide coupling followed the principles of Fmoc/*t*Bu solid-phase peptide synthetic strategy, which implied the use of N_α-Fmoc protected amino acids and *t*Bu-protected side chains. Thus, every protective group orthogonal to Fmoc appeared suitable for the protection of reactive moieties of the side chains and allowed the selective deprotection of the N_α-amine and regioselective coupling. In general, a qualitative ninhydrin test was used to monitor the reaction progress.

Coupling with the Fmoc-protected amino acid was performed using the highly effective coupling reagent COMU and DIPEA in DMF (product **C**).[21] Eventually, the resin-bound peptide was coupled with the respective fatty acid (product **D**) and the product was cleaved off as fully protected modified lipo-dipeptide **E** using HFIP/DCM (1:4) within 15 min. Notably, longer exposure of **D** to more acidic conditions, e.g., HFIP/DCM (1:1 to 1:3), led to the partial cleavage of the Boc-protective groups and isolation of a mixture of mono- and diprotected derivatives. The obtained lipodipeptides were globally deprotected using 95% TFA in DCM and purified using reverse-phase preparative high pressure liquid chromatography (HPLC) to yield multimilligram amounts of analytical pure (*E*)-barnesin derivatives (Figure 2). Here, it needs to be noted that reaction sequences containing arginine derivatives were prone to side reactions (e.g., partial Boc deprotection) and epimerization if conditions were not accurately followed. To separate the resulting diastereomers and monoprotected species required occasionally an additional HPLC purification step resulting in overall lower yields of the desired end product (see the Supporting Information). Methyl esters (**13**, **14**) were obtained after treatment of cleaved and fully protected peptides (**15** and **16**) with TMS-diazomethane, followed by global deprotection.

In summary, the synthesis of 14 barnesin derivatives was achieved in only seven or eight synthetic steps (instead of previous nine steps),[1] and only one final purification protocol was generally required to yield analytical pure samples.

We then tested the inhibitory activity of all barnesin derivatives against two pharmacologically important papain-like cysteine proteases, human cathepsin L (hCatL) and rhodesain (Rd) (Table 1, reference compounds: Table S2).[22] Cathepsin L is a lysosomal endopeptidase, which is involved in the initiation of physiologically important protein degradation reactions.[23] An increased expression of hCatL and other

https://dx.doi.org/10.1021/acs.orglett.0c00723
Org. Lett. 2020, 22, 3744 3748

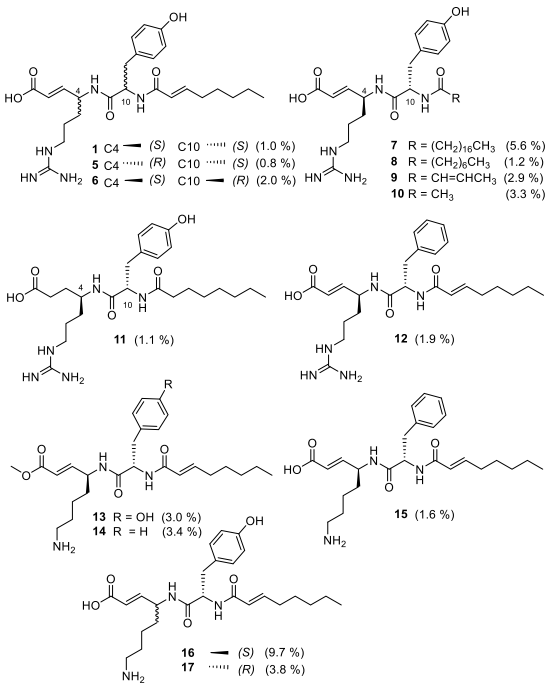

Figure 2. Synthesized barnesin derivatives (**1**, **5**–**17**) using an HWE-based solid-phase synthesis approach (overall yields after seven or eight steps, respectively).

proteases, however, has been reported in many cancer types and tumor-associated fibroblasts and macrophages, thus rendering them promising drug targets. Rhodesain (Rd), also a clan CA papain-family cysteine protease plays a central role in the life cycle of *Trypanosoma brucei* and its related subspecies,[24] which are parasitic hemoflagellate protists and the major cause of *Human African Trypanosomiasis* (HAT),[25] more commonly known as "African sleeping sickness".[26] The selective inhibition of cysteine proteases in *Trypanosoma* represents a promising strategy for the development of new drugs with antiparasitic activity.

We used an established fluorescence-based assay to determine the activity of all synthesized barnesin derivatives against hCatL and Rd,[27] and an initial screening at inhibitor concentrations of 20 μM was performed to identify ligands with an inhibition of hCatL and Rd above 60%. For active compounds, continuous assays at different inhibitor concentrations were carried out. All inhibitors with more than 60% inhibition in the initial screening were found to act in a time-dependent manner and compared to reference standards (Supporting Information, Table S2). During kinetic analyses of the substrate conversion, the maximum inactivation rates k_{inact}, the apparent dissociation constants K_i^{app}, and the second-order rates of inhibition k_{second} were determined. The reversible enzyme inhibitor complex constants K_i were calculated according to the Cheng-Prusoff equation.[28] To evaluate the potential of all compounds regarding their systemic application in mammalians, we determined in vitro pharmacokinetic properties in metabolic assays using human liver microsomes (HLM) and glutathione (GSH).

As depicted in Table 1, barnesin A (**1**) revealed K_i values of 1.5 (±0.39) and 0.081 (±0.013) μM against hCatL and Rd, respectively. The stereochemistry at position C-4 and C-10 was found to be of crucial importance as diastereoisomer **5** (4*R*,10*S*) showed only very low activity against rhodesain, and **6** (4*S*,10*R*) was found to be inactive (nd) against both enzymes. In accordance with previous findings, the fully reduced barnesin A derivative **11** showed no inhibitory activity against both proteases. In a next step, different acyl derivatives of barnesin A (**7**–**10**) were tested. The results illustrated that the chain length, but not saturation degree, is of significant importance for activity. While long-chain derivative **7**, propenyl derivatives **9** and acyl derivative **10** showed significant reduction in activity, octanyl derivative **8** revealed properties similar to barnesin A. Furthermore, the exchange of tyrosine (**1**) against phenylalanine (**12**) did not significantly alter the activity. As shown in Table 1, all tested vinyl-Arg derivatives (**1**–**12**) were found to be stable in our microsomal and

Table 1. Inhibitory Activity (K_i Values) of Synthesized Compounds against Cathepsin L and Rhodesain and Their Metabolic Stability

	cat L		Rd			
compd	K_i (μM)	k_{second} (M^{-1} s^{-1})	K_i (μM)	k_{second} (M^{-1} s^{-1})	HLM[a] (%)	GSH[b] (%)
1	**1.5 ± 0.39**	**2216 ± 347**	**0.081 ± 0.013**	**144427 ± 23974**	**83**	**94**
5	nd	nd	3.6 ± 1.0	2130 ± 144	68	≥99
6	nd	nd	nd	nd	87	99
7	**nd**	**nd**	**nd**	**nd**	**90**	**93**
8	7.0 ± 2.1	749 ± 85	0.080 ± 0.012	84579 ± 7358	92	≥99
9	nd	nd	2.8 ± 1.1	6847 ± 1627	≥99	88
10	35 ± 7.6	105 ± 10	0.91 ± 0.34	4862 ± 736	≥99	≥99
11	nd	nd	nd	nd	≥98	≥99
12	**6.4 ± 2.2**	**1,110 ± 601**	**0.075 ± 0.017**	**104631 ± 14066**	**79**	**≥99**
13	1.9 ± 0.4	3004 ± 292	0.21 ± 0.049	54716 ± 5982	25	53
14	0.047 ± 0.005	103802 ± 1573	0.024 ± 0.005	797250 ± 151069	<5	76
15	4.3 ± 1.0	1704 ± 167	0.048 ± 0.01	157543 ± 25248	≥99	≥99
16	**0.11 ± 0.02**	**22436 ± 897**	**0.012 ± 0.005**	**673809 ± 32619**	**≥99**	**97**
17	4.2 ± 0.39	904 ± 43	0.045 ± 0.02	239099 ± 85338	80	98

[a]Microsomal stability assays using human liver microsomes (HLM). [b]Glutathione (GSH) stability assays. Values are given in % based on relative peak areas of the extracted ion chromatograms after 90 min (assay) versus time of initiation (100%).

https://dx.doi.org/10.1021/acs.orglett.0c00723
Org. Lett. 2020, 22, 3744 3748

glutathione-based stability assays (HLM and GSH) over a period of more than 90 min (Supporting Information). This is quite surprising as the intrinsic mechanism-based reactivity of unsaturated barnesins would imply interference with nucleophiles or oxidative metabolic degradation pathways. In case of lysine derivatives **13** **17**, both methyl esters (**13**, **14**) showed higher inhibitory activity against both cysteine proteases compared to the free acids (**15** **17**); presumably due to an increased electrophilicity of the vinylogous warhead. At the same time, the ester moiety reduced the metabolic stability, presumably due to spontaneous trans-acylation reactions.

Thus, overall, derivative **16** was determined as the most active and stable derivative. We then analyzed literature reports of other natural products with similar structural features with respect to protease inhibitory activities against Cat L and Rd. Although inhibitory activities values across different assays and literature reports needs to be handled with extreme care, our survey (Table S2) showed that barnesin derivative **14** had similar inhibitory activity against CatL as the fungal dipeptide E-64[29] (E-64: IC_{50} 0.05 μM versus **14**: IC_{50} 0.093 μM), while a structural analogue of E-64, named kojistatin A, was found to be 2 orders of magnitude more potent (0.0048 μM).[30] Interestingly, both fungal protease inhibitors carry a epoxysuccinate moiety as warhead. However, to the best of our knowledge, none of the related reports included inhibitory activity studies against rhodesain (Rd) or stability assays to evaluate their systemic application.

In conclusion, we have developed a new and efficient synthesis of barnesin and derivatives using a largely underexplored HWE reaction on solid support. Only seven synthetic steps and one purification procedure were needed to yield derivatives on a multimilligram scale. Subsequent biological studies of all synthesized compounds showed an intriguing metabolic stability and clear structure activity relationships against human cathepsin L (hCatL) and rhodesain (Rd). The replacement of tyrosine to phenylalanine and vinyl arginine to vinyl lysine generally increased inhibitory activities of barnesin derivatives, without significant loss of metabolic stability. Overall, these encouraging bioassay results will guide future studies on this intriguing natural product scaffold. The modularity of the synthetic approach presented further sets the stage for extensive combinatorial studies necessary for the targeted generation of leads in the field of cysteine protease inhibitors.

■ ASSOCIATED CONTENT

Supporting Information

The Supporting Information is available free of charge at https://pubs.acs.org/doi/10.1021/acs.orglett.0c00723.

Experimental procedures, bioactivity studies, and NMR tables (PDF)

NMR spectra (PDF)

■ AUTHOR INFORMATION

Corresponding Author

Christine Beemelmanns *Leibniz Institute for Natural-Product Research and Infection Biology - Hans Knöll Institute (HKI), 07745 Jena, Germany;* orcid.org/0000-0002-9747-3423; Email: christine.beemelmanns@leibniz-hki.de

Authors

Dávid Roman *Leibniz Institute for Natural-Product Research and Infection Biology - Hans Knöll Institute (HKI), 07745 Jena, Germany*

Luka Raguž *Leibniz Institute for Natural-Product Research and Infection Biology - Hans Knöll Institute (HKI), 07745 Jena, Germany;* orcid.org/0000-0001-5383-3012

François Keiff *Leibniz Institute for Natural-Product Research and Infection Biology - Hans Knöll Institute (HKI), 07745 Jena, Germany*

Florian Meyer *Leibniz Institute for Natural-Product Research and Infection Biology - Hans Knöll Institute (HKI), 07745 Jena, Germany*

Fabian Barthels *Institute of Pharmaceutical and Biomedical Sciences, Johannes Gutenberg University Mainz, 55128 Mainz, Germany*

Tanja Schirmeister *Institute of Pharmaceutical and Biomedical Sciences, Johannes Gutenberg University Mainz, 55128 Mainz, Germany*

Florian Kloss *Leibniz Institute for Natural-Product Research and Infection Biology - Hans Knöll Institute (HKI), 07745 Jena, Germany*

Complete contact information is available at: https://pubs.acs.org/10.1021/acs.orglett.0c00723

Notes

The authors declare the following competing financial interest(s): The authors declare a financial conflict of interest. A patent application has been filed (registration number: EP 18 160 274.9: Barnesin A, derivatives and uses thereof) at the European patent office.

■ ACKNOWLEDGMENTS

We are grateful for financial support from the German Research Foundation (DFG, BE 4799/2-1). C.B. greatly acknowledges funding by the ERC (ERC Starting Grant project 802736 MORPHEUS). F.M. and F.K. have been supported by InfectControl 2020 (FKZ 03ZZ0803A, FKZ 03ZZ0826A, and FKZ 03ZZ0835A). We wish to thank Ms. Heike Heinecke (Leibniz Institute for Natural Product Research and Infection Biology - Hans Knöll Institute, Jena) for measurement of NMR spectra.

■ REFERENCES

(1) Rischer, M.; Raguž, L.; Guo, H.; Keiff, F.; Diekert, G.; Goris, T.; Beemelmanns, C. *ACS Chem. Biol.* **2018**, *13*, 1990 1995.

(2) Stolz, J. F.; Ellis, D. J.; Blum, J. S.; Ahmann, D.; Lovley, D. R.; Oremland, R. S. *Int. J. Syst. Evol. Microbiol.* **1999**, *49*, 1177 1180.

(3) (a) Behnken, S.; Hertweck, C. *Appl. Microbiol. Biotechnol.* **2012**, *96*, 61 67. (b) Letzel, A.-C.; Pidot, S. J.; Hertweck, C. *Nat. Prod. Rep.* **2013**, *30*, 392 428.

(4) Walsh, C. T.; O'Brien, R. V.; Khosla, C. *Angew. Chem., Int. Ed.* **2013**, *52*, 7098 7124.

(5) Tabares, P.; Degel, B.; Schaschke, N.; Hentschel, U.; Schirmeister, T. *Pharmacogn. Res.* **2012**, *4*, 63 66.

(6) Nakao, Y.; Fujita, M.; Warabi, K.; Matsunaga, S.; Fusetani, N. *J. Am. Chem. Soc.* **2000**, *122*, 10462 10463.

(7) Konno, H.; Kubo, K.; Makabe, H.; Toshiro, E.; Hinoda, N.; Nosaka, K.; Akaji, K. *Tetrahedron* **2007**, *63*, 9502 9513.

(8) Kolodziejek, I.; Misas-Villamil, J. C.; Kaschani, F.; Clerc, J.; Gu, C.; Krahn, D.; Niessen, S.; Verdoes, M.; Willems, L. I.; Overkleeft, H. S.; Kaiser, M.; van der Hoorn, R. A. L. *Plant Physiol.* **2011**, *155*, 477 489.

https://dx.doi.org/10.1021/acs.orglett.0c00723
Org. Lett. 2020, 22, 3744 3748

(9) Schellenberg, B.; Bigler, L.; Dudler, R. *Environ. Microbiol.* **2007**, *9*, 1640 1650.
(10) Krahn, D.; Ottmann, C.; Kaiser, M. *Nat. Prod. Rep.* **2011**, *28*, 1854 67.
(11) Kaysser, L. *Nat. Prod. Rep.* **2019**, *36*, 1654 1686.
(12) Groll, M.; Schellenberg, B.; Bachmann, A. S.; Archer, C. R.; Huber, R.; Powell, T. K.; Lindow, S.; Kaiser, M.; Dudler, R. *Nature* **2008**, *452*, 755 758.
(13) Gobec, S.; Frlan, R. *Curr. Med. Chem.* **2006**, *13*, 2309 2327.
(14) Varnava, K. G.; Sarojini, V. *Chem. - Asian J.* **2019**, *14*, 1088 1097.
(15) Behrendt, R.; White, P.; Offer, J. *J. Pept. Sci.* **2016**, *22*, 4 27.
(16) Johnson, C. R.; Zhang, B. *Tetrahedron Lett.* **1995**, *36*, 9253 9256.
(17) Sun, S.; Murray, W. V. *J. Org. Chem.* **1999**, *64*, 5941 5945.
(18) Ando, K.; Suzuki, Y. *Tetrahedron Lett.* **2010**, *51*, 2323 2325.
(19) Wu, Y.; Matsueda, G. R.; Bernatowicz, M. *Synth. Commun.* **1993**, *23*, 3055 3060.
(20) Blanchette, M. A.; Choy, W.; Davis, J. T.; Essenfeld, A. P.; Masamune, S.; Roush, W. R.; Sakai, T. *Tetrahedron Lett.* **1984**, *25*, 2183 2186.
(21) Subiros-Funosas, R.; Nieto-Rodriguez, L.; Jensen, K. J.; Albericio, F. *J. Pept. Sci.* **2013**, *19*, 408 414.
(22) Powers, J. C.; Asgian, J. L.; Ekici, Ö.D.; James, K. E. *Chem. Rev.* **2002**, *102*, 4639 4750.
(23) Li, Y.-Y.; Fang, J.; Ao, G.-Z. *Expert Opin. Ther. Pat.* **2017**, *27*, 643 656.
(24) Rocha, D. A.; Silva, E. B.; Fortes, I. S.; Lopes, M. S.; Ferreira, R. S.; Andrade, S. F. *Eur. J. Med. Chem.* **2018**, *157*, 1426 1459.
(25) Cullen, D. R.; Mocerino, M. *Curr. Med. Chem.* **2017**, *24*, 701 717.
(26) Barrett, M. P. *PLoS Neglected Trop. Dis.* **2018**, *12*, No. e0006925.
(27) Giroud, M.; Ivkovic, J.; Martignoni, M.; Fleuti, M.; Trapp, N.; Haap, W.; Kuglstatter, A.; Benz, J.; Kuhn, B.; Schirmeister, T.; Diederich, F. *ChemMedChem* **2017**, *12*, 257 270.
(28) Cheng, Y.-Ch.; Prusoff, W. H. *Biochem. Pharmacol.* **1973**, *22*, 3099 3108.
(29) Hanada, K.; Tamai, M.; Yamagishi, M.; Ohmura, S.; Sawada, J.; Tanaka, I. *Agric. Biol. Chem.* **1978**, *42*, 523.
(30) Sato, N.; Horiuchi, T.; Hamano, M.; Sekine, H.; Chiba, S.; Yamamoto, H.; Yoshioka, T.; Kimura, I.; Satake, M.; Ida, Y. *Biosci., Biotechnol., Biochem.* **1996**, *60*, 1747.

https://dx.doi.org/10.1021/acs.orglett.0c00723
Org. Lett. 2020, 22, 3744 3748

“

5 Open-source Technologies for Life Sciences

5.1 A Low-cost 3D-printable Differential Scanning Fluorometer for Drug Discovery and Biochemistry

5.1.1 Context, Project Summary, and own Contribution

Biophysical methods are indispensable tools in elucidating protein- and RNA-ligand interactions for drug discovery efforts. One approach is the thermal study of protein/RNA stability after ligand-binding since the free energy of binding of complex formation usually stabilizes the complex.[307] In this context, a fluorometric reporter dye can be used to determine the degree of (un)folding on a linear temperature heating ramp.[308] PANTOLIANO et al. developed a protocol in the early 2000s to perform such experiments, now known as differential scanning fluorimetry (DSF), in a conventional real-time polymerase chain reaction (qPCR) thermocycler.[309] Despite the simplicity of the experimental setup, the accessibility of several 10,000 € qPCR instruments is still limiting for performing DSF experiments.[310] In this context, HOESER et al. developed a protocol to transform a conventional 96-well plate reader into a DSF thermocycler but with the prerequisite of ownership.[311]

In this project, we demonstrated that the accessibility of a DSF-capable instrument can be significantly improved by combining 3D printing and microelectronics for the development of an open-source differential scanning fluorometer (openDSF) for 176 €. The openDSF system consists of a 3D-printed polyoxymethylene (POM) chassis, the ESP32 microcontroller as the heart piece for temperature resp. fluorescence measurement, a fluorescence measurement pathway consisting of high-power LEDs, and stage light foil as a low-cost filter component (λ_{ex}=490 nm/λ_{em}=624 nm). We were able to show that the I^2S interface of the ESP32 microcontroller, which was developed for processing audio data, is perfectly suited for recording analog measurement data such as thermistor and photodiode signals. Samples were prepared in PCR tubes and tempered during the measurement by airflow heating, resulting in an absolute temperature accuracy of (±0.1 °C). With exemplary protein and RNA melting experiments from the fields of drug discovery and biochemistry, we could demonstrate that the openDSF system is suitable for the investigation of high-resolution protein/RNA ligand-binding.

Own contributions: Conceptualization, 3D printing, Programming of the software, Assembly of electronics and mechanical parts, Characterization of the instrumentation, Execution of example applications & Writing of the manuscript.

Contributions from other authors: Protein expression and purification & In vitro transcription of RNA.

This work has been published in: HardwareX (impact factor: 4.33).

5.1.2 Publication

The following publication quoted (within “”) from page 243 to page 268 is exactly the same as the manuscript cited on page 242:”

HardwareX 11 (2022) e00256

Contents lists available at ScienceDirect

HardwareX

journal homepage: www.elsevier.com/locate/ohx

A low-cost 3D-printable differential scanning fluorometer for protein and RNA melting experiments

Fabian Barthels *, Stefan J. Hammerschmidt, Tim R. Fischer, Collin Zimmer, Elisabeth Kallert, Mark Helm, Christian Kersten, Tanja Schirmeister

Institute for Pharmaceutical and Biomedical Sciences, Johannes Gutenberg-University, Staudinger Weg 5, 55128 Mainz, Germany

ARTICLE INFO

Article history:
Received 26 October 2021
Received in revised form 2 December 2021
Accepted 1 January 2022

Keywords:
Differential scanning fluorimetry
Thermal shift assay
ESP32
Protein melting point
Biophysical chemistry

ABSTRACT

Differential scanning fluorimetry (DSF) is a widely used biophysical technique with applications to drug discovery and protein biochemistry. DSF experiments are commonly performed in commercial real-time polymerase chain reaction (qPCR) thermal cyclers or nanoDSF instruments. Here, we report the construction, validation, and example applications of an open-source DSF system for 176 €, which, in addition to protein-DSF experiments, also proved to be a versatile biophysical instrument for less conventional RNA-DSF experiments. Using 3D-printed parts made of polyoxymethylene, we were able to fabricate a thermostable machine chassis for protein-melting experiments. The combination of blue high-power LEDs as the light source and stage light foil as filter components was proven to be a reliable and affordable alternative to conventional optics equipment for the detection of SYPRO Orange or Sybr Gold fluorescence. The ESP32 microcontroller is the core piece of this openDSF instrument, while the in-built I^2S interface was found to be a powerful analog-to-digital converter for fast acquisition of fluorescence and temperature data. Airflow heating and inline temperature control by thermistors enabled high-accuracy temperature management in PCR tubes (±0.1 °C) allowing us to perform high-resolution thermal shift assays (TSA) from exemplary biological applications.

Specifications table

Hardware name	openDSF
Subject area	Chemistry and biochemistry
Hardware type	Measuring physical properties and in lab sensors
Closest commercial analog	Real time PCR thermocycler: e.g., Qiagen Rotor Gene Q
Open source license	GNU General Public License (GPL) 3.0
Cost of hardware	176 €
Source file repository	openDSF (Mendeley data): https://doi.org/10.17632/73rt8s7pwd.2

* Corresponding author.
E-mail address: barthels@uni-mainz.de (F. Barthels).

https://doi.org/10.1016/j.ohx.2022.e00256
2468-0672/

Hardware in context

Differential scanning fluorimetry (DSF) is a method of biophysical protein analysis, which is utilized for the investigation of thermal protein unfolding [1 3]. In this context, protein binding ligands may increase the protein stability and result in the protein unfolding being shifted to a higher melting temperature. The difference between the melting temperature of a protein in the presence or absence of a ligand is termed "thermal shift". Thermal shift assays (TSA) are among the most com mon ligand characterization techniques with numerous applications for drug discovery and structural biology [4,5]. TSAs are easy to establish and are typically performed in commercial real time polymerase chain reaction thermal cycler (qPCR) instruments [6,7]. To perform a typical DSF experiment, a sample containing a protein or protein complex is added with the SYPRO Orange dye. SYPRO Orange has a low intrinsic fluorescence with the natively folded protein present. Only upon heating, when hydrophobic patches of the protein are exposed, the merocyanine type dye binds to them, resulting in a sig nificant increase in fluorescence [3]. The apparent melting point (T_m) is usually determined as the inflection point of the flu orescence versus temperature curve and is considered a measure of protein stabilization [8]. Widely used qPCR machines used for this purpose utilize halogen lamps, laser diodes, or LEDs to monitor the fluorescence changes allowing the measure ment of the SYPRO Orange fluorescence. Besides the high cost of commercial qPCR instruments, the factory filter sets fre quently do not optimally fit the large Stokes shift of the SYPRO Orange dye (λ_{ex} 490 nm/λ_{em} 624 nm) and cause reduced quantum yield and signal to noise (S/N) ratios [9]. This might lead to the absence of a measurable melting curve for small and less hydrophobic proteins [3]. In contrast, fluorescence spectrometers with variable settings of wavelengths are limited in their temperature management, making them mostly impractical for DSF experiments.

To address this issue, Hoeser et al. developed a cheap and easy to build heating device for a 96 well plate reader that is coupled with a fluorescence spectrometer [10]. However, this requires the availability of a likewise expensive plate reader. Recently, open source qPCR machines have been presented and described for DIY reproduction [11,12]. However, some of these open source qPCR devices (including some commercial instruments) were designed and proven for nucleic acid quan tification and will likely be impractical for performing high resolution DSF experiments because they show temperature homogeneity ranging up to ± 0.5 °C so that thermal shifts smaller than the temperature resolution limit might not be accu rately detected [11,13].

In addition to proteins, numerous RNA molecules also possess a native tertiary structure that can be characterized in the course of a thermal unfolding process. Similar to protein ligand binding, small molecule modulators of RNA often lead to stabilization and increased melting points [14,15]. This can be obtained in the course of melting experiments from the intrin sic fluorescence properties of the nucleic bases or with an intercalating dye. For this purpose, Silvers et al. developed a DSF protocol using dyes from the Sybr series, which allow quantification with the same fluorescence setup as for SYPRO Orange when using the Sybr Gold dye (λ_{ex} 495 nm/λ_{em} 537 nm) [16].

In this work, we describe the construction and performance of an optics free 3D printable low cost differential scanning fluorometer (openDSF) with high sensitivity for SYPRO Orange (protein DSF) or Sybr Gold (RNA DSF) fluorescence detection and a melting temperature resolution of < 0.1 °C.

Hardware description

We designed an open source differential scanning fluorometer as a low cost alternative to existing qPCR thermal cyclers and commercial nanoDSF devices for biophysical characterization of protein ligand complexes (Fig. 1). To support low budget academic research campaigns, only inexpensive and easily available components (e.g., 3D printed pieces, basic elec tronics) were used, so that the costs (176 €) are several magnitudes lower than those of a commercial counterpart (~20,000 €) [17]. The fundamental principle of the system is that four DSF reaction mixtures, prepared in PCR tubes, are flo wed with heated air, while both the temperature and the SYPRO Orange fluorescence of each PCR tube are measured and recorded. To achieve this functionality, the design of the device combines five modules to form the whole open source dif ferential scanning fluorometer: 1) the 3D printed chassis, 2) the ESP32 microcontroller, 3) the air heating system, 4) the tem perature probes, and 5) the fluorescence measurement path (Fig. 2B).

3D printed device chassis

Structural parts forming the chassis of the device were fabricated by fused deposition modeling with an Anycubic 4Max 3D printer either from polyethylene terephthalate (PETG, diameter: 1.75 mm) or from polyoxymethylene (POM, diameter: 1.75 mm) filament. Functional tasks of the chassis are the assembly of the measuring, lighting, and heating modules as well as the directional flow control of the air heating system. DSF experiments are performed in the temperature range of 20 95 °C, which sets special requirements for the temperature stability of the 3D printed parts. Hence, POM filament was used for parts with increased temperature demands (POM is dimensionally stable up to at least 130 °C [18]). To meet the known constructional limitations of POM 3D printing, sharp corners and edges were avoided in the design of the POM parts, because these are particularly prone to warping [19]. The openDSF chassis consisted of 14 different 3D printed parts (Fig. 2A). POM parts were designed double walled and printed with an infill of 20% so that the high air content inside these parts makes

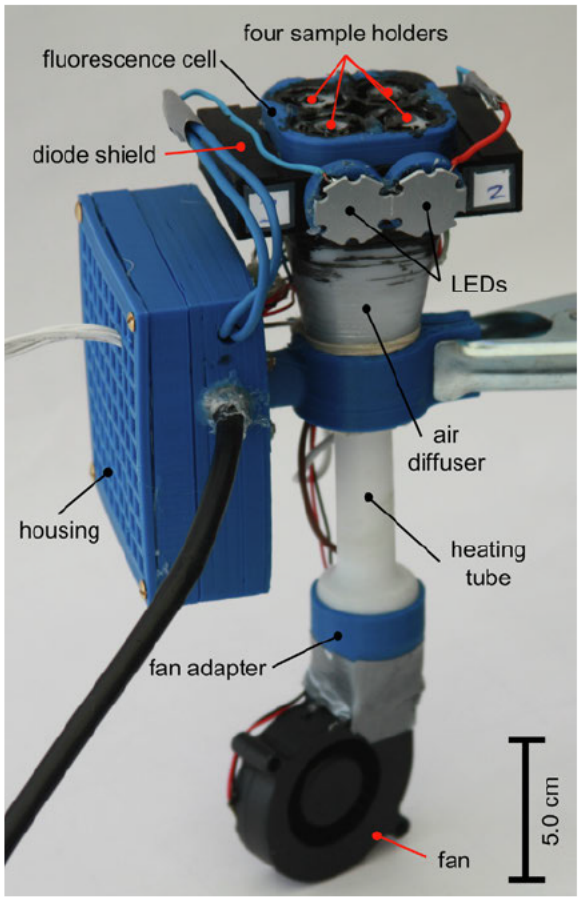

Fig. 1. Device overview. Photograph of the openDSF instrument with opened sample holders and labeling of important features.

them good thermal insulators. The low thermal losses allow for reproducible heating ramps and eliminate hot zones on the device surface so that it can be safely touched by the user at any time.

ESP32 microcontroller

The Espressif ESP32 wrover microcontroller (dual core CPU, 8 MB PSRAM, 240 MHz clock) was chosen as the central control unit of the fluorometer. The ESP32 is a low cost and relatively recent microcontroller family (released in 2016) [20]. The digital outputs of the chip were used to control the excitation LEDs, the air supplying fan, and the heating wire. The peripheral I^2S interface of the chip, which has been designed for transmitting audio data, has proven suitable for recording thermistor and photodiode analog input signals in the microsecond range (Fig. 2B). In this regard, two onboard multi channel successive approximation analog to digital converters (SAR ADCs) were polled with a sampling rate of 60 kHz and the temperature resp. fluorescence values were recorded *via* direct memory access (DMA) protocol. Online data processing was handled by one of the two CPU cores, while the other core was tasked with general control and communication *via* the PC's serial interface. The firmware for the ESP32 was developed on the Espressif ESP IDF 4.2 platform, while the serial interface was implemented with Python, Matplotlib, NumPy, SciPy, and Tkinter. A serial/USB driver must be installed on the connected PC.

Air heating system

Temperature control of the sample PCR tubes was performed by airflow heating, in which the air was tempered with a heating wire and conveyed by a radial fan (Fig. 3A). The heating power (heating wire current) was controlled by a 13 bit PWM MOSFET circuit, while the air volume (fan speed) was controlled by an 11 bit circuit. A Sunon Blower (MF50151V2

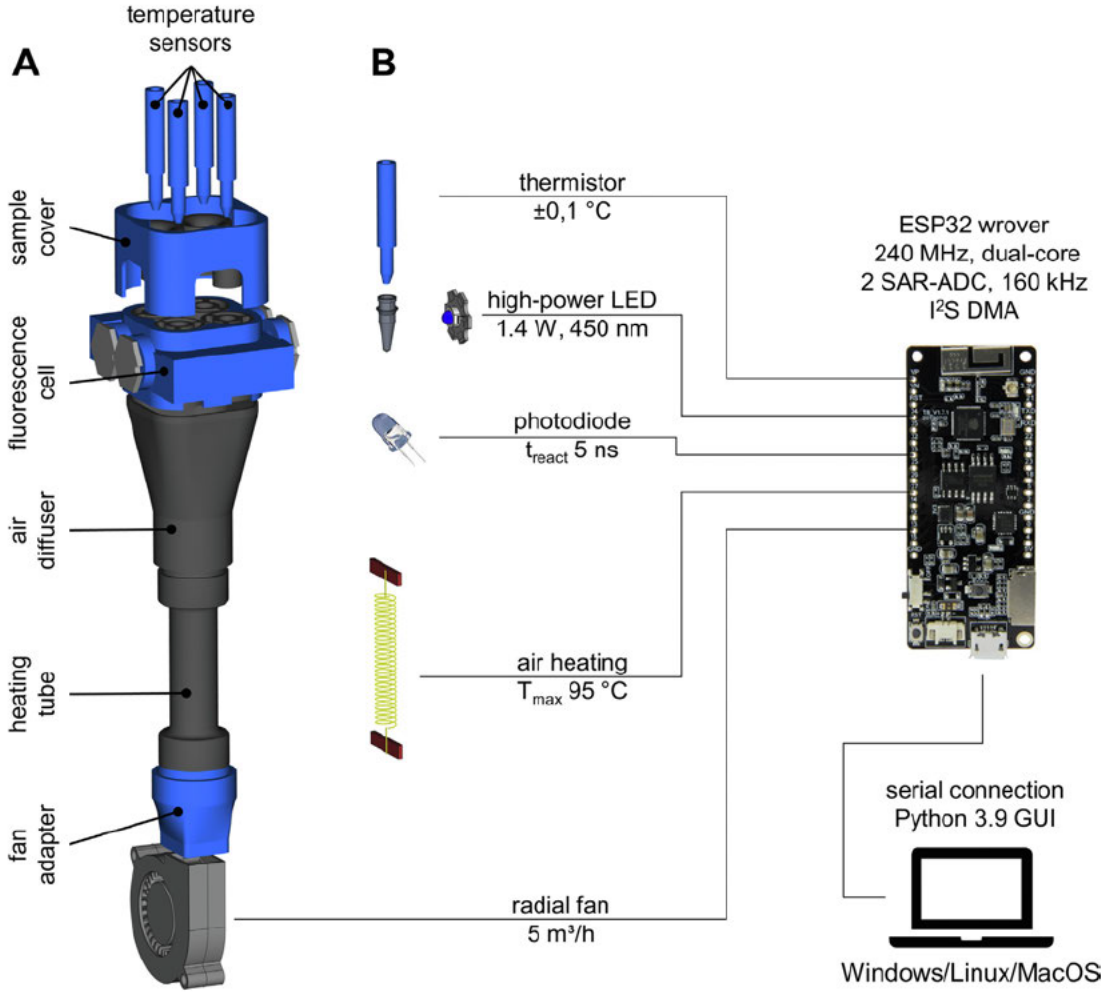

Fig. 2. (**A**) Explosion drawing of the openDSF chassis. 3D-printed parts made of PETG are shown in blue. POM parts are shown in gray. A detailed explosion drawing and a cross-section of the fluorescence cell are shown in the figures below. (**B**) Schematic overview of all modules included in the system with information on characteristic specifications of the components. (For interpretation of the references to color in this figure legend, the reader is referred to the web version of this article.)

B00U A99) was used as a radial fan, which was designed to convey approx. 5 m^3/h of air along an SS430 awg30 heating wire (stainless steel 430, l 70 cm, d 0.25 mm, R 12.2 Ω/m, X6Cr17). The power consumption of the heating module was designed to be max. 150 W to be able to run both slow and fast (0.1 9 °C/min) heating ramps for up to 4 PCR tube samples. A homogeneous temperature cross section was ensured by turbulent airflow within the device's mixing cell. The dimensions of the air flowed round parts of the chassis were designed based on a calculated Reynolds number (Re ~ 10,000). Addition ally, to increase the velocity of the airflow and thus the heat transfer in the proximity of the sample vessels, the sample hold ers were shaped as Laval nozzles. The resulting pressure loss promotes uniform distribution of the airflow to the 4 individual sample holders.

Temperature probes

The temperature of each sample can be determined separately using negative temperature coefficient (NTC) thermistors (NTC3950, 100 kΩ) within the airspace of the individual PCR tube. The temperature probes were dimensioned in a manner that they can be inserted into the PCR tube and thereby seal the upper opening. A thermistor circuit was designed in such a way that a voltage divider (V_{ref} 5.02 V) enabled the recording of relevant measurement temperatures (20 95 °C) within the

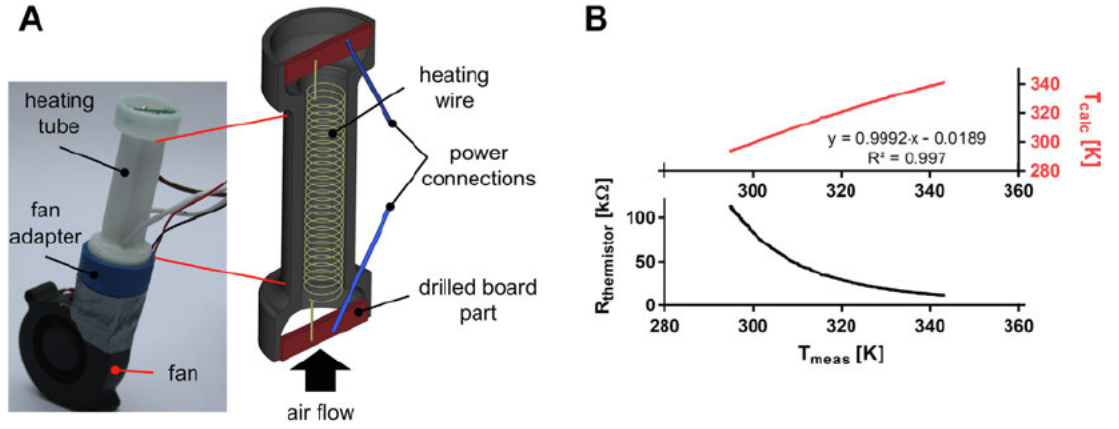

Fig. 3. (**A**) Photograph and cross-section of the heating module. The air heating system works according to the principle that the fan conveys ambient air through the heating tube, in which the air is heated and turbulated on the coiled heating wire. The heating coil is self-supporting and is connected to the power supply at the ends on cut-to-size drilled board parts. (**B**) Bottom: The air heating system was calibrated using the thermistors of the sample holders. The resistance of the thermistors follows the logarithmic Steinhart-Hart relationship to the actual temperature. Top: Determination of the coefficients of the Steinhart-Hart equation ($\frac{1}{T} = 0.0009614 + 0.0002096 \cdot \ln(R) + 0 \cdot \ln^3(R)$) allows temperature adjustment in the PCR tubes with an absolute accuracy of 0.1 °C.

ADC's 12 bit resolution. The measured temperature dependent voltages were recorded every second by the ESP32 chip and stabilized by oversampling (SAR ADC at 60 kHz sampling rate). The conversion of voltages to sample temperatures was performed using the modified Steinhart Hart equation ($\frac{1}{T} = a_0 + a_1 \ln(R) + a_2 \ln^3(R)$) [21]. The apparent resistance was calculated from the measured voltages and the dimensions of our design: $R_{thermistor} = 12k\Omega(\frac{5.02V}{0.0008 U + 0.0624} - 1)$. The thermistors were calibrated by determining the coefficients (a_i) using a precision contact thermometer (Pt100). With this setup, we were able to achieve linear heating ramps over the entire temperature range, with an absolute temperature inaccuracy of ± 0.1 °C (Fig. 3B).

Fluorescence measurement path

The conventional DSF dye SYPRO Orange is a merocyanine type fluorescent dye with absorption and emission maxima of λ_{ex} 490 nm and λ_{em} 624 nm (Fig. 4A). Commercial qPCR instruments often use costly lamps, optics, or filter equipment, which we have circumvented by using cheap high power OSRAM Oslon SSL 80 royal blue LEDs as the light source (on 20 mm stars, LD CQ7P). The fluorescent dye in the samples was excited with a 50 ms pulse of the high power blue LED (λ 450 nm,

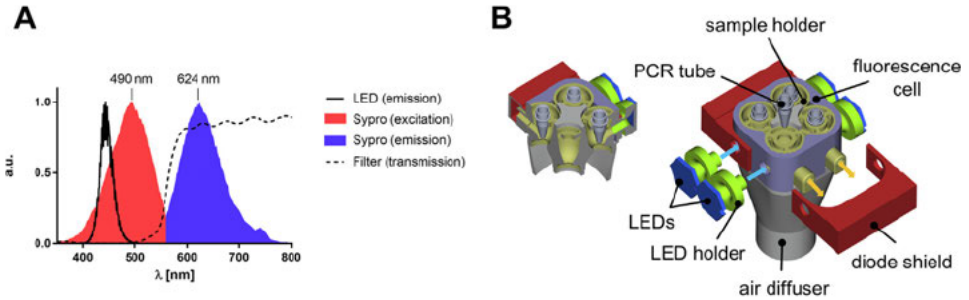

Fig. 4. (**A**) Normalized spectra of the SYPRO Orange fluorescence, LED emission, and filter foil transmission (all measured on a Tecan Spark 10 M spectrometer). The LED emission showed good spectral overlap with the excitation characteristics of SYPRO Orange, whereas the orange filter foil efficiently filtered out excitation light but allowed the SYPRO Orange emission to pass with a transmission rate of > 80%. (**B**) Exploded view drawing and cross-section of the fluorescence cell with labeling of the most important components. The blue arrows show the path of the excitation light while the orange arrows illustrate the emitted radiation path. (For interpretation of the references to color in this figure legend, the reader is referred to the web version of this article.)

W_{max} 1400 mW, ϕ_E 630 mW). Longer pulse widths resulted in significant photobleaching of the dye during long term experiments, but since the fluorescence signal is recorded at a sampling rate of 60 kHz, a 50 ms pulse width was found to be sufficient to achieve low noise recordings. Since the output fluorescence depends on the protein, the buffer, and the sample volume, the irradiation intensity can be modulated with the 11 bit PWM controller of a constant current source (LED BUCK V2, 1000 mA, 42 V, PWM < 5 kHz). Excitation of the sample solution was performed through the lateral outer wall of the PCR tube, with the emitted fluorescence captured at a 90° angle by OSRAM SFH 203 photodiodes (Fig. 4B). The SFH 203 photodiode was selected because of its exceptionally fast switching operational performance (rise/fall time: 5 ns). However, this photodiode exhibits sensitivity throughout the entire visible spectrum, so that the scattered and reflected excitation light must be eliminated with a filter. We have found that filter foils for stage spotlights are an excellent alternative to expensive optical filters. In this regard, the receiver photodiode was shielded with a piece of the LEE 158 Deep Orange filter foil, which efficiently prevented the passage of light with a wavelength of < 500 nm. The current of the receiver photodiode was evaluated with a transimpedance amplifier (Texas Instruments OPA380, R_F 12 MΩ) and the resulting out put voltage was measured by the ESP32 SAR ADC (sampling rate of 60 kHz, bit depth of 12 bit).

Data acquisition and processing

During a DSF run, both fluorescence and temperature data are acquired for each of the four holders individually (ADC serial inputs: 8 channels 4 each for photodiodes and thermistors). In this regard, two values per data point, i. e. tempera ture and fluorescence, are recorded for regular intervals. The interval between two measurement points has been established with 1000 ms by default but can also be modified (def TEMP_SAMPLE_PERIOD). At the beginning of each interval, a sampling phase is performed in which the PCR tube is irradiated, and fluorescence resp. temperature values are recorded. The default duration for the sampling phase is determined by the LED pulse width (int led_on; default: 50 ms). The sampling frequency is 60 kHz on 8 channels (4 temperature, 4 fluorescence), hence, for each data point 375 raw values per channel ($= \frac{60kHz}{4+4channels} \cdot \frac{50ms}{1000ms}$) are recorded. Subsequently, these raw values are combined by arithmetic averaging and the mean fluo rescence values are written to a log file for online plot and CSV export at specified temperatures (0.1 1 °C/datapoint). For post acquisition processing, a smoothing function according to the Savitzky Golay filtering algorithm was implemented (scipy.signal.savgol_filter). The signal acquisition and processing pipeline of the openDSF system is shown in SI Fig. 1.

- The open source differential scanning fluorometer (openDSF) allows fast, accurate, and reliable protein and RNA DSF measurements.
- The combination of high power LEDs as the light source and stage light foil as filter components is a cost effective alter native to laser lamps and optics equipment for fluorometric measuring cells.
- Airflow heating and temperature control by thermistors allow high accuracy temperature management in PCR tubes (±0.1 °C).
- The ESP32 microcontroller with the I^2S interface is a powerful system for fast acquisition of analog measurement data (sampling rate 60 kHz).
- A 3D printable polyoxymethylene (POM) chassis allows biological experiments at up to 130 °C.

Design files summary

The repository containing the design data for reproduction and modification of an openDSF instrument can be found at https://doi.org/10.17632/73rt8s7pwd.2

Design file name	File type	Open source license	Location of the file
AirDiffuser	FreeCAD 0.18/.stl	GNU General Public License(GPL) 3.0	https://data.mendeley.com/public_files/datasets/73rt8s7pwd/files/379d19e4_fff5_46a2_91db_4fb37df472aa/file_downloaded
DiodeShield	FreeCAD 0.18/.stl	GNU General Public License(GPL) 3.0	https://data.mendeley.com/public_files/datasets/73rt8s7pwd/files/9aad5e3f_d962_4a97_987c_37b4ce739f63/file_downloaded
FanAdapter	FreeCAD 0.18/.stl	GNU General Public License(GPL) 3.0	https://data.mendeley.com/public_files/datasets/73rt8s7pwd/files/dbea3546_4454_4188_a598_3fc66c4576a4/file_downloaded
FluorescenceCell	FreeCAD 0.18/.stl	GNU General Public License(GPL) 3.0	https://data.mendeley.com/public_files/datasets/73rt8s7pwd/files/39770286_5fe0_428f_8ff6_876545f331f1/file_downloaded

(*continued*)

Design file name	File type	Open source license	Location of the file
HeatingTube	FreeCAD 0.18/.stl	GNU General Public License(GPL) 3.0	https://data.mendeley.com/public_files/datasets/73rt8s7pwd/files/ff45fdf5_d84d_4854_b236_5c6c7ad228d0/file_downloaded
Housing	FreeCAD 0.18/.stl	GNU General Public License(GPL) 3.0	https://data.mendeley.com/public_files/datasets/73rt8s7pwd/files/81528873_8264_4cd5_867f_d2622c1baa20/file_downloaded
LEDHolder	FreeCAD 0.18/.stl	GNU General Public License(GPL) 3.0	https://data.mendeley.com/public_files/datasets/73rt8s7pwd/files/be717870_22ea_4ec6_99fb_e4f30555df45/file_downloaded
openDSF	Python 3.9.2/.zip	GNU General Public License(GPL) 3.0	https://data.mendeley.com/public_files/datasets/73rt8s7pwd/files/93d80e7b_d63a_40f8_94b5_1498d167c9f0/file_downloaded
PhotoDiodePCB	.zip	GNU General Public License(GPL) 3.0	https://data.mendeley.com/public_files/datasets/73rt8s7pwd/files/81dcaa9e_9a6d_44c0_a272_a710958638ab/file_downloaded
SampleCover	FreeCAD 0.18/.stl	GNU General Public License(GPL) 3.0	https://data.mendeley.com/public_files/datasets/73rt8s7pwd/files/1be70242_af16_4df3_83d9_10014a03d285/file_downloaded
SampleHolder	FreeCAD 0.18/.stl	GNU General Public License(GPL) 3.0	https://data.mendeley.com/public_files/datasets/73rt8s7pwd/files/34ad26df_501d_41e0_9515_676d01cdf948/file_downloaded
TemperatureSensor	FreeCAD 0.18/.stl	GNU General Public License(GPL) 3.0	https://data.mendeley.com/public_files/datasets/73rt8s7pwd/files/f215b2f0_f524_43d0_aced_cbc2421c98db/file_downloaded
WiringDiagram	KiCad Eeschema/.zip	GNU General Public License(GPL) 3.0	https://data.mendeley.com/public_files/datasets/73rt8s7pwd/files/2dbbf304_9985_4c7c_988e_8e972766ae3e/file_downloaded
3D printing profiles	Cura profile/.ini	GNU General Public License(GPL) 3.0	https://data.mendeley.com/public_files/datasets/73rt8s7pwd/files/99881b79_0276_4043_9df3_e98d1b81148e/file_downloaded

AirDiffuser: The air diffuser (POM) divides the heated airflow among the four individual measuring cells and leads to turbu lent air mixing and thus to a homogeneous temperature profile.

DiodeShield: The diode shield (PETG) is designed to shield the photodiodes from external light or daylight to reduce the noise of the recorded fluorescence signal.

FanAdapter: The fan adapter (PETG) converts the rectangular outlet of the Sunon radial fan to a circular fitting of the heat ing tube.

FluorescenceCell: The fluorescence cell (PETG) creates a framework into which the sample holders are mounted.

HeatingTube: The heating tube (POM) incorporates the coiled heating wire.

Housing: The housing of the circuit boards protects the electronic components during use.

LEDHolder: High power LEDs are glued onto the LED holders and serve to stabilize them.

openDSF: Project folder (openDSF.zip) for insertion into an ESP_IDF development environment. Python GUI (openDSF.py) to control the device from the user's PC.

PhotoDiodePCB: Material for the fabrication of printed circuit boards of the photodiode modules.

SampleCover: A light and temperature shielding cover (PETG + POM) is placed over the measuring cell, through which the temperature sensors are inserted into the PCR tubes. The heated airflow of the instrument exits through this cover, which is why the contact points to the hot air were protected with thermally robust POM inserts.

SampleHolder: The sample holders (POM) are shaped as Laval nozzles to ensure optimal airflow and heat transfer. Due to the pressure loss of the nozzle, homogeneous air distribution is achieved. The sample holders provide holes for the LEDs and photodiodes.

TemperatureSensor: The temperature sensors (PETG) hold the individual thermistors and shield the sensitive electrical contacts from moisture and physical contact.

WiringDiagram: Circuit diagram overview of the electronic components of the openDSF system created with KiCad Eeschema.

3D printing profiles: List of 3D printer settings (.ini) for the different filaments used (PETG and POM).

Bill of materials summary

Designator	Component	Number	Cost per unit currency	Total cost currency	Source of materials	Material type
Constant current power supply	LED BUCK V2 constant current power supply (1000 mA, 42 V), PWM 2.5 V, < 5 kHz	1	12.90 €	12.90 €	https://bit.ly/31gELmI	Semi conductor
ESP32 board	ESP32 wrover 8 MB Psram, development board	1	7.21 €	7.21 €	https://bit.ly/3l1rbda	Semi conductor
Fan	Sunon Blower MF50151V2 B00U A99	1	6.93 €	6.93 €	https://bit.ly/3yV6btO	Composite
Heating wire	SS430 awg30 stainless steel wire 430, 0.25 mm, resistance 12.2 Ω/m,	1	3.95 €	3.95 €	https://bit.ly/3EbirKD	Metal
High Power LED	OSRAM Oslon SSL 80 royal blue on 20 mm star	4	2.99 €	11.96 €	https://bit.ly/38XAg0Y	Semi conductor
PETG filament	Maertz 1.75 mm PETG,1.0 kg spool	1	14.31 €	14.31 €	https://bit.ly/2VqAYkk	Polymer
Photodiodes	OSRAM SFH 203	4	0.67 €	2.56 €	https://bit.ly/2X7wqQc	Semi conductor
Polyurethane varnish	OBI PU color varnish deep black semi gloss, 125 mL	1	6.99 €	6.99 €	https://bit.ly/3Eh1luS	Organic
POM filament	Hobbyking 1.75 mm POM, 1.0 kg spool	1	22.70 €	22.70 €	https://bit.ly/3ngNkad	Polymer
Power supply	36 V / 10 A	1	18.15 €	18.15 €	https://bit.ly/3jZoZDP	Composite
Power supply	12 V / 3 A	1	12.99 €	12.99 €	Local electronics store	Composite
Power supply	5 V / 3 A	1	10.50 €	10.50 €	Local electronics store	Composite
Stage light filter foil	LEE Filters: 158 Deep Orange	1	5.50 €	5.50 €	https://bit.ly/3yZGmbX	Other
Superglue	UHU Superflex Gel 3.0 g	1	2.70 €	2.70 €	Local store	Other
Thermistors	NTC3950, 100 kΩ	4	0.95 €	3.80 €	https://bit.ly/2X4BPrg	Semi conductor
Transimpedance amplifier	TI OPA380AIDGKR	4	4.49 €	17.96 €	https://bit.ly/3l5jiUl	Semi conductor
Accessories and electronic consumables	Resistors, capacitors, MOSFETs, diodes, ...	var.	15.00 €	15.00 €	Local electronics store	Other
Sum				**176.11** €		

Build instructions

Safety hazards

Never heat or turn on the LED lights while the openDSF instrument is disassembled. Although the device uses low voltages (36 V), hot parts are inside the apparatus (heating wire). When assembled correctly, the high power LEDs are directed into the interior of the apparatus, so they emit very little stray light to the environment. However, looking directly into the disassembled LEDs can irritate the user's eyes. The SYPRO Orange resp. Sybr Gold DSF dye does not have a hazardous material classification, however, the biological samples and chemicals used in individual DSF experiments may harbor specific hazards. We recommend that the openDSF instrument, like all heating laboratory equipment, should not be left running unattended for several hours as they pose a potential fire risk in the event of a malfunction.

3D printing:

We fabricated the 3D printed parts with an Anycubic 4Max printer. Utilizing the open source software FreeCAD 0.18 and Ultimaker Cura 15.04.6 39, we designed, meshed, and sliced individual components. We performed printing through a 0.4 mm nozzle with 1.75 ± 0.02 mm PETG filament at 225 °C. The layer thickness was set to 0.2 mm. POM was printed at 240 250 °C and a bed temperature of 70 °C. The infill percentage and infill style were 20% resp. the zig zag pattern for both filaments. The complete printer settings were added as Cura profiles (.ini) to the repository of design files. An overview of all 3D printed components can be seen in Fig. 2. For better adhesion to the printing table, POM was printed on a three layer bed of PETG filament. A layer printing time of 6 8 s/layer was found to be most effective against warping effects for the POM filament.

Winding of the heating tube:

In the POM heating tube, a coil of the heating wire (8 mm diameter with 28 windings corresponding to a total length of approx. 0.7 m; pitch approx. 1.8 mm) was inserted (Fig. 3A). The ends of the coil were screwed onto cut to size drilled board parts (24 × 5 mm). To fix the coil vertically, the drilled board parts were clamped in the inlet and outlet of the heating tube, respectively. The power connections were soldered on the drilled boards and the connections were led out through 3 mm drilled holes in the heating tube.

Mounting of 3D printed parts:

Before the 3D printed parts, the heating tube, and the fan were assembled by their plug in joints, the inner surfaces of the colorless POM parts (diffuser, sample holder, and LED holder) were coated with a black polyurethane varnish layer to absorb stray light. Alternatively, the corresponding parts might be printed with a non transparent material, e.g., black filament. Previously, we also found that the mechanical durability of varnished 3D printed parts is increased compared to the raw form [22]. Subsequently, a rolled piece of orange filter foil was inserted into the four individual sample holders and the foil was fixed with superglue (Fig. 5A). Caution: The filter foil is attacked by the contained solvents.

The individual parts of the openDSF instrument were assembled according to the exploded view drawings (Fig. 2A and 4B). Note: Make sure that the joints are well sealed! Any printing imperfections must be corrected by filing. The critical plug connections (fan fan connector heating tube diffuser) can optionally be sealed with Teflon insulating tape. To facilitate rebuilding, we have added a 3D model of the exploded view drawing from Fig. 2A to the repository of design files (https://data.mendeley.com/public_files/datasets/73rt8s7pwd/files/90f0a996_645d_4283_8ca8_ae1a65b3404b/file_downloaded), so that a rebuilder can examine the topology of the design while zooming in or moving parts around.

Assembly of the fluorescence cell:

For assembly of the fluorescence cell, two LED modules and two photodiode modules were fabricated, so that a sample holder is equipped with one LED and one photodiode each (Fig. 4B). For a single LED module, two high power LEDs were soldered together with proper polarity and provided with connecting cables so that they could be glued onto their LED holder with hot glue and inserted into the cut outs at the fluorescence cell. To assemble the photodiode module, two photodiodes were mounted (20 mm apart from each other) on a PCB board according to the PCB layout specifications (https://data.mendeley.com/public_files/datasets/73rt8s7pwd/files/81dcaa9e_9a6d_44c0_a272_a710958638ab/file_downloaded).

We manufactured the PCBs ourselves using the toner transfer method [23]. The electronic components were soldered onto the circuit board using a standard soldering iron. For the operational amplifier, assembly instructions from the manufacturer's datasheet are to be followed. The photodiodes were inserted into the holes provided in the fluorescence cell and later covered by the two PETG diode shields (Fig. 4B).

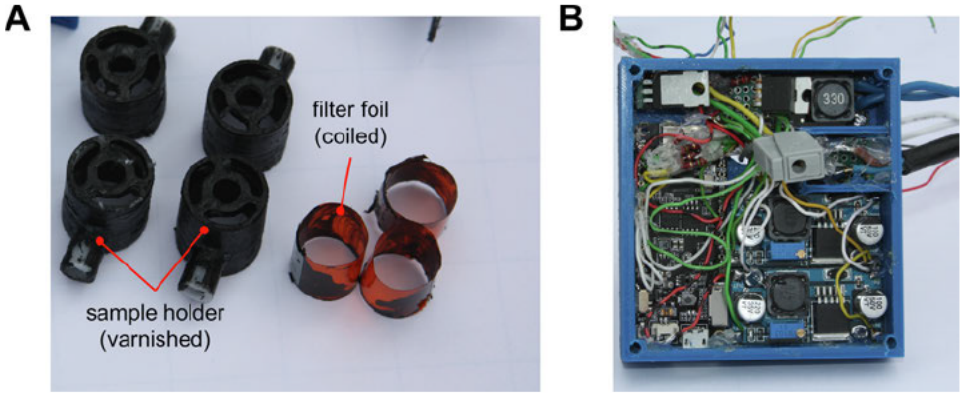

Fig. 5. (**A**) Example of black painted POM parts: The four sample holders were varnished black because the colorless filament, in its untreated form, acts as an effective optical fiber to disperse stray light and causes significant tube-to-tube bleeding. Next to them, the rolled filter foil inserts, which shield the photodiodes from the blue excitation light. (**B**) Housing of the electronic components (ESP32 development board, MOSFET circuits, and constant current power supply). (For interpretation of the references to color in this figure legend, the reader is referred to the web version of this article.)

Wiring of electronic components:

The thermistors were inserted into the 3D printed temperature sensors and fixed so that the glass sphere of the thermistor just peeks out of the bottom hole (Fig. 6B). The MOSFET circuits (fan and heater) were assembled on drilled boards. A flyback diode was provided for the fan. The resistance values from the PWM supply were 15 Ω and 10 kΩ to the ground. Subsequently, the ESP32 development board, the constant current power supply, and the MOSFET circuits were placed in the housing (Fig. 5B). Finally, the individual electronic components were cabled according to the circuit diagram (https://data.mendeley.com/public-files/datasets/73rt8s7pwd/files/2dbbf304-9985-4c7c-988e-8e972766ae3e/file_downloaded). We noticed that using a USB cable without supplying voltage between the ESP32 and the computer leads to more stable ADC characteristics. The possible interference between simultaneous supply *via* the USB voltage common collector (VCC) and the 5 V pin of the ESP32 board has already been described for V_{ext} < 5.2 V [24]. Therefore, we prepared a data only USB cable from a standard micro USB cable for data transfer to the computer according to literature instructions [25].

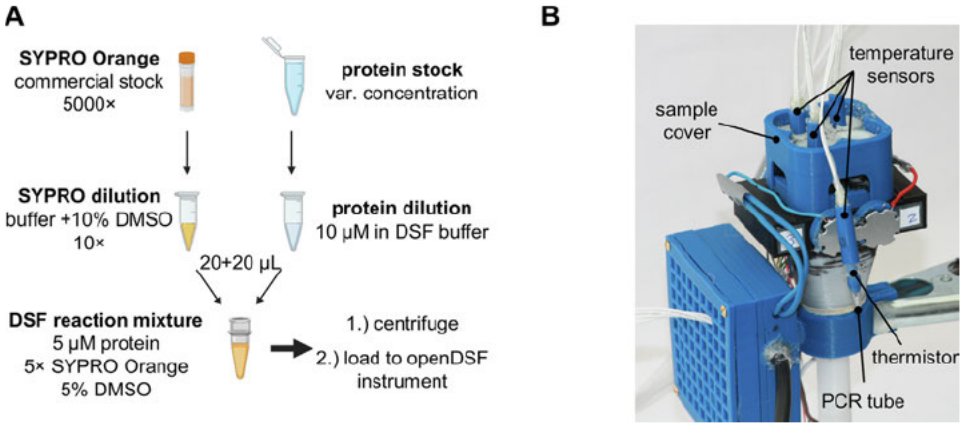

Fig. 6. (**A**) Overview of sample preparation instructions (mix, centrifuge, and load) based on a commercially available SYPRO Orange solution (5000 ×) and a protein stock solution. (**B**) Close-up of the openDSF instrument with the sample holders closed by the sample cover highlighting the thermistors in the 3D-printed temperature sensors. Three temperature sensors are inserted ready-for-use in their respective sample holders, while one PCR tube equipped with a temperature sensor hangs in front of the instrument for illustration purposes. The thermistor can only be seen by its glass sphere, which extends a few millimeters from the temperature sensor. (For interpretation of the references to color in this figure legend, the reader is referred to the web version of this article.)

Firmware compilation & openDSF GUI:

The firmware was built in the ESP IDF development environment (v4.2.2). The steps for installing the development environment have been described in detail by the manufacturer: https://docs.espressif.com/projects/esp_idf/en/v4.2.2/esp32/get_started/index.html. After the development environment has been installed, proceed as follows (here for Windows users): The archive "openDSF.zip" (https://data.mendeley.com/public_files/datasets/73rt8s7pwd/files/ba2f88ef_547c_4ca7_8ef7_ed597cbf53b8/file_downloaded) has been unpacked. The unpacked openDSF folder was copied into the root directory of the development environment. Before the firmware can be compiled, the development environment was slightly modified. The file "...\components\driver\esp32\adc.c" was replaced by the custom file "...\openDSF\adc.c". Subsequently, the firmware was compiled and transferred to the ESP32 board *via* USB cable.

During experimental usage, the ESP32 board is controlled by a GUI programmed in Python (version 3.9.2). Installation instructions for Python can be found here: https://docs.python.org/3/using/windows.html. The following libraries and modules must be installed in the Python environment: signal, time, datetime, serial, threading, queue, serial.tools.list_ports, scipy.optimize, numpy, tkinter, matplotlib, pyplot, backend_bases, backends.backend_tkagg, scipy.signal.savgol_filter.

Operation instructions

Sample preparation:

The following instructions are described as examples for the preparation of a single DSF reaction mixture but can be scaled up as desired. Prepare 30 μL of a protein solution (10 μM) in an appropriate buffer (e.g., 50 mM HEPES pH 7.5, 150 mM NaCl). In parallel, prepare 30 μL of a 10 × SYPRO Orange dilution (1:500 dilution of the commercial 5000 × stock solution) in the same buffer as used for the protein solution but supplemented with 10% DMSO. Mix 20 μL of the protein solution with 20 μL of the 10 × SYPRO Orange dilution to yield the DSF reaction mixture (final concentration: 5 μM protein and 5 × SYPRO Orange). Note: Other concentrations may also be possible, which could be determined for each protein in the course of an assay optimization. For the study of protein ligand interactions, compounds or mock treatment additives can be added from DMSO or buffered solutions. Centrifuge (1 min at 300 rcf) and transfer 30 μL of the particle free solution into a PCR tube (Fig. 6A). Insert 1 4 PCR tubes into the sample holders of the openDSF instrument, seal the reaction tubes with the thermistor caps, and close the instrument with the sample cover (Fig. 6B).

Run a DSF experiment:

0.) Switch on the openDSF instrument by connecting the power supply. 1.) To establish proper communication between the computer and instrument, start the Python script ("openDSF.py") from a console and press the "Ports" button to select the serial port to the openDSF instrument (Fig. 7). Then click "Connect" to establish the connection. 2.) Initialize the heating module by entering the default parameter "1000" in the "Fan" input box. Other fan speeds can be selected (300 2047) and varied for assay optimization. 3.) Click on "Start" to initiate the acquisition of temperature data to check the function of the thermistors and to verify the temperature homogeneity between the different holders. 4.) Subsequently, the physical parameters of fluorescence detection and heating ramp are defined: Start the LED illumination by entering the default parameter "1000" in the "LED" input field. Check if the initial protein dependent fluorescence value is between 20 and 300 mV and, if necessary, adjust the value to this range by varying the LED strength (0 2047). If a starting temperature above the prevailing room temperature is desired, a heating intensity parameter (0 4096) can be chosen in the "Heating" input field. The terminal temperature of the melting experiment is entered in the "MaxT" input field. The DSF experiment is started by launching the heating ramp, which can be run in varying gradients (0.1 20.0) *via* the "Step" input field. 5.) Once the melting process is completed and the specified maximum temperature has been reached, the data acquisition can be terminated by clicking the "Stop" button. The device cools back to room temperature automatically.

6.) For post run processing of the melting curve data, the resolution of the temperature steps (typically: 0.1 1 °C) in the output file is defined. 7.) Since the acquired raw data is subject to ADC related noise, it may be reasonable to smooth the raw data. A Savitzky Golay filter function can be applied to the raw data by clicking on "Filter" and specifying the window size ($x_0 \ldots x_n$) and polynomial order (x^n) of the smoothing function. The smoothing can be reversed by clicking on "Raw". 8.) Both raw or filtered melting curves can be exported ("Save" button) as a CSV file for analysis with an external program. In this regard, various mathematical evaluation procedures for analyzing DSF datasets have already been described in the literature [3,6,8,26]. The data sets of the following model applications were analyzed with the open source DSF analysis software DSFworld (https://github.com/gestwicki_lab/dsfworld) and simpleDSFviewer (https://github.com/hscsun/SimpleDSFviewer_5.0) which were downloaded from their GitHub repositories for desktop usage [3,8]. An example openDSF CSV data set can be found in the repository (https://data.mendeley.com/public_files/datasets/73rt8s7pwd/files/60ecd57d_24a1_4234_b7a9_4cbdbefd6794/file_downloaded).

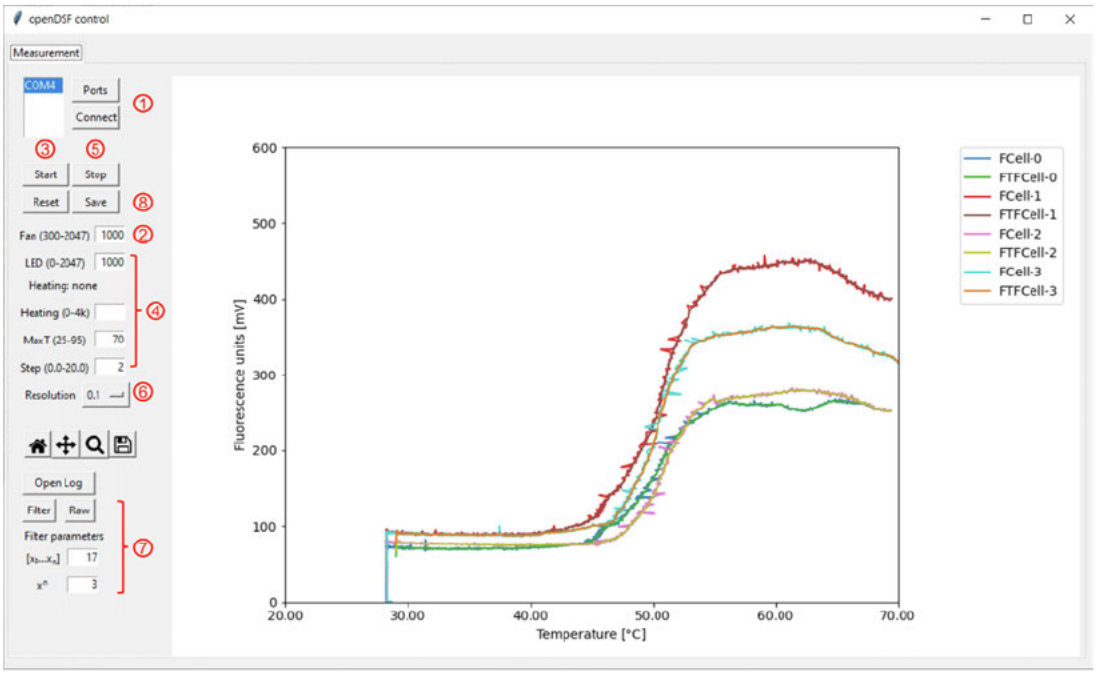

Fig. 7. Graphical user interface of the openDSF.py control program. In the left control bar, the elementary functions of the openDSF instrument can be controlled (e.g., fan rpm, heating power, and LED power). The display panel on the right shows the raw and filtered data of the fluorescence *vs.* temperature plot (melting curves). The functionalities in the GUI are labeled according to the operating instructions (1–8) in the section "Run a DSF experiment".

Validation and characterization

Characterization of the instrument

To assess the capabilities of the openDSF system, various relevant benchmarks (absolute temperature accuracy, cross holder temperature homogeneity, maximum heating/cooling rates, linear dynamic range, detector saturation, S/N ratios, and tube to tube bleeding) were examined.

By online temperature control of each sample holder, we were able to obtain linear temperature ramps (R^2 0.997) over the entire heating range we investigated (25 80 °C) (Fig. 3B). Calibration of the thermistors as temperature sensors resulted in an absolute temperature error of < 0.1 °C. This error was below the fluctuations caused by sample preparation (e.g., pipet ting errors and material variations of the PCR tubes), which is why we qualified the temperature control by air heating and thermistor measurement as valid. However, due to the differential nature of DSF experiments, the reproducibility of the same temperature has to be evaluated prior to the absolute temperature accuracy. We did this by the reproduction of protein melting points in different holders during one experiment or during separate experiments (see below). The absolute devia tion of protein melting points was in the range of 0.1 0.2 °C (Table 1). This error includes the statistical and systematic inac curacy due to temperature inhomogeneities between different holders but also the variations caused during sample preparation. The standard error of the determined protein melting points is thus in the same range as commercial qPCR solu tions [3,10,27,28].

Typical heating rates for DSF experiments are in the range of 0.5 4 °C/min [3]. For the openDSF system, these depend on both the power of the heating tube and the flow rate of the fan. We have performed the following example DSF experiments at a heating rate of 2 °C/min (GUI: Fan speed 1000 and step 2.0). However, even at very high heating rates of 9 °C/min (step 9.0), we were still able to achieve good temperature homogeneity and melting point reproducibility (SI Fig. 3C). When operating the fan without heating, the openDSF system is also able to cool the sample holders uniformly with air. The cooling curve (with fan speed 1000) follows an exponential relationship between the temperature reached (T_{max}) and the ambient temperature (T_R): $T(t) = (T_{max} \quad T_R)e^{\ 0\,0122\,t} + T_R$. This feature can be utilized for a sequence of oscillating heating and cool ing events, for example, to study protein unfolding and subsequent refolding (SI Fig. 3D) [29].

Using blue high power LEDs and orange filter foil, we were able to remodel the fluorescence characteristics of the DSF reaction mixture (fluorescence transmission rate > 80%), while avoiding the need for expensive optics, lamps, or filter units

Table 1
Overview of various protein melting points and S/N-ratios as recorded with the openDSF instrument in comparison to respective literature values. DSF reaction mixtures contained 5 μM protein and 5 × SYPRO Orange in 50 mM HEPES buffer at pH 7.5.

Protein	Melting point [°C]	N (replicates)	Lit. melting point [°C]	S/N [dB]
M^{pro}	57.09 ± 0.08	12	55.74[31]	27.1 ± 0.32
SrtA	49.84 ± 0.13	16	50.50[32]	31.1 ± 0.32
Cruzain	64.90 ± 0.14	8	66.40[33]	30.5 ± 0.29
Thrombin	52.10 ± 0.08	4	58.30[30]	28.8 ± 0.29
Lysozyme	67.58 ± 0.10	4	71.90[29]	27.3 ± 0.27
BSA	58.72 ± 0.13	4	56.00[3]	21.6 ± 0.53
Calpain I	44.60 ± 0.11	4	47.00[34]	20.5 ± 0.16
NS2B/NS3	50.01 ± 0.07	4	49.00[35]	27.9 ± 0.26

(Fig. 4A). The practical fluorescence measurement range of the fluorometer is characterized by its linear dynamic range, which was determined by a series of different SYPRO Orange dilutions (SI Fig. 2A). The linear dynamic range of the openDSF was found to be between 0 and 3000 mV, which should be aimed at during DSF measurements. Above 3000 mV, the detector saturates and finally reaches its upper maximum at 3500 mV. Besides detector linear responsivity, S/N ratios were determined as quality parameters for the fluorescence measurements and can be used as benchmarks for reproducing the system. The S/N ratio was calculated as the absolute fluorescence increase during unfolding divided by the dark noise: $S/N = \frac{FL_{unfolded} - FL_{folded}}{darknoise}$. Where the dark noise corresponds to the standard deviation of 100 fluorescence data points before the actual heating ramp was started. In addition to the intrinsic protein properties, the S/N ratio of the fluorescence measurement depends on the intensity of the LED illumination which was therefore optimized at the beginning of each run. An initial fluorescence value of 20 300 mV has been empirically found to be optimal for obtaining low noise traces. The protein specific S/N ratios are shown in Table 1.

As described during the build instructions, it is necessary to varnish or print the POM parts black, otherwise, they will act as an effective optical fiber and transport stray light from one sample to the neighboring PCR tube thereby falsifying the measurements. This so called tube to tube bleeding has been quantified and must be requalified when building a comparable design. Using our setup, within the linear dynamic range, no tube to tube bleeding could be detected with varnished POM parts (SI Fig. 2B). In order to detect tube to tube bleeding, an overload of the detector far beyond the saturation limits (>3500 mV) was required, which in our case was correlated with optically perceptible fluorescence despite a closed device (250 × SYPRO Orange in 9:1 glycerol/water).

DSF experiments in the openDSF system were established for a sample volume of 30 μL in PCR tubes with the thermistor measuring temperature just above the liquid level (Fig. 6). The minimum sample volume was tested with additional sample sizes using 20, 10, and 5 μL of a DSF reaction mixture. The signal intensity decreased with lower sample volumes, leading to worse S/N ratios (SI Fig. 3A). The lowest practical volume that could be measured was 10 μL. On the other hand, when loading sample volumes>40 μL, these resulted in increased noise from the temperature sensors, as the thermistors were too close to the liquid level with these volumes.

To test the gas tightness of the openDSF system, the evaporation loss of the samples during the heating phases was investigated gravimetrically. A temperature ramp of 25 70 °C resulted in a loss of about 0.3 μL for a 30 μL sample (SI Fig. 3B). However, at higher temperatures (25 95 °C), the evaporation loss was increased to approx. 2 μL. Prolonged heating (10 min) at 95 °C also resulted in a similar loss of approx. 2 μL, leading to the hypothesis that the gas space in the temperature sensor becomes saturated with humidity and the liquid does not continuously evaporate at a leaky point. This hypothesis could be confirmed by repeated temperature ramps or heating intervals at 95 °C, as the evaporation loss was much lower in the following heating cycles (SI Fig. 3B).

We cannot yet conclusively judge the longevity of our design, but after about 100 heating ramps (25 80 °C), we did not notice any signs of wear or benchmark drops. Since the system is modular and open source, broken parts can be replaced easily.

Exemplary DSF applications

To challenge the capabilities of the openDSF system eight different proteins were analyzed by their melting profiles: SARS CoV2 main protease (M^{pro}), *S. aureus* sortase A (srtA), *T. cruzi* cathepsin L (cruzain), bovine thrombin, hen egg white lysozyme, bovine serum albumin (BSA), human calpain I, and Zika virus (ZIKV) NS2B/NS3 protease. DSF reaction mixtures (5 μM protein, 5 × SYPRO Orange, 50 mM HEPES pH 7.5, 150 mM NaCl, 5% DMSO) were heated at temperature ramps of 2 °C/min from 25 to 80 °C, and subsequently, the melting points (T_m) were determined with the open source analysis tool of DSFworld from the sigmoid RFU *vs.* temperature curves [3]. The melting curves of a representative replicate and the corresponding melting points are shown in Fig. 8.

A comprehensive overview of melting points and S/N ratios is given in Table 1. Protein melting points determined by the openDSF instrument showed good agreement with the melting points determined by DSF or differential scanning calorimetry (DSC) as reported in the literature (Table 1). Only for thrombin (Fig. 8D), our measured T_m value deviates significantly

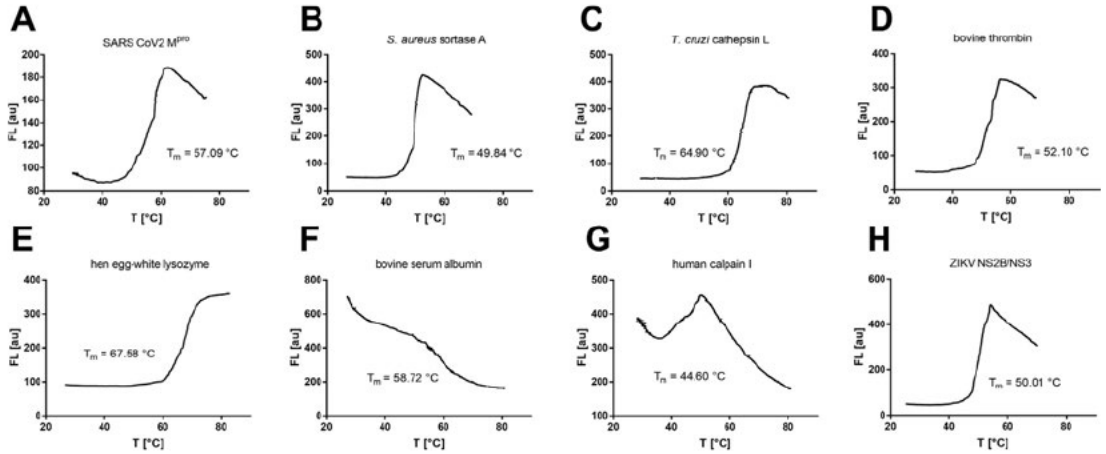

Fig. 8. Representative melting curve examples of various proteins (5 μM) and 5 × SYPRO Orange in 50 mM HEPES buffer at pH 7.5. (**A**) SARS-CoV2 main protease (M^{pro}), (**B**) *S. aureus* sortase A (srtA), (**C**) *T. cruzi* cathepsin L (cruzain), (**D**) bovine thrombin, (**E**) hen egg-white lysozyme, (**F**) bovine serum albumin (BSA), (**G**) human calpain I, (**H**) Zika virus (ZIKV) NS2B/NS3 protease.

from the literature melting point (52.10 °C *vs.* 58.30 °C), but this might be attributed to a different buffer composition in the literature experiment [30]. For BSA, we obtained a negative DSF curve (Fig. 8F). This is also in agreement with the literature since BSA binds SYPRO Orange already at room temperature due to numerous hydrophobic cavities and at higher temper atures, this binding is entropically reduced [3]. The melting point variance between different holders (intra assay variation) and between different DSF runs (inter assay variation) was 0.1 0.2 °C for all protein samples studied, which is low enough to investigate the influence of ligands on the thermal shift of the apparent melting point [2,6,7].

To demonstrate the practical applicability of the openDSF system to biological problems, selected protein ligand inter actions were investigated by DSF. The bacterial transpeptidase srtA utilizes calcium as a stabilizing cofactor. The protein melting point of srtA in the absence and presence of calcium has already been determined by DSC and differs by ΔT_m 3.4 ° C [36]. Using ITC, the dissociation constant of this

srtA Ca^{2+} complex was determined to be K_D 55 μM [37]. By studying a solution of 5 μM srtA supplemented with differ ent concentrations of calcium chloride, we were able to reproduce the thermodynamic parameters determined with the other two biophysical methods using the openDSF instrument (Fig. 9A). In detail, we titrated 0, 10, 50, 100, and 500 μM cal cium chloride to the DSF reaction mixtures and determined the dissociation constant K_D(srtA Ca^{2+}) 42.5 μM from the bind ing isotherm of the melting points versus the calcium concentration (Fig. 9B) [6].

DSF is also useful for the identification and study of small molecule drug substances on their protein targets. If a ligand binds to a protein, the free energy of ligand binding mostly results in protein stabilization and increased T_m values [7]. Here, we studied the cysteine protease calpain I with or without treatment of the protease inhibitors leupeptin and E64 (structures in SI Fig. 4). The melting point of the untreated protease (5 μM) was determined with T_m 44.60 °C (Fig. 10A). After treat ment with 100 μM of the inhibitors leupeptin or E64, the melting point increased to 51.10 °C and 53.47 °C, respectively (Fig. 10B,C). The molecular background of this stabilization becomes evident from the crystal structures of the apo structure and the inhibitor bound complexes [38,39]. The structural rigidity of a protein can be determined by B' factor analysis of the corresponding crystallographic dataset [40]. In the regions of the crystal structure where the inhibitor binds, a significant stabilization of the protein backbone takes place, which explains the increase in melting points (Fig. 10D,E). Here, it is shown that the combination of thermodynamic parameters from openDSF experiments with spatially resolved methods such as XRAY or NMR complement each other well.

Furthermore, to compare a melting curve example with a commercial qPCR system, DSF reaction mixtures of the ZIKV NS2B/NS3 protease were analyzed using both the Bio Rad C1000/CFX384 (Fig. 11C) and our openDSF instrument (Fig. 11A). The protein melting point was 49.60 °C and 50.01 °C, respectively, for both instruments, very close to the literature value (Table 1) [35]. The ZIKV protease is known to adopt multiple conformations due to the dynamic interaction of both NS2B and NS3 proteins. A catalytically active (mostly substrate bound) form is referred to as the "closed" conformation, whereas the "open" conformation describes the predominate species of the protein resting state [41]. However, the addition of substrate mimetic inhibitors was reported to cause to the stabilization of the closed conformation and an increased melt ing point [42,43]. In a DSF experiment, the presence of a cyclic peptide inhibitor (10 μM, structure in SI Fig. 4 [42]) led to an increase of the melting point by ΔT_m 2.46 °C (Fig. 11B).

To investigate the ability of our instrument to perform DSF analysis of RNA molecules, we examined two examples of literature known tertiary structured RNA aptamers. For this purpose, RNA (500 nM) was mixed with a suitable intercalating

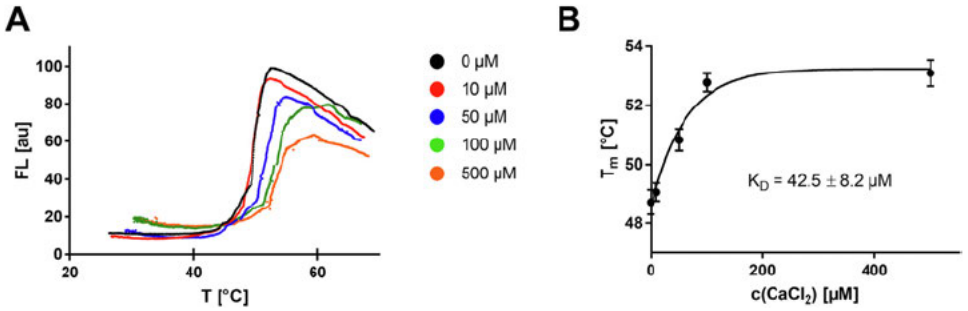

Fig. 9. (**A**) Representative srtA melting curves in the presence of different $CaCl_2$ concentrations. At higher calcium concentrations, the srtA protein is stabilized towards higher melting points. (**B**) Determination of the thermodynamic dissociation constant K_D for the srtA-Ca^{2+} complex from the melting point *vs.* $CaCl_2$-concentration relationship by regression with a binding isotherm $T_m(c) \quad T_m(min) + (T_m(max) - T_m(min)) \cdot (1 - e^{\ kc})$ with $K_D \quad \frac{\ln(2)}{k}$. Shown are means ± standard deviation (n = 3).

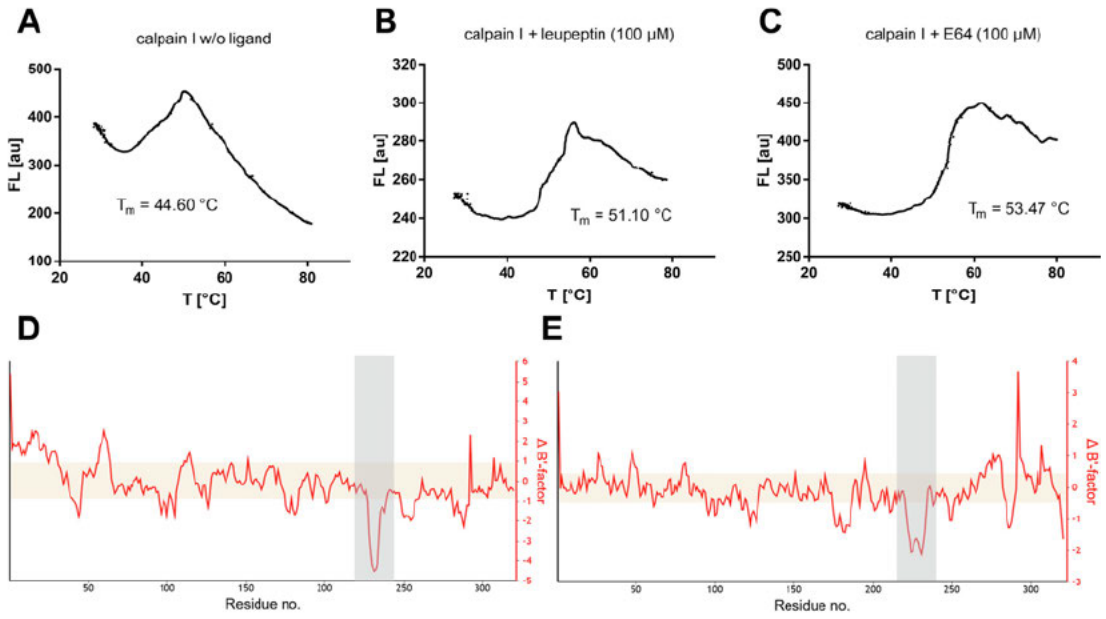

Fig. 10. DSF experiments on calpain I ligand complexes. (**A**) Melting curve of native calpain I (5 µM) in absence of a ligand, (**B**) Melting curve of calpain I (5 µM) in presence of the inhibitor leupeptin (100 µM), (**C**) Melting curve of calpain I (5 µM) in presence of the inhibitor E64 (100 µM), (**D**) B'-factor analysis with the open-source BANΔIT-web server [40]: The calpain-leupeptin complex (pdb: 1TL9) reveals rigidization (negative ΔB') of the ligand-binding site (Asp259–Leu268) compared to the corresponding apo structure (pdb: 1KXR), (**E**) The calpain-E64 complex (pdb: 1TLO) reveals rigidization (negative ΔB') of the ligand-binding site (Ile252–Lys266) compared to the corresponding apo structure (pdb: 1KXR).

dye (1 × Sybr Gold) in a reaction buffer and, analogously to the protein DSF experiments, heated at a temperature ramp of 2 °C/min (25 70 °C). Melting points (T_m) were calculated using the differentiation methodology of Silvers et al. and the sim pleDSFviewer software [8,16].

The aptamer domain of the $preQ_1$ riboswitch from *B. subtilis* folds into a pseudoknot structure upon binding of its natural ligand $preQ_1$. When $preQ_1$ (10 µM, structure in SI Fig. 4) was added to the riboswitch (500 nM in 1 × phosphate buffered saline, pH 7.5), the unliganded melting curve changed significantly (Fig. 12A). Examination of the ligand free reaction mix ture by the derivative analysis method yielded two melting points in agreement with the literature ($T_{m,1}$ 27.30 °C, $T_{m,2}$ 54. 16 °C, Fig. 12B) [44]. In summary, the addition of the ligand $preQ_1$ (10 µM) resulted in a shift of the second melting point towards higher temperatures ($T_{m,2}$ 56.12 °C, Fig. 12C).

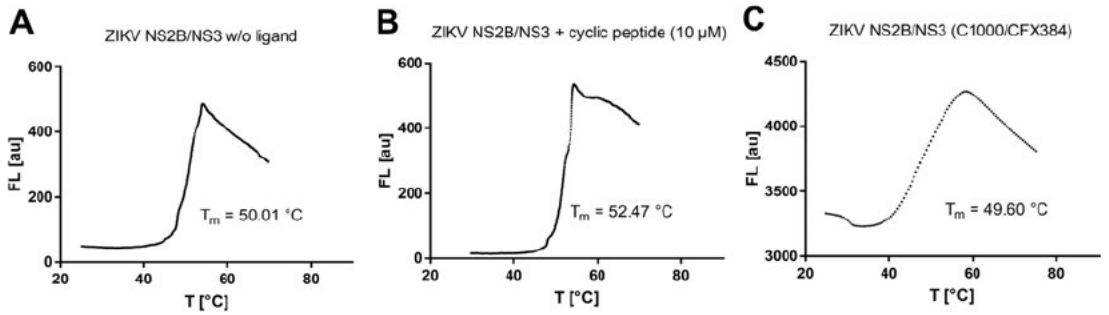

Fig. 11. DSF experiments on the ZIKV NS2B/NS3 protease. (**A**) ZIKV NS2B/NS3 fluorescence *vs.* temperature curve recorded with the openDSF instrument. (**B**) Fluorescence *vs.* temperature curve of ZIKV NS2B/NS3 in presence of the cyclic peptide ligand (10 µM, pdb: 6Y3B). (**C**) NS2B/NS3 fluorescence *vs.* temperature curve recorded with the C1000/CFX384.

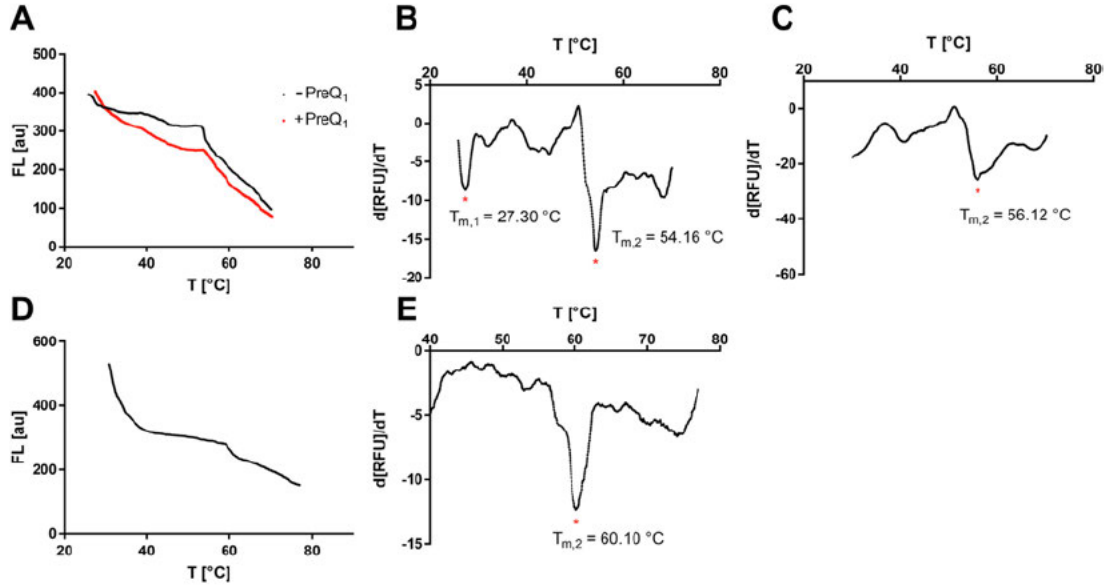

Fig. 12. RNA-aptamer DSF experiments. (**A**) RNA-DSF trace for the $preQ_1$ riboswitch aptamer domain (500 nM) with and without its natural ligand $preQ_1$ (10 µM). (**B**) Derivative plot of the $preQ_1$ aptamer in absence of a ligand. (**C**) Derivative plot of the $preQ_1$ aptamer supplemented with 10 µM of $preQ_1$. (**D**) RNA-DSF trace for a trypanosome-specific RNA aptamer. (**E**) Derivative plot of the trypanosome-specific RNA aptamer (temperature range: 40–75 °C).

Secondly, a trypanosome specific RNA aptamer was investigated by DSF in 50 mM cacodylate buffer (pH 6.5) supplemented with 0.5 mM $MgCl_2$ [45]. This parasite specific aptamer was previously characterized with a melting point of 58 °C. Here, we could confirm the identity of our RNA construct by recording a DSF trace matching the melting point ($T_{m,2}$ 60.10 °C, Fig. 12E). In contrast, the strong decrease in fluorescence at temperatures between 30 and 40 °C has not been observed in the literature, suggesting that some of the aptamer molecules are not in their native fold. In this respect, RNA DSF is also suitable for an assessment of sample quality [16].

Declaration of Competing Interest

The authors declare that they have no known competing financial interests or personal relationships that could have appeared to influence the work reported in this paper.

Acknowledgments

Research in the laboratories of Mark Helm and Tanja Schirmeister was funded by DFG grants (TRR 319 "RMaP" projects A01, C01, and A05). Cruzain was a gift from the group of Dr. Avninder Bhambra (University of Leicester, UK). We thank Prof. Torsten Steinmetzer (University of Marburg, Germany) for providing the cyclic peptide ligand (1 ((8*R*,15*S*,18*S*) 15,18 bis(4 aminobutyl) 4,7,14,17,20 pentaoxo 3,6,13,16,19 pentaaza 1(1,3) benzenacyclohenicosaphane 8 yl)guanidine).

Appendix A. Supplementary data

Supplementary data to this article can be found online at https://doi.org/10.1016/j.ohx.2022.e00256.

References

[1] M.-C. Lo, A. Aulabaugh, G. Jin, R. Cowling, J. Bard, M. Malamas, G. Ellestad, Evaluation of fluorescence-based thermal shift assays for hit identification in drug discovery, Anal. Biochem. 332 (1) (2004) 153–159, https://doi.org/10.1016/j.ab.2004.04.031.
[2] M.W. Pantoliano, E.C. Petrella, J.D. Kwasnoski, V.S. Lobanov, J. Myslik, E. Graf, T. Carver, E. Asel, B.A. Springer, P. Lane, F.R. Salemme, High-density miniaturized thermal shift assays as a general strategy for drug discovery, J. Biomol. Screening. 6 (6) (2001) 429–440, https://doi.org/10.1177/108705710100600609.
[3] T. Wu, J. Yu, Z. Gale-Day, A. Woo, A. Suresh, M. Hornsby, J.E. Gestwicki, Three Essential Resources to Improve Differential Scanning Fluorimetry (DSF) Experiments, preprint (BioRxiv), 2020. https://doi.org/10.1101/2020.03.22.002543 (accessed November 24, 2020)..
[4] D.E. Scott, C. Spry, C. Abell, Differential Scanning Fluorimetry as Part of a Biophysical Screening Cascade, in: D.A. Erlanson, W. Jahnke (Eds.), Methods and Principles in Medicinal Chemistry, Wiley-VCH Verlag GmbH & Co. KGaA, Weinheim, Germany, 2016: pp. 139–172. http://doi.wiley.com/10.1002/9783527683604.ch07..
[5] K. Gao, R. Oerlemans, M.R. Groves, Theory and applications of differential scanning fluorimetry in early-stage drug discovery, Biophys. Rev. 12 (1) (2020) 85–104, https://doi.org/10.1007/s12551-020-00619-2.
[6] N. Bai, H. Roder, A. Dickson, J. Karanicolas, Isothermal analysis of thermofluor data can readily provide quantitative binding affinities, Sci. Rep. 9 (2019) 2650, https://doi.org/10.1038/s41598-018-37072-x.
[7] F.H. Niesen, H. Berglund, M. Vedadi, The use of differential scanning fluorimetry to detect ligand interactions that promote protein stability, Nat. Protoc. 2 (9) (2007) 2212–2221, https://doi.org/10.1038/nprot.2007.321.
[8] C. Sun, Y. Li, E.A. Yates, D.G. Fernig, SimpleDSFviewer: A tool to analyze and view differential scanning fluorimetry data for characterizing protein thermal stability and interactions, Protein Sci. 29 (1) (2020) 19–27, https://doi.org/10.1002/pro.v29.110.1002/pro.3703.
[9] T.H. Steinberg, H.M. White, V.L. Singer, Optimal filter combinations for photographing SYPRO orange or SYPRO red dye-stained gels, Anal. Biochem. 248 (1) (1997) 168–172, https://doi.org/10.1006/abio.1997.2117.
[10] J. Hoeser, E. Gnandt, T. Friedrich, Low cost, microcontroller based heating device for multi-wavelength differential scanning fluorimetry, Sci Rep. 8 (2018) 1457, https://doi.org/10.1038/s41598-018-19702-6.
[11] R.A. Mendoza-Gallegos, A. Rios, J.L. Garcia-Cordero, An affordable and portable thermocycler for real-time PCR made of 3D-printed parts and off-the-shelf electronics, Anal. Chem. 90 (9) (2018) 5563–5568, https://doi.org/10.1021/acs.analchem.7b04843.
[12] G. Mulberry, K.A. White, M. Vaidya, K. Sugaya, B.N. Kim, 3D printing and milling a real-time PCR device for infectious disease diagnostics, PLoS ONE. 12 (2017) e0179133. https://doi.org/10.1371/journal.pone.0179133..
[13] J.T. Keer, Chapter 7:Quantitative Real-time PCR Analysis, in: Essentials of Nucleic Acid Analysis, 2008: pp. 132–166. https://doi.org/10.1039/9781847558213-00132..
[14] D.E. Draper, T.C. Gluick, Melting studies of RNA unfolding and RNA—Ligand interactions, in: J. Abelson, M. Simon, G. Verdine, A. Pyle (Eds.), Methods in Enzymology, Elsevier, 1995, pp. 281–305, https://doi.org/10.1016/0076-6879(95)59049-8.
[15] F. Zamani, T. Suzuki, Synthetic RNA modulators in drug discovery, J. Med. Chem. 64 (11) (2021) 7110–7155, https://doi.org/10.1021/acs.jmedchem.1c00154.
[16] R. Silvers, H. Keller, H. Schwalbe, M. Hengesbach, Differential scanning fluorimetry for monitoring RNA stability, ChemBioChem. 16 (7) (2015) 1109–1114, https://doi.org/10.1002/cbic.v16.710.1002/cbic.201500046.
[17] QIAGEN Rotor-Gene Q - Average price, Bimedis. (2021). https://bimedis.com/qiagen-rotor-gene-q-m21547 (accessed November 18, 2021)..
[18] S. Brinkmann, K. Oberbach, E. Baur, E. Schmachtenberg, T.A. Osswald, International Plastics Handbook, 29th ed., Carl Hanser Verlag GmbH, Munich, 2006, https://www.hanser-elibrary.com/isbn/9783446229051.
[19] I. Muro-Fraguas, E. Sainz-García, A. Pernía-Espinoza, F. Alba-Elías, Atmospheric pressure air plasma treatment to improve the 3D printing of polyoxymethylene, Plasma Process Polym. 16 (7) (2019), https://doi.org/10.1002/ppap.v16.710.1002/ppap.201900020.
[20] M. Babiuch, P. Foltýnek, P. Smutný, Using the ESP32 Microcontroller for Data Processing, in: 2019 20th International Carpathian Control Conference (ICCC), 2019: pp. 1–6. https://doi.org/10.1109/CarpathianCC.2019.8765944..
[21] W.Y. Lee, T.M. Kim, M.J. Kim, Y.W. Ko, J.D. Kim, User-friendly calibration tool for temperature measurements of PCR devices with NTC thermistors, Int. J. Control Autom. 8 (7) (2015) 13–24.
[22] F. Barthels, U. Barthels, M. Schwickert, T. Schirmeister, FINDUS: An open-source 3D printable liquid-handling workstation for laboratory automation in life sciences, SLAS Technol. 25 (2) (2020) 190–199, https://doi.org/10.1177/2472630319877374.
[23] simpletronic, Heatless (cold) Toner Transfer for PCB Making, Instructables. (2021). https://www.instructables.com/Heatless-cold-Toner-Transfer-for-PCB-Making/ (accessed September 11, 2021)..
[24] J. Kim, Analysis and Optimization of DC Supply Range for the ESP32 Development Board, preprint (TechRxiv), 2020. https://doi.org/10.36227/techrxiv.12798410.v3 (accessed September 12, 2021)..
[25] DavisT2, DIY Data Only USB Type B, Instructables. (2021). https://www.instructables.com/DIY-Data-Only-USB-Type-B/ (accessed September 12, 2021)..
[26] T.A. Wright, J.M. Stewart, R.C. Page, D. Konkolewicz, Extraction of thermodynamic parameters of protein unfolding using parallelized differential scanning fluorimetry, J. Phys. Chem. Lett. 8 (3) (2017) 553–558, https://doi.org/10.1021/acs.jpclett.6b02894.
[27] M. Vivoli, H.R. Novak, J.A. Littlechild, N.J. Harmer, Determination of protein-ligand interactions using differential scanning fluorimetry, J Vis Exp. (2014) 51809, https://doi.org/10.3791/51809.
[28] N. Rosa, M. Ristic, S.A. Seabrook, D. Lovell, D. Lucent, J. Newman, Meltdown: A tool to help in the interpretation of thermal melt curves acquired by differential scanning fluorimetry, J Biomol Screen. 20 (7) (2015) 898–905, https://doi.org/10.1177/1087057115584059.
[29] H.L. Svilenov, T. Menzen, K. Richter, G. Winter, Modulated scanning fluorimetry can quickly assess thermal protein unfolding reversibility in microvolume samples, Mol. Pharmaceutics. 17 (7) (2020) 2638–2647, https://doi.org/10.1021/acs.molpharmaceut.0c00330.
[30] J. Crossen, S.L. Diamond, Thermal shift assay to probe melting of thrombin, fibrinogen, fibrin monomer, and fibrin: Gly-Pro-Arg-Pro induces a fibrin monomer-like state in fibrinogen, Biochim Biophys Acta Gen Subj. 1865 (2) (2021) 129805, https://doi.org/10.1016/j.bbagen.2020.129805.

[31] C. Ma, M.D. Sacco, B. Hurst, J.A. Townsend, Y. Hu, T. Szeto, X. Zhang, B. Tarbet, M.T. Marty, Y.u. Chen, J. Wang, Boceprevir, GC-376, and calpain inhibitors II, XII inhibit SARS-CoV-2 viral replication by targeting the viral main protease, Cell Res. 30 (8) (2020) 678–692, https://doi.org/10.1038/s41422-020-0356-z.
[32] F. Barthels, G. Marincola, T. Marciniak, M. Konhäuser, S. Hammerschmidt, J. Bierlmeier, U. Distler, P.R. Wich, S. Tenzer, D. Schwarzer, W. Ziebuhr, T. Schirmeister, Asymmetric disulfanylbenzamides as irreversible and selective inhibitors of Staphylococcus aureus sortase A, ChemMedChem. 15 (10) (2020) 839–850, https://doi.org/10.1002/cmdc.201900687.
[33] L. Cianni, F.D.R. Rocho, F. Rosini, V. Bonatto, J.F.R. Ribeiro, J. Lameira, A. Leitão, A. Shamim, C.A. Montanari, Optimization strategy of single-digit nanomolar cross-class inhibitors of mammalian and protozoa cysteine proteases, Bioorg. Chem. 101 (2020) 104039, https://doi.org/10.1016/j.bioorg.2020.104039.
[34] T. Moldoveanu, Z. Jia, P.L. Davies, Calpain activation by cooperative Ca2+ binding at two non-EF-hand sites, J. Biol. Chem. 279 (7) (2004) 6106–6114, https://doi.org/10.1074/jbc.M310460200.
[35] F. Hammerstein, L.M. Lauth, S. Hammerschmidt, A. Wagner, T. Schirmeister, U.A. Hellmich, Cis autocatalytic cleavage of glycine-linked Zika virus NS2B-NS3 protease constructs, FEBS Lett. 593 (16) (2019) 2204–2213, https://doi.org/10.1002/feb2.v593.1610.1002/1873-3468.13507.
[36] I. Ugur, M. Schatte, A. Marion, M. Glaser, M. Boenitz-Dulat, I. Antes, Ca2+ binding induced sequential allosteric activation of sortase A: An example for ion-triggered conformational selection, PLoS One. 13 (2018) e0205057. https://doi.org/10.1371/journal.pone.0205057..
[37] X. Wang, J.-L. Chen, G. Otting, X.-C. Su, Conversion of an amide to a high-energy thioester by Staphylococcus aureus sortase A is powered by variable binding affinity for calcium, Sci. Rep. 8 (2018) 16371, https://doi.org/10.1038/s41598-018-34752-6.
[38] T. Moldoveanu, C.M. Hosfield, D. Lim, J.S. Elce, Z. Jia, P.L. Davies, A Ca2+ switch aligns the active site of calpain, Cell. 108 (5) (2002) 649–660, https://doi.org/10.1016/S0092-8674(02)00659-1.
[39] T. Moldoveanu, R.L. Campbell, D. Cuerrier, P.L. Davies, Crystal structures of Calpain–E64 and – leupeptin inhibitor complexes reveal mobile loops gating the active site, J. Mol. Biol. 343 (5) (2004) 1313–1326, https://doi.org/10.1016/j.jmb.2004.09.016.
[40] F. Barthels, T. Schirmeister, C. Kersten, BANΔIT: B'-factor analysis for drug design and structural biology, Mol. Inf. 40 (1) (2021) 2000144, https://doi.org/10.1002/minf.v40.110.1002/minf.202000144.
[41] M.C. Mahawaththa, B.J.G. Pearce, M. Szabo, B. Graham, C.D. Klein, C. Nitsche, G. Otting, Solution conformations of a linked construct of the Zika virus NS2B-NS3 protease, Antivir. Res. 142 (2017) 141–147, https://doi.org/10.1016/j.antiviral.2017.03.011.
[42] N.J. Braun, J.P. Quek, S. Huber, J. Kouretova, D. Rogge, H. Lang-Henkel, E.Z.K. Cheong, B.L.A. Chew, A. Heine, D. Luo, T. Steinmetzer, Structure-based macrocyclization of substrate analogue NS2B-NS3 protease inhibitors of Zika, West Nile and Dengue viruses, ChemMedChem. 15 (15) (2020) 1439–1452, https://doi.org/10.1002/cmdc.v15.1510.1002/cmdc.202000237.
[43] Y. Li, Z. Zhang, W.W. Phoo, Y.R. Loh, W. Wang, S. Liu, M.W. Chen, A.W. Hung, T.H. Keller, D. Luo, CongBao Kang, Structural dynamics of zika virus NS2B-NS3 protease binding to dipeptide inhibitors, Structure 25 (8) (2017) 1242–1250.e3, https://doi.org/10.1016/j.str.2017.06.006.
[44] J.E. Hoeher, M.A. Veirs, J.R. Widom, Impacts of fluorescent base analogue substitution on the folding of a riboswitch, preprint (BioRxiv) (2021), https://doi.org/10.1101/2021.07.22.453416.
[45] A. Adler, N. Forster, M. Homann, H.U. Göringer, Post-SELEX chemical optimization of a trypanosome-specific RNA aptamer, Comb Chem High Throughput Screen. 11 (2008) 16–23, https://doi.org/10.2174/138620708783398331.

Fabian Barthels received his M.Sc. in Biochemistry from the University of Tübingen (Germany) and after graduation, he joined the research group of Prof. Dr. Tanja Schirmeister for a Ph.D. in the field of Pharmaceutical Chemistry at the University of Mainz (Germany). During his doctorate, he discovered his interest in open-source hard- and software for drug discovery applications. Previously, he has developed and published an open-source liquid handling workstation (FINDUS) and a crystallographic B-factor analysis toolkit (BANΔIT). His current research interests involve designing biophysical instrumentations for the study of protein & RNA ligand interactions.

A low-cost 3D-printable differential scanning fluorometer for protein and RNA melting experiments

Authors
Fabian Barthels*,[1], Stefan J. Hammerschmidt[1], Tim R. Fischer[1], Collin Zimmer[1], Elisabeth Kallert[1], Mark Helm[1], Christian Kersten[1], and Tanja Schirmeister[1]

Affiliations
[1]Institute for Pharmaceutical and Biomedical Sciences, Johannes Gutenberg-University, Staudinger Weg 5, 55128 Mainz, Germany.

Corresponding author's email address
barthels@uni-mainz.de

Source of protein and RNA materials

The following proteins were obtained commercially: bovine thrombin (Sigma-Aldrich), hen egg-white lysozyme (Sigma-Aldrich), bovine serum albumin (Sigma-Aldrich), and human Calpain I (Calbiochem). Cruzain was a gift from the group of Dr. Avninder Bhambra (University of Leicester, UK). SARS-CoV2 main protease, *S. aureus* sortase A, and ZIKV NS2B/NS3 protease were obtained by recombinant protein expression (see below for protocols). The ligands used in this study $PreQ_1$ (Sigma-Aldrich), E64 (Cayman Chemical), and leupeptin (Sigma-Aldrich) were purchased. The cyclic peptide ligand (1-((8*R*,15*S*,18*S*)-15,18-bis(4-aminobutyl)-4,7,14,17,20-pentaoxo-3,6,13,16,19-pentaaza-1(1,3)-benzenacyclohenicosaphane-8-yl)guanidine was a gift from Prof. Torsten Steinmetzer (University of Marburg, Germany). The $preQ_1$ r boswitch aptamer domain and trypanosome-specific RNA aptamer were obtained by *in vitro* transcription (see below for protocols).

Protein expression of SARS-CoV2 main protease

Expression of SARS-CoV2 M^{pro} was performed as described previously [1]. The M^{pro}-sequence containing pMal expression construct (Prof. John Ziebuhr, Justus-Liebig-University Gießen, Germany) was transformed into competent *Escherischia coli* (*E. coli*) strain BL21-Gold (DE3) cells (Agilent Technologies, Santa Clara, California, USA) which were grown in 100 µM ampicillin containing LB medium at 37 °C until reaching an OD_{600} of ~0.5. Expression was induced by the addition of 0.3 mM isopropyl-D-thiogalactoside (IPTG) for 16 h at 18 °C. After harvesting by centrifugation (10 min, 10 krpm), cells were resuspended in M^{pro}-lysis buffer (20 mM Tris-HCl pH 7.8, 150 mM NaCl, 20 mM imidazole) and lysed by sonication (Sonoplus, Bandelin, Berlin, Germany). The cleared lysate (45 min, 15 krpm) was immediately subjected

to immobilized metal affinity chromatography (IMAC) using a HisTrap HP 5 mL column (GE Healthcare, Chicago, Illinois, USA) to isolate the protein. After extensive washing with 20 column volumes (CV) of $IMAC_{Mpro}$ buffer A (20 mM Tris-HCl pH 7.8, 200 mM NaCl, 20 mM imidazole) protein was eluted in a linear gradient of $IMAC_{Mpro}$ buffer B (20 mM Tris-HCl pH 7.8, 200 mM NaCl, 500 mM imidazole). Throughout IMAC, buffers were cooled on ice. Fractions containing protein were subsequently administered to a gel-filtration (size exclusion chromatography, SEC) step on a HiLoad 16/600 Superdex 75°pg column (GE Healthcare, Chicago, Illinois, USA) in the M^{pro} SEC buffer (20 mM Tris-HCl pH 7.8, 150 mM NaCl, 1 mM ethylenediaminetetraacetic acid (EDTA), 1 mM dithiothreitol (DTT)). Purified M^{pro} was diluted to a final concentration of 10 µM and adjusted to 10% (v/v) glycerol. Aliquots were shock frozen in liquid nitrogen and stored at –80 °C until further usage. Throughout all purification steps, protein concentrations were measured *via* absorbance at 280 nm on a NanoDrop 2000 Spectrophotometer (Thermo Scientific Waltham, Massachusetts) and sample purity was assessed *via* coomassie brilliant blue-stained sodium dodecyl sulfate−polyacrylamide gel electrophoresis (SDS-PAGE).

Protein expression of *S. aureus* Sortase A

Expression of *S. aureus* SrtA was performed as described previously [2]. The pET23b vector containing the SrtA sequence, received from the group of Prof. Dirk Schwarzer (University of Tübingen, Germany)[3], was transformed into competent *E. coli* strain BL21-Gold (DE3) cells which were grown in 100 µM ampicillin containing LB medium at 37 °C until reaching an OD_{600} of ~0.6–0.8. Expression was induced by the addition of 1 mM IPTG for 16 h at 20 °C. Pelleted cells were resuspended in SrtA-lysis buffer (20 mM Tris-HCl, pH 6.9, 300 mM NaCl, 0.1% (v/v) $Triton_{X\text{-}100}$, DNase, lysozyme) and lysed by sonication. The centrifugation-cleared lysate (45 min, 15 krpm) was subjected to IMAC using a HisTrap HP 5 mL column to isolate SrtA. After washing with 5 CV of $IMAC_{SrtA}$ buffer A (20 mM Tris-HCl pH 7.2, 300 mM NaCl, 30 mM imidazole) protein was eluted in a linear gradient of $IMAC_{SrtA}$ buffer B (20 mM Tris-HCl pH 7.2, 500 mM NaCl, 300 mM imidazole). Fractions containing protein were subsequently administered to SEC on a HiLoad 16/600 Superdex 75°pg column in the SEC_{SrtA} buffer (20 mM Tris-HCl pH 7.5, 150 mM NaCl). Purified SrtA was shock frozen in liquid N_2 and stored at –80 °C until further usage. Throughout purification, protein concentrations were measured *via* absorbance at 280 nm and sample purity was assessed *via* SDS-PAGE.

Protein expression of Zika virus NS2B-NS3 protease

Expression of ZIKV $NS2B_{cf}$-$NS3_{pro}$ was performed as described previously [4]. To abolish autocatalytic cleavage of the covalently linked protease construct, an R95A mutant was used instead of the wild-type protein [5]. The pET11a vector containing the sequence of ZIKV $NS2B_{cf}$-$NS3_{pro}$ was transformed into competent *E. coli* strain BL21-Gold (DE3) cells which were grown in 100 µM ampicillin containing LB medium at 37 °C until reaching an OD_{600} of ~0.6–0.8. Expression was induced with the addition of 1 mM IPTG for 16 h at 20 °C. Pelleted cells were resuspended in $lysis_{Z\,KV}$ buffer (20 mM Tris-HCl pH 8.0, 300 mM NaCl, 20 mM imidazole, 0.1% (v/v) $Triton_{X\text{-}100}$, DNase, lysozyme, 1 mM dithiothreitol (DTT)) and lysed by sonication. The cleared lysate (45 min, 15 krpm) was subjected to IMAC using a HisTrap HP 5 mL column to isolate the ZIKV protease. After washing with 5 CV of $IMAC_{Z\,KV}$ buffer A (20 mM Tris-HCl pH 8.0, 300 mM NaCl, 20 mM imidazole) protein was eluted in a linear gradient of $IMAC_{Z\,KV}$ buffer B (20 mM Tris-HCl pH 8.0, 300 mM NaCl, 250 mM imidazole). Fractions containing protein were subsequently administered to SEC on a HiLoad 16/600 Superdex 75°pg column in the $SEC_{Z\,KV}$ buffer (50 mM Tris-HCl pH 8.0, 150 mM NaCl). Purified ZIKV $NS2B_{cf}$-$NS3_{pro}$ was shock frozen in liquid nitrogen and stored at –80 °C until further usage. Throughout purification, protein concentrations were measured *via* absorbance at 280 nm and sample purity was assessed *via* SDS-PAGE.

In vitro transcription (IVT) and purification of $preQ_1$ riboswitch aptamer domain

Polymerase Chain Reaction (PCR)

The *B. subtilis* $preQ_1$ riboswitch sequence (5‘ GGA GAG GUU CUA GCU ACA CCC UCU AUA AAA AAC UAA 3‘) was retrieved from Roth *et al*. [PMID: **17384645**].

For the preparation of IVT templates, PCR reactions were carried out in final volumes of 200 µL. 5 U/µL Taq DNA Polymerase (NEB; units defined by the supplier) were added to the reaction buffer (10 mM Tris-HCl (pH 8.3), 50 mM KCl, 1.5 mM $MgCl_2$) containing 3 mM $MgCl_2$, 400 µM dNTP-Mix, 2 µM of each primer and 10 nM template DNA. After an initial denaturation step (2 min at 90 °C), 30 PCR cycles were performed with annealing (30 s at 45 °C), elongation (45 s at 72 °C) and denaturation (30 s at 90 °C) with a final elongation step of 5 min.

***In vitro* transcription of preQ$_1$ riboswitch RNA and purification**

400 µL of PCR reaction product were added without further purification to transcription buffer (40 mM Tris-HCl (pH 7.9), 2 mM spermidine, 10 mM DTT,10 mM NaCl) together with 40 mM $MgCl_2$, 5 mM DTT, 5 mM of each NTP, 2.5 µg/mL BSA and 0.6 U/µL of T7 polymerase (ThermoFisher Scientific; units defined by the supplier). Reactions were carried out in a final volume of 1 mL at 37 °C for 4 h.

In vitro transcribed RNA was purified by 10 % denaturing polyacrylamide gel electrophoresis (PAGE) for 90 min at 15 W. RNA was visualized by UV shadowing and the corresponding gel area was excised from the gel. After overnight elution in 0.5 M NH_4OAc and nanosep filtering (0.45 µm, VWR), the RNA was precipitated with EtOH.

Purified RNA was dissolved in MilliQ water and the quality was checked on 10 % denaturing PAGE gels. The concentration was determined on a Nanodrop 2000 Spectrometer (Thermo Scientific, Waltham, USA) by measuring the absorption at 260 nm and 280 nm.

Table 1: Oligos used for RNA preparation.

Oligo	Sequence
Template	5‘ TAG TCG TAA GCT GAT ATG GCT GAT TAG TCG GAA GCA TCG AAC GCT GAT TTA GTT TTT TAT AGA GGG TGT AGC TAG AAC CTC TCC TAT AGT GAG TCG TAT TA 3‘
Forward primer	5‘ CGC GCG AAG CTT AAT ACG ACT CAC TAT A 3‘
Reverse primer	5‘ TTA GTT TTT TAT AGA GGG TG 3‘

In vitro transcription and purification of a trypanosome-specific RNA aptamer

A modified version of “aptamer 2-16”, originally published by Adler et al. with an added 3’-terminal adenosine was synthesized [6]. The complementary DNA sequence for this construct, incorporated in a pUC19 plasmid under the control of a T7 promoter and terminated by an AseI restriction site, was commercially synthesized (GenScript). Prior to run-off *in vitro* transcription (IVT), the template plasmid was digested by *Aquaspirillum serpens* nuclease (AseI, New England Biolabs) according to the vendors’ protocol and used in IVT without further purification. T7 RNA polymerase was expressed following standard procedures. The aptamer was produced by run-off transcription in a 40 mM Tris buffer pH 8 in the presence

of 65 ng/µL DNA template, 5 mM of each ATP/CTP/GTP/UTP, 1 mM spermidine, 15 mM DTT, 5 µg/mL BSA, 40 mM $MgCl_2$ and appropriate amounts of T7 RNA polymerase. After IVT, a DNase I (Jena Bioscience) digest was performed, and the sample was purified by preparative 10% PAGE. The RNA was visualized under UV light and manually excised. RNA was eluted in 0.3 M sodium acetate buffer pH 5, precipitated, and redissolved in MQ water. Samples were stored at –20 °C.

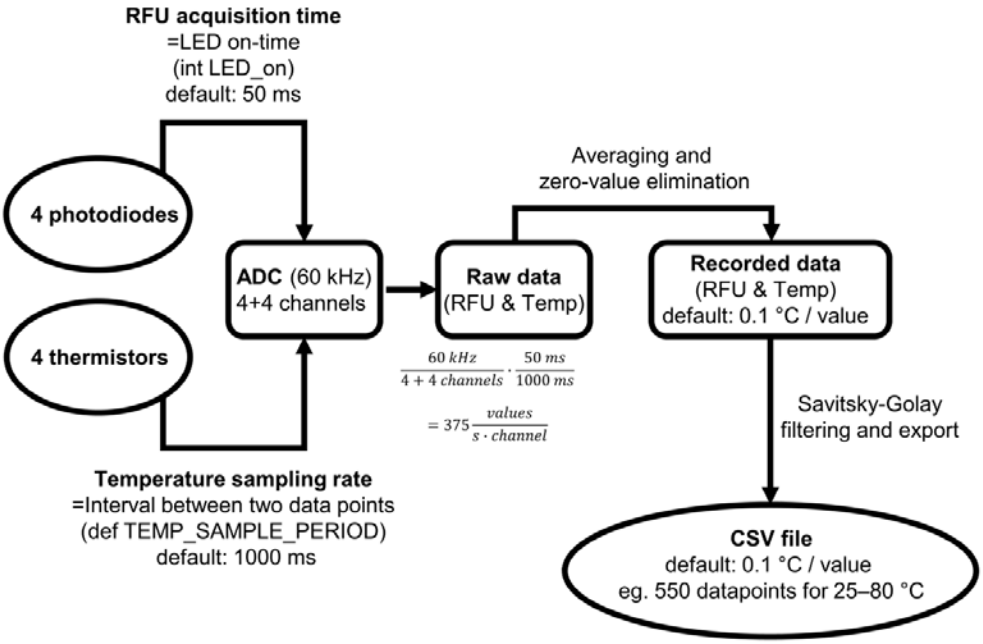

Figure 1: Flowchart of data acquisition and processing in the openDSF system. The analog signals measured by the thermistors and photodiodes are converted by the ADC into digital raw data which is averaged and smoothed until it is written to a log file as a tuple of [channel; temperature; fluorescence].

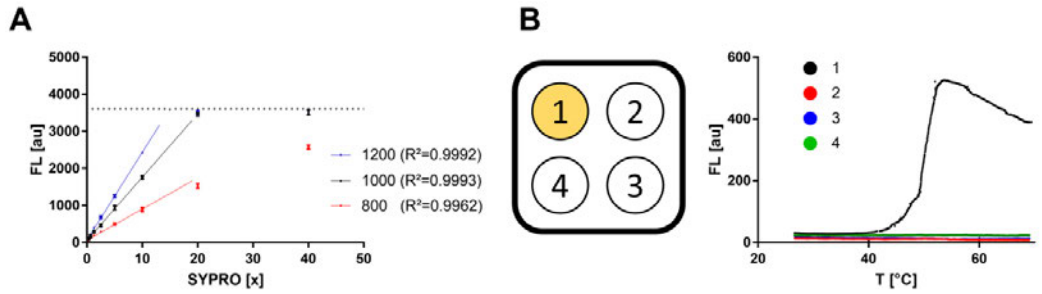

Figure 2: Characterization of the fluorescence detector. (**A**) A concentration series of SYPRO Orange (40–0.15×) in glycerol/water (9:1) was measured in 30 µL triplicates for all four holders at an LED excitation power of 800, 1000, or 1200 and the fluorescence data were plotted for linear regression. Within the detection range of 0–3000 mV, the photodiode shows a linear response to the concentration. At 3500 mV, the detector reaches its upper detection limit (oversaturation). (**B**) To investigate tube-to-tube bleeding, a 30 µL sample with srtA (5 µM) and SYPRO Orange (5×) was loaded into a holder (e.g., holder 1). In the other holders (2–4), only srtA (5 µM, 30 µL) was loaded. A melting curve of 25–70 °C was measured and the fluorescence traces were examined. Stray light could not be quantified in any neighboring detector cell for all four holders (N=8).

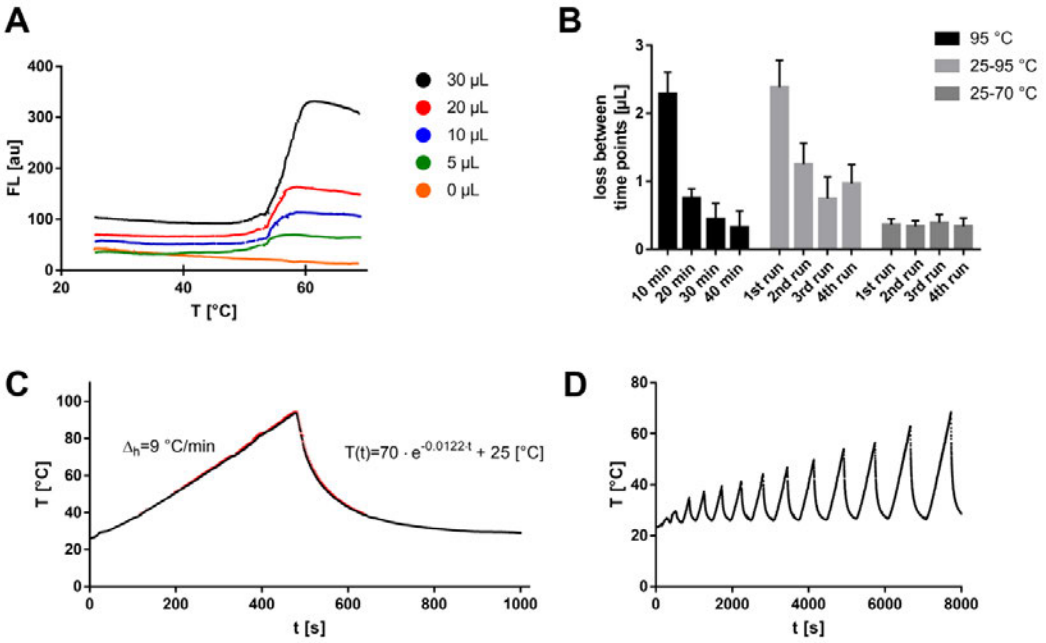

Figure 3: Characterization of the heating system and PCR tube parameters. (**A**) Determination of the minimum sample volume (0–30 µL with SARS CoV2 M^{pro} protein samples (5 µM/5×). S/N ratios [dB] for the M^{pro} samples: 30 µL (27.1), 20 µL (24.7), 10 µL (20.5), 5 µL (18.7). (**B**) Gravimetric determination of the evaporation loss of a 30 µL sample (50 mM HEPES buffer) sealed with a thermistor cap after (i) 10–40 min heating at 95 °C; (ii) 1–4 temperature ramps (2 °C/min) from 25 to 95 °C; (iii) 1–4 temperature ramps (2 °C/min) from 25 to 70 °C. 4 replicates were measured. (**C**) Fastest established heating curve (9 °C/min, 25–95 °C) followed by a cooling curve with air at room temperature (25 °C) which follows an exponential relationship. Three replicates for all four holders (N=12) were performed. The error bars (standard deviation) are shown with red symbols. (**D**) Oscillating sequence of heating and cooling cycles with a heating rate of 2 °C/min (holder 1).

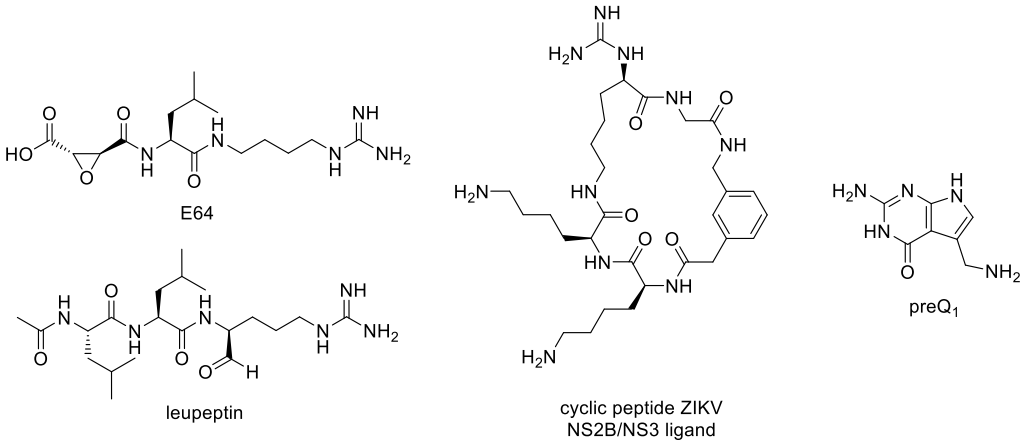

Figure 4: Molecular structures of the ligands used in the protein- and RNA-DSF experiments of this study.

References:

[1] G. Amendola, R. Ettari, S. Previti, C. Di Chio, A. Messere, S. Di Maro, S.J. Hammerschmidt, C. Zimmer, R.A. Zimmermann, T. Schirmeister, M. Zappalà, S. Cosconati, Lead Discovery of SARS-CoV-2 Main Protease Inh bitors through Covalent Docking-Based Virtual Screening, J. Chem. Inf. Model. 61 (2021) 2062–2073. https://doi.org/10.1021/acs.jcim.1c00184.

[2] F. Barthels, G. Marincola, T. Marciniak, M. Konhäuser, S. Hammerschmidt, J. Bierlmeier, U. Distler, P.R. Wich, S. Tenzer, D. Schwarzer, W. Ziebuhr, T. Schirmeister, Asymmetric Disulfanylbenzamides as Irreversible and Selective Inhibitors of Staphylococcus aureus Sortase A, ChemMedChem. 15 (2020) 839–850. https://doi.org/10.1002/cmdc.201900687.

[3] L. Schmohl, J. Bierlmeier, N. von Kügelgen, L. Kurz, P. Reis, F. Barthels, P. Mach, M. Schutkowski, C. Freund, D. Schwarzer, Identification of sortase substrates by specificity profiling, Bioorg. Med. Chem. 25 (2017) 5002–5007. https://doi.org/10.1016/j.bmc.2017.06.033.

[4] H. Maus, F. Barthels, S.J. Hammerschmidt, K. Kopp, B. Millies, A. Gellert, A. Ruggieri, T. Schirmeister, SAR of novel benzothiazoles targeting an allosteric pocket of DENV and ZIKV NS2B/NS3 proteases, Bioorganic & Medicinal Chemistry. 47 (2021) 116392. https://doi.org/10.1016/j.bmc.2021.116392.

[5] F. von Hammerstein, L.M. Lauth, S. Hammerschmidt, A. Wagner, T. Schirmeister, U.A. Hellmich, Cis autocatalytic cleavage of glycine-linked Zika virus NS2B-NS3 protease constructs, FEBS Lett. 593 (2019) 2204–2213. https://doi.org/10.1002/1873-3468.13507.

[6] A. Adler, N. Forster, M. Homann, H.U. Göringer, Post-SELEX Chemical Optimization of a Trypanosome-Specific RNA Aptamer, Comb Chem High Throughput Screen. 11 (2008) 16–23. https://doi.org/10.2174/138620708783398331.

“

5.2 FINDUS: An Open-Source 3D Printable Liquid-Handling Workstation for Laboratory Automation in Life Sciences

5.2.1 Context, Project Summary, and own Contribution

Liquid-handling plays a crucial role in most biochemical and synthetic experiments. The volumes transferred are often in the low microliter range and the number of pipetting steps can be very high when combinatorial or sequential experimental designs are involved. Manual pipetting is therefore often impractical and subject to inherent human error.[312] To address the needs for pipetting automation, commercial liquid-handling workstations have been developed in the past, but they cost several 10,000 € and are often inaccessible to academic research.[313] In this project, we decided to develop a low-cost (400 €) fully integrable non-commercial dispensing utility system (FINDUS) to address our research needs (e.g., synthesis of a SrtA substrate and to increase the enzyme inhibition assay accuracy).

The core piece of the FINDUS is an air displacement pipette such as can be found in any laboratory. With the FINDUS, we have removed the spring mechanism of the pipette, so that the pipetting piston can be moved via a gear. The rotation of a stepper motor pulls the pipetting piston and enables it to aspirate a liquid from a reservoir. We have chosen the ESP8266 as a microcontroller to control the four stepper motors in order to move the pipetting arm. The automation is done by means of a Python-based user interface developed for this project which is freely available for adaptation. Another characteristic of the FINDUS is the flexible design of the workspace through a modular system consisting of 3D-printed racks in which so-called bins, i.e. vessels like PCR tubes or 96-well plates can be mounted. Calibration of the FINDUS according to the standard gravimetric method (ISO8655) resulted in a maximum statistical pipetting error of 0.3%. This accuracy qualifies the system for analytical purposes and we could demonstrate the practical use of the FINDUS for our research with biochemical (protease inhibition assays) and synthetic (solid-phase peptide synthesis) application examples.

Based on 3D printing and Arduino microcontrollers, the FINDUS system was in 2019 the first fully non-commercial open-source solution of a precision liquid-handling system. In the following two years, two adapted and extended pipetting systems (EvoBot & Open workstation) have been developed and published in the spirit of the open-source philosophy.[314,315]

Own contributions: Conceptualization, Assembly of electronic and 3D-printed parts, Development of the user interface, Gravimetric calibration, Execution of example applications & Writing of the manuscript.

Contributions from other authors: Solid-phase peptide synthesis & Computer-aided design of the gear rack.

This work has been published in: SLAS Technology (impact factor: 3.12).

The 'Supporting Information' can be accessed online at doi: 10.1177/2472630319877374.

5.2.2 Publication

The following publication quoted (within "") from page 271 to page 280 is exactly the same as the manuscript cited on page 270:"

Original Research

FINDUS: An Open-Source 3D Printable Liquid-Handling Workstation for Laboratory Automation in Life Sciences

SLAS Technology
2020, Vol. 25(2) 190–199

DOI: 10.1177/2472630319877374
journals.sagepub.com/home/jla
SAGE

Fabian Barthels[1], Ulrich Barthels[1], Marvin Schwickert[1], and Tanja Schirmeister[1]

Abstract

3D-printed laboratory devices can enable ambitious research purposes even at a low-budget level. To follow this trend, here we describe the construction, calibration, and usage of the FINDUS (Fully Integrable Noncommercial Dispensing Utility System). We report the successful 3D printing and assembly of a liquid-handling workstation for less than $400. Using this setup, we achieve reliable and flexible liquid-dispensing automation with relative pipetting errors of less than 0.3%. We show our system is well suited for several showcase applications from both the biology and chemistry fields. In support of the open-source spirit, we make all 3D models, assembly instructions, and source code available for free download, rebuild, and modification.

Keywords

liquid-handling automation, open-source, 3D print, ESP8266, Arduino, Python

Introduction

The open-source movement, originating from Do-It-Yourself-scene software engineers during the late 1960s, has outlasted the decade but also changed paradigms with the availability of cost-efficient 3D printers.[1,2] About 10 years ago, 3D printers were still unaffordable for end consumers, but the costs have decreased dramatically since about 2013, due to the expiration of crucial fused deposition modeling (FDM) patents.[3–6]

Most 3D printer users share their ready-to-print assembly instructions in online repositories such as MakerBot Thingiverse[7] or the National Institutes of Health's 3D-print exchange.[8] Consequently, users with access to a 3D printer can freely reprint and modify the relevant model.

3D printers operate by melting a filament of plastic, such as polyethylene terephthalate glycol-modified (PETG), at the heated nozzle to build a 3D object in layers.[9] By now, most midrange 3D printers cost a few hundred dollars, with marginal operating expenses of about $30/kg printed material.[10]

It comes as no surprise that scientists from diverse fields use these technologies to build or customize laboratory equipment. Recently reported devices include constructions ranging from optics equipment[11] to biomolecular models,[12] handheld pipets,[13] synthesis reaction-ware,[14] nutating mixers,[15] continuous-flow reactors,[16] and other inventions summarized in several reviews.[17–20]

A nearly unlimited spectrum of possibilities emerges when 3D-printed mechanical parts are combined with microcontroller electronics. Recently, scientists developed several laboratory equipment instruments with low-budget open-source microcontrollers like Arduino[21] and Raspberry Pi,[22] yielding highly specialized laboratory equipment such as arthropod venom extractors,[23] microfluidic flow cytometers,[24] solid-phase peptide synthesizers,[25] environmental data collection systems,[26] RNA/DNA extractors,[27] and radiochemistry synthesis devices.[28]

Handling of liquids plays a central role in most experiments for the life sciences. The volumes are usually in the low-microliter range, and the number of transferred samples can be large when a combinatorial design of experiment is used. Therefore, manual liquid handling is often impractical, tedious, and prone to human error.[29,30] Consequently, there is a need for automated liquid-handling methods with higher accuracy and consistency. Commercially available liquid-handling workstations fulfill these needs but are often unaffordable (>$30,000) for academic research institutions.[31]

[1]Institute of Pharmacy and Biochemistry, Johannes Gutenberg University Mainz, Mainz, Germany

Received Jun 13, 2019, and in revised form Aug 18, 2019. Accepted for publication Aug 29, 2019.

Supplemental material is available online with this article.

Corresponding Author:
Fabian Barthels, Institute of Pharmacy and Biochemistry, Johannes Gutenberg University Mainz, Staudinger Weg 5, Mainz, 55128, Germany.
Email: barthels@uni-mainz.de

Furthermore, most commercial devices use a proprietary system architecture unsuitable for adaptive changes in the hard- or software components, although such changes are often needed for innovative research projects.

Open-source-based approaches to liquid handling were widely unknown before 2016, but recent advances led to a significant change in the landscape, with many producers introducing cheaper and more interoperable devices. The Andrew robot[32] can pick up conventional pipets from built-in racks using a camera to guide the movement of the robotic arm. Liquid-handling robots from Opentron are almost one order of magnitude cheaper than previous devices ($4000)[33] and contain an XYZ-gantry system that can handle standard pipets by mechanical control. Opentron's open-source concept recently led to innovative applications (e.g., devices for the production of human cell spheroids[34] or malaria parasite culturing[35]). Another invention, the OpenLH robot, integrates a commercially available robotic arm with custom 3D-printed parts and was set up for less than $1000.[36] Gerber et al. constructed a liquid-handling device around the LEGO Education EV3 core set.[37] While being primarily designed for education, this device shows also potential for research applications.

To contribute to this highly active research field, we report the design, 3D printing, and proof of an easy-to-rebuild liquid-handling robot for less than $400 in material costs, less than 50 hours of construction work, and an additional 50 hours of 3D-printing time.

Materials and Methods

Materials for Construction

We purchased precision shafts, linear bearings, tooth belts, belt pulleys, and joints from Motedis (Ensdorf, Germany). **Supplemental Table 1** shows detailed specifications on the hardware components integrated in the FINDUS (Fully Integrable Noncommercial Dispensing Utility System).

3D Printing

We fabricated the 3D-printed parts with an Anycubic 4Max printer (Shenzhen, China). By means of the open-source software FreeCAD[38] (LPGLv2+) and Ultimaker Cura 15.04.6[39] (LPGLv3), we designed, meshed, and sliced individual components. For the design of gears, we used the FreeCAD workbench "gear." We performed printing through a 0.4 mm nozzle with 1.75 mm ± 0.02 mm PETG filament (3D Hero, purchased on amazon.de) at 225 °C. The layer thickness was 0.2 mm. By soaking the printed parts, we reinforced mechanically stressed parts like the gear housing, X-slide, and Z-support with SR555 epoxy resin (Sicomin, Chateauneuf Les Martigues, France). 3D models (FCstd- and stl-files) can be downloaded for modification and reprinting from https://github.com/FBarthels/FINDUS.

Electronics

We chose an ESP8266 12F microcontroller from Espressif Systems (Shanghai, China) to control the movable parts of the FINDUS and programmed the microcontroller with Arduino IDE (integrated development environment) 1.8.8 [General Public License (GPL)]. OMC Corporation Ltd. (Nanjing City, China) was the commercial source for all NEMA (National Electrical Manufacturers Association) stepper motors used in this work. For the XY drives, we used bipolar NEMA 17 stepper motors (2 A, 1.8 °/step, 59 Ncm); for the Z drive, a bipolar NEMA 17 (26 Ncm); and for the pipet drive, a NEMA 11 (6 Ncm). Step-down boards provided a voltage of 3.3 V for the ESP8266 12F. DRV8825 controller boards from Pololu Electronics (Las Vegas, NV) controlled stepper motors using a motor library provided by Laurentiu Badea under MIT license.[40] Parameters used for this library were microstepping=32, speed profile=LINEAR_SPEED, Accel-Param=1000, and Decel-Param=1000. The ESP8266 was in access point mode. We set up a 10.0.0.0 private WiFi network for communication with the control computer. **Supplemental Figures 1–3** show the layout circuit boards for the ESP8266 FINDUS mainboard and the peptide synthesis module.

Software

After completion of the FINDUS board, we programmed it via the Arduino development interface and flashed it using a serial FTDI (Future Technology Devices International) adaptor from AZDelivery (Deggendorf, Germany). Only the primary flashing required the serial adaptor. We performed further program updates via WiFi using the HTTPUpdateServer library available in the Arduino environment.

We installed an information library and standard library for the ESP8266 microcontroller via the PC board manager. Among the available board settings, we selected the following NodeMCU 1.0 ESP-12E Module settings: FlashSize, 4M (1M SPIFFS); DebugPort, disabled; DebugLevel, none; CPU Frequency, 80 MHz; and UploadSpeed, 115000.

Based on Python (GPL-compatible license), we developed a FINDUS module in an object-oriented programming style, which contained all functions to control the robot. For the communication with the microcontroller, we used the Python library requests (Apache2 license) and the Python library dill (3-clause BSD license) to store instantiated classes. The complete source code can be obtained from https://github.com/FBarthels/FINDUS.

Configuring the Motorized Piston Stroke and Calibration

We accomplished a gravimetric calibration procedure as prescribed in DIN EN ISO 8655 to configure the motorized piston stroke and to assay the accuracy and precision of the liquid-handling workstation.[41] The model pipet Pipetman P200 and P1000 from Gilson (Middleton, WI) contained a displacement piston (4 mm diameter for the 200 µL pipet and 8 mm for the 1000 µL pipet) made of ground and polished hardened steel, which was moved directly by a computer-controlled, stepper motor–driven lifting axle. We determined the volume of deionized water dispensed by density-corrected[42] weightings in 1.5 mL polypropylene Eppendorf tubes (CarlRoth, Karlsruhe, Germany). In terms of gravimetric methods, we exploited the conventional guidelines for the use of a semi-microbalance. On a Quintix35-1S (Sartorius, Göttingen, Germany) analytical balance, we performed gravimetric analysis with 10 technical replicates for each data point and repetition thrice on 3 nonconsecutive days. We developed a calibration program as shown in the supplemental materials.

Inhibition of Cathepsin B by the E-64 Inhibitor

We investigated the inhibition of human cathepsin B (Calbiochem, Merck Millipore, Burlington, MA) by the epoxide inhibitor E-64 (AppliChem, Darmstadt, Germany) by means of a fluorometric enzyme assay as reported previously.[43] We prepared a stock solution of the cathepsin B protease (final concentration: 2 pM) in assay buffer (20 mM Tris-HCl, pH 6.0, containing 5 mM EDTA, 2.5 mM DTT, 200 mM NaCl, and 0.005% Brij 35). An Infinite F200 Pro (Tecan, Männedorf, Switzerland) multiplate reader monitored the increase of fluorescence on cleavage of the fluorogenic substrate Cbz–Phe–Arg–AMC (Bachem, Bubendorf, Switzerland). We performed all pipetting steps to set up the assay using the automation script as shown in the supplemental materials. Stock solutions of the substrate (final concentration: 100 µM) and E-64 were prepared in DMSO. We carried out three technical replicates in a volume of 90 µL in black flat-bottomed 96-well microtiter half-area plates (Greiner Bio-One, Kremsmünster, Austria) and negative inhibition control by mock treatment with pure DMSO. Fitting of the k_{obs} values against the inhibitor concentrations to the hyperbolic equation $k_{obs} = k_{inac}[I] / (K_{Iapp} + [I])$ gave the individual values of K_{Iapp} and k_{inac}. We corrected the K_{Iapp} values to the substrate concentration by the Cheng–Prusoff equation $K_I = K_{Iapp} / (1 + [S] / K_M)$.[44]

Solid-Phase Peptide Synthesis

An ESP8266 from Espressif Systems controlled the solid-phase synthesis module by connecting the WiFi station to the microcontroller of the FINDUS base system (access point). For the shaker, we used a NEMA 17 stepper motor (59 Ncm), and for vacuum aspiration a 12 V vacuum pump (120/−65 KPa, 5 L/min), from Aiyima (Shanghai, China). **Supplemental Table 2** shows a full list of the hardware components integrated in the peptide synthesis module.

We synthesized peptides by Fmoc-based solid-phase peptide chemistry using the homemade peptide synthesis module of the workstation and the script shown in the supplemental materials. Sigma-Aldrich (St. Louis, MO) supplied the chemicals used for the peptide synthesis. We performed the synthesis on Novabiochem (Merck Millipore) Wang resin (1.1 mmol/g) and a standard TBTU coupling protocol[45] by coupling each amino acid in threefold molar excess for 60 min with 2-(1*H*-benzotriazole-1-yl)-1,1,3,3-tetramethyluronium-hexafluorophosphate (TBTU) and *N*-methylmorpholine (NMM). We removed the Fmoc group twice with 40% piperidine in dimethylformamide (DMF) for 10 min and 20 min, respectively, and finally cleaved the peptide from the resin with trifluoroacetic acid (TFA)/triisopropylsilane/water (90/5/5) for 3 h. Precipitation with −80 °C cold ether, centrifugation, and lyophilization from water/acetonitrile (1:1) yielded the crude peptides. We determined success and purity by combined high-performance liquid chromatography (HPLC)/electrospray ionization mass spectrometry (ESI-MS) analysis using an Agilent (Santa Clara, CA) 1100 series HPLC system with an Agilent Poroshell 120 EC-C18 column (150×2.10 mm 4 µm column; mobile phase: ACN/H_2O 45:55 + 0.1% formic acid; flow rate: 0.4 mL/min). The HPLC detection wavelength was 254 nm. We used the Agilent 1100 series LC/MSD (Liquid Chromatography/Mass Selective Detector) trap in positive ionization mode.

Results and Discussion

Designing the Pipetting Arm

We designed the FINDUS primarily to automatize repetitive liquid-handling tasks in a modern life science laboratory. The basis for the liquid transfer machinery was a commercially available micropipet integrated with a displacement piston (**Fig. 1a**). For conventional handheld pipets, the piston stroke is controlled with a variable prestressed spring. The amount of liquid taken into the pipet tip is proportional to the piston stroke. We removed the spring and replaced it with 3D-printed bolt and nut adaptors. By separating both the handle and button part, we controlled the piston stroke by means of a stepper motor with a gear converting rotary motion into axial motion (**Fig. 1c**). The computer control guaranteed reproducible values of stroke, stroke speed, and acceleration, as well as intermediate pauses. This can be achieved by a gearbox with a

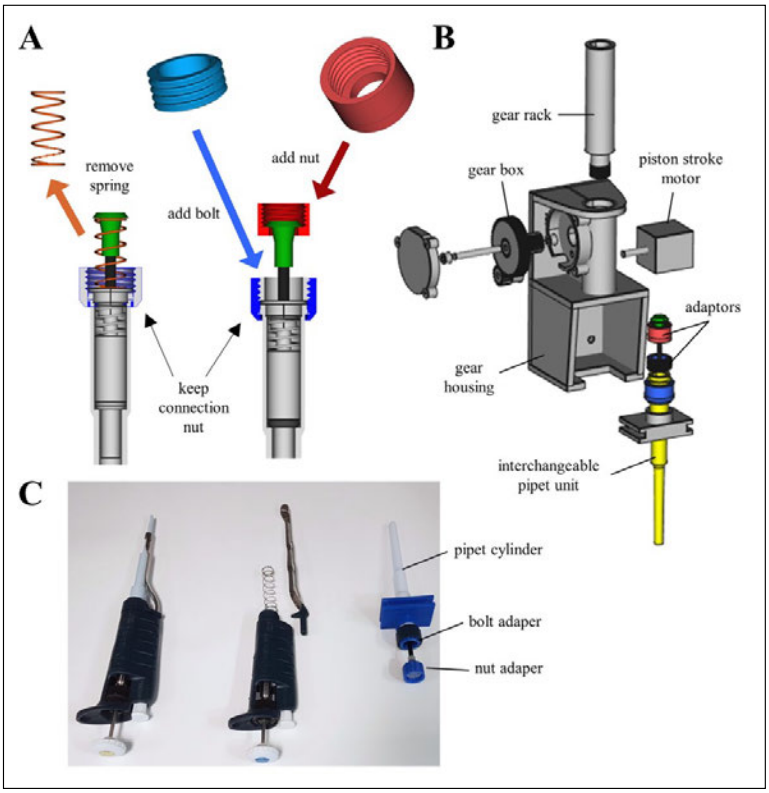

Figure 1. Construction of the FINDUS (Fully Integrable Noncommercial Dispensing Utility System) pipet arm and housing. (**A**) The modification of a conventional handheld pipet yielded the FINDUS centerpiece pipet unit. (**B**) Exploded-view drawing of the pipet cylinder and its piston adaptors within the pipet housing. (**C**) A micropipet with a displacement piston (left) was converted to an interchangeable pipet unit (right) by removing the spring, handle, and button (middle).

trapezoidal threaded spindle or a gear rack. While a threaded spindle allows better resolution, we chose the latter because of several advantages: (1) 3D-printing capability, (2) lower hysteresis (lower thread clearance) due to pressed fit, and (3) higher maximum axial speeds. We selected a gear rack with a gear ratio of 1:3.375 for 435 steps/mm, which enables a positional accuracy of the piston stroke of approximately 2 µm. We designed the housing for the motor and the gearbox so that different commercially available pipets can be exchanged with minimal effort (**Fig. 1b**). The exchange of the interchangeable pipet unit requires the manual action of the operator but is completed within 10 s by screwing the nut adaptor (**Fig. 1b and 1c**).

Setting Up a Working Area

We chose the size of the available working area of the robot to be 300×420 mm, allowing the placement of several experimental setups at the same time (**Fig. 2a and 2b**). The maximum upstroke of the Z-slide measured 100 mm but can be adjusted to the user's demands.

We constructed the FINDUS base frame from a corner-stiffened slot profile system, facilitating the dismantling of the device. The robot's XYZ system consisted of 10 mm and 8 mm precision shafts, linear bearings, GT2 profile tooth belts, belt pulleys, and PETG 3D-printed joints. We evaluated an aluminum composite panel and found it suitable for the base plate. The stiffened slot profiles served for the mounting of the XY-traverse, the Z-slide, and the pipet housing (**Fig. 3**).

An essential characteristic of the FINDUS was the flexibility in (re)placing the bins on the base plate. We designed different racks for liquid vessels, so-called Bins, printed in PETG. To fix the racks, we used double-sided adhesive tape because it allows rearrangement without great effort. Since the relative distances within the rack were not changed, only the new rack position had to be acquired in a new arrangement. We designed racks for 1.5 and 2.0 mL Eppendorf tubes, 6–25 mL glass vials, 100 mL bottles, 96-well plates, and spring-loaded racks for pipet tips (200 and 1000 µL) to allow automatic tip changing and release (**Fig. 2a and 2b**).

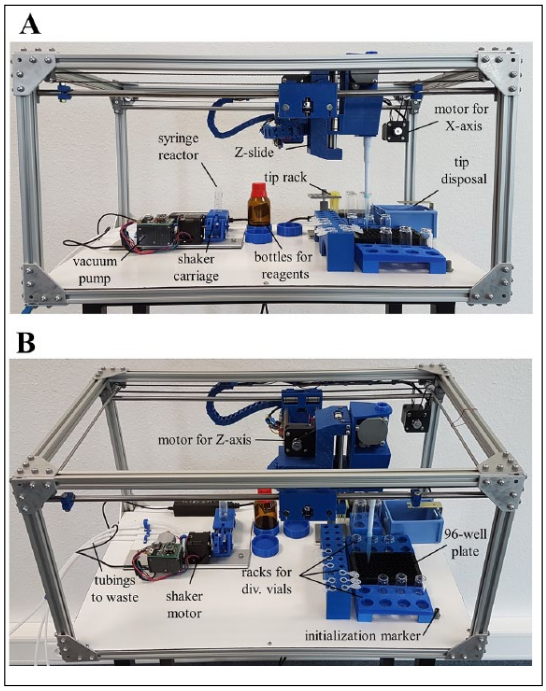

Figure 2. The FINDUS (Fully Integrable Noncommercial Dispensing Utility System) working area with sample models of 3D-printed racks used in our setup. (**A**) Photograph of the liquid-handling workstation as it is used in the author's laboratory, front view. (**B**) Photograph, top view.

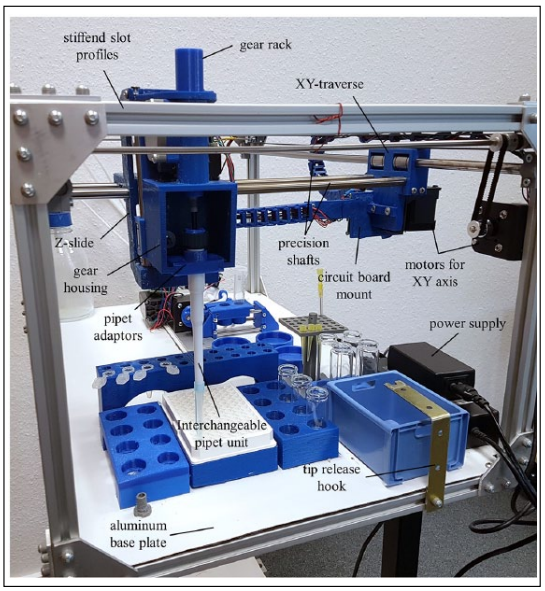

Figure 3. The FINDUS (Fully Integrable Noncommercial Dispensing Utility System) from the side view. The interchangeable pipet unit is mounted to the gear housing with a gear rack. The Z-slide and XY-traverse are moved on precision shafts and linear bearings by three stepper motors (XYZ).

ESP8266 Implementation

Among hundreds of available microcontrollers, the ESP8266 offered at least two advantages compared to most competitors in the price range of less than $10: (1) It was easy to implement the Arduino development environment;[46] and (2) the ESP8266 can run in access point mode, allowing the installation of additional ESP8266-driven modules without changing the network structure or the existing source code.[47] The software implemented on the ESP8266 controlled only the basic features of the stepper motors. We implemented the actual workstation in a Python environment on a remote-controlling personal computer (PC) or smartphone (**Fig. 4a**).

The ESP8266 operated as an access point with a private 10.0.0.0 network using the WPA+WPA2 standard and managed up to 10 clients simultaneously. Communication took place via a web server to which the PC sent commands via HTTP-Post requests. We implemented the following requests: INIT, RESET, SET_POS, MOVE_XY, MOVE_X, MOVE_Y, MOVE_Z, and MOVE_PIP. The MOVE requests required a parameter speed [revolutions per minute (rpm)] to control the speed of the robot over a wide range.

For stepper motor control, we integrated a library,[40] which made speed ramping of the steppers available. The stepper motors for the XY coordinates operated as multidrivers so that both motors started simultaneously, and whichever reached the endpoint first stopped while the other continued to run. We maintained the absolute position of the stepper motors (number of steps after initialization) over requests and returned as a reply with each request. This ensured that after initialization of the zero point, the stepper motors do not attempt to move robot parts beyond the physical limits.

FINDUS Python Script

We developed a Python-based FINDUS module and made it available for download, adaptation, and extension to the user's choice from GitHub (**Fig. 4b**). At the lowest level of this scenario, the class "Bin" instantiated bins, which had values defined in a dictionary ("bin_types"). One level higher, racks grouped specific bins together (i.e., an instantiated class, Rack). The Rack class implemented methods for handling bins (e.g., volume management) and the rack

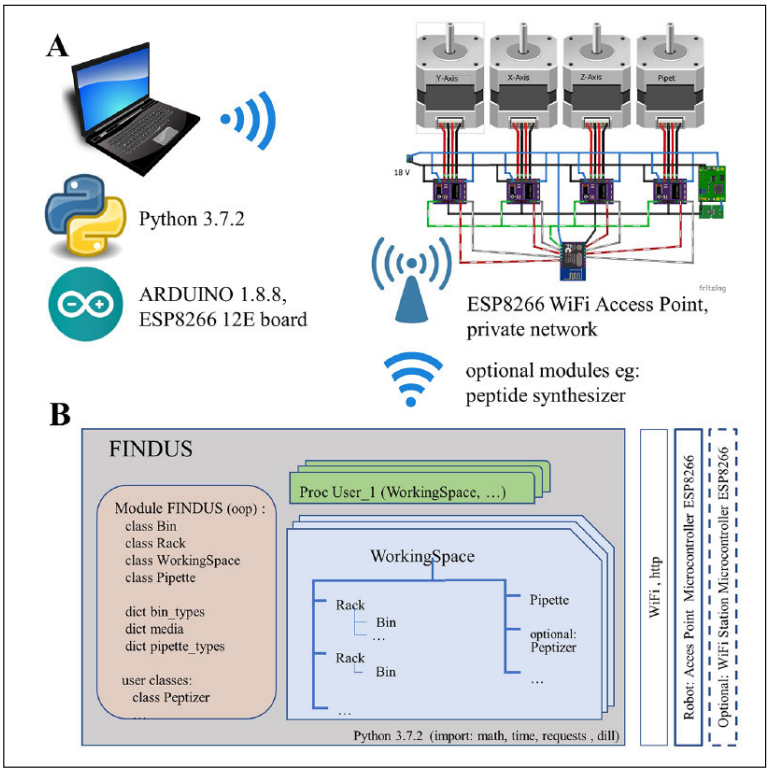

Figure 4. Soft- and hardware architecture to manage and control the FINDUS (Fully Integrable Noncommercial Dispensing Utility System). (**A**) WiFi-based communication system. The ESP8266 was limited to control basic motor movements, while a Python/Arduino-enabled computer was transmitting program instructions by HTTP protocol via WiFi connectivity. (**B**) Software architecture of the object-oriented FINDUS program, including the different classes. Licensing: Canopus49; Tango Project; Arduino CC-BY-SA 3.0 Unported. Fritzing, CC-BY-SA 2.0 de.

Table 1. Determination of the Pipetting Performance by Means of the Gravimetric Protocol, as Described in ISO8655.

	Nominal Volume	Maximum Permissible Systematic Error		Maximum Permissible Random Error	
Pipet[a]	[µL]	[%]	[µL]	[%]	[µL]
P200	20	±0.610	±0.122	±0.309	±0.062
P200	30	±0.679	±0.203	±0.338	±0.100
P200	50	±0.495	±0.247	±0.249	±0.124
P200	90	±0.197	±0.178	±0.243	±0.218
P200	140	±0.061	±0.085	±0.111	±0.155
P200	200	±0.094	±0.189	±0.109	±0.219
P1000	200	±0.489	±0.979	±0.179	±0.356
P1000	400	±0.249	±0.999	±0.215	±0.866
P1000	600	±0.216	±1.299	±0.132	±0.790
P1000	800	±0.119	±0.959	±0.081	±0.650
P1000	1000	±0.024	±0.240	±0.080	±0.808

a. The 200 µL pipet (P200) was tested at six different nominal volumes, and the 1000 µL pipet (P1000) was tested at five nominal volumes.

position. In this way, several physical bins can be combined to form a virtual one.

Methods in the Pipette class controlled the pipet action. The pipet was instantiated using a dictionary with pipet types, URL of the robot, and so on. Instantiated racks and pipets defined a WorkingSpace. The WorkingSpace class implemented the actual methods for a logical pipetting order or tip changing. Additional modules (e.g., a peptide synthesizer) can optionally be integrated into a WorkingSpace. A sequence of calls of

WorkingSpace methods fulfilled the actual pipetting task. We implemented liquid transfers between source and target, or more complex tasks like dilution series, on this level. In addition, the pipetting step can be specified in more detail with further parameters such as speed, humidification, or multidispensing from the pipet.

To group this sequence, there was a truncated class ("UserProc"), which implemented standard methods. The methods "init()" and "run()" were defined by the user. These instantiated user classes can be saved and reloaded. For verification of the program flow, we included a simulation mode in offline setup.

Setting Up the Motorized Pipet Arm

We configured the motorized piston stroke by fitting the stepper motor's rotation to the gravimetrically determined pipetting volume at five different nominal volumes. For the 200 µL pipet, nominal volumes were 20, 50, 90, 140, and 200 µL. The 1000 µL pipet nominal volumes were 200, 400, 600, 800, and 1000 µL. We assumed for both pipets a linear relation between the piston stroke and the dispensed volume. Thus, we started the calibration in the middle of the working range at 90 µL and 600 µL, respectively, with an estimated calibration value based on the displaced volume of the piston diameter of the pipet (4 mm and 8 mm).

We performed an iterative calibration procedure by linear interpolation from the nominal volume and the averaged measured masses. By this, we determined a refined calibration value for each pipet. With this refined calibration value, we carried out a new series of measurements. After three iterations, the calibration value was stable for both pipets. With the iterated calibration value for 90 µL and 600 µL, respectively, we performed measurement series for all nominal volumes and fitted these using linear regression (see script in the supplemental materials).

Calibration of the FINDUS Performance

Devices for liquid handling should be calibrated to ensure their performance with accepted standards, such as DIN12560 or ISO8655.[41] Skilled experimenters are usually capable of limiting the permissible random error to 1–2%.[29] Semac et al. and Lochner et al. probed and summarized frequent error sources in the life science laboratory and their contribution: uneven rhythm (1.5%), incorrect tip immersion depth (1%), and deviation from verticality (1%).[48,49] By separating the conventional handle and button part of a pipet, we controlled the piston stroke by means of a stepper motor. The stepper motor allowed a positional accuracy of the piston stroke of approximately 2 µm. With our setup, we could avoid all significant sources of errors for manual pipetting precision.

We tested the accuracy of the pipetting performance after calibration at all nominal volumes for both pipets. Thus, we performed five independent replicates to determine the maximum relative error for each pipet given from the gravimetric analysis (**Fig. 6a and 6b**). The maximum permissible systematic error and random error for the 1000 µL pipet and the 200 µL pipet are shown in **Table 1**. The permissible error limits according to ISO8655 were 1.4% to 2.8% of the nominal volume.[29] These results proved that the pipetting performance of the FINDUS complied with ISO8655 standards, even in our average life science laboratory, and is most likely outperforming skilled human pipetting operators.

Pre-wetting of the pipet tip by a single dispensing of the nominal volume led to a significant improvement in the reliability and was integrated into all pipetting steps in the enzyme assay. If pre-wetting was omitted, Joyce et al. found the first values of a measurement series were significantly smaller because of insufficient water vapor saturation in the tip.[50]

We identified two further factors as critical parameters for reproducible pipetting results: the piston stroke speed and the immersion depth of the pipet. We limited the piston stroke speed to 4 mm/s to allow the quasi-stationary uptake of the liquid into the tip without a latent negative pressure in the dead volume of the pipet. We chose the immersion depth (3 mm) below the liquid surface to be as small as possible without risking the absorption of air bubbles. The current filling level was simultaneously calculated from the quantity of liquid removed or added.

Our system design goals were accuracy performance and accessibility rather than speed. We benchmarked the FINDUS operating speed at a piston stroke speed of 4 mm/s. With a single-channel pipet, we filled a 96-well plate in 03:30 min. By using eight-channel pipets, the fill time can be drastically reduced to approximately 25 s per 96-well plate. We also set up a standard biological assay (24 wells total) with multidispensing variable volumes in about 01:00 min. We performed a video presentation illustrating the pipetting performance for the 24-well assay (www.github.com/FBarthels/FINDUS/tree/master/videos).

Solid-Phase Peptide Synthesis

We designed the peptide synthesis module to synthesize small to medium-sized peptides (4–20 amino acids) on a small scale (<0.5 mmol). We selected 2×10 mL disposable syringes as the reactive receptacle to carry out two parallel synthesis batches and introduced a polypropylene frit into each syringe (**Fig. 5a**). A vacuum pump sucked off the

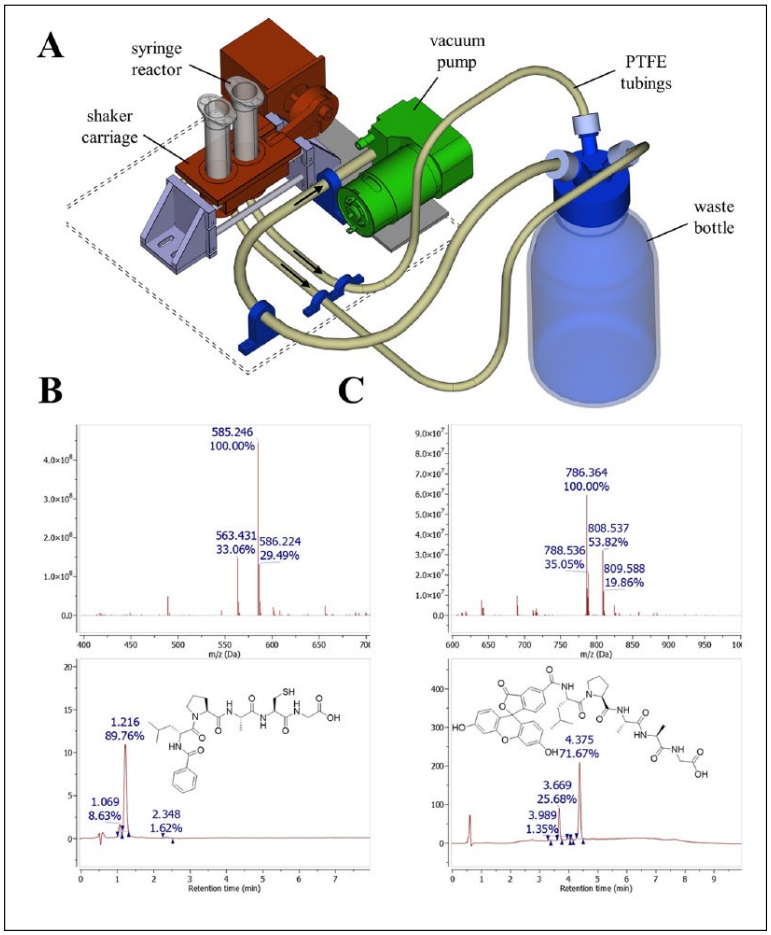

Figure 5. Peptide synthesis module. (**A**) Schematic depiction of the solid-phase synthesizer. The shaker carriage holds the syringes during the synthesis, while the vacuum pump is used to empty the reaction chamber. Arrows indicate the liquid and airflow of the vacuum pump. (**B**) High-performance liquid chromatography (HPLC) purity and electrospray ionization mass spectrometry (ESI-MS) of the synthesized peptide Bz-LPACG-OH. $[M+H]^+$ = 563.1 Da. (**C**) HPLC and ESI-MS of FAM-LPAAG-OH. $[M+H]^+$ = 786.2 Da.

liquid, while the solid phase remained in the reaction vessel. The extracted liquid passed through polytetrafluoroethylene (PTFE) hoses and was collected in the waste container, where it separated from the gas flow. We positioned the disposable syringes on a carriage, which is moved back and forth by a stepper motor via an eccentric. This movement caused an intimate mixing of the suspension in the syringe. We achieved sufficient mixing for a homogeneous suspension at approximately 300 rpm of the stepper motor. We synthesized a small test peptide, Bz-LPACG-OH, on a 132 µmol scale with a crude yield of 70.0% and a purity of 89.7% after precipitation from trifluoroacetic acid (**Fig. 5b**). A second test peptide, FAM-LPAAG-OH, was successfully synthesized on a 72 µmol scale with a crude yield of 66.0% and 71.6% purity (**Fig. 5c**). We concluded the FINDUS peptide synthesis module can synthesize short to medium-sized peptides in an acceptable yield and purity. We performed a video demonstration illustrating the basic features (filling, shaking, and emptying) of the FINDUS peptide synthesis module (www.github.com/FBarthels/FINDUS/tree/master/videos).

Cathepsin B Assay

Lysosomal cathepsin B is strongly inhibited by the naturally occurring epoxide E-64 extracted from *Aspergillus japonicus*.[51] The epoxide reacts with an active-site thiol group of cysteine proteases to form a thioether. Inhibition of cathepsin B by E-64 was previously assayed with a fluorometric Z-Phe-Arg-AMC assay (**Fig. 6c**).[52,53] Literature values for the inhibition constant K_I of E-64 on cathepsin B ranged from 43 nM to 51 nM. Therefore, we assumed this to be a valid enzyme inhibitor system to assess the reproducibility of enzyme assays. The FINDUS prepared a dilution series of the inhibitor at seven different concentrations

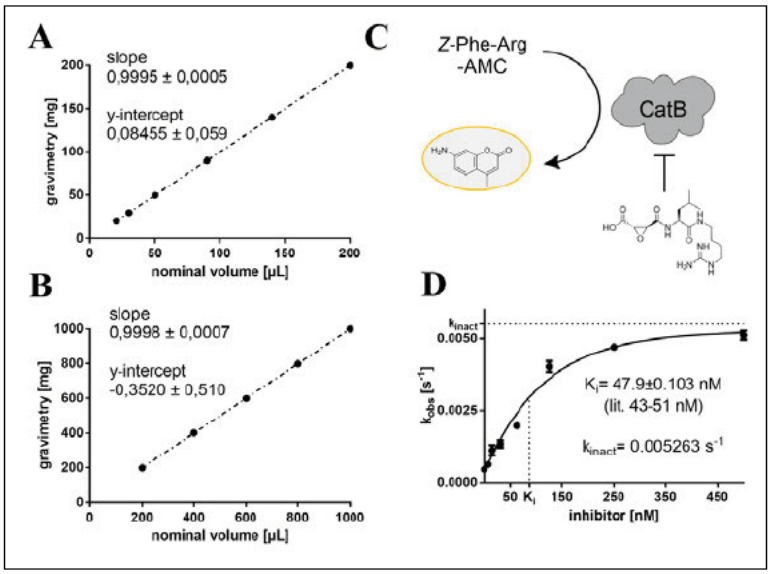

Figure 6. Calibration of the FINDUS (Fully Integrable Noncommercial Dispensing Utility System) and pipetting performance during an enzyme assay. (**A**) Calibration results of the 200 µL pipet. (**B**) Calibration results of the 1000 µL pipet. (**C**) Schematic depiction of the enzyme assay to determine the inhibition parameters of E-64 on cathepsin B. (**D**) Fluorometric assay results and calculation of the inhibitor-specific kinetic parameters.

(500 nM to 7.81 nM) prior to fluorometric measurement. Fitting of the fluorometric data to hyperbolas and zero-substrate correction gave the inhibition constant K_I at 47.9 nM ± 0.103 nM (**Fig. 6d**). Therefore, we concluded the enzyme assay performed with the FINDUS system is of high consistency and in agreement with literature values.

Declaration of Conflicting Interests

The authors declared no potential conflicts of interest with respect to the research, authorship, and/or publication of this article.

Funding

The authors disclosed receipt of the following financial support for the research, authorship, and/or publication of this article: Johannes Gutenberg University of Mainz.

ORCID iD

Fabian Barthels https://orcid.org/0000-0001-7950-2158

References

1. Anderson, C. *Makers: Das Internet der Dinge: die nächste industrielle Revolution*. Carl Hanser: Munich, 2013.
2. Rundle, G. *A Revolution in the Making*. Affirm Press: Melbourne, Australia, 2014.
3. Hull, C. W. Method for Production of Three-Dimensional Objects by Stereolithography. US Patent US5762856A, June 9, 1998.
4. Childers, C. M.; Hull, C. W. Method of Making a Three-Dimensional Object by Stereolithography. US Patent US5609812A, March 11, 1997.
5. Smalley, D. R.; Vorgitch, T. J.; Manners, C. R.; et al. Simultaneous Multiple Layer Curing in Stereolithography. US Patent US5597520A, January 28, 1997.
6. Almquist, T. A.; Smalley, D. R. Thermal Stereolithography. US Patent US5569349A, October 29, 1996.
7. Makerbot. Thingiverse—Digital Designs for Physical Objects. https://www.thingiverse.com.
8. National Institutes of Health. NIH 3D Print Exchange: A Collection of Biomedical 3D Printable Files and 3D Printing Resources Supported by the National Institutes of Health (NIH). https://3dprint.nih.gov.
9. Gross, B. C.; Erkal, J. L.; Lockwood, S. Y.; et al. Evaluation of 3D Printing and Its Potential Impact on Biotechnology and the Chemical Sciences. *Anal. Chem.* **2014**, *86*, 3240–3253.
10. Baden, T.; Chagas, A. M.; Gage, G.; et al. Open Labware: 3-D Printing Your Own Lab Equipment. *PLoS Biol.* **2015**, *13*, e1002086.
11. Zhang, C.; Anzalone, N. C.; Faria, R. P.; et al. Open-Source 3D-Printable Optics Equipment. *PLoS ONE.* **2013**, *8*, e59840.
12. Da Veiga Beltrame, E.; Tyrwhitt-Drake, J.; Roy, I.; et al. 3D Printing of Biomolecular Models for Research and Pedagogy. *J. Vis. Exp. JoVE.* **2017**. http://dx.doi.org/10.3791/55427.
13. Baden, T. Biropette: Customisable, High Precision Pipette. BadenLab. https://www.thingiverse.com/thing:255519.
14. Symes, M. D.; Kitson, P. J.; Yan, J.; et al. Integrated 3D-Printed Reactionware for Chemical Synthesis and Analysis. *Nat. Chem.* **2012**, *4*, 349–354.
15. Trivedi, D. K.; Pearce, J. M. Open Source 3-D Printed Nutating Mixer. *Appl. Sci.* **2017**, *7*, 942.
16. Neumaier, J. M.; Madani, A.; Klein, T.; et al. Low-Budget 3D-Printed Equipment for Continuous Flow Reactions. *Beilstein J. Org. Chem.* **2019**, *15*, 558–566.

17. Capel, A. J.; Rimington, R. P.; Lewis, M. P.; et al. 3D Printing for Chemical, Pharmaceutical and Biological Applications. *Nat. Rev. Chem*. **2018**, *2*, 422.
18. Gross, B.; Lockwood, S. Y.; Spence, D. M. Recent Advances in Analytical Chemistry by 3D Printing. *Anal. Chem*. **2017**, *89*, 57–70.
19. He, Y.; Wu, Y.; Fu, J.; et al. Developments of 3D Printing Microfluidics and Applications in Chemistry and Biology: A Review. *Electroanalysis*. **2016**, *28*, 1658–1678.
20. Courtemanche, J.; King, S.; Bouck, D. Engineering Novel Lab Devices Using 3D Printing and Microcontrollers. *SLAS Technol. Transl. Life Sci. Innov*. **2018**, *23*, 448–455.
21. Arduino Foundation. Arduino—Home. https://www.arduino.cc.
22. Raspberry Pi Foundation. Raspberry Pi—Teach, Learn, and Make with Raspberry Pi. https://www.raspberrypi.org.
23. Besson, T.; Debayle, D.; Diochot, S.; et al. Low Cost Venom Extractor Based on Arduino® Board for Electrical Venom Extraction from Arthropods and Other Small Animals. *Toxicon*. **2016**, *118*, 156–161.
24. Chaturvedi, A.; Gorthi, S. S. Automated Blood Sample Preparation Unit (ABSPU) for Portable Microfluidic Flow Cytometry. *SLAS Technol. Transl. Life Sci. Innov*. **2017**, *22*, 73–80.
25. Gali, H. An Open-Source Automated Peptide Synthesizer Based on Arduino and Python. *SLAS Technol. Transl. Life Sci. Innov*. **2017**, *22*, 493–499.
26. Ali, A. S.; Zanzinger, Z.; Debose, D.; et al. Open Source Building Science Sensors (OSBSS): A Low-Cost Arduino-Based Platform for Long-Term Indoor Environmental Data Collection. *Build. Environ*. **2016**, *100*, 114–126.
27. Bitting, A. L.; Bordelon, H.; Baglia, M. L.; et al. Automated Device for Asynchronous Extraction of RNA, DNA, or Protein Biomarkers from Surrogate Patient Samples. *J. Lab. Autom*. **2016**, *21*, 732–742.
28. Maurer, A.; Bowden, G.; Cotton, J.; et al. Acetuino—A Handy Open-Source Radiochemistry Module for the Preparation of [1-^{11}C]Acetate. *SLAS Technol. Transl. Life Sci. Innov*. **2018**, 247263031881234.
29. Huzly, D. Stellungnahme Zur Richtlinie DKD-R 8-1. 2015.
30. Physikalisch-Technische Bundesanstalt. Richtlinie DKD-R 8-1. Kalibrierung von Kolbenhubpipetten Mit Luftpolster. 2011.
31. Kong, F.; Yuan, L.; Zheng, Y. F.; et al. Automatic Liquid Handling for Life Science: A Critical Review of the Current State of the Art. *J. Lab. Autom*. **2012**, *17*, 169–185.
32. Andrew Alliance. Pipetting Tools and Software for the Scientific Lab. https://www.andrewalliance.com.
33. Opentrons. Open-Source Pipetting Robots for Biologists. https://opentrons.com.
34. Langer, K.; Jonsson, H. Draft: Robotic Automation of Production and the Recovery of Cell Spheroids. *bioRxiv*. **2019**, 552687.
35. Sanderson, T.; Rayner, J. C. PlasmoTron: An Open-Source Platform for Automated Culture of Malaria Parasites. *bioRxiv*. **2018**, 241596.
36. Gome, G.; Waksberg, J.; Grishko, A.; et al. OpenLH: Open Liquid-Handling System for Creative Experimentation with Biology. In *Proceedings of the Thirteenth International Conference on Tangible, Embedded, and Embodied Interaction*; TEI '19. ACM: New York, 2019; pp. 55–64.
37. Gerber, L. C.; Calasanz-Kaiser, A.; Hyman, L.; et al. Liquid-Handling Lego Robots and Experiments for STEM Education and Research. *PLoS Biol*. **2017**, *15*, e2001413.
38. The FreeCAD Team. FreeCAD: Your Own 3D Parametric Modeler. https://www.freecadweb.org.
39. Cura, U. Advanced 3D Printing Software, Made Accessible. https://www.ultimaker.com/en/products/ultimaker-cura-software.
40. Badea, L. StepperDriver: Arduino Library for A4988, DRV8825, DRV8834, DRV8880 and Generic Two-Pin (DIR/STEP) Stepper Motor Drivers. https://github.com/laurb9/StepperDriver.
41. International Organization for Standardization. ISO 8655-2:2002: Piston-Operated Volumetric Apparatus—Part 2: Piston Pipettes. http://www.iso.org/cms/render/live/en/sites/isoorg/contents/data/standard/02/97/29727.html.
42. Bigg, P. H. Density of Water in SI Units over the Range 0–40 C. *Br. J. Appl. Phys*. **1967**, *18*, 521–525.
43. Vicik, R.; Busemann, M.; Gelhaus, C.; et al. Aziridide-Based Inhibitors of Cathepsin L: Synthesis, Inhibition Activity, and Docking Studies. *ChemMedChem*. **2006**, *1*, 1126–1141.
44. Ettari, R.; Nizi, E.; Di Francesco, M. E.; et al. Development of Peptidomimetics with a Vinyl Sulfone Warhead as Irreversible Falcipain-2 Inhibitors. *J. Med. Chem*. **2008**, *51*, 988–996.
45. Schmohl, L.; Bierlmeier, J.; von Kügelgen, N.; et al. Identification of Sortase Substrates by Specificity Profiling. *Bioorg. Med. Chem*. **2017**, *25*, 5002–5007.
46. Schwartz, M. *Internet of Things with ESP8266*. Packt Publishing Ltd: Birmingham, UK, 2016.
47. Bhadoria, S.; Ramos, R. O. *Raspberry Pi 3 Home Automation Projects: Bringing Your Home to Life Using Raspberry Pi 3, Arduino, and ESP8266*; Packt Publishing Ltd: Birmingham, UK, 2017.
48. Semac, I.; Horak, G.; Jordan, A.; et al. *Pipetting Performances by Means of the Andrew Robot*. Andrew Alliance: Geneva, 2013; p. 20.
49. Lochner, K. H.; Ballweg, T.; Fahrenkrog, H.-H. Untersuchungen Zur Meßgenauigkeit von Kolbenhubpipetten Mit Luftpolster. *Lab. J. Lab. Med*. **2009**, *20*, 430–441.
50. Joyce, D. N.; Tyler, J. P. Accuracy, Precision and Temperature Dependence of Disposable Tip Pipettes. *Med. Lab. Technol*. **1973**, *30*, 331–334.
51. Hanada, K.; Tamai, M.; Yamagishi, M.; et al. Isolation and Characterization of E–64, a New Thiol Protease Inhibitor. *Agric. Biol. Chem*. **1978**, *42*, 523–528.
52. Schaschke, N.; Assfalg-Machleidt, I.; Machleidt, W.; et al. E-64 Analogues as Inhibitors of Cathepsin B: On the Role of the Absolute Configuration of the Epoxysuccinyl Group. *Bioorg. Med. Chem*. **1997**, *5*, 1789–1797.
53. Inaba, T.; Hirayama, Y.; Fujinaga, N. Inhibition of Cathepsin B1 by E-64, a Thiol Proteinase Inhibitor, and Its Derivatives. *Agric. Biol. Chem*. **1979**, *43*, 655–656.

"

5.3 BANΔIT: B’-factor Analysis for Drug Design and Structural Biology

5.3.1 Context, Project Summary, and own Contribution

Crystal structure analysis is the gold standard for structure-based inhibitor development. In addition to the static 3D coordinates, a crystallographic dataset also contains the often-neglected data on the dynamics of the elucidated structures, known as the B-factors, giving information on the atomistic mobility in the biomolecule.[316] However, B-factors between two different crystallographic sets cannot be directly compared because the resolution and refinement methods used lead to a non-linear distortion of the native B-factors; instead, normalization (calculation of B'-factors) is necessary which allows the subtractive analysis of two crystallographic sets to determine the rigidization hotspot upon ligand-binding.[317]

The idea to develop a toolkit for the analysis of B’-factor profiles arose during the analysis of the intrinsic flexibility of different SrtA crystal structures, as ligands and substrate binding led to the rigidization of the protein and these interactions should be quantified and exploited for the design of SrtA inhibitors (see chapter 3). Even though B-factor normalization has been repeatedly described as a widely accepted method for the analysis of protein-ligand interactions and corresponding applications have already been collected in reviews or contributed to drug design in the pharmaceutical industry, there was no publicly available toolkit that reads in crystal structures and outputs B’-factors.[318,319] Therefore, an open-source HTML/JavaScript-based toolkit (BANΔIT) was developed which allows the calculation of B'-factors, structural alignment, and graphical inspection of the results in a dynamic website environment. Since all calculations are completed on the client-side of the web toolkit, a processed crystallographic dataset never leaves the user's computer which satisfies the confidentiality of recently solved crystal structures.

Retrospective application examples from the fields of rational drug design showed that BANΔIT is suitable to support orthogonal biophysical investigations if a crystal structure of the protein of interest has been solved. To confirm the usability and the scope of usage, we have given exemplary conclusions for drug optimization including the development of a B’-factor-supported pharmacophore model for SARS-CoV2 main protease inhibitors from the recently solved XChem fragment screening campaign.[50]

Own contributions: Programming of the web toolkit, Execution of example applications & Writing of the manuscript.

Contributions from other authors: Conceptualization of the project.

This work has been published in: Molecular Informatics (impact factor: 3.35).

5.3.2 Publication

The following publication quoted (within "") from page 283 to page 288 is exactly the same as the manuscript cited on page 282:"

Application Note www.molinf.com molecular informatics

DOI: 10.1002/minf.202000144

BANΔIT: B′-Factor Analysis for Drug Design and Structural Biology

Fabian Barthels,[a] Tanja Schirmeister,[a] and Christian Kersten*[a]

Abstract: The analysis of B-factor profiles from X-ray protein structures can be utilized for structure-based drug design since protein mobility changes have been associated with the quality of protein-ligand interactions. With the BANΔIT (B′-factor analysis and ΔB′ interpretation toolkit), we have developed a JavaScript-based browser application that provides a graphical user interface for the normalization and analysis of B′-factor profiles. To emphasize the usability for rational drug design applications, we have analyzed a selection of crystallographic protein-ligand complexes and have given exemplary conclusions for further drug optimization including the development of a B′-factor-supported pharmacophore model for SARS CoV-2 main protease inhibitors. BANΔIT is available online at https://bandit.uni-mainz.de. The source code can be downloaded from https://github.com/FBarthels/BANDIT.

Keywords: B-factor · Protein flexibility · Molecular modeling · Drug design · Bioinformatics

The inherent mobility of proteins is a long-standing challenge in drug design, but a summary of recent examples showed that the understanding of structural-dynamic processes can be exploited for rational drug design.[1] Analysis of protein crystal structures is a routine tool for ligand studies. In structure-based drug design, focus has been put into understanding of the molecular interactions from the 3D-coordinates, but X-ray crystal structures naturally also include atomic displacement factors, known as the B-, Debye-Waller- or temperature factors, which give atomic resolution information on the mobility in the structure.[2] However, the distribution of raw B-factors is irregular comparing different crystallographic sets, because these are highly influenced by the resolution, crystal packing and the quality of the refinement methods used.[3] Due to these circumstances, it is necessary to normalize B-factors before they can be compared between different protein structures. The normalized B-factor (B′-factor) is a statistic expression of the raw experimental B-factor for which different calculation methods have been developed.[4–6]

B′-factor analysis was previously used to analyze the distribution of active site vs. non-active site residues,[7] to investigate the flexibility at protein-DNA interfaces,[8] to differentiate between protein binding sites and crystal-packing contacts,[9] to estimate protein-ligand binding affinities,[10] and many other applications summarized in reviews.[11] Recently, this methodology has also been explored for rational drug design because changes in B′-factors indicate an enhancement or weakening of molecular interactions on an atomic resolution level.[12–14] The binding of reversible ligands to their targets usually leads to a rigidification of the protein scaffold and manifests itself in a reduction of the B′-factor which was found to be in approximate correlation to the binding strength of the ligand.[15]

The BANΔIT toolkit (https://bandit.uni-mainz.de) enables facile B′-factor analysis for users from medicinal and biological chemistry fields by accessing the graphical user interface through a web browser. For offline usage, the underlying source code can be downloaded from https://github.com/FBarthels/BANDIT. The open-source program package was realized in a client-side dynamic website environment with HTML/JavaScript and is distributed under LGPL license. Even if the program is accessed via the web appearance, the client-side content is generated on the user's local computer. By this, the submitted crystallographic data never leaves the user's computer, an important implication that underlies the fact many solved crystal structures are confidential. Besides data security, this approach is robust, offers excellent cross-platform usability and the client-side rendering takes less than a second. The BANΔIT implementation includes the following modules:

(i) Creating a B-factor record set from a PDB-file: The parse pdb library was developed to create a JavaScript *recordSet*, which is used for handling of either local PDB-files or fetching from the rcsb.org repository. The respective

[a] *F. Barthels, T. Schirmeister, C. Kersten*
Institute for Pharmaceutical and Biomedical Sciences, Johannes Gutenberg-Universität Mainz, Staudingerweg 5, 55128 Mainz, Germany
(+49)6131-39-25714
E-mail: kerstec@uni-mainz.de

Application Note www.molinf.com molecular informatics

fileData is transferred to a *parseBuffer*, parsed by the library and finally accessible through a *pdbObject*.

Crystallographic B-factors are a quantity with atomic resolution, i.e. there is an individual B-factor for each heavy atom of a structure. However, the most common approach to study protein mobility is the residue-wise analysis of B′-factors as the flexibility index. The choice of which B-factors should represent a single residue is guided by the respective application. Thus, the *tempFactors* (B-factors) specified by the ATOM-records can be selectively extracted from a *recordSet*. The comparison of C_α B′-factor profiles is the gold standard in the characterization of backbone mobility that results from protein dynamics, but the normalization of an averaged value over all backbone heavy atoms (N, C_α, C, O) has also been reported in representative studies.[16] For the analysis of side-chain mobility, all heavy atoms of the structure were considered for B-factor normalization.[12,17]

The choice of the input atoms has further implications: Amino acid side chains might be present in alternate locations. By default, the most frequent location is considered for a residue, but it is also possible to determine an averaged B′-factor using the occupancy π of all alternate locations *l* (eq. 1).

$$B'(i) \quad \sum \pi(l) B'(i,l) \tag{1}$$

(ii) Normalization of B-factors: B-factor normalization is the transformation of experimental B-factors so that the resulting distribution is defined in terms of the expected value and the variance, which allows the comparison of B′-factors for different datasets in a way that eliminates gross influences. The normalization procedure is carried out by the process pdb library and the normalized data are transferred to a *tempSet*, i.e. a *recordSet* of B′-factors per residue.

The first literature-described algorithm for B-factor normalization was proposed by Karplus and Schulz and related the experimental B-factor of a residue *i* to the arithmetic mean of all B-factors in a structure (eq. 2).[4]

$$B'(i) \quad \frac{B(i) + D}{\left[\frac{1}{N}\sum_{i\ 1}^{N} B(i)\right] + D} \tag{2}$$

The value of *D* for a given structure was iterated in such a way that the root mean square deviation of the resulting B′-values was equal to 0.3 (eq. 3). This algorithm was previously found to be useful to correlate mobility to different amino acids,[4,18] however, in recent times it was largely replaced by other methods.

$$0.3 \quad \sqrt{\frac{1}{N}\sum_{i\ 1}^{N} (B' \quad B'(i))^2} \tag{3}$$

A more recent normalization method for B-factors is the z-transformation that relates the arithmetic mean to the standard deviation (eq. 4). B′-factors normalized with this method show zero mean and unit variance.[5]

$$B'(i) \quad \frac{B(i) \quad \frac{1}{N}\sum_{i\ 1}^{N} B(i)}{\sqrt{\frac{1}{N\ 1}\sum_{i\ 1}^{N} (B \quad B(i))^2}} \tag{4}$$

However, both estimators used in the standard z-score, the sample mean and the standard deviation, can be disturbed by even a single outlier value. Smith *et al.* found that experimental B-factors follow not a normal distribution, but a Gumbel distribution.[6] They developed an approach for the identification of outliers by the median absolute deviation (*MAD*) as a robust measure for the variability of experimental B-factors around the median *B* (eq. 5). Following the recommendation of Iglewicz and Hoaglin, a modified z-score cut-off value of $M(i) > 3.5$ was chosen to label B-factor outliers (eq. 6).[19]

$$MAD \quad median\left[\sqrt{(B(i) \quad B)^2}\right] \tag{5}$$

$$M(i) \quad \frac{0.674 \quad (B(i) \quad B)}{MAD} \tag{6}$$

With raw B-factors filtered for outliers, a standard z-score with the arithmetic mean B_{noout} and the standard deviation σ_{noout} can be calculated (eq. 7).

$$B'(i) \quad \frac{B(i) \quad B_{noout}}{\sigma_{noout}} \tag{7}$$

IBM developed a particularly robust modified z-transformation algorithm (MAD_E method) which completely relies on the median *B* for calculating the z-score.[20] Depending on the value of the *MAD*, modified z-scores were calculated in one of two ways (eq. 8). Although this approach has found its way into the B-factor literature only rarely,[13] it might be advantageous because it is the least influenced by outliers.

$$B'(i) \quad \begin{cases} \frac{B(i) \quad B}{\frac{1.235}{N}\sum_{i=1}^{N} \left(B(i) \quad B\right)^2}, & MAD \quad 0 \\ \\ \frac{B(i) \quad B}{1.486 \cdot MAD} & MAD / 0 \end{cases} \tag{8}$$

(iii) Post-processing of B′-factors: B′-factors in a *tempSet* can optionally be post-processed with various analytical methods. Representative examples have been included: E.g. residue-wise determination of RMSF-values from MD simulations are often weighted proportionally to the atomic masses of the included atoms. A similar approach has been proposed for the prediction of B-factors from RMSF-values.[21] The atoms *a* of a residue *i* can therefore optionally

Application Note www.molinf.com molecular informatics

be weighted to their molecular weight *M(a)* (eq. 9). For ordinary residues the difference might be small (C 12 u–S 32 u), but for selenomethionines (Se 79 u) and high-resolution X-ray structures which enable the positioning of hydrogen atoms (H 1 u) significant deviations are known[22,23]

$$B'(i,a) \quad \frac{1}{M(i)}\sum M(a)B'(i,a) \tag{9}$$

If a B′-factor profile resolution greater than a single residue is desired, the fluctuating atomic resolution of B′-factors was found to be a hindrance, e.g. if B′-factors are used for the characterization of secondary structure motives. Since abrupt changes in flexibility within a closed backbone sequence are physically not to be expected, a smoothing method for B′-factors was implemented.[24] Smoothed B'_{sm}-factors can be calculated by a moving average with a variable residue window size *n* (eq. 10).

$$B'_{sm}(i) \quad \frac{1}{n}\sum_{k\ 0}^{n\ 1} B'(i \quad k) \tag{10}$$

(iv) Alignment of structures: B-factors are primarily normalized to be compared between different data sets. It is possible to calculate the difference $\Delta B' \quad B'_{complex} \quad B'_{apo}$ only if two corresponding B′-factors exist, thus, incompletely resolved atomic records must be excluded by the process pdb library. To derive structural-biologically relevant statements ΔB′-values have to be finally checked for their significance in the ΔB′-population ($p < 0.05$).[12,25]

To perform a comparative analysis, an alignment between the target data sets may be necessary. Based on the optimization algorithm proposed by Needleman and Wunsch a common sequence-based alignment was implemented for standard use on nearly identical proteins.[27] Furthermore, based on the MMLigner package,[28] which allows structural alignments built on Bayesian and information-theoretic principles, the possibility was implemented to align structurally conserved but sequentially different proteins. Since the MMLigner program has been developed in C++, the complementary JavaScript code was ported with the LLMV-JS compiler Emscriptem.[29]

However, the MMLigner algorithm is computationally quite demanding, hence, an accelerated B′-factor-based dynamic programming procedure for a three-dimensional fuzzy alignment was developed. A method of Blankenbecler *et al.* was adapted that matched residues by comparing structural categories by an optimization algorithm (eq. 11).[30]

$$F(i,j) \quad max\begin{cases} F(i \quad 1,j \quad 1) + w(x_i,y_i) \\ F(i \quad 1,j) + f \\ F(i,j \quad 1) + f \end{cases} \tag{11}$$

Based on the B′-factors, a scoring function $w(x_i,y_i)$ was developed which assigns each residue to a category (A–G) according to its absolute B′-factor value ($F > 2.8 > D > 1.4 > B > 0.6 > A > \quad 0.6 > C > \quad 1.4 > E > \quad 2.8 > G$). Scores were calculated based on the similarity of the B′-factor categories (e.g. $w(A,A) \quad 3$, $w(A,B) \quad 2$, $w(A,E) \quad 1$, $w(A,F) \quad 0$). Gaps were penalized relatively high (f 3) to ensure correct alignment in domains with varying mobility.

(v) Visualization of the results: The graphical presentation of the calculated B′-factors was realized in the HTML and JavaScript environment for display in a web browser. The free-for-academic charting API canvasJS (https://canvasjs.com/) was used for data presentation and interactive B-factor profile analysis. The NGL WebGL-based molecular viewer was implemented for the interactive display of protein structures.[26] Furthermore, the data can also be exported in pdb- or csv-format for external processing. A screen dump of the toolkit's user interface and usage instructions are shown in Figure 1. For interaction hotspot analysis of B′-factor profiles across multiple structures these can be visualized in a heatmap format with the open-source charting API ApexCharts (https://apexcharts.com/).

To demonstrate the scope of BANΔIT, we have briefly analyzed a selection of literature examples that have investigated the dynamic processes of protein-ligand binding by conventional techniques like nuclear magnet resonance spectroscopy (NMR) and molecular dynamic (MD) simulations. With our toolkit, we aimed to reproduce the statements regarding dynamics and flexibility by a retrospective analysis of corresponding crystallographic B-factors which have not yet received any attention. To demonstrate the applicability for relevant prospective studies, we have also developed a B′-factor-supported pharmacophore model for SARS CoV-2 main protease inhibitors based on a recently solved crystallographic fragment screening dataset.

Example 1 Tyrosine phosphatase 1E PDZ domain: Dhulesia *et al.* described the changes in dynamic processes that occur in the second PDZ domain of the human tyrosine phosphatase 1E (PTP1E) upon binding of the small peptide RA-GEF2 by protein NMR and MD simulations.[31] The selective inhibition of PDZ-mediated protein-protein interactions was considered to be an approach for drug development in cancers that are based on abnormal activities in the underlying pathways.[32] The rational design of inhibitors of protein-protein interactions is still considered difficult because of the inherent protein flexibility.[33,34] We see a special potential in our toolkit supporting rational drug design in this context.

Application Note www.molinf.com molecular informatics

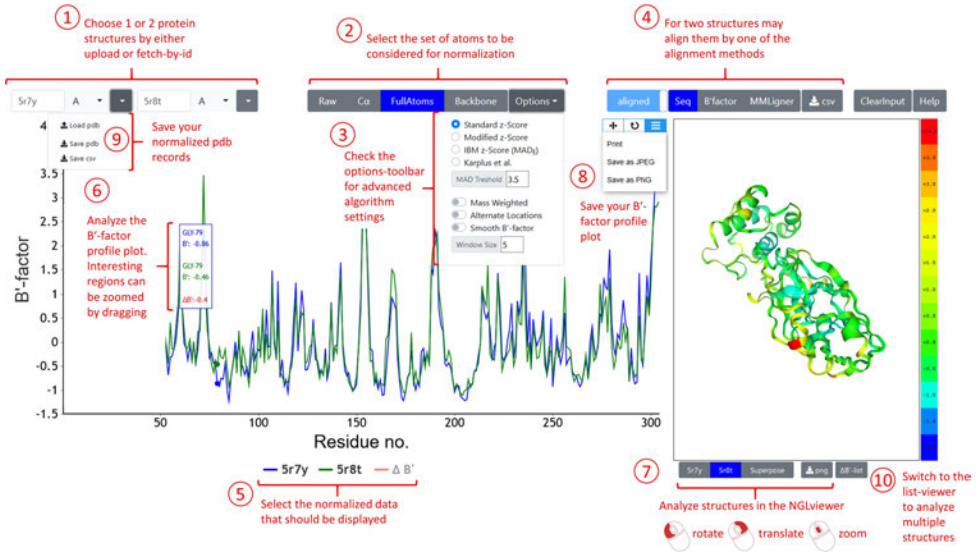

Figure 1. User interface of the BANΔIT with numbered instruction steps for pairwise analysis of B′-factor profiles. (1) Choose 1 or 2 protein structures by either upload or fetch-by-id. (2) Select the set of atoms to be considered for normalization. (3) Check the options-toolbar for advanced algorithm settings. (4) For two structures may align them by one of the alignment methods. (5) Select the normalized data that should be displayed. (6) Analyze the B′-factor profile plot. Interesting regions can be zoomed by dragging. (7) Analyze the 3D-models colored by their B′-factors in the NGLviewer.[26] (8) Save the B′-factor profile plot. (9) Save the normalized PDB-records. (10) Switch to the list-viewer interface for multiple structure alignment and heatmap visualization

The B′-factor analysis of the PTP1E crystal structures in the absence or presence of the RA-GEF2 ligand perfectly reflects the same results of the NMR-order parameter restrained MD calculations.[35] The β2/β3-loop (T28–G34) and a distal surface region (L66–E76) are significantly rigidified once the RA-GEF2 ligand binds (Figure 2A).

In the ribbon model with a coloring relative to the C_α B′-factor of a residue (B-factor putty) the key mediators of rigidification (S29, R31, K72 and Q93) can be visualized (Figure 2B). This information might be useful to determine which residues should be kept flexible in an induced-fit docking protocol.[36] In cases where residues are characterized by high B′-factors, several conformations will probably exist in solution. A mechanistic model for ligand binding was developed from the rigidified residues: K72, which protrudes into the binding pocket in the apo-structure, is displaced by the ligand and rigidified via backbone interactions. S29 interacts with the ligand via the side-chain hydroxyl group and thus stabilizes the entire β2/β3-loop, resulting in a reorientation of R31 ultimately interacting with the distal Q93 (Figure 2C).

Example 2 Src kinase SH2 domain: In extensive NMR and MD studies of Src kinase ligand complexes, it was found that a comparison of natural and conformationally constrained ligands leads to NMR chemical shift deviations across the binding site. MD simulations supported these findings and the investigators concluded that the observed enthalpic penalty is a result of increased flexibility in the binding site.[37] By B′-factor analysis we could confirm these results and showed that there is a significant dynamic increase in the βD′-sheet (K60–L64, Figure 2D&E). Inspection of the ligand poses revealed this is a consequence of the poor cation-π interaction of K60 with the constrained ligand (Figure 2F&G). By this example, we showed B′-factor analysis can be helpful to understand thermodynamic ligand binding issues. Based on the results, it might be advisable to place the conformational constrain at a different position in the ligand.

Example 3 SARS CoV-2 main protease: At the Diamond Light Source of the UK national synchrotron facility a high throughput crystallographic fragment screening was performed (yet unpublished[38]), which solved 44 covalent and 22 non-covalent fragment complexes of the SARS CoV-2 main protease (Mpro). Since a drug to treat COVID-19 is desperately needed in 2020,[39] our toolkit was used to develop a B′-factor-supported pharmacophore model of the 22 non-covalent fragment complexes in the active site binding pocket.

While it can be easily seen from the crystal structures that in the center of the active site pocket (S2- and S3-site) an overlap of aromatic core structures dominates, superposition of all fragment poses leads to a diverse pattern of interactions with distal residues of the substrate-binding site.[38] Common practice would be to examine the set of

Application Note www.molinf.com molecular informatics

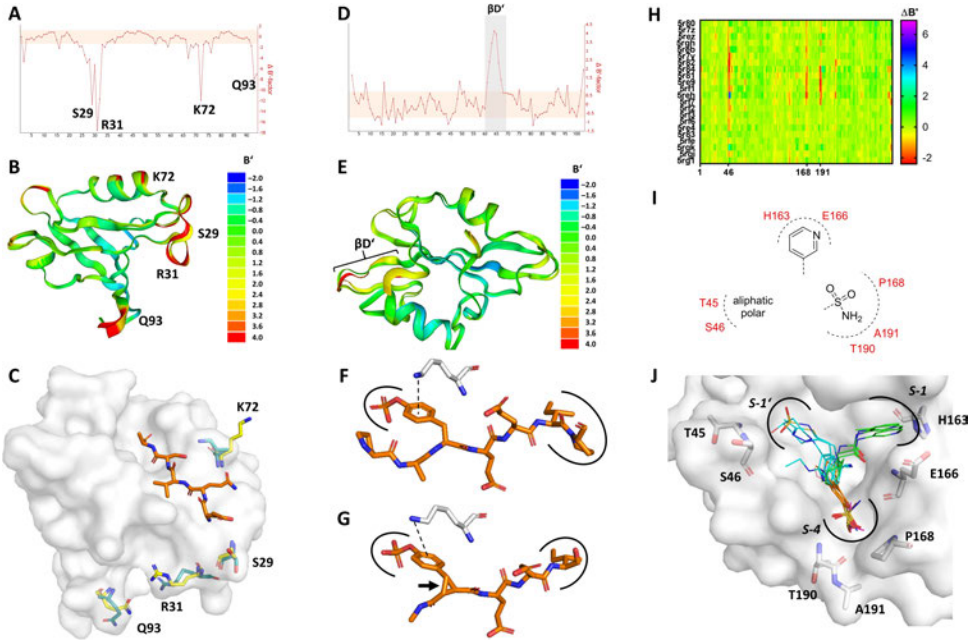

Figure 2. Presentation of the B′-factor analysis from representative drug design examples. (**A**) Plot of ΔB′ for PTP1E apo-structure (PDB: 3LNX) *vs.* PTP1E in complex with the RA-GEF ligand (PDB: 3LNY). ΔB′-values outside the salmon-colored horizontal box are statistically significant ($p < 0.05$). (**B**) Superposed crystal structures for PTP1E with and without the RA-GEF ligand colored by the B′-factors. (**C**) Representation of the most rigidified residues in the RA-GEF2 PTP1E complex. *Turquoise*: PTP1E apo-structure; *Yellow*: PTP1E holo-structure; *Orange*: RA-GEF2 peptide ligand. (**D**) Plot of ΔB′ for the Src kinase in complex with the conformationally constrained ligand (PDB: 1IS0) *vs.* Src in complex with the natural ligand (PDB: 1SPS). (**E**) Superposed crystal structures for the respective Src complexes with both ligands colored by the B′-factors. (**F**) The natural phosphopeptide ligand reveals a favourable cation-π interaction with K60. (**G**) The cyclopropyl constraint (*arrow*) leads to a suboptimal cation-π interaction, which induces increased mobility in the neighboring residues (K60–L64). (**H**) B′-factor analysis of SARS CoV-2 main protease in complex with multiple fragments. Clustering of 22 non-covalent complexes *vs.* the non-liganded apo-structure (PDB: 5R8T). (**I**) Development of a B′-factor-based pharmacophore hypothesis. (**J**) Superposition of selected crystal structures from a crystallographic fragment screening to the SARS CoV-2 main protease. In the center, aromatic structural elements are predominant. Sulfonamides interact with T190, A191 and P168 (PDB: 5R80, 5R81, 5RF1; Carbons colored in orange). DMSO molecules were also found in this S-4 pocket (PDB: 5REH, 5R82, 5RE9; Carbons colored in magenta). Various polar fragments interact with T45, S46 (PDB: 5REB, 5R7Y, 5R82, 5RGH; Carbons colored in cyan). Pyridine containing ligands show interactions with H163 and E166 (PDB: 5RE4, 5R83, 5R84; Carbons colored in green).

fragments for a superposition of structural features,[40] but this does not allow quantification of the interaction quality. Therefore, we have chosen a different approach and calculated ΔB′-factor profiles of all non-covalent fragment complexes versus the apo-structure. Hotspots of mobility changes due to specific ligand features were clustered and presented in a heat map (Figure 2H).

In total, three hotspots for ligand-induced protein rigidification were identified. We found that sulfonamides strongly stabilize the backbone atoms of T190, A191 and the side chain atoms of P168 in the S4-pocket. For some crystal structures where this pocket is not occupied by a ligand, analogously a DMSO molecule is located in this pocket, which has also a rigidifying effect. In general, the binding of sulfoxides and sulfonamides to this pocket seems to be preferred. Secondly, T45 and S46 at the edge of the S1′-pocket are also strongly rigidified by ligands that encompass various polar-decorated structural elements. However, a clear structural trend was not identified. Primarily aliphatic scaffolds with polar decoration such as 4-hydroxypiperidines, N-ethylmethanesulfonamides, 2-ethylamino pyridines or 2-methylthiadiazoles should be considered. A single complex (PDB: 5REH) showed significantly increased mobility of S46. However, since this ligand has no contact with S46 and a large part of the ligand is solvent-exposed, we believe that this is an artifact without relevance for ligand binding.

In contrast, the S1-pocket (H163, E166) was often occupied by heteroaromatic structural features such as pyridines. However, no significant change in the ΔB′ of the surrounding residues was observed. This can be explained by the fact that a water network is perturbated when

Application Note www.molinf.com molecular informatics

ligands bind into this pocket.[41] A prospective analysis of this putative entropically dominated binding by water displacement is outside the scope of B′-factor analysis. From the combined results a B′-factor-supported pharmacophore model was developed, which might be complementary to upcoming conventional fragment clustering, linking and merging efforts (Figure 2I&J).[42]

In conclusion, we demonstrated the BANΔIT can be used for rational drug design applications. It provides an additional tool based on a measure that is already existing in crystal structures. Especially in the combination with NMR- and MD-experiments, pioneering results in drug design can be expected in the future.

Conflict of Interest

None declared.

Acknowledgements

This work has been supported by the Johannes Gutenberg-Universität Mainz. Open access funding enabled and organized by Projekt DEAL.

References

[1] S. J. Teague, *Nat. Rev. Drug Discovery* **2003**, *2*, 527–541.
[2] K. N. Trueblood, H.-B. Bürgi, H. Burzlaff, J. D. Dunitz, C. M. Gramaccioli, H. H. Schulz, U. Shmueli, S. C. Abrahams, *Acta Crystallogr. Sect. A* **1996**, *52*, 770–781.
[3] D. E. Tronrud, *J. Appl. Crystallogr.* **1996**, *29*, 100–104.
[4] P. A. Karplus, G. E. Schulz, *Sci. Nat. (Heidelberg)* **1985**, *72*, 212–213.
[5] O. Carugo, P. Argos, *Protein Eng. Des. Sel.* **1997**, *10*, 777–787.
[6] D. K. Smith, P. Radivojac, Z. Obradovic, A. K. Dunker, G. Zhu, *Protein Sci.* **2003**, *12*, 1060–1072.
[7] Z. Yuan, J. Zhao, Z.-X. Wang, *Protein Eng. Des. Sel.* **2003**, *16*, 109–114.
[8] B. Schneider, J.-C. Gelly, A. G. de Brevern, J. Černý, *Acta Crystallogr. Sect. D* **2014**, *70*, 2413–2419.
[9] Q. Liu, Z. Li, J. Li, *BMC Bioinf.* **2014**, *15*, 3–14.
[10] Q. Liu, C. K. Kwoh, J. Li, *J. Chem. Inf. Model.* **2013**, *53*, 3076–3085.
[11] Z. Sun, Q. Liu, G. Qu, Y. Feng, M. T. Reetz, *Chem. Rev.* **2019**, *119*, 1626–1665.
[12] T. W. Johnson, R. A. Gallego, A. Brooun, D. Gehlhaar, M. McTigue, *ACS Med. Chem. Lett.* **2018**, *9*, 878–883.
[13] X. Li, M. Anderson, D. Collin, I. Muegge, J. Wan, D. Brennan, S. Kugler, D. Terenzio, C. Kennedy, S. Lin, M. E. Labadia, B. Cook, R. Hughes, N. A. Farrow, *J. Biol. Chem.* **2017**, *292*, 11618–11630.
[14] G. J. P. van Westen, J. K. Wegner, A. Bender, A. P. IJzerman, H. W. T. van Vlijmen, *Protein Sci.* **2010**, *19*, 742–752.
[15] T. T. Waldron, K. P. Murphy, *Biochemistry* **2003**, *42*, 5058–5064.
[16] G. M. Clore, C. D. Schwieters, *J. Mol. Biol.* **2006**, *355*, 879–886.
[17] S. C. Lovell, J. M. Word, J. S. Richardson, D. C. Richardson, *Proc. Mont. Acad. Sci.* **1999**, *96*, 400–405.
[18] M. Vihinen, E. Torkkila, P. Riikonen, *Proteins Struct. Funct. Bioinf.* **1994**, *19*, 141–149.
[19] B. Iglewicz, D. C. Hoaglin, *How to Detect and Handle Outliers*, Asq Press, Milwaukee, WI, **1993**.
[20] L. S. Meyers, G. C. Gamst, A. J. Guarino, *Performing Data Analysis Using IBM SPSS*, John Wiley & Sons, Hoboken, NJ, **2013**.
[21] T. L. Rodgers, D. Burnell, P. D. Townsend, E. Pohl, M. J. Cann, M. R. Wilson, T. C. McLeish, *BMC Bioinf.* **2013**, *14*, 183.
[22] J. Błaszczyk, *Biochem. Anal. Biochem.* **2014**, *3*, 1–9.
[23] L. Tong, T. C. Warren, J. King, R. Betageri, J. Rose, S. Jakes, *J. Mol. Biol.* **1996**, *256*, 601–610.
[24] S. Parthasarathy, M. R. Murthy, *Protein Sci.* **1997**, *6*, 2561–2567.
[25] A. Sigliocolo, R. Gerace, S. Pascarella, *Biophys. Chem.* **2010**, *153*, 104–114.
[26] A. S. Rose, A. R. Bradley, Y. Valasatava, J. M. Duarte, A. Prlić, P. W. Rose, *Bioinformatics* **2018**, *34*, 3755–3758.
[27] S. B. Needleman, C. D. Wunsch, *J. Mol. Biol.* **1970**, *48*, 443–453.
[28] J. H. Collier, L. Allison, A. M. Lesk, P. J. Stuckey, M. Garcia de la Banda, A. S. Konagurthu, *Bioinformatics* **2017**, *33*, 1005–1013.
[29] C. Jiang, X. Jin, *J. Chem. Inf. Model.* **2017**, *57*, 2407–2412.
[30] R. Blankenbecler, M. Ohlsson, C. Peterson, M. Ringnér, *Proc. Mont. Acad. Sci.* **2003**, *100*, 11936–11940.
[31] A. Dhulesia, J. Gsponer, M. Vendruscolo, *J. Am. Chem. Soc.* **2008**, *130*, 8931–8939.
[32] N. X. Wang, H.-J. Lee, J. Zheng, *Drug News Perspect.* **2008**, *21*, 137–141.
[33] H. Jubb, T. L. Blundell, D. B. Ascher, *Prog. Biophys. Mol. Biol.* **2015**, *119*, 2–9.
[34] X. Ran, J. E. Gestwicki, *Curr. Opin. Chem. Biol.* **2018**, *44*, 75–86.
[35] J. Zhang, P. J. Sapienza, H. Ke, A. Chang, S. R. Hengel, H. Wang, G. N. Phillips, A. L. Lee, *Biochemistry* **2010**, *49*, 9280–9291.
[36] H. A. Carlson, J. A. McCammon, *Mol. Pharmacol.* **2000**, *57*, 213–218.
[37] J. M. Ward, N. M. Gorenstein, J. Tian, S. F. Martin, C. B. Post, *J. Am. Chem. Soc.* **2010**, *132*, 11058–11070.
[38] Diamond Light Source, "XChem @ Diamond," can be found under https://fragalysis.diamond.ac.uk/viewer/react/projects/2/3, **2020**.
[39] M. Phadke, S. Saunik, *Drug. Dev. Res.* **2020**, in press.
[40] D. Patel, J. D. Bauman, E. Arnold, *Prog. Biophys. Mol. Biol.* **2014**, *116*, 92–100.
[41] A. Paasche, A. Zipper, S. Schäfer, J. Ziebuhr, T. Schirmeister, B. Engels, *Biochemistry* **2014**, *53*, 5930–5946.
[42] R. L. M. van Montfort, P. Workman, B. Lamoree, R. E. Hubbard, *Essays Biochem.* **2017**, *61*, 453–464.

Received: June 10, 2020
Accepted: August 21, 2020
Published online on September 6, 2020

6 Outlook

This doctoral research on covalent cysteine protease inhibitors fits neatly into the current publication landscape of medicinal chemistry. The initial approval of the cysteine protease inhibitor nirmatrelvir in 2021, as well as several other clinically advanced inhibitors such as odanacatib, belnacasan, and petesicatib, give hope that the coming years will usher in the regulatory era of cysteine protease inhibitors.[105,107,109,110] The use of electrophilic warheads beyond the so-far tested nitrile and carbonyl-based electrophiles could make a decisive contribution mitigating the currently limiting toxicity problems associated with long-term administration of the drugs.[102,103]

In addition to the development of potent, selective, and pharmacokinetically advantageous inhibitors, the selection of an appropriate cysteine protease target is critical to the success of the drug discovery campaign. During the studies of this dissertation, it has become apparent that *S. aureus* SrtA is an extremely challenging target for the development of potent yet selective inhibitors due to the reverse protonation and its striking intrinsic flexibility.[192] Using state-of-the-art drug design methodologies, several SrtA inhibitors with potency in the low micromolar range were developed which also showed promising results as in vitro lead structures.[7,320] However, cell experiments indicated that inhibition of *S. aureus* SrtA is not a ubiquitous strategy to avoid virulence parameters such as bacterial biofilm formation, as propagated in the previous literature. Some strains such as *S. aureus* USA300 already harbor intrinsic resistance to inhibition of their SrtA, making the designation of SrtA as a low-resistance target obsolete.[321] Here, it has been shown that the *S. aureus* SrtA is an excellent model system for exploring the mechanism of novel covalent inhibitors, however, the chances of developing a clinically effective anti-bacterial agent must be considered rather low.

In contrast, the covalent-reversible *T. brucei* rhodesain inhibitors studied during this dissertation have been shown to provide potencies in the (sub)nanomolar range and to have advantageous selectivity properties over related human cysteine proteases. In the course of other works in this field, α-fluorovinyl sulfones have shown to be warheads with excellent metabolic and biodistribution properties.[322] Upcoming studies will mainly focus on the pharmacokinetic optimization of the predominantly peptidomimetic drugs since rhodesain inhibitors have to cross the blood-brain barrier to access their site of action. The "on-target" benzyl ester prodrug concept characterized during this dissertation might provide a contribution to this.[5,6] However, whether the most potent rhodesain inhibitors are suitable for clinical investigation will remain to be proven by studies in mammals and advanced disease model systems.

7 Bibliography

(1) Levene The Cleavage Products of Proteoses *J. Biol. Chem.* **1905**, *1* (1), 45–58
(2) Beynon & Bond *Proteolytic Enzymes: A Practical Approach*; Oxford University Press Oxford, 2001; Vol 2
(3) Goettig Reversed Proteolysis—Proteases as Peptide Ligases *Catalysts* **2021**, *11* (1), 33
(4) Stauffer & Zeffren Concerning the Mechanism of Ester Hydrolysis by Proteases *J. Biol. Chem.* **1970**, *245* (13), 3282–3284
(5) Klein et al New Cysteine Protease Inhibitors: Electrophilic (Het)Arenes and Unexpected Prodrug Identification for the Trypanosoma Protease Rhodesain *Molecules* **2020**, *25* (6), 1451
(6) Klein et al Naphthoquinones as Covalent Reversible Inhibitors of Cysteine Proteases—Studies on Inhibition Mechanism and Kinetics *Molecules* **2020**, *25* (9), 2064
(7) Barthels et al Asymmetric Disulfanylbenzamides as Irreversible and Selective Inhibitors of Staphylococcus Aureus Sortase A *ChemMedChem* **2020**, *15* (10), 839–850
(8) Bustamante et al Mechanisms of Cellular Proteostasis: Insights from Single-Molecule Approaches *Annu. Rev. Biophys.* **2014**, *43* (1), 119–140
(9) Neurath & Walsh Role of Proteolytic Enzymes in Biological Regulation (a Review) *Proc. Natl. Acad. Sci.* **1976**, *73* (11), 3825–3832
(10) Seife Blunting Nature's Swiss Army Knife *Science* **1997**, *277* (5332), 1602–1603
(11) Ehrmann & Clausen Proteolysis as a Regulatory Mechanism *Annu. Rev. Genet.* **2004**, *38* (1), 709–724
(12) Sauer et al Sculpting the Proteome with AAA+ Proteases and Disassembly Machines *Cell* **2004**, *119* (1), 9–18
(13) Siegel Caspases at the Crossroads of Immune-Cell Life and Death *Nat. Rev. Immunol.* **2006**, *6* (4), 308–317
(14) López-Otín & Overall Protease Degradomics: A New Challenge for Proteomics *Nat. Rev. Mol. Cell Biol.* **2002**, *3* (7), 509–519
(15) Page-McCaw et al Matrix Metalloproteinases and the Regulation of Tissue Remodelling *Nat. Rev. Mol. Cell Biol.* **2007**, *8* (3), 221–233
(16) Ciechanover Proteolysis: From the Lysosome to Ubiquitin and the Proteasome *Nat. Rev. Mol. Cell Biol.* **2005**, *6* (1), 79–87
(17) Mariño et al Human Autophagins, a Family of Cysteine Proteinases Potentially Implicated in Cell Degradation by Autophagy *J. Biol. Chem.* **2003**, *278* (6), 3671–3678
(18) Puente et al Human and Mouse Proteases: A Comparative Genomic Approach *Nat. Rev. Genet.* **2003**, *4* (7), 544–558
(19) Davie & Neurath Identification Of A Peptide Released During Autocatalytic Activation Of Trypsinogen *J. Biol. Chem.* **1955**, *212* (2), 515–529
(20) Davie & Ratnoff Waterfall Sequence for Intrinsic Blood Clotting *Science* **1964**, *145* (3638), 1310–1312
(21) Suzuki et al Calcium-Activated Neutral Protease and Its Endogenous Inhibitor Activation at the Cell Membrane and Biological Function *FEBS Lett.* **1987**, *220* (2), 271–277
(22) Kamphuis et al Structure of Papain Refined at 1 65 Å Resolution *J. Mol. Biol.* **1984**, *179* (2), 233–256
(23) Glickman & Ciechanover The Ubiquitin-Proteasome Proteolytic Pathway: Destruction for the Sake of Construction *Physiol. Rev.* **2002**, *82* (2), 373–428
(24) Schomburg & Schomburg Enzyme Databases In *Data Mining Techniques for the Life Sciences*; Carugo, O , Eisenhaber, F , Eds ; Methods in Molecular Biology; Humana Press: Totowa, NJ, 2010; pp 113–128
(25) Rawlings et al MEROPS: The Database of Proteolytic Enzymes, Their Substrates and Inhibitors *Nucleic Acids Res.* **2014**, *42* (D1), D503–D509
(26) Rawlings & Barrett Evolutionary Families of Peptidases *Biochem. J.* **1993**, *290* (1), 205–218
(27) Rawlings et al Asparagine Peptide Lyases: A Seventh Catalytic Type Of Proteolytic Enzymes *J. Biol. Chem.* **2011**, *286* (44), 38321–38328
(28) Madala et al Update 1 of: Proteases Universally Recognize Beta Strands In Their Active Sites *Chem. Rev.* **2010**, *110* (6), PR1–PR31
(29) Fairlie et al Conformational Selection of Inhibitors and Substrates by Proteolytic Enzymes: Implications for Drug Design and Polypeptide Processing *J. Med. Chem.* **2000**, *43* (7), 1271–1281
(30) Berger & Schechter On the Size of Active Site in Proteases I Papain *Biochem Biophys Res Commun* **1967**, *27*, 157–162
(31) Turk Targeting Proteases: Successes, Failures and Future Prospects *Nat. Rev. Drug Discov.* **2006**, *5* (9), 785–799
(32) Barrett et al *Handbook of Proteolytic Enzymes, Volume 1*; Elsevier, 2012; Vol 1
(33) Drag & Salvesen Emerging Principles in Protease-Based Drug Discovery *Nat. Rev. Drug Discov.* **2010**, *9* (9), 690–701
(34) Polgár Catalytic Mechanisms of Cysteine Peptidases In *Handbook of Proteolytic Enzymes*; Elsevier, 2013; pp 1773–1784
(35) Schirmeister & Welker Erfolgreiches Konzept: Proteasen Als Zielstrukturen Für Antiinfektiva Neue Angriffspunkte In Der Infektionstherapie *Pharm. Unserer Zeit* **2009**, *38* (6)
(36) Qiu et al Identification of the Putative Staphylococcal AgrB Catalytic Residues Involving the Proteolytic Cleavage of AgrD to Generate Autoinducing Peptide *J. Biol. Chem.* **2005**, *280* (17), 16695–16704
(37) Choi et al The Autocatalytic Protease P29 Encoded by a Hypovirulence-Associated Virus of the Chestnut Blight Fungus Resembles the Potyvirus-Encoded Protease HC-Pro *Virology* **1991**, *183* (2), 747–752
(38) Marr et al Expression of the Rubella Virus Nonstructural Protein ORF and Demonstration of Proteolytic Processing *Virology* **1994**, *198* (2), 586–592
(39) Laskar et al Modeling and Structural Analysis of PA Clan Serine Proteases *BMC Res. Notes* **2012**, *5*, 256
(40) Buller & Townsend Intrinsic Evolutionary Constraints on Protease Structure, Enzyme Acylation, and the Identity of the Catalytic Triad *Proc. Natl. Acad. Sci. U. S. A.* **2013**, *110* (8), E653-661
(41) Elsässer & Goettig Mechanisms of Proteolytic Enzymes and Their Inhibition in QM/MM Studies *Int. J. Mol. Sci.* **2021**, *22* (6), 3232
(42) Wilson et al Structure and Mechanism of Interleukin-Lβ Converting Enzyme *Nature* **1994**, *370* (6487), 270–275
(43) McGrath et al Crystallographic Structure at 1 6-Å Resolution of the Human Adenovirus Proteinase in a Covalent Complex with Its 11-Amino-Acid Peptide Cofactor: Insights on a New Fold *Biochim. Biophys. Acta BBA* **2003**, *1648* (1), 1–11
(44) Odagaki et al The Crystal Structure of Pyroglutamyl Peptidase I from Bacillus Amyloliquefaciens Reveals a New Structure for a Cysteine Protease *Structure* **1999**, *7* (4), 399–411
(45) Suree et al The Structure of the Staphylococcus Aureus Sortase-Substrate Complex Reveals How the Universally Conserved LPXTG Sorting Signal Is Recognized *J. Biol. Chem.* **2009**, *284* (36), 24465–24477
(46) Lorenz et al Structure of the Catalytic Domain of the Hepatitis C Virus NS2-3 Protease *Nature* **2006**, *442* (7104), 831–835
(47) Shin et al Structural and Functional Insights into Alphavirus Polyprotein Processing and Pathogenesis *Proc. Natl. Acad. Sci.* **2012**, *109* (41), 16534–16539
(48) Kim et al Enterococcus Faecium Secreted Antigen A Generates Muropeptides to Enhance Host Immunity and Limit Bacterial Pathogenesis *eLife* **2019**, *8*, e45343
(49) Suh et al Crystal Structure of DeSI-1, a Novel DeSUMOylase Belonging to a Putative Isopeptidase Superfamily *Proteins* **2012**, *80* (8), 2099–2104
(50) Douangamath et al Crystallographic and Electrophilic Fragment Screening of the SARS-CoV-2 Main Protease *Nat. Commun.* **2020**, *11* (1), 5047
(51) Kneller et al Unusual Zwitterionic Catalytic Site of SARS–CoV-2 Main Protease Revealed by Neutron Crystallography *J. Biol. Chem.* **2020**, *295* (50), 17365–17373
(52) Stennicke & Salvesen Catalytic Properties of the Caspases *Cell Death Differ.* **1999**, *6* (11), 1054–1059
(53) Ton-That et al Anchoring of Surface Proteins to the Cell Wall of Staphylococcus Aureus *J. Biol. Chem.* **2002**, *277* (9), 7447–7452
(54) Sárkány et al Thiolate-Imidazolium Ion Pair Is Not an Obligatory Catalytic Entity of Cysteine Peptidases: The Active Site of Picornain 3C *Biochemistry* **2001**, *40* (35), 10601–10606
(55) Chou et al Quaternary Structure of the Severe Acute Respiratory Syndrome (SARS) Coronavirus Main Protease *Biochemistry* **2004**, *43* (47), 14958–14970
(56) Paasche et al Evidence for Substrate Binding-Induced Zwitterion Formation in the Catalytic Cys-His Dyad of the SARS-CoV Main Protease *Biochemistry* **2014**, *53* (37), 5930–5946
(57) Shrestha & Wereszczynski Discerning the Catalytic Mechanism of Staphylococcus Aureus Sortase A with QM/MM Free Energy Calculations *J. Mol. Graph. Model.* **2016**, *67*, 33–43
(58) Tian & Eriksson Catalytic Mechanism and Roles of Arg197 and Thr183 in the Staphylococcus Aureus Sortase A Enzyme *J. Phys. Chem. B* **2011**, *115* (44), 13003–13011

(59) Świderek & Moliner Revealing the Molecular Mechanisms of Proteolysis of SARS-CoV-2 Mpro by QM/MM Computational Methods *Chem. Sci.* **2020**, *11* (39), 10626–10630
(60) Fernandes et al New Insights into the Catalytic Mechanism of the SARS-CoV-2 Main Protease: An ONIOM QM/MM Approach *Mol. Divers.* **2021**, 1–9
(61) Diamond Methods for Mapping Protease Specificity *Curr. Opin. Chem. Biol.* **2007**, *11* (1), 46–51
(62) Biedermann *Biedermann's Centralblatt Für Agrikulturchemie Und Rationellen Landwirtschaftsbetrieb*; Akademische Verlagsgesellschaft, 1879; Vol 8
(63) Drenth et al Structure of Papain *Nature* **1968**, *218* (5145), 929–932
(64) Vernet et al Structural and Functional Roles of Asparagine 175 in the Cysteine Protease Papain *J. Biol. Chem.* **1995**, *270* (28), 16645–16652
(65) Lewis et al Potentiometric Determination of Ionizations at the Active Site of Papain *Biochemistry* **1976**, *15* (23), 5009–5017
(66) Lewis et al Effect of Cysteine-25 on the Ionization of Histidine-159 in Papain as Determined by Proton Nuclear Magnetic Resonance Spectroscopy Evidence for a Histidine-159-Cysteine-25 Ion Pair and Its Possible Role in Catalysis *Biochemistry* **1981**, *20* (1), 48–51
(67) Migliorini & Creighton Active-Site Ionizations of Papain *Eur. J. Biochem.* **1986**, *156* (1), 189–192
(68) Mladenovic et al On the Origin of the Stabilization of the Zwitterionic Resting State of Cysteine Proteases: A Theoretical Study *J. Am. Chem. Soc.* **2008**, *130* (27), 8696–8705
(69) Chaiken & Smith Reaction of the Sulfhydryl Group of Papain with Chloroacetic Acid *J. Biol. Chem.* **1969**, *244* (19), 5095–5099
(70) Arad et al A Simulation of the Sulfur Attack in Catalytic Pathway of Papain Using Molecular Mechanics and Semiempirical Quantum Mechanics *J. Am. Chem. Soc.* **1990**, *112* (2), 491–502
(71) Harrison et al Catalytic Mechanism of the Enzyme Papain: Predictions with a Hybrid Quantum Mechanical/Molecular Mechanical Potential *J. Am. Chem. Soc.* **1997**, *119* (50), 12285–12291
(72) Angelides & Fink Cryoenzymology of Papain: Reaction Mechanism with an Ester Substrate *Biochemistry* **1978**, *17* (13), 2659–2668
(73) Lowe & Yuthavong Kinetic Specificity in Papain-Catalysed Hydrolyses *Biochem. J.* **1971**, *124* (1), 107–115
(74) Fekete & Komáromi Modeling the Archetype Cysteine Protease Reaction Using Dispersion Corrected Density Functional Methods in ONIOM-Type Hybrid QM/MM Calculations; the Proteolytic Reaction of Papain *Phys. Chem. Chem. Phys.* **2016**, *18* (48), 32847–32861
(75) Ma et al Molecular Dynamics Simulations of the Catalytic Pathway of a Cysteine Protease: A Combined QM/MM Study of Human Cathepsin K *J. Am. Chem. Soc.* **2007**, *129* (44), 13633–13645
(76) Han et al QM/MM Study of the Active Site of Free Papain and of the NMA-Papain Complex *J. Biomol. Struct. Dyn.* **1999**, *16* (5), 1019–1032
(77) Wei et al Reaction Pathway and Free Energy Profile for Papain-Catalyzed Hydrolysis of N-Acetyl-Phe-Gly 4-Nitroanilide *Biochemistry* **2013**, *52* (30), 5145–5154
(78) Polgár & Bender The Nature Of General Base-General Acid Catalysis In Serine Proteases *Proc. Natl. Acad. Sci. U. S. A.* **1969**, *64* (4), 1335–1342
(79) Sulpizi et al Reaction Mechanism of Caspases: Insights from QM/MM Car–Parrinello Simulations *Proteins* **2003**, *52* (2), 212–224
(80) Elsässer et al Distinct Roles of Catalytic Cysteine and Histidine in the Protease and Ligase Mechanisms of Human Legumain As Revealed by DFT-Based QM/MM Simulations *ACS Catal.* **2017**, *7* (9), 5585–5593
(81) Abbenante & Fairlie Protease Inhibitors in the Clinic *Med. Chem.* **2005**, *1* (1), 71–104
(82) Leeson et al Target-Based Evaluation of "Drug-Like" Properties and Ligand Efficiencies *J. Med. Chem.* **2021**, *64* (11), 7210–7230
(83) Fujio et al Method of Treating Diseases Associated with Plasmin Activity US2939817 (A), June 7, 1960
(84) Alkjaersig et al ε-Aminocaproic Acid: An Inhibitor of Plasminogen Activation *J. Biol. Chem.* **1959**, *234* (4), 832–837
(85) Brockway & Castellino The Mechanism of the Inhibition of Plasmin Activity by ε-Aminocaproic Acid *J. Biol. Chem.* **1971**, *246* (14), 4641–4647
(86) Wu et al The Refined Structure of the Epsilon-Aminocaproic Acid Complex of Human Plasminogen Kringle 4 *Biochemistry* **1991**, *30* (43), 10589–10594
(87) Anderson The Process of Structure-Based Drug Design *Chem. Biol.* **2003**, *10* (9), 787–797
(88) Lenci & Trabocchi Peptidomimetic Toolbox for Drug Discovery *Chem. Soc. Rev.* **2020**, *49* (11), 3262–3277
(89) Vagner et al Peptidomimetics, a Synthetic Tool of Drug Discovery *Curr. Opin. Chem. Biol.* **2008**, *12* (3), 292–296
(90) Acharya et al ACE Revisited: A New Target for Structure-Based Drug Design *Nat. Rev. Drug Discov.* **2003**, *2* (11), 891–902
(91) Navia et al Three-Dimensional Structure of Aspartyl Protease from Human Immunodeficiency Virus HIV-1 *Nature* **1989**, *337* (6208), 615–620
(92) Ghosh et al Recent Progress in the Development of HIV-1 Protease Inhibitors for the Treatment of HIV/AIDS *J. Med. Chem.* **2016**, *59* (11), 5172–5208
(93) Manasanch & Orlowski Proteasome Inhibitors in Cancer Therapy *Nat. Rev. Clin. Oncol.* **2017**, *14* (7), 417–433
(94) Copeland et al Drug–Target Residence Time and Its Implications for Lead Optimization *Nat. Rev. Drug Discov.* **2006**, *5* (9), 730–739
(95) Sutanto et al Covalent Inhibitors: A Rational Approach to Drug Discovery *RSC Med. Chem.* **2020**, *11* (8), 876–884
(96) de Leuw & Stephan Protease Inhibitors for the Treatment of Hepatitis C Virus Infection *GMS Infect. Dis.* **2017**, *5*, Doc08
(97) Deacon A Review of Dipeptidyl Peptidase-4 Inhibitors Hot Topics from Randomized Controlled Trials *Diabetes Obes. Metab.* **2018**, *20 Suppl 1*, 34–46
(98) Khadse et al Advances in the Development of Novel Factor Xa Inhibitors: A Patent Review *Mini Rev. Med. Chem.* **2018**, *18* (16), 1332–1353
(99) Scott Sitagliptin: A Review in Type 2 Diabetes *Drugs* **2017**, *77* (2), 209–224
(100) Garnock-Jones Boceprevir *Drugs* **2012**, *72* (18), 2431–2456
(101) Otto & Schirmeister Cysteine Proteases and Their Inhibitors *Chem. Rev.* **1997**, *97* (1), 133–172
(102) Siklos et al Cysteine Proteases as Therapeutic Targets: Does Selectivity Matter? A Systematic Review of Calpain and Cathepsin Inhibitors *Acta Pharm. Sin. B* **2015**, *5* (6), 506–519
(103) Verma et al Cysteine Proteases: Modes of Activation and Future Prospects as Pharmacological Targets *Front. Pharmacol.* **2016**, *7*, 107
(104) Dai et al Cathepsin K: The Action in and Beyond Bone *Front. Cell Dev. Biol.* **2020**, *8*, 433
(105) Owen et al An Oral SARS-CoV-2 Mpro Inhibitor Clinical Candidate for the Treatment of COVID-19 *Science 374* (6575), 1586–1593
(106) Zhao et al Crystal Structure of SARS-CoV-2 Main Protease in Complex with Protease Inhibitor PF-07321332 *Protein Cell* **2021**, 1–5
(107) Gauthier et al The Discovery of Odanacatib (MK-0822), a Selective Inhibitor of Cathepsin K *Bioorg. Med. Chem. Lett.* **2008**, *18* (3), 923–928
(108) Doyle et al Discovery of Second Generation Reversible Covalent DPP1 Inhibitors Leading to an Oxazepane Amidoacetonitrile Based Clinical Candidate (AZD7986) *J. Med. Chem.* **2016**, *59* (20), 9457–9472
(109) Flores et al Pre-Symptomatic Caspase-1 Inhibitor Delays Cognitive Decline in a Mouse Model of Alzheimer Disease and Aging *Nat. Commun.* **2020**, *11* (1), 4571
(110) Theron et al Pharmacodynamic Monitoring of RO5459072, a Small Molecule Inhibitor of Cathepsin S *Front. Immunol.* **2017**, *8*, 806
(111) Linton et al First-in-Class Pan Caspase Inhibitor Developed for the Treatment of Liver Disease *J. Med. Chem.* **2005**, *48* (22), 6779–6782
(112) Brömme & Lecaille Cathepsin K Inhibitors for Osteoporosis and Potential Off-Target Effects *Expert Opin. Investig. Drugs* **2009**, *18* (5), 585–600
(113) Je et al Low Doses of the Novel Caspase-Inhibitor GS-9450 Leads to Lower Caspase-3 and -8 Expression on Peripheral CD4+ and CD8+ T-Cells *Apoptosis Int. J. Program. Cell Death* **2011**, *16* (9), 959–966
(114) Lonsdale & Ward Structure-Based Design of Targeted Covalent Inhibitors *Chem. Soc. Rev.* **2018**, *47* (11), 3816–3830
(115) Lonsdale et al Expanding the Armory: Predicting and Tuning Covalent Warhead Reactivity *J. Chem. Inf. Model.* **2017**, *57* (12), 3124–3137
(116) Schirmeister et al Quantum Chemical-Based Protocol for the Rational Design of Covalent Inhibitors *J. Am. Chem. Soc.* **2016**, *138* (27), 8332–8335
(117) Strelow A Perspective on the Kinetics of Covalent and Irreversible Inhibition *SLAS Discov.* **2017**, *22* (1), 3–20
(118) Mayr & Patz Scales of Nucleophilicity and Electrophilicity: A System for Ordering Polar Organic and Organometallic Reactions *Angew. Chem. Int. Ed. Engl.* **1994**, *33* (9), 938–957
(119) Lee & Grossmann Reversible Covalent Inhibition of a Protein Target *Angew. Chem. Int. Ed Engl.* **2012**, *51* (35), 8699–8700
(120) Bandyopadhyay & Gao Targeting Biomolecules with Reversible Covalent Chemistry *Curr. Opin. Chem. Biol.* **2016**, *34*, 110–116
(121) Gehringer & Laufer Emerging and Re-Emerging Warheads for Targeted Covalent Inhibitors: Applications in Medicinal Chemistry and Chemical Biology *J. Med. Chem.* **2019**, *62* (12), 5673–5724
(122) Statsyuk Let K-Ras Activate Its Own Inhibitor *Nat. Struct. Mol. Biol.* **2018**, *25* (6), 435–437
(123) Zhou et al Selective Inhibition of Cullin 3 Neddylation through Covalent Targeting DCN1 Protects Mice from Acetaminophen-Induced Liver Toxicity *Nat. Commun.* **2021**, *12* (1), 2621
(124) Parr et al Electrophilicity Index *J. Am. Chem. Soc.* **1999**, *121* (9), 1922–1924

(125) Lucius et al Kinetic Studies of Carbocation–Carbanion Combinations: Key to a General Concept of Polar Organic Reactivity *Angew. Chem. Int. Ed.* **2002**, *41* (1), 92–95
(126) LoPachin & Gavin Reactions of Electrophiles with Nucleophilic Thiolate Sites: Relevance to Pathophysiological Mechanisms and Remediation *Free Radic. Res.* **2016**, *50* (2), 195–205
(127) Mayer & Ofial Nucleophilicity of Glutathione: A Link to Michael Acceptor Reactivities *Angew. Chem. Int. Ed.* **2019**, *58* (49), 17704–17708
(128) Moon et al Reversible Covalent Inhibition of Papain by a Peptide Nitrile Carbon-13 NMR Evidence for a Thioimidate Ester Adduct *J. Am. Chem. Soc.* **1986**, *108* (6), 1350–1351
(129) Berteotti et al Predicting the Reactivity of Nitrile-Carrying Compounds with Cysteine: A Combined Computational and Experimental Study *ACS Med. Chem. Lett.* **2014**, *5* (5), 501–505
(130) Quesne et al Cysteine Protease Inhibition by Nitrile-Based Inhibitors: A Computational Study *Front. Chem.* **2013**, *1*, 39
(131) Ramos-Guzmán et al Computational Simulations on the Binding and Reactivity of a Nitrile Inhibitor of the SARS-CoV-2 Main Protease *Chem. Commun.* **2021**, *57* (72), 9096–9099
(132) Mihalovits et al The Role of Quantum Chemistry in Covalent Inhibitor Design *Int. J. Quantum Chem.* **2021**, *10.1002/qua.26768*
(133) Martin et al Characterising Covalent Warhead Reactivity *Bioorg. Med. Chem.* **2019**, *27* (10), 2066–2074
(134) Citarella & Micale Peptidyl Fluoromethyl Ketones and Their Applications in Medicinal Chemistry *Molecules* **2020**, *25* (17), 4031
(135) Mittl et al Structure of Recombinant Human CPP32 in Complex with the Tetrapeptide Acetyl-Asp-Val-Ala-Asp Fluoromethyl Ketone *J. Biol. Chem.* **1997**, *272* (10), 6539–6547
(136) Powers et al Irreversible Inhibitors of Serine, Cysteine, and Threonine Proteases *Chem. Rev.* **2002**, *102* (12), 4639–4750
(137) Finn et al The Pfam Protein Families Database: Towards a More Sustainable Future *Nucleic Acids Res.* **2016**, *44* (D1), D279–D285
(138) Dramsi et al Sorting Sortases: A Nomenclature Proposal for the Various Sortases of Gram-Positive Bacteria *Res. Microbiol.* **2005**, *156* (3), 289–297
(139) Mazmanian et al Staphylococcus Aureus Sortase, an Enzyme That Anchors Surface Proteins to the Cell Wall *Science* **1999**, *285* (5428), 760–763
(140) Ton-That et al Purification and Characterization of Sortase, the Transpeptidase That Cleaves Surface Proteins of Staphylococcus Aureus at the LPXTG Motif *Proc. Natl. Acad. Sci. U. S. A.* **1999**, *96* (22), 12424–12429
(141) Navarre & Schneewind Surface Proteins of Gram-Positive Bacteria and Mechanisms of Their Targeting to the Cell Wall Envelope *Microbiol. Mol. Biol. Rev.* **1999**, *63* (1), 174–229
(142) Comfort & Clubb A Comparative Genome Analysis Identifies Distinct Sorting Pathways in Gram-Positive Bacteria *Infect. Immun.* **2004**, *72* (5), 2710–2722
(143) Schneewind et al Sorting of Protein A to the Staphylococcal Cell Wall *Cell* **1992**, *70* (2), 267–281
(144) Perry et al Anchoring of Surface Proteins to the Cell Wall of Staphylococcus Aureus III Lipid II Is an in Vivo Peptidoglycan Substrate for Sortase-Catalyzed Surface Protein Anchoring *J. Biol. Chem.* **2002**, *277* (18), 16241–16248
(145) Bentley et al Mutagenesis Studies of Substrate Recognition and Catalysis in the Sortase A Transpeptidase from Staphylococcus Aureus *J. Biol. Chem.* **2008**, *283* (21), 14762–14771
(146) Ilangovan et al Structure of Sortase, the Transpeptidase That Anchors Proteins to the Cell Wall of Staphylococcus Aureus *Proc. Natl. Acad. Sci.* **2001**, *98* (11), 6056–6061
(147) Marraffini et al Anchoring of Surface Proteins to the Cell Wall of Staphylococcus Aureus A Conserved Arginine Residue Is Required for Efficient Catalysis of Sortase A *J. Biol. Chem.* **2004**, *279* (36), 37763–37770
(148) Frankel et al Staphylococcus Aureus Sortase Transpeptidase SrtA: Insight into the Kinetic Mechanism and Evidence for a Reverse Protonation Catalytic Mechanism *Biochemistry* **2005**, *44* (33), 11188–11200
(149) Huang et al Kinetic Mechanism of Staphylococcus Aureus Sortase SrtA *Biochemistry* **2003**, *42* (38), 11307–11315
(150) Clancy et al Sortase Transpeptidases: Insights into Mechanism, Substrate Specificity, and Inhibition *Pept. Sci.* **2010**, *94* (4), 385–396
(151) Connolly et al Sortase from Staphylococcus Aureus Does Not Contain a Thiolate-Imidazolium Ion Pair in Its Active Site *J. Biol. Chem.* **2003**, *278* (36), 34061–34065
(152) Weiner et al The Sortase A Enzyme That Attaches Proteins to the Cell Wall of Bacillus Anthracis Contains an Unusual Active Site Architecture *J. Biol. Chem.* **2010**, *285* (30), 23433–23443
(153) Mock Theory of Enzymatic Reverse-Protonation Catalysis *Bioorganic Chem.* **1992**, *20* (4), 377–381
(154) Ke et al Active Site Cysteine Is Protonated in the PAD4 Michaelis Complex: Evidence from Born-Oppenheimer Ab Initio QM/MM Molecular Dynamics Simulations *J. Phys. Chem. B* **2009**, *113* (38), 12750–12758
(155) Sims et al Reverse Protonation Is the Key to General Acid−Base Catalysis in Enolase *Biochemistry* **2003**, *42* (27), 8298–8306
(156) Zong et al Crystal Structures of Staphylococcus Aureus Sortase A and Its Substrate Complex *J. Biol. Chem.* **2004**, *279* (30), 31383–31389
(157) Jacobitz et al Sortase Transpeptidases: Structural Biology and Catalytic Mechanism In *Advances in Protein Chemistry and Structural Biology*; Elsevier, 2017; Vol 109, pp 223–264
(158) Chen et al 3D Structure Determination of an Unstable Transient Enzyme Intermediate by Paramagnetic NMR Spectroscopy *Angew. Chem. Int. Ed.* **2016**, *55* (44), 13744–13748
(159) Ruzin et al Further Evidence That a Cell Wall Precursor [C(55)-MurNAc-(Peptide)-GlcNAc] Serves as an Acceptor in a Sorting Reaction *J. Bacteriol.* **2002**, *184* (8), 2141–2147
(160) Li et al Irreversible Site-Specific Hydrazinolysis of Proteins by Use of Sortase *Angew. Chem. Int. Ed.* **2014**, *53* (8), 2198–2202
(161) Naik et al Staphylococcus Aureus Sortase A Transpeptidase Calcium Promotes Sorting Signal Binding By Altering The Mobility And Structure Of An Active Site Loop *J. Biol. Chem.* **2006**, *281* (3), 1817–1826
(162) Pang & Zhou Disorder-to-Order Transition of an Active-Site Loop Mediates the Allosteric Activation of Sortase A *Biophys. J.* **2015**, *109* (8), 1706–1715
(163) Ugur et al Ca2+ Binding Induced Sequential Allosteric Activation of Sortase A: An Example for Ion-Triggered Conformational Selection *PLOS ONE* **2018**, *13* (10), e0205057
(164) Wang et al Conversion of an Amide to a High-Energy Thioester by Staphylococcus Aureus Sortase A Is Powered by Variable Binding Affinity for Calcium *Sci. Rep.* **2018**, *8* (1), 16371
(165) Kappel et al The Binding Mechanism, Multiple Binding Modes, and Allosteric Regulation of Staphylococcus Aureus Sortase A Probed by Molecular Dynamics Simulations *Protein Sci.* **2012**, *21* (12), 1858–1871
(166) Kruger et al Analysis of the Substrate Specificity of the Staphylococcus Aureus Sortase Transpeptidase SrtA *Biochemistry* **2004**, *43* (6), 1541–1551
(167) Jacobitz et al Structural and Computational Studies of the Staphylococcus Aureus Sortase B-Substrate Complex Reveal a Substrate-Stabilized Oxyanion Hole *J. Biol. Chem.* **2014**, *289* (13), 8891–8902
(168) Chan et al Structure of the Bacillus Anthracis Sortase A Enzyme Bound to Its Sorting Signal: A Flexible Amino-Terminal Appendage Modulates Substrate Access *J. Biol. Chem.* **2015**, *290* (42), 25461–25474
(169) Zong et al The Structure of Sortase B, a Cysteine Transpeptidase That Tethers Surface Protein to the Staphylococcus Aureus Cell Wall *Structure* **2004**, *12* (1), 105–112
(170) Al-Mebairik et al A Review of Virulence Factors, Pathogenesis, and Antibiotic Resistance in Staphylococcus Aureus *Rev. Med. Microbiol.* **2016**, *27* (2), 50–56
(171) Lowy Staphylococcus Aureus Infections *N. Engl. J. Med.* **1998**, *339* (8), 520–532
(172) Noble et al Carriage of Staphylococcus Aureus in Random Samples of a Normal Population *J. Hyg. (Lond.)* **1967**, *65* (4), 567–573
(173) Casewell & Hill The Carrier State: Methicillin-Resistant Staphylococcus Aureus *J. Antimicrob. Chemother.* **1986**, *18* (Suppl A), 1–12
(174) Vercellotti et al Bacterial Adherence to Fibronectin and Endothelial Cells: A Possible Mechanism for Bacterial Tissue Tropism *J. Lab. Clin. Med.* **1984**, *103* (1), 34–43
(175) Schneewind & Missiakas Sortases, Surface Proteins, and Their Roles in Staphylococcus Aureus Disease and Vaccine Development *Protein Secret. Bact.* **2019**, *7* (1), 173–188
(176) Marrack & Kappler The Staphylococcal Enterotoxins and Their Relatives *Science* **1990**, *248* (4956), 705–711
(177) McCrae *Molecular Aspects of Host-Pathogen Interactions*; Cambridge University Press, 1997
(178) Koo et al Targeting Microbial Biofilms: Current and Prospective Therapeutic Strategies *Nat. Rev. Microbiol.* **2017**, *15* (12), 740–755
(179) Flemming et al Biofilms: An Emergent Form of Bacterial Life *Nat. Rev. Microbiol.* **2016**, *14* (9), 563–575

(180) Tsompanidou et al The Sortase A Substrates FnbpA, FnbpB, ClfA and ClfB Antagonize Colony Spreading of Staphylococcus Aureus *PLOS ONE* **2012**, *7* (9), e44646
(181) Ponnuraj et al A "Dock, Lock, and Latch" Structural Model for a Staphylococcal Adhesin Binding to Fibrinogen *Cell* **2003**, *115* (2), 217–228
(182) Falugi et al Role of Protein A in the Evasion of Host Adaptive Immune Responses by Staphylococcus Aureus *mBio* **2013**, *4* (5), e00575-13
(183) Wardenburg et al Surface Proteins and Exotoxins Are Required for the Pathogenesis of Staphylococcus Aureus Pneumonia *Infect. Immun.* **2007**, *75* (2), 1040–1044
(184) O´Brien et al Multiple Mechanisms for the Activation of Human Platelet Aggregation by Staphylococcus Aureus: Roles for the Clumping Factors ClfA and ClfB, the Serine–Aspartate Repeat Protein SdrE and Protein A *Mol. Microbiol.* **2002**, *44* (4), 1033–1044
(185) Pishchany et al IsdB-Dependent Hemoglobin Binding Is Required for Acquisition of Heme by Staphylococcus Aureus *J. Infect. Dis.* **2014**, *209* (11), 1764–1772
(186) Schaffer et al Immunization with Staphylococcus Aureus Clumping Factor B, a Major Determinant in Nasal Carriage, Reduces Nasal Colonization in a Murine Model *Infect. Immun.* **2006**, *74* (4), 2145–2153
(187) Wertheim et al Key Role for Clumping Factor B in Staphylococcus Aureus Nasal Colonization of Humans *PLOS Med.* **2008**, *5* (1), e17
(188) Weiss et al Effect of SrtA and SrtB Gene Expression on the Virulence of Staphylococcus Aureus in Animal Models of Infection *J. Antimicrob. Chemother.* **2004**, *53* (3), 480–486
(189) Mazmanian et al Staphylococcus Aureus Sortase Mutants Defective in the Display of Surface Proteins and in the Pathogenesis of Animal Infections *Proc. Natl. Acad. Sci.* **2000**, *97* (10), 5510–5515
(190) Dickey et al Different Drugs for Bad Bugs: Antivirulence Strategies in the Age of Antibiotic Resistance *Nat. Rev. Drug Discov.* **2017**, *16* (7), 457–471
(191) Maresso & Schneewind Sortase as a Target of Anti-Infective Therapy *Pharmacol. Rev.* **2008**, *60* (1), 128–141
(192) Cascioferro et al Sortase A Inhibitors: Recent Advances and Future Perspectives *J. Med. Chem.* **2015**, *58* (23), 9108–9123
(193) Zhang et al Antiinfective Therapy with a Small Molecule Inhibitor of Staphylococcus Aureus Sortase *Proc. Natl. Acad. Sci.* **2014**, *111* (37), 13517–13522
(194) Mu et al Isovitexin, a Potential Candidate Inhibitor of Sortase A of Staphylococcus Aureus USA300 *J Microbiol Biotechnol* **2018**, *28* (9), 1426–1432
(195) Yeo et al The FDA-Approved Anti-Cancer Drugs, Streptozotocin and Floxuridine, Reduce the Virulence of Staphylococcus Aureus *Sci. Rep.* **2018**, *8* (1), 2521
(196) Scott et al Irreversible Inhibition of the Bacterial Cysteine Protease-Transpeptidase Sortase (SrtA) by Substrate-Derived Affinity Labels *Biochem. J.* **2002**, *366* (3), 953–958
(197) Liew et al Localization and Mutagenesis of the Sorting Signal Binding Site on Sortase A from Staphylococcus Aureus *FEBS Lett.* **2004**, *571* (1–3), 221–226
(198) Ton-That & Schneewind IV Inhibitors of the Cell Wall Sorting Reaction *J. Biol. Chem.* **1999**, *274* (34), 24316–24320
(199) Chenna et al Synthesis and Structure Activity Relationship Studies of Novel Staphylococcus Aureus Sortase A Inhibitors *Eur. J. Med. Chem.* **2010**, *45* (9), 3752–3761
(200) Oniga et al New 2-Phenylthiazoles as Potential Sortase A Inhibitors: Synthesis, Biological Evaluation and Molecular Docking *Molecules* **2017**, *22* (11), 1827
(201) Parrino et al 1,2,4-Oxadiazole Topsentin Analogs as Staphylococcal Biofilm Inhibitors Targeting the Bacterial Transpeptidase Sortase A *Eur. J. Med. Chem.* **2021**, *209*, 112892
(202) Jaudzems et al Targeting Bacterial Sortase A with Covalent Inhibitors: 27 New Starting Points for Structure-Based Hit-to-Lead Optimization *ACS Infect. Dis.* **2020**, *6* (2), 186–194
(203) Zhulenkovs et al Discovery and Structure–Activity Relationship Studies of Irreversible Benzisothiazolinone-Based Inhibitors against Staphylococcus Aureus Sortase A Transpeptidase *Bioorg. Med. Chem.* **2014**, *22* (21), 5988–6003
(204) Chan et al Discovery of Staphylococcus Aureus Sortase A Inhibitors Using Virtual Screening and the Relaxed Complex Scheme *Chem. Biol. Drug Des.* **2013**, *82* (4), 418–428
(205) Wehrli et al Discovery and Development of Substituted Thiadiazoles as Inhibitors of Staphylococcus Aureus Sortase A *Bioorg. Med. Chem.* **2019**, *27* (19), 115043
(206) Yang et al Tideglusib and Its Analogues As Inhibitors of Staphylococcus Aureus SrtA *J. Med. Chem.* **2020**, *63* (15), 8442–8457
(207) Sapra et al Chemical Biology of Sortase A Inhibition: A Gateway to Anti-Infective Therapeutic Agents *J. Med. Chem.* **2021**, *64* (18), 13097–13130
(208) Mackey et al A Cathepsin B-like Protease Is Required for Host Protein Degradation in Trypanosoma Brucei *J. Biol. Chem.* **2004**, *279* (46), 48426–48433
(209) Kerr et al Crystal Structures of TbCatB and Rhodesain, Potential Chemotherapeutic Targets and Major Cysteine Proteases of Trypanosoma Brucei *PLoS Negl. Trop. Dis.* **2010**, *4* (6), e701
(210) Caffrey & Steverding Kinetoplastid Papain-like Cysteine Peptidases *Mol. Biochem. Parasitol.* **2009**, *167* (1), 12–19
(211) Langousis & Hill Motility and More: The Flagellum of Trypanosoma Brucei *Nat. Rev. Microbiol.* **2014**, *12* (7), 505–518
(212) Losos & Ikede Review of Pathology of Diseases in Domestic and Laboratory Animals Caused by Trypanosoma Congolense, T Vivax, T Brucei, T Rhodesiense and T Gambiense *Vet. Pathol.* **1972**, *9* (1), 1–79
(213) Ponte-Sucre An Overview of Trypanosoma Brucei Infections: An Intense Host-Parasite Interaction *Front. Microbiol.* **2016**, *7*, 2126
(214) Simarro et al Estimating and Mapping the Population at Risk of Sleeping Sickness *PLoS Negl. Trop. Dis.* **2012**, *6* (10), e1859
(215) Steverding et al Trypanosoma Brucei: Chemical Evidence That Cathepsin L Is Essential for Survival and a Relevant Drug Target *Int. J. Parasitol.* **2012**, *42* (5), 481–488
(216) Nikolskaia et al Blood-Brain Barrier Traversal by African Trypanosomes Requires Calcium Signaling Induced by Parasite Cysteine Protease *J. Clin. Invest.* **2006**, *116* (10), 2739–2747
(217) Kennedy Human African Trypanosomiasis of the CNS: Current Issues and Challenges *J. Clin. Invest.* **2004**, *113* (4), 496–504
(218) Bullard et al Haptoglobin-Hemoglobin Receptor Independent Killing of African Trypanosomes by Human Serum and Trypanosome Lytic Factors *Virulence* **2012**, *3* (1), 72–76
(219) Oli et al Serum Resistance-Associated Protein Blocks Lysosomal Targeting of Trypanosome Lytic Factor in Trypanosoma Brucei *Eukaryot. Cell* **2006**, *5* (1), 132–139
(220) Stephens & Hajduk Endosomal Localization of the Serum Resistance-Associated Protein in African Trypanosomes Confers Human Infectivity *Eukaryot. Cell* **2011**, *10* (8), 1023–1033
(221) Pays et al The VSG Expression Sites of Trypanosoma Brucei: Multipurpose Tools for the Adaptation of the Parasite to Mammalian Hosts *Mol. Biochem. Parasitol.* **2001**, *114* (1), 1–16
(222) McCulloch et al Emerging Challenges in Understanding Trypanosome Antigenic Variation *Emerg. Top. Life Sci.* **2017**, *1* (6), 585–592
(223) Triggs & Bangs Glycosylphosphatidylinositol-Dependent Protein Trafficking in Bloodstream Stage Trypanosoma Brucei *Eukaryot. Cell* **2003**, *2* (1), 76–83
(224) Steverding The Transferrin Receptor of Trypanosoma Brucei *Parasitol. Int.* **2000**, *48* (3), 191–198
(225) Grab et al Protease Activated Receptor Signaling Is Required for African Trypanosome Traversal of Human Brain Microvascular Endothelial Cells *PLoS Negl. Trop. Dis.* **2009**, *3* (7), e479
(226) Yadati et al The Ins and Outs of Cathepsins: Physiological Function and Role in Disease Management *Cells* **2020**, *9* (7), 1679
(227) Caffrey et al Active Site Mapping, Biochemical Properties and Subcellular Localization of Rhodesain, the Major Cysteine Protease of Trypanosoma Brucei Rhodesiense *Mol. Biochem. Parasitol.* **2001**, *118* (1), 61–73
(228) Stoka et al Lysosomal Cathepsins and Their Regulation in Aging and Neurodegeneration *Ageing Res. Rev.* **2016**, *32*, 22–37
(229) Johé et al Structure, Interdomain Dynamics, and PH-Dependent Autoactivation of pro-Rhodesain, the Main Lysosomal Cysteine Protease from African Trypanosomes *J. Biol. Chem.* **2021**, *296*, 100565
(230) Carmona et al Potency and Selectivity of the Cathepsin L Propeptide as an Inhibitor of Cysteine Proteases *Biochemistry* **1996**, *35* (25), 8149–8157
(231) Kerr et al Vinyl Sulfones as Antiparasitic Agents and a Structural Basis for Drug Design *J. Biol. Chem.* **2009**, *284* (38), 25697–25703
(232) Choe et al Substrate Profiling of Cysteine Proteases Using a Combinatorial Peptide Library Identifies Functionally Unique Specificities *J. Biol. Chem.* **2006**, *281* (18), 12824–12832
(233) Ettari et al Inhibition of Rhodesain as a Novel Therapeutic Modality for Human African Trypanosomiasis *J. Med. Chem.* **2013**, *56* (14), 5637–5658

(234) Arafet et al Computational Study of the Catalytic Mechanism of the Cruzain Cysteine Protease *ACS Catal.* **2017**, *7* (2), 1207–1215
(235) Arafet et al Computational Study of the Michaelis Complex Formation and the Effect on the Reaction Mechanism of Cruzain Cysteine Protease *ACS Omega* **2018**, *3* (12), 18613–18622
(236) Abdulla et al RNA Interference of Trypanosoma Brucei Cathepsin B and L Affects Disease Progression in a Mouse Model *PLoS Negl. Trop. Dis.* **2008**, *2* (9), e298
(237) Scory et al The Cysteine Proteinase Inhibitor Z-Phe-Ala-CHN2 Alters Cell Morphology and Cell Division Activity of Trypanosoma Brucei Bloodstream Forms in Vivo *Kinetoplastid Biol. Dis.* **2007**, *6*, 2
(238) Troeberg et al Cysteine Proteinase Inhibitors Kill Cultured Bloodstream Forms of Trypanosoma Brucei Brucei *Exp. Parasitol.* **1999**, *91* (4), 349–355
(239) Steverding et al Trypanosoma Brucei: Inhibition of Cathepsin L Is Sufficient to Kill Bloodstream Forms *Mol. Biochem. Parasitol.* **2020**, *235*, 111246
(240) Giroud et al Repurposing a Library of Human Cathepsin L Ligands: Identification of Macrocyclic Lactams as Potent Rhodesain and Trypanosoma Brucei Inhibitors *J. Med. Chem.* **2018**, *61* (8), 3350–3369
(241) Mott et al Identification and Optimization of Inhibitors of Trypanosomal Cysteine Proteases: Cruzain, Rhodesain, and TbCatB *J. Med. Chem.* **2010**, *53* (1), 52–60
(242) dos Santos Nascimento et al Cruzain and Rhodesain Inhibitors: Last Decade of Advances in Seeking for New Compounds Against American and African Trypanosomiases *Curr. Top. Med. Chem.* **2021**, *21* (21), 1871–1899
(243) Ettari et al The Inhibition of Cysteine Proteases Rhodesain and TbCatB: A Valuable Approach to Treat Human African Trypanosomiasis *Mini-Rev. Med. Chem.* **2010**, *16* (17), 1374–1391
(244) Nkemgu et al Improved Trypanocidal Activities of Cathepsin L Inhibitors *Int. J. Antimicrob. Agents* **2003**, *22* (2), 155–159
(245) Löser et al Interaction of Papain-like Cysteine Proteases with Dipeptide-Derived Nitriles *J. Med. Chem.* **2005**, *48* (24), 7688–7707
(246) Yang et al Design, Synthesis and Biological Evaluation of Potent Azadipeptide Nitrile Inhibitors and Activity-Based Probes as Promising Anti-Trypanosoma Brucei Agents *Chem. – Eur. J.* **2012**, *18* (21), 6528–6541
(247) Schirmeister et al Evaluation of Dipeptide Nitriles as Inhibitors of Rhodesain, a Major Cysteine Protease of Trypanosoma Brucei *Bioorg. Med. Chem. Lett.* **2017**, *27* (1), 45–50
(248) Ehmke et al Optimization of Triazine Nitriles as Rhodesain Inhibitors: Structure-Activity Relationships, Bioisosteric Imidazopyridine Nitriles, and X-Ray Crystal Structure Analysis with Human Cathepsin L *ChemMedChem* **2013**, *8* (6), 967–975
(249) Arafet et al Quantum Mechanics/Molecular Mechanics Studies of the Mechanism of Cysteine Proteases Inhibition by Dipeptidyl Nitroalkenes *Chem. – Eur. J.* **2020**, *26* (9), 2002–2012
(250) Dunny et al Vinyl Sulfone-Based Peptidomimetics as Anti-Trypanosomal Agents: Design, Synthesis, Biological and Computational Evaluation *J. Med. Chem.* **2013**, *56* (17), 6638–6650
(251) Bryant et al Novel Non-Peptidic Vinylsulfones Targeting the S2 and S3 Subsites of Parasite Cysteine Proteases *Bioorg. Med. Chem. Lett.* **2009**, *19* (21), 6218–6221
(252) Zhang et al Synthesis, Biological Evaluation and Molecular Docking of 2-Phenyl-Benzo[d]Oxazole-7-Carboxamide Derivatives as Potential Staphylococcus Aureus Sortase A Inhibitors *Bioorg. Med. Chem. Lett.* **2016**, *26* (16), 4081–4085
(253) Chen et al Synthesis of Macrocyclic Trypanosomal Cysteine Protease Inhibitors *Bioorg. Med. Chem. Lett.* **2008**, *18* (22), 5860–5863
(254) Ettari et al Development of Peptidomimetics with a Vinyl Sulfone Warhead as Irreversible Falcipain-2 Inhibitors *J. Med. Chem.* **2008**, *51* (4), 988–996
(255) Previti et al Development of Novel Peptide-Based Michael Acceptors Targeting Rhodesain and Falcipain-2 for the Treatment of Neglected Tropical Diseases (NTDs) *J. Med. Chem.* **2017**, *60* (16), 6911–6923
(256) Royo et al Dipeptidyl Enoates As Potent Rhodesain Inhibitors That Display a Dual Mode of Action *ChemMedChem* **2015**, *10* (9), 1484–1487
(257) Latorre et al Dipeptidyl Nitroalkenes as Potent Reversible Inhibitors of Cysteine Proteases Rhodesain and Cruzain *ACS Med. Chem. Lett.* **2016**, *7* (12), 1073–1076
(258) González et al Dipeptidyl-α,β-Epoxyesters as Potent Irreversible Inhibitors of the Cysteine Proteases Cruzain and Rhodesain *Bioorg. Med. Chem. Lett.* **2007**, *17* (24), 6697–6700
(259) Ettari et al Development of Rhodesain Inhibitors with a 3-Bromoisoxazoline Warhead *ChemMedChem* **2013**, *8* (12), 2070–2076
(260) Ettari et al Development of Novel Dipeptide-like Rhodesain Inhibitors Containing the 3-Bromoisoxazoline Warhead in a Constrained Conformation *Bioorg. Med. Chem.* **2015**, *23* (21), 7053–7060
(261) Vicik et al Aziridine-2,3-Dicarboxylate Inhibitors Targeting the Major Cysteine Protease of Trypanosoma Brucei as Lead Trypanocidal Agents *Bioorg. Med. Chem. Lett.* **2006**, *16* (10), 2753–2757
(262) Fey et al New Aziridine-Based Inhibitors of Cathepsin L-like Cysteine Proteases with Selectivity for the Leishmania Cysteine Protease LmCPB2 8 *Eur. J. Med. Chem.* **2018**, *156*, 587–597
(263) Anderson *Makers: Das Internet der Dinge: die nächste industrielle Revolution*; Carl Hanser Verlag GmbH & Co KG, 2013
(264) Rundle *A Revolution in the Making*; Affirm Press, 2014
(265) GitHub: Where the world builds software https://github com/ (accessed 2021 -12 -12)
(266) Zenodo - Research Shared https://zenodo org/ (accessed 2021 -12 -12)
(267) Mendeley Data https://data mendeley com/ (accessed 2021 -12 -12)
(268) Courtemanche et al Engineering Novel Lab Devices Using 3D Printing and Microcontrollers *SLAS Technol.* **2018**, *23* (5), 448–455
(269) PubMed https://pubmed ncbi nlm nih gov/ (accessed 2021 -12 -12)
(270) HardwareX - Journal - Elsevier: An open access scientific hardware journal https://www journals elsevier com/journals elsevier com/hardwarex (accessed 2021 -12 -12)
(271) Raspberry Pi Foundation Raspberry Pi — Teach, Learn, and Make with Raspberry Pi https://www raspberrypi org (accessed 2019 -03 -03)
(272) Arduino foundation Arduino - Home https://www arduino cc/ (accessed 2019 -03 -03)
(273) Schwartz *Internet of Things with ESP8266*; Packt Publishing Ltd, 2016
(274) Jolles Broad-scale Applications of the Raspberry Pi: A Review and Guide for Biologists *Methods Ecol. Evol.* **2021**, *12* (9), 1562–1579
(275) Babiuch et al Using the ESP32 Microcontroller for Data Processing In *2019 20th International Carpathian Control Conference (ICCC)*; 2019; pp 1–6
(276) Cressey The DIY Electronics Transforming Research *Nature* **2017**, *544* (7648), 125–126
(277) Kondaveeti et al A Systematic Literature Review on Prototyping with Arduino: Applications, Challenges, Advantages, and Limitations *Comput. Sci. Rev.* **2021**, *40*, 100364
(278) Gross et al Evaluation of 3D Printing and Its Potential Impact on Biotechnology and the Chemical Sciences *Anal. Chem.* **2014**, *86* (7), 3240–3253
(279) Symes et al Integrated 3D-Printed Reactionware for Chemical Synthesis and Analysis *Nat. Chem.* **2012**, *4* (5), 349–354
(280) Almquist & Smalley Thermal Stereolithography US5569349A, October 29, 1996
(281) Childers & Hull Method of Making a Three-Dimensional Object by Stereolithography US5609812A, March 11, 1997
(282) Hull Method for Production of Three-Dimensional Objects by Stereolithography US5762856A, June 9, 1998
(283) Smalley et al Simultaneous Multiple Layer Curing in Stereolithography US5597520A, January 28, 1997
(284) Gross et al Recent Advances in Analytical Chemistry by 3D Printing *Anal. Chem.* **2017**, *89* (1), 57–70
(285) Baden et al Open Labware: 3-D Printing Your Own Lab Equipment *PLOS Biol.* **2015**, *13* (3), e1002086
(286) Capel et al 3D Printing for Chemical, Pharmaceutical and Biological Applications *Nat. Rev. Chem.* **2018**, *2* (12), 422
(287) Pearce Economic Savings for Scientific Free and Open Source Technology: A Review *HardwareX* **2020**, *8*, e00139
(288) Pearce *Open-Source Lab: How to Build Your Own Hardware and Reduce Research Costs*; Newnes, 2013
(289) Da Veiga Beltrame et al 3D Printing of Biomolecular Models for Research and Pedagogy *J. Vis. Exp. JoVE* **2017**, *121*, e55427
(290) Watson & Crick Molecular Structure of Nucleic Acids; a Structure for Deoxyribose Nucleic Acid *Nature* **1953**, *171* (4356), 737–738
(291) Corey & Pauling Molecular Models of Amino Acids, Peptides, and Proteins *Rev. Sci. Instrum.* **1953**, *24* (8), 621–627
(292) Bauer et al 2-Sulfonylpyrimidines: Mild Alkylating Agents with Anticancer Activity toward P53-Compromised Cells *Proc. Natl. Acad. Sci.* **2016**, *113* (36), 5271–5280
(293) Förster et al 2-Sulfonylpyrimidines Target the Kinesin HSET via Cysteine Alkylation *Eur. J. Org. Chem.* **2019**, *2019* (31–32), 5486–5496
(294) Lyu et al Characterization of Lead Compounds Targeting the Selenoprotein Thioredoxin Glutathione Reductase for Treatment of Schistosomiasis *ACS Infect. Dis.* **2020**, *6* (3), 393–405

(295) Li et al Discovery of Highly Potent 2-Sulfonyl-Pyrimidinyl Derivatives for Apoptosis Inhibition and Ischemia Treatment *ACS Med. Chem. Lett.* **2017**, *8* (4), 407–412
(296) Gao et al Exploration of Multiple Sortase A Protein Conformations in Virtual Screening *Sci. Rep.* **2016**, *6*, 20413
(297) Suree et al Discovery and Structure–Activity Relationship Analysis of Staphylococcus Aureus Sortase A Inhibitors *Bioorg. Med. Chem.* **2009**, *17* (20), 7174–7185
(298) Chan et al NMR Structure-Based Optimization of Staphylococcus Aureus Sortase A Pyridazinone Inhibitors *Chem. Biol. Drug Des.* **2017**, *90* (3), 327–344
(299) Baell & Nissink Seven Year Itch: Pan-Assay Interference Compounds (PAINS) in 2017—Utility and Limitations *ACS Chem. Biol.* **2018**, *13* (1), 36–44
(300) Baell & Walters Chemistry: Chemical Con Artists Foil Drug Discovery *Nat. News* **2014**, *513* (7519), 481
(301) Gilberg et al X-Ray Structures of Target–Ligand Complexes Containing Compounds with Assay Interference Potential *J. Med. Chem.* **2018**, *61* (3), 1276–1284
(302) Valente et al The 1,4-Naphthoquinone Scaffold in the Design of Cysteine Protease Inhibitors *Bioorg. Med. Chem.* **2007**, *15* (15), 5340–5350
(303) Rohrbach et al Concerted Nucleophilic Aromatic Substitution Reactions *Angew. Chem. Int. Ed.* **2019**, *58* (46), 16368–16388
(304) Steert et al Dipeptidyl α-Fluorovinyl Michael Acceptors: Synthesis and Activity against Cysteine Proteases *Bioorg. Med. Chem. Lett.* **2007**, *17* (23), 6563–6566
(305) Rischer et al Biosynthesis, Synthesis, and Activities of Barnesin A, a NRPS-PKS Hybrid Produced by an Anaerobic Epsilonproteobacterium *ACS Chem. Biol.* **2018**, *13* (8), 1990–1995
(306) Stolz et al Sulfurospirillum Barnesii Sp Nov and Sulfurospirillum Arsenophilum Sp Nov , New Members of the Sulfurospirillum Clade of the ε-Proteobacteria *Int. J. Syst. Evol. Microbiol.* **1999**, *49* (3), 1177–1180
(307) Gao et al Theory and Applications of Differential Scanning Fluorimetry in Early-Stage Drug Discovery *Biophys. Rev.* **2020**, *12* (1), 85–104
(308) Niesen et al The Use of Differential Scanning Fluorimetry to Detect Ligand Interactions That Promote Protein Stability *Nat. Protoc.* **2007**, *2* (9), 2212–2221
(309) Pantoliano et al Microplate Thermal Shift Assay Apparatus for Ligand Development and Multi-Variable Protein Chemistry Optimization US6849458B2, February 1, 2005
(310) Keer Chapter 7:Quantitative Real-Time PCR Analysis In *Essentials of Nucleic Acid Analysis*; 2008; pp 132–166
(311) Hoeser et al Low Cost, Microcontroller Based Heating Device for Multi-Wavelength Differential Scanning Fluorimetry *Sci. Rep.* **2018**, *8* (1), 1457
(312) Lochner et al Untersuchungen Zur Meßgenauigkeit von Kolbenhubpipetten Mit Luftpolster *Lab. J. Lab. Med.* **2009**, *20* (7–8), 430–441
(313) Kong et al Automatic Liquid Handling for Life Science: A Critical Review of the Current State of the Art *J. Lab. Autom.* **2012**, *17* (3), 169–185
(314) Faiña et al EvoBot: An Open-Source, Modular, Liquid Handling Robot for Scientific Experiments *Appl. Sci.* **2020**, *10* (3), 814
(315) Eggert et al OpenWorkstation: A Modular Open-Source Technology for Automated in Vitro Workflows *HardwareX* **2020**, *8*, e00152
(316) Trueblood et al Atomic Dispacement Parameter Nomenclature Report of a Subcommittee on Atomic Displacement Parameter Nomenclature *Acta Crystallogr. A* **1996**, *52* (5), 770–781
(317) Tronrud Knowledge-Based B-Factor Restraints for the Refinement of Proteins *J. Appl. Crystallogr.* **1996**, *29* (2), 100–104
(318) Sun et al Utility of B-Factors in Protein Science: Interpreting Rigidity, Flexibility, and Internal Motion and Engineering Thermostability *Chem. Rev.* **2019**, *119* (3), 1626–1665
(319) Johnson et al Reviving B-Factors: Retrospective Normalized B-Factor Analysis of c-Ros Oncogene 1 Receptor Tyrosine Kinase and Anaplastic Lymphoma Kinase L1196M with Crizotinib and Lorlatinib *ACS Med. Chem. Lett.* **2018**, *9* (9), 878–883
(320) Barthels et al 2-Sulfonylpyrimidines as Privileged Warheads for the Development of S Aureus Sortase A Inhibitors *Front. Mol. Biosci.* **2022**, *8*, 1284
(321) Cascioferro et al Sortase A: An Ideal Target for Anti-Virulence Drug Development *Microb. Pathog.* **2014**, *77*, 105–112
(322) Jung et al Fluorovinylsulfones and -Sulfonates as Potent Covalent Reversible Inhibitors of the Trypanosomal Cysteine Protease Rhodesain: Structure–Activity Relationship, Inhibition Mechanism, Metabolism, and In Vivo Studies *J. Med. Chem.* **2021**, *64* (16), 12322–12358

8 Curriculum Vitae